

**Synthesis and characterization of new bioactive  
metal complexes with imine-based pincer  
ligands: Exploration of potential chemical and  
biological activities**

*Thesis*

*Submitted for the degree of*

**Doctor of Philosophy (Science)**

*by*

**BISWAJIT BERA**



**Department of Chemistry  
Jadavpur University, Kolkata - 700 032  
India**

**FEBRUARY-2024**

**Dr. T. K. Mondal, Ph. D.**  
**Professor**  
**Department of Chemistry**  
**Inorganic Chemistry Section**



**JADAVPUR UNIVERSITY**  
**Kolkata – 700 032, India**  
**Telephone: 91-033-2457-2970**  
**tapank.mondal@jadavpuruniversity.in**

**CERTIFICATE FROM THE SUPERVISOR(S)**

This is to certify that the thesis entitled “**Synthesis and characterization of new bioactive metal complexes with imine-based pincer ligands: Exploration of potential chemical and biological activities**” submitted by **Mr. Biswajit Bera**, M.Sc., who got his name registered on **27.07.2020** for the award of Ph.D. (Science) degree of Jadavpur University, is absolutely based upon his own work under the supervision of Dr. Tapan Kumar Mondal and that neither this thesis nor any part of it has been submitted for either any degree / diploma or any other academic award anywhere before.

16/02/2024

(Signature of the Supervisor(s) date with official seal

**Dr. TAPAN KUMAR MONDAL**  
Professor  
Department of Chemistry  
Jadavpur University  
Kolkata-700032

*“Fail early and fail first” and “be wrong as fast as you can”*

*~ Ed Catmull*

*Dedicated to*  
*My parents*



## ACKNOWLEDGEMENTS

My research journey, which began on July 2<sup>nd</sup>, 2018, has come to an end, having improved and matured both as a researcher and as a person. Throughout this journey, so many people had a profound influence on my way of thinking that either directly or indirectly benefited me. This is my chance to thank my supervisor, Dr. Tapan Kumar Mondal, Department of Chemistry at Jadavpur University in Kolkata - 700 032, for letting me work freely in his group. Without his unwavering support and inspiring direction during this journey, I could not have completed the work at hand. I am appreciative of him for following through on the thesis and for his insightful advice throughout my research journey.

I would like to sincerely thank all the faculty members of the Department of Chemistry at Jadavpur University, including Prof. Kajal Krishna Rajak, Head of the Department, Dr. Ashis Kumar Sarkar, Dean of Science at J.U, Prof. Partha Roy, Section-In-Charge, Inorganic Chemistry Section, and all other faculty members. I would want to thank all the teaching and non-teaching staff members at this department and university for their assistance in various aspects.

Financial assistance received from CSIR, New Delhi, India is gratefully acknowledged.

I would also like to thank all my lab colleagues, both former and present: Dr. Krishnendu Aich, Dr. Saswati Gharami, Dr. Puspendu Roy, Dr. Subrata Jana, Dr. Apurba Sau Mondal, Dr. Sujan Biswas, Dr. Samik Acharyya, Dr. Lakshman Patra, Dr. Rahul Naskar, Mr. Akash Das, Mr. Atanu Maji, Mr. Sandipan Mandal, Mr. Amitav Biswas, Mr. Subrata Mandal, Mr. Arpan Halder, Mr. Chandrasekhar Mandi, Miss Moumita Ghosh and Mr. Wasim Akram for their constant assistance and support during my research process. My research period's greatest asset will be the recollections I have of them. The mere fact that they were all there, made the journey much smoother and enthusiastic. My senior lab partner and hostel roommate, Dr. Krishnendu Aich (Krishnendu Da), sparked my interest in the synthesis of organic compounds and supported me with invaluable assistance during my research. I am very grateful to Dr. Lakshman Patra, Dr. Chandan Kumar Manna and Dr. Rahul Naskar as they showed me their guidance when I had no clue where and how to start.

I express my gratitude to my M.Sc. sir Dr. Nabakumar Bera, Jhargram Raj College, as the inspiration he gave for getting 'NET' qualified and initializing the spirit of research through me during my masters which led me to begin this journey. I really enjoyed my tenure of research because of the smooth working environment of my lab and for the supportive nature of my labmates. I am deeply thankful to Dr. Saswati Gharami, my senior labmate, for her priceless assistance in every single time when I needed. When we first met, she encouraged me to "do not take too much pressure about the degree," as I recalled, without her help and support, my research work would not have been successful enough. I am grateful to Mr. Subrata Mandal, who helped me gain various knowledge about the work and always entertain everyone in the Lab by creating friendly environment. Every single person in my lab has helped me a lot to grow gracefully and gave me enough encouragement to meet my goal which is to accomplish my Ph.D with ease. I will never forget the annual lab tours that I used to go with all of my lab mates, our guide, and his family. I will never forget those memories, and I was able to fully get to know them all because of those trips. Without this lab, my doctoral journey would not have been as successful and memorable.

I am deeply thankful to all those who became my friend while staying at university hostel. Without them in my everyday life, my research would not be fulfilled enough. I would also like to thank my friends Mr. Uttam Kumar Bera and Mr. Shantanu Samanta for their supports.

I am truly grateful to my closest friend Miss Moumita Maiti for her continued and unfailing love, support and understandings during my pursuit of Ph.D degree that made the completion of my thesis possible and also thankful to her family for their moral supports. Finally, I am very much indebted as well as lucky enough to have Mr. Haripada Bera and Mrs. Nilima Bera as my parents for their unconditional love, support, teachings and blessings which brought me this far without any pressure. I would also like to thank my younger brother Mr. Indrajit Bera who stand strong and tall with me in these past years. I express my sincere gratitude each and every one of the individuals listed above for their unwavering support, encouragement, and love, which gave me the fortitude and tenacity to effectively complete my journey.

*Biswajit Bera* 16.02.24  
(Biswajit Bera)

Department of Chemistry  
Jadavpur University

# CONTENTS

	<b>Page no.</b>
<b>PREFACE</b>	i – ii
<b>CHAPTER-I</b>	1 – 38
Introduction	
Synthesis and characterization of new bioactive metal complexes with imine-based pincer ligands: Exploration of potential chemical and biological activities	
<b>CHAPTER-II</b>	39 – 65
Palladium(II) and Platinum(II) complexes with ONN donor pincer ligand: Synthesis, characterization and <i>in vitro</i> cytotoxicity study	
<b>CHAPTER-III</b>	66 – 102
New palladium(II) and platinum(II) complexes with coumarin based O,N,N pincer: Synthesis, structure elucidation, BSA protein binding studies and anticancer activity	
<b>CHAPTER-IV</b>	103 – 167
Fabrication of thiosemicarbazone based Pd(II) complexes: Structural elucidations, catalytic activity towards Suzuki-Miyaura Coupling reaction, biomolecular interactions and antitumor activity against human TNBC cells (MDA-MB-231)	
<b>CHAPTER-V</b>	168 – 218
Synthesis of acetate bridged copper(II) 1D polymer containing morpholine based NNO donor Schiff base ligand: Exploration of potential catalytic and biological activity	
<b>CHAPTER-VI</b>	219 – 255
Heavy metal based binuclear luminescent complexes for selective and swift sensing of nitro-explosives in solution and solid phase	
<b>LIST OF PUBLICATION</b>	256

## PREFACE

The work embodied in my thesis entitled “*Synthesis and characterization of new bioactive metal complexes with imine-based pincer ligands: Exploration of potential chemical and biological activities*” was initiated on 2<sup>nd</sup> July 2018 to explore the synthesis of new metal complexes using different type of N O S donor imine-based base pincer ligands, and their spectral characterization and catalytic properties. In addition, biomolecular interaction and cytotoxicity properties of the metal complexes are investigated.

A review of the ligands containing N O S donor site and different complexes of palladium(II), platinum(II), copper(II) and some heavy metal has been described including their several catalytic activities specially towards C-C cross coupling reaction and also interaction with biomolecules with their anti-cancer activities in **Chapter I** along with the purpose of the present investigations.

**Chapter II** deals with the synthesis of Pd(II) and Pt(II) complexes with NNO donor pincer ligand. At the same time the X-ray structure of the complexes and computational study has also been performed. In addition, the cytotoxic activity of the two complexes is investigated against different cancerous cell lines.

**Chapter III** is on the synthesis and characterization of two new Pd(II) and Pt(II) complex with ONN donor Schiff base including their X-ray crystallography study and computational study. Furthermore, interaction of the two complexes with BSA protein and *in vitro* anti-cancer activity are performed.

**Chapter IV** deals with the fabrication of thiosemicarbazone ligands and their Pd(II) complexes. Structure of the complexes is confirmed by single crystal X-ray diffraction method. Electronic structure of the complex is interpreted by DFT computations. Catalysis study of the complexes is explored towards Suzuki-Miyaura cross coupling reaction. Additionally, the interaction with the biomolecules (like CT DNA and BSA protein) and antitumor activity against human breast tumor cells is examined.

**Chapter V** describes the synthesis and characterization of an one dimensional copper(II) coordination polymer (CUPM) along with its structural elucidations. Catecholase activity is performed in acetonitrile medium along with its interaction with the DNA and BSA



protein molecules. Furthermore, Cytotoxic nature of the complex has also been carried out in cancer cell lines.

**Chapter VI** contains synthesis and spectral characterization of three heavy metal based binuclear luminescent complexes  $[M_2(HL)_2Cl_4]$ ;  $M = Zn, Cd$  and  $Hg$ ]. The complexes are employed for the selective detection of explosive nitro-aromatic compounds especially 2,4,6-trinitrophenol (TNP) in solution phase as well as in solid phase.

In brief, this thesis accounts the chemistry of different metals with the imine-based pincer ligands of phenol and thiosemicarbazide derivatives. I am happy to note that the work has been published in international journals (**List of Publications**).

When the work is stated to be based on the findings of other researchers, appropriate acknowledgment has been made in accordance with the standard procedure for reporting scientific observations. I undertake full responsibility for any inadvertent missteps or mistakes that may have occurred despite taking the necessary safety measures.

Biswajit Bera  
(Biswajit Bera) 16.02.24

Department of Chemistry  
Jadavpur University

## CHAPTER - I

# INTRODUCTION

---

*Synthesis and characterization of new bioactive metal complexes with imine-based pincer ligands: Exploration of potential chemical and biological activities*

---

## 2 | Chapter I

---

### I.1. General Introduction

A substantial corpus of inorganic chemistry research is included in coordination chemistry. The primary focus of this field has captivated and motivated researchers worldwide: the chemistry of metal complexes. Awareness of the metal complexes of organic chelating ligands is growing in academia, industry, and biology. Since they may control the reactivity of a metal center and identify the reactive sites that are available, ligands that bind to transition metal ions in a predictable manner are crucial to modern coordination chemistry. In coordination chemistry, ligands in particular, Schiff base ligands are still crucial. Since they are synthetically flexible, selective and sensitive to the central metal atom, and structurally comparable to naturally occurring biological molecules, Schiff bases are an important class of ligands. Significant anticancer, antifungal, and diuretic properties have been reported for research in this area. The food, dye, analytical chemistry, catalysis, fungicidal, agrochemical, and biological industries all make extensive use of Schiff bases.<sup>1-8</sup> It is also possible to envision a number of catalytic organic transformations in which the ligands regulate the chemical processes.<sup>9,10</sup>

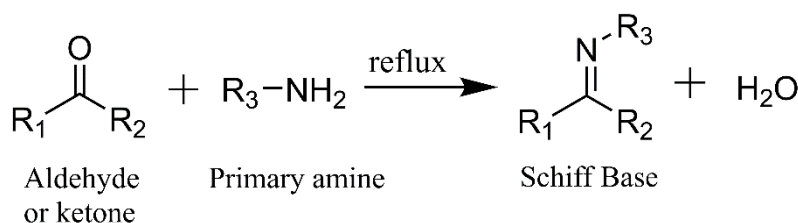
Palladium and platinum were the transition metals that piqued our interest because of their remarkable molecular and electronic structures, redox characteristics, and diverse biological activities that highlight the close relationship between inorganic chemistry and biology.<sup>11-14</sup> Additionally, their utility in a range of homogeneous catalytic applications and analytical applications is noteworthy.<sup>15-17</sup> In addition to catalysis, metal complexes have intriguing uses in a number of other domains, including biology and medicine. The use of inorganic substances in medicine dates back to Hippocrates' day. He suggested using metallic salts medicinally. Metal complexes have been applied in medicine and diagnosis. Some of the most active research areas in bio-inorganic chemistry right now include studies on metal-based anticancer medications and arthritis agents. Numerous metal complexes based on palladium and platinum, particularly those involving Schiff bases, have been investigated with the goal of employing them as antimicrobial and anticancer medications. Moreover, numerous research groups have been occupied with the precise design and fabrication of metal complex chemosensors for the distinct recognition of toxic organic analytes and explosive compounds due to their major impact on environment as well as on human life. This chapter presents an overview of Schiff bases, their metal complexes, and their general applications.



## 3 | Chapter I

### I.2. Schiff base ligands

Hugo Schiff, a German chemist, created a new class of organic compounds in 1864. These compound groups, called imines, bear his name. Schiff bases are usually formed by condensation of an aldehyde or ketone and a primary amine (Scheme I.1). Schiff base ligands are referred to as "privileged ligands" because they contain an azomethine group ( $-\text{HC}=\text{N}-$ ),<sup>18</sup> which is particularly useful for binding to metal ions through the N atom lone pair. When the Schiff bases contain one or more donor atoms in addition to the  $-\text{HC}=\text{N}-$  group, they function as polydentate chelating ligands or macrocycles. Both aldehydes and ketones form Schiff bases, but the formation of ketone is less common than that of aldehyde. Even now, a huge variety of complexes with intriguing structures are being synthesized due to the Schiff bases' flexibility. While Schiff bases formed from aromatic aldehydes are more stable, those derived from aliphatic aldehydes are unstable and easily polymerize.<sup>19</sup> The typical Schiff bases are weakly basic and crystalline. Schiff bases are often produced using heat, acid or base catalysis, or both. Schiff bases are widely employed in a variety of domains, including drug synthesis, inorganic chemistry, biology, and analysis. The intriguing and significant characteristics of a wide variety of Schiff bases and their complexes, such as catalytic activity and amino group transfer,<sup>20</sup> photochromic behavior,<sup>21</sup> and the capacity to form complexes with specific hazardous metals,<sup>22</sup> have been investigated. Certain Schiff bases are used in spectrofluorimetric monitoring of minute pH changes as fluorescent indicators.<sup>23</sup>



Scheme I.1. Simple formation of Schiff base ligand

### I.3. Metal complexes of Schiff base ligands

The evolution of coordination chemistry has been significantly influenced by Schiff bases. The performance of metals in a wide range of beneficial catalytic transformations can really be controlled by Schiff bases, which could stabilize a wide variety of metals in varied oxidation states. Because of Schiff base metal complexes' appealing chemical and physical

## 4 | Chapter I

---

characteristics and their many uses in organic synthesis,<sup>24</sup> liquid crystals,<sup>25</sup> molecular switches in logic or memory circuits,<sup>26</sup> UV stabilizers,<sup>27</sup> laser dyes,<sup>28</sup> and other applications, a great deal of research has been done on them. These versatile classes of ligands can be made into a combinatorial library of ligands based on their size and charge.<sup>29</sup> As homogenous catalysts for a variety of reactions, Schiff base complexes of numerous transition metal ion complexes have been found. These complexes have demonstrated remarkable homogeneity, repeatability, selectivity, and high activity to catalyze reactions under mild circumstances. Additionally, the construction of supramolecular architecture, such as coordination polymers, double helices, and triple helicates, has shown that Schiff base ligands are highly helpful.<sup>30</sup> Distinct metal centers involving distinct coordination modes can be accommodated by Schiff base ligands, enabling the effective synthesis of homo- and heterometallic complexes with a variety of stereochemical configurations.<sup>31,32</sup> The modelling of active sites in biological systems makes use of this property. The oxygen and nitrogen donor Schiff bases in transition metal complexes are particularly interesting due to their unique topologies, structural lability, and sensitivity to molecular environments.<sup>33,34</sup> Significant biological functions of Schiff base complexes include photosynthesis and oxygen transport in mammalian and other respiratory systems.<sup>35</sup> It has also been demonstrated that Schiff bases are essential to bacteriorhodopsin's biological activity.<sup>36</sup> A protonated Schiff base forms a covalent bond between the protein and the retinal chromophore.<sup>37</sup> Furthermore, the dioxygen absorption and oxidative catalysis of Schiff base complexes have been investigated.<sup>38-40</sup> It is possible to adjust the steric and electronic effects surrounding the metal core by carefully choosing the bulky, electron-donating, or electron-withdrawing substituents that are added to the Schiff bases. The chelated Schiff bases' two donor atoms, O and N, have opposing electronic effects. Hard donors like phenolate oxygen are known to stabilize the metal atom's higher oxidation state, whereas soft donors like imine nitrogen stabilize the metal's lower oxidation state.<sup>41</sup> Palladium (II) complexes are known for their exceptional stability, which is mostly due to the presence of ligands in the coordination sphere that contain donor atoms like N, P, S, or O. The literature covers a wide range of practical aspects related to the synthesis of Schiff base metal complexes.

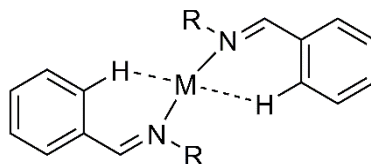
### I.4. Diverse bonding modes of Schiff base ligands

The Schiff bases co-ordinate to the metal ion as:

## 5 | Chapter I

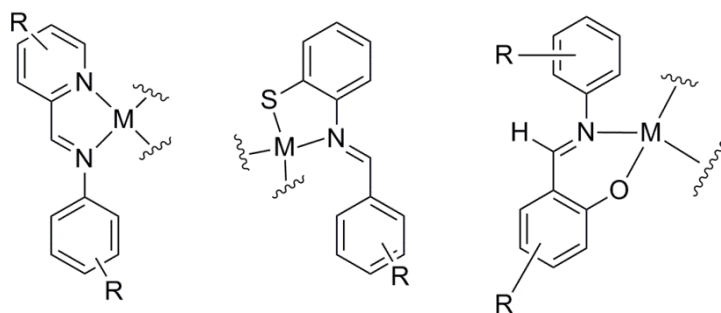
### (i) Monodentate

To coordinate the imino nitrogen atom to a metal ion and create stable complexes, the C=N group's fundamental strength is insufficient. Therefore, the metal-nitrogen bond should be stabilized by the creation of chelate rings when at least one additional donor atom is present and appropriately close to the nitrogen atom.



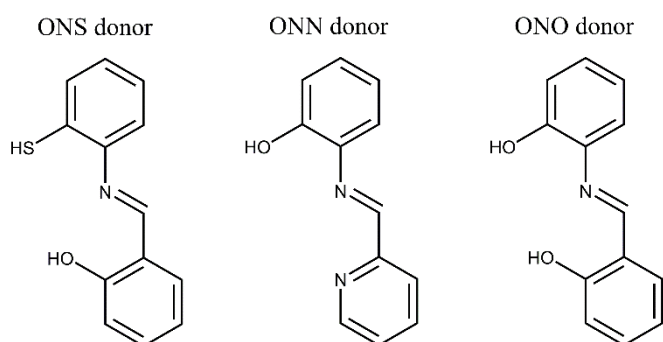
### (ii) Bidentate

The Schiff bases can coordinate to the metal ion through N, O or S donor atom as follows:



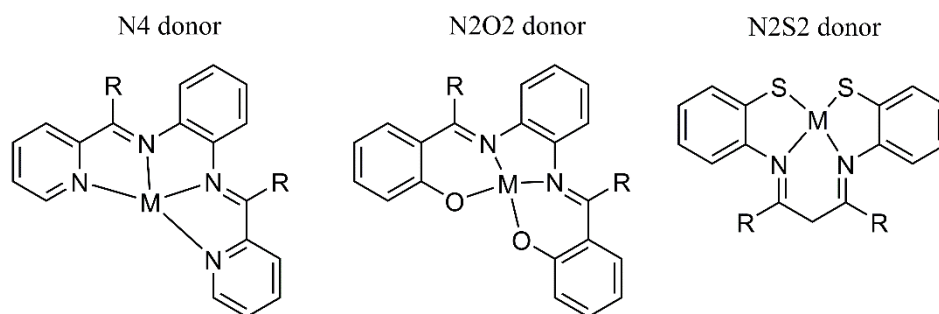
### (iii) Tridentate

Many tridentate Schiff bases have been utilized as anionic ligands with different donor sets.



### (iv) Tetradentate

Schiff bases coordinating to the metal as N<sub>4</sub>, N<sub>2</sub>S<sub>2</sub>, N<sub>2</sub>O<sub>2</sub> donor sets have been widely studied for their ability to coordinate metal ions.



### I.5. Polydentate ligands

From the outset, efforts have been made in academic, industrial, and pharmaceutical laboratories to synthesize novel and inventive ligand complexes for a variety of uses. One of the many significant functions that the ligands that form complexes with transition metal ions can play is controlling the metals, coordination number, coordination shape, and formal oxidation state.<sup>42</sup> The increased stability of metal-ligand complexes that these species provide to the metal site to which they are coupled has sparked interest in the production of polydentate ligand. The resulting metal-chelate complexes exhibit a greater degree of stability towards the circumstances than are seen when using equivalent monodentate ligands.<sup>43,44</sup> Due to the wide range of potential coordination environments that the metal center offers, there is great interest in the synthesis of unsymmetrical polydentate ligands that comprise many electrically distinct donor sites.<sup>45</sup> When a ligand possesses both soft and hard donor moieties, it can partially dissociate, creating an empty coordination site at the metal that is "masked" in the ground state.<sup>46</sup> This could result in some unusual behavior. Because the ligand remains in the metal's coordination sphere during the catalytic cycles, this phenomenon holds enormous promise for utilization in catalytic applications.

It is possible to responsively control the coordination at a particular metal centre by varying the ligand's structure and the type of its donor sites. Thus, a substantial effect on the reactivity of the metal complexes should result from the existence of electrically distinct donor pieces inside the same metal scaffold. It is anticipated that soft late transition metals will bind more strongly to softer, more polarizable donor moieties based on Pearson's "hard-soft-acid-base" (HSAB) theorem, and that harder, less polarizable donor segments will preferentially attach to the earlier metals.<sup>47</sup> For this reason, it is preferable to incorporate several electronically distinct donors into a single ligand framework, for example, a variety of softer donors like phosphines and thiols to contrast with more rigid oxygen and amine donors. The *trans* effects of different donor atoms can potentially be utilized in the resulting

complexes by incorporating them. Specifically, organo-chalcogen ligands tend to exhibit greater *trans* influences than nitrogen donors, which in turn exhibit smaller *trans* influences than tertiary phosphines.<sup>48-50</sup> Most notably, the systematic change of the donor functionality results in a family of closely related ligands, which makes it possible to thoroughly examine the complete coordination capabilities of the resulting multidentate ligand family using metal centers.

### I.6. Nitrogen donor ligands

Since the early 19th century, the Classical or Werner's complexes where the metal bonds to a heteroatom have been understood. Some of the most basic ligands and metal-ligand linkages are found in these complexes. These kinds of complexes were the starting point for coordination chemistry study. Organometallic chemistry does not use amine ligands as often as coordination chemistry, despite coordination chemistry having researched them extensively. This is due to two main factors: first, amines favour class A metals, whereas most organometallic chemistry concentrates on class B metals, which often coordinate only weakly; second, the N-H bond of the coordinated amine tends to be particularly reactive. In organometallic chemistry, amines are typically found in conjunction with borderline metals, where there is less of a hard/soft mismatch. Because of the chelate effect, polydentate ligands like ethylenediamine can be used to replace monodentate amines in order to improve the coordination.<sup>51</sup>

There are many different types of nitrogen donor ligands, ranging from simple amines like the previously described ethylenediamine to pyridine ligands like phenanthroline (phen) and 2,2'-bipyridine (bipy), oxazolines, porphyrins, and imines. Because they are softer than amines, ligands based on pyridine, imine, and oxazoline are more frequently found in organometallic chemistry.<sup>52,53</sup> Many times, the ligands are multidentate, containing oxygen and phosphorus among other heteroatoms. The salens are a well-known class of N, O donor ligands that have been applied to coordination chemistry as well as catalysis. Chiral amines can be used to create chiral salens that are appropriate for asymmetric catalysis, such as the Jacobsen epoxidation.<sup>54</sup>

### I.7. Oxygen or Sulphur containing ligands

The literature is replete with examples of ligands based on sulphur and oxygen as well as a wide range of applications for them. In contrast, the harder oxygen donors, specifically those found in oxo-ethers, exhibit greater interactions with s-block and the earlier metals; crown

ethers are likely the greatest example of these donor ligands. An intriguing area of coordination chemistry is the synthesis of ligands with thioether donor centers in chelated environments with extra N and O donors in acyclic/macrocyclic backbones to create reliable working models that take into account the function of metal ions in biological systems. Numerous research teams are attempting to synthesize various ligands with N and S donor sites in order to investigate the function of metal ions in biological systems and remove ecologically hazardous heavy metal ions from everyday products. Numerous  $N_xS_y$  donor ligands have been developed, in which N is a member of aromatic nitrogenous systems such as pyridine, imidazole, benzimidazole, and so on. The reactivity of these ligands has been examined using various transition and non-transition metals.<sup>55-62</sup> The synthesis of chemical analogues of metalloproteins' active sites has attracted a lot of study interest, and some of the bioactive compounds have N and S donor centers. In coordination chemistry, it is crucial to synthesize ligands with thioether donor centers in chelated environments with extra N and O donors on acyclic/macrocyclic platforms in order to create effective working models.<sup>63-65</sup> Regarding their capacity to donate soft or hard tissues, their excited state and photophysical characteristics, the production of anticancer platinum medicines with lower nephrotoxicity, etc. Various scientific fields are showing interest in  $N_xS_y$  systems.

### I.8. Phosphorus donor ligands

Because phosphorus has a lone pair that can be supplied to the metal, phosphones are thought of as  $\sigma$ -donors. When electron-donating substituents on R are used to raise the electron density on phosphorus, the strength of  $\sigma$ -donation increases. They can also function as  $\pi$ -acceptors, also called  $\pi$ -acids, in which case the acceptor is the  $\sigma^*$ -orbital of the P-R bonds (Figure I.1). The weakest  $\pi$ -acceptors are alkyl phosphines, which are followed by aryl phosphines and phosphites while  $PF_3$  is comparable to CO.<sup>66</sup>  $\pi$ -back donation is favoured by substituents on R that remove electrons. While separating the  $\pi$ -acceptor and  $\sigma$ -donor characteristics of phosphine through experimental means is challenging, there are a variety of computational techniques that can be used.<sup>67</sup> These findings confirm that phosphines are both  $\pi$ -acceptors and  $\sigma$ -donors,  $\pi$ -bonding results from the donation of electron density from the metal into an empty orbital of the ligand that exhibits phosphorus 3p character, whereas  $\sigma$ -bonding largely originates from the lone pair of phosphorus.

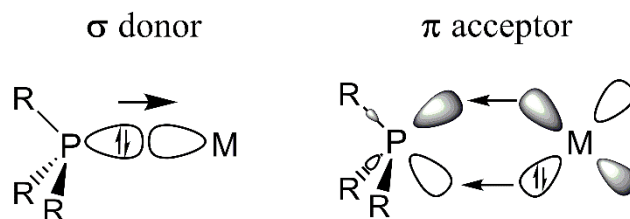


Figure I.1. Phosphines as  $\sigma$ -donor and  $\pi$ -acceptor

Triethylphosphine platinum trichloride, the first phosphorus-metal compound, was initially reported by Hofmann in 1857.<sup>68</sup> Since then, phosphines ( $\text{PR}_3$ ) have established themselves as a conventional and adaptable ligand class for transition metal complex. By changing R (R = aryl, alkyl), the steric and electrical characteristics of  $\text{PR}_3$  can be changed in a methodical and predictable way, providing access to a variety of ligand reactivity profiles.<sup>69,70</sup>

## I.9. Heavy metals

“Heavy metals” are natural elements characterized by their relatively high atomic mass and their high density. Although typically occurring in rather low concentration, they can be found all through the crust of our planet. Commonly, a density of at least  $5 \text{ g cm}^{-3}$  is used to define a heavy metal and to differentiate it from other, “light” metals. Other, broader definitions for “heavy metals” require an atomic mass higher than 23 or an atomic number exceeding 20. Heavy metals enter our bodies through food, water, or air. Consumption of very high concentrations of heavy metals can lead to toxicity and associated health problems. Heavy metals enter wastewater mainly from industrial, agricultural, or other human activities.<sup>71,72</sup> Many of these metals are toxic to humans even at very trace levels. Others cause serious health hazards to humans and living organisms. Therefore, heavy metal removal has become a critical goal in many wastewater treatment facilities. This led to the development of several methods for removing pollution caused by heavy metals. Essential heavy metals are those required by living organisms for carrying out the fundamental processes like growth, metabolism, and development of different organs. There are numerous essential heavy metals like Cu, Fe, Mn, Co, Zn, and Ni required by plants as they form cofactors that are structurally and functionally vital for enzymes and other proteins. Among them, Zn(II) ions are very much important for the human body.<sup>73,74</sup> They are involved in a range of biological processes whereas Cd(II) and Hg(II) are extremely toxic and carcinogenic metals.<sup>75,76</sup> Cadmium is chiefly found in electroplated steel, electric batteries, pigments



in plastics and their exposure can cause enhanced risks of cardiovascular diseases, cancer mortality and damage to liver and kidneys.<sup>76,77</sup> Mercury can be found from many sources such as gold production, coal plants, thermometers, barometers, caustic soda, and mercury lamps and it can contaminate air, water and soil.<sup>78,79</sup> [10] It also causes severe damage to the central nervous system, Minamata disease etc.<sup>80</sup> Commonly, Schiff base complex of soft metal ions, like Zn(II), Cd(II) and Hg(II), are utilized for optoelectronic devices, owing to their brilliant photoluminescence properties.<sup>81,82</sup> This characteristic property can be used to recognize them because the presence of the  $d^{10}$  electronic configuration hinders the application of the analytical techniques such as Mössbauer, EPR spectroscopy and magnetic susceptibility measurements. But fluorescence spectroscopy can be efficiently used as these metal ions effortlessly modify the fluorescence intensity of organic fluorophore.<sup>83</sup> Therefore fluorescence spectroscopy is most leading tool to recognize these metal ions.<sup>84</sup> Copper is used alongside iron to form red blood cells. It helps to maintain healthy bones, nerves, and immune function. Copper nutritional deficiencies are associated with high cholesterol and high blood pressure. Significant attention has been provided to copper-based therapeutics as alternatives since copper is a fundamental growth factor of organisms as a noteworthy constituent of the active site of many metalloproteins such as hemocyanin, catecholase and tyrosinase.<sup>85-87</sup> Various Cu(II) complexes have also been reported to hinder tumor growth in animal models and their relevant nature with biological research areas can help diminish the side effects.<sup>88</sup> Thus, copper complexes have turned into a new cancer chemotherapeutic agent, but their indisputable anticancer mechanism has not yet been established.

### I.10. Palladium

Palladium, denoted by the symbol Pd and having an atomic number of 46, is a rare chemical element that falls within the 10<sup>th</sup> and 5<sup>th</sup> periods of the current periodic table. William Hyde Wollaston found the brilliant silvery-white palladium metal in 1803. After the Greek goddess of wisdom "pallas," he had given it the name palladium. Approximately 50% of the palladium and its congener platinum supply is utilized in catalytic converters, which change up to 90% of the toxic chemicals found in car exhaust (nitrogen dioxide, carbon monoxide, and hydrocarbons) into less harmful forms (nitrogen, carbon dioxide, and water vapour). Palladium has the oxidation states of 0, +1, +2, +4, and +6. The stable oxidation states that are most prevalent are +2, +4, and 0. There are seven isotopes of palladium that exist naturally; six of them are stable and are known as <sup>102</sup>Pd, <sup>104</sup>Pd, <sup>105</sup>Pd, <sup>106</sup>Pd, <sup>108</sup>Pd, and <sup>110</sup>Pd. With an abundance of 27.33%, <sup>106</sup>Pd is the most stable isotope.

Palladium complexes have found extensive application in catalytic processes involving a range of environments that include the formation of carbon-carbon bonds, such as carbon-hetero atom interactions, carbonylations, and allylic-alkylations. Scheme I.2 provides a comprehensive overview of some of the most useful catalysts. Chloropalladic acid (**1**) solution is formed when palladium metal is submerged in a concentrated hydrochloric acid solution in the presence of chlorine environment. Following the evaporation of this reddish-brown solution, palladium (II) chloride (**2**) is produced as a brown polymeric solid.<sup>89</sup> It is used as a carbonylation catalyst (Wacker-Hoechst process) in the large-scale chemical production industry to convert ethylene to acetaldehyde, produce acetone from propene, and create glycol derivatives.<sup>90-93</sup> An orange-yellow crystalline solid is produced by the reaction of **2** in acetonitrile solution under refluxing conditions to generate dichlorobis(acetonitrile)palladium(II) (**3**). It is employed as a hydro carboxylation catalyst and in a number of cross-coupling processes, including Heck, Negishi, and Grignard.<sup>94-99</sup> By reacting (**3**) with the bis(diphenylphosphino)ferrocene in dichloromethane, the dichloro(bis(diphenylphosphino)ferrocene)palladium(II) dichloromethane (**4**) complex is created. It is employed as a catalyst in the Buchwald-Hartwig, Stille, and Grignard coupling processes.<sup>100-103</sup> By reacting triphenylphosphine with ethanol at 60°C, dichlorobis(triphenylphosphine)palladium(II), (**5**) produces a light yellow crystalline powder in an almost quantifiable yield.<sup>104,105</sup> It is employed as a carbonylation catalyst to produce specific lactones as well as a catalyst in the Sonogashira coupling of terminal alkynes with aryl halides.<sup>106,107</sup> Tris(dibenzylideneacetone)dipalladium(0) (**6**) was generated by the reaction of (**2**) with dibenzylideneacetone and sodium acetate in methanol at 60°C. As a catalyst, it is highly useful in a wide range of carbon-carbon and carbon-heteroatom coupling processes. In order to form biphenyls through the Suzuki coupling of aryl chlorides with an Arduengo imidazolium salt, it is also employed in specialized catalysis. By reacting (**6**) with tri-tert-butylphosphene in dimethylformamide solution, two sterically hindered phosphines (P<sup>t</sup>Bu<sub>3</sub>) are produced, which are linearly coordinated to the palladium metal in the center of another significant complex, bis(tri-tert-butylphosphine)palladium(0), (**7**). The Negishi cross coupling of aryl and vinyl chlorides is carried out by means of this zero valent complex catalyst.<sup>108-110</sup> The reaction of palladium powder dissolved in acetic acid in the presence of nitric acid under refluxing conditions yields the palladium(II) acetate salt, (**8**). It is used as a catalyst to help butadiene undergo telomerization, forming substituted 1,6- and 1,7-dienes.<sup>111</sup> The reaction of (**1**) with 1,5-COD in ethanol yields the dichloro(1,5-

cyclooctadiene)palladium(II) (**9**) complex, which is employed in a number of organometallic coupling processes as well as a catalyst to preserve hydroxyl groups.<sup>112</sup> In addition to its fascinating use in catalysing [3,3] sigmatropic rearrangements, the tetrakis(triphenylphosphine)-palladium(0) (**10**) is employed in catalysis for coupling reactions, especially the Sonogashira process.<sup>113</sup> By reacting (**2**) with allyl chloride in methanol solvent in the presence of carbon monoxide, the significant catalyst  $\pi$ -allylpalladium(II), (**11**) was generated. It is widely used in asymmetric alkylation, where the generation of a quaternary center by azolactone alkylation has been replaced by a novel method that is employed in the synthesis of sphingosines, an antifungal drug.<sup>114-116</sup>

stability in the presence of heat, oxygen, and water, and how simple it is to handle and separate the reaction mixtures' boron-containing byproducts.<sup>119</sup> Furthermore, compared to other organometallic reagents, boron-containing byproducts are easier to handle and remove, particularly during large-scale synthesis. Beller,<sup>120</sup> Buchwald,<sup>121</sup> Genet,<sup>122</sup> Leadbeater,<sup>123</sup> Miyaura,<sup>124</sup> Plenio,<sup>125</sup> and Shaughnessy<sup>126</sup> all made significant contributions to this discipline. In general, the exceptional complexation capacity of pyridoxal hydrazone-based ligands towards transition metals and the potential for analytical applications made the coordination chemistry of these ligands highly intriguing. Depending on the pH, these chelating ligands can exist in two distinct deprotonated forms, such as neutral and anionic. Tridentate is the most common coordination mode, which is attained by the oxygen atoms of carbonyl, phenolic, and hydrazine nitrogen.<sup>127</sup> Hydrazone metal complexes have demonstrated potential uses as molecular sensors,<sup>128</sup> luminous probes,<sup>129</sup> and catalysts.<sup>130</sup> The importance of the SMC reaction in organic synthesis over the past few decades is evident from the availability of multiple articles in the literature. As a result, a wealth of material on the topic exists, including several excellent reviews.<sup>131</sup> The catalytically active palladium complexes with thiosemicarbazone ligands were reported by D. Pandiarajan *et al.*<sup>132</sup> Palladium complexes with Schiff base ligands comprising S or Se have been reported by B. R. Steele *et al.* to be effective catalysts for the Suzuki–Miyaura Cross-Coupling Reaction.<sup>133</sup> M. J. Jin *et al.* have created the ( $\beta$ -Oxoiminato) (phosphanyl) palladium complexes as extremely active catalysts in Suzuki–Miyaura coupling processes.<sup>134</sup> Additionally, for the Suzuki–Miyaura reaction, the Pd(II)-Schiff base complex supported by a mesoporous matrix has been reported.<sup>135</sup> The Suzuki–Miyaura reaction was created by P. Liu *et al.* using palladium(II) complexes that catalyze bis(imino)pyridine.<sup>136</sup> Since then, many groups have documented noteworthy advancements in the field of palladium-mediated S-M reactions; however, the development of the Suzuki–Miyaura coupling reaction catalysed by palladium complexes remains a major issue for chemists.

Because palladium(II) chelates allow the metal to engage directly with the target deoxyribonucleic acid (DNA) molecule, they are more potent anticancer medicines than other metal chelates, including platinum (Das and Livingstone 1978). Pd(II) ions easily combine with other macromolecules such as vitamin B6 as well as proteins, DNA, and amino acids (Rîmbu *et al.* 2014). When looking for medicinal metals, palladium(II) is the metal of choice due to its structural stability and liability. Moreover, it has been demonstrated that

compounds containing palladium are not carcinogenic; as a result, they can be safely used in medicinal applications (Melber 2002).

### **I.11. Theoretical calculations**

#### **Basic ideas behind DFT**

A strong tool for calculating the quantum states of atoms, molecules, and solids as well as molecular dynamics is density functional theory, or DFT. With regard to the atomic-level simulation of condensed matter phases, electronic structure of matter-wave functions with density functional and quantum chemical systems, it has firmly established itself as the workhorse.<sup>137</sup> The advent of density functional theory approaches has substantially helped the theoretical description of charge distribution and related features, such as chemical reactivity descriptors of chemical compounds.<sup>138</sup> But during the past ten years, DFT has made it possible for theoretical chemistry to precisely forecast the energetics and structures of molecules and clusters. As a result, these reactivity descriptors that are derived straight from DFT calculations now require further consideration.

#### **Significance of Density Functional Theory (DFT)**

- The density functional theory (DFT) is presently the most successful (and also the most promising) approach to compute the electronic structure of matter and chemical reactivity.
- Its applicability ranges from atoms, molecules and solids to nuclei and quantum and classical fluids.
- In its original formulation, the density functional theory provides the ground state properties of a system, and the electron density plays a key role.
- DFT predicts a great variety of molecular properties: molecular structures, vibrational frequencies, atomization energies, ionization energies, electric and magnetic properties, reaction paths, etc.
- Extremistic electrons, spin polarized systems, multicomponent systems like nuclei and electron hole droplets, free energy, superconductors with electronic pairing mechanisms, time-dependent phenomena and excited states, bosons, molecular dynamics, etc. are all situations that the original density functional theory can handle.

#### **General Application Density Functional Theory (DFT)**

1. Total molecular energy calculation and study of tautomerisation
2. Molecular Geometry optimization and to assign electronic structure

3. Frequency calculation is done for vibrational mode and thermochemical analysis
4. Spin density calculation and to explain EPR, magnetic and redox properties
5. IRC (Intrinsic reaction coordinate) is done to follow the reaction path ways
6. Scanning of potential energy surface.
7. Potential energy surface
8. To test the stability of wave functions
9. Predicting and interpreting of other molecular properties and some common spectra

### **Time-dependent density function theory (TDDFT)**

#### **Outline**

A quantum mechanical theory called time-dependent density functional theory is applied in physics and chemistry to study the dynamics and characteristics of many-body systems when time-dependent potentials like electric or magnetic fields are present. TDDFT can be used to study the impact of such fields on molecules and solids in order to extract attributes such as photo-absorption spectra, excitation energies, and frequency-dependent response characteristics.

The Runge-Gross (RG) theorem (1984), the time-dependent equivalent of the Hohenberg-Kohn (HK) theorem (1964), serves as the formal basis for Time-dependent density function theory (TDDFT).<sup>139,140</sup> The RG theorem demonstrates that there is a unique mapping between a system's time-dependent density and its time-dependent external potential for a given starting wave function. This suggests that the density, which depends only on three factors, is equal to the many-body wave function, which depends on three variables. As a result, all system features may be ascertained just by understanding the density. Time-dependent quantum mechanics does not have a general minimization principle, in contrast to DFT. As a result, the RG theorem requires more work to prove than the HK theorem.

Finding the imaginary non-interacting system with the same density as the physical (interacting) system of interest. also known as the (time-dependent) Kohn-Sham system, is the next step towards creating a computationally feasible method, given the RG theorem. This system is formally found as the stationary point of an action functional defined in the Keldysh formalism.<sup>141</sup>

The calculation of excited state energies in isolated systems and, less frequently, solids is the most widely used application of TDDFT. These computations are predicated on the observation that a system's exact excitation energies have poles in the linear response function, which describes how the electron density varies in response to changes in the

external potential. The exchange-correlation kernel, which is the functional derivative of the exchange-correlation potential with respect to the density, is also needed for these computations in addition to the exchange-correlation potential.<sup>142,143</sup>

### Utility of Time-dependent density functional theory

Time-dependent density functional theory TDDFT is an extension of density functional theory (DFT), and the conceptual and computational foundations are analogous - to show that the (time-dependent) wave function is equivalent to the (time-dependent) electronic density, and then to derive the effective potential of a fictitious non-interacting system which returns the same density as any given interacting system. Building such a system is more difficult using TDDFT, primarily because the time-dependent effective potential at any given moment depends on the density value at all earlier times. As a result, the development of time-dependent approximations for TDDFT implementation is progressing more slowly than DFT.

### Basis set

In theoretical and computational chemistry, a basis set is a collection of functions, also referred to as basis functions, that are coupled in a linear fashion to produce molecular orbitals, usually as a component of a quantum chemical calculation.<sup>144-146</sup> Quantum chemical computations in contemporary computational chemistry are usually carried out with a limited number of fundamental functions. In these situations, the system's wave functions are shown as vectors, each of whose components is a coefficient in a linear combination of the fundamental functions in the basis set that was employed.

### Popular Software

- Gaussian Software Package (chemistry, Hartree-Fock, correlated approaches. current version: Gaussian09)
- Amsterdam Density Functional (ADF)
- Gamess-UK (chemistry, Hartree-Fock, DFT, correlated approaches)
- VASP (DFT, planewave, ultrasoft, PAW)
- ORCA
- Jaguar
- Turbomole
- Spartan



### I.12. Physical measurements

- (i) **Elemental analysis:** Microanalytical data (C, H, N) were collected on a Series–II CHN-2400 CHNS/O elemental analyzer, Perkin Elmer, USA using the pure solid sample.
- (ii) **Conductance measurements:** The solution electrical conductivity were measured using Systronics conductivity meter (Model 304) using a solution concentration of ca.  $10^{-3}$  M in acetonitrile.
- (iii) **FTIR spectra:** FTIR spectra were obtained on a Perkin Elmer; model RX–1 (KBr disk,  $4000\text{--}400\text{ cm}^{-1}$ ) spectrometer with samples prepared as KBr pellets.
- (iv) **UV-VIS spectra:** Absorption spectra were studied on a Perkin Elmer, Lambda 750 spectrophotometer using the solution of required concentration in acetonitrile. Solution will be kept in a quartz cell and absorption spectra will be recorded starting from visible to UV region.
- (v)  **$^1\text{H}$  NMR spectra:**  $^1\text{H}$  NMR spectra were recorded by Bruker (AC) 300 MHz FTNMR spectrometer.
- (vi) **Single crystal X-ray diffraction study:** Attempts were taken to obtain single crystals of the compounds by slow evaporation of solvent from solutions, or from the diffusion of another solvent into a solution of the compounds. Data were collected with an automated Bruker AXS Kappa equipped with an Apex-II CCD diffractometer with area detector using a graphite monochromated Mo-K $\alpha$  radiation ( $\lambda = 0.71073\text{ \AA}$ ). X-ray data reduction, structure solution and refinement will be done by using SHELXS-97 and SHELXL-97 programs. The structures were solved by direct method.
- (vii) **Mass Spectroscopic study:** ESI mass spectra were recorded on a micro mass Q-OF mass spectrometer.
- (viii) **Emission Measurements:** Emission properties were measured using Shimadzu RF-6000 spectro-fluorophotometer at room temperature (298 K).
- (ix) **Fluorescence Lifetime:** Fluorescence lifetimes were measured using a time-resolved spectrofluorometer from IBH, UK. The instrument uses a picoseconds diode laser (NanoLed-07, 370 nm) as the excitation source and works on the principle of time-correlated single photon counting (TSPC). The instrument response's function is  $\sim 230\text{ ps}$  at FWHM. To eliminate depolarization effects on the fluorescence decays, measurements were done with magic angle geometry ( $54.7^\circ$ ) for the excitation and emission polarizers. The decays of compounds fit with single exponential decay or with a bi-exponential decay as in the following equation where  $\tau$  is the fluorescence lifetime and  $\alpha$  is the pre-

exponential factor. For the fits, the reduced  $\chi^2$  values were within 0.97 – 1.1 and the distribution of the weighted residuals were random among the data channels.  $\tau_f$  is mean fluorescence life time (meaning of the symbols are usual).

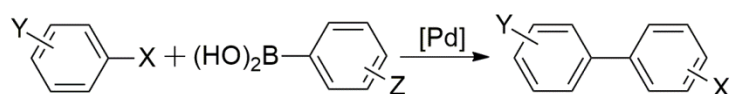
$$I(t) = [\alpha_1 \exp(-t / \tau_1) - \alpha_2 \exp(-t / \tau_2)] \quad (2)$$

$$\tau_f = \alpha_1 \tau_1 + \alpha_2 \tau_2 \quad (3)$$

### I.13. Catalysis

#### The Suzuki-Miyaura cross coupling reaction

Cross-coupling reactions mediated by transition metals have revolutionized organic synthesis in a way.<sup>147</sup> There have been numerous reports in the past regarding mild and effective protocols for C-C bond formation after cross coupling processes. In terms of catalyst utilized and reaction conditions, the Suzuki-Miyaura reaction is a better coupling reaction than other cross-coupling processes, such as the Heck or Stille reaction.<sup>148-150</sup> Under basic circumstances, the Suzuki-Miyaura reaction is a coupling of organic halides or triflates with organoboranes catalyzed by palladium (Scheme I.4).



X = I, Br, Cl, OTf

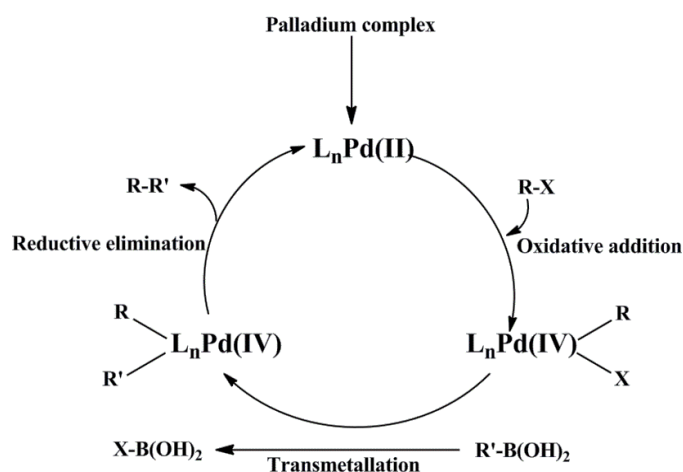
Y = Ester, Aldehyde, Ketone, Amine, Ether etc.

Z = CH<sub>3</sub>, C<sub>2</sub>H<sub>5</sub>, Phenyl

Scheme I.3. General reaction scheme for the Suzuki-Miyaura reaction

This reaction's primary benefit is that it may be applied to a wide range of functional groups, including ethers, alcohols, protected amines, aldehydes, ketones, and esters. High regio- and stereo selectivity, ease of separating inorganic boron compounds, ease of using the reaction in both aqueous and heterogeneous reaction conditions, and most importantly, high yields are among the other benefits. The Suzuki-Miyaura reaction has the potential to be utilised in macromolecular chemistry as a polycondensation technique due to its elevated yields. The Suzuki-Miyaura cross coupling process follows a three-step mechanistic pathway, as illustrated in Scheme I.4, that entails oxidative addition, transmetalation, and reductive elimination in order to obtain the coupling partner. The Pd(0) complex is placed between the R1-X (aryl halide) link after the catalyst precursor's ligands dissociate. A stable trans-R1-

$\text{Pd(II)-X}$  complex (**II**) is produced by the oxidative addition of organic halides to a catalytically active  $\text{Pd (0)}$  species. In a typical catalytic cycle, this step is frequently the one that determines the rate. Before reductive elimination, Suzuki *et al.*<sup>151</sup> suggested one intermediary step for transmetalation, but Canary *et al.* suggested two, as seen in Scheme I.4. According to Suzuki *et al.*, the  $\text{R1-Pd(II)-X}$  complex (**II**) produces biaryl  $\text{Pd}$  intermediate **IV** (transmetalation step) when it combines with aryl boronic acids or esters. The catalytic cycle is maintained by the regeneration of the catalytically active  $\text{Pd (0)}$  species following the reductive elimination of the biaryl product (**IV**). Canary and colleagues suggested that  $\text{B} \rightarrow \text{Pd}$  undergoes transmetalation to generate a *trans* diarylpalladium species (**III**); the *trans* isomer is then isomerized into the *cis* isomer to yield **IV**.<sup>152</sup> The transmetalation phase is less well understood than the two steps of oxidative addition and reductive elimination, which are both very well recognized.



Scheme I.4. Postulated reaction mechanisms ( $\text{X}$  = halogens, OTf or ONf and  $\text{L}$  = ligand)

Based only on experimental results, Suzuki *et al.* and Canary *et al.* postulated two distinct reaction pathways for the SCC reaction. Prior to reductive elimination, Suzuki *et al.* [161] hypothesised a chemical cycle that included the creation of intermediate **IV**. But Canary *et al.* showed that **III** is a likely transition using electro spray ionisation mass spectrometry (ESIMS).<sup>152</sup> We looked at the Suzuki cross coupling reaction between pyridyl bromide and three structurally related phenyl boronic acids. According to the catalytic cycle, the two important intermediates, **II** and **IV**, were present in the reaction mixture. Given that the replacement of one anion by another in the halide depends on the coupling reaction's substrates and reaction circumstances, these processes are not inherently incompatible.

Product yields from the Suzuki-Miyaura cross coupling process are typically very high. Suzuki couplings are employed in industrial settings as well as research labs.<sup>153,154</sup> The biaryl motif can be found in conducting polymers, liquid crystalline materials, herbicides, and a variety of medications and natural goods.<sup>155</sup>

### **I.14. Biological Activities**

Antitumor studies of Schiff base ligands and their metal complexes are numerous reported.<sup>156-159</sup> The biological activity of Schiff bases either increase or decrease upon chelation with metal ions.

#### **I.14.1. Cytotoxic activities**

Cancer is a major public health and financial issue, and its impact has been predicted to expand broadly over the coming decades. Globally, cancer claimed the lives of around 10 million individuals in 2020.<sup>160</sup> It is anticipated that there would be 28.4 million new instances of cancer worldwide in 2040, which is 47% rise from 2020.<sup>161</sup> Therefore, it is crucial to design novel treatment plans and chemotherapy medications. Despite being a well-known anticancer medication, the use of cisplatin in cancer chemotherapy has been constrained by multifactorial resistance, harmful side effects on normal cells, and general toxicity.<sup>162,163</sup> So, in order to increase the selectivity of anticancer medications and lessen their adverse effects, less toxic and highly effective metal-based anticancer compounds have been sought after and produced. Interaction of DNA with transition metal complexes has gained considerable current interest due to its various applications in cancer research and nucleic acid chemistry.<sup>164-166</sup> To understand clearly the binding behavior of DNA with Schiff base metal complexes, a brief description about structure of DNA, nucleic acid and heredity, DNA binding modes and DNA cleavage is given below.

#### **I.14.2. Structure of DNA and BSA**

Deoxyribonucleic acid, or DNA, is the genetic substance found in humans and nearly all other living things. Every cell in an individual's body contains the same DNA. Nuclear DNA refers to the majority of the DNA molecules found in the cell nucleus; however, mitochondrial DNA, or mtDNA, also contains a tiny quantity of DNA. Adenine (A), Guanine (G), Cytosine (C), and Thymine (T) are the four chemical bases that make up the code that contains the information in DNA. There are roughly three billion bases in human DNA. In all humans, more than 99 percent of these bases are the same. Watson and Crick presented the most commonly recognized model for the structure of the DNA molecule in 1953; for this

work, Crick was granted the 1962 Nobel Prize in Medicine. As to his assertion, the DNA molecule is composed of two helices (Figure I.2). Two antiparallel polynucleotide strands that are spirally wound around one another in a right-handed helix make up the molecule. Hydrogen bonds hold the two strands together. Major and minor grooves on the double stranded helical molecule alternate. A lengthy polynucleotide of deoxyribonucleotides makes up each strand. In terms of the bases' arrangement inside the two strands, they are complementary to one another. Purines and pyrimidines, or (A and T) and (G and C), are thus found as base pairs within the double helix. Because of this, it is simple to determine the base sequence of the complementary strand of DNA provided the base sequence of one strand of DNA is known. Phosphate and deoxyribose sugar molecules are stacked alternately and connected by phosphodiester connections to create the strand's backbone.

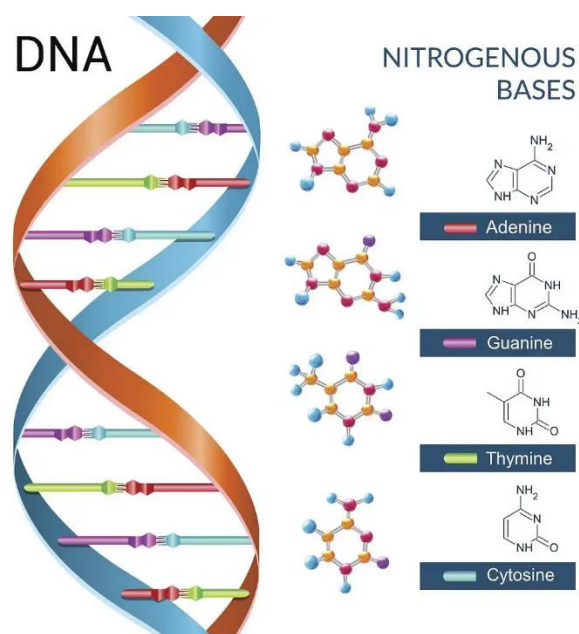


Figure I.2. Structure of DNA.

Of all the molecules encountered in living organisms, proteins are the most abundant and diverse from a functional point of view. From the hormones and enzymes that control metabolism, the framework forming collagen in bones, the contractile proteins in muscles, to the haemoglobin and albumin in the bloodstream and immunoglobulins fighting infections, almost every life process relies on this class of molecules.

Albumin is the most abundant protein in the vertebrates' organisms (up to 40 mg/ml) and the most prominent plasma protein (about 60% of the total protein content of plasma). It is one of

the first discovered and most intensely studied proteins. When approaching the evaluation of small molecules affinity for albumins, bovine serum albumin (BSA) is usually selected as a relevant model, due to its structural similarity with human serum albumin (76%), its low cost and wide availability. The BSA molecule consists of 583 amino acids, bound in a single chain cross-linked with 17 cystine residues (eight disulfide bonds and one free thiol group), and has a molecular mass of 66400 Da.<sup>167</sup> The amino acid chain is made up of three homologous but structurally distinct domains (I, II and III), divided into nine loops by the disulfide bonds and arranged in a heart-shaped molecule. Each domain consists of two subdomains, A and B. The secondary structure of the protein is mainly  $\alpha$ -helical (74%), with the remaining polypeptide chain occurring in turns and in extended or flexible regions between subdomains.<sup>167-169</sup>

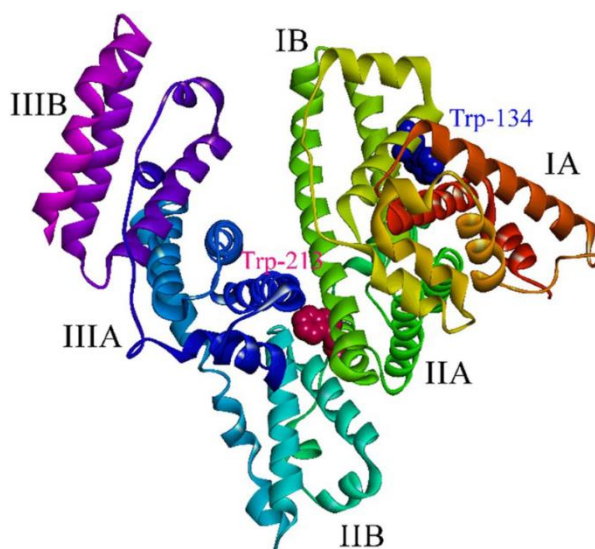


Figure I.2. Structure of BSA molecule.

Many endogenous and exogenous compounds (including drugs, hormones, xenobiotics and fatty acids,<sup>170</sup> once entered the blood stream, are transported and disposed of as a consequence of forming a complex with serum albumins. This class of proteins also contribute to the colloid blood osmotic pressure and the maintenance of blood pH,<sup>171,172</sup> but one of the most important property of albumins is that they bind to different compounds in a reversible manner. The protein often increases the apparent solubility of hydrophobic drugs in the plasma and influences the circulation, metabolism and efficacy of drugs.



**I.14.3. Binding Modes of DNA and BSA**

DNA is the fundamental genetic material of living things and the building block of gene expression. DNA can interact with small molecules through intercalative binding, electrostatic binding, and groove binding (Figure I.3).<sup>173-175</sup> When tiny molecules or the medication intercalate into the non-polar interior of the DNA helix, intercalative binding occurs. When ligands of the proper size and chemical makeup fit themselves in between DNA base pairs, an aromatic group is stacked between the base pairs in this sort of binding. The majority of ligands that are appropriate for intercalation are planar, aromatic, and polycyclic; as a result, they frequently function well as nucleic acid stains. DNA strand design and synthesis are currently of interest since these compounds have the potential to be used as chemotherapeutic medicines. In groove binding interactions, the bound molecule directly interacts with base pair edges in the major (G-C) or minor (A-T) grooves of the nucleic acids. Methyl groups in the antibiotic netropsin function as a model groove binder by preventing intercalation.<sup>176</sup> It is uncommon for tiny molecules to bind within the double helix's main groove. Electrostatic interaction occurs between molecules that have a positive charge. They interact electrostatically with the DNA chain's negatively charged phosphate backbone. Under physiological conditions, electrostatic attraction is typically weak. Intercalation into the base pair stack at the double helix's core and insertion into the minor groove are the two most frequent binding mechanisms. Usually, cationic compounds with planar aromatic rings exhibit intercalation. The positive charge could be on a substituent instead of in the ring structure. To form a binding pocket for the ligand in this binding mode, two neighbouring base pairs must split apart.<sup>177</sup> Conversely, minor groove binders typically possess some degree of flexibility because this enables the molecule to modify its structure in order to track the groove as it twists around the helix's central axis.<sup>178,179</sup> When binding in the minor groove as opposed to intercalative binding, significantly less DNA distortion is needed. Often employed techniques to shed light on the binding mechanisms of tiny compounds include UV-vis spectroscopy, fluorescence spectroscopy, circular dichroism (CD) and viscosity.

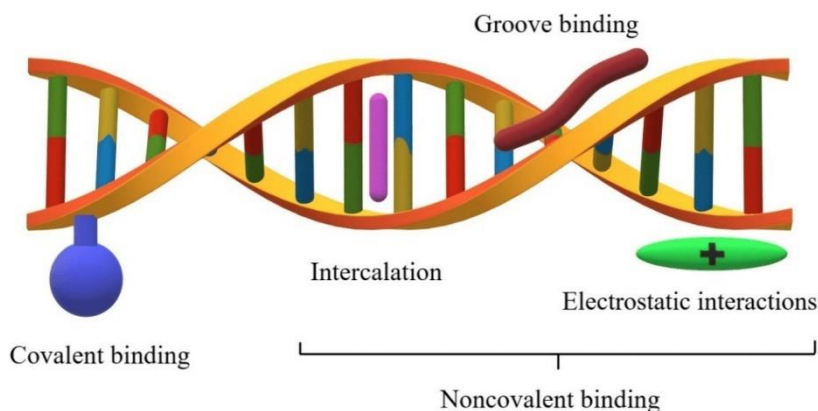


Figure I.3. Binding modes of DNA

The BSA interaction and binding ability of a large variety of mononuclear and polynuclear  $\text{Cu}^{2+}$ ,  $\text{Ni}^{2+}$ ,  $\text{Zn}^{2+}$ ,  $\text{Co}^{2+}$ ,  $\text{Pt}^{2+}$  complexes with aromatic ligands (some of them bearing known pharmacologically active moieties) has been investigated. As in the case of the interaction of metal complexes with other classes of biomolecules, it has been suggested that the planarity of the ligands coordinating the metal center plays an important role in enhancing protein binding ability. A certain degree of binding specificity was observed for metal complexes, due to weak interactions between the ligand sphere and the protein binding site, as some studies suggested that metal complexes most likely affect the Trp-134 residue, found on the surface of the protein, and thus more accessible.<sup>180</sup>

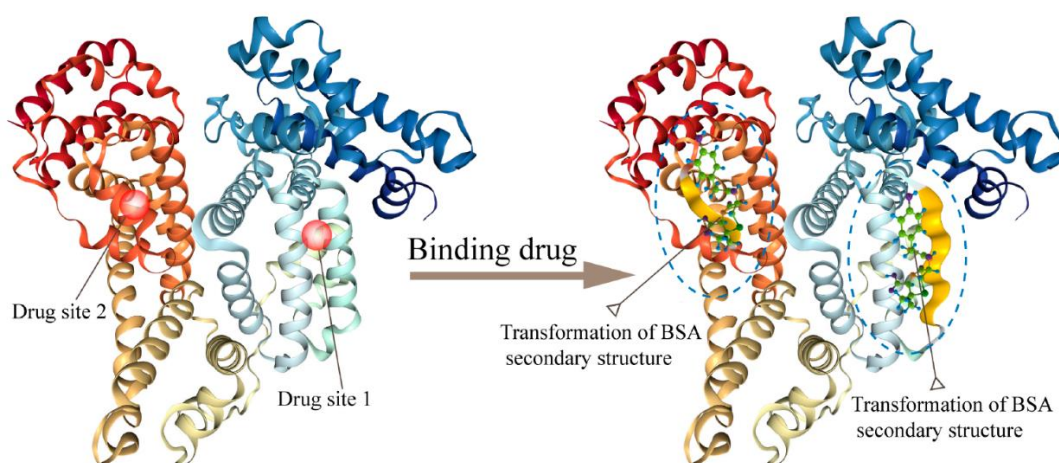


Figure I.4. Schematic illustration of the structure and conformational variation of BSA in complex with a drug.

Other research groups, after performing displacement experiments, concluded that complexes preferentially bind to subdomain IIA.<sup>181</sup> An interaction between BSA and metal complexes often leads to a perturbation of the secondary structure of the protein, by disrupting the disulfide bonds and leading to a partial loss of  $\alpha$ -helix conformation with the subsequent unfolding of the protein,<sup>181</sup> or a change in the polarity of the environment to which the tryptophan residues are exposed,<sup>182</sup> as a result of molecular interactions, such as excited-state reactions, molecular rearrangements, energy transfer, ground-state complex formation or collision quenching (Figure I.4).

#### **I.14.4. Transition metal complexes as chemical probes for DNA and BSA**

Researching the design of molecules with a high binding affinity for DNA is a difficult task. These compounds, which exert their biological activity through interactions with DNA, can function as good chemotherapeutic reagents.<sup>183-188</sup> The biological activity of these molecules is not only determined by their interactions with DNA; however, their method of binding with DNA is frequently connected with their reactivity and selectivity. Therefore, the rational design of diverse DNA-targeted chemotherapeutic drugs and molecular probes for DNA depends critically on a better knowledge of the mechanisms that influence the interactions of small molecules with DNA. As biological system probes, stable, inert compounds with active metal centers are very helpful. Palladium complexes are among the transition metal complexes that are currently widely employed to investigate the interactions between metal complexes and DNA.<sup>189-193</sup>

The selectivity and affinity of metal complexes' binding to DNA have attracted a lot of attention. The development of biotechnological instruments and chemotherapy may benefit from the findings of such studies. Extensive efforts have been made to comprehend the non-covalent interactions between metal complexes and DNA. We have investigated the palladium complexes' interactions with DNA by electrochemical and absorption spectroscopy investigations. One of the most effective methods for examining metal ion DNA interactions is electronic absorption spectroscopy.<sup>194,195</sup> DNA's double helix structure is characterized by two spectral features: the "hyperchromic" and "hypochromic" effects. "Hypochromism" is caused by both conformational changes on DNA and the concentration of DNA along the helix axis, whereas "hyperchromism" is caused by structural damage to DNA.<sup>196,197</sup> On the other hand, either hyperchromism or hypochromism may result in metal complexes that bind non-intercalatively or electrostatically with DNA.<sup>198,199</sup> The degree of hyperchromism indicates the strength of intercalative binding. In order to track their interaction with DNA,

palladium(II) complexes do not exhibit a strong d-d or charge transfer band. Thus, the changes are tracked using the absorption band. DNA content was varied while maintaining a fixed complex concentration of 100  $\mu\text{M}$  in DMSO at 25  $^{\circ}\text{C}$  for the electronic absorption titration of the complexes. Palladium complexes in DMSO-buffer solutions exhibit bands corresponding to ligand to metal charge transfer (LMCT) transitions, with a wavelength range of 290–370 nm. Because of either hyperchromism or hypochromism, the charge transfer band's intensity varies as DNA concentration rises. Plotting the  $[\text{DNA}]/(\epsilon_a - \epsilon_f)$  against  $[\text{DNA}]$  allowed for the determination of the intrinsic binding constant,  $K_b$ , which was used to compare the binding strengths of metal complexes.<sup>200</sup>

$$[\text{DNA}]/(\epsilon_a - \epsilon_f) = [\text{DNA}]/(\epsilon_b - \epsilon_f) + 1/K_b (\epsilon_b - \epsilon_f),$$

Where,  $[\text{DNA}]$  = Concentration of DNA in base pairs,  $\epsilon_a$  = the apparent extinction coefficient =  $A_{\text{obsd}}/[\text{Complex}]$

$\epsilon_f$  = the extinction coefficient for free metal complex

$\epsilon_b$  = the extinction coefficient for free metal complex in the fully bound form

From the plot of  $[\text{DNA}]/\epsilon_a - \epsilon_f$  versus  $[\text{DNA}]$ ,  $K_b$  was measured from the ratio of slope to intercept of the plot.

An efficient approach in evaluating the interaction between metal complexes and BSA is the use of fluorescence spectroscopy. BSA has fluorescent properties and emits intensely upon excitation. Responsible for its intrinsic fluorescence are three amino acid residues found in its structure: tryptophan, tyrosine and phenylalanine,<sup>167</sup> but as the relative ratio of fluorescence intensity for these amino acids is 100:9:0.5, it seems probable that the fluorescence of BSA arises mainly from its two tryptophan residues: Trp-134 located on the surface of sub-domain IB and Trp-212 located within a hydrophobic binding pocket in sub-domain IIA. The fluorescence spectra are recorded in the absence and in the presence of increasing concentrations of metal complex. In the case of an interaction with the coordination compound, the fluorescence intensity of the protein at around 345 nm decreases regularly as the concentration of the probe increases. Moreover, a red or blue shift of the emission maximum in the fluorescence spectrum of the albumin is indicative of an increase in the hydrophobicity of the microenvironment around the tryptophan residues,<sup>201</sup> while no change in the position of the emission maximum suggests no alteration in the local dielectric environment of BSA. Fluorescence quenching can occur by different mechanisms, usually classified as static quenching (a non-fluorescent ground-state complex is formed between the fluorophore and the quencher), dynamic quenching (a collisional process, the fluorophore and

the quencher interact during the transient existence of the excited state), or a simultaneous static and dynamic quenching. A series of parameters are used to define and evaluate the interaction between BSA and the probe: the Stern-Volmer quenching constant, the quenching rate constant, the binding constant and the number of binding sites. The fluorescence quenching is described by the Stern-Volmer equation.

$$I_0/I = 1 + K_{SV}[Q] = 1 + k_q\tau_0[Q]$$

where  $I_0$  and  $I$  are the fluorescence intensities of BSA in the absence and in the presence of the quencher (i.e. the metal complex), respectively,  $K_{SV}$  is the Stern-Volmer quenching constant,  $[Q]$  is the concentration of the quencher,  $k_q$  is the quenching rate constant of the biomolecule and  $\tau_0$  is the average lifetime of the molecule in the absence of the quencher.

A linear  $I_0/I$  vs.  $[Q]$  plot indicates that a single type of quenching mechanism is involved, either static or dynamic, while a deviation from linearity suggests a mixed quenching mechanism.<sup>202</sup> The  $K_{SV}$  value is obtained from the plot  $I_0/I$  vs  $[Q]$ . Values with a magnitude order of  $10^5 \text{ M}^{-1}$  for  $K_{SV}$  are considered to be indicative of a relatively strong interaction between BSA and metal complexes.<sup>203,204</sup>

Dynamic and static quenching show certain characteristics, such as their different dependence on temperature reflected in the changes in the fluorescence spectrum of the fluorophore. In the case of static quenching, an increase in temperature leads to a lower stability of the complex and a decrease in the quenching constant. In the case of dynamic quenching, a faster diffusion is a consequence of an increase in temperature and, thus, the quenching rate increases. When small molecules bind independently to a set of equivalent sites on a molecule, the equilibrium between free and bound molecules is represented by the Scatchard equation.

$$\log[(I_0 - I)/I] = \log[K_b] + n \log[Q]$$

where  $I_0$  and  $I$  are the fluorescence intensities of the protein in the absence and in the presence of the quencher (i.e. the metal complex) respectively,  $[Q]$  is the concentration of the quencher,  $K_b$  is the binding constant and  $n$  is the number of binding sites.

The  $K_b$  values are obtained from the plot  $\log[(I_0 - I)/I]$  vs  $\log[Q]$ . Values with a magnitude order in the range of  $10^3$ – $10^6 \text{ M}^{-1}$  for  $K_b$  are reported as being indicative of an efficient interaction with the protein.<sup>205</sup> Generally, the binding constant of a compound to serum albumin should be high enough to ensure that a significant amount gets transported and distributed through the organism, but, at the same time, low enough so that the compound can

be released once it reaches its target. Such an optimum range is considered to be  $10^4 - 10^6 \text{ M}^{-1}$ .

### **I.15. Objectives and scope of the present work**

Interesting uses for the metal complexes of Schiff bases can be found in material science, medicine, and catalysis. The synthesis of novel Schiff bases and their complexes is therefore still of interest. Therefore, it was thought to be beneficial to create a few new Schiff base complexes, investigate their physicochemical characteristics, and use them as hydrogenation, oxidation, and DNA cleaving catalysts. The primary focus of the study in this thesis is on metal complexes of Schiff bases with O N S donor ligands. Given that the ligand field strengths of these Schiff bases with an electron-withdrawing heterocyclic system should be lower than those of the Schiff bases produced from salicylaldehyde, they would be intriguing. Furthermore, it is anticipated that the catalytic and DNA cleaving capabilities of these ligand complexes will differ significantly from those of the salen complexes. The majority of transition metal complexes were synthesized in order to investigate the binding characteristics of BSA and DNA. These complexes are used in biological activity as well as catalysis. The effectual recognition of nitroaromatic-based explosives (NACs) has achieved lots of attention in present time owing to the threat towards security and human wellbeing. Scientists are putting great efforts in developing chemosensors which can not only recognize nitro-aromatics at a very tiny level but at the same time, it should be cost-effective. Of all the nitro explosives, 2,4,6-trinitrophenol (TNP) has gained the most attention because it is more powerful explosive than the others. Hence, proficient recognition of TNP is vital and accordingly here we fabricated three heavy metal complex-based probes which selectively recognize TNP.

**Therefore, the work presented in this thesis was carried out with the following objectives**

- ❖ To synthesize some new palladium(II) and platinum(II) complexes with N, S and O donor imine functional ligands by very facile and economically cheap synthetic route and studied their properties, chemical and biological activities.
- ❖ Phosphine based palladium(II) complexes which possess significant bio-activities and catalytic activities towards the C-C cross-coupling reactions.



- ❖ To design and development one-dimensional copper(II) coordination polymer which shows admirable biological activity.
- ❖ Fabrication of heavy metal-based complexes for the selective and sensitive recognition of nitro-aromatics in environment.

Details of these studies are embodied in this thesis.

## I.16. References

1. P. M. Thakor, R. J. Patel, R. Kr. Giri, S. K. Chaki, A. J. Khimani, Y. H. Vaidya, P. Thakor, A. B. Thakkar and J. D. Patel, *ACS Omega*, 2023, **8**, 33069.
2. M. Li, J. Tang, Y. Luo, J. Yang, J. Liu, J. Peng and Y. Fang, *Anal. Chem.*, 2023, **95**, 2094.
3. M. T. Kaczmarek, M. Zabiszak, M. Nowak and R. Jastrzab, *Coord. Chem. Rev.*, 2018, **370**, 42.
4. M. S. More, P. G. Joshi, Y. K. Mishra and P. K. Khanna, *Materials Today. Chemistry.*, 2019, **14**, 100195.
5. A. M. Khan, O. R. Abid and S. Mir, *Biopolymers.*, 2020, **111**, 23338.
6. L. H. A. Rahman, A. M. A. Dief, M. O. Aboelez and A. A. H. A. Mawgoud, *J. Photochem. Photobiol. B.*, 2017, **170**, 271.
7. H. E. Salama, G. R. Saad and M. W. Sabaa, *Int. J. Biol. Macromol.*, 2015, **79**, 996.
8. S. Omid and A. Kakanejadifard, *RSC Adv.*, 2020, **10**, 30186.
9. A. Das, C. Hessin, Y. Ren and M. D. E. Murr, *Chem. Soc. Rev.*, 2020, **49**, 8840.
10. J. A. Stubbe, W. A. van der Donk, *Chem. Rev.*, 1998, **98**, 705.
11. B. N. Nguyen, L. A. Adrio, T. Albrecht, A. J. P. White, M. A. Newton, M. Nachtegaal, S. J. A. Figueroa and K. K. Hii, *Dalton Trans.*, 2015, **44**, 16586.
12. C. H. Yu, C. Zhu, X. Ji, W. H. Xie, N. Bhuvanesh, L. Fang and O. V. Ozerov, *Inorg. Chem. Front.*, 2020, **7**, 4357.
13. J. Wu, B. Xu, Y. Xu, L. Yue, J. Chen, G. Xie and J. Zhao, *Inorg. Chem.*, 2023, **62**, 19142.
14. L. Li, M. Zhang, D. Jia, Z. Liu, N. Zhang, B. Sun, Z. Wang, M. Liu and Q. Wang, *Dalton Trans.*, 2023, **52**, 147.
15. A. K. King, A. Brar, G. Li and M. Findlater, *Organometallics*, 2023, **42**, 2353.
16. P. N. Swami, N. Meena, H. Joshi, K. Rangan and A. Kumar, *Organometallics*, 2023, **42**, 2359.
17. C. Arroniz, G. Chaubet and E. A. Anderson, *ACS Catal.*, 2018, **8**, 8290.
18. P. G. Cozzi, *Chem. Soc. Rev.*, 2004, **33**, 410.
19. Z. Li, K. R. Conser and E. N. Jacobsen, *J. Am. Chem. Soc.*, 1993, **115**, 5326.
20. G. H. Olie and S. Olive, Springer, Berlin, 1984, 152.
21. H. Dugas and C. Penney, *Bioorganic Chemistry*, Springer, New York, 1981, 435.
22. K. Sancak, Mustafa Er, Y. Ünver, M. Yildirim and I. Degirmencioglu, *Transition Met. Chem.*, 2007, **32**, 16.
23. M. N. Ibrahim and S. E. A. Sharif, *E-J. Chem.*, 2007, **4**, 531.
24. K. Wang, H. Yang, Z. Liao, S. Li, M. Hambsch, G. Fu, S. C. B. Mannsfeld, Q. Sun and T. Zhang, *J. Am. Chem. Soc.*, 2023, **145**, 5203.
25. H. Liu, Z. Fu, K. Xu, H. Cai, X. Liu and M. Chen, *J. Phys. Chem. B*, 2011, **115**, 7568.
26. S. Pu, Z. Tong, G. Liu and R. Wang, *J. Mater. Chem. C*, 2013, **1**, 4726.

27. N. Shaalan, N. Laftah, G. A. El-Hiti, M. H. Alotaibi, R. Muslih, D. S. Ahmed and E. Yousif, *Molecules*, 2018, **23**, 913.
28. Y. Dong, R. Fan, P. Wang, L. Wei, X. Wang, H. Zhang, S. Gao, Y. Yang and Y. Wang, *Dalton Trans.*, 2015, **44**, 5306.
29. W. J. Evans, C. H. Ziller and J. W. Ziller, *Polyhedron*, 2002, **21**, 1683.
30. (a) R. Ziessel, *Coord. Chem. Rev.*, 2001, **195**, 216; (b) M. Albrect, *Chem. Rev.*, 2001, **101**, 3457.
31. T. Chakraborty, A. Sarkar, A. Adhikary, N. Chakiroy and D. Das, *Cryst. Growth Des.*, 2019, **19**, 7336.
32. Y-C. Su, G-L. Liu and B-T. Ko, *Inorg. Chem.*, 2023, **62**, 8565.
33. C. T. Prabhakara, S. A. Patil, S. S. Toragalmath, S. M. Kinnal and P. S. Badami, *J. Photochem. Photobiol. B*, 2016, **157**, 1.
34. L. Rigamonti, A. Forni, S. Righetto and A. Pasinic, *Dalton Trans.*, 2019, **48**, 11217.
35. W. Zoubia, A. S. Al-Hamdanib and M. Kaseema, *Appl. Organometal. Chem.*, 2016, **30**, 810.
36. L. Roussio, N. Friedman, M. Sheves and O. Ottolenghi, *Biochemistry*, 1995, **34**, 12059.
37. J. K. Lanyi, *Biophys. Acta.*, 1993, **241**, 241.
38. M. Pająk, M. Woźniczka, M. E. Lichawska, B. Czerwiński, J. Włodarczyk, and J. Fichna, *Int. J. Mol. Sci.*, 2022, **23**, 5492.
39. G. Givaja, M. Volpe, M. A. Edwards, A. J. Blake, C. Wilson, M. Schroder and J. B. Love, *Angew. Chem. Int. Ed.*, 2007, **46**, 584.
40. W. A. Zoubi and Y. G. Ko, *J. Organomet. Chem.*, 2016, **822**, 173.
41. (a) P. Gueerriero, S. Tamburin and P. A. Vigato, *Coord. Chem. Rev.*, 1995, **139**, 17; (b) P. A. Vigato and S. Tamburini, *Coord. Chem. Rev.*, 2004, **248**, 1717.
42. (a) G. J. P. Britovsek, V. C. Gibson and D. F. Wass, *Angew. Chem. Int. Ed Engl.*, 1999, **38**, 428; (b) R. E. Morris and L. Brammer, *Chem. Soc. Rev.*, 2017, **46**, 5444.
43. A. E. Martell, R. D. Hancock and R. J. Motekaitis, *Coord. Chem. Rev.*, 1994, **133**, 39.
44. E. Peris and R. H. Crabtree, *Chem. Soc. Rev.*, 2018, **47**, 1959.
45. X. Liu and J. Hamon, *Coord. Chem. Rev.*, 2019, **389**, 94.
46. P. Braunstein and F. Naud, *Angew. Chem. Int. Ed.*, 2001, **40**, 680.
47. R. G. Pearson, *J. Am. Chem. Soc.*, 1963, **85**, 3533.
48. M. Mukai, S. Hagiwara, R. Tanaka, H. Tabe, T. Nakazono and Y. Yamada, *Inorg. Chem.*, 2023, **62**, 18098.
49. M. S. M. Holmsen, A. Nova and M. Tilset, *Acc. Chem. Res.*, 2023, **56**, 3654.
50. Y. Yang, L. Eberle, F. F. Mulks, J. F. Wunsch, M. Zimmer, F. Rominger, M. Rudolph and A. S. K. Hashmi, *J. Am. Chem. Soc.*, 2019, **141**, 17414.
51. M. G. Gardiner and C. C. Ho, *Coord. Chem. Rev.*, 2018, **375**, 373.

52. (a) K. Buldurun and M. Özdemir, *J. Mol. Struct.*, 2020, **1202**, 127266; (b) M. Ramesh and G. Venkatachalam, *J. Organomet. Chem.*, 2019, **880**, 47.
53. H. A. McManus and P. J. Guiry, *Chem. Rev.*, 2004, **104**, 4151.
54. E. M. McGarrigle and D. G. Gilheany, *Chem. Rev.*, 2005, **105**, 1563.
55. E. A. M. Geary, L. J. Yellowlees, L. A. Jack, I. D. H. Oswald, S. Parsons, N. Hirata, J. R. Durrant and N. Robertson, *Inorg. Chem.*, 2005, **44**, 242.
56. X. Yang, F. Drepper, B. Wu, W. Sun, W. Haehnelb and C. Janiak, *Dalton Trans.*, 2005, **2**, 256.
57. X. Chen, P. Sun, B. Mo, C. Chen, and J. Peng, *J. Org. Chem.*, 2021, **86**, 352.
58. J. Yu, J. Li, P. Wang and J. Yu, *Angew. Chem.*, 2019, **131**, 18309.
59. G. Cheng, Y. Weng, X. Yang, and X. Cui, *Org. Lett.*, 2015, **17**, 3790.
60. S. Budagumpi and S. Endud, *Organometallics*, 2013, **32**, 1537.
61. K. E. Prosser, S. W. Chang, F. Saraci, P. H. Le and C. J. Walsby, *J. Inorg. Biochem.*, 2017, **167**, 89.
62. N. Anbu, A. Dhakshinamoorthy, *J. Ind. Eng. Chem.*, 2018, **65**, 120.
63. A. Bhanja, R. Herchel, Z. Travnicek and D. Ray, *Inorg. Chem.*, 2019, **58**, 12184.
64. R. Balamurugan, M. Palaniandaver and R. S. Gopalan, *Inorg. Chem.*, 2001, **40**, 2246.
65. M. Kalita, P. Gogoi, P. Barman, B. Sarma, A. K. Buragohain and R. D. Kalita, *Polyhedron*, 2014, **74**, 93.
66. R. H. Crabtree, *The Organometallic Chemistry of the Transition Metals*, 2nd ed.; Wiley: New York, 1994, Chapter 4.
67. (a) M. P. Mitoraj and A. Michalak, *Inorg. Chem.*, 2010, **49**, 578; (b) D. Woska, A. Prock and W. P. Giering, *Organometallics*, 2000, **19**, 4629.
68. (a) A. W. Hofmann, *Ann. Chem. Pharm.*, 1857, **104**, 1; (b) B. W. Malerbi, *Platinum Metal Rev.*, 1965, **9**, 47.
69. (a) J. Jover, N. Fey, J. N. Harvey, G. C. Lloyd-Jones, A. G. Orpen, G. J. J. Owen-Smith, P. Murray, D. R. J. Hose, R. Osborne and M. Purdie, *Organometallics*, 2010, **29**, 6245; (b) T. Sawano, Z. Lin, D. Bours, B. An, C. Wang, and W. Lin, *J. Am. Chem. Soc.*, 2016, **138**, 9783; (c) M. E. van der Boom and D. Milstein, *Chem. Rev.*, 2003, **103**, 1759.
70. H. P. Stevens, J. Olsen, J. K. Kirkland and D. H. Ess, *Organometallics*, 2024, **43**, 40.
71. J. Ahmed, A. Thakur and A. Goyal, in *Biological Treatment of Industrial Wastewater*, ed. M. P. Shah, The Royal Society of Chemistry, 2021, pp. 1-14.
72. S. S. Sonone, S. Jadhav, M. S. Sankhla and R. Kumar, *Lett. Appl. NanoBioScience*, 2020, **10**, 2148.
73. M. P. Cuajungco, M. S. Ramirez, M. E. Tolmasky, *Biomedicines*, 2021, **9**, 208.
74. M. I. Costa, A. B. Sarmiento-Ribeiro and A. C. Gonçalves, *Int. J. Mol. Sci.*, 2023, **24**, 4822.

75. M. Balali-Mood, K. Naseri, Z. Tahergorabi, M. R. Khazdair, M. Sadeghi, *Front. Pharmacol.*, 2021, **12**, 643972.
76. G. Genchi, M. S. Sinicropi, G. Lauria, A. Carocci, A. Catalano, *Int. J. Environ. Res. Public Health*, 2020, **17**, 3782.
77. E. García-Esquinas, M. Pollan, M. Tellez-Plaza, K. A. Francesconi, W. Goessler, E. Guallar, J. G. Umans, J. Yeh, L. G. Best and A. Navas-Acien, *Environ. Health Perspect.*, 2014, **122**, 363.
78. S. Chaudhuri, G. Sigmund, S. E. Bone, N. Kumar and T. Hoffman, *Environ. Sci. Technol.*, 2022, **56**, 11354.
79. L. Wang, D. Hou, Y. Cao, Y. S. Ok, F. M. G. Tack, J. Rinklebe and D. O'Connor, *Environ. Int.*, 2020, **134**, 105281.
80. K.-H. Kim, E. Kabir and S. A. Jahan, *J. Hazard. Mater.*, 2016, **306**, 376.
81. D. Temerova, T.-C. Chou, K. S. Kisel, T. Eskelinen, N. Kinnunen, J. Jänis, A. J. Karttunen, P.-T. Chou and I. O. Koshevoy, *Inorg. Chem.*, 2022, **61**, 19220.
82. D. C. Onwudiwe and P. A. Ajibade, *Mater. Lett.*, 2011, **65**, 3258.
83. P. Jiang and Z. Guo, *Coord. Chem. Rev.*, 2004, **248**, 205.
84. (a) T. Chattopadhyay, M. Mukherjee, K. S. Banu, A. Banerjee, E. Suresh, E. Zangrando and D. Das, *J. Coord. Chem.*, 2009, **6**, 967; (b) A. Guha, R. Sanyal, T. Chattopadhyay, Y. G. Han, T. K. Mondal and D. Das, *J. Mol. Struct.*, 2013, **1042**, 104; (c) M. Khorshidifard, H. Amiri Rudbari, Z. Kazemi-Delikani, V. Mirkhani and R. Azadbakht, *J. Mol. Struct.*, 2015, **1081**, 494; (d) S. Shit, A. Sasmal, P. Dhal, C. Rizzoli and S. Mitra, *J. Mol. Struct.*, 2016, **1108**, 475; (e) S. Roy, B. N. Sarkar, K. Bhar, S. Satapathi, P. Mitra and B. K. Ghosh, *J. Mol. Struct.*, 2013, **1037**, 160; (f) R. Golbedaghi, M. Rezaeivala and L. Albeheshti, *J. Mol. Struct.*, 2014, **1076**, 673.
85. A. Paul, S. Anbu, G. Sharma, M. L. Kuznetsov, B. Koch, M. Fatima, C. G. da Silva and A. J. L. Pombeiro, *Dalton Trans.*, 2015, **44**, 19983.
86. C. Marzano, M. Pellei, F. Tisato and C. Santini, *Anti-Cancer Agents Med. Chem.*, 2009, **9**, 185.
87. C. Santini, M. Pellei, V. Gandin, M. Porchia, F. Tisato and C. Marzano, *Chem. Rev.*, 2014, **114**, 815.
88. L. Jia, J. Xu, X. L. Zhao, S. S. Shen, T. Zhou, Z. Q. Xu, T. F. Zhu, R. H. Chen, T. L. Ma, J. Xie, K. Dong and J. C. Huang, *J. Inorg. Biochem.*, 2016, **159**, 107.
89. J. P. Wolfe, S. Wagaw, J. F. Marcoux and S. L. Buchwald, *Acc. Chem. Res.*, 1998, **31**, 805.
90. P. H. Espeel, G. D. Peuter, M. C. Tielen and P. A. Jacobs, *J. Phys. Chem.*, 1994, **98**, 11588.
91. M. Watanabe, T. Yamamoto and M. Nishiyama, *Angew. chemie.*, 2000, **112**, 2620.
92. M. Opanasenko, P. Stepnicka and J. Cejka, *RSC Adv.*, 2014, **4**, 65137.
93. S. Paul, M. Islamc and M. Islam, *RSC Adv.*, 2015, **5**, 42193.
94. G. Ferguson, R. McCrindle, A. J. McAlees and M. Parvez, *Acta Cryst.*, 1982, **B38**, 2679.
95. R. F. Heck, *J. Am. Chem. Soc.*, 1963, **85**, 657.

96. R. F. Heck, *J. Am. Chem. Soc.*, 1968, **90**, 313.
97. E. Negishi and L. Anastasia, *Chem. Rev.*, 2003, **103**, 1979.
98. E. Negishi, *Acc. Chem. Res.*, 1982, **15**, 340.
99. V. Grignard, *J. Ind. Eng. Chem.*, 1917, **9**, 1142.
100. J. F. Hartwig, *Acc. Chem. Res.*, 1998, **31**, 852.
101. J. F. Hartwig, *Inorg. Chem.*, 2007, **46**, 1936.
102. J. K. Stille, *Organometallics*, 1990, **9**, 3007.
103. J. K. Stille and R. Divakaruni, *J. Am. Chem. Soc.*, 1978, **100**, 1303.
104. J. Tsuji, I. Shimizu, I. Minami, Y. Ohashi and T. Sugiura, *J. Org. Chem.*, 1985, **50**, 1523.
105. B. M. Trost and Z. Shi, *J. Am. Chem. Soc.*, 1996, **118**, 3037.
106. K. Sonogashira, S. Takahashi and N. Hagihara, *Macromolecules*, 1977, **10**, 879.
107. A. C. Skapski and M. L. Smart, *Chem. Commun.*, 1970, **8**, 658.
108. R. Martin and S. L. Buchwald, *Acc. Chem. Res.*, 2008, **41**, 1461.
109. B. M. Trost and M. Lautens, *J. Am. Chem. Soc.*, 1985, **107**, 1781.
110. R. B. Bedford, C. S. J. Cazin and D. Holder, *Coord. Chem. Rev.*, 2004, **248**, 2283.
111. R. Jackstell, A. Grotevendt, D. Michalik, L. E. Firdoussi and M. Beller, *J. Organometal. Chem.*, 2007, **692**, 4737.
112. J. K. Stille and D. E. James, *J. Organometal. Chem.*, 1976, **108**, 401.
113. P. Fitton and E. A. Rick, *J. Organometal. Chem.*, 1971, **28**, 287.
114. T. R. Hoye, C. J. Dinsmore, D. S. Johnson and P. F. Korkowski, *J. Org. Chem.*, 1990, **55**, 4518.
115. Y. Tatsuno, T. Yoshida and S. Otsuka, *Inorg. Synth.*, 1990, **28**, 342.
116. B. M. Trost and C. B. Lee, *J. Am. Chem. Soc.*, 1998, **120**, 6818.
117. (a) N. Miyaura and A. Suzuki, *Chem. Rev.*, 1995, **95**, 2457; (b) L. Yin and J. Liebscher, *Chem. Rev.*, 2007, **107**, 133; (c) A. F. Littke and G. C. Fu, *Angew. Chem.*, 2002, **114**, 4350; (d) A. F. Littke and G. C. Fu, *Angew. Chem. Int. Ed.*, 2002, **41**, 4176; (e) R. Martin and S. L. Buchwald, *Acc. Chem. Res.*, 2008, **41**, 1461.
118. (a) A. O. King, N. Yasuda in *Organometallics in Process Chemistry* (Ed.: R. D. Larsen), Springer, Berlin, 2004, 205; (b) N. Miyaura, *Top. Curr. Chem.*, 2002, **219**, 11; (c) A. Suzuki in *Modern Arene Chemistry* (Ed.: D. Astruc), Wiley-VCH, Weinheim, 2002, 53; (d) A. Suzuki, *J. Organomet. Chem.*, 2002, **653**, 54.
119. R. M. Appa, S. S. Prasad, J. Lakshmidhevi, B. R. Naidu, M. Narasimhulu and K. Venkateswarlu, *Appl. Organometal. Chem.*, 2019, **33**, 5126.
120. (a) M. Beller, J. G. E. Krauter, A. Zapf and S. Bogdanovic, *Catal. Today*, 1999, **48**, 279; (b) M. Beller, J. G. E. Krauter and A. Zapf, *Angew. Chem., Int. Ed. Engl.*, 1997, **36**, 772.
121. K. W. Anderson and L. Buchwald, *Angew. Chem., Int. Ed.*, 2005, **44**, 6173.



122. (a) J. P. Genêt, A. Linquist, E. Blart, V. Mouries and M. Savignac, *Tetrahedron Lett.*, 1995, **36**, 1443; (b) C. Dupuis, K. Adiey, L. Charruault, V. Michelet, M. Savignac and J. P. Genêt, *Tetrahedron Lett.*, 2001, **42**, 6523.
123. N. E. Leadbeater, *Chem. Commun.*, 2005, **23**, 2881.
124. M. Ueda, M. Nishimura and N. Miyaura, *Synlett*, 2000, **6**, 856.
125. (a) C. A. Fleckenstein and H. Plenio, *Green Chem.*, 2007, **9**, 1287; (b) C. A. Fleckenstein, S. Roy, S. Leuthauser and H. Plenio, *Chem. Commun.*, 2007, **27**, 2870; (c) C. A. Fleckenstein and H. Plenio, *Chem. Eur. J.*, 2007, **13**, 2701; (d) C. A. Fleckenstein and H. Plenio, *J. Org. Chem.*, 2008, **73**, 3236; (e) C. A. Fleckenstein and H. Plenio, *Chem. Eur. J.*, 2008, **14**, 4267.
126. (a) L. R. Moore and K. H. Shaughnessy, *Org. Lett.*, 2001, **3**, 2757; (b) L. R. Moore and K. H. Shaughnessy, *Org. Lett.*, 2004, **6**, 225; (c) R. Huang and K. H. Shaughnessy, *Organometallics*, 2006, **25**, 4105; (d) L. R. Moore, E. C. Western, R. Craciun, J. M. Spruell, D. A. Dixon, K. P. O'Halloran and K. H. Shaughnessy, *Organometallics*, 2008, **27**, 576.
127. E. W. Y. Tido, E. J. M. Vertelman, A. Meetsma, P. J. van Koningsbruggen, *Inorg. Chim. Acta*, 2007, **360**, 3896.
128. X. Su and I. Aprahamian, *Chem. Soc. Rev.*, 2014, **43**, 1963.
129. Y. Yang, C. Gao, J. Liu and D. Dong, *Anal. Methods*, 2016, **8**, 2863.
130. M. R. Maurya, N. Chaudhary, F. Avecilla, P. Adaoc and J. C. Pessoa, *Dalton Trans.*, 2015, **44**, 1211.
131. (a) D. Zhang and Q. Wang, *Coord. Chem. Rev.*, 2015, **286**, 1. (b) A. Chatterjee and T. R. Ward, *Catal. Lett.*, 2016, **146**, 820. (c) I. Hussain, J. Capricho and M. A. Yawer, *Adv. Synth. Catal.*, 2016, **358**, 3320.
132. D. Pandiarajan, R. Ramesh, Y. Liu and R. Suresh, *Inorg. Chem. Commun.*, 2013, **33**, 33.
133. I. D. Kostas, B. R. Steele, A. Terzis, S. V. Amosova, A. V. Martynov and N. A. Makhaeva, *Eur. J. Inorg. Chem.*, 2006, **13**, 2642.
134. D. H. Lee, J. Y. Jung, I. M. Lee and M. J. Jin, *Eur. J. Org. Chem.*, 2008, **2**, 356.
135. K. Dhara, K. Sarkar, D. Srimani, S. K. Saha, P. Chattopadhyay and A. Bhaumik, *Dalton Trans.*, 2010, **39**, 6395.
136. P. Liu, M. Yan and R. He, *Appl. Organometal. Chem.*, 2010, **24**, 131.
137. W. Kohn, *Rev. Mod. Phys.*, 1998, **71**, 1253.
138. John Wiley & Sons, Inc. *J Comput Chem.*, 1999, **20**, 129.
139. E. Runge and E. K. U. Gross, *Phys. Rev. Lett.*, 1984, **52**, 997.
140. P. Hohenberg and W. Kohn, *Phys. Rev.*, 1964, **136**, B864.
141. R. V. Leeuwen, *Phys. Rev. Lett.*, 1998, **80**, 1280.
142. M. E. Casida, C. Jamorski, F. Bohr, J. Guan, D. R. Salahub Washington, D.C.: ACS Press., 1996 p. 145.

143. M. Petersilka, U. J. Gossmann, and E. K. U. Gross, *Phys. Rev. Lett.*, 1996, **76**, 1212.
144. E. R. Davidson, *Chem. Rev.*, 1986, **86**, 681.
145. R. Ditchfield, W. J. Hehre and J. A. Pople, *J. Chem. Phys.*, 1971, **54**, 724.
146. Thorn H. Dunning, Jr., *J. Chem. Phys.*, 1989, **90**, 1007.
147. K. Zhao, L. Shen, Z. Shen and T. Loh, *Chem. Soc. Rev.*, 2017, **46**, 586.
148. (a) H. A. Dieck and R. F. Heck, *J. Am. Chem. Soc.*, 1974, **96**, 1133; (b) G. T. Crisp, *Chem. Soc. Rev.*, 1998, **27**, 427.
149. J. K. Stille, *Angew. Chem. Int. Ed.*, 1986, **25**, 508.
150. N. Miyaura, T. Yanagi and A. Suzuki, *Synth. Commun.*, 1981, **11**, 513.
151. N. Miyaura, K. Yamada, H. Suginome and A. Suzuki, *J. Am. Chem. Soc.*, 1985, **107**, 972.
152. A. O. Aliprantis and J. W. Canary, *J. Am. Chem. Soc.*, 1994, **116**, 6985.
153. (a) J. Hassan, M. Sévignon, C. Gozzi, E. Schulz and M. Lemaire, *Chem. Rev.*, 2002, **102**, 1359; (b) S. Kotha and K. Mandal, *Eur. J. Org. Chem.*, 2006, **23**, 5387; (c) N. E. Leadbeater and M. Marco, *J. Org. Chem.*, 2003, **68**, 5660; (d) Y. Jie, Z. Min and Z. Zhongshi, *Eur. J. Org. Chem.*, 2006, **9**, 2060.
154. (a) D. S. Ennis, J. McManus, W. Wood-Kaczmar, J. Richardson, G. E. Smith, A. Carstairs, *Org. Proc. Res. Dev.*, 1999, **3**, 248; (b) R. M. Appa, S. S. Prasad, J. Lakshmidevi, B. R. Naidu, M. Narasimhulu, K. Venkateswarlu, *Appl. Organometal. Chem.*, 2019, **33**, 5126; (c) J. El-Maiss, T. M. El Dine, C.-S. Lu, I. Karamé, A. Kanj, K. Polychronopoulou and J. Shaya, *Catalysts*, 2020, **10**, 296.
155. (a) I. T. Raheem, S. N. Goodman and E. N. Jacobsen, *J. Am. Chem. Soc.*, 2004, **126**, 706. (b) Y. Hu, X. Hao, L. Xu, X. Xie, B. Xiong, Z. Hu, H. Sun, G. Yin, X. Li, H. Peng and H. Yang, *J. Am. Chem. Soc.*, 2020, **142**, 6285.
156. Y. Toubi, F. Abridach, S. Radi, F. Souana, A. Hakkou, A. Alsayari, A. B. Muhsinah and Y. N. Mabkhot, *Molecules*, 2019, **24**, 3250.
157. C. E. Satheesha, P. Raghavendra Kumara, N. Shivakumarb, K. Lingarajuc, P. Murali Krishnab, H. Rajanaikac and A. Hosamani, *Inorg. Chim. Acta.*, 2019, **495**, 118929.
158. G. Kumaravel, P. U. Ponnukalai, D. Mahendiran and N. Raman, *Int. J. Biol. Macromol.*, 2019, **126**, 1303.
159. M. Manimohan, S. Pugalmani and M. A. Sithique, *Int. J. Biol. Macromol.*, 2019, **136**, 738.
160. H. Sung, J. Ferlay, R. L. Siegel, M. Laversanne, I. Soerjomataram, A. Jemal and F. Bray, *CA-Cancer J. Clin.*, 2021, **71**, 209–249.
161. J. Lopes, C. M. P. Rodrigues, M. M. Gaspar and C. P. Reis, *Cancers*, 2022, **14**, 4652.
162. (a) T. C. Johnstone, K. Suntharalingam and S. J. Lippard, *Chem. Rev.*, 2016, **116**, 436–3486; (b) J. J. Wilson and S. J. Lippard, *Chem. Rev.*, 2014, **114**, 4470–4495.

163. I. B. Lozada, B. Huang, M. Stilgenbauer, T. Beach, Z. Qiu, Y. Zheng, D. E. Herbert, *Dalton Trans.* 2020, **49**, 6557–6560.
164. C. J. Dhanaraj, I. Ul Hassan, J. Johnson, J. Joseph and R. S. Joseyphus, *J. Photochem. Photobiol. B.*, 2016, **162**, 115.
165. Q. X. Wang, W. Li, F. Gao, S. Li, J. Ni and Z. Zheng, *Polyhedron*, 2010, **29**, 539.
166. A. C. Komor and J. K. Barton, *Chem. Commun.*, 2013, **49**, 3617.
167. T. J. Peters, San Diego: Academic Press; 1995.
168. K. A. Majorek, P. J. Porebski, A. Dayal, M. D. Zimmerman, K. Jablonska, A. J. Stewart, M. Chruszcz, W. Minor, *Mol Immunol.*, 2012, **52**, 174.
169. F. Jalali, P. S. Dorraji, H. Mahdiuni, *J. Lumin.*, 2014, **148**, 347.
170. W. Bal, J. Christodoulou, P. J. Sadler, A. Tucker, *J. Inorg. Biochem.*, 1998, **70**, 33.
171. M. Gharagozlou, D. M. Boghaei, *Spectrochim. Acta A Mol. Biomol. Spectrosc.*, 2008, **71**, 1617.
172. P. Krishnamoorthy, P. Sathyadevi, A. H. Cowley, R. R. Butorac, N. Dharmaraj, *Eur. J. Med. Chem.*, 2011, **46**, 3376.
173. J. A. Mountzouris, L. H. Hurley In: S.M. Hecht Ed, *Bioorganic chemistry: nucleicacids*. Oxford University Press, New York, 1996, 288.
174. J. A. Cowan, *Curr. Opin. Chem. Biol.*, 2001, **5**, 634.
175. L. N. Ji, X. H. Zou and J. G. Liu, *Coord. Chem. Rev.*, 2001, **216**, 513.
176. H. Mei and J. Barton, *J. Am. Chem. Soc.*, 1986, **108**, 7414.
177. L. S. Lerman, *J. Mol. Biol.*, 1961, **3**, 18.
178. B. H. Geierstanger, D. E. Wemmer, R. Annu, *Biophys. Biomol. Struct.*, 1995, **24**, 463.
179. B. A. Armitage, *Top. Curr. Chem.*, 2005, **253**, 55.
180. F. Xue, C.-Z. Xie, Y.-W. Zhang, Z. Qiao, X. Qiao, J.-Y. Xu, S.-P. Yan, *J. Inorg. Biochem.*, 2012, **115**, 78.
181. F. Samari, B. Hemmateenejad, M. Shamsipur, M. Rashidi, H. Samouei, *Inorg. Chem.*, 2012, **51**, 3454.
182. M. Ehteshami, F. Rasoulzadeh, S. Mahboob, M.-R. Rashidi, *J. Lumin.*, 2013, **135**, 164.
183. B. J. Pages, D. L. Ang, E. P. Wright and J. R. Aldrich-Wright, *Dalton Trans.*, 2015, **44**, 3505.
184. H. Liu and P. J. Sadler, *Acc. Chem. Res.*, 2011, **44**, 349.
185. M. Lazoua, A. Tarushia, P. Gritzapisb and G. Psomas, *J. Inorg. Biochem.*, 2020, **206**, 111019.
186. E. Moradinia, M. Mansournia, Z. Aramesh-Boroujeni and A. Bordba, *Appl. Organometal. Chem.*, 2019, **33**, 4893.
187. N. Vamsikrishna, S. Daravath, N. Ganji, N. Pasha, Shivaraj, *Inorg. Chem. Commun.*, 2020, **113**, 107767.
188. M. Lazoua, A. Tarushia, P. Gritzapisb and G. Psomasa, *J. Inorg. Biochem.*, 2020, **206**, 111019.

189. D. Cocica, S. Jovanovica, S. Radisavljevic, J. Korzekwab, A. Scheurerb, R. Puchtab, D. Baskice, D. Todorovicf, S. Popovice, S. Maticg and B. Petrovic, *J. Inorg. Biochem.*, 2018, **189**, 91.
190. E. A. Popova, A. V. Protas, A. V. Mukhametshina, G. K. Ovsepyan, R. V. Suezov, A. V. Eremin, E. I. Stepchenkova, E. R. Tarakhovskaya, A. V. Fonin, G. L. Starova, O. V. Mikolaichuk, Y. B. Porozov, M. A. Gureev and R. E. Trifonov, *Polyhedron*, 2019, **158**, 36.
191. G. Onar, C. Gürses, M. O. Karatas, S. Balcioglu, N. Akbay, N. Ozdemir, B. Ates, B. Alici, *J. Organomet. Chem.*, 2019, **886**, 48.
192. A. Ziannaa, G. D. Geromichalosa, A. G. Hatzidimitrioua, E. Coutouli-Argyropouloub, M. Lalia-Kantouria, G. Psomas, *J. Inorg. Biochem.*, 2019, **194**, 85.
193. A. Querino, J. Silva, J. Teixeira Silva, G. M. Alvarenga, C. H. Silveira, M. T. Q. Magalhaes, O. A. Chaves, B. A. Iglesias, R. Diniz and H. Silva, *J. Biol. Inorg. Chem.*, 2019, **24**, 1087.
194. Q. Wang, Z. Y. Yang, G. F. Qi, D. D. Qin, *Eur. J. Med. Chem.*, 2009, **44**, 2425.
195. X. H. Zou, B. H. Ye, H. Li, J. G. Liu, Y. Xiong, L. N. Ji, *J. Chem. Soc., Dalton Trans.*, 1999, 1423.
196. F. Q. Liu, Q. X. Wang, K. Jiao, F. F. Jian, G. Y. Liu and R. X. Li, *Inorg. Chim. Acta.*, 2006, **359**, 1524.
197. D. Lawrence, V. G. Vaidyanathan and B. Unni Nair, *J. Inorg. Biochem.*, 2006, **100**, 1244.
198. E. C. Long and J. K. Barton, *Acc. Chem. Res.*, 1990, **23**, 271.
199. S. Tabassum and I. U. H. Bhat, *Chem. Pharm. Bull.*, 2010, **58**, 318.
200. A. Wolfe, G. H. Shimer Jr., T. Meehan, *Biochemistry.*, 1987, **26**, 6392.
201. A. Ray, B. Koley Seth, U. Pal and S. Basu, *Spectrochim. Acta A Mol. Biomol. Spectrosc.*, 2012, **92**, 164.
202. M. R. Eftink and C. A. Ghiron, *Anal. Biochem.*, 1981, **114**, 199.
203. S. Mandal, S. K. Tarai, P. Patra, P. Nandi, S. Sing, B. Rajak and S. C. Moi, *Langmuir*, 2022, **38**, 13613.
204. L. Côte-Real, V. Pósa, M. Martins, R. Colucas, N. V. May, X. Fontrodona, I. Romero, F. Mendes, C. P. Reis, M. M. Gaspar, J. C. Pessoa, É. A. Enyedy, and I. Correia, *Inorg. Chem.*, 2023, **62**, 11466.
205. C. Kakoulidou, C. T. Chasapis, A. G. Hatzidimitriou, K. C. Fylaktakidou and G. Psomas, *Dalton Trans.*, 2022, **51**, 16688.

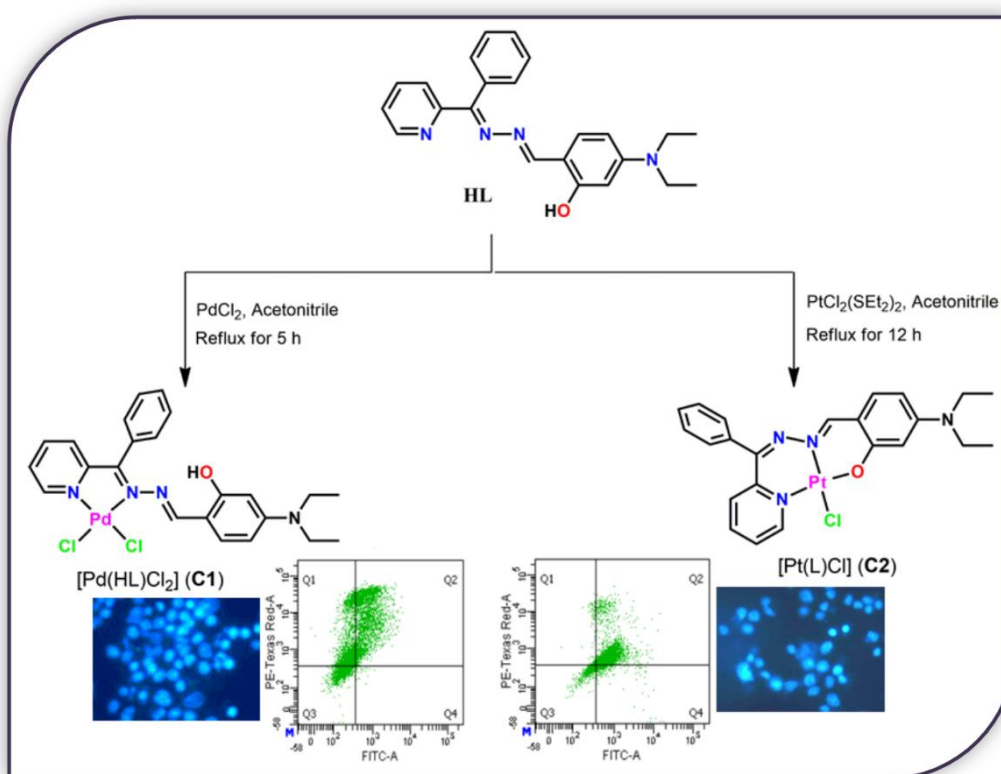
## **CHAPTER - II**

**Palladium(II) and Platinum(II) complexes with  
ONN donor pincer ligand: Synthesis,  
characterization and *in vitro* cytotoxicity study**

## *Palladium(II) and Platinum(II) complexes with ONN donor pincer ligand: synthesis, characterization and in vitro cytotoxicity study*

### Abstract

New Pd(II) and Pt(II) complexes,  $[Pd(HL)Cl_2]$  (**C1**) and  $[Pt(L)Cl]$  (**C2**) with ONN donor pincer ligand, 5-(diethylamino)-2-((Z)-((E)-(phenyl(pyridin-2-yl)methylene)hydrazono)methyl)phenol (HL) were synthesized and thoroughly characterized using spectroscopic techniques. X-ray structures of the complexes revealed that HL acts as bidentate N,N and tridentate O,N,N chelator in Pd(II) and Pt(II) complexes, respectively. The antiproliferative activity of the complexes was explored against four different human cancer (MCF-7, HCT116, A549, HepG2) cell lines. However, the maximum cytotoxicity was seen in the HepG2 cell line  $[IC_{50} = 6-12 \mu M]$  for both the complexes.  $IC_{50}$  for both complexes, **C1** and **C2**, toward human peripheral blood mononuclear cells (hPBMC) cells were found to be  $>200 \mu M$ . The cytotoxicity of platinum complex (**C2**) was comparable to that of the cisplatin in HepG2 cell lines.





### II.1. Introduction

According to WHO, cancer is the second major reason of death worldwide.<sup>1</sup> So any new effective anticancer agents with nominal side effects remain of crucial significance to the world research society.<sup>2-4</sup> The advancement of drug resistance and disease relapse are foremost challenges in anticancer drug design.<sup>5</sup> Now metals have always been handy in dealing with a variety of illnesses found globally.<sup>6</sup> Owing to their exclusive nature, metal complexes, particularly those consisting of transition metals have achieved remarkable consideration as anticancer agents.<sup>7</sup> Transition metal complexes as antitumor agents have been broadly utilized after *cis*-platin proved to be so successful as an anti-cancer drug. Lately, *cis*-platin has been recognized as one of the most extensively used antitumor drugs in the world due to its high effectiveness for testicular and ovarian cancers and in the treatment of cervical, bladder and many other varieties of carcinoma.<sup>8</sup> Nevertheless, regardless of the positive outcomes of platinum compounds in destroying cancer cells, they also have lethal side effects which include nausea, vomiting, lessening of blood cell and platelet production in bone marrow thereby affecting response to infection.<sup>9</sup> Hence to prevail over these drawbacks, numerous platinum complexes were designed and fabricated and examined for their anticancer activities.<sup>10-12</sup> The cytotoxic properties of these Pt(II) complexes were evaluated with respect to cell growth inhibition against different types of human cancer cell lines.

On the other hand, other than the platinum compounds, the palladium(II) compounds are the ones that are being used for cancer treatment as palladium(II) derivatives have antitumor activity similar to the *cis*-platin drug and they also show a lesser amount of kidney toxicity.<sup>13-15</sup> Thus the development of new palladium based anti-cancer drugs is very crucial for effective and efficient use as chemotherapeutic agents. So far significant importance has been given in studying Pd(II) complexes as anticancer drugs,<sup>16-20</sup> among all the other metal ions owing to its numerous resemblance with Pt(II). Although one obstacle of this Pd-based anticancer drugs is that the ligand-exchange and a quation rates of Pd(II) complexes are about 105 times faster than those of the Pt(II) analogues.<sup>21</sup> So, palladium could prevent interaction with the target DNA by associating with the other donor groups present in the bloodstream thereby enhancing their toxicity and diminishing their beneficial potential. Hence an appropriate choice of ligands is vital in order to fabricate a better and competitive palladium complex based anticancer agents.<sup>15</sup> Additionally, the palladium compounds have improved solubility compared to Pt(II) analogues generally. Recent studies reveal that numerous Pd(II)

compounds demonstrated a vastly proficient biological activity *in vitro* which is mostly notably preferable than their Pt(II) equivalents or cisplatin.<sup>13-15,22</sup>

Metal complexes have achieved an escalating attention and significance in medicinal chemistry since the discovery of anticancer activity of cisplatin, *cis*-[PtCl<sub>2</sub>(NH<sub>3</sub>)<sub>2</sub>].<sup>23-27</sup> The more efficient and less lethal second- and third-generation platinum-based anticancer agents, carboplatin and oxaliplatin were effectively tested and eventually achieved global scientific recognition.<sup>28</sup> Regardless of the extensive use of *cis*-platin (cis-diamminedichloroplatinum(II)) and second-generation platinum compounds as anticancer drugs in healthcare organizations,<sup>29</sup> the disadvantages such as systemic toxicity, the generation of resistance and the deficiency of selectivity have driven several scientists to get involved in the fabrication of metal compounds with non-classical anticancer mechanisms.<sup>30-38</sup> The binding of cisplatin to DNA is usually acknowledged to be accountable for the cytotoxicity of this drug<sup>38-40</sup> and so as a result, the concept of a novel design of platinum compounds should be taken as the major task to yield new anticancer agents with a diverse range of biological activity, along with improved toxicological and pharmacokinetics properties.<sup>31,32,40-42</sup>

The ligand, 5-(diethylamino)-2-((Z)-((E)-(phenyl(pyridin-2-yl)methylene)hydrazono)methyl)phenol (HL) used in this current article, to fabricate the palladium and platinum complexes was reported by our group earlier<sup>43</sup> although the previous report was regarding the selectivity and sensitivity mechanism and studies with Zn(II) and Hg(II). In this paper, we have investigated the coordination behaviour of ONN donor pincer ligand (HL) towards Pd(II) and Pt(II) through synthesizing Pd(II) and Pt(II) complexes having general formula, [Pd(HL)Cl<sub>2</sub>] (**C1**) and [Pt(L)Cl] (**C2**) and characterizing both of them by using spectrometric techniques like NMR, IR, Mass, UV-Vis as well as single crystal X-ray diffraction study. Cytotoxicity study of the complexes was carried out on human liver (HepG2), colorectal (HTCT116), human breast (MCF-7) and human lung (A549) cancer cell lines along with cell imaging studies in HepG2 cell line which explains the DNA fragmentation. Cell migration study has also been executed to observe the inhibitory action of both Pd(II) and Pt(II) complexes in HepG2 cell line. To elucidate the electronic structure and UV-Vis spectra of the complexes DFT and TD-DFT calculations were executed.

## II.2. Experimental

### II.2.1. Materials and methods

All reagents and solvents used in this synthesis were purchased from Aldrich. All other organic chemicals and inorganic salts were available from commercial sources and used without further purification. Ligand HL was synthesized following the published procedure.<sup>43</sup> Dulbecco's modified Eagle's medium (DMEM), Fetal Bovine Serum (FBS), penicillin, streptomycin, neomycin (PSN) antibiotic, ethylenediaminetetraacetic acid (EDTA) and trypsin were bought from Gibco BRL (Grand Island, NY, USA). 3-(4, 5-Dimethylthiazol-2-yl)-2,5-diphenyltetrazolium bromide (45989, MTT-CAS298-93-1-Calbiochem), DMSO, Flow Collect Annexin Red kit (Cat. No. FCCH100108) were bought from Merck-Millipore. Tissue culture plastic wares were bought from Genetix Biotech Asia Pvt. Ltd. Zinc acetate was purchased from Sigma-Aldrich. HepG2 cell line was obtained from National Centre for Cell Science (NCCS), Pune.

<sup>1</sup>H, <sup>1</sup>H-<sup>1</sup>H-2D COSY and <sup>13</sup>C NMR spectra were recorded on Bruker 300 MHz instrument in CDCl<sub>3</sub>. Chemical shifts are expressed in  $\delta$  units and <sup>1</sup>H-<sup>1</sup>H and <sup>1</sup>H-C coupling constants in Hz. HRMS mass spectra were recorded on Waters quadrupole time-of-flight mass spectrometer (Xevo G2 Q-TOF). Electronic spectra were taken on a Shimadzu UV-1900i spectrophotometer. IR spectra were recorded on PerkinElmer Spectrum Two FT-IR Spectrometer.

### II.2.2. Synthesis

#### II.2.2.1. Synthesis of Pd(II) complex, [Pd(HL)Cl<sub>2</sub>] (C1)

At first, PdCl<sub>2</sub> (0.087 g, 0.5 mmol) was dissolved in acetonitrile and then the solution was added to the solution of previously synthesized ligand, HL (0.186 g, 0.5 mmol) and refluxed for 5 h. After completion of the reaction, the resulted mixture was cooled to room temperature and filtered. The solvent was then removed under reduced pressure to yield a red coloured solid mass of complex **C1**. The yield was, 0.187 g, 71%.

Anal. Calc. for C<sub>23</sub>H<sub>24</sub>Cl<sub>2</sub>N<sub>4</sub>OPd: C, 50.25; H, 4.40; N, 10.19. Found: C, 49.97; H, 4.21; N, 9.95. IR (KBr, cm<sup>-1</sup>): 3455  $\nu$ (O-H); 3055, 2970, 2918  $\nu$ (C-H); 1616  $\nu$ (C=N). <sup>1</sup>H NMR (300 MHz, CDCl<sub>3</sub>):  $\delta$  1.13-1.23 (m, 6H), 3.34-3.43 (m, 4H), 6.27 (d, J = 9 Hz, 1H), 6.33 (s, 1H), 7.07 (d, J = 9 Hz, 1H), 7.36 (t, J = 6 Hz, 2H), 7.48-7.59 (m, 5H), 7.80 (t, J = 9 Hz, 1H), 8.19 (s, 1H), 10.24 (d, J = 5 Hz, 1H), 11.63 (s, 1H). HRMS: calculated for C<sub>23</sub>H<sub>24</sub>ClN<sub>4</sub>OPd [M-Cl]<sup>+</sup> (m/z): 513.0673; found: 513.0325. UV-Vis (in CH<sub>3</sub>CN),  $\lambda_{\max}$  ( $\epsilon$ , M<sup>-1</sup>cm<sup>-1</sup>): 267 (7478), 325 (12100), 354 (sh.), 453 (sh.), 496 (13860).

**II.2.2.2. Synthesis of Pt(II) complex, [Pt(L)Cl] (C2)**

To synthesize [Pt(L)Cl] (**C2**) complex, mixture of HL (0.074 g, 0.2 mmol) and  $\text{PtCl}_2(\text{SEt}_2)_2$  (0.089 g, 0.2 mmol) in 10 mL acetonitrile was refluxed for 12 h. After completion of the reaction, the mixture was cooled to room temperature and then filtered. The solvent was then removed under reduced pressure to yield a deep red coloured solid mass of complex **C2**. The yield was, 0.086 g, 72%.

Anal. Calc. for  $\text{C}_{23}\text{H}_{23}\text{ClN}_4\text{OPt}$ : C, 45.89; H, 3.85; N, 9.31. Found: C, 45.67; H, 3.72; N, 9.15. IR (KBr,  $\text{cm}^{-1}$ ): 3051, 2971, 2923  $\nu(\text{C-H})$ , 1608  $\nu(\text{C=N})$ .  $^1\text{H}$  NMR (300 MHz,  $\text{CDCl}_3$ ):  $\delta$  1.15-1.24 (m, 6H), 3.35-3.42 (m, 4H), 6.24 (d,  $J = 6$  Hz, 1H), 6.36 (s, 1H), 7.16-7.2 (m, 1H), 7.41 (d,  $J = 6$  Hz, 1H), 7.5-7.64 (m, 6H), 7.89 (t,  $J = 9$  Hz, 1H), 10.70 (d,  $J = 6$  Hz, 1H). HRMS: calculated for  $\text{C}_{23}\text{H}_{23}\text{N}_4\text{OPt} [\text{M} - \text{Cl}]^+$  ( $m/z$ ): 566.1520; found: 566.1490. UV-Vis (in  $\text{CH}_3\text{CN}$ ),  $\lambda_{\text{max}}$  ( $\epsilon$ ,  $\text{M}^{-1}\text{cm}^{-1}$ ): 270 (9068), 348 (14258), 438 (9778), 505 (16277).

**II.2.3. Theoretical study**

Full geometry optimizations were carried out by density functional theory (DFT) method using B3LYP<sup>44</sup> hybrid exchange correlation functional for the complexes. All elements except Pd and Pt were assigned the 6-31G(d) basis set. LanL2dz<sup>45</sup> basis set with effective core potential was employed for Pd and Pt atoms. Vibrational frequency calculations were performed on the optimized geometries to ensure that each configuration is indeed a local minimum on the potential energy surface. All calculations were performed with Gaussian09 program<sup>46</sup> with the aid of the Gauss-View, Version 5 visualization program. Electronic transitions were calculated using the time-dependent density functional theory (TDDFT) formalism<sup>47</sup> using conductor-like polarizable continuum model (CPCM)<sup>48</sup> in acetonitrile to simulate the solvent. GaussSum<sup>49</sup> was used to calculate the fractional contributions of various groups to each molecular orbital.

**II.2.4. Crystal structure determination and refinement**

Details of crystal analysis, data collection and structure refinement data for  $[\text{Pd}(\text{HL})\text{Cl}_2]$  (**C1**) and  $[\text{Pt}(\text{L})\text{Cl}]$  (**C2**) are given in Table II.1. Diffraction data was collected using Bruker AXS D8 Quest CMOS diffractometer using graphite monochromatized Mo- $\text{K}\alpha$  radiation ( $\lambda = 0.71073$  Å) at 293°C. Reflection data were recorded using the  $\omega$  scan technique. The data were integrated using the SAINT program<sup>50</sup>, and the absorption corrections were made with SADABS<sup>51</sup>. All data were corrected for Lorentz and polarization effects, and the non-hydrogen atoms were refined anisotropically. Hydrogen atoms were included in the

refinement process as per the riding model. The structures were solved by direct method and refined using SHELXL-2016/6 program<sup>52</sup> by full-matrix least-squares techniques.

Table II.1. Crystallographic data and refinement parameters of **C1** and **C2**

Complex	[Pd(HL)Cl <sub>2</sub> ] ( <b>C1</b> )	[Pt(L)Cl] ( <b>C2</b> )
Formula	C <sub>23</sub> H <sub>24</sub> Cl <sub>2</sub> N <sub>4</sub> OPd	C <sub>23</sub> H <sub>23</sub> ClN <sub>4</sub> OPt
Formula Weight	549.76	601.99
Crystal System	<i>Triclinic</i>	<i>Triclinic</i>
Space group	<i>P</i> - <i>1</i>	<i>P</i> - <i>1</i>
a, b, c [Å]	9.2645(16), 10.3915(18), 24.989(4)	8.3273(7), 10.4097(8), 13.1711(11)
α	80.629(4)	76.354(3)
β	84.019(4)	79.382(3)
γ	79.944(4)	79.593(3)
V [Å <sup>3</sup> ]	2330.1(7)	1079.20(15)
Z	4	2
D(calc) [g/cm <sup>3</sup> ]	1.567	1.853
Mu(MoKa) [ /mm]	1.048	6.647
F(000)	1112	584
Temperature (K)	293(2)	293(2)
Radiation [Å]	0.71073	0.71073
θ(Min-Max) [°]	2.012 - 25.000	2.034 - 25.499
Dataset (h; k; l)	-11 to 11, -12 to 12, -29 to 29	-10 to 10, -12 to 12, -15 to 15
R, wR <sub>2</sub>	0.0983, 0.1925	0.0462, 0.1083
Goodness of fit(S)	1.071	1.031

Table II.2. Some selected X-ray and calculated bond distances and angles of **C1** and **C2**

<b>C1</b>			<b>C2</b>		
Bonds(Å)	X-ray	Calc.	Bonds(Å)	X-ray	Calc.
Pd1-N2	2.065(8)	2.028	Pt1-N2	1.971(6)	2.021
Pd1-N1	2.067(8)	2.044	Pt1-N1	2.014(6)	2.055
Pd1-Cl1	2.270(3)	2.263	Pt1-O1	1.989(5)	2.014
Pd1-Cl2	2.290(3)	2.294	Pt1-Cl1	2.329(2)	2.381
N2-N3	1.363(12)	1.396	N2-N3	1.394(9)	1.352
O1-C15	1.348(14)	1.347	O1-C15	1.296(10)	1.298
Angles (°)					
Cl1-Pd1-Cl2	89.33(11)	89.73039	O1-Pt1-N1	172.4(2)	174.348
N2-Pd1-N1	81.3(3)	80.74118	O1-Pt1-N2	92.5(2)	92.304
N2-Pd1-Cl1	95.5(2)	95.21670	O1-Pt1-Cl1	82.41(18)	83.269
N2-Pd1-Cl2	174.9(2)	175.03813	N2-Pt1-N1	91.9(2)	90.964
N1-Pd1-Cl1	176.9(2)	175.05901	N2-Pt1-Cl1	170.6(2)	173.729
N1-Pd1-Cl2	93.8(2)	94.33672	N1-Pt1-Cl1	94.04(18)	93.812

### **II.2.5. In Vitro Cytotoxicity Study**

#### **II.2.5.1. Cell Culture**

HepG2 cells were cultured in DMEM mixed with 10% FBS and 1% antibiotic (PSN) at 37°C in humidified incubator with 5% CO<sub>2</sub>. The HepG2 cell line was cultured in DMEM containing 10% FBS at 37°C in a humidified atmosphere under 5% CO<sub>2</sub>. Cells were harvested with 0.5% trypsin and seeded at a required density to allow them to re-equilibrate a day before the start of experiment. All experiments were conducted in DMEM containing 10% FBS and 1% PSN antibiotic.

#### **II.2.5.2. Cell Viability Assay**

MTT [(4,5-dimethyl-thiazol-2-yl)-2,5-diphenyl tetrazolium bromide] assay was carried out to determine the cytotoxic effect of palladium(II) and platinum(II) complexes **C1** and **C2**. Cells (1×10<sup>6</sup>/well) were seeded in 96-well plate and treated with different concentrations of **C1** and **C2** (2.5, 5, 10, 20, 40, 60, 80 and 100µM) and were kept in incubator for 24h at 37°C in a humidified (5%CO<sub>2</sub>) atmosphere. After 24h incubation MTT (4 mg/mL) was added and the plates were further incubated for another 4h. At 595 nm the absorbance of DMSO-solubilized intracellular formazan salt was recorded using ELISA reader. This experiment was done in triplicate.

#### **II.2.5.3. Detection of DNA fragmentation/cell death by ELISA**

Cell death was assessed using an ELISA based cell death detection that quantitatively detects histone exposed from DNA fragments. Briefly, cells treated with or without different concentrations of two complexes for 24 h were lysed and centrifuged. Supernatant containing histone containing DNA fragments were taken as source of antigen in a sandwich ELISA with primary anti-histone monoclonal antibody coated to the streptavidin-coated well. This was followed by a second anti-DNA monoclonal antibody coupled to peroxidase. The amount of histones was measured by the peroxidase retained in the immune-complex. Peroxidase activity was determined spectrophotometrically at 405 nm with 2,2-azino-di (3-ethylbenzthiazolin-sulfonate) (ABTS) as a substrate.

#### **II.2.5.4. Cell Imaging Study**

HepG2 cells were used as model for further study on cytotoxicity induced by the complexes. Cancer cell death through apoptosis is a desirable aim. Characteristic apoptotic changes in cell morphology like cell shrinkage and cell rounding were observed in complex treated cells in fluorescence microscopy.



### II.2.5.5. In Vitro Cell Migration Assay

Cells were grown in 12-well plates for 24 h. A straight scratch was made on the confluent cell using a pipette tip following the washing with PBS for three times. Then the cells were treated with **C1** and **C2** in serum-free DMEM medium. After incubating for 0 h, 12 h and 24 h, the gap width of scratch repopulation was measured and recorded which was then compared with the initial gap size at 0 h. The gap was measured using ImageJ image processing program and the size of the denuded area was determined at each time point from the digital images.

### II.2.5.6. Quantification of Apoptosis by Flow Cytometry

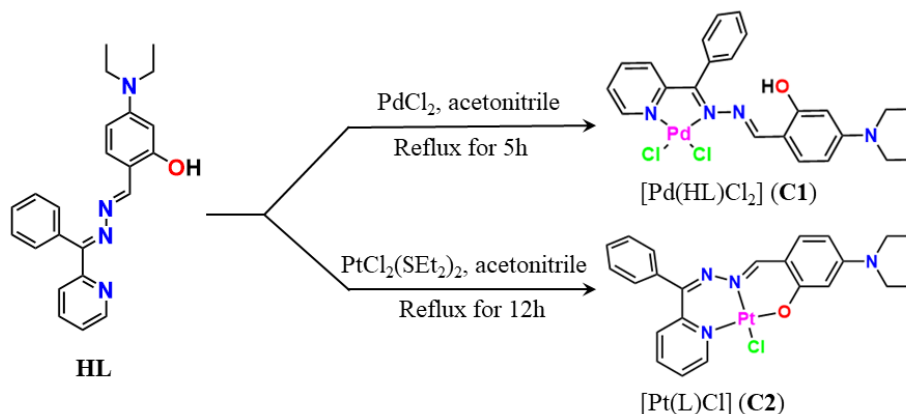
Determination of apoptosis and necrosis were analyzed by flow cytometry using Annexin-V/FITC/PI detection kit (Calbiochem, CA, USA). HepG2 cells were seeded in a 6 well plate and treated with both **C1** and **C2** ( $IC_{70}$ ) for 24h and were stained with Annexin-V/FITC-PI as per the direction of manufacturer. The percentage of viable, apoptotic (early and late), necrotic cells were calculated by flow cytometry (BD LSR Fortessa, San Jose, CA, USA).

### II.2.5.7. Cell cycle analysis

After treatment with the complexes **C1** and **C2**, cells were pelleted and fixed overnight in 70% ethanol at 4°C. Next day the cells were pelleted and suspended in PBS containing 25 µg/ml RNase and Triton X-100 (0.5%) and incubated for 1 h at 37°C. Next, they were stained with 50 µg /ml PI at 4°C for 15 min and analysed using flow cytometry. A total of  $1 \times 10^4$  cells were counted.

## II.3. Results and discussion

Synthesis of palladium(II) and platinum(II) complexes,  $[Pd(HL)Cl_2]$  (**C1**) and  $[Pt(L)Cl]$  (**C2**) involved the reaction of previously reported NNO donor pincer ligand, 5-(diethylamino)-2-((Z)-(E)-(phenyl(pyridin-2-yl)methylene)hydrazono)methylphenol (HL)<sup>43</sup> with  $PdCl_2$  and  $PtCl_2(SEt_2)_2$  respectively under reflux condition in acetonitrile (scheme II.1). The chemical structures of both **C1** and **C2** were confirmed by  $^1H$  NMR spectroscopy and ESI mass spectrometry along with single crystal X-ray crystallography method.



Scheme II.1. Synthetic scheme for  $[\text{Pd}(\text{HL})\text{Cl}_2]$  (**C1**) and  $[\text{Pt}(\text{L})\text{Cl}]$  (**C2**)

### II.3.1. Spectral studies

IR spectrum of **C1** displays a broad peak at  $3459\text{ cm}^{-1}$  corresponds to  $\nu(\text{O-H})$  stretching while the peaks at  $2970\text{--}3055\text{ cm}^{-1}$  and  $1616\text{ cm}^{-1}$  corresponding to  $\nu(\text{C-H})$  and  $\nu(\text{C=N})$  respectively (Fig. II.1). IR spectrum of **C2** exhibits  $\nu(\text{C-H})$  at  $2923\text{--}2971\text{ cm}^{-1}$  while  $\nu(\text{C=N})$  appears at  $1608\text{ cm}^{-1}$  (Fig. II.1).  $\nu(\text{C=N})$  for free **HL** ( $1632\text{ cm}^{-1}$ ) (Fig. II.1) is significantly shifted to lower frequency region ( $1608\text{--}1616\text{ cm}^{-1}$ ) upon complexation with Pd(II) and Pt(II). Similarly, the  $\nu(\text{O-H})$  stretching frequency ( $3460\text{ cm}^{-1}$ ) of **HL** disappeared due to the formation of O-Pt bond in **C2**.  $^1\text{H}$  NMR spectra of **C1** and **C2** were recorded in  $\text{CDCl}_3$ . In case of **C1**, the peak at 8.19 ppm corresponds to the imine ( $\text{N=CH}$ ) proton while the O-H proton appears at 11.63 ppm (Fig. II.2). The aromatic protons appear at the region of 6.23–7.83 ppm. The proton ortho to the coordinated pyridyl-N appeared as doublet in the downfield region (10.24 ppm) compare to the free ligand ( $\sim 8.7$  ppm), this downfield shift is because of the coordination of pyridyl-N with Pd(II). The O-H proton signal for free **HL** at 11.59 ppm<sup>43</sup> disappeared in Pt(II) complex (**C2**) due to the dissociation of O-H bond and coordination of O atom to Pt(II) (Fig. II.3). Imine ( $\text{CH=N}$ ) proton appears as singlet at 8.59 ppm and  $\text{HC=N}$  (pyridyl) proton, H1 appears as doublet at 10.7 ppm.

To better understand the coupling of neighbouring protons,  $^1\text{H}$ - $^1\text{H}$ -2D COSY NMR spectra of the complexes were taken. The coupling of H1 proton ( $\text{HC=N}$  (pyridyl)) with the neighbour H2 proton (at 7.36 ppm) is seen in the  $^1\text{H}$ - $^1\text{H}$ -2D COSY NMR spectra of both the complexes (Figs. II.4 and II.5). The coupling between  $\text{H}_a$  and  $\text{H}_b$  aromatic is also observed in the aromatic region. The  $-\text{CH}_2$  and  $-\text{CH}_3$  protons of  $-\text{CH}_2\text{CH}_3$  moiety appear as multiplet at 3.34–3.43 ppm and 1.13–1.24 ppm probably because of the two different types

(diastereotopic) of  $-\text{CH}_2$  protons and also diastereotopic protons of  $-\text{CH}_3$  group. This connection between  $-\text{CH}_2$  protons with  $-\text{CH}_3$  protons is seen in the  $^1\text{H}$ - $^1\text{H}$ -2D COSY NMR spectra of the complexes. Mass spectrum of  $[\text{Pd}(\text{HL})\text{Cl}_2](\text{C1})$  shows  $m/z$  peak corresponding to  $[\text{M}-\text{Cl}]^+$  at 513.0325 (Fig. II.6) while  $[\text{Pt}(\text{L})\text{Cl}](\text{C2})$  exhibits  $m/z$  peak at 566.1490 corresponds to  $[\text{M}-\text{Cl}]^+$  (Fig. II.7).

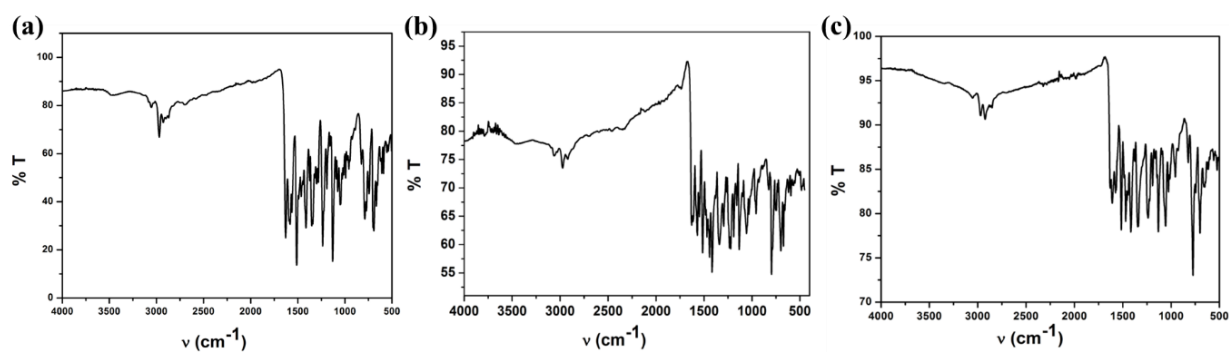


Figure II.1. IR spectra of (a) ligand (**HL**), (b)  $[\text{Pd}(\text{HL})\text{Cl}_2]$  (**C1**) and (c)  $[\text{Pt}(\text{L})\text{Cl}]$  (**C2**)

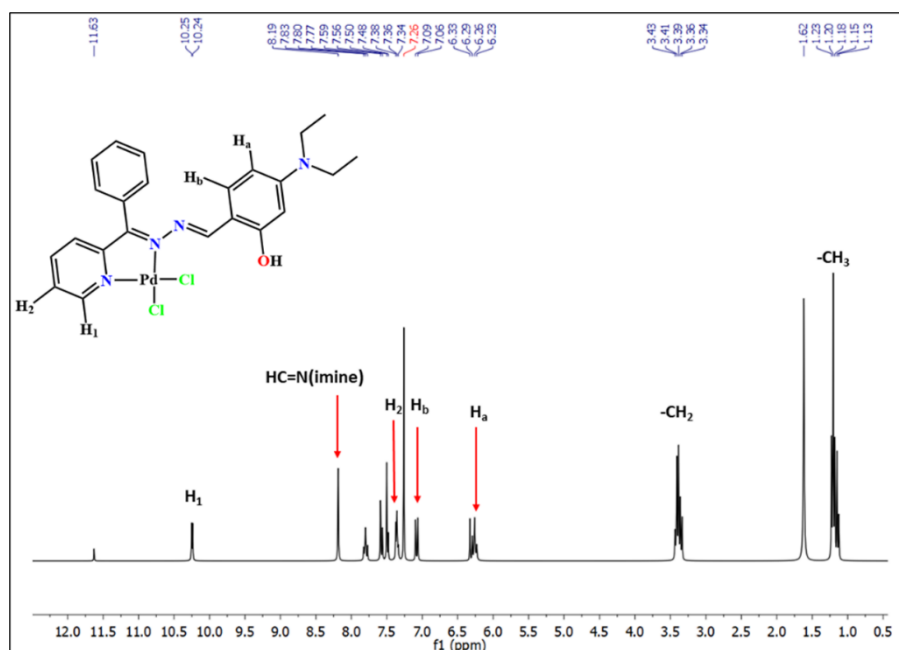
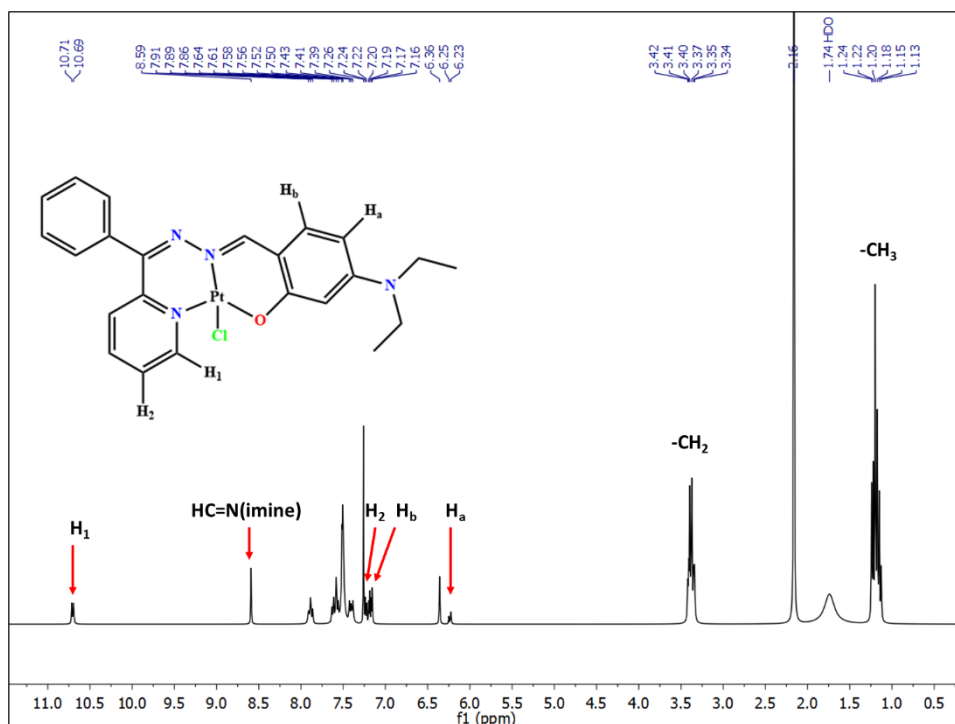
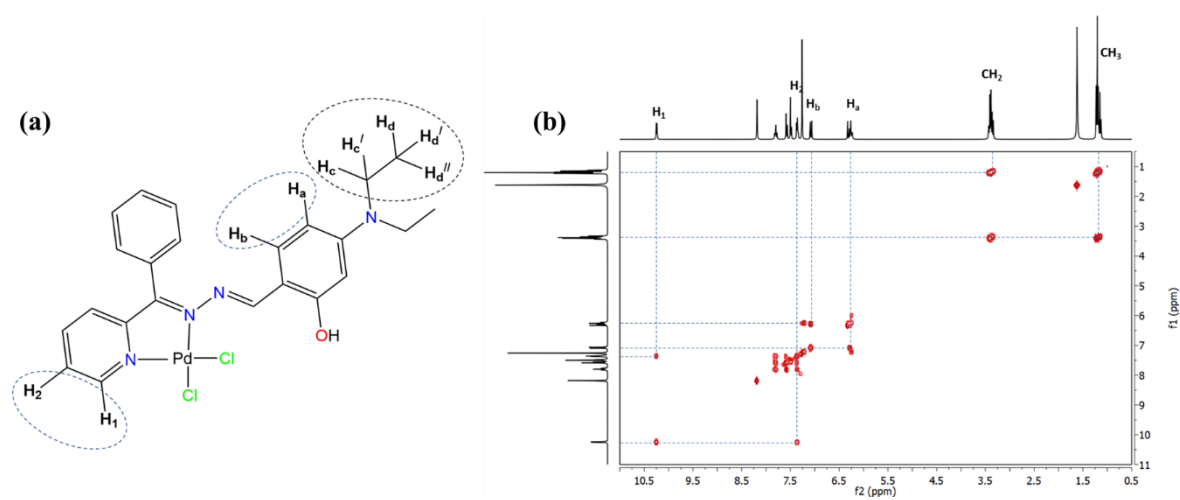


Figure II.2. IR spectra of complex  $[\text{Pd}(\text{HL})\text{Cl}_2]$  (**C1**) in  $\text{CDCl}_3$

Figure II.3. IR spectra of complex [Pt(L)Cl] (**C2**) in CDCl<sub>3</sub>Figure II.4. (a) Coupling between H<sub>1</sub> and H<sub>2</sub>, between H<sub>a</sub> and H<sub>b</sub> and diastereotopic hydrogens (H<sub>c</sub>, H<sub>c'</sub>, H<sub>d</sub>, H<sub>d'</sub> and H<sub>d''</sub>) in **C1** and (b) <sup>1</sup>H-<sup>1</sup>H-2D COSY NMR spectrum of **C1** in CDCl<sub>3</sub>

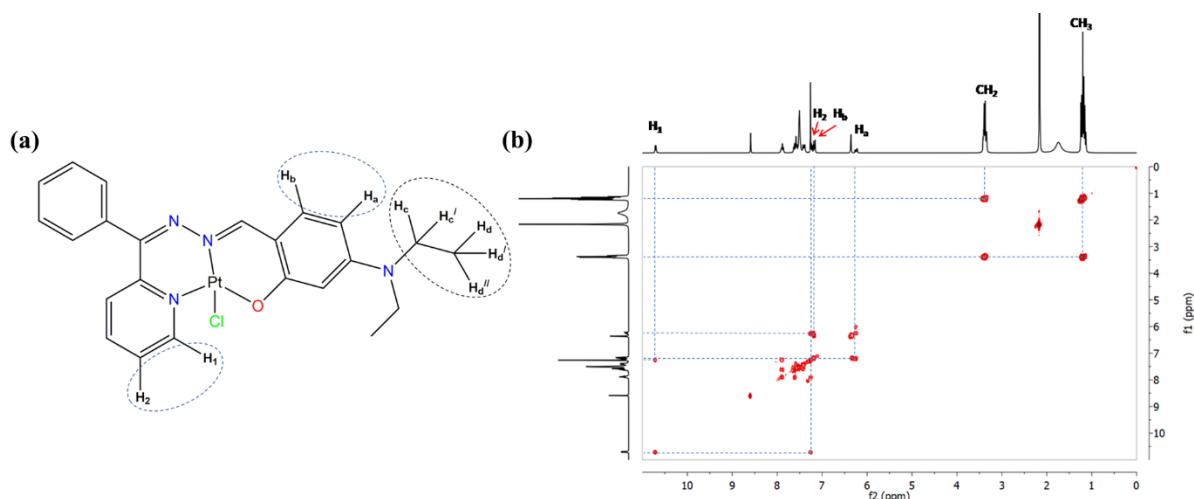


Figure II.5. (a) Coupling between  $H_1$  and  $H_2$ , between  $H_a$  and  $H_b$  and diastereotopic hydrogens ( $H_c$ ,  $H_c'$ ,  $H_d$ ,  $H_d'$  and  $H_d''$ ) in **C2** and (b)  $^1\text{H}$ - $^1\text{H}$ -2D COSY NMR spectrum of **C2** in  $\text{CDCl}_3$

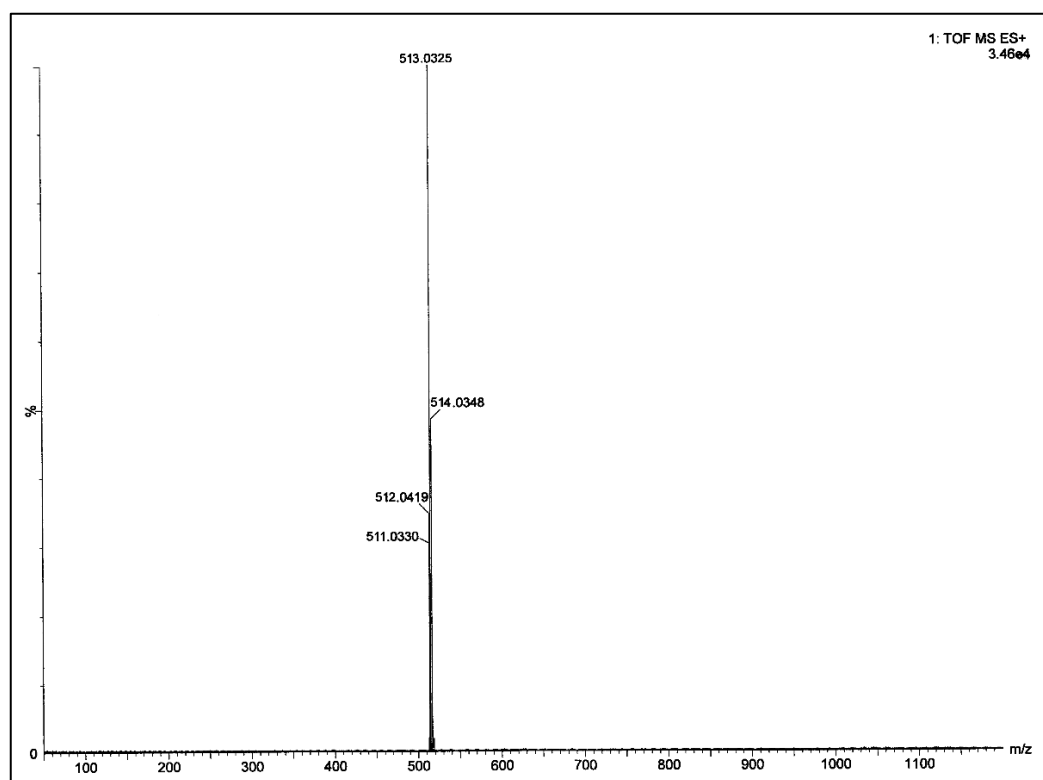


Figure II.6. HRMS of  $[\text{Pd}(\text{HL})\text{Cl}_2]$  (**C1**) in acetonitrile

Absorption spectra of **C1** and **C2** complexes were taken in acetonitrile. **C1** exhibits one sharp moderately intense low energy peak at 496 nm ( $\epsilon$ ,  $13860 \text{ M}^{-1}\text{cm}^{-1}$ ) along with a shoulder band at 453 nm. A sharp high energy band appears at 325 nm ( $\epsilon$ ,  $12100 \text{ M}^{-1}\text{cm}^{-1}$ ) along with two shoulder peaks at 267 and 354 nm (Fig. II.8). For **C2** the low energy band is slightly red

shifted and appears at 505 nm ( $\epsilon$ ,  $16277 \text{ M}^{-1}\text{cm}^{-1}$ ). A low energy shoulder peak appears at 438 nm. A high energy sharp band observed at 348 nm ( $\epsilon$ ,  $14258 \text{ M}^{-1}\text{cm}^{-1}$ ) along with a shoulder peak at 270 nm (Fig. II.8).

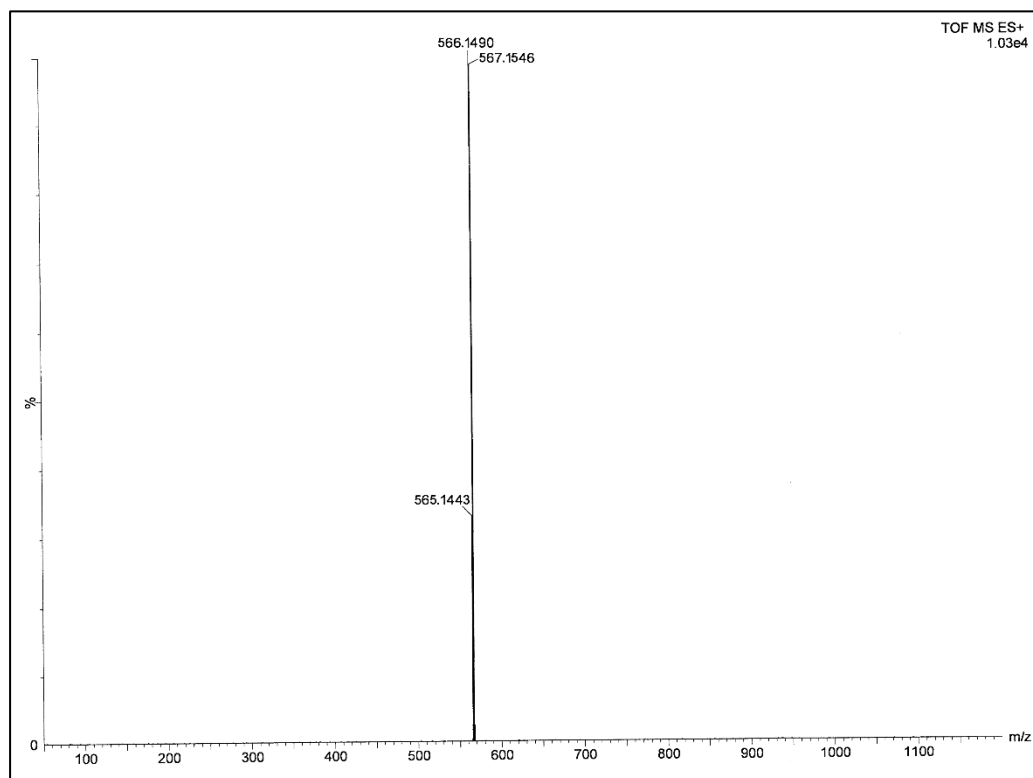


Figure II.7. HRMS of  $[\text{Pt}(\text{L})\text{Cl}]$  (**C2**) in acetonitrile

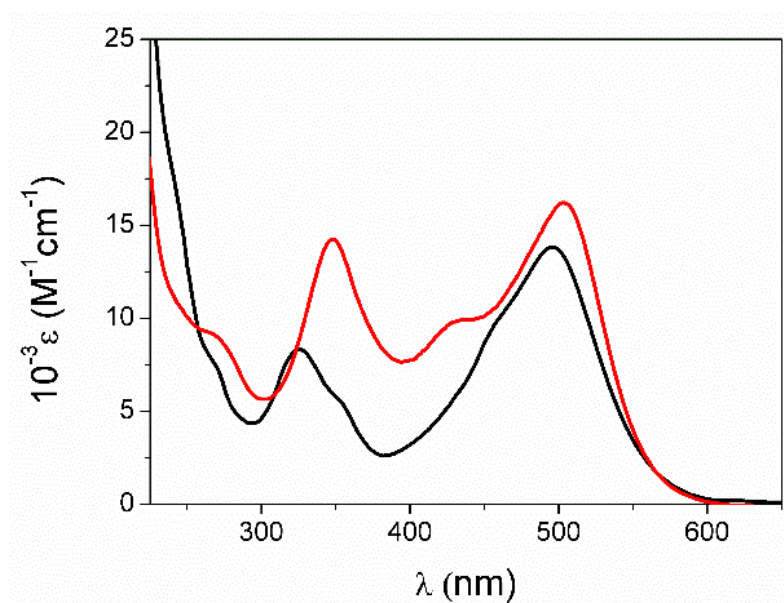


Figure II.8. UV-Vis spectra of  $[\text{Pd}(\text{HL})\text{Cl}_2]$  (**C1**) and  $[\text{Pt}(\text{L})\text{Cl}]$  (**C2**) in acetonitrile

### II.3.2. Crystallographic study

The structure of  $[\text{Pd}(\text{HL})\text{Cl}_2]$  (**C1**) and  $[\text{Pt}(\text{L})\text{Cl}]$  (**C2**) were determined by single crystal X-ray diffraction method. The ORTEP plots of **C1** and **C2** are shown in Figure II.9. HL acts as tridentate N, N, O donor pincer ligand in the complexes. In complex **C1**, Pd metal is coordinated with HL through imine nitrogen atom (N2) and pyridyl nitrogen atom (N1) via formation five-membered (Pd1-N2-C6-C5-N1) chelate ring with chelate bite angle  $\angle\text{N2-Pd1-N1}$ ,  $81.3(3)^\circ$ . In complex **C2**, Pt metal is coordinated with HL through imine nitrogen atom (N2), pyridyl nitrogen atom (N1) and oxygen atom (O1) via formation of two six-membered (Pt1-N2-N3-C6-C5-N1) and (Pt1-N2-C13-C14-C15-O1) chelate ring with chelate bite angles  $\angle\text{N2-Pt1-N1}$  and  $\angle\text{N2-Pt1-O1}$ ,  $91.9(2)^\circ$  and  $92.5(2)^\circ$  respectively. The selected bond distances and bond angles of the complexes are summarized in Table II.2. The Pt1-N1(pyridyl) bond length ( $2.014(6)$  Å) is shorter compared to Pd1-N1(pyridyl) bond length ( $2.067(8)$  Å) that indicates strong interaction of Pt(II) with pyridyl-N (N1) in complex **C2**. Similarly, Pt1-N2(imine) bond distance ( $1.971(6)$  Å) in **C2** is significantly shorter compared to Pd1-N2(imine) bond distance ( $2.065(8)$  Å) in **C1**. Moreover, the M-N(pyridyl) and M-N(imine) (M = Pd (**C1**) and Pt (**C2**)) bond distances are well corroborated with the reported M-N(pyridyl) and M-N(imine) bond distances of Pd and Pt complexes.<sup>53</sup> Pd1-Cl1 and Pd1-Cl2 bond distances are found to be  $2.270(3)$  Å and  $2.290(3)$  Å respectively in **C1** while for complex **C2**, Pt1-Cl1 bond distance is found to be at  $2.329(2)$  Å which are in well agreement with the reported palladium and platinum complexes.<sup>3,54</sup> The two trans angles for the Pd(II) complex,  $\angle\text{Cl1-Pd1-N1}$  and  $\angle\text{Cl2-Pd1-N2}$  were found to be  $176.9(2)^\circ$  and  $174.9(2)^\circ$  respectively and for Pt(II) complex,  $\angle\text{O1-Pt1-N1}$  and  $\angle\text{Cl1-Pt1-N2}$  were found to be  $172.4(2)^\circ$  and  $170.6(2)^\circ$  respectively, these are deviated from the ideal angle  $180^\circ$  leading significant distortion in the square planar geometry of the two complexes.

### II.3.3. Computational study

The geometries of **C1** and **C2** were optimized in singlet ground state by DFT/B3LYP method. The optimized geometric parameters are given in Table II.2. The calculated bond parameters of the two complexes are reasonably well reproducing the X-ray crystal structures data. Contour plots of selected molecular orbitals **C1** and **C2** are given in Fig. II.10 and Fig. II.11 respectively. Energy and compositions of selected molecular orbitals are given in Table II.3. For **C1** the higher energy occupied molecular orbital (HOMO) has 97% contribution of ligand, HL and the low-lying virtual orbital, LUMO also has 94% contribution of ligand  $\pi^*$



orbital. For **C2**, HOMO has 72% contribution of ligand and 17% contribution of Pt(d $\pi$ ) orbitals, while LUMO has 96% contribution of ligand.

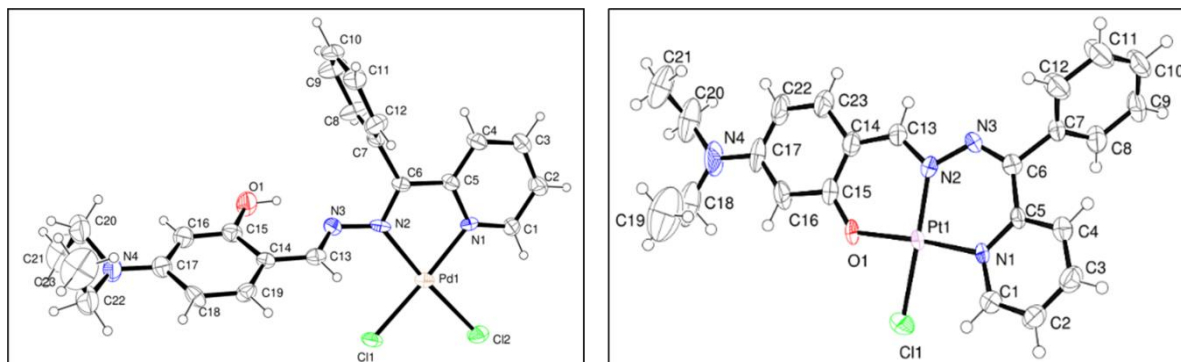


Figure II.9. ORTEP view of **C1** and **C2** with 35% ellipsoidal probability

Table II.3. Energy and % of composition of some selected molecular orbitals of **C1** and **C2**

C1					C2			
MO	Energy	% Composition			Energy	% Composition		
		Pd	HL	Cl		Pt	L	Cl
LUMO+5	-0.58	01	99	0	-0.24	03	97	00
LUMO+4	-0.87	01	99	0	-0.47	02	98	00
LUMO+3	-1.00	04	94	02	-0.64	54	34	12
LUMO+2	-1.54	02	97	01	-0.99	03	97	00
LUMO+1	-2.01	47	23	30	-1.42	02	98	00
LUMO	-2.85	05	94	01	-2.36	04	96	00
HOMO	-5.44	01	97	02	-5.21	17	72	11
HOMO-1	-5.90	29	03	68	-5.42	15	84	01
HOMO-2	-6.04	14	13	73	-5.98	25	30	45
HOMO-3	-6.17	28	21	51	-6.07	25	08	67
HOMO-4	-6.20	06	84	10	-6.25	86	05	09
HOMO-5	-6.23	15	04	81	-6.70	06	89	05
HOMO-6	-6.45	84	04	12	-6.83	53	46	01
HOMO-7	-7.14	08	80	12	-7.01	01	93	06
HOMO-8	-7.30	03	89	08	-7.20	29	58	13
HOMO-9	-7.47	03	95	02	-7.24	10	63	27

HOMO-10	-7.57	05	77	18	-7.31	07	79	14
---------	-------	----	----	----	-------	----	----	----

For details about the electronic transitions, TDDFT calculation on the optimized geometries of the complexes were performed. For **C1** the low energy transition at 533 nm (HOMO→LUMO+1 transition) corresponds to the experimental band at 496 nm ( $\epsilon$ , 13860 M<sup>-1</sup>cm<sup>-1</sup>) having mixed ligand to metal charge transfer (LMCT) and intra-ligand charge transfer (ILCT) character. The experimentally observed shoulder band 453 nm is well corroborated with the calculated transition at 470 nm (HOMO-2/HOMO-4→LUMO+1 transitions) having mixed ILCT and XMCT (halogen to metal charge transfer) character. Other high energy bands at 354 nm, 325 nm and 267 nm correspond to ILCT transitions. For **C2** the low energy experimental band at 505 nm ( $\epsilon$ , 16277 M<sup>-1</sup>cm<sup>-1</sup>) corresponds to the HOMO→LUMO transition at 492 nm has mixed ILCT and metal to ligand charge transfer (MLCT) character. Similarly, the band at 432 nm ( $\epsilon$ , 9778 M<sup>-1</sup>cm<sup>-1</sup>) corresponds to mixed ILCT and MLCT character (Table II.4). The bands at 348 nm and 270 nm correspond to ILCT character.

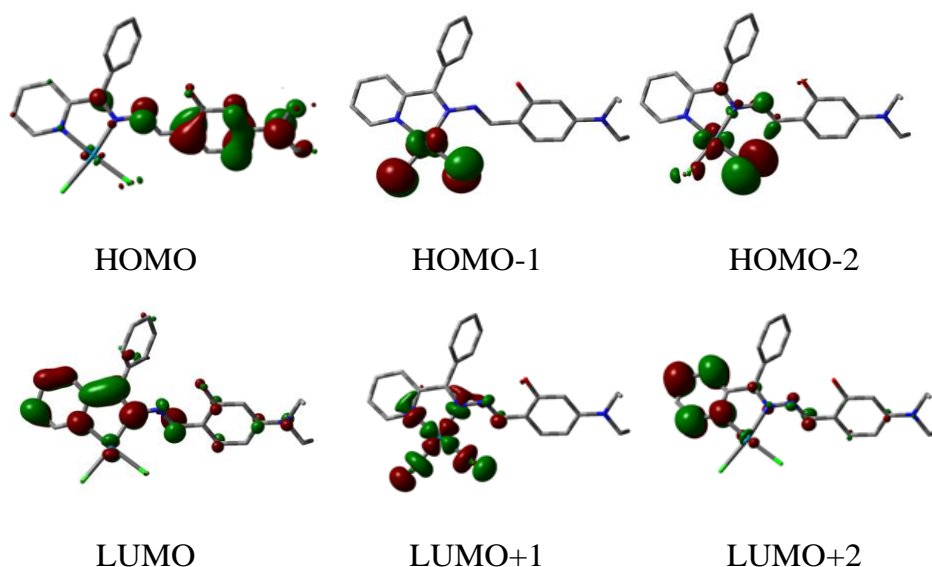
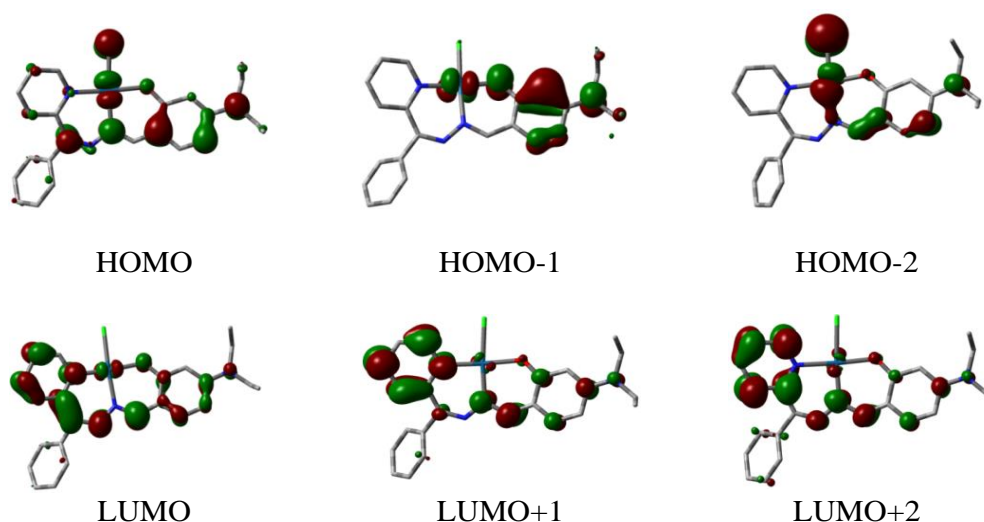


Figure II.10. Contour plots of selected molecular orbital of **C1**

Figure II.11. Contour plots of selected molecular orbital of **C2**Table II.4. Vertical electronic transition calculated by TDDFT/CPCM method of **C1** and **C2**

Compd.	$\lambda$ (nm)	E (eV)	Osc. Strength (f)	Key excitations	Character	$\lambda_{\text{expt.}}$ (nm) ( $\epsilon$ , $\text{M}^{-1}\text{cm}^{-1}$ )
<b>C1</b>	533.0	2.3261	0.3738	(59%)HOMO→LUMO+1 (27%)HOMO→LUMO	LMCT/ILCT	496 (13860)
	469.6	2.6402	0.0289	(51%)HOMO-4→LUMO+1 (37%)HOMO-2→LUMO+1	LMCT/XMCT	453 (sh.)
	375.4	3.3024	0.1254	(73%)HOMO-3→LUMO	MLCT/XLCT	
	346.6	3.5775	0.1549	(67%)HOMO→LUMO+2	ILCT	354 (sh.)
	316.9	3.9119	0.3436	(49%)HOMO-9→LUMO	ILCT	325 (12100)
	269.6	4.5982	0.1055	(68%)HOMO→LUMO+5	ILCT	267 (7478)
<b>C2</b>	492.1	2.5196	0.6759	(96%)HOMO→LUMO	ILCT/MLCT	505 (16277)
	454.2	2.7298	0.0352	(97%)HOMO-1→LUMO	ILCT/MLCT	432 (9778)
	360.7	3.4376	0.1339	(59%)HOMO→LUMO+1	ILCT/MLCT	
	340.2	3.6441	0.2962	(67%)HOMO-5→LUMO	ILCT	348 (14258)
	277.8	4.4636	0.1107	(86%)HOMO-7→LUMO	ILCT	270 (9068)

### II.3.4. Cytotoxicity Study

#### II.3.4.1. Pd(II) and Pt(II) complexes induced cytotoxicity in cancer cells

The cytotoxic activity of the Pd(II) and Pt(II) complexes (**C1/C2**) were evaluated against four different human cancer (MCF-7, HCT116, A549, HepG2) cell lines. The half-minimum inhibitory concentration ( $IC_{50}$ ) values of the complexes in 24h are tabulated (Table II.5). Both the complexes showed different degree of cytotoxicity in these cell lines. Platinum complex (**C2**) showed higher cytotoxicity than palladium complex (**C1**) in all these cell lines, which may be due the different in coordination environment around Pd and Pt centres in complexes **C1** and **C2** respectively. Highest sensitivity was seen in HepG2 cell line [ $IC_{50}$  = 6-12  $\mu$ M] for both the complexes. Moreover, antiproliferative activity of the present complexes is much better towards HepG2 cell line than the reported Pd(II) and Pt(II) complexes.<sup>55</sup> Interestingly, cytotoxicity of platinum complex was nearly comparable to that of the standard anticancer drug, cisplatin in HepG2 cell line. Whereas the free ligand HL didn't show any noticeable cytotoxicity towards the above-mentioned cell lines. Moreover, the  $IC_{50}$  value of both the complexes **C1** and **C2** were higher than 200  $\mu$ M in human peripheral blood mononuclear cells (hPBMC). We have chosen HepG2 cell line for further cytotoxic study of Pd(II) and Pt(II) complexes.

Table II.5.  $IC_{50}$  values (in  $\mu$ M) of HL, [Pd(HL)Cl<sub>2</sub>] (**C1**) and [Pt(L)Cl] (**C2**) against various cancer and normal cell lines\*

Compounds	MCF-7	HCT-116	A549	HepG2	PBMC
<b>HL</b>	>200	>200	>200	>200	>200
<b>[Pd(HL)Cl<sub>2</sub>](C1)</b>	48.1±3.4	57.4±4.5	33.6±2.7	11.4±3.1	>200
<b>[Pt(L)Cl](C2)</b>	36.2±2.3	44.3±2.8	25.8±1.7	6.45±1.4	>200
<b>Cisplatin</b>	14.2±1.8	11.7±1.6	12.3±2.5	7.8±2.2	>200

\*MCF-7, A549, HCT116, HepG2 and PBMC cells ( $1 \times 10^6$  cells/mL) were treated with different concentrations of ligand, Pd- complex and Pt- complex ranging from 0 to 200  $\mu$ M for 24 h. The  $IC_{50}$  values were calculated from an MTT assay. Results presented here are one of the three representative experiments  $\pm$ S.D.

### II.3.4.2. Pd(II) and Pt(II) complexes induced DNA fragmentation and ROS generation in cancer cells

Cell death results from DNA fragmentation. So, we examined DNA fragmentation level induced by **C1** and **C2** complexes in HepG2 cells. Level of fragmented DNA increases with increasing concentration of both the compounds upto 80  $\mu\text{M}$  in HepG2 (Fig. II.12a). The redox properties of transition metal complexes offer one of the routes for anticancer therapy. Activation of ROS generation enhances cancer cell death.<sup>56</sup> So, ROS level was measured in Pt(II) and Pd(II) complex treated HepG2 cells spectrofluorometrically. Similar rise in ROS level like DNA fragmentation are observed in the Pd(II) and Pt(II) complex treated cells (Fig. II.12b).

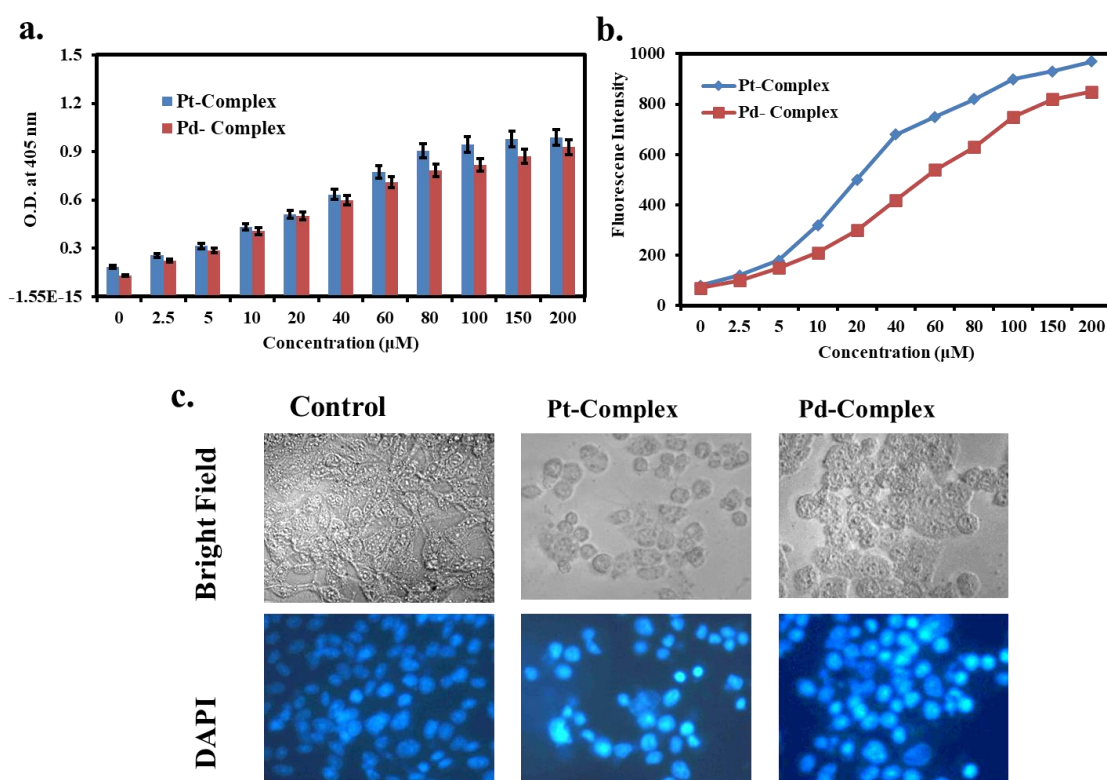


Figure II.12. (a) and (b) HepG2 (Human Hepatocellular Carcinoma) cells ( $1 \times 10^6$  cells/mL) were treated with different concentrations of Pd(II) and Pt(II) complexes ranging from 0 to 200  $\mu\text{M}$  for 24 h. DNA fragmentation by using Death detection kit (a) and ROS generation by spectrofluorometrically (b) were monitored. Results presented here are one of the three representative experiments  $\pm$ S.D. (c) HepG2 cells ( $1 \times 10^6$  cells/mL) were treated with  $\text{IC}_{50}$  value of Pd(II) and Pt(II) complexes for 24 h. Morphological changes (upper row), and nuclear condensation/ DNA fragmentation (lower row) were monitored under fluorescence microscope.

### II.3.4.3. Cell Image study

HepG2 cells were used as model for further study on cytotoxicity induced by the Pt(II) and Pd(II) complexes (**C1/C2**). Cancer cell death through apoptosis is a desirable aim. Characteristic apoptotic changes in cell morphology like cell shrinkage and cell rounding are observed in complex treated cells. Apoptotic feature in nucleus such as chromatin condensation and DNA fragmentation were seen after treatment with **C1** and **C2** for 24h.<sup>57</sup> Increased numbers of condensed bright fragmented nuclei are evident from the DAPI staining (a nuclear staining dye) (Fig. II.12c).<sup>58</sup> Increased number of DNA fragments in complex treated cells was found from the DNA-fragmentation study using death detection kit (Fig. II.12a) which corroborates with the findings in Figure II.12c. Thus, cytotoxicity induced by complex in HepG2 cells may involve apoptosis.

### II.3.4.4. In Vitro Cell Migration study

Cancerous cells exhibit uncontrolled cell migration. To detect the inhibitory action of both the complexes on cell migration of HepG2 cells, the scratch assay was carried out.<sup>59-61</sup> When treated with IC<sub>50</sub> of Pd(II) and Pt(II) complexes, cell migration of HepG2 was reduced in 12h and 24h.<sup>62</sup> The result also revealed that the number of cells was significantly reduced in the denuded area, suggesting that both the complexes could minimize the site-specific cell migration as well as trigger the cell death (Fig. II.13).

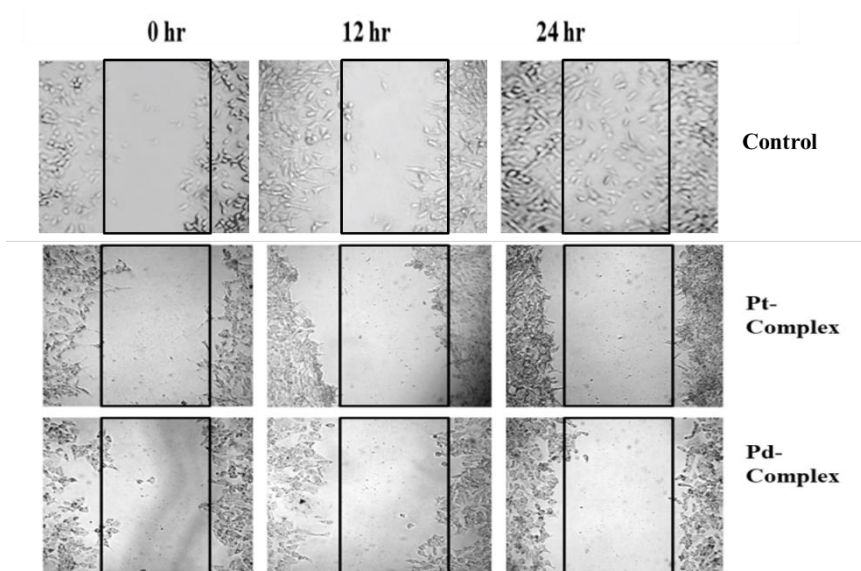


Figure II.13. HepG2 cells ( $1 \times 10^6$  cells/mL) were treated with IC<sub>50</sub> value of Pd(II) and Pt(II) complexes for 0 h, 12h and 24 h. Scratch assay (migration inhibition study) were monitored under microscope.



### II.3.4.5. Apoptotic analysis by annexin-V/FITC-PI binding assay

Binding of annexin V with phosphatidyl serine exposed to the outer membrane of apoptotic cells indicate apoptotic cells.<sup>63-65</sup> Annexin V-FITC is the apoptosis detection kit. Propidium Iodide binds with the DNA exposed from the necrotic cells and it can be detected by the PE/Texas Red channel. Annexin V positive - PI negative populations represent cells in early apoptosis (Q4). Annexin V positive - PI positive staining indicates cells in the late apoptosis (Q2). Annexin V positive - PI negative staining cells are live (Q3). Annexin V negative - PI positive cells are necrotic cells (Q1). Q2+Q4 represent total apoptotic cells. Q1+Q2+Q4 indicate total dead cells.<sup>58</sup>

Accordingly, Figure II.14a shows that live cells are 94.3 % in untreated sample compared to 27.3% and 9.4% in palladium(II) complex, **C1** and platinum(II) complex, **C2** treated cells. Total apoptotic cells are 2.8% (1.3+1.5), 40.7% (40.1+0.6), and 89.0% (79.1+9.9) and total dead cells are 5.8%, 72.8% and 90.6% in untreated, **C1** and **C2** treated samples respectively. Thus the data indicates the presence of markedly higher percentage of apoptotic cells as well as total dead cells in Pd(II) and Pt(II)-complex treated sets compared to untreated control. Also, percentage of apoptotic and total dead cells is found to be significantly higher in Pt(II) complex (**C2**) treated experiments than that of treated with Pd(II) complex (**C1**).

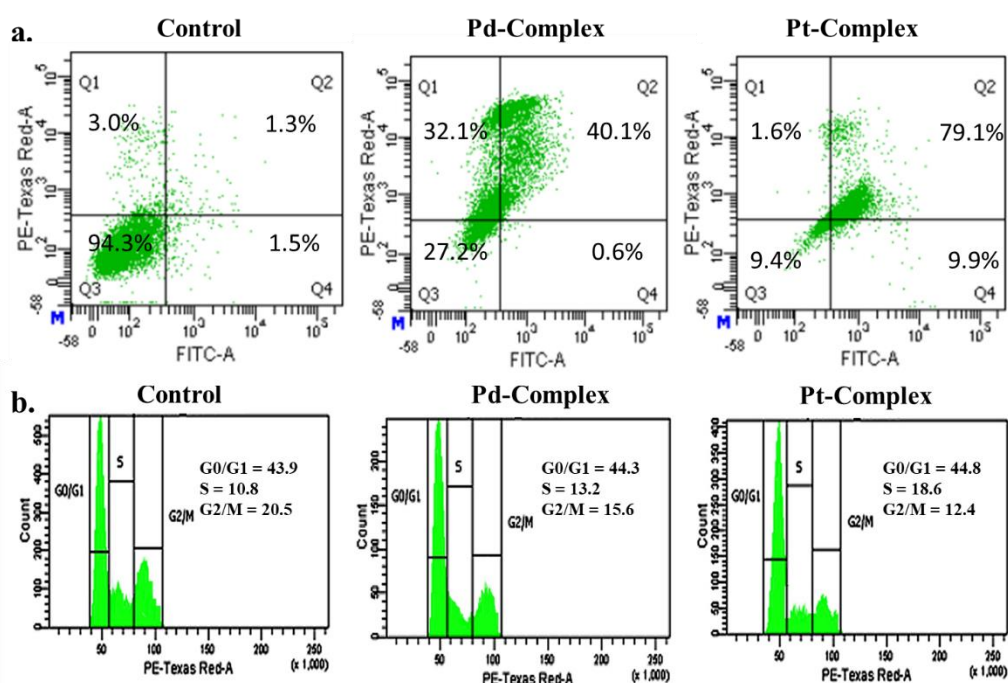


Figure II.14. (a) AnnexinV-FITC binding study (apoptotic changes) were monitored and by FACS analysis. (b) Effect on cell cycle arrest in HepG2 cells of treatment with prior to treatment Pd- and Pt-complexes.



### II.3.4.6. Pd(II) and Pt(II) complexes (C1/C2) cause G2/M cell cycle arrest in HepG2 cells

To determine ROS mediated cell cycle arrest, we have tested the cell cycle status after treating cells with complexes **C1** and **C2**. G2/M cell cycle arrest occurred after Pd- and Pt-complex treatment as the proportion of cells in G2/M phase decreased by 4.9% for Pd(II) complex (**C1**) and 8.1% for Pt(II) complex (**C2**) (Fig. II.14b).

## II.4. Conclusion

New Pd(II) and Pt(II) complexes (**C1/C2**) with ONN donor pincer ligand, HL are synthesized and thoroughly characterized. X-ray structures of the complexes revealed that HL acts as bidentate NN and tridentate ONN chelator in Pd(II) and Pt(II) complexes. The antiproliferative activity of the complexes showed that Pt(II) complex (**C2**) is more potent than Pd(II) complex (**C1**) in HCT116, HepG2, MCF-7 and A549 cell lines. Apoptotic analysis by annexin-V/FITC-PI binding assay shows that the percentage of apoptotic and total dead cells is significantly higher in Pt(II) complex (**C2**) than that of Pd(II) complex (**C1**).

## II.5. References

1. H. Sung, J. Ferlay, R. L. Siegel, M. Laversanne, I. Soerjomataram, A. Jemal, and F. Bray, *Ca Cancer J. Clin.*, 2021, **71**, 209-249.
2. G. P. Nagaraju, G. Srivani, B. Dariya, G. Chalikonda, B. Farran, S. K. Behera, A. Alam and M. A. Kamal, *Semin. Cancer Bio.*, 2021, **69**, 69-76.
3. S. N. Mbugua, N. R. S. Sibuyi, L. W. Njenga, R. A. Odhiambo, S. O. Wandiga, M. Meyer, R. A. Lalancette and M. O. Onani, *ACS Omega*, 2020, **25**, 14942-14954.
4. E. Petruzzella, R. Sirota, I. Solazzo, V. Gandin and D. Gibson, *Chem. Sci*, 2018, **9**, 4299-4307.
5. M. Hallek, *Am. J. Hematol.*, 2019, **94**, 1266-1287.
6. R. J. Ward and R. R. Crichton, *Met. Ions Life Sci.*, 2019, **19**, 87-122.
7. (a) R. Paprocka, M. Wiese-Szadkowska, S. Janciauskiene, T. Kosmalski, M. Kulik and A. Helmin-Basa. *J. Coord. Chem. Rev.*, 2022, 452, 214307; (b) E. Sánchez-López, D. Gomes, G. Esteruelas, L. Bonilla, A. L. Lopez-Machado, R. Galindo, A. Cano, M. Espina, M. Ettcheto, A. Camins, A. M. Silva, A. Durazzo, A. Santini, M. L. Garcia and E. B. Souto, *Nanomaterials*, 2020, **10**, 292.
8. (a) S. Ghosh, *Bioorg. Chem.*, 2019, **88**, 102925; (b) S. Dasari and P. B. Tchounwou, *Eur. J. Pharmacol.*, 2014, **740**, 364-378.
9. A. M. Florea and D. Büsselberg, *Cancers*, 2011, **3**, 1351-1371.
10. T. C. Johnstone, K. Suntharalingam and J. Lippard, *Chem. Rev.*, 2016, **116**, 3436-3486.
11. T. C. Johnstone, G. Y. Park and S. J. Lippard, *Cancer Res.*, 2014, **34**, 471-476.
12. U. Ndagi, N. Mhlongo and M. E. Sliman, *Drug. Des. Devel. Ther.* 2017, **11**, 599-616.
13. J. Espino, E. Fernández-Delgado, S. Estirado, F. de la Cruz-Martinez, S. Villa-Carballar, E. Viñuelas-Zahínos, F. Luna-Giles and J. A. Pariente, *Sci. Rep.*, 2020, **10**, 1-16.
14. H. A. Rudbari, N. Kordestani, J. V. Cuevas-Vicario, M. Zhou, T. Efferth, I. Correia, T. Schirmeister, F. Barthels, M. Enamullah, A. R. Fernandes and N. Micale. *New J. Chem.*, 2022, **46**, 6470-6483.
15. Md N. Alam, F. Huq, *Coord. Chem. Rev.*, 2016, **316**, 36-67.
16. A. R. Kapdi and I. J. S. Fairlamb, *Chem. Soc. Rev.*, 2014, **43**, 4751-4777.
17. T. Lazarević, A. Rilak and Ž. D. Bugarčić, *Eur. J. Med. Chem.*, 2017, **142**, 8-31.
18. H. H. Repich, V. V. Orysyk, L. G. Palchykovska, S. I. Orysyk, Y. L. Zborovskii, O. V. Vasylenko, O. V. Storozhuk, A. A. Biluk, V. V. Nikulina, L. V. Garmanchuk, V. I. Pekhnyo and M. V. Vovk, *J. Inorg. Biochem.*, 2017, **168**, 98-106.
19. (a) D. Simić, M. Zarić, I. Nikolić, R. Živković-Zarić, P. Čanović, A. Kočović, I. Radojević, I. Raković, S. Jovičić Milić, Đ. Petrović, D. Stojković, N. Vuković, M. Kačaniová, M. Vukić and

- V. Jevtić, *Dalton Trans.*, 2022, **51**, 1191-1205; (b) A. Eskandari, A. Kundu, A. Johnson, S. Karmakar, S. Ghosh and K. Suntharalingam, *Dalton Trans.*, 2020, **49**, 4211-4215.
20. M. Fanelli, M. Formica, V. Fusi, L. Giorgi, M. Micheloni and P. Paoli, *Coord. Chem. Rev.*, 2016, **310**, 41-79.
21. Ž. D. Bugarčić, J. Bogojeski and R. van Eldik, *Coord. Chem. Rev.*, 2015, **292**, 91-106.
22. M. N. Alam and F. Huq, *Coord. Chem. Rev.*, 2016, **316**, 36-67.
23. C. Orvig and M. J. Abrams, *Chem. Rev.*, 1999, **99**, 2201-2204.
24. C. S. Allardyce, A. Dorcier, C. Scolaro, and P. J. Dyson, *App. Organomet. Chem.*, 2005, **19**, 1.
25. P. J. Dyson and G. Sava, *Dalton Trans.*, 2006, **16**, 1929-1933.
26. M. J. Hannon, *Pure Appl. Chem.*, 2007, **79**, 2243-2261.
27. K. B. Garbutcheon-Singh, M. P. Grant, B. W. Harper, A. M. Krause-Heuer, M. Manohar, N. Orkey and J. R. Aldrich Wright, *Current Topics in Med. Chem.*, 2011, **11**, 521-542.
28. P. Marques-Gallego, H. Dulk, J. Brouwer, H. Kooijman, A. L. Spek, O. Roubeau, S. J. Teat and J. Reedijk, *Inorg. Chem.*, 2008, **47**, 11171-11179.
29. N. J. Wheate, S. Walker, G. E. Craig and R. Oun, *Dalt. Trans.*, 2010, **39**, 8113-8127.
30. A. Bergamo and G. Sava, *Chem. Soc. Rev.*, 2015, **44**, 8818-8835.
31. M. Hanif and C. G. Hartinger, *Future Med. Chem.*, 2018, **10**, 615-617.
32. L. Bai, C. Gao, Q. Liu, C. Yu, Z. Zhang, L. Cai, B. Yang, Y. Qian, J. Yang and X. Liao, *Eur. J. Med. Chem.*, 2017, **140**, 349-382.
33. C. S. Allardyce and P. J. Dyson, *Dalton Trans.*, 2016, **45**, 3201-3209.
34. R. G. Kenny, S. W. Chuah, A. Crawford and C. J. Marmion, *Eur. J. Inorg. Chem.*, 2017, **12**, 1596-1612.
35. K. Laws and K. Suntharalingam, *ChemBioChem*, 2018, **19**, 2246-2253.
36. B. S. Murray, M. V Babak, C. G. Hartinger and P. J. Dyson, *Coord. Chem. Rev.*, 2016, **306**, 86-114.
37. E. Alessio, *Eur. J. Inorg. Chem.*, 2017, **12**, 1549-1560.
38. J. Reedijk, *Eur. J. Inorg. Chem.*, 2009, **10**, 1303-1312.
39. D. Wang and S. J. Lippard, *Nat. Rev. Drug Discov.*, 2005, **4**, 307-320.
40. V. Brabec, O. Hrabina and J. Kasparkova, *Coord. Chem. Rev.*, 2017, **351**, 2-31.
41. S. Komeda, *Metallomics*, 2011, **3**, 650-655.
42. T. C. Johnstone, K. Suntharalingam and S. J. Lippard, *Chem. Rev.*, 2016, **116**, 3436-3486.
43. S. Gharami, K. Aich, L. Patra and T. K. Mondal, *New J. Chem.*, 2018, **42**, 8646-8652.
44. (a) A. D. Becke, *J. Chem. Phys.*, 1993, **98**, 5648-5652; (b) C. Lee, W. Yang and R. G. Parr, *Phys. Rev. B: Condens. Matter Mater. Phys.*, 1988, **37**, 785-789.
45. (a) P. J. Hay and W. R. Wadt, *J. Chem. Phys.*, 1985, **82**, 270-283; (b) W. R. Wadt and P. J. Hay, *J. Chem. Phys.*, 1985, **82**, 284-298; (c) P. J. Hay and W. R. Wadt, *J. Chem. Phys.*, 1985, **82**, 299-310.

46. M. J. Frisch, G. W. Trucks, H. B. Schlegel, G. E. Scuseria, M. A. Robb, J. R. Cheeseman, G. Scalmani, V. Barone, B. Mennucci, G. A. Petersson, H. Nakatsuji, M. Caricato, X. Li, H. P. Hratchian, A. F. Izmaylov, J. Bloino, G. Zheng, J. L. Sonnenberg, M. Hada, M. Ehara, K. Toyota, R. Fukuda, J. Hasegawa, M. Ishida, T. Nakajima, Y. Honda, O. Kitao, H. Nakai, T. Vreven, J. A. Montgomery, Jr., J. E. Peralta, F. Ogliaro, M. Bearpark, J. J. Heyd, E. Brothers, K. N. Kudin, V. N. Staroverov, R. Kobayashi, J. Normand, K. Raghavachari, A. Rendell, J. C. Burant, S. S. Iyengar, J. Tomasi, M. Cossi, N. Rega, J. M. Millam, M. Klene, J. E. Knox, J. B. Cross, V. Bakken, C. Adamo, J. Jaramillo, R. Gomperts, R. E. Stratmann, O. Yazyev, A. J. Austin, R. Cammi, C. Pomelli, J. W. Ochterski, R. L. Martin, K. Morokuma, V. G. Zakrzewski, G. A. Voth, P. Salvador, J. J. Dannenberg, S. Dapprich, A. D. Daniels, O. Farkas, J. B. Foresman, J. V. Ortiz, J. Cioslowski and D. J. Fox, Gaussian 09, Revision D.01, Gaussian, Inc., Wallingford CT, 2009.
47. (a) R. Bauernschmitt and R. Ahlrichs, *Chem. Phys. Lett.*, 1996, **256**, 454-464; (b) R. E. Stratmann, G. E. Scuseria and M. J. Frisch, *J. Chem. Phys.*, 1998, **109**, 8218; (c) M. E. Casida, C. Jamorski, K. C. Casida and D. R. Salahub, *J. Chem. Phys.*, 1998, **108**, 4439-4449.
48. (a) V. Barone and M. Cossi, *J. Phys. Chem. A*, 1998, **102**, 1995-2001; (b) M. Cossi and V. Barone, *J. Chem. Phys.*, 2001, **115**, 4708-4717; (c) M. Cossi, N. Rega, G. Scalmani and V. Barone, *J. Comput. Chem.*, 2003, **24**, 669-681.
49. N. M. O'Boyle, A. L. Tenderholt, K. M. Langner, *J. Comput. Chem.*, 2008, **29**, 839-845.
50. Bruker. SAINT v8.38A. Bruker AXS Inc., Madison, Wisconsin, USA.
51. L. Krause, R. Herbst-Irmer, G. M. Sheldrick, D. Stalke, *J. Appl. Cryst.*, 2015, **48**, 3-10.
52. (a) G. M. Sheldrick, *Acta Cryst.*, 2008, **A64**, 112-122; (b) G. M. Sheldrick, *Acta Cryst.*, 2015, **C71**, 3-8.
53. (a) J. -A. Alvarez-Hernández, N. Andrade-López, J. G. Alvarado-Rodríguez, S. González-Montiel, L. Á. Zárate-Hernández and J. Cruz-Borbolla, *Polyhedron*, 2022, **214**, 115635; (b) S. Biswas, P. Roy and T. K. Mondal, *J. Mol. Struct.*, 2017, **1142**, 110-115; (c) D. Qiu, Y. Guo, H. Wang, X. Bao, Y. Feng, Q. Huang, J. Zeng and G. Qiu, *Inorg. Chem. Commun.*, 2011, **14**, 1520-1524.
54. (a) E. Fernández-Delgado, F. de la Cruz-Martínez, C. Galán, L. Franco, J. Espino, E. Viñuelas-Zahínos, F. Luna-Giles, I. Bejarano, *J. Inorg. Biochem.*, 2020, **202**, 110870; (b) E. Fernández-Delgado, S. Estirado, J. Espino, E. Viñuelas-Zahínos, F. Luna-Giles, A. B. R. Moratinos and J. A. Pariente, *J. Inorg. Biochem.*, 2022, **227**, 111688.
55. (a) S. Rubino, R. Busà, A. Attanzio, R. Alduina, V. Di Stefano, M. A. Girasolo, S. Orecchio and L. Tesoriere, *Bioorg. Med. Chem.*, 2017, **25**, 2378-2386; (b) N. Miklášová, E. Fischer-Fodor, P. Lönnecke, C. I. Tomuleasa, P. Virag, M. P. Schrepler, R. Mikláš, L. S. Dumitrescu and E. Hey-Hawkins, *Eur. J. Med. Chem.*, 2012, **49**, 41-47; (c) S. Rubino, V. Di Stefano, A. Attanzio, L. Tesoriere, M. A. Girasolo, F. Nicolò, G. Bruno, S. Orecchio and G.C. Stocco,

- Inorg. Chim. Acta*, 2014, **418**, 112-118; (d) L. Masaryk, P. Zoufalý, K. Słoczyńska, E. Zahradníková, D. Milde, P. Koczurkiewicz-Adamczyk and P. Štarha, *Inorg. Chim. Acta*, 2022, **536**, 120891; (e) L. Niu, G. Ren, T. Hou, X. Shen and D. Zhu, *Inorg. Chem. Commun.*, 2021, **130**, 108737.
56. A. Brozovic, A. Ambriović-Ristov and M. Osmak, *Crit. Rev. Toxicol.*, 2010, **40**, 347-359.
57. S. Hadizadeh, N. Najafzadeh, M. Mazani, M. Amani, H. M. Torshizi and A. Niapour, *Biochem. Res. Int.*, 2014, 813457.
58. Y. Li, S. Man, J. Li, H. Chai, W. Fan, Z. Liu and W. Gao, *Chemico-Bio. Interac.*, 2014, **220**, 193-199.
59. W. Dai, F. Wang, L. He, C. Lin, S. Wu, P. Chen, Y. Zhang, M. Shen, D. Wu, C. Wang, J. Lu, Y. Zhou, X. Xu, L. Xu and C. Guo, *Mol. Carcinogenesis*, 2013, **54**, 301-311.
60. I. K. Sani, S. H. Marashi and F. Kalalinia, *Toxicology in Vitro*, 2015, **29**, 893-900.
61. Y. Chang, Y. Yuan, Q. Zhang, Y. Rong, Y. Yang, M. Chi, Z. Liu, Y. Zhang, P. Yu, and Y. Teng, *RSC Adv.*, 2020, **10**, 1191-1197.
62. F. U Rahman, M. Z. Bhatti, A. Ali, H. Q. Duong, Y. Zhang, B. Yang, S. Koppireddi, Y. Lin, H. Wang, Z. T. Li and D. W. Zhang, *Euro. J. Med. Chem.*, 2018, **143**, 1039-1052.
63. S. -H. Lee, X. W. Meng, K. S. Flatten, D. A. Loegering and S. H. Kaufmann, *Cell Death & Differentiation*, 2013, **20**, 64-76.
64. G. Zhang, V. Gurtu, S. R. Kain and G. Yan, *BioTechniques*, 1997, **23**, 525-531.
65. V. Turinetto and C. Giachino, *Nucleic Acids Res.*, 2015, **43**, 2489-2498.

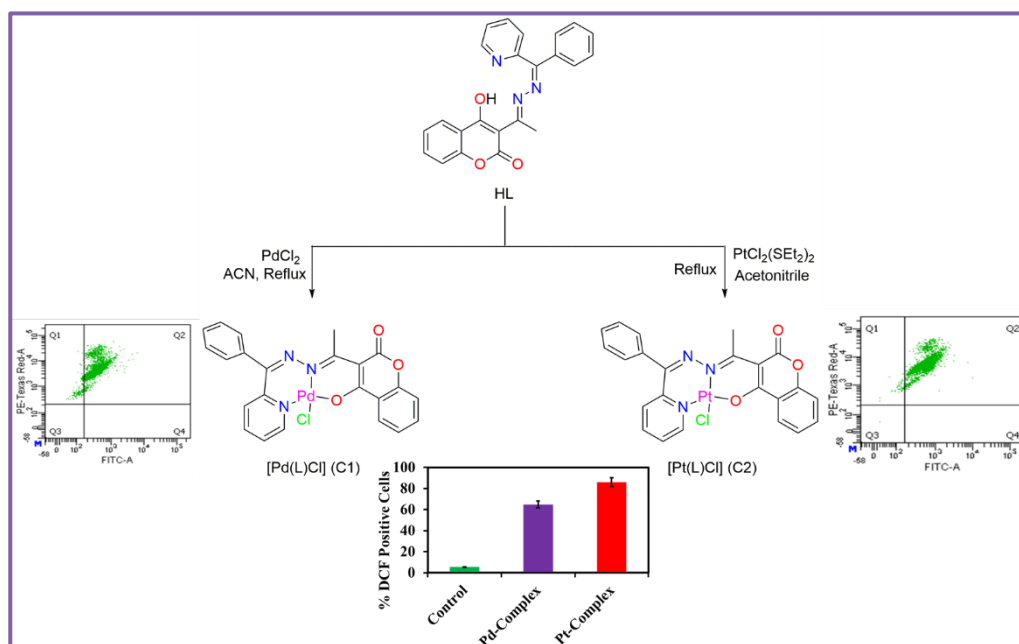
## **CHAPTER - III**

**New palladium(II) and platinum(II) complexes  
with coumarin based O,N,N pincer: Synthesis,  
structure elucidation, BSA protein binding  
studies and anticancer activity**

## *New palladium(II) and platinum(II) complexes with coumarin based O,N,N pincer: Synthesis, structure elucidation, BSA protein binding studies and anticancer activity*

### Abstract

New Pd(II) and Pt(II) complexes (**C1/C2**) with a O,N,N donor pincer ligand, 4-hydroxy-3-((*E*)-1-(((*Z*)-phenyl(pyridin-2-yl)methylene)hydrazono)ethyl)-2H-chromen-2-one (**HL**) were synthesized and methodically characterized by several spectroscopic and XRD techniques. Absorption and fluorescence techniques were used to assess the mechanism of interaction of the complexes with BSA protein. MTT assay was executed to investigate the antiproliferative activity of the complexes with several cancer cell lines (MCF-7, HCT116, A549 and HepG2) along with a normal cell line (PBMC). Both **C1** and **C2** showed better antiproliferative activity with HepG2 cell line ( $IC_{50}$  value of 15.3 and 5.1  $\mu$ M respectively). A cytotoxicity study was performed and complex **C2** exhibited a better antiproliferative activity as compared to **C1**. The morphological changes were also examined by staining methods and fragmented DNA unveiled that the cell death took place through apoptosis.





### III.1. Introduction

Unquestionably, one of the most important health problems that modern society faces is cancer, which is a key focus in the field of medicinal chemistry. Therefore, every new and effective anticancer treatment with few side effects stands out as being of utmost significance to the global scientific community.<sup>1-3</sup> The emergence of drug resistance and illness relapse are the fundamental obstacles in the development of anti-cancer medications.<sup>4</sup> Metals have constantly been utilized to take care of an array of disorders around the world.<sup>5</sup> Due to their elite nature, anticancer activity of transition metal complexes are comprehensively explored.<sup>6</sup> Following the incredibly successful adoption of cisplatin as an anti-cancer therapy in 1965, these transition metal complexes are widely used as antitumor medicine.<sup>7,8</sup> Due to its superior efficacy, particularly in the treatment of cervical, ovarian, bladder, metastatic testicular and several other types of cancers, cisplatin has recently been recognized as one of the most extensively and exclusively utilized anticancer drug in the globe along with the more effectual and less fatal 2<sup>nd</sup> and 3<sup>rd</sup>-generation Pt-based anticancer medicines, carboplatin and oxaliplatin.<sup>9</sup> Later on, however, a number of serious adverse effects including nephrotoxicity, hair loss, blood clots, weariness, weakness, and treatment resistance of the tumor cells were discovered.<sup>10,11</sup> Additionally, the therapeutic applicability of Pt-based medicines is restricted by cellular resistance, whole system toxicity, and pitiable activity against specific types of malignancies.<sup>12-15</sup> Now the dose restrictive side effects of cisplatin made the scientists think about such discovery of platinum complexes which will have less toxic side-effects and be effective against a wide variety of categories of carcinoma.<sup>16,17</sup> Irrespective of the encouraging effects and applications of platinum compounds in various cancer cells, they too show severe side effects like nausea, vomiting, a decrease in the fabrication of blood cells and platelets in the bone marrow, and a consequent alteration in the body's response to infection.<sup>18</sup> These shortcomings provide a compelling reason to find more effective cytotoxic compounds including additional transition metals.<sup>19,20</sup> Because of the commonalities between Pt(II) and Pd(II), the study of palladium(II) complexes has gained a lot more attention as anticancer medicines.<sup>21,22</sup> Now the highly brisk ligand-exchange and hydration rates of Pd(II) complexes about 105 times quicker than their Pt(II) equivalents result in one drawback for these Pd-based anticancer medications.<sup>23</sup> Accordingly, this presumption suggests that palladium's greatly elevated reactivity may hinder engagement with the target DNA by interacting with other donor moieties already present in the circulation, magnifying their toxicity and decreasing their potential for positive effects. As a result, an appropriate ligand

preference is crucial in the growth of better and more efficient palladium complex-based anticancer medicines.<sup>19,24-27</sup> Schiff base ligands, produced by the reaction between amines and carbonyl compounds play crucial role in transition metal complexes. They are also known as imine compounds and has nitrogen atom which forms a dative bond with metal ion by donating its lone pair of electrons along with the other donor atoms present in the compound. This causes the change in the structure, electronic nature and reactivity.<sup>28</sup> So, we name them as bidentate, tridentate, tetradentate ligands according to the number of donor atoms present in the Schiff base compounds. They have useful applications in the treatment of various diseases but their transition-metal complexes show higher medical importance especially as anticancer agents.<sup>29-32</sup> Therefore, transition metal complexes of their Schiff base ligand is quite important in the field of human health.

A vastly growing awareness and importance are gradually noticed in case of the metal complexes for their application in medicinal chemistry from the time of the innovation of anticancer activity of cisplatin, *cis*-[PtCl<sub>2</sub>(NH<sub>3</sub>)<sub>2</sub>] in the 1970s.<sup>33-36</sup> The interaction of cisplatin with DNA is typically recognized to be liable for the cytotoxicity of this drug<sup>37-39</sup> which consequently results in the perception of a fresh model of Pt-complexes. This concept leads to produce new antineoplastic drugs with variety of biological activity and improved toxicological and pharmacological kinetics properties.<sup>34,40-42</sup>

The primary biological endpoint for anticancer medicines is DNA. Therefore, the concept and subsequent production of DNA-aiming metal-based anticancer medicines have gained prominence in current years.<sup>43</sup> The covalent interactions of platinum-based medicines with DNA are widely established to be the source of their anticancer effect.<sup>12</sup> The ability of transition metal complexes to move themselves to the intended location of the target should be considered while creating effective anticancer compounds. Therefore, the study of interaction modes of anti-cancer drugs to serum albumins is very much important. The most prevalent proteins in the circulatory systems of a broad range of organisms are serum albumins.<sup>44</sup> It is a multi-functional protein with various biological handling.<sup>45</sup> Serum albumin may change the binding pattern of the drug thereby changing the structure of the protein which eventually can affect its function.<sup>46,47</sup> Because of its structural resemblance to human serum albumin (HSA), bovine serum albumin (BSA), one of the serum albumins, is frequently used as a prototype in biophysical and biochemical experiments.<sup>48</sup> The choice of this serum albumin is also greatly influenced by its short rate and intriguing ligand binding characteristics. Therefore, researching the BSA binding potential of various biologically relevant compounds could provide a wealth of knowledge on the structural properties of

pharmaceuticals. There are a few reports that provide in-depth analyses of both Pd and Pt complexes as well as the complexes' interactions with the BSA protein, but more research is required in this area.<sup>49,50</sup>

Herein, we synthesized two new Pd(II) and Pt(II) complexes (**C1** and **C2**) with a O,N,S donor pincer ligand, *4-hydroxy-3-((E)-1-(((Z)-phenyl(pyridin-2-yl)methylene)hydrazono)ethyl)-2H-chromen-2-one* (HL). We also investigate synchronous, absorption-emission, and CD spectroscopic methods to characterise how the complexes interact with the BSA protein. Furthermore, the complexes' cytotoxicity was tested on human breast (MCF-7), human colorectal (HCT116), human liver (HepG2), and human lung (A549) cancer cell lines. In the HepG2 cell line, bright-field morphology and apoptosis tests of the complexes were conducted. Theoretical calculations (DFT and TD-DFT) were performed to get more information to corroborate the experimental findings.

## III.2. Experimental

### III.2.1. Materials and physical measurements

This synthesis's reagents and solvents were all bought from Aldrich. Without additional purification, all other organic compounds and inorganic salts were employed as they were readily available from commercial sources. <sup>1</sup>H NMR spectra were recorded on a Bruker 300 MHz equipment in CDCl<sub>3</sub>. Mass spectra were taken on a Waters (Xevo G2 Q-TOF) mass spectrometer. Shimadzu UV-1900i spectrophotometer was used to measure the electronic spectra. IR spectra were recorded on a RX-1 PerkinElmer spectrometer.

Penicillin, streptomycin, neomycin (PSN) antibiotic, ethylenediaminetetraacetic acid (EDTA), and trypsin were purchased from Gibco BRL along with Dulbecco's modified Eagle's medium (DMEM) (Grand Island, NY, USA). Flow Collect Annexin Red kit (Cat. No. FCCH100108), DMSO, and 3-(4, 5-Dimethylthiazol-2-yl)-2,5-diphenyltetrazolium bromide (45989, MTT-CAS 298-93-1-Calbiochem) were purchased from Merck-Millipore. We purchased plastic tissue culture tools from Genetix Biotech Asia Pvt. Ltd. We bought zinc acetate from Sigma-Aldrich. The National Centre for Cell Science (NCCS), located in Pune, provided the HepG2 cell line.

**III.2.2. Synthesis****III.2.2.1. Synthesis of 4-hydroxy-3-((E)-1-((Z)-(phenyl(pyridine-2-yl)methylene)hydrazono)ethyl)-2H-chromen-2-one (HL)**

To an ethanolic solution (15 mL) of previously synthesized compound (2)<sup>51</sup> (0.5 g, 2.5 mmol), 3-acetyl-4-hydroxycoumarin (0.51 g, 2.5 mmol) [prepared by a reported procedure<sup>52</sup>] was mixed and refluxed for 4 hours. The reaction mixture was then given time to reach room temperature. The precipitate was collected, cleaned with ethanol after cooling, and HL was obtained as a yellow solid. The yield was 0.718g (75%).

Anal. Calc. for C<sub>23</sub>H<sub>17</sub>N<sub>3</sub>O<sub>3</sub>: C, 72.05; H, 4.47; N, 10.96. Found: C, 71.77; H, 4.31; N, 10.85. <sup>1</sup>H-NMR (300 MHz, CDCl<sub>3</sub>, ppm): δ 3.18 (s, 3H), 7.13-7.19 (m, 2H), 7.34-7.51 (m, 5H), 7.67-7.98 (m, 4), 8.19 (d, J = 8 Hz, 1H), 8.65 (d, J = 6 Hz, 1H), 14.3 (s, 1H). <sup>13</sup>C NMR (75 MHz, CDCl<sub>3</sub>, ppm): δ 17.72, 116.49, 123.01, 123.42, 124.74, 126.47, 128.39, 128.65, 128.9, 129.58, 130.54, 134.2, 136.52, 137.46, 149.65, 153.79, 154.62, 161.08, 173.65, 181.4. IR (cm<sup>-1</sup>) in KBr: ~3404 ν(O-H); 3058, 2920 ν(C-H); 1701 ν(C=O of cyclic ester); 1612ν(C=N). HRMS: Calculated for C<sub>23</sub>H<sub>17</sub>N<sub>3</sub>O<sub>3</sub> [M + H]<sup>+</sup> (m/z): 384.1348; found: 384.1360. UV-Vis (in CH<sub>3</sub>CN), λ<sub>max</sub> (ε, M<sup>-1</sup>cm<sup>-1</sup>): 378 (43000), 246 (22580).

**III.2.2.2. Synthesis of [Pd(L)Cl] complex (C1)**

0.023 g (0.13mmol) PdCl<sub>2</sub> was dissolved in 10 mL acetonitrile solvent, to it 0.05 g (0.13 mmol) ligand, HL solution in 10 mL acetonitrile was poured. After that, the reaction mixture was refluxed for 5 hours. This reaction produced a reddish-colored solution that was filtered. By allowing the solvent to slowly evaporate for one week, red-colored single crystals of the complex were produced. The yield was 0.048 g (70%).

Anal. Calc. for C<sub>23</sub>H<sub>16</sub>ClN<sub>3</sub>O<sub>3</sub>Pd: C, 52.69; H, 3.08; N, 8.02. Found: C, 52.37; H, 2.97; N, 7.88. <sup>1</sup>H-NMR (300 MHz, CDCl<sub>3</sub>, ppm): δ 2.96 (s, 3H), 7.25-7.31 (m, 3H), 7.53-7.7 (m, 7H), 7.97 (t, J = 7.8 Hz, 2H), 8.21 (d, J = 7.7 Hz, 1H), 9.61 (d, J = 6 Hz, 1H). <sup>13</sup>C NMR (75 MHz, CDCl<sub>3</sub>, ppm): δ 22.42, 106.15, 116.25, 117.8, 124.2, 126.5, 127.3, 127.6, 129, 129.6, 131.5, 134.2, 135.5, 139.6, 140.8, 153.5, 155.8, 160.7, 162.6, 168.8, 173.4. HRMS: Calculated mass C<sub>23</sub>H<sub>16</sub>N<sub>3</sub>O<sub>3</sub>Pd [M-Cl]<sup>+</sup> (m/z): 488.0226; found: 487.0265. IR (cm<sup>-1</sup>) in KBr: 3050, 3020, 2920 ν(C-H); 1700 ν(C=O of cyclic ester); 1598 ν(C=N). UV-Vis (in CH<sub>3</sub>CN), λ<sub>max</sub> (ε, M<sup>-1</sup>cm<sup>-1</sup>): 428 (6180), 338 (5987), 250 (23283).

**III.2.2.3. Synthesis of [Pt(L)Cl] complex (C2)**

0.057 g (0.13mmol)  $\text{Pt}(\text{SEt}_2)_2\text{Cl}_2$  was dissolved in 10 mL acetonitrile solvent, to it 0.05 g (0.13 mmol) ligand, HL solution in 10 mL acetonitrile was poured. The reaction mixture was then refluxed for 10 hours. As a result of this reaction, a red-colored solution appeared which was filtered. Red colored crystals of the complex suitable for X-ray diffract were achieved by deliberate evaporation of solvent for 15 days. Yield 0.057 g (72%).

Anal. Calc. for  $\text{C}_{23}\text{H}_{16}\text{ClN}_3\text{O}_3\text{Pt}$ : C, 45.07; H, 2.63; N, 6.86. Found: C, 44.88; H, 2.51; N, 6.71.  $^1\text{H}$  NMR (300 MHz,  $\text{CDCl}_3$ ):  $\delta$  2.91 (s, 3H), 7.23-7.31 (m, 3H), 7.46 (t,  $J = 6.6$  Hz, 1H), 7.55-7.67 (m, 5H), 7.97 (t,  $J = 7.7$  Hz, 2H), 8.22 (d,  $J = 7.8$  Hz, 1H), 9.95 (d,  $J = 6$  Hz, 1H).  $^{13}\text{C}$  NMR (75 MHz,  $\text{CDCl}_3$ , ppm):  $\delta$  22.24, 104.8, 116.3, 117.3, 124.3, 126.65, 127.18, 128.98, 129.68, 131.19, 134.11, 135.96, 138.58, 139.22, 153.03, 155.73, 158.63, 162.05, 167.67, 172.1. HRMS: calculated for  $\text{C}_{23}\text{H}_{16}\text{N}_3\text{O}_3\text{Pt}$   $[\text{M}-\text{Cl}]^+$  (m/z): 577.0839; found: 577.0871. IR (KBr,  $\text{cm}^{-1}$ ): 3055, 2968, 2926  $\nu(\text{C}-\text{H})$ ; 1702  $\nu(\text{C}=\text{O}$  of cyclic ester); 1607  $\nu(\text{C}=\text{N})$ . UV-Vis (in  $\text{CH}_3\text{CN}$ ),  $\lambda_{\text{max}}$  ( $\epsilon$ ,  $\text{M}^{-1}\text{cm}^{-1}$ ): 462 (7480), 372 (6900), 262 (19280).

**III.2.3. Theoretical study**

Density functional theory (DFT) was used to optimize the complexes' whole geometry using the B3LYP<sup>53</sup> hybrid exchange correlation functional. The 6-31G(d) basis set was applied to all elements apart from Pd and Pt. For the Pd and Pt atoms, the LanL2dz<sup>54</sup> basis set with effective core potential was used. The present correlation functional (B3LYP) and basis set (LanL2dz) has been widely used for several Pd and Pt complexes.<sup>55</sup> The Gaussian-09 program<sup>56</sup> and the Gauss-View, Version 5 visualization package were used for all calculations. Electronic transitions were estimated using the conductor-like polarizable continuum model (CPCM)<sup>57</sup> in acetonitrile as the model solvent using the time-dependent density functional theory (TDDFT) formalism.<sup>58</sup> To determine the fractional contributions of distinct groups to each equation, GaussSum<sup>59</sup> was employed.

**III.2.4. X-ray diffraction**

Suitable single crystal of the two complexes **C1** and **C2** were performed for collecting the X-ray data with a Bruker Smart Apex CCD diffractometer equipped with graphite monochromatized Mo-K $\alpha$  radiation ( $\lambda = 0.71073$  Å) at 293 K. The SAINT program<sup>60</sup> was used to scale and integrate the data, while SADABS<sup>61</sup> was used to adjust for absorption. The non-hydrogen atoms were anisotropically purified after all data were corrected for Lorentz and polarization effects. According to the riding model, hydrogen atoms were added

throughout the refinement process. The SHELXL-2016/6 programme<sup>62</sup> was used to solve the structures using the direct method and refine them using full-matrix least-squares techniques on  $F^2$ . The SQUEEZE function of PLATON<sup>63</sup> was used to eliminate several unassignable peaks that were seen on the electron density map.

### III.2.5. Protein binding studies

#### III.2.5.1. UV-Vis and fluorescence studies

By measuring absorption and emission, it was possible to determine how the BSA protein interacted with the complexes. For this, a BSA stock solution ( $1 \times 10^{-5}$  M) was prepared in 500 mM phosphate buffer saline (PBS) at pH 7.4 and kept in the dark at 4° C. The complex solutions ( $1 \times 10^{-4}$  M) were prepared in DMSO solvent and was suitably diluted with PBS whenever necessary. The BSA ( $1 \times 10^{-5}$  M) concentration was kept constant throughout the absorption titration tests while the complexes' addition concentrations were changed. A fixed BSA concentration was used for fluorescence titrations in a similar manner. A micropipette was used to manually add the compounds to both the absorbance and emission titrations. The identical concentrations of BSA and the complexes were also employed for synchronous fluorescence spectra at two distinct  $\Delta\lambda$  values (difference between the excitation and emission wavelengths of BSA), such as 15 and 60 nm.

#### III.2.5.2. CD spectral study

Circular dichroism (CD) measurements were obtained by employing JASCO (J-815) spectropolarimeter at 298 K using a quartz cuvette of 1 cm cell path length. The spectra were carried out by keeping a constant BSA concentration (0.6  $\mu$ M) and the spectra were recorded in the absence and presence of the two complexes with a mole ratio ( $r_i$ ) ranged from 0 to 4, where  $r_i = [\text{complex}]/[\text{BSA}] = 0, 2$  and 4. The CD results were expressed in terms of the mean residual ellipticity (MRE) in  $\text{deg cm}^2 \text{dmol}^{-1}$  according to the following equation (1).

$$\text{MRE} = \text{observed CD (mdeg)} / 10C_p n l \quad (1)$$

Where,  $C_p$  represents the molar concentration of the protein,  $n$  stands for the number of amino acid residues (583 for BSA) and  $l$  is the path length of the cell (1 cm). The  $\alpha$ -helical (%) contents of the free and bound BSA were calculated from the mean MRE values at 208 nm using the following equation (2).

$$\alpha\text{-helix (\%)} = [(-\text{MRE}_{208} - 4000) / (33,000 - 4000)] \times 100 \quad (2)$$

Where,  $MRE_{208}$  is the MRE value observed at 208 nm, 4000 is the MRE of the  $\beta$ -form and random coil conformation at 208 nm, and 33000 is the MRE value of a pure  $\alpha$ -helix at 208 nm.

### III.2.6. Cytotoxicity Studies

#### III.2.6.1. Cell Culture

HepG2 cells were cultured in DMEM mixed with 10% FBS and 1% antibiotic (PSN) in a humidified incubator containing 95% air and 5%  $CO_2$  at 37°C. The HepG2 cell line was cultured in DMEM containing 10% FBS in a humidified atmosphere under 5%  $CO_2$  at 37°C. A Day before the start of experiment cells were harvested with 0.5% trypsin and seeded at a required density to let them re-equilibrate. All experiments were conducted in DMEM containing 10% FBS and 1% PSN antibiotic.

#### III.2.6.2. MTT Assay

Cell viability was carried out by using MTT metabolic activity assay to investigate the cytotoxic effect of the complexes. Cells ( $1 \times 10^6$  /well) were seeded in 96-well plate and treated with different concentrations of Pd & Pt -complexes (2.5, 5, 10, 20, 40, 60, 80 and 100  $\mu$ M) and were kept in incubator for 24h in a humidified (5%  $CO_2$ ) atmosphere at 37°C. After 24h incubation MTT (4 mg/mL) was added and the plates were further incubated for another 4h. The absorbance of DMSO-solubilized intracellular formazan salt was recorded using ELISA reader at 595 nm. This experiment was done in triplicate.

#### III.2.6.3. Detection of DNA fragmentation/cell death by ELISA

Cell death was evaluated using an ELISA cell death detection that quantitatively spots histone exposed from DNA fragments. Briefly, cells treated with or without different concentrations of two complexes for 24 h were lysed and centrifuged. Supernatant containing histone containing DNA fragments were taken as source of antigen in a sandwich ELISA with primary anti-histone monoclonal antibody coated to the streptavidin-coated well. This was followed by a second anti-DNA monoclonal antibody coupled to peroxidase. The amount of histones was measured by the peroxidase retained in the immune-complex. Peroxidase activity was determined spectrophotometrically at 405 nm with 2,2-azino-di (3-ethylbenzthiazolin-sulfonate) (ABTS) as a substrate.



### III.2.6.4. Intracellular ROS production

Mitochondria are the primary source of the multiplication of reactive oxygen species (ROS) creation in mammalian cells and generation of reactive oxygen species (ROS) is a key factor of apoptotic cell death. For the determination of intracellular ROS formation, treated cells were loaded with 10  $\mu$ M of H<sub>2</sub>DCFH-DA (2', 7'-dichlorodihydrofluoresceindiacetate) for 20 min by incubation before the analysis by flow cytometer (BD LSR Fortessa™, Becton Dickinson, Franklin Lakes, NJ, USA) at 37°C. The elevation of DCF fluorescence directly redirects the generated ROS inside cells which were represented as mean fluorescence intensity of DCF.

### III.2.6.5. Cell Imaging Study

HepG2 cells were used as model for further study on cytotoxicity induced by complex. Cancer cell death through apoptosis is a desirable aim. Distinctive apoptotic changes in cell morphology like cell shrinkage and cell rounding were observed in complex treated cells. Apoptotic feature in nucleus such as chromatin condensation and DNA crumbling were seen after 40 $\mu$ M Complex treatment for 24h. Increased numbers of condensed bright fragmented nuclei were evident from the DAPI staining (a nuclear staining dye). Increased number of DNA fragments in drug treated cell was also found from the DNA-fragmentation study using death detection kit.

### III.2.6.6. Quantification of Apoptosis by Flow Cytometry

Determination of apoptosis and necrosis were analyzed by flow cytometry using Annexin-V/FITC/PI detection kit (Calbiochem, CA, USA). HepG2 cells were seeded in a 6 well plate and treated with both drugs (IC<sub>70</sub>) time dependently upto 24h and were stained with Annexin-V/FITC-PI as per the direction of manufacturer. The percentage of viable, apoptotic (early and late), necrotic cells were calculated by flow cytometry (BD LSR Fortessa, San Jose, CA, USA).

### III.2.6.7. Caspase activity

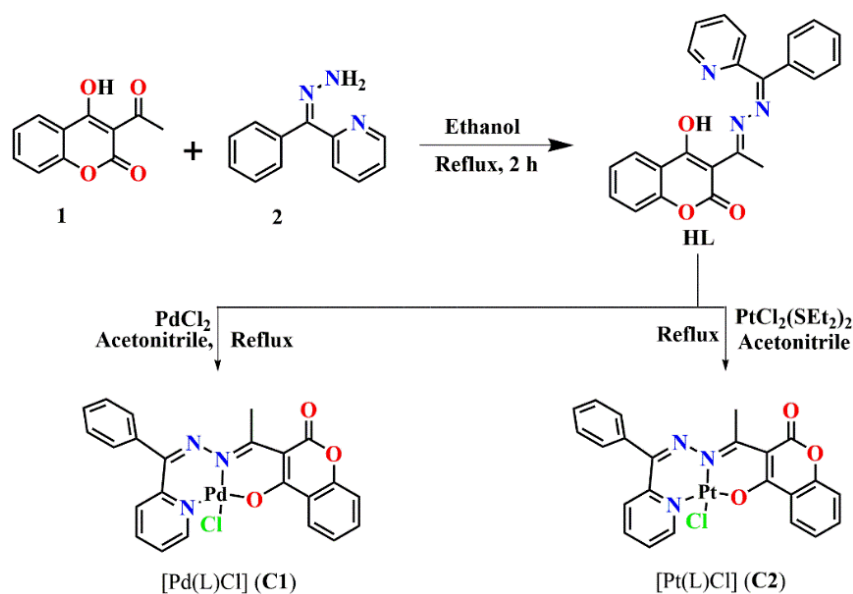
The activity of apoptosis initiation caspase (caspase-9) and apoptosis executioner caspase (caspase-3) were quantified by using a commercially available colorimetric assay kits from Invitrogen. The proteolytic cleavage of chromophore *p*-nitroaniline (*p*-NA) by Caspase-3 from its labelled substrate, Ac-DEVD-*p*-NA and by Caspase-9 from its labeled substrate, LEHD-*p*-NA. were detected at 405 nm by an ELISA reader. Cells after treatment with compounds were lysed and processed according to the manufacturer's instructions.

### III.3. Results and discussion

#### III.3.1. Synthesis and spectral analysis

New Pd(II) and Pt(II) complexes,  $[\text{Pd}(\text{L})\text{Cl}]$  (**C1**) and  $[\text{Pt}(\text{L})\text{Cl}]$  (**C2**) were synthesized by the reaction of HL with  $\text{PdCl}_2$  and  $\text{Pt}(\text{SEt}_2)_2\text{Cl}_2$  respectively in a 1:1 molar ratio under refluxing condition in acetonitrile (scheme III.1). Elemental analysis, IR, HRMS and  $^1\text{H}$  NMR spectroscopy were employed to fully comprehend the structures of the complexes, **C1** and **C2**, (see the experimental section) and single-crystal X-ray crystallography was used to corroborate these findings.

IR spectrum of ligand (HL) shows a wide band at  $3404\text{ cm}^{-1}$  which corresponds to  $\nu_{\text{O-H}}$  stretching while a sharp stretching band at  $1701\text{ cm}^{-1}$  corresponds to keto group of cyclic ester and a peak range from  $2900$  to  $3100\text{ cm}^{-1}$  corresponding to C-H stretching (Fig. III.1(a)). Another vibration was detected at  $1610\text{ cm}^{-1}$  in HL corresponding to  $\nu_{\text{C=N}}$  stretching which after coordination of nitrogen atom with metal ion was shifted to  $1598\text{ cm}^{-1}$  and  $1607\text{ cm}^{-1}$  in **C1** and **C2** respectively.



Scheme III.1. Synthetic layout for complexes **C1** and **C2**

Both the complexes exhibit a peak range between  $2900$  and  $3060\text{ cm}^{-1}$  that is consistent with C-H stretching. A sharp band at  $1700\text{ cm}^{-1}$  and  $1702\text{ cm}^{-1}$  for **C1** and **C2** respectively, corresponding to the keto group of the cyclic ester and no broad peak of O-H stretching are

present in either of the complexes, indicating that the phenolic OH group was involved in the bonding with the metal ions ( $\text{Pd}^{2+}$  and  $\text{Pt}^{2+}$ ) (Fig. III.1 (b) and (c)).

$^1\text{H}$  NMR spectrum of **HL**, **C1** and **C2** were recorded in  $\text{CDCl}_3$ . The proton peak of OH group appeared at 14.3 ppm for free ligand (**HL**) which is disappeared for the complexes [**C1** and **C2**] as a result of coordination of oxygen atom with palladium and platinum metal ion respectively (Figs. III.2, III.4 and III.6). The proton peak due to  $\text{CH}=\text{N}$  in the pyridyl component of **C1** and **C2** occurred at 9.61 and 9.95 ppm, respectively, compared to 8.65 ppm in the parent ligand, **HL**. This is because the coordination of pyridyl nitrogen atom with metal (Pd or Pt) which caused the electron density of nitrogen atom to move towards metal atom (Pd or Pt).  $^{13}\text{C}$  NMR of the three compounds were taken in  $\text{CDCl}_3$  (Figs. III.3, III.5 and III.7).

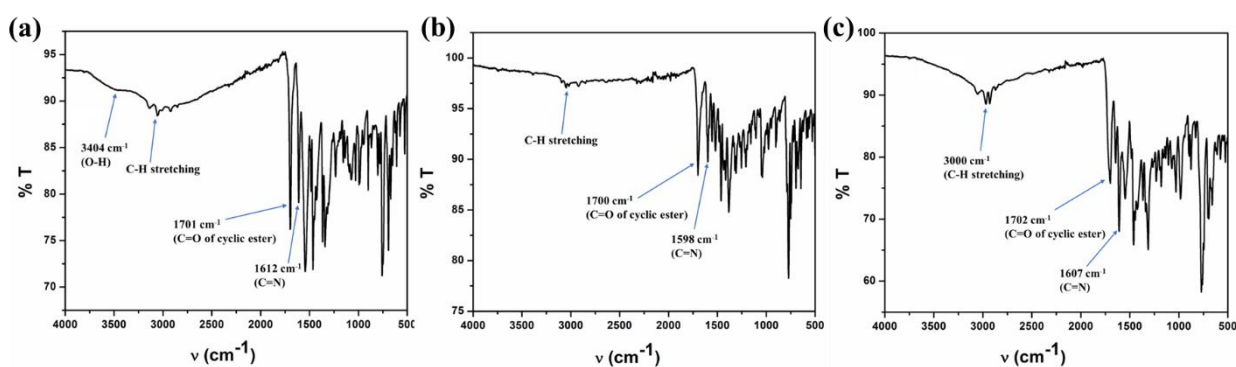
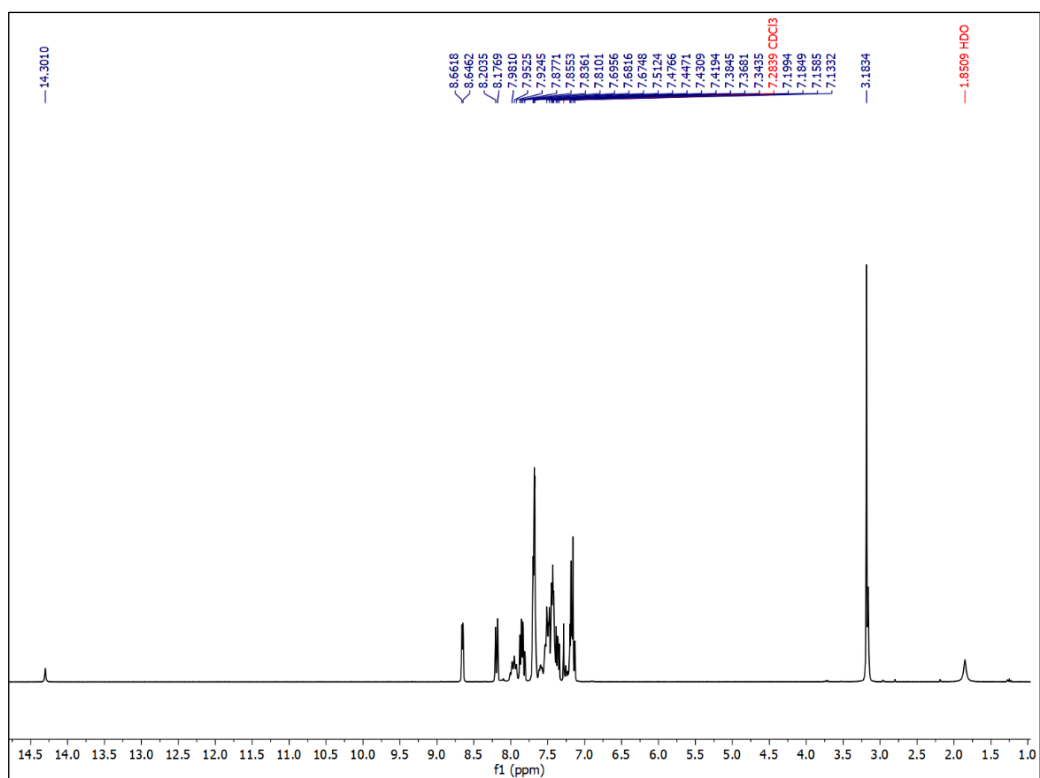
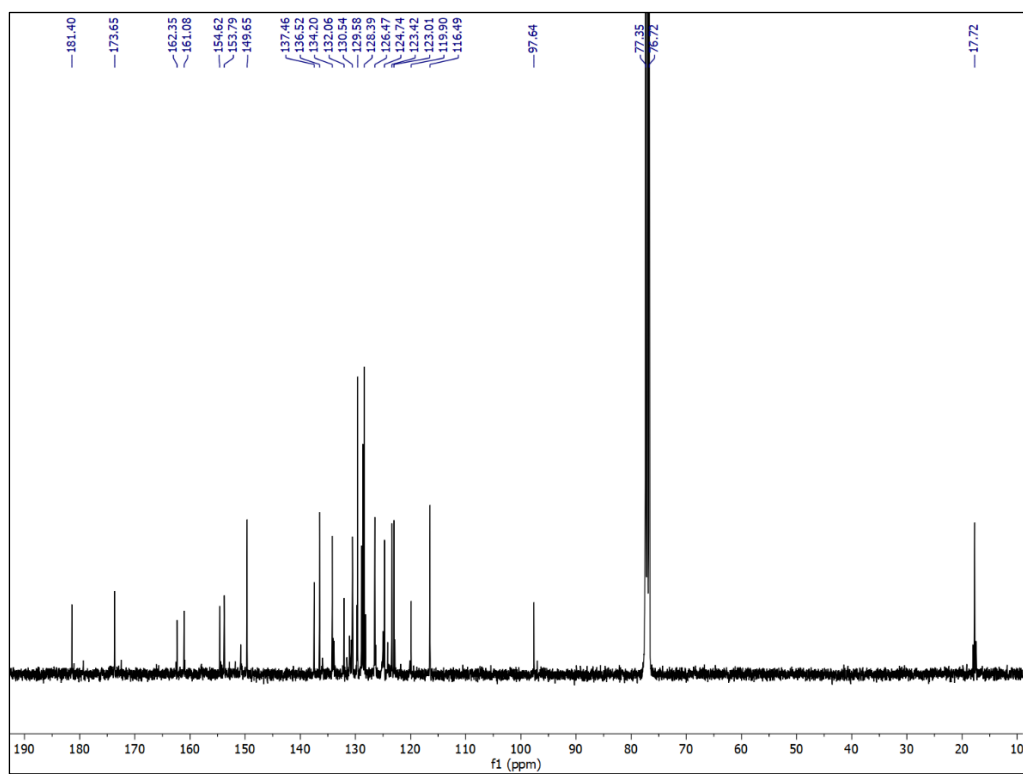
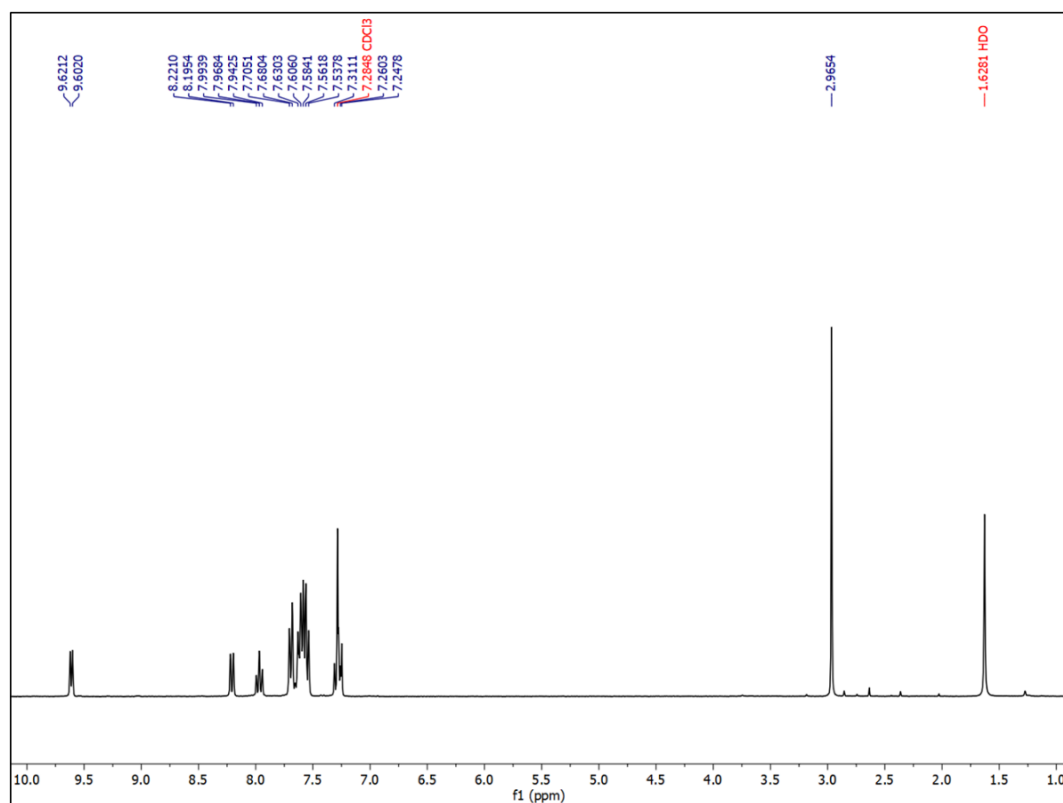
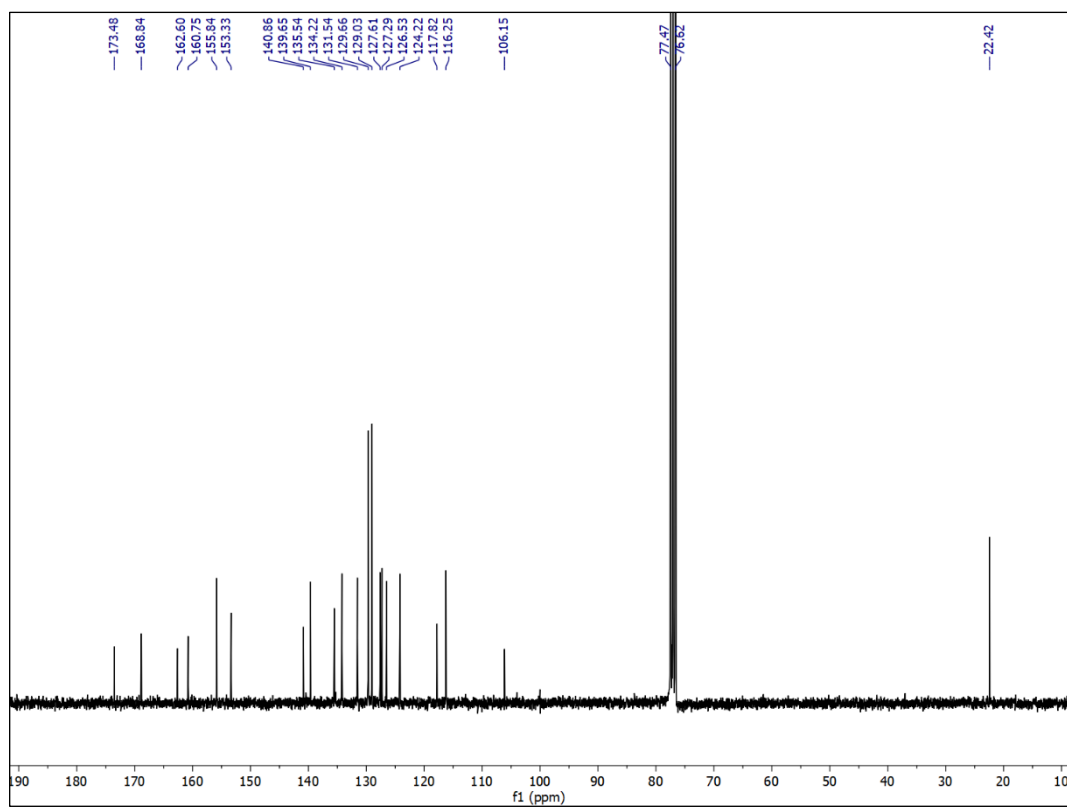
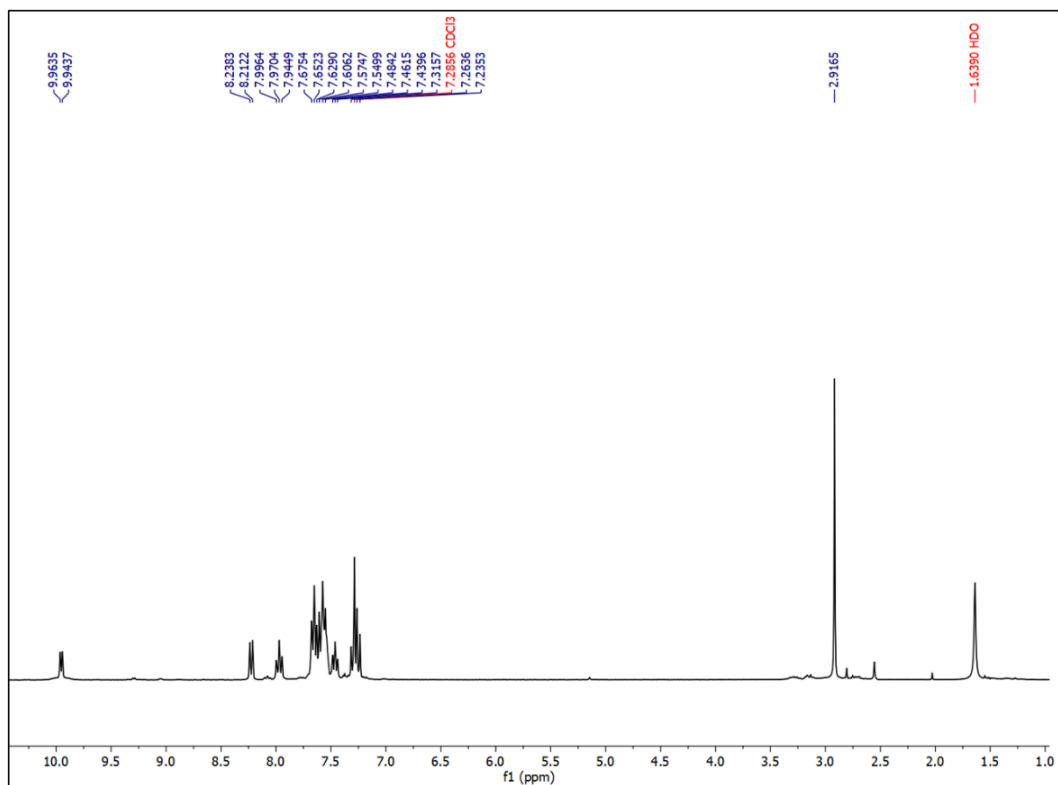
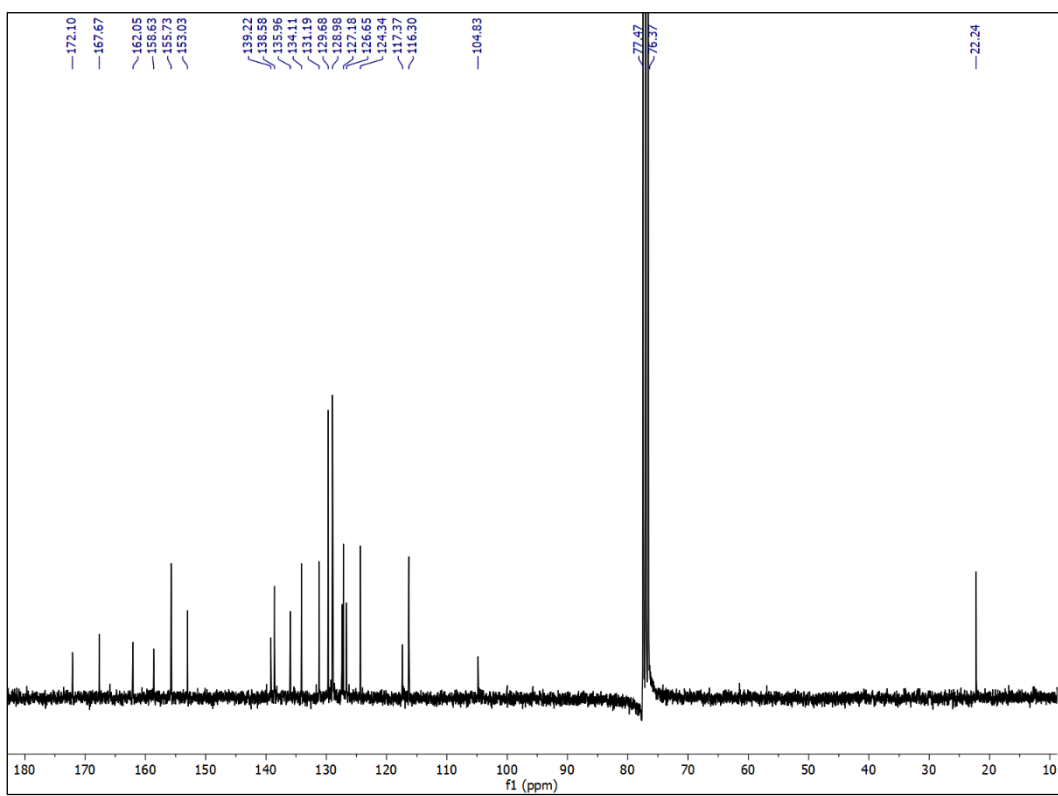


Figure III.1. IR spectra of (a) ligand (**HL**), (b)  $[\text{Pd}(\text{HL})\text{Cl}_2]$  (**C1**) and (c)  $[\text{Pt}(\text{L})\text{Cl}]$  (**C2**)

For the details about the coupling between the adjacent protons,  $^1\text{H}$ - $^1\text{H}$ -2D COSY NMR spectra of the compounds were performed in  $\text{CDCl}_3$  (Figs. III.8 and III.9). A strong coupling was observed between H6 proton ( $\text{HC}=\text{N}$ , pyridyl) and H5 proton (ortho coupling) and a weak coupling between H6 proton and H4 (1,3-coupling) was also noticed for both the complexes **C1** and **C2** in  $^1\text{H}$ - $^1\text{H}$ -2D COSY NMR spectra. HRMS spectra of ligand, **HL** display molecular ion peak as  $[\text{M} + \text{H}]^+$  at 384.1360 [error = 3.12 ppm] (Fig. III.10). While HRMS spectra of the two complexes (**C1** and **C2**) exhibit molecular ion peaks as  $[\text{M} - \text{Cl}]^+$  which are at 488.0265 [error = 7.99 ppm] and 577.0871 [error = 5.54 ppm] respectively (Figs. III.11 and III.12).

Figure III.2.  $^1\text{H}$  NMR spectra of **HL** in  $\text{CDCl}_3$ Figure III.3.  $^{13}\text{C}$  NMR spectra of **HL** in  $\text{CDCl}_3$

Figure III.4. <sup>1</sup>H NMR spectra of complex **C1** in CDCl<sub>3</sub>Figure III.5. <sup>13</sup>C NMR spectra of the complex **C1** in CDCl<sub>3</sub>

Figure III.6. <sup>1</sup>H NMR spectra of complex **C2** in CDCl<sub>3</sub>Figure III.7. <sup>13</sup>C NMR spectra of the complex **C2** in CDCl<sub>3</sub>

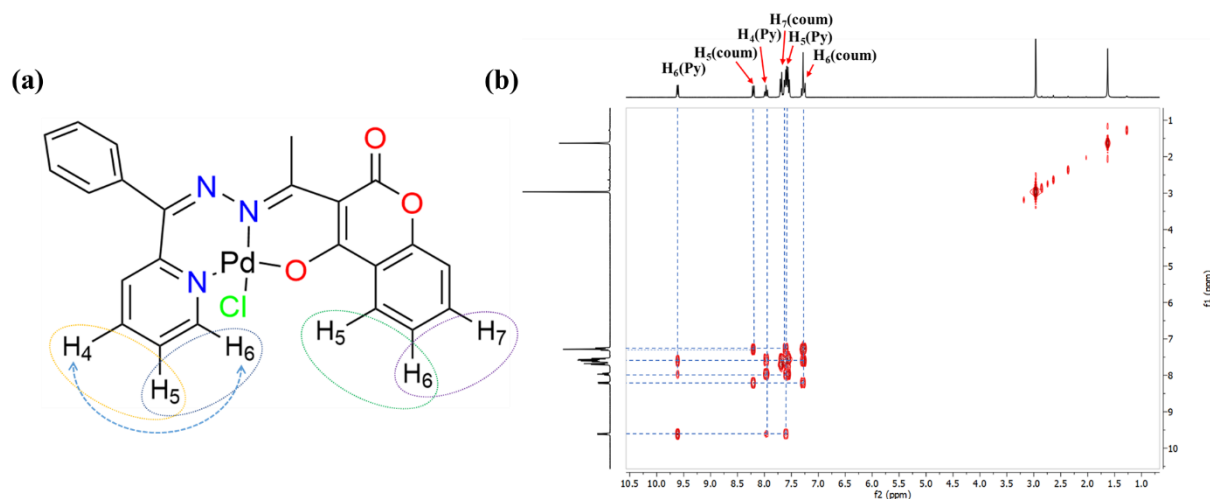


Figure III.8. (a) Coupling between the circled hydrogens in **C1** and (b) <sup>1</sup>H-<sup>1</sup>H-2D COSY NMR spectrum of **C1** in CDCl<sub>3</sub>

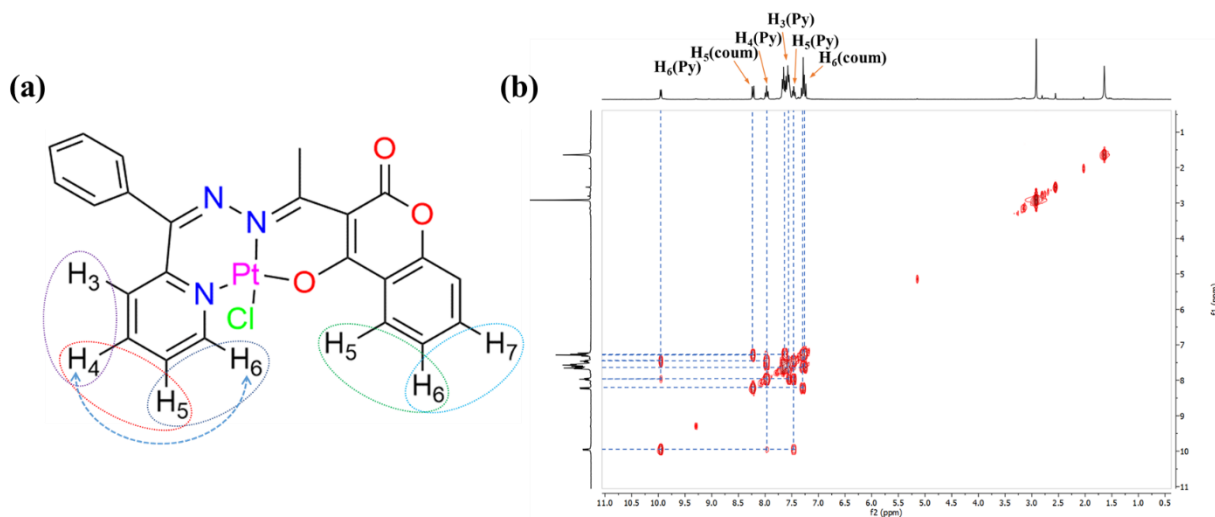
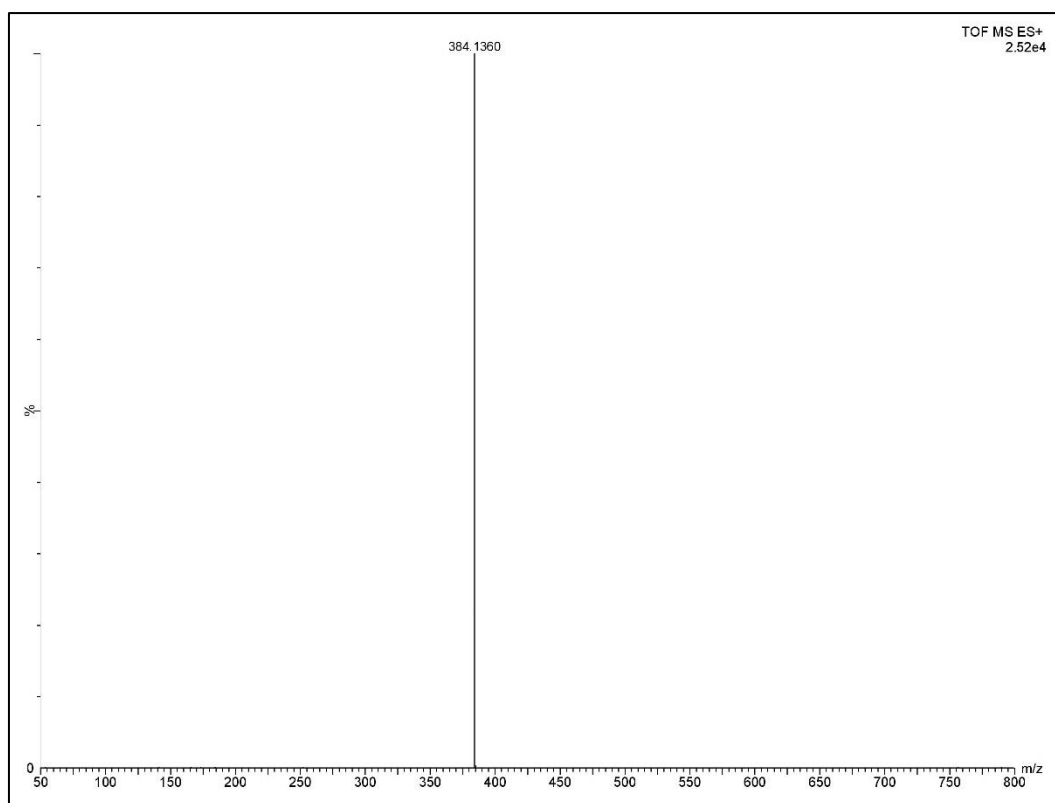
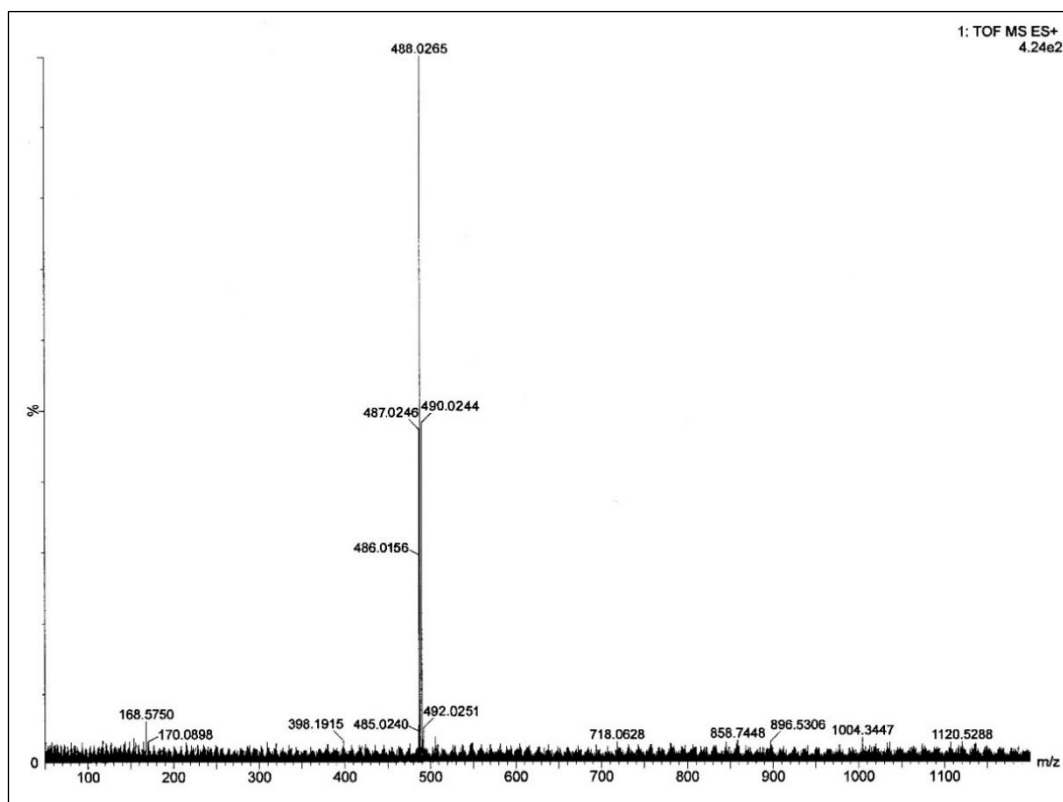


Figure III.9. (a) Coupling between the circled hydrogens in **C2** and (b) <sup>1</sup>H-<sup>1</sup>H-2D COSY NMR spectrum of **C2** in CDCl<sub>3</sub>



Figure III.10. HRMS of ligand **HL** in acetonitrileFigure III.11. HRMS of the complex **C1** in acetonitrile

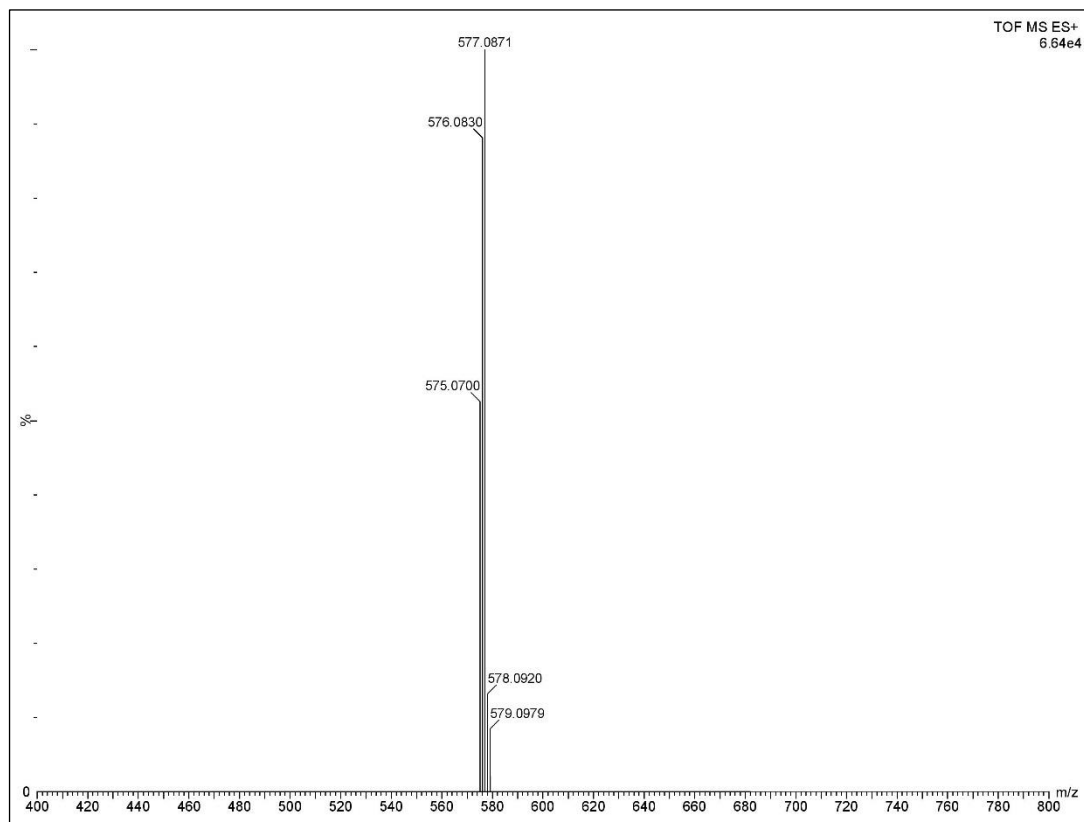


Figure III.12. HRMS of the complex **C2** in acetonitrile

UV-Vis spectral properties of the ligand (HL) and its Pd(II) and Pt(II) complexes were studied in acetonitrile solution at the 200-700 nm range. When HL (10  $\mu\text{M}$ ) is dissolved in acetonitrile, the absorption spectrum shows a band at 378 nm ( $\epsilon$ , 42809  $\text{M}^{-1}\text{cm}^{-1}$ ) and a hump at 246 nm ( $\epsilon$ , 22510  $\text{M}^{-1}\text{cm}^{-1}$ ). The corresponding Pd(II) complex (10  $\mu\text{M}$ ) shows two moderate peaks at 428 nm ( $\epsilon$ , 6180  $\text{M}^{-1}\text{cm}^{-1}$ ) and 338 nm ( $\epsilon$ , 5987  $\text{M}^{-1}\text{cm}^{-1}$ ) respectively as well as a high intensity band at 250 nm ( $\epsilon$ , 23283  $\text{M}^{-1}\text{cm}^{-1}$ ). Two substantial absorption peaks were also seen for the Pt(II) complex (10  $\mu\text{M}$ ) at 462 nm ( $\epsilon$ , 7480  $\text{M}^{-1}\text{cm}^{-1}$ ) and 372 nm ( $\epsilon$ , 6900  $\text{M}^{-1}\text{cm}^{-1}$ ) respectively accompanied with an intense hump at 262 nm ( $\epsilon$ , 19280  $\text{M}^{-1}\text{cm}^{-1}$ ) (Fig. III.13).

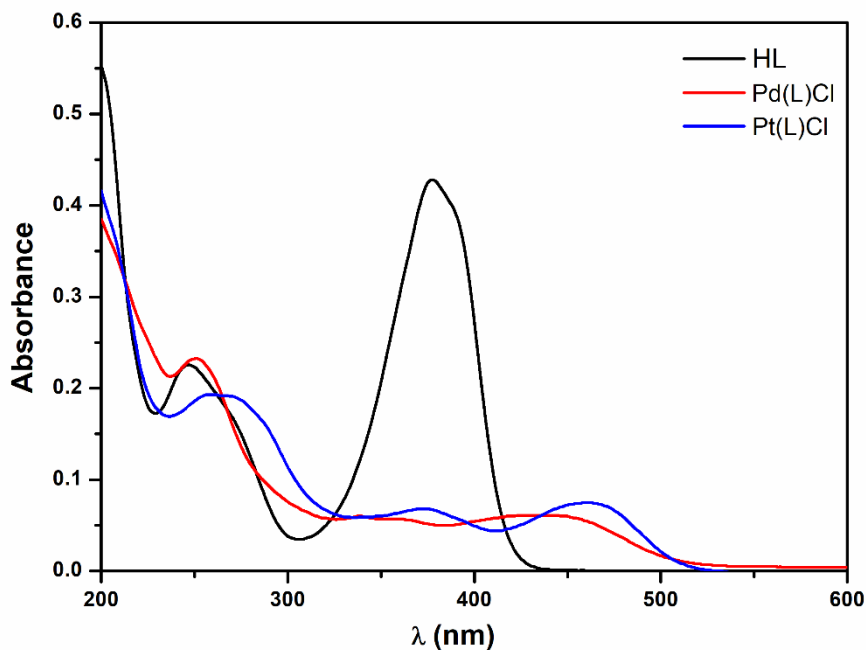


Figure III.13. UV-Vis spectra of **HL**, **C1** and **C2** in acetonitrile

### III.3.2. Crystal structure descriptions

The structures of **C1** and **C2** crystallized in the monoclinic system with  $P2_1/n$  space group. Table III.1 contains information on crystal analysis, data collecting, and structural refining. ORTEP plots are shown in Fig. III.14. HL acts as N, N, O donor tridentate chelator in both the complexes. HL interacts with metal ions [Pd(II) and Pt(II)] via pyridyl nitrogen atom (N1), imine nitrogen atom (N3), and oxygen atom (O1) via production of two six-membered chelate rings [Pd1-N3-N2-C6-C5-N1 and Pd1-N3-C13-C15-C16-O1 for **C1** and Pt1-N3-N2-C6-C5-N1 and Pt1-N3-C13-C15-C16-O1 for **C2**] causing a square planar geometry around the two metal ions [Pd(II) and Pt(II)]. In case of **C1** chelate bite angles  $\angle O1-Pd1-N3$  and  $\angle N3-Pd1-N1$  are  $89.79(8)^\circ$  and  $89.05(8)^\circ$  respectively while for **C2** chelate bite angles  $\angle N3-Pt1-N1$  and  $\angle N3-Pt1-O1$  are  $89.52(12)^\circ$  and  $90.16(11)^\circ$  respectively. The trans angles  $\angle O1-Pd1-N1$  for **C1** and  $\angle N1-Pt1-O1$  for **C2** are discovered to be  $173.61(8)^\circ$  and  $173.05(11)^\circ$  respectively. These deviations from the ideal trans angle of  $180^\circ$  caused a considerable deformation in the complexes' square planar geometry. In **C1**, Pd1-N1 ( $1.998(2)$  Å), Pd1-N3 ( $1.992(2)$  Å) and Pd1-Cl1 ( $2.3026(7)$  Å) bond distances are in good agreement with the reported values of known palladium complexes<sup>64-68</sup>, while for **C2**, Pt1-N1 ( $1.988(3)$  Å), Pt1-N3 ( $1.989(3)$  Å) and Pt1-Cl1 ( $2.3032(10)$  Å) bond distances are also found to be comparable with the reported values (Table III.2).<sup>64,67-72</sup>

Table III.1. Crystallographic data and refinement parameters of **C1** and **C2**

Complex	[Pd(L)Cl] ( <b>C1</b> )	[Pt(L)Cl] ( <b>C2</b> )
Formula	C <sub>23</sub> H <sub>16</sub> Cl N <sub>3</sub> O <sub>3</sub> Pd	C <sub>23</sub> H <sub>16</sub> Cl N <sub>3</sub> O <sub>3</sub> Pt
Formula Weight	524.24	612.93
Crystal System	<i>monoclinic</i>	<i>monoclinic</i>
Space group	<i>P21/n</i>	<i>P21/n</i>
a, b, c [Å]	10.7397(9), 13.7223(11), 14.0399(12)	10.7879(8), 13.6464(10), 14.0301(11)
$\alpha$	90	90
$\beta$	98.660(3)	98.521(2)
$\gamma$	90	90
V [Å <sup>3</sup> ]	2045.5(3)	2042.7(3)
Z	4	4
D(calc) [g/cm <sup>3</sup> ]	1.702	1.993
Mu(MoKa) [ /mm]	1.069	7.032
F(000)	1048	1176
$\theta$ (Min-Max) [°]	2.087 - 27.619	2.093- 27.536
Dataset (h; k; l)	-13 to 14, -17 to 17, -18 to 18	-14 to 13, -17 to 17, -18 to 18
No. of measured reflections	30660	72191
Total reflection (N <sub>tot</sub> )/	4712/4058	4673/4246
Unique reflection (N <sub>ref</sub> )		
R, wR <sub>2</sub>	0.0291, 0.0617	0.0231, 0.0557
Goodness of fit(S)	1.073	1.055

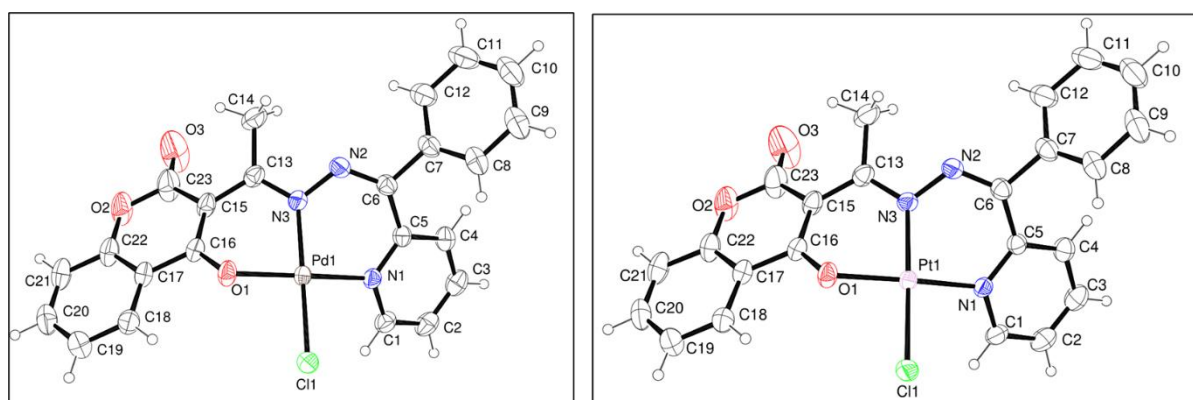
Figure III.14. ORTEP view of **C1** and **C2** respectively with 35% ellipsoidal probability

Table III.2. Some selected X-ray and calculated bond distances and angles of **C1** and **C2**

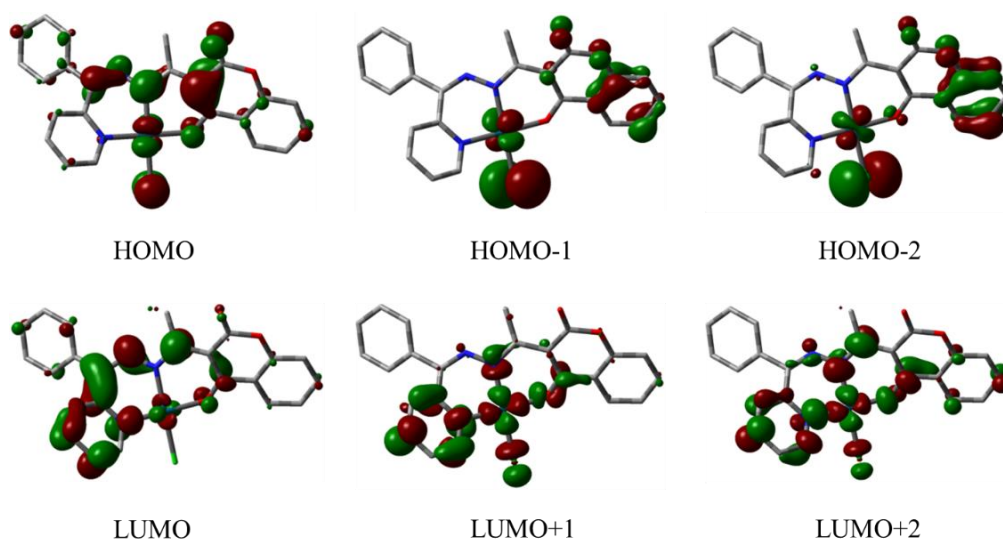
<b>C1</b>			<b>C2</b>		
Bonds(Å)	X-ray	Calc.	Bonds(Å)	X-ray	Calc.
Pd1–O1	1.9870(17)	2.009	Pt1–O1	1.997(2)	2.016
Pd1–N3	1.992(2)	2.033	Pt1–N3	1.989(3)	2.032
Pd1–N1	1.998(2)	2.051	Pt1–N1	1.988(3)	2.037
Pd1–Cl1	2.3026(7)	2.344	Pt1–Cl1	2.3032(10)	2.366
O1–C16	1.290(3)	1.278	O1–C16	1.290(4)	1.281
N3–C13	1.316(3)	1.338	N3–C13	1.326(5)	1.342
N2–N3	1.393(3)	1.365	N2–N3	1.396(4)	1.365
N1–C1	1.347(3)	1.349	N1–C1	1.352(4)	1.354
N1–C5	1.352(3)	1.356	N1–C5	1.361(4)	1.361
Angles (°)					
O1–Pd1–N3	89.79(8)	89.399	O1–Pt1–N3	90.16(11)	89.968
O1–Pd1–N1	173.61(8)	174.108	O1–Pt1–N1	173.05(11)	174.698
N3–Pd1–N1	89.05(8)	89.618	N3–Pt1–N1	89.52(12)	90.589
O1–Pd1–Cl1	87.71(5)	88.360	O1–Pt1–Cl1	86.98(8)	86.695
N3–Pd1–Cl1	173.36(6)	175.378	N3–Pt1–Cl1	173.28(9)	174.396
N1–Pd1–Cl1	94.11(6)	118.518	N1–Pt1–Cl1	94.06(9)	93.147

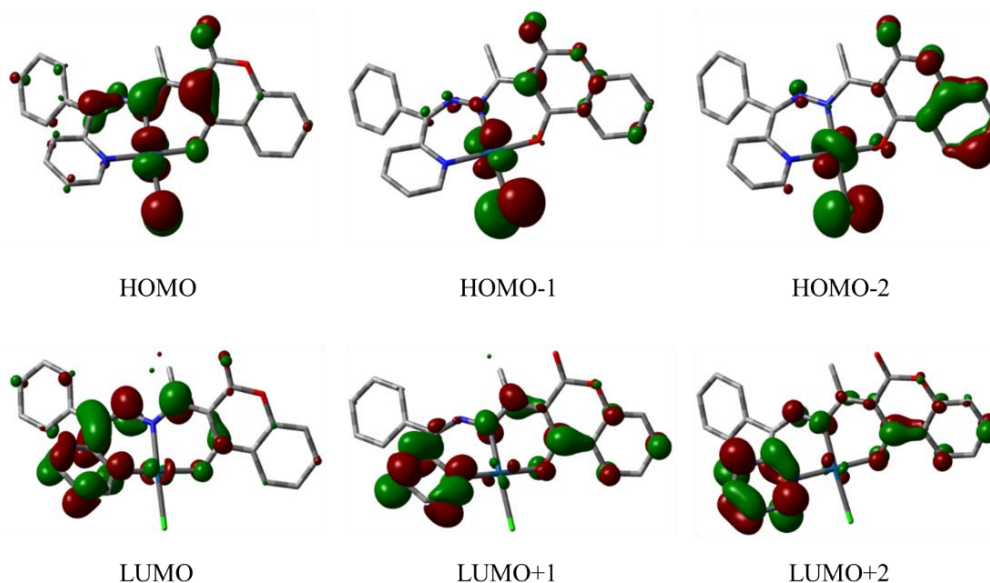
### III.3.3. Computational study

By applying the DFT approach and the B3LYP exchange-correlation functional, the geometries of the two complexes (**C1** and **C2**) were optimized. The data from the X-ray crystal structures are reasonably well reproduced by the computed bond distances and angles of the complexes (Table III.2). Contour plots of some chosen molecular orbitals of the complexes are provided in Figs. III.15 and III.16. Energy and compositions of chosen molecular orbitals are provided in Table III.3. In the case of **C1**, the ligand contributes 75% of the higher energy occupied molecular orbital (HOMO), and the Pd( $d\pi$ ) orbitals contribute less. The ligand  $\pi^*$  orbitals contribute 95% of the low-lying virtual orbital, LUMO. On the other hand, for **C2**, the lower energy unoccupied orbital, LUMO has 96% contribution from ligand  $\pi^*$  orbitals, whereas the higher energy occupied orbital (HOMO) has 58% contribution from HL and 24% contribution from Pt( $d\pi$ ) orbitals.

Table III.3. Energy and % of composition of some selected molecular orbitals of **C1** and **C2**

MO	<b>C1</b>				<b>C2</b>			
	Energy	% Composition			Energy	% Composition		
		Pd	L	Cl		Pt	L	Cl
LUMO+5	-0.55	02	98	0	-0.54	03	97	00
LUMO+4	-1.09	01	99	0	-1.01	41	49	10
LUMO+3	-1.56	02	98	0	-1.06	10	88	02
LUMO+2	-1.76	23	72	05	-1.54	03	97	00
LUMO+1	-2.05	30	62	08	-1.95	03	97	00
LUMO	-2.82	04	95	01	-2.81	04	96	00
HOMO	-5.92	13	75	12	-5.81	24	58	18
HOMO-1	-6.41	15	32	53	-6.38	22	28	50
HOMO-2	-6.5	12	36	52	-6.49	22	45	33
HOMO-3	-6.56	12	58	30	-6.53	34	56	10
HOMO-4	-6.78	75	13	12	-6.68	72	11	17
HOMO-5	-6.99	28	72	0	-6.83	33	64	03
HOMO-6	-7.24	03	94	03	-7.24	03	97	00
HOMO-7	-7.31	04	90	06	-7.32	02	94	04
HOMO-8	-7.33	10	86	04	-7.34	05	92	03
HOMO-9	-7.46	09	73	18	-7.54	08	74	18
HOMO-10	-7.73	30	60	10	-7.69	16	66	18

Figure III.15. Contour plots of selected molecular orbital of **C1**

Figure III.16. Contour plots of selected molecular orbital of **C2**

TDDFT computations on the optimized geometries were also performed to retrieve additional information about the electronic transitions. Complex **C1** features a low energy transition (HOMO→LUMO+1 transition) that is close to 423 nm and corresponds to the observed band at 428 nm with mixed intra-ligand charge transfer (ILCT) and ligand to metal charge transfer (LMCT) characteristics while, HOMO → LUMO+2 transition at 335 nm which has a mixture of ILCT and LMCT characteristics, correlates to the fairly bright experimental peak at 338 nm. The moderately bright bands at 462 nm and 372 nm for **C2** correspond to estimated bands featuring mixed ILCT and MLCT character at 469 nm (HOMO→LUMO transition) and 369 nm (HOMO-3→LUMO transition), respectively. Furthermore, the complexes' high-energy bands at 250–262 nm exhibit ILCT characteristics (Table III.4).

Table III.4. Vertical electronic transition calculated by TDDFT/CPCM method of **C1** and **C2**

Compd.	$\lambda$ (nm)	E (eV)	Osc. Strength (f)	Key excitations	Character	$\lambda_{\text{expt.}}$ (nm) ( $\epsilon$ , $\text{M}^{-1}\text{cm}^{-1}$ )
<b>C1</b>	479.14	2.5877	0.1811	(72%) HOMO→LUMO	ILCT	
	422.99	2.9311	0.2253	(67%)HOMO→LUMO+1	ILCT/LMCT	428 (6180)
	335.06	3.7003	0.0607	(78%)HOMO→LUMO+2	ILCT/LMCT	338 (5987)
	272.49	4.5500	0.1614	(79%)HOMO→LUMO+4	ILCT	



	267.54	4.6342	0.1096	(61%)HOMO-5→LUMO+2	ILCT/LMCT	
	251.13	4.9371	0.1395	(71%)HOMO→LUMO+5	ILCT	250 (23283)
	468.71	2.6452	0.3797	(96%)HOMO→LUMO	ILCT/ MLCT	462 (7480)
	368.90	3.3609	0.1230	(76%)HOMO-3→LUMO	ILCT/ MLCT	372 (6900)
<b>C2</b>	297.05	4.1739	0.2394	(70%)HOMO-2→LUMO+1	ILCT/ MLCT/XLCT	
	257.25	4.8196	0.1923	(70%)HOMO-2→LUMO+2	ILCT	262 (19280)

### III.3.4. Protein binding studies

Electronic absorption spectra of BSA protein (10  $\mu$ M in PBS at pH 7.4) were acquired in the 200-500 nm range in presence of different concentration of the complexes as shown in Fig. III.17. BSA exhibits a 280 nm distinctive absorption band. Complexes are gradually added to the BSA solution, which causes a slight blue shift and a steady increase in 280 nm absorbance. This hypsochromic shift corresponds to ground-state association (static quenching) between the complex and protein.<sup>73,74</sup> The apparent association constant ( $K$ ) was calculated from the plot of  $1/(A_{obs}-A_0)$  vs  $1/[complex]$  (Table III.5 and Fig. III.17 inset) adopting the following equation.

$$\frac{1}{A_{obs} - A_0} = \frac{1}{A_c - A_0} + \frac{1}{K (A_c - A_0)[complex]}$$

Where  $A_0$  and  $A_c$  are the absorbance of BSA alone and serum albumin with the complex, respectively, and  $A_{obs}$  is the observed absorbance (at 280 nm) of the solution bearing various concentrations of the complex.

Fluorescence measurements were used to determine how the two complexes (**C1** and **C2**) interacted with BSA at room temperature. The fluorescence activity of BSA is due to tryptophan, tyrosine and phenylalanine protein residues.<sup>75</sup> The inherent fluorescence of BSA is caused mostly by tryptophan residues.<sup>76</sup> Complex is non-fluorescent in DMSO solution. However, an aqueous solution of BSA protein (10  $\mu$ M in PBS buffer, pH 7.4) produces a bright fluorescence at ~336 nm following excitation at 280 nm. The fluorescence intensity of BSA at ~336 nm now gradually decreases with the incremental addition of complexes (59.9% and 60.2% quenching for **C1** and **C2** respectively) with a little blue shift (Fig. III.18(a) and

III.19(a)). The interaction of complexes with the protein is primarily responsible for this hypochromicity in the spectra.

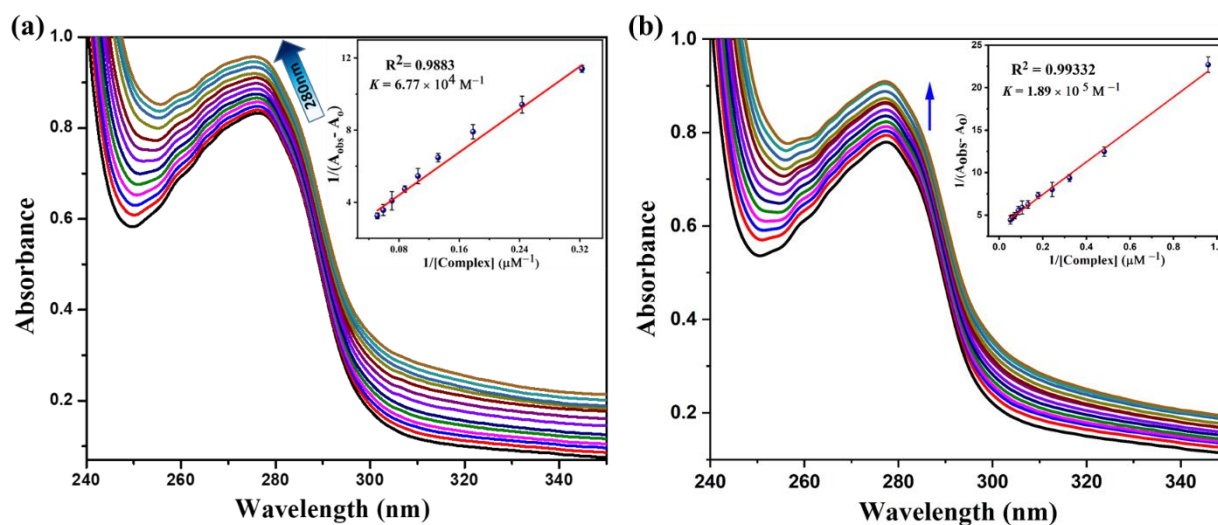


Figure III.17. Absorption spectral titration of BSA with (a) **C1** and (b) **C2** [inset: plot of  $1/[\text{complex}]$  vs  $1/(A-A_0)$ ]. The arrow shows the intensity changes.

Fluorescence quenching can be described by using Stern-Volmer equation:  $F_0/F = 1 + K_{sv}[Q]$ , where  $[Q]$  is the quencher concentration.  $F$  and  $F_0$  are the fluorescence strengths of BSA with and without the presence of the complex, respectively.  $K_{sv}$  is the Stern–Volmer quenching constant (Figs. III.18(b) and III.19(b) and Table III.5). The equilibrium binding constant ( $K_b$ ) and number of available binding sites ( $n$ ) for the complex were assessed from the plot of  $\log[(F_0-F)/F]$  versus  $\log[\text{complex}]$  (Figs. III.18(a) inset and III.19(a) inset) using by the Scatchard equation below:

$$\log(F_0 - F/F) = \log K_b + n \log[Q]$$

Where,  $K_b$  is the binding constant of the complexes with BSA, and  $n$  is the number of binding sites per albumin molecule. The slope and intercept of the plot of  $\log[(F_0-F)/F]$  versus  $\log[\text{complex}]$  are used to determine the  $K_b$  values and  $n$ , and these values reflects the higher affinity of complexes for BSA (Table III.5). As the calculated value of  $n$  is nearly equal to 1, it was predicted that both **C1** and **C2** with BSA form a system with a 1:1 molar ratio.<sup>77</sup>

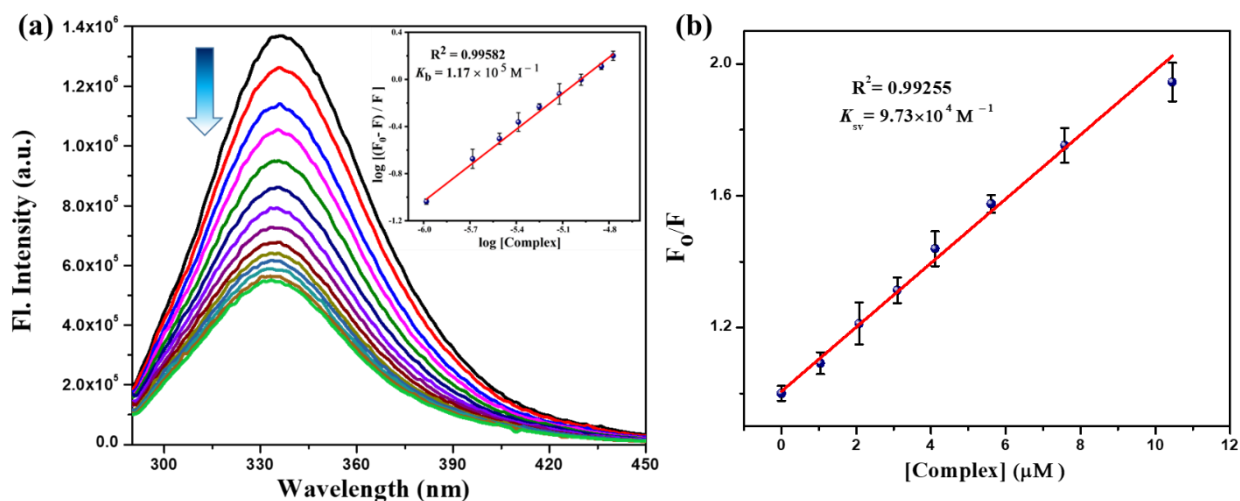


Figure III.18. Fluorescence spectral titration of BSA with Pd(II) complex (**C1**) (the arrow shows the intensity changes) and Stern-Volmer plot for **C1** ([complex] vs  $F_0/F$ ).

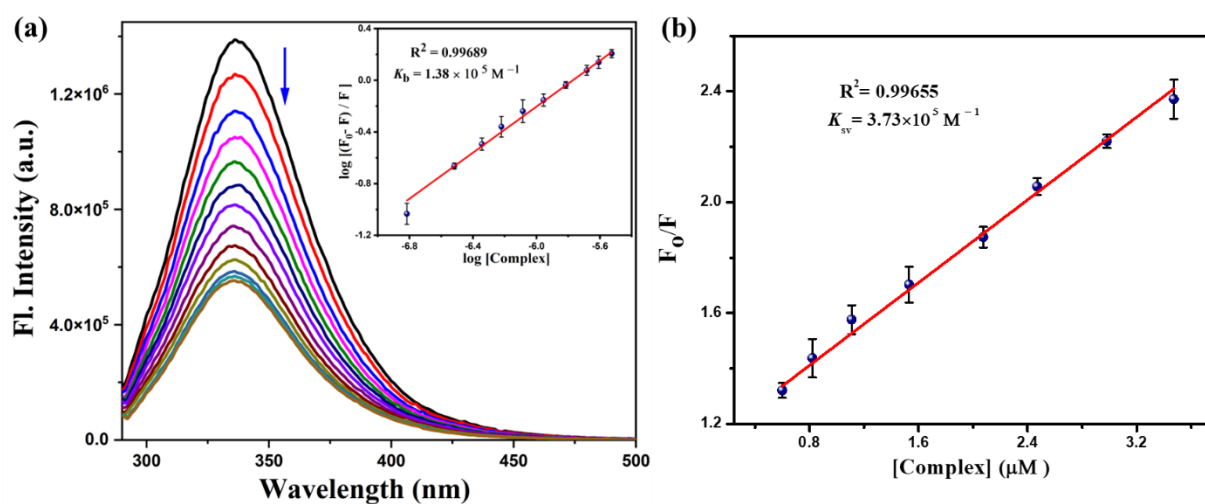


Figure III.19. Fluorescence spectral titration of BSA with Pt(II) complex (**C2**) (the arrow shows the intensity changes) and Stern-Volmer plot for **C2** ([complex] vs  $F_0/F$ ).

Table III.5. Apparent association constant ( $K$ ), quenching constant ( $K_{sv}$ ), binding constant ( $K_b$ ), and number of the binding sites ( $n$ ) of the BSA-**C1** and BSA-**C2** systems

Compound	UV Method	Fluorescence Method		
	$K (\times 10^4) (\text{M}^{-1})$	$K_b (\times 10^5) (\text{M}^{-1})$	$K_{sv} (\times 10^5) (\text{M}^{-1})$	$n$
BSA + <b>C1</b>	$6.77 \pm 0.18$	$1.17 \pm 0.029$	$0.973 \pm 0.03$	$1.01 \pm 0.02$
BSA + <b>C2</b>	$18.9 \pm 1.1$	$1.38 \pm 0.026$	$3.73 \pm 0.08$	$0.89 \pm 0.01$

#### III.3.4.1. Characteristics of the synchronous fluorescence spectra

Synchronous fluorescence spectra of BSA were taken in order to look into the structural modifications that the two complexes caused. According to Miller,<sup>78</sup> the spectra of different chromophores can be seen in the difference between the emission and excitation wavelengths ( $\Delta\lambda = \lambda_{em} - \lambda_{ex}$ ) in synchronous fluorescence spectroscopy. Tyrosine residue exhibits synchronous fluorescence when the  $\Delta\lambda$  value is 15 nm, but tryptophan exhibits synchronous fluorescence when the  $\Delta\lambda$  value is 60 nm.<sup>79</sup> At  $\Delta\lambda = 15$  nm and  $\Delta\lambda = 60$  nm, the synchronous fluorescence spectra of BSA with changing amounts of the complexes were captured (Fig. III.20). When the complexes were added to the BSA solution, the fluorescence intensity of BSA at 300 nm decreases slightly (~35% quenching for **C1** and **C2**) without any shift of  $\lambda_{max}$  in the synchronous fluorescence spectra of BSA at  $\Delta\lambda = 15$  nm while at  $\Delta\lambda = 60$  nm, adding the complexes (**C1** and **C2**) to BSA solution bring about in a significant fluorescence quenching of BSA at 336 nm (59.8% and 55.77% for **C1** and **C2** respectively). From the synchronous fluorescence studies, we can conclude that tyrosine fluorescence intensity was not altered much with the increasing amount of complexes, while a significant decrease and a blue shift of tryptophan fluorescence intensity has been observed, which suggest that the binding of the complexes with BSA influences the conformation of tryptophan only and not the microenvironment of tyrosine. Thus, the results of BSA protein interaction studies manifest that the interaction of the complexes with BSA is mostly because of the hydrophobic and electrostatic interactions. Therefore, it will be fascinating to research the complexes' pharmacological characteristics, such as cytotoxicity.

#### III.3.4.2. CD spectral studies

CD spectra were taken to investigate the modifications to BSA's secondary structure in presence of **C1** and **C2**. Two negative absorption bands that are indicative of the  $\alpha$ -helical structure of BSA may be seen in BSA at wavelengths of 208 nm ( $\pi \rightarrow \pi^*$ ) and 220 nm ( $n \rightarrow \pi^*$ ).<sup>80</sup> These negative band intensities decreased without any appreciable peak shifting when complexes **C1** and **C2** were added individually to BSA solution in various molar ratios (Fig. III.21). The CD spectra of BSA at physiological pH in different molar ratios of protein to drug (1:0, 1:2 and 1:4) indicate that the secondary structure of the proteins was altered by the interaction of **C1** and **C2** with BSA. According to calculations (by the equations (1) and (2)), the secondary structure of BSA's  $\alpha$ -helix content changed by 58.53% (1:0), 52.55% (1:2), and 48.18% (1:4) for **C1** and 55.92% (1:0), 47.18% (1:2), and 38.29% (1:4) for complex **C2**.

The outcomes thus show that the shape of the protein structure is altered as a result of the two complexes' binding to BSA.<sup>77</sup>

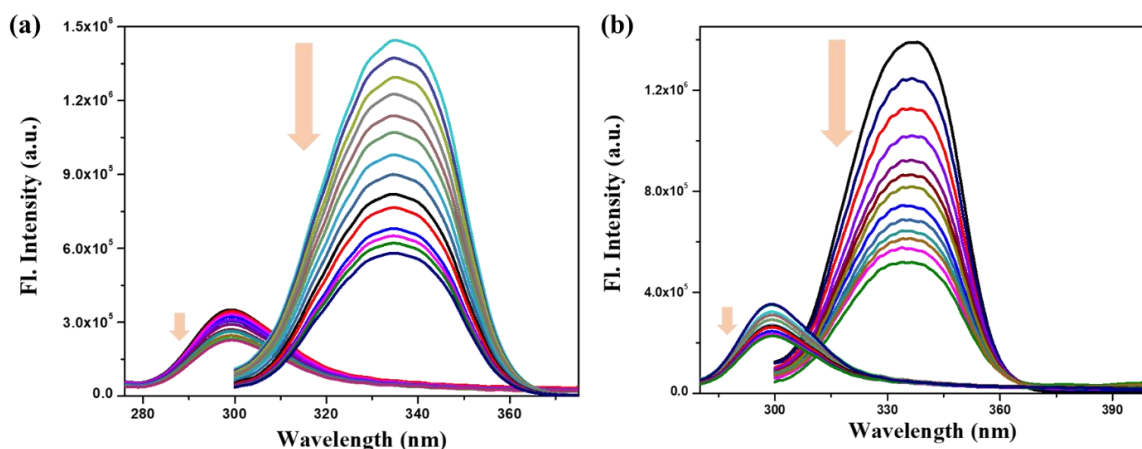


Figure III.20. Synchronous fluorescence spectral titration of BSA with (a) **C1** and (b) **C2** at  $\Delta\lambda = 15$  nm (for tyrosine residue) and  $\Delta\lambda = 60$  nm (for tryptophan residue).

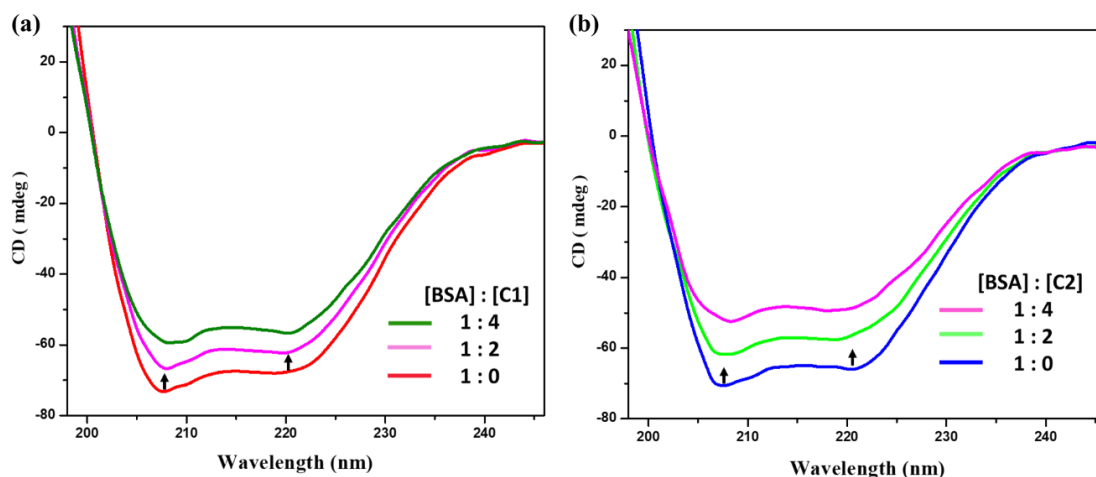


Figure III.21. CD spectra of BSA in the absence and presence of the Pd(II) complex (**C1**). The arrow shows the intensity changes.

### III.3.5. In vitro cytotoxicity studies

#### III.3.5.1. Cytotoxicity study of Pd- & Pt-Complexes

The toxicity of **C1** and **C2** was assessed in against four different cancer (MCF-7, HCT116, A-549, HepG2) cell lines and normal cell PBMC. The toxicity curves were plotted using different dose of the complexes and the  $IC_{50}$  values of each complex were compared for each cell line (Table III.6). Both the complexes were most active in the HepG2 cell line [ $IC_{50} =$

5–15  $\mu\text{M}$ ], which stated the selectivity of the complexes. Cisplatin was taken as a positive control and the  $\text{IC}_{50}$  value of the Pt-complex (**C2**) ( $5.1 \pm 0.8 \mu\text{M}$ ) was comparable to that of the Cisplatin ( $6.6 \pm 1.9 \mu\text{M}$ ). But the high  $\text{IC}_{50}$  value of the ligand (HL) revealed the nontoxic nature of it. The  $\text{IC}_{50}$  value of the Pd-complex (**C1**) ( $15.3 \pm 1.8$ ) was higher than that of Pt-complex (**C2**). So, it can be stated that the ligand was not the key factor of the cytotoxicity as inspite of having the same ligand Pt-complex showed a better activity than that of Pd-complex.<sup>64</sup> The  $\text{IC}_{50}$  value for **C1** and **C2** towards normal cells PBMC were found to be higher than 200  $\mu\text{M}$ , suggesting that the complexes were less toxic toward the normal cell line.

Table III.6. In vitro cytotoxic activity of the compounds against several cancer cell lines and normal cell (PBMC)\*.

Compounds	MCF-7	HCT-116	A549	HepG2	PBMC
<b>HL</b>	>500	>500	>500	>500	>500
<b>C1</b>	39.3 $\pm$ 2.2	38.2 $\pm$ 2.7	29.9 $\pm$ 1.8	15.3 $\pm$ 1.8	>200
<b>C2</b>	28.3 $\pm$ 1.7	26.1 $\pm$ 3.4	21.5 $\pm$ 2.1	5.1 $\pm$ 0.8	>200
<b>cis-platin</b>	21.8 $\pm$ 5.3	12.8 $\pm$ 2.1	11.4 $\pm$ 2.3	6.6 $\pm$ 1.9	>200

\* Cells ( $1 \times 10^6$  cells per mL) were treated with different concentrations of HL, Pd and Pt-complexes (0 to 200  $\mu\text{M}$ ) for 24 h. The  $\text{IC}_{50}$  values were evaluated by MTT assay. The results are expressed as the mean  $\pm$  S.D (n = 3).

### III.3.5.2. DNA fragmentation and ROS generation

The change in shape and size of the cells during apoptosis include breakage of DNA. So, we have studied DNA fragmentation level induced by **C1** and **C2** in HepG2 cells. The level of fragmented DNA became higher gradually with the rising concentration of both the complexes upto 20  $\mu\text{M}$  in HepG2 (Fig. III.22A). The formation of reactive oxygen species (ROS) increases the cancer cell death.<sup>81</sup> Often, anticancer agents elevated the ROS generation so, ROS level was measured in drug (**C1** and **C2**) treated HepG2 cells spectroscopically. Similar rise in ROS level like DNA fragmentation was detected (Fig. III.22B). The cellular ROS level was determined in HepG2 cells by flow cytometry analysis using DCF-DA. It can penetrate through the cell membrane and esterase enzymes will cleave off the acetate groups trapping the DCF (2,7-dichlorodihydrofluorescein) within the cell. Then the DCF can be oxidized by reactive oxygen species like peroxynitrite, hydroxyl radicals, and peroxides to

generate a highly fluorescent end product. So, increase in fluorescent intensity indicated the increase in ROS level (Fig. III.23). The % of DCF positive cells were higher for **C2** (Fig. III.22C). Thus, **C1** and **C2** can induce DNA fragmentation and ROS generation.

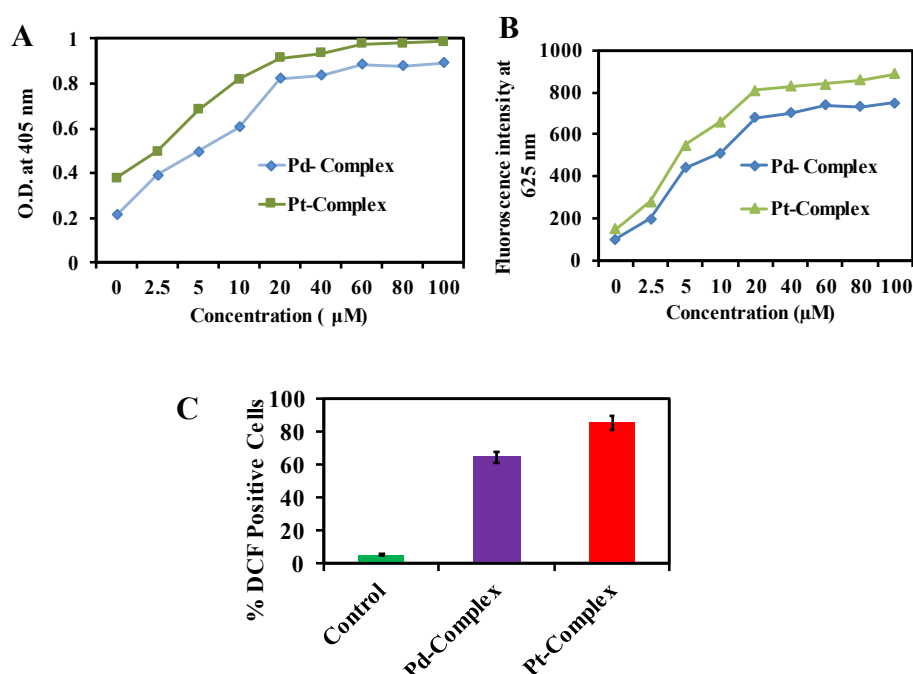


Figure III.22. Cells ( $1 \times 10^6$  cells per mL) were treated with different concentrations of **C1** and **C2** (0 to 100  $\mu$ M) for 24 h. (A) DNA fragments resulted in **C1** and **C2** treated HepG2 (B) ROS generation from **C1** and **C2** treated HepG2 (C) Graphical representation of FACS (fluorescence activated cell sorting) data; Results are one of the representative experiments  $\pm$  sd.

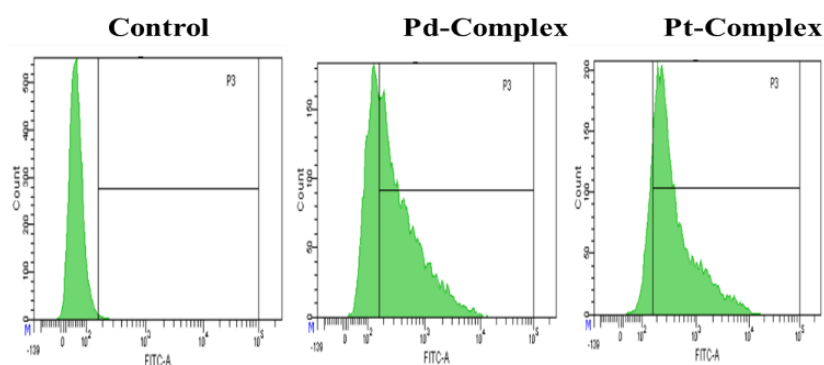


Figure III.23. Cells ( $1 \times 10^6$  cells per mL) were treated **C1** and **C2** in HepG2 cells. ROS generation was measured by FACS analysis. x-axis corresponds to the signal intensity while the y-axis represents the number of cells at a particular measurement value.



### III.3.5.3. Cell Image study

The process of programmable cell death is called apoptosis. The major steps involve in apoptosis are cell compression and cell fragmentation which were noticed in complex treated cancer cells in this present study. After cells were treated with 10  $\mu$ M complex for 24 h, chromatin condensation and DNA fragmentation were observed in the nucleus which is a significant feature of apoptosis.<sup>82</sup> The nucleus of the cells was stained by DAPI (a nuclear staining dye). The increasing numbers of condensed bright nuclei were evidence of the fragmentation of nucleus. (Fig. III.24).<sup>83</sup> DNA-fragmentation study using death detection kit also showed the rise in number of DNA fragments in complex treated cells (Fig. III.22A) which validated with the results in Fig. III.24. So, we can say that the complex may induced cytotoxicity via apoptosis in HepG2 cells.

### III.3.5.4. Detection of apoptosis and caspase 3/9 activity

HepG2 cells were treated with the IC<sub>90</sub> value of the metal complexes for 24 h and the apoptotic activity was determined using Annexin V. The initiation of apoptosis was quantified by the reactivity of Annexin V towards externalized phosphatidyl serine in the apoptotic cells.<sup>84,85</sup> Flow cytometric data suggested that the complexes did not show early apoptosis. The percentage (%) of Annexin V positive HepG2 cells increases with the treatment of the **C1** and **C2** compared to the untreated cells (Fig. III.25A) and **C2** showed higher apoptotic activity than **C1**, implies the better effect of **C2**.

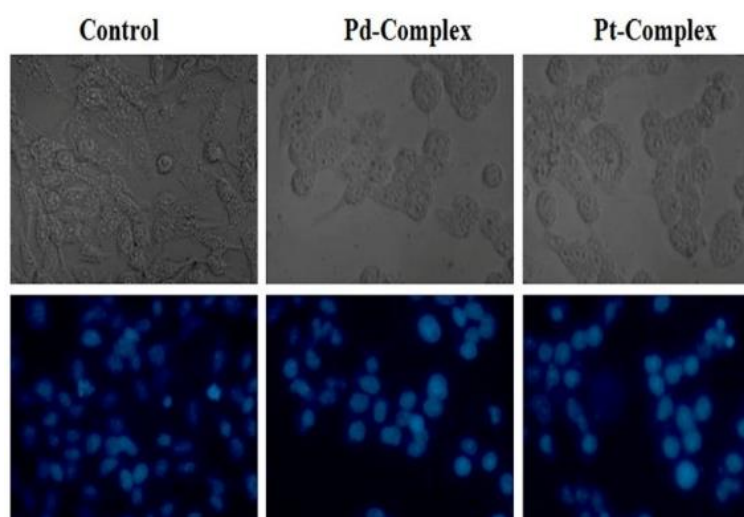


Figure III.24. HepG2 cells ( $1 \times 10^6$  cells/mL) were treated **C1** and **C2** for 24 h. Under a fluorescent microscope, morphological alterations (upper row) and nuclear condensation/DNA fragmentation (bottom row) were seen.

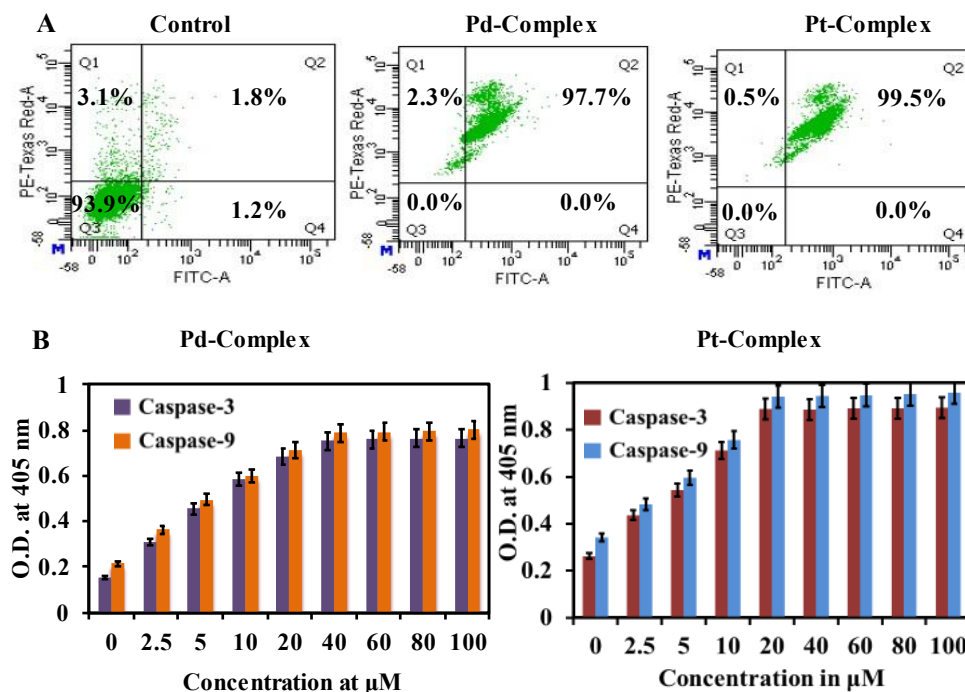


Figure III.25.  $1 \times 10^6$  cells/mL have been treated with indicated doses of **C1** and **C2** for 24h. (A) FACS analysis for Phosphatidyl serine exposure to outer membrane cells after treatment with  $IC_{90}$  of the **C1** and **C2** for 24h. (B) Level of fragmented caspase-3 and caspase-9 for **C1** and **C2** complexes by using colorimetric assay kit.

Since caspases-3 and -9 are two key factors for apoptosis, the activation of these two caspases in HepG2 cells treated with **C1** and **C2** was evaluated using assay kit for 24 h. Figure III.25B showed the dose-dependent increase of caspase-3/9 activity which proved that both the compound can activate the caspase 3/9 path. The result showed that activation of caspases occur by **C2** was comparatively higher than that of **C1**.

### III.4. Conclusions

Herein, we reported the synthesis of two innovative Pd(II) and Pt(II) complexes with O N N donor ligand (HL). The complexes' X-ray structures showed that HL functioned in both of them as a tridentate O,N,N chelator. Fluorescence quenching experiments with BSA established the static type of quenching for the complexes. Additionally, the complexes caused a minor alteration in the protein's secondary structure, according to the results of the synchronous and CD spectral analysis. Studies on the cytotoxicity of the complexes revealed that **C1** and **C2** are more effective against the chosen cell lines, such as MCF-7, HCT-116, A-

549, and HepG2, than the free ligand (HL). In the aforementioned cell lines, it can be noted that Pt(II) complex (**C2**) is more efficacious than Pd(II) complex (**C1**), and **C2** also displayed IC<sub>50</sub> values that were lower than those of cisplatin against HepG2 cell line. The percentage of apoptotic and total dead cells were much greater in the Pt(II) complex (**C2**), according to apoptosis analyses. Therefore, it will be helpful in creating and developing novel alternative Pd(II) and Pt(II) complexes as prospective anticancer drugs.

## III.5. References

1. G. P. Nagaraju, G. Srivani, B. Dariya, G. Chalikonda, B. Farran, S. K. Behera, A. Alam and M. A. Kamal, *Semin. Cancer Bio.*, 2021, **69**, 69.
2. S. N. Mbugua, N. R. S. Sibuyi, L. W. Njenga, R. A. Odhiambo, S. O. Wandiga, M. Meyer, R. A. Lalancette and M. O. Onani, *ACS Omega*, 2020, **25**, 14942.
3. E. Petruzzella, R. Sirota, I. Solazzo, V. Gandin and D. Gibson, *Chem. Sci.*, 2018, **9**, 4299.
4. M. Hallek, *Am. J. Hematol.*, 2019, **94**, 1266.
5. R. J. Ward, R. R. Crichton, *Met. Ions Life Sci.*, 2019, **19**, 87.
6. (a) R. Paprocka, M. Wiese-Szadkowska, S. Janciauskiene, T. Kosmalski, M. Kulik and A. Helmin-Basa, *J. Coord. Chem. Rev.*, 2022, **452**, 214307; (b) E. Sánchez-López, D. Gomes, G. Esteruelas, L. Bonilla, A. L. Lopez-Machado, R. Galindo, A. Cano, M. Espina, M. Ettcheto, A. Camins, A. M. Silva, A. Durazzo, A. Santini, M. L. Garcia and E. B. Souto, *Nanomaterials*, 2020, **10**, 292.
7. B. Rosenberg, L. Van Camp and T. Krigas, *Nature*, 1965, **205**, 698.
8. J. Zhang, L. Li, L. Wang, F. Zhang and X. Li, *Eur. J. Med. Chem.*, 2010, **45**, 5337.
9. (a) S. Ghosh, *Bioorg. Chem.*, 2019, **88**, 102925; (b) S. Dasari and P. B. Tchounwou, *Eur. J. Pharmacol.*, 2014, **740**, 364.
10. L. Kelland, *Nat. Rev. Cancer*, 2007, **7**, 573.
11. S. R. McWhinney, R. M. Goldberg and H. L. McLeod, *Mol. Cancer Ther.*, 2009, **8**, 10.
12. X. Wang, *Anti-Cancer Agents Med. Chem.*, 2010, **10**, 396.
13. X. Wang and Z. Guo, *Chem. Soc. Rev.*, 2013, **42**, 202.
14. M. Jamshidi, R. Yousefi, S. M. Nabavizadeh, M. Rashidi, M. G. Haghighi, A. Niazi and A.-A. Moosavi-Movahedi, *Int. J. Biol. Macromol.*, 2014, **66**, 86.
15. Z. Pouryasini, R. Yousefi, S. M. Nabavizadeh, M. Rashidi, P. Hamidizadeh, M.-M. Alavianmehr and A. A. Moosavi-Movahedi, *Appl. Biochem. Biotechnol.*, 2014, **172**, 2604.
16. M. E. Moghadam, M. Saidifar, A. Divsalar, H. Mansouri-Torshizi, A. A. Saboury, H. Farhangian and M. Ghadamgahi, *J. Biomol. Struct. Dyn.*, 2016, **34**, 206.
17. M.-C. Zhu, X.-T. Cui, F.-C. Zhao, X.-Y. Ma, Z.-B. Han and E.-J. Gao, *RSC Adv.*, 2015, **5**, 47798.
18. A. M. Florea and D. Büsselberg, *Cancers*, 2011, **3**, 1351.
19. A. R. Kapdi and I. J. S. Fairlamb, *Chem. Soc. Rev.*, 2014, **43**, 4751.
20. A. Garoufis, S. K. Hadjikakou and N. Hadjiladis, *Coord. Chem. Rev.*, 2009, **253**, 1384.
21. N. V. Loginova, H. I. Harbatsevich, N. P. Osipovich, G. A. Ksendzova, T. V. Koval'chuk and G. I. Polozov, *Curr. Med. Chem.*, 2020, **27**, 5213.
22. T. W. Hambley, *Science*, 2007, **318**, 1392.
23. Ž. D. Bugarčić, J. Bogojeski and R. van Eldik, *Coord. Chem. Rev.*, 2015, **292**, 91.

24. T. Lazarević, A. Rilak and Ž. D. Bugarčić, *Eur. J. Med. Chem.*, 2017, **142**, 8.
25. H. H. Repich, V. V. Orysyk, L. G. Palchykovska, S. I. Orysyk, Y. L. Zborovskii, O. V. Vasylichenko, O. V. Storozhuk, A. A. Biluk, V. V. Nikulina, L. V. Garmanchuk, V. I. Pekhnyo and M. V. Vovk, *J. Inorg. Biochem.*, 2017, **168**, 98.
26. (a) D. Simić, M. Zarić, I. Nikolić, R. Živković-Zarić, P. Čanović, A. Kočović, I. Radojević, I. Raković, S. Jovičić Milić, D. Petrović, D. Stojković, N. Vuković, M. Kačaniová, M. Vukić and V. Jevtić, *Dalton Trans.*, 2022, **51**, 1191; (b) A. Eskandari, A. Kundu, A. Johnson, S. Karmakar, S. Ghosh and K. Suntharalingam, *Dalton Trans.*, 2020, **49**, 4211.
27. M. Fanelli, M. Formica, V. Fusi, L. Giorgi, M. Micheloni and P. Paoli, *Coord. Chem. Rev.*, 2016, **310**, 41.
28. M. Stradiotto, R. L. Lundgren, *Wiley & Sons*, 2016, 1–13.
29. G. Matela, *Anticancer Agents Med Chem.* 2020, **20**, 1908-1917.
30. K. T. Tadele, T. W. Tsega, *Anticancer Agents Med Chem.* 2019, **19**, 1786-1795.
31. S. H. Sumrra, M. Ibrahim, S. Ambreen, M. Imran, M. Danish, F. S. Rehmani, *Bioinorg. Chem. Appl.* 2014, **2014**, 812924.
32. L. A. Alfonso-Herrera, S. Rosete-Luna, D. Hernández-Romero, J. M. Rivera-Villanueva, J. L. Olivares-Romero, J. A. Cruz-Navarro, A. Soto-Contreras, A. Arenaza-Corona, D. Morales-Morales, R. Colorado-Peralta, *ChemMedChem*, 2022, **17**, e202200367.
33. C. S. Allardyce, A. Dorcier, C. Scolaro, and P. J. Dyson, *App. Organomet. Chem.*, 2005, **19**, 1.
34. P. J. Dyson and G. Sava, *Dalton Trans.*, 2006, **16**, 1929.
35. K. B. Garbutcheon-Singh, M. P. Grant, B. W. Harper, A. M. Krause-Heuer, M. Manohar, N. Orkey and J. R. Aldrich Wright, *Current Topics in Med. Chem.*, 2011, **11**, 521.
36. J. Reedijk, *Eur. J. Inorg. Chem.*, 2009, **10**, 1303.
37. D. Wang and S. J. Lippard, *Nat. Rev. Drug Discov.*, 2005, **4**, 307.
38. V. Brabec, O. Hrabina and J. Kasparkova, *Coord. Chem. Rev.*, 2017, **351**, 2.
39. M. Hanif and C. G. Hartinger, *Future Med. Chem.*, 2018, **10**, 615.
40. L. Bai, C. Gao, Q. Liu, C. Yu, Z. Zhang, L. Cai, B. Yang, Y. Qian, J. Yang and X. Liao, *Eur. J. Med. Chem.*, 2017, **140**, 349.
41. S. Komeda, *Metallomics*, 2011, **3**, 650.
42. T. C. Johnstone, K. Suntharalingam and S. J. Lippard, *Chem. Rev.*, 2016, **116**, 3436.
43. D. B. Zamble, Y. Mikata, C. H. Eng, K. E. Sandman and S. J. Lippard, *J. Inorg. Biochem.*, 2002, **91**, 451.
44. A. R. Timerbaev, C. G. Hartinger, S. S. Aleksenko and B. K. Keppler, *Chem. Rev.*, 2006, **106**, 2224.
45. T. A. Wani, A. H. Bakheit, S. Zargar, H. Rizwana and A. A. Al-Majed, *Spectrochim. Acta Part A*, 2020, **227**, 117691.
46. T. Topală, A. Bodoki, L. Oprean and R. Oprean, *Clujul Med.*, 2014, **87**, 215.

47. W. Bal, J. Christodoulou, P. J. Sadler and A. Tucker, *J. Inorg. Biochem.*, 1998, **70**, 33.
48. W. Bal, M. Sokołowska, E. Kurowska and P. Faller, *Biochim. Biophys. Acta, Gen. Subj.*, 2013, **1830**, 5444.
49. S. Jovanović, K. Obrenčević, Ž. D. Bugarčić, I. Popović, J. Žakula and B. Petrović, *Dalton Trans.*, 2016, **45**, 12444.
50. D. Ćoćić, S. Jovanović-Stević, R. Jelić, S. Matić, S. Popović, P. Djurdjević, D. Baskić and B. Petrović, *Dalton Trans.*, 2020, **49**, 14411.
51. S. Gharami, K. Aich, L. Patra and T. K. Mondal, *New J. Chem.*, 2018, **42**, 8646.
52. Shaily, A. Kumar and N. Ahmed, *New J. Chem.*, 2017, **41**, 14746.
53. (a) A. D. Becke, *J. Chem. Phys.*, 1993, **98**, 5648; (b) C. Lee, W. Yang and R. G. Parr, *Phys. Rev. B: Condens. Matter Mater. Phys.*, 1988, **37**, 785.
54. (a) P. J. Hay and W. R. Wadt, *J. Chem. Phys.*, 1985, **82**, 270; (b) W. R. Wadt and P. J. Hay, *J. Chem. Phys.*, 1985, **82**, 284; (c) P. J. Hay and W. R. Wadt, *J. Chem. Phys.*, 1985, **82**, 299.
55. (a) B. Bera, S. Mondal, S. Gharami, R. Naskar, K. Das Saha, T. K. Mondal, *New J. Chem.*, 2022, **46**, 11277; (b) A. Das, M. Saha, S. Mandal, S. Das, K. Das Saha, T. K. Mondal, *New J. Chem.*, 2023, **47**, 4931-4943.
56. M. J. Frisch, G. W. Trucks, H. B. Schlegel, G. E. Scuseria, M. A. Robb, J. R. Cheeseman, G. Scalmani, V. Barone, B. Mennucci, G. A. Petersson, H. Nakatsuji, M. Caricato, X. Li, H. P. Hratchian, A. F. Izmaylov, J. Bloino, G. Zheng, J. L. Sonnenberg, M. Hada, M. Ehara, K. Toyota, R. Fukuda, J. Hasegawa, M. Ishida, T. Nakajima, Y. Honda, O. Kitao, H. Nakai, T. Vreven, J. A. Montgomery, Jr., J. E. Peralta, F. Ogliaro, M. Bearpark, J. J. Heyd, E. Brothers, K. N. Kudin, V. N. Staroverov, R. Kobayashi, J. Normand, K. Raghavachari, A. Rendell, J. C. Burant, S. S. Iyengar, J. Tomasi, M. Cossi, N. Rega, J. M. Millam, M. Klene, J. E. Knox, J. B. Cross, V. Bakken, C. Adamo, J. Jaramillo, R. Gomperts, R. E. Stratmann, O. Yazyev, A. J. Austin, R. Cammi, C. Pomelli, J. W. Ochterski, R. L. Martin, K. Morokuma, V. G. Zakrzewski, G. A. Voth, P. Salvador, J. J. Dannenberg, S. Dapprich, A. D. Daniels, O. Farkas, J. B. Foresman, J. V. Ortiz, J. Cioslowski and D. J. Fox, Gaussian 09, Revision D.01, Gaussian, Inc., Wallingford CT, **2009**.
57. (a) V. Barone and M. Cossi, *J. Phys. Chem. A*, 1998, **102**, 1995; (b) M. Cossi and V. Barone, *J. Chem. Phys.*, 2001, **115**, 4708; (c) M. Cossi, N. Rega, G. Scalmani and V. Barone, *J. Comput. Chem.*, 2003, **24**, 669.
58. (a) R. Bauernschmitt and R. Ahlrichs, *Chem. Phys. Lett.*, 1996, **256**, 454; (b) R. E. Stratmann, G. E. Scuseria and M. J. Frisch, *J. Chem. Phys.*, 1998, **109**, 8218; (c) M. E. Casida, C. Jamorski, K. C. Casida and D. R. Salahub, *J. Chem. Phys.*, 1998, **108**, 4439.
59. N. M. O'Boyle, A. L. Tenderholt, K. M. Langner, *J. Comput. Chem.*, 2008, **29**, 839.
60. Bruker. SAINT v8.38A. Bruker AXS Inc., Madison, Wisconsin, USA.
61. L. Krause, R. Herbst-Irmer, G.M. Sheldrick, D. Stalke, *J. Appl. Cryst.*, 2015, **48**, 3.

62. (a) G.M. Sheldrick, *Acta Cryst.*, 2008, **A64**, 112; (b) G.M. Sheldrick, *Acta Cryst.*, 2015, **C71**, 3.
63. A. L. Spek, *Acta Crystallogr., Sect. D: Biol. Crystallogr.*, 2009, **65**, 148.
64. B. Bera, S. Mondal, S. Gharami, R. Naskar, K. Das Saha, T. K. Mondal, *New J. Chem.*, 2022, **46**, 11277.
65. S. Roy, R. Saha, T. K. Mondal, C. Sinha, *Inorg. Chim. Acta*, 2014, **423**, 52.
66. A. Shanmugapriya, F. Dallemer and R. Prabhakaran, *New J. Chem.*, 2018, **42**, 18850.
67. G. Lupaşcu, E. Pahonţu, S. Shova, Ş. F. Bărbuceanu, M. Badea, C. Paraschivescu, J. Neamţu, M. Dinu, R. V. Ancuceanu, D. Drăgănescu, C. E. Dinu-Pîrvu, *Appl. Organomet. Chem.*, 2021, **35**, e6149.
68. M.-H. Huang, W.-Y. Lee, X.-R. Zou, C.-C. Lee, S.-B. Hong, L.-C. Liang, *Appl. Organomet. Chem.*, 2021, **35**, e6128.
69. C. M. Almeida, P. H. S. Marcon, É. C. M. Nascimento, J. B. L. Martins, M. A. S. Chagas, M. Fujimori, P. G. F. De Marchi, E. L. França, A. C. Honorio-França, C. C. Gatto, *Appl. Organomet. Chem.*, 2022, **36**, e6761.
70. C. Icsel, V. T. Yilmaz, M. Aygun, B. Cevatemre, P. Alper and E. Ulukaya, *Dalton Trans.*, 2018, **47**, 11397.
71. S. N. Mbugua, N. R. S. Sibuyi, L. W. Njenga, R. A. Odhiambo, S. O. Wandiga, M. Meyer, R. A. Lalancette and M. O. Onani, *ACS Omega*, 2020, **5**, 14942.
72. I. B. Lozada, J. A. G. Williams, D. E. Herbert, *Inorg. Chem. Front.*, 2022, **9**, 10.
73. E. Ramachandran, D. S. Raja, N. P. Rath, K. Natarajan, *Inorg. Chem.*, 2013, **52**, 1504.
74. D. S. Raja, N. S. P. Bhuvanesh, K. Natarajan, *Inorg. Chem.*, 2011, **50**, 12852.
75. N. Biswas, S. Khanra, A. Sarkar, S. Bhattacharjee, D. P. Mandal, A. Chaudhuri, S. Chakraborty, C. Roy Choudhury, *New J. Chem.*, 2017, **41**, 12996.
76. D. S. Raja, N. S. P. Bhuvanesh, K. Natarajan, *Dalton Trans.*, 2012, **41**, 4365.
77. F. Darabi, H. Hadadzadeh, J. Simpsonb and A. Shahpiric, *New J. Chem.*, 2016, **40**, 9081.
78. J. N. Miller, *Proc.: Anal. Div. Chem. Soc.*, 1979, **16**, 203.
79. J. Tang, F. Luan and X. Chen, *Bioorg. Med. Chem.*, 2006, **14**, 3210.
80. N. Stevanović, D. Apostolović, M. Milčić, A. Lolić, M. van Hage, T. Č. Veličković, R. Baošić, *New J. Chem.*, 2021, **45**, 6231.
81. A. Brozovic, A. Ambriović-Ristov and M. Osmak, *Crit. Rev. Toxicol.*, 2010, **40**, 347.
82. S. Hadizadeh, N. Najafzadeh, M. Mazani, M. Amani, H. M. Torshizi and A. Niapour, *Biochem. Res. Int.*, 2014, 813457.
83. Y. Li, S. Man, J. Li, H. Chai, W. Fan, Z. Liu and W. Gao, *Chemico-Bio. Interac.*, 2014, **220**, 193.
84. S-H Lee, X. W. Meng, K. S. Flatten, D. A. Loegering and S. H. Kaufmann, *Cell Death & Differentiation*, 2013, **20**, 64.
85. V. Turinetto and C. Giachino, *Nucleic Acids Res.*, 2015, **43**, 2489.



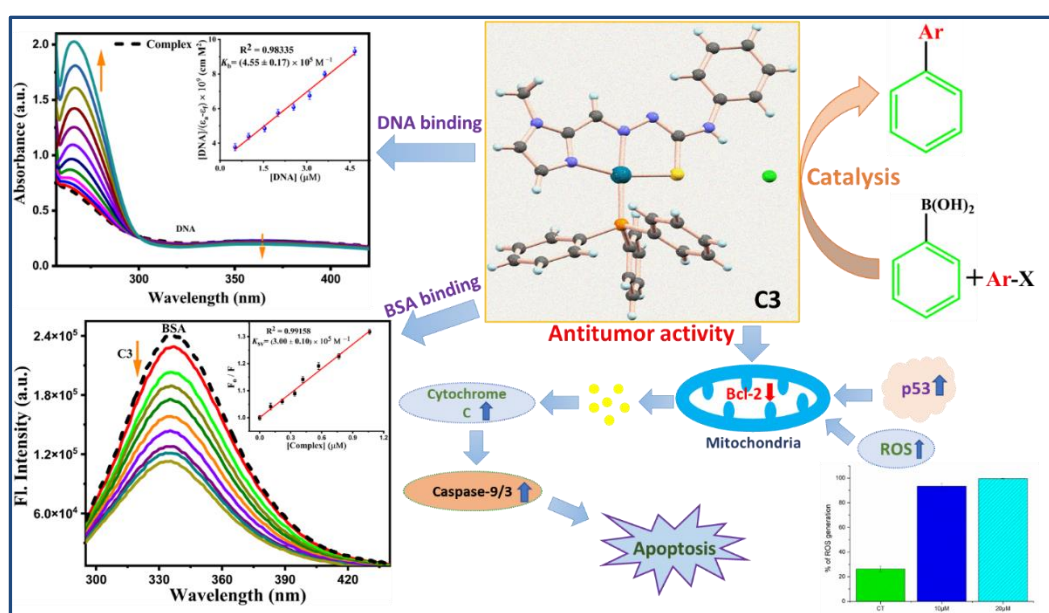
## **CHAPTER - IV**

**Fabrication of thiosemicarbazone based Pd(II) complexes: Structural elucidations, catalytic activity towards Suzuki-Miyaura Coupling reaction, biomolecular interactions and antitumor activity against human TNBC cells (MDA-MB-231)**

## *Fabrication of Thiosemicarbazone Based Pd(II) Complexes: Structural Elucidations, Catalytic Activity Towards Suzuki-Miyaura Coupling Reaction, Biomolecular Interactions and Antitumor Activity Against Human TNBC Cells (MDA-MB-231)*

### Abstract

Herein we report three heterocyclic-thiosemicarbazone based Pd(II) complexes [Pd(**HL**<sup>1</sup>)Cl] (**C1**), [Pd(**L**<sup>2</sup>)(PPh<sub>3</sub>)] (**C2**) and [Pd(**L**<sup>3</sup>)(PPh<sub>3</sub>)]Cl (**C3**) having coligands Cl and PPh<sub>3</sub>. Thiosemicarbazone ligands (**HL**<sup>1</sup>, **HL**<sup>2</sup> and **L**<sup>3</sup>) and the complexes (**C1–C3**) were characterized methodically by several spectroscopic techniques. The application of these complexes as catalysts toward Suzuki–Miyaura coupling reaction has been done with various aryl halides and phenyl boronic acid in PEG 400 solvent. The reaction's optimization revealed that complex **C2** is more efficient than other complexes. The complexes displayed good biomolecular interactions with DNA/protein with the binding constant value in the order of 10<sup>5</sup> M<sup>-1</sup>. **C3** showed greater binding efficacy toward these biomolecules than the other complexes which might be due to the cationic nature of **C3**. Furthermore, antitumor activity of the complexes was studied against human triple negative breast cancer (TNBC) cell line MDA-MB-231. Additionally, the complex induced apoptosis was confirmed and occurred via mitochondria-dependent (intrinsic) pathway.



## IV.1. Introduction

Thiosemicarbazones are a class of N, S donor ligands that have been widely employed in coordination chemistry because of their structural adaptability and versatility since they can exist as thione-thiol tautomers and accordingly bind to metal centres as monodentate, bidentate, or bridging ligands.<sup>1,2</sup> Due to their pharmacological characteristics, particularly as antiphrastic, antibacterial, antioxidant, and anticancer agents, thiosemicarbazone derivatives and their metal complexes have attracted significant interest in chemistry and biology.<sup>3-8</sup> Specifically, heterocyclic thiosemicarbazones have good therapeutic characteristics in mammalian cells by blocking the enzyme ribonucleotide reductase, which prevents DNA synthesis.<sup>6,9</sup> Numerous heterocyclic thiosemicarbazone based transition metal complexes have received interest due to their favourable biomolecular interactions and anticancer properties.<sup>6,10-13</sup>

Cancer is a major public health and financial issue, and its impact has been predicted to expand broadly over the coming decades. Globally, cancer claimed the lives of around 10 million individuals in 2020.<sup>14</sup> It is anticipated that there would be 28.4 million new instances of cancer worldwide in 2040, which is 47% rise from 2020.<sup>15</sup> Therefore, it is crucial to design novel treatment plans and chemotherapy medications. Despite being a well-known anticancer medication, the use of cisplatin in cancer chemotherapy has been constrained by multifactorial resistance, harmful side effects on normal cells, and general toxicity.<sup>16,17</sup> So, in order to increase the selectivity of anticancer medications and lessen their adverse effects, less toxic and highly effective metal-based anticancer compounds have been sought after and produced.<sup>18,19</sup> As the palladium complexes are closely related to their platinum analogues because of their similarities in coordination chemistry, palladium complexes have gained a lot more attention as anticancer medication.<sup>20-23</sup> Palladium complexes were promoted as potential anticancer agents in one of Graham and coworkers' early experiments.<sup>24</sup> Since the publication of this study, a large number of novel palladium complexes have been created, several of which have shown potential antitumor activity against lung, prostate, and other tumour cell lines. In several cases, palladium(II) complexes have shown better antitumor activity than their platinum analogues (cisplatin, carboplatin, etc.).<sup>21,25,26</sup>

The primary molecular targets for anticancer medications are DNA and protein, and DNA plays a crucial role as it houses all of the genetic data required for cellular function. As a result, it is thought that the metal complexes that bind and break DNA under physiological settings provide suitable candidates for use as therapeutic agents in medical applications and

genetic research.<sup>27,28</sup> There are numerous physiological uses for bovine serum albumin (BSA), a significant soluble protein of the circulatory system.<sup>29</sup> Examining drug-protein interactions is crucial since most medications bound to serum albumins are often delivered as a protein complex.<sup>28,30,31</sup> As a result, understanding the binding characteristics of metal complexes with proteins is crucial for the logical development of novel medications.

One of the most potent synthetic pathways used in organic chemistry is transition metal-catalyzed coupling reactions, which are used to create medicines, pesticides, natural compounds, and sophisticated functional materials.<sup>32-35</sup> In particular, the Pd-catalyzed Suzuki-Miyaura cross-coupling (SMC) reaction of aryl halides with aryl boronic acids, for which Professor Suzuki was awarded the 2010 Nobel Prize in Chemistry, has attracted significant interest to produce biaryls or substituted aromatic moieties. This is mainly because the cross-coupling reaction can be conducted under mild reaction conditions with fast reaction rates, high production yields, high turnover frequency, high stereoselectivity and great functional group tolerance.<sup>36,37</sup> In the past ten years, the use of novel ligands has significantly increased the efficiency and selectivity possible in these cross-coupling reactions. Bulky dialkylbiaryl and triarylphosphines continue to be the most employed ligands for cross-coupling processes, followed by N-heterocyclic carbenes (NHCs).<sup>38-43</sup> However, there are small number of Pd(II) triphenylphosphine catalysts bearing heterocyclic thiosemicarbazone ligands in the SMC reaction have been reported.<sup>44-47</sup>

So, herein we have presented three heterocyclic thiosemicarbazone ligand (**HL**<sup>1</sup>, **HL**<sup>2</sup> and **L**<sup>3</sup>) and their corresponding complexes [Pd(**HL**<sup>1</sup>)Cl] (**C1**), [Pd(**L**<sup>2</sup>)(PPh<sub>3</sub>)] (**C2**) and [Pd(**L**<sup>3</sup>)(PPh<sub>3</sub>)]Cl (**C3**) having coligands Cl and PPh<sub>3</sub>. All the compounds were characterized methodically by different spectroscopic techniques (elemental analysis, <sup>1</sup>H and <sup>13</sup>C NMR, UV-Vis, IR and HRMS). Single crystal X-ray diffraction (SC-XRD) study reveals that complex **C2** has a square planar geometry around the metal centre while **C1** and **C3** have a slight distorted square planar structure. Suzuki-Miyaura cross coupling reaction was conducted by varying the different reaction conditions and the results showed complex **C2** has highest catalytic efficiency followed by **C3** and **C1**. The metal complexes show admirable binding interaction with biomolecules CT-DNA and BSA protein with the binding constant value in the order of 10<sup>5</sup> M<sup>-1</sup>. Furthermore, the antiproliferative activity of the three complexes was assessed against human TNBC (triple negative breast cancer) cells MDA-MB-231. Complex **C3** showed low IC<sub>50</sub> value (10 ± 2.90 μM) than the other two complexes. The mechanism of the cytotoxic activity of **C3** was explained in detail via cell viability

studies, ROS generation, mitochondrial membrane potential (MMP) and confocal microscopy.

## IV.2. Experimental

### IV.2.1. Materials and Methods

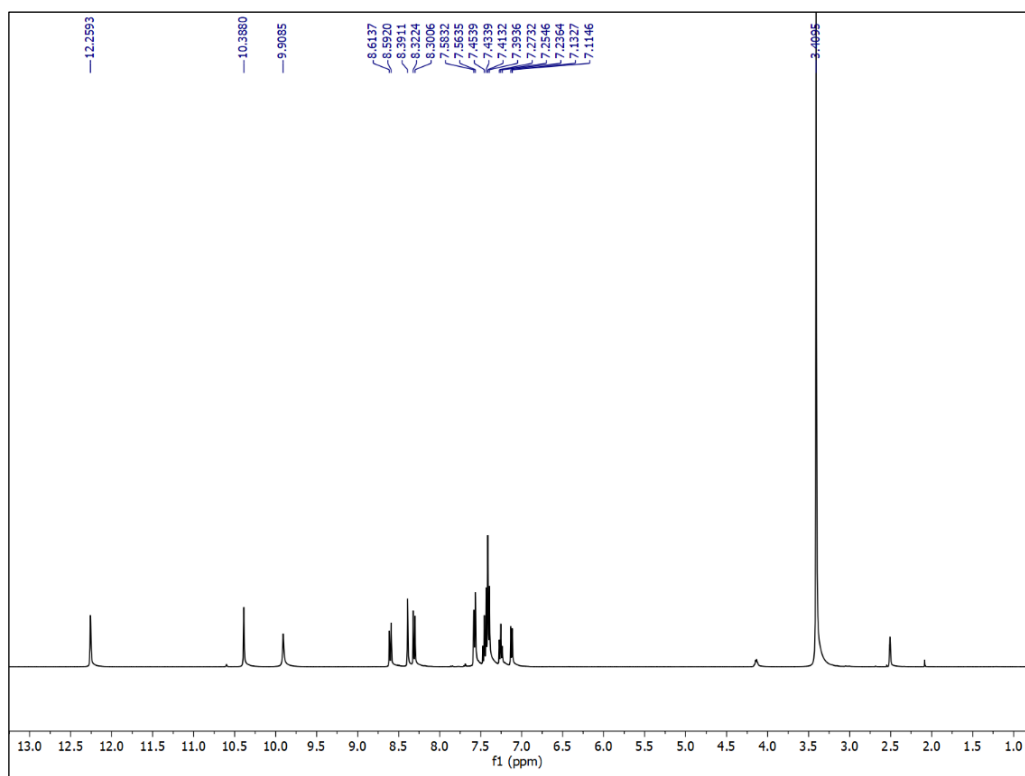
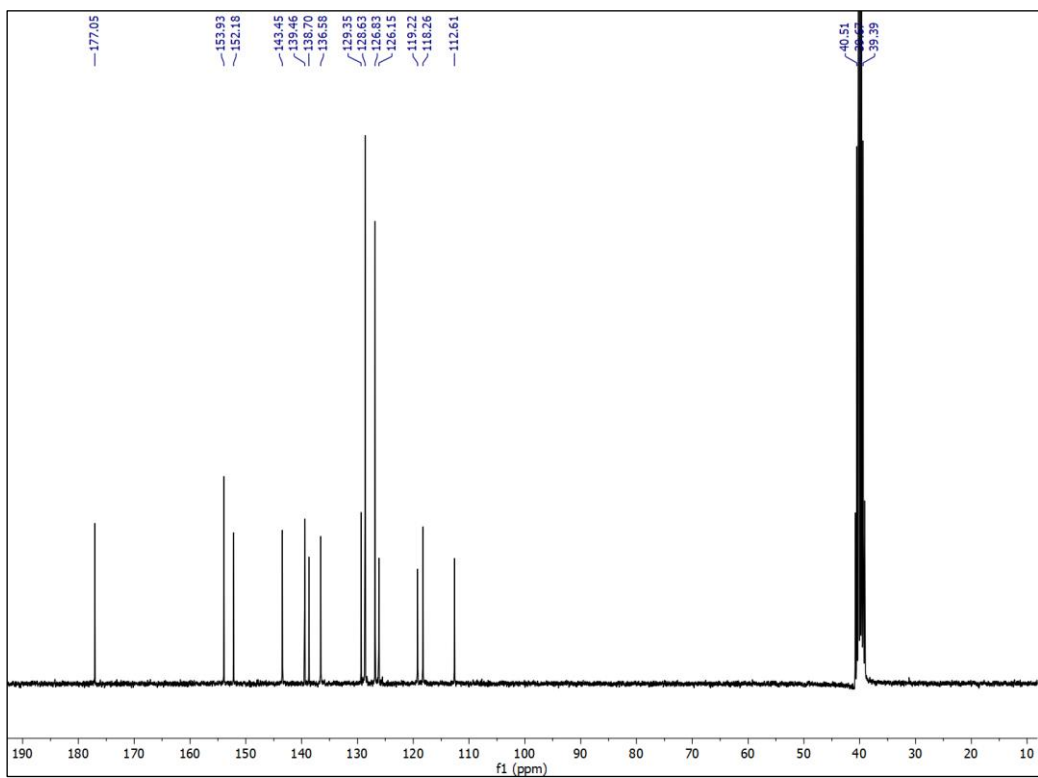
All reagents and solvents used in this synthesis were purchased from Aldrich. All other organic chemicals and inorganic salts were available from commercial sources and used without further purification.  $^1\text{H}$ , and  $^{13}\text{C}$  NMR spectra were recorded on Bruker 300 MHz and 400 MHz instruments (mentioned in each spectrum) in DMSO- $\text{d}_6$  solvent. HRMS mass spectra were recorded on Waters quadruple time-of-flight mass spectrometer (Xevo G2 Q-TOF). Electronic spectra were taken on a Shimadzu UV-1900i spectrophotometer. IR spectra were recorded on PerkinElmer Spectrum Two FT-IR Spectrometer.

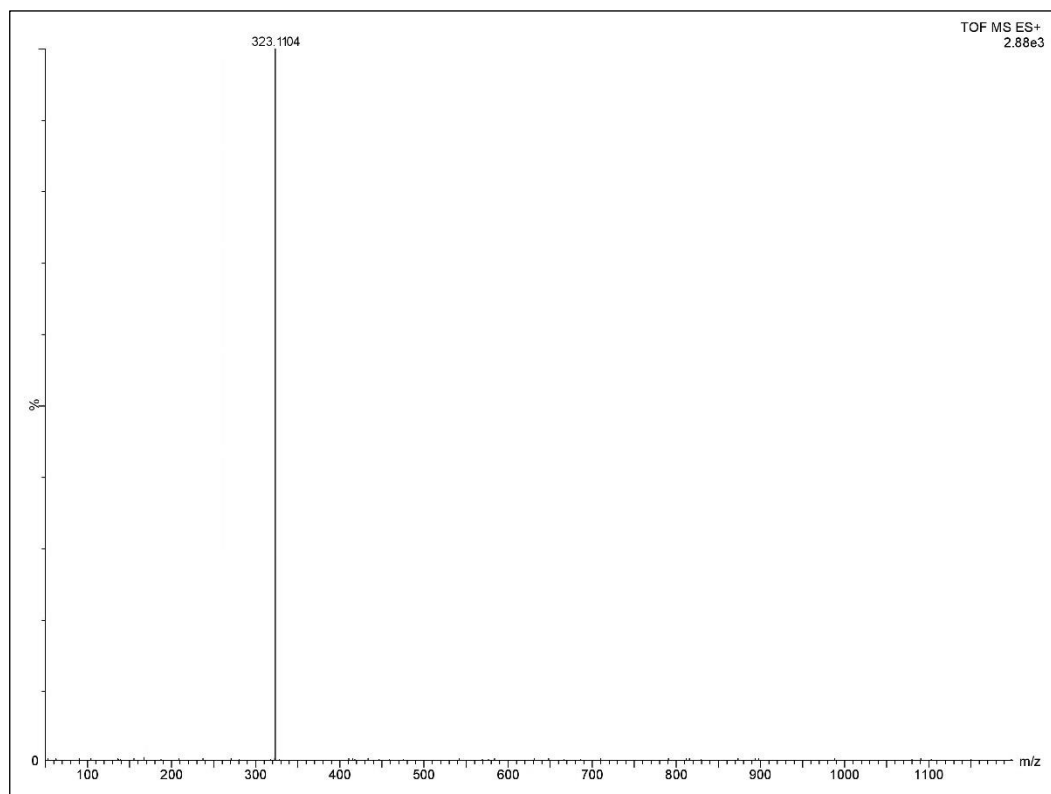
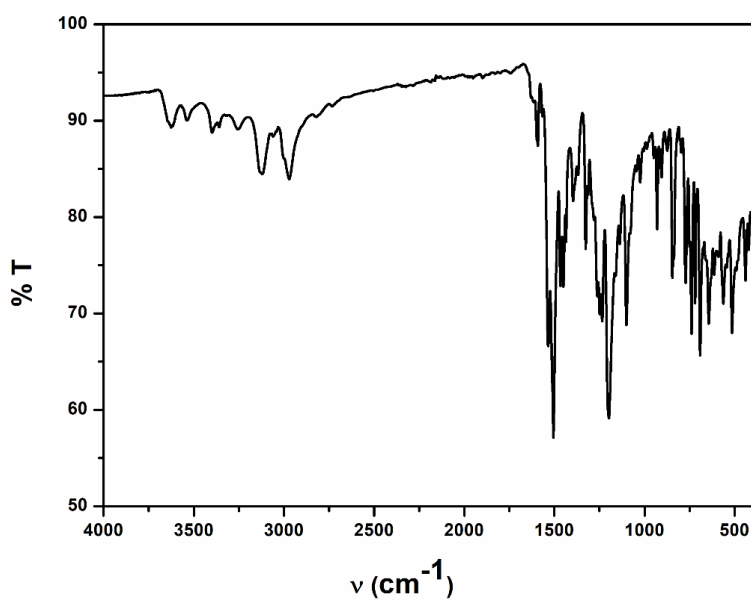
### IV.2.2. Synthesis

#### IV.2.2.1. Synthesis of (E)-2-((8-hydroxyquinolin-2-yl)methylene)-N-phenylhydrazine-1-carbothioamide ( $\text{HL}^1$ )

A methanolic solution of 4-phenylthiosemicarbazide (0.1 g, 0.6 mmol) was added to a solution of 8-hydroxyquinoline-2-carbaldehyde (0.103 g, 0.6 mmol) in methanol and the resulting mixture was refluxed for 2 h. After the completion of the reaction a light brown colour precipitate was appeared which was filtered and washed with methanol. The yield was 0.14 g (75%).

Anal. Calc. for  $\text{C}_{17}\text{H}_{14}\text{N}_4\text{OS}$ : C, 63.34; H, 4.38; N, 17.38. Found: C, 63.39; H, 4.41; N, 17.45.  $^1\text{H}$  NMR (400 MHz, DMSO- $\text{d}_6$ ):  $\delta$  7.12 (d,  $J$  = 7.24 Hz, 1H), 7.25 (t,  $J$  = 7.28 Hz, 1H), 7.39-7.45 (m, 3H), 7.57 (d,  $J$  = 7.88 Hz, 2H), 8.31 (d,  $J$  = 8.7 Hz, 2H), 8.39 (s, 1H), 8.6 (d,  $J$  = 8.68 Hz, 1H), 9.9 (s, 1H), 10.38 (s, 1H), 12.26 (s, 1H).  $^{13}\text{C}$  NMR (75 MHz, DMSO- $\text{d}_6$ ) in ppm:  $\delta$  112.6, 118.26, 119.22, 126.15, 126.83, 128.63, 129.35, 136.58, 138.7, 139.46, 143.45, 152.18, 153.93, 177.05. IR ( $\text{cm}^{-1}$ ) in KBr: 3624  $\nu(\text{O-H})$ ; 3398, 3256  $\nu(\text{N-H})$ ; 3122, 2971  $\nu(\text{C-H})$ ; 1592  $\nu(\text{C=N})$ ; 1200  $\nu(\text{C=S})$ . HRMS: Calculated for  $\text{C}_{17}\text{H}_{15}\text{N}_4\text{OS}$   $[\text{M} + \text{H}]^+$  ( $m/z$ ): 323.0967; found: 323.1104. UV-Vis (in  $\text{CH}_3\text{CN}$ ),  $\lambda_{\text{max}}$  ( $\epsilon$ ,  $\text{M}^{-1}\text{cm}^{-1}$ ): 346 (29944), 310 (26196), 257 (15473).

Figure IV.1.  $^1\text{H}$ -NMR spectrum of **HL**<sup>1</sup> in  $\text{DMSO-d}_6$ Figure IV.2.  $^{13}\text{C}$ -NMR spectrum of **HL**<sup>1</sup> in  $\text{DMSO-d}_6$

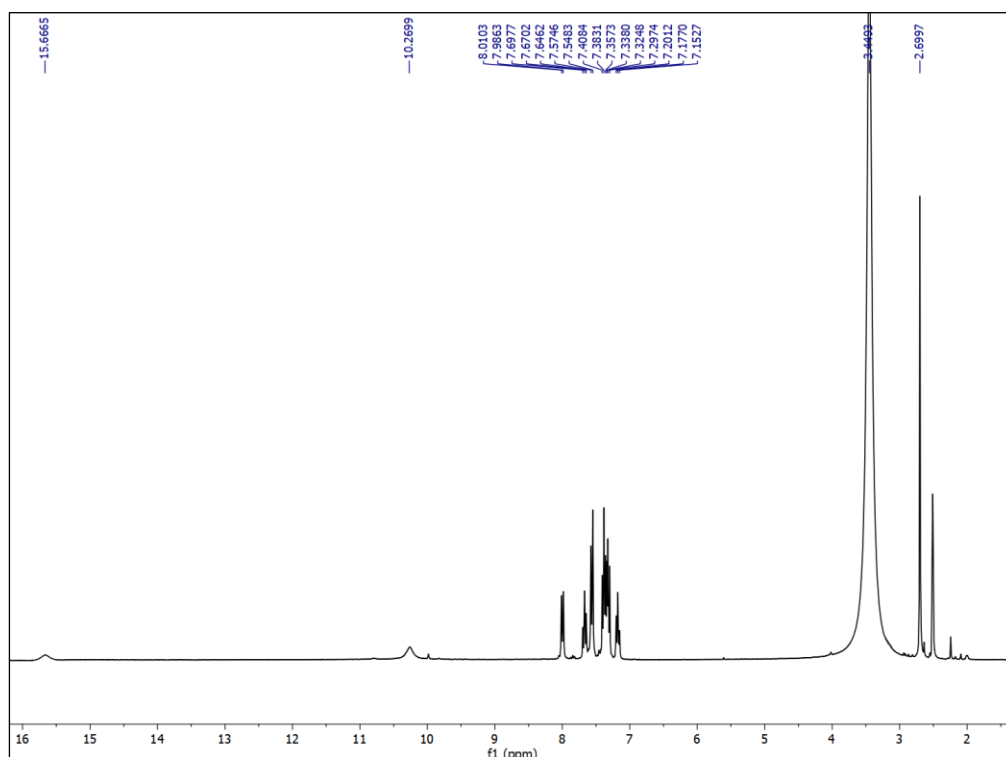
Figure IV.3. HRMS of **HL**<sup>1</sup> in acetonitrileFigure IV.4. IR spectra of **HL**<sup>1</sup>

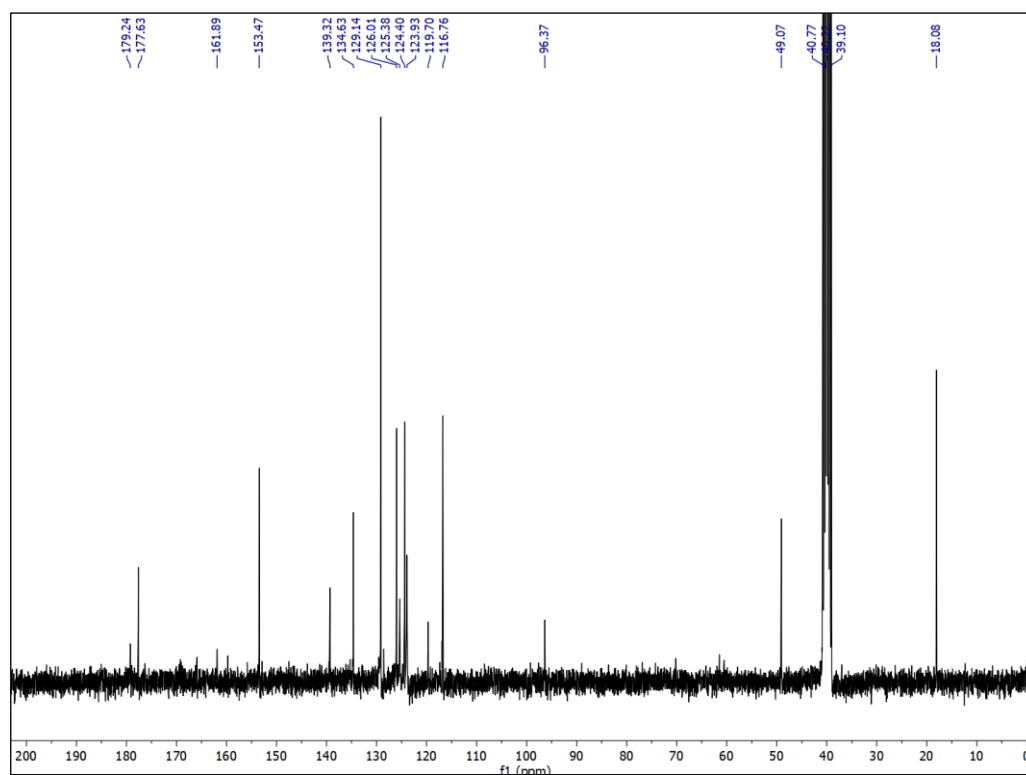
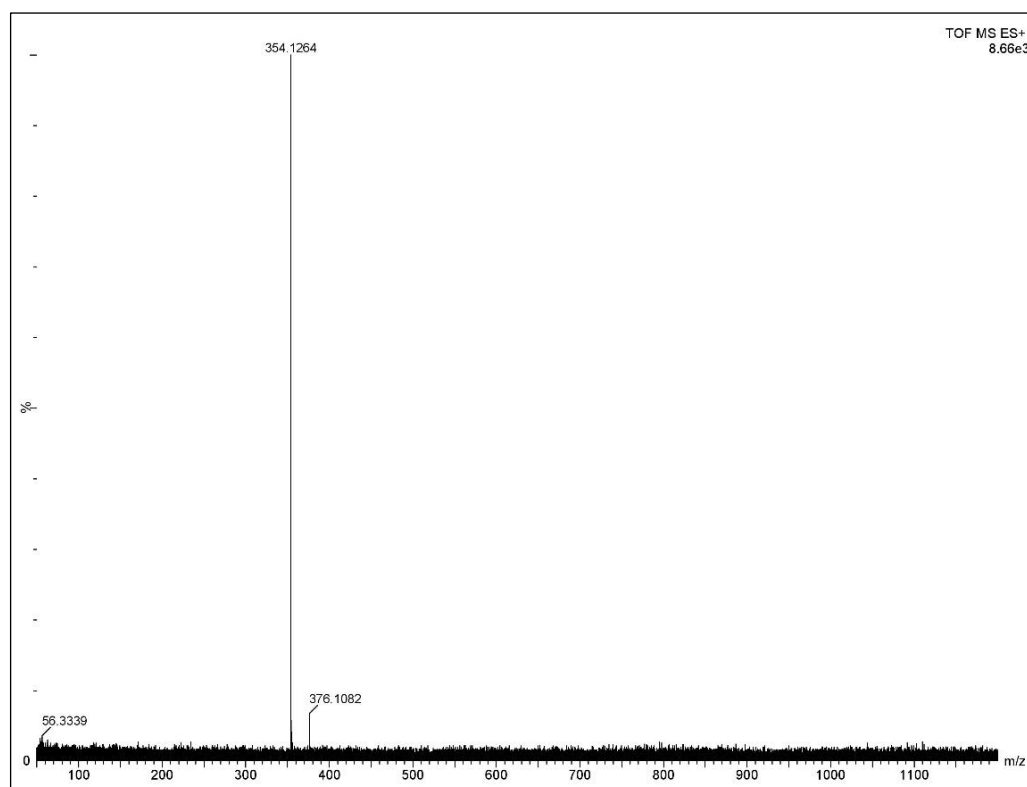


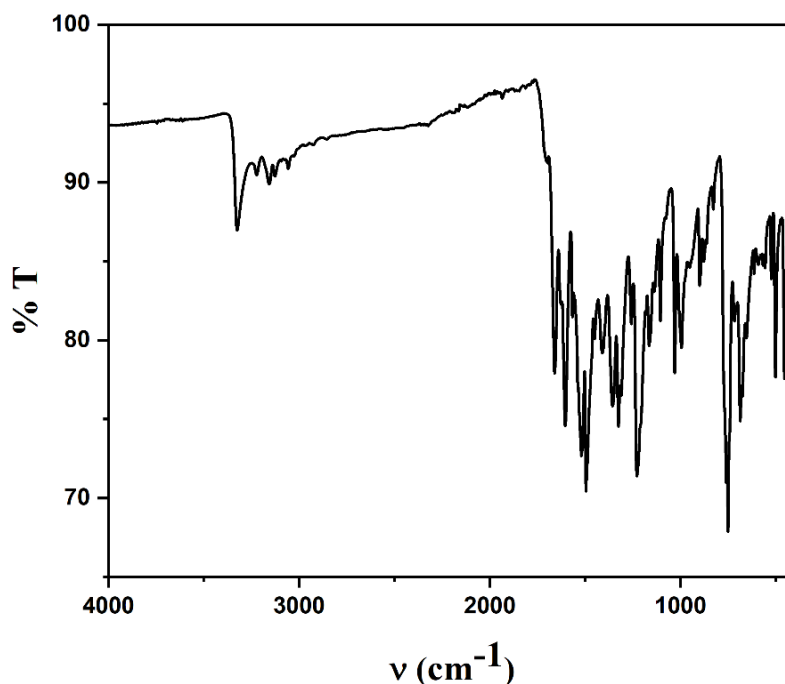
#### IV.2.2.2. Synthesis of (E)-2-(1-(4-hydroxy-2-oxo-2H-chromen-3-yl)ethylidene)-N-phenylhydrazine-1-carbothioamide (**HL**<sup>2</sup>)

0.1 g (0.5 mmol) of 3-acetyl-4-hydroxycoumarin was dissolved in 8 mL methanol, to it 0.083 g (0.5 mmol) 4-phenylthiosemicarbazide was added and the mixture was refluxed for 2 h. A light-yellow precipitate was appeared which is filtered and washed with methanol. The yield was 0.124 g (72%).

Anal. Calc. for  $C_{18}H_{15}N_3O_3S$ : C, 61.18; H, 4.28; N, 11.89. Found: C, 61.11; H, 4.21; N, 11.96.  $^1H$  NMR (300 MHz, DMSO- $d_6$ ):  $\delta$  2.69 (s, 3H), 7.18 (t,  $J = 7.29$  Hz, 1H), 7.29-7.4 (m, 4H), 7.56 (d,  $J = 7.89$  Hz, 2H), 7.67 (t,  $J = 7.2$  Hz, 1H), 8 (d,  $J = 7.2$  Hz, 1H), 10.27 (s, 1H), 15.66 (s, 1H).  $^{13}C$  NMR (75 MHz, DMSO- $d_6$ ) in ppm:  $\delta$  18.08, 49.07, 96.37, 116.76, 119.7, 123.93, 124.4, 125.38, 126.01, 129.14, 134.63, 139.32, 153.47, 161.89, 177.63, 179.24. IR ( $cm^{-1}$ ) in KBr: 3325  $\nu$ (O-H); 3223, 3157  $\nu$ (N-H); 3057, 2924  $\nu$ (C-H); 1660  $\nu$ (C=O, cyclic ester); 1605  $\nu$ (C=N); 1228  $\nu$ (C=S). HRMS: Calculated for  $C_{18}H_{16}N_3O_3S$   $[M + H]^+$  ( $m/z$ ): 354.0912; found: 354.1246. UV-Vis (in  $CH_3CN$ ),  $\lambda_{max}$  ( $\epsilon$ ,  $M^{-1}cm^{-1}$ ): 327 (11255).



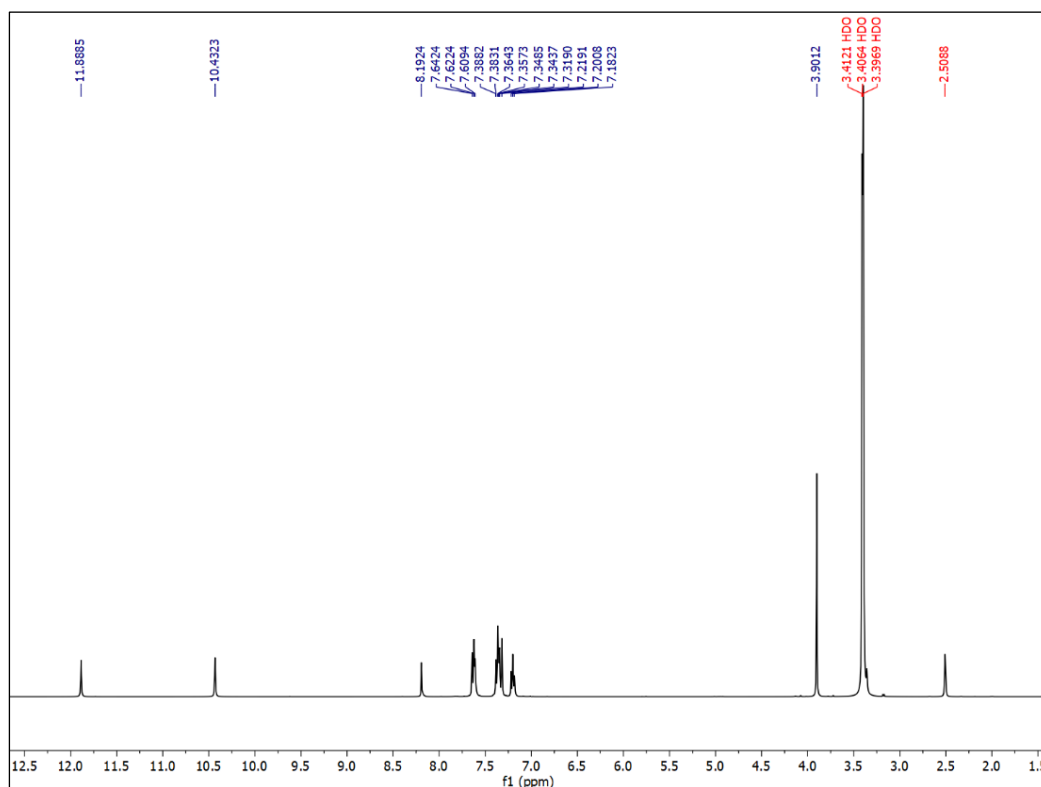
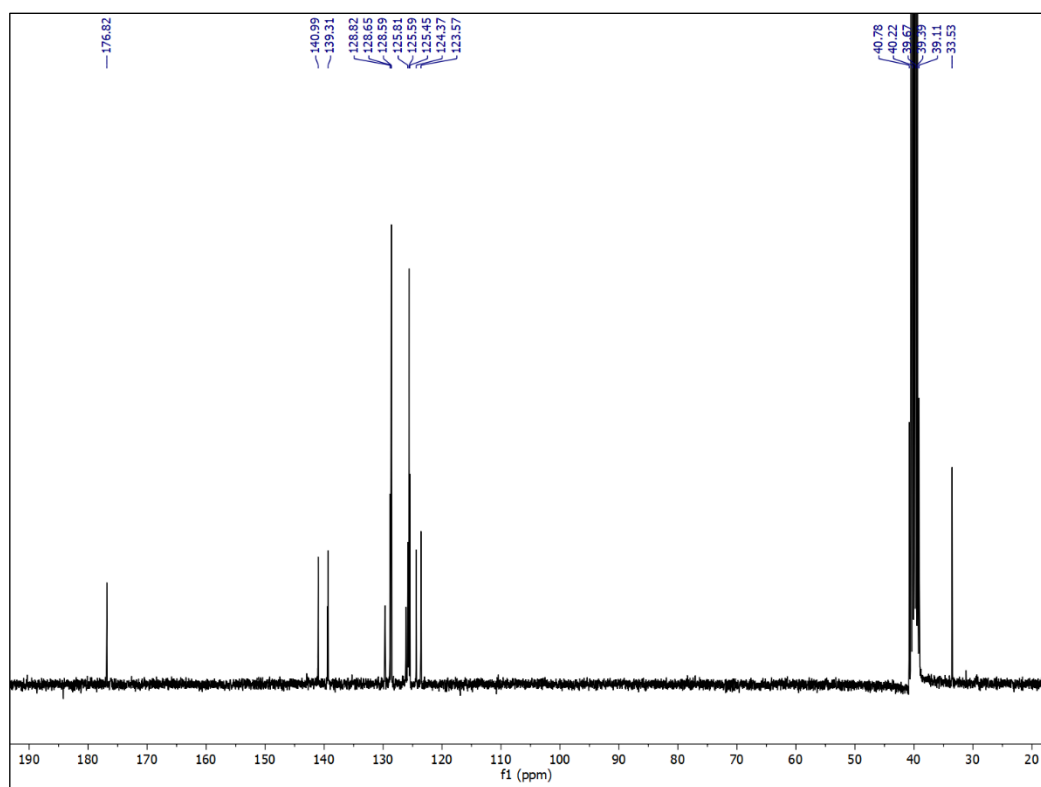
Figure IV.6.  $^{13}\text{C}$ -NMR spectrum of  $\text{HL}^2$  in  $\text{DMSO-d}_6$ Figure IV.7. HRMS of  $\text{HL}^2$  in acetonitrile

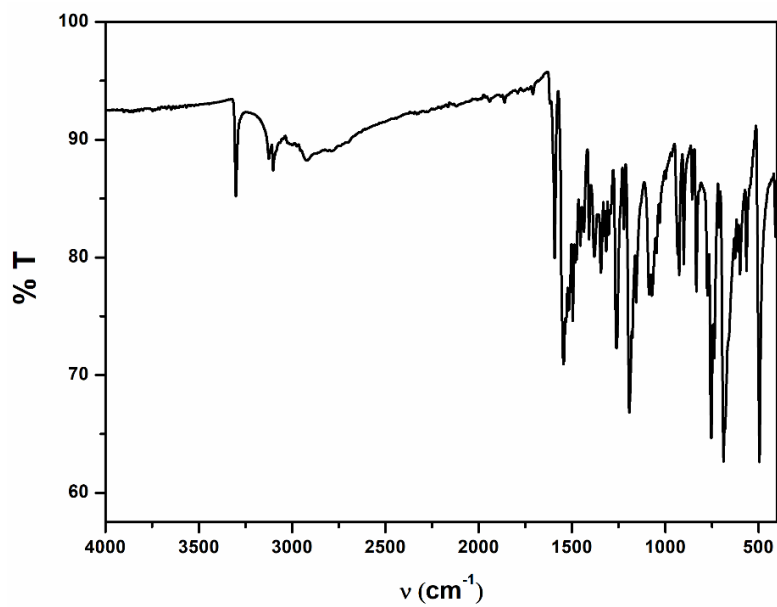
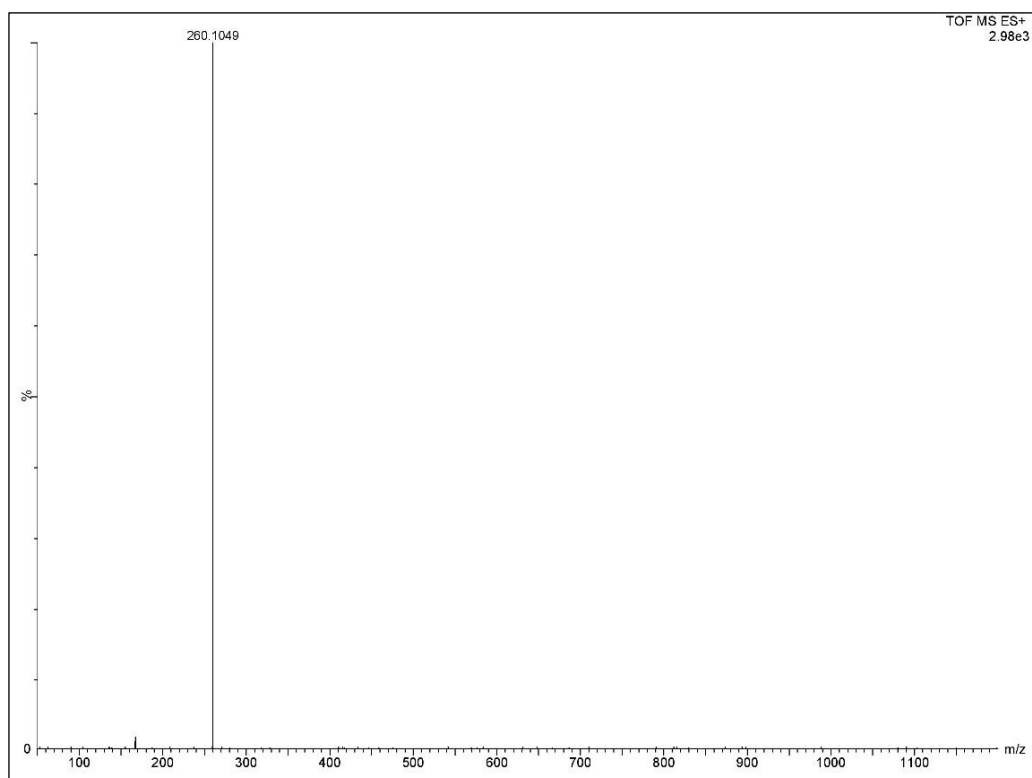
Figure IV.8. IR spectra of **HL**<sup>2</sup>

#### IV.2.2.3. Synthesis of (E)-2-((1-methyl-1H-imidazol-2-yl)methylene)-N-phenylhydrazine-1-carbothioamide (**L**<sup>3</sup>)

To a methanolic solution (8 mL) of 1-methyl-2-imidazolecarbaldehyde (0.06 mL), 0.1 g (0.6 mmol) of 4-phenylthiosemicarbazide was added and heated for 3 h. The reaction mixture was filtered after the completion of the reaction and kept it for the slow evaporation of solvent. Needle shape colourless crystals appropriate for X-ray diffraction of the ligand were appeared. The yield was 0.12 g (78%).

Anal. Calc. for C<sub>12</sub>H<sub>13</sub>N<sub>5</sub>S: C, 55.58; H, 5.05; N, 27.01. Found: C, 55.65; H, 4.98; N, 27.03. <sup>1</sup>H NMR (400 MHz, DMSO-d<sub>6</sub>): δ 3.9 (s, 3H), 7.2 (t, J = 7.28 Hz, 1H), 7.31-7.38 (m, 4H), 7.62 (t, J = 8 Hz, 2H), 8.19 (s, 1H), 10.43 (s, 1H), 11.88 (s, 1H). <sup>13</sup>C NMR (75 MHz, DMSO-d<sub>6</sub>) in ppm: δ 33.53, 123.57, 124.37, 125.45, 125.59, 125.81, 128.59, 128.65, 128.82, 139.31, 140.99, 176.82. IR (cm<sup>-1</sup>) in KBr: 3301, 3124, ν(N-H); 3100, 3000, 2922, ν(C-H); 1593 ν(C=N); 1192 ν(C=S). HRMS: Calculated for C<sub>12</sub>H<sub>14</sub>N<sub>5</sub>S [M + H]<sup>+</sup> (m/z): 260.0970; found: 260.1049. UV-Vis (in CH<sub>3</sub>CN), λ<sub>max</sub> (ε, M<sup>-1</sup>cm<sup>-1</sup>): 330 (30770), 246 (8735).

Figure IV.9.  $^1\text{H}$ -NMR spectrum of  $\text{L}^3$  in  $\text{DMSO-d}_6$ Figure IV.10.  $^{13}\text{C}$ -NMR spectrum of  $\text{L}^3$  in  $\text{DMSO-d}_6$

Figure IV.11. IR spectra of  $L^3$ Figure IV.12. HRMS of  $L^3$  in acetonitrile

IV.2.2.4. Synthesis of  $[\text{Pd}(\text{HL}^1)\text{Cl}]$  (**C1**)

0.06 g (0.338 mmol) of palladium chloride ( $\text{PdCl}_2$ ) was dissolved in acetonitrile by heating the solution and then it was added to the solution of **HL**<sup>1</sup> (0.1 g, 0.338 mmol) in acetonitrile and refluxed the resulting mixture for 12 h. Then the mixture was cooled to r.t and filtered it. Red colour single crystals of the complex suitable for diffraction were obtained after few days by the slow evaporation of the solvent. The yield was 0.11 g (70 %).

Anal. Calc. for  $\text{C}_{17}\text{H}_{13}\text{ClN}_4\text{OSPd}$ : C, 44.08; H, 2.83; N, 12.09; S, Found: C, 44.16; H, 2.90; N, 12.19. IR (KBr,  $\text{cm}^{-1}$ ): 3418  $\nu(\text{O-H})$ ; 3347  $\nu(\text{N-H})$ ; 3058  $\nu(\text{C-H})$ ; 1531  $\nu(\text{C=N})$ ; 760  $\nu(\text{C-S})$ .  $^1\text{H}$  NMR (300 MHz,  $\text{DMSO-d}_6$ ):  $\delta$  7.01 (t,  $J = 7.14$  Hz, 1H), 7.09-7.16 (m, 2H), 7.23-7.35 (m, 4H) 7.85 (d,  $J = 8.43$  Hz, 1H), 8.34 (d,  $J = 8.78$  Hz, 1H), 8.45 (s, 1H), 8.79 (d,  $J = 8.4$  Hz, 1H), 9.76 (s, 1H), 10.43 (s, 1H). HRMS: Calculated for  $\text{C}_{17}\text{H}_{13}\text{N}_4\text{OSPd} [\text{M} - \text{Cl}]^+$  ( $m/z$ ): 426.9845; found: 426.9903. UV-Vis (in  $\text{CH}_3\text{CN}$ ),  $\lambda_{\text{max}}$  ( $\epsilon$ ,  $\text{M}^{-1}\text{cm}^{-1}$ ): 391 (3045), 325 (2274), 250 (7370).

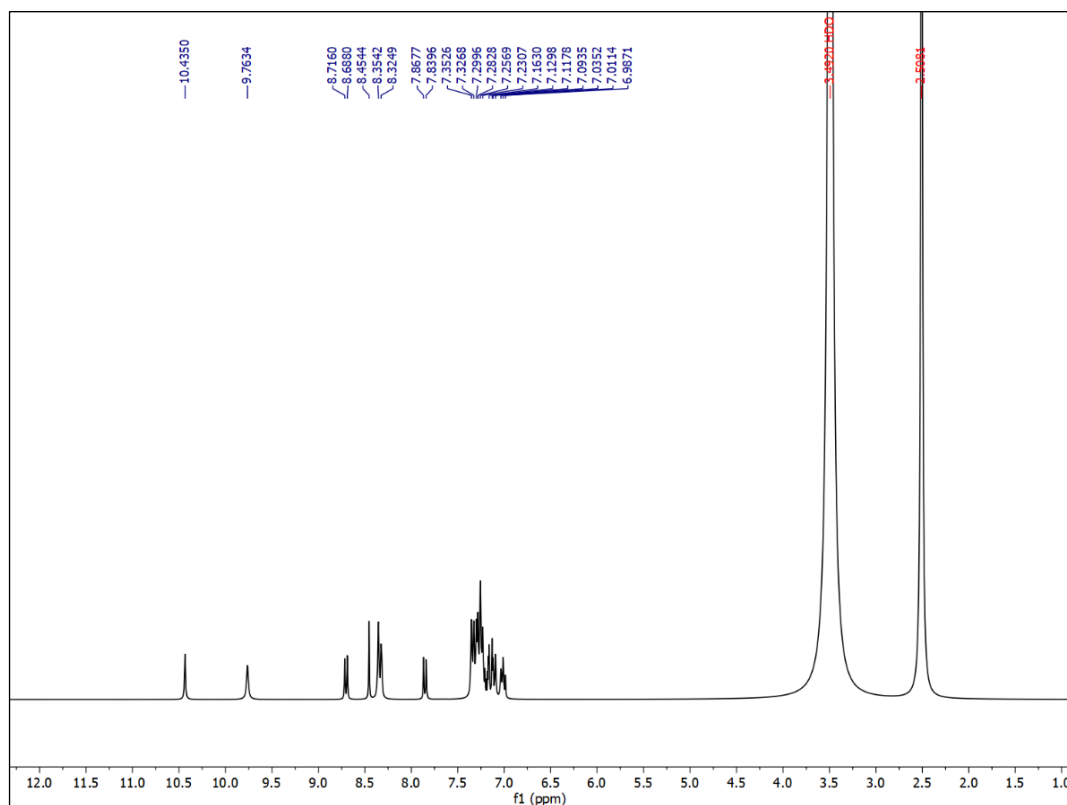
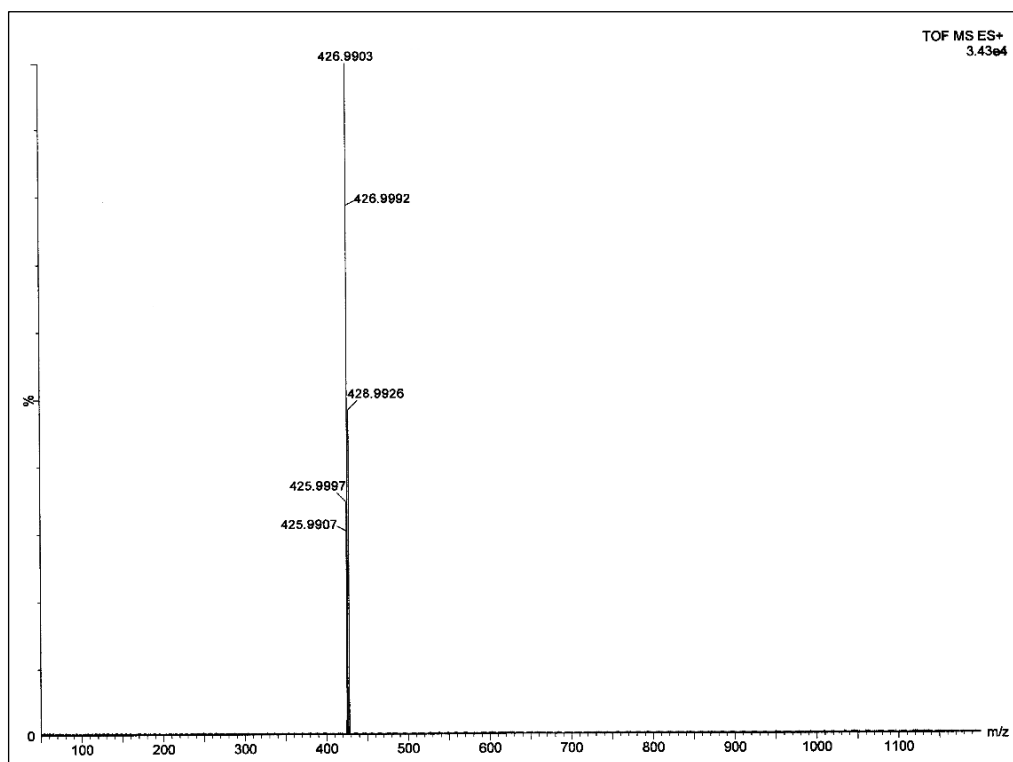
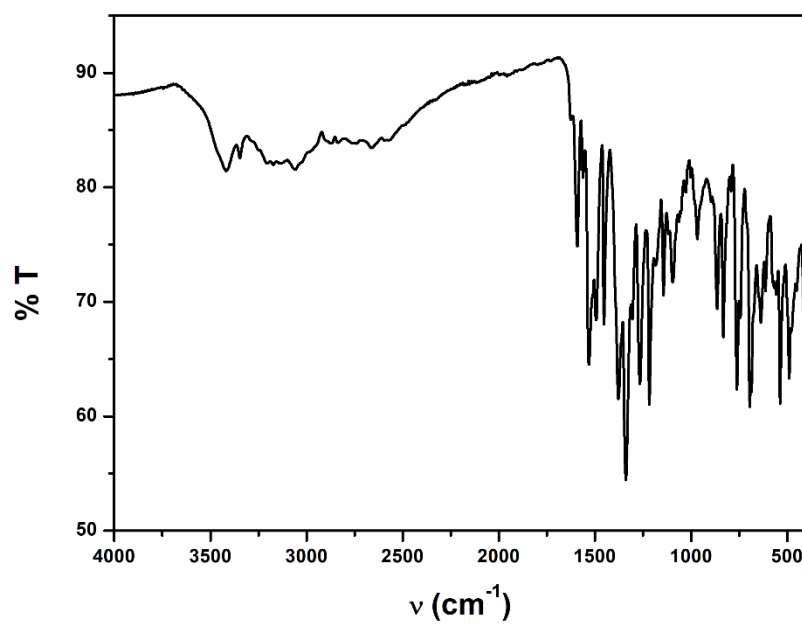


Figure IV.13.  $^1\text{H}$ -NMR spectrum of **C1** in  $\text{DMSO-d}_6$

Figure IV.14. HRMS of **C1** in acetonitrileFigure IV.15. IR spectra of **C1**



#### IV.2.2.5. Synthesis of [Pd(L<sup>2</sup>)(PPh<sub>3</sub>)] (C2)

PdCl<sub>2</sub> (0.05 g, 0.28 mmol) solution (in acetonitrile) was added to a solution of **HL**<sup>2</sup> (0.1 g, 0.28 mmol) in acetonitrile and refluxed for 2 h and then PPh<sub>3</sub> (0.11 g, 0.42 mmol) was added to the reaction mixture and refluxed the resultant mixture for 5 h. Orange colour crystals of **C2** were obtained after the evaporation of the solvent. The yield was, 0.14 g, 68%.

Anal. Calc. for C<sub>36</sub>H<sub>28</sub>N<sub>3</sub>O<sub>3</sub>SPPd: C, 60.05; H, 3.92; N, 5.84. Found: C, 60.14; H, 3.96; N, 5.92. IR (KBr, cm<sup>-1</sup>): 3345 ν(N-H); 3060, 2922, 2853 ν(C-H), 1691 ν(C=O, cyclic ester); 1600 ν(C=N); 744 ν(C-S). <sup>1</sup>H NMR (300 MHz, DMSO-d<sub>6</sub>): δ 2.75 (s, 3H) 6.63 (d, J = 7.56 Hz, 1H), 6.88-6.95 (m, 2H), 7.22-7.31 (m, 4H), 7.47-7.71 (m, 17H) 9.56 (s, 1H). HRMS: Calculated for C<sub>36</sub>H<sub>28</sub>N<sub>3</sub>O<sub>3</sub>SPPd [M + H]<sup>+</sup> (m/z): 720.0702; found: 720.0710. UV-Vis (in CH<sub>3</sub>CN), λ<sub>max</sub> (ε, M<sup>-1</sup>cm<sup>-1</sup>): 372 (4018), 287 (sh.), 252 (sh.).

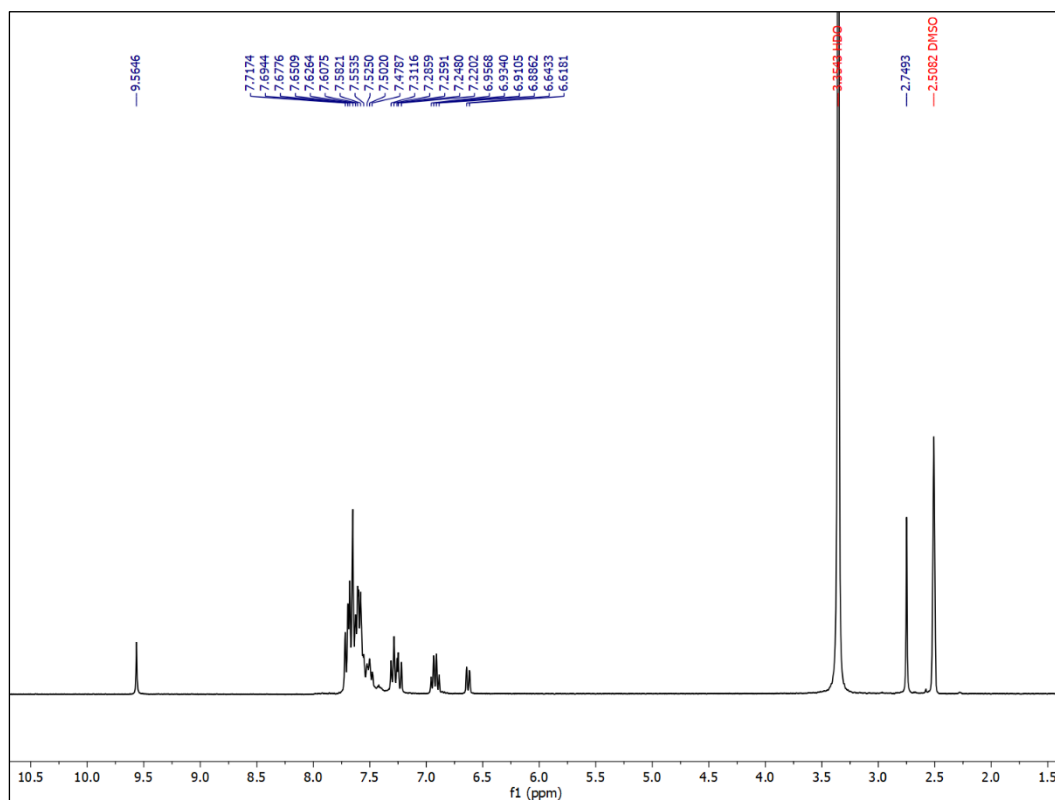


Figure IV.16. <sup>1</sup>H-NMR spectrum of **C2** in DMSO-d<sub>6</sub>

#### IV.2.2.6. Synthesis of [Pd(L<sup>3</sup>)(PPh<sub>3</sub>)]Cl (C3)

The procedure for the synthesis of **C3** was same as **C2**, here ligand was **L**<sup>3</sup> (0.07 g, 0.28 mmol). After the addition of PPh<sub>3</sub>, orange red colour solution appear which was filtered and

kept it for crystallization. Red colour crystals of **C3** were appeared after few days. Yield was 0.09 g (72 %).

Anal. Calc. for  $C_{30}H_{27}ClN_5SPPd$ : C, 57.47; H, 4.34; N, 11.17. Found: C, 57.58; H, 4.45; N, 11.25. IR (KBr,  $cm^{-1}$ ): 3345  $\nu(N-H)$ ; 3049, 2923, 2853  $\nu(C-H)$ , 1541  $\nu(C=N)$ ; 743  $\nu(C-S)$ .  $^1H$  NMR (300 MHz, DMSO- $d_6$ ):  $\delta$  3.94 (s, 3H), 7.08-7.73 (m, 4H), 8.5 (s, 1H), 10.3 (s, 1H). HRMS: Calculated for  $C_{30}H_{27}N_5SPPd$   $[M - Cl]^+$  (m/z): 626.0760; found: 625.9386. UV-Vis (in  $CH_3CN$ ),  $\lambda_{max}$  ( $\epsilon$ ,  $M^{-1}cm^{-1}$ ): 348 (8121), 257 (sh.).

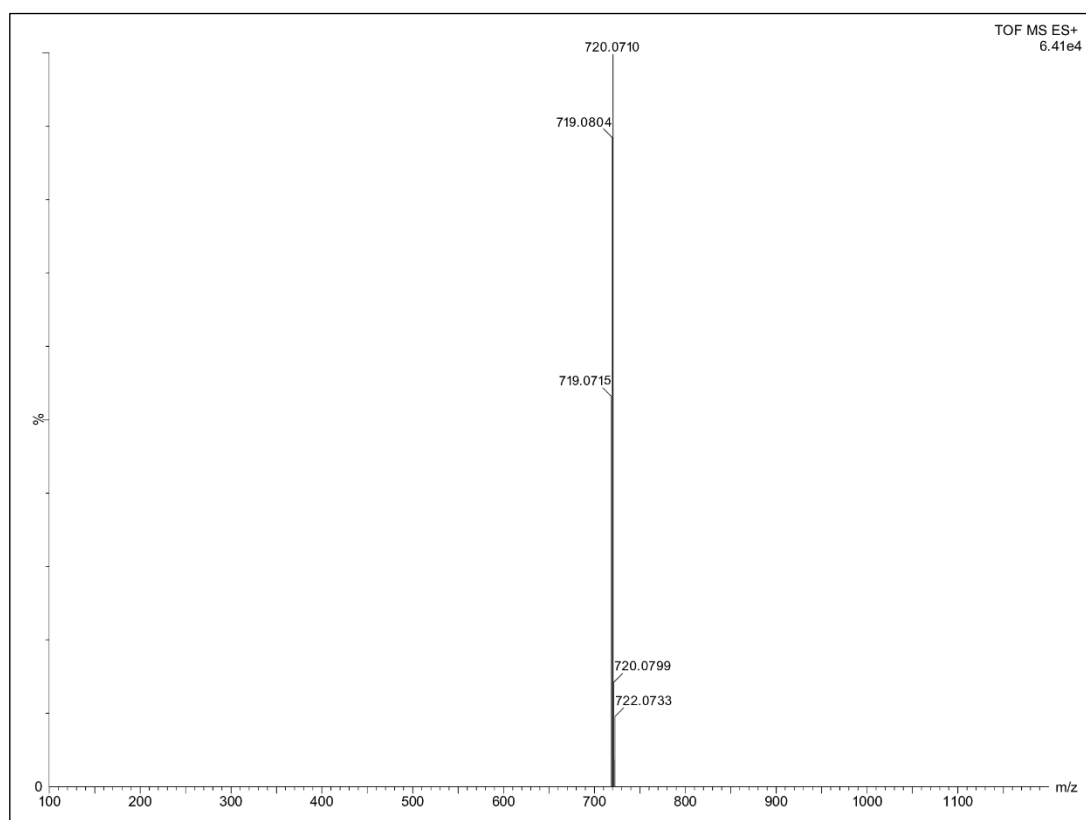
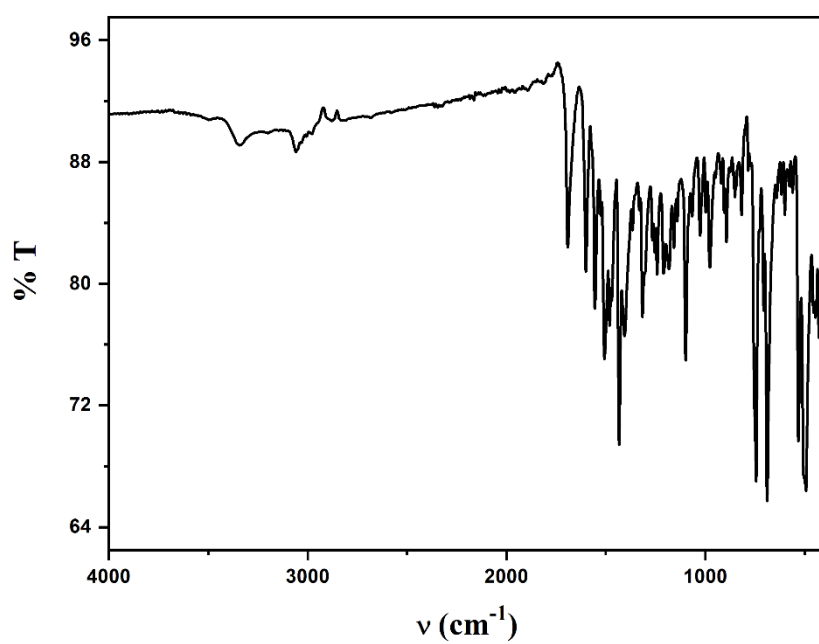
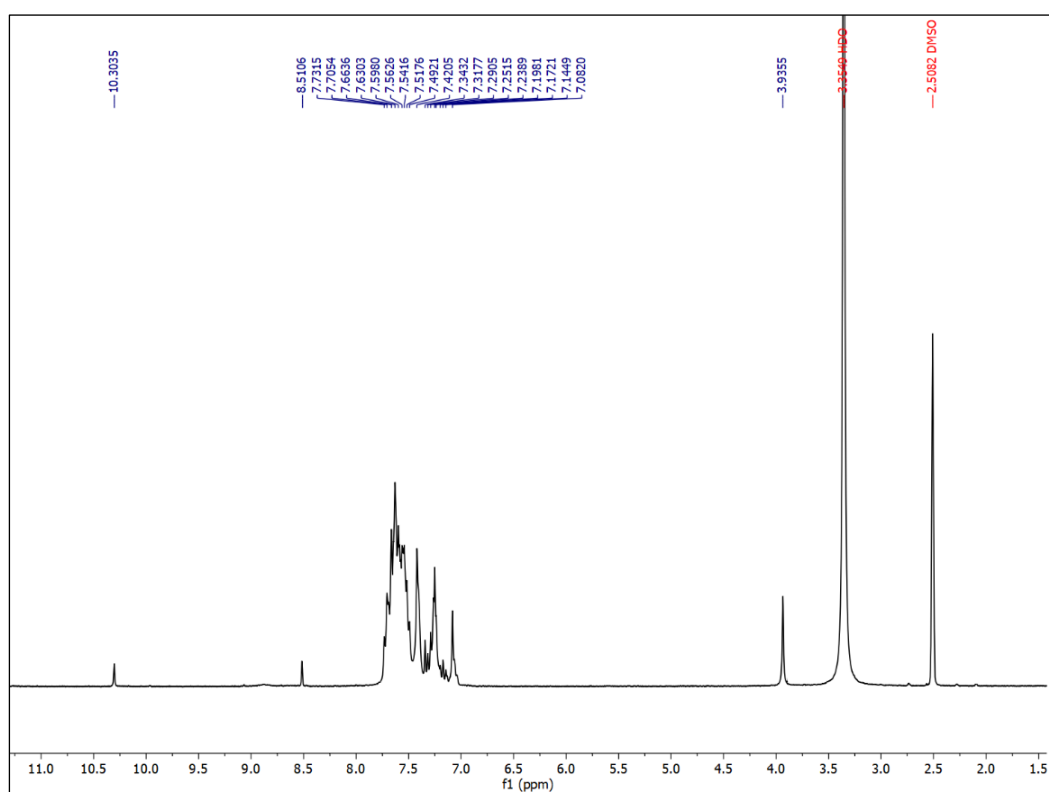


Figure IV.17. HRMS of **C2** in acetonitrile

Figure IV.18. IR spectra of **C2**Figure IV.19.  $^1\text{H}$ -NMR spectrum of **C3** in DMSO- $\text{d}_6$

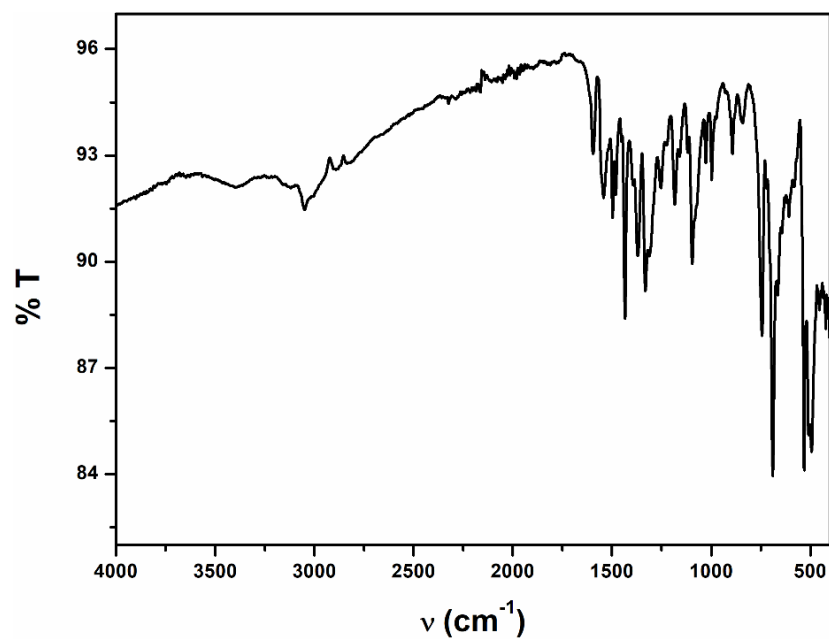


Figure IV.20. IR spectra of C3

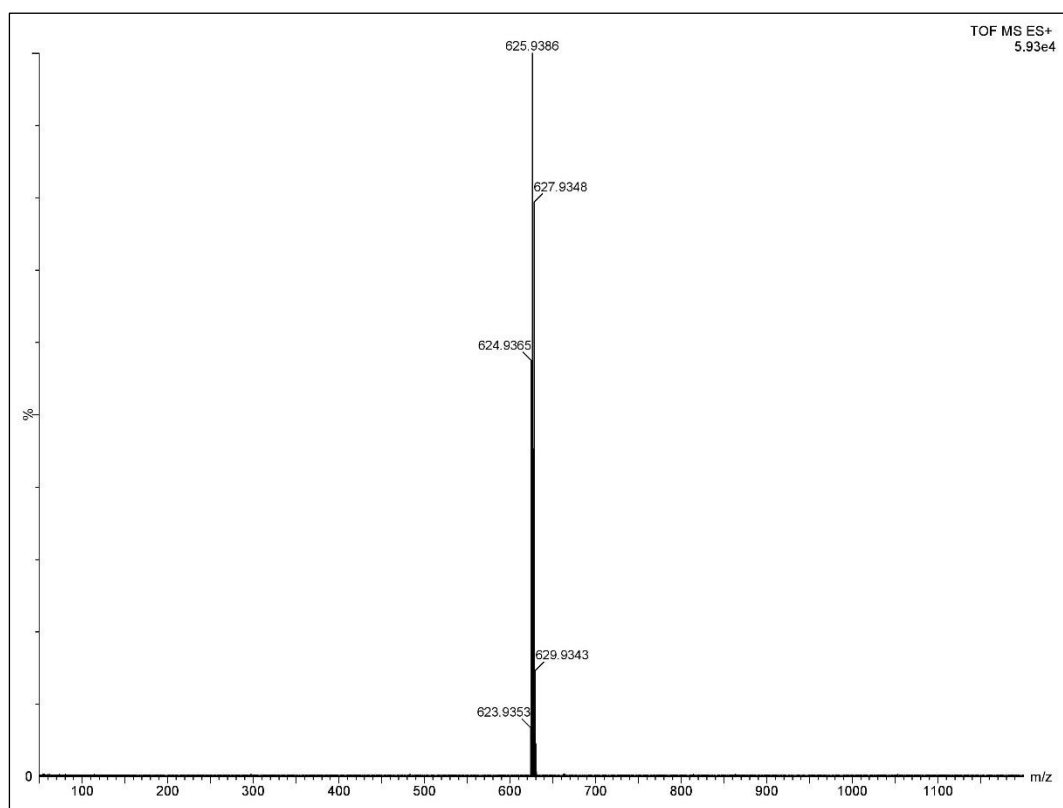


Figure IV.21. HRMS of C3 in acetonitrile

### IV.2.3. Procedure for the Suzuki Coupling Reaction

Aryl halide (1 mmol), phenylboronic acid (1 mmol),  $K_2CO_3$  (2 mmol) and catalyst (**C1/C2/C3**, 1 mol%) were mixed in 5 mL PEG 400 solvent and stirred under reflux condition (90° C) for 6-7 h. The product formation was primarily examined by TLC. Solvent was evaporated under reduced pressure after the completion of the reaction and the residue was poured in water and extracted using diethyl ether. The catalyst was separated and washed with diethyl ether. The diethyl ether part was dried using anhydrous sodium sulfate. Then the solvent was evaporated and the residue was purified by column chromatography on silica gel and identified by  $^1H$  NMR spectroscopy. The yields were determined by GC.

### IV.2.4. Crystal Structure Determination and Refinement

Details of crystal analysis, data collection and structure refinement data for **L<sup>3</sup>**, **C1**, **C2** and **C3** are given in Table S1. The Bruker AXS D8 Quest CMOS diffractometer was used to acquire diffraction data using graphite monochromatized Mo-K $\alpha$  radiation ( $\lambda = 0.71073$ ) at 293 K and reflection data were recorded using the  $\omega$  scan technique. The SAINT program<sup>48</sup> was used to integrate the data, and SADABS<sup>49</sup> was used to make the absorption corrections. All data were polarization and Lorentz adjusted, and the non-hydrogen atoms were anisotropically refined. The refinement procedure took into account hydrogen atoms in accordance with the riding model. The structures were resolved by direct method and refined using SHELXL-2016/6 program<sup>50</sup> by full-matrix least-squares techniques.

### IV.2.5. Theoretical Study

Density functional theory (DFT) was used to optimize the complexes' full geometry using the B3LYP<sup>51</sup> hybrid exchange correlation functional. All elements except Pd were assigned with 6-31G(d) basis set while for Pd atoms LanL2dz<sup>52</sup> basis set with effective core potential was employed. On the optimized geometries, vibrational frequency calculations were done to make sure that each configuration is actually a local minimum on the potential energy surface. The Gaussian09 program<sup>53</sup> and the Gauss-View, Version 5 visualization program were used for all calculations. Electronic transitions were calculated using the time-dependent density functional theory (TDDFT) formalism<sup>54</sup> using conductor-like polarizable continuum model (CPCM)<sup>55</sup> in acetonitrile to simulate the solvent. The fractional contributions of various groups to each molecular orbital were calculated using GaussSum.<sup>56</sup>

#### IV.2.6. DNA Interaction Studies

The binding experiments of metal complexes with calf thymus (CT) DNA were performed in Tris HCl/50 mM NaCl buffer (pH 7.4). A stock solution of CT DNA was prepared in that buffer and the concentration of the CT DNA was determined by dividing its absorption value at 260 nm with the molar extinction coefficient value i.e.,  $6600 \text{ M}^{-1} \text{ cm}^{-1}$ .<sup>57</sup> The stock solution of the complexes was prepared in DMSO medium ( $\sim 10^{-4} \text{ M}$ ) and was suitably diluted with Tris-buffer whenever necessary. By keeping constant concentration of complexes, absorption titration was carried out by gradually adding the CT DNA solution. The competitive studies of the complexes with ethidium bromide (EB) were investigated with fluorescence spectroscopy in order to examine whether the compound can displace EB from its EB-CT DNA complex. The EB-CT DNA adduct was prepared by adding  $15 \mu\text{M}$  EB and  $30 \mu\text{M}$  CT DNA in buffer (Tris-HCl/NaCl buffer at pH 7.4). The influence of the addition of the complexes to the EB-CT DNA adduct solution has been obtained by recording the emission spectra and the observed quenching is attributed to the displacement of EB from its EB-CT DNA adduct.

The viscosity of the CT-DNA solution ( $30 \mu\text{M}$ ) was measured by increasing the concentration of the complexes using an Ostwald viscometer placing in a thermostated water bath at  $20.0^\circ\text{C}$ . Flow time has been measured three times for each concentration of the compound and then the average flow time was calculated. Viscosity values were calculated from the observed flow time of DNA-containing solutions ( $t$ ) corrected for the flow time of buffer alone ( $t_0$ ),  $\eta = t - t_0$ . The data is reported as  $(\eta / \eta_0)^{1/3}$  versus the ratio of the concentration of the compound to CT-DNA ( $R$ ), where  $\eta$  is the viscosity of CT-DNA in the presence of the compound and  $\eta_0$  is the viscosity of CT-DNA solution alone.

#### IV.2.6. BSA Protein Binding Studies

It was feasible to ascertain how the BSA protein interacted with the complexes by measuring absorption and emission. In order to do this, a BSA stock solution ( $5 \mu\text{M}$ ) in 500 mM phosphate buffer saline (PBS) at pH 7.4 was produced and stored at  $4^\circ\text{C}$  in the dark. The complex solutions ( $\sim 10^{-4} \text{ M}$ ) were prepared in DMSO solvent and was suitably diluted with PBS whenever necessary. During the absorption titration tests, the addition concentrations of the complexes were varied while the BSA ( $5 \mu\text{M}$ ) concentration was maintained constant. Similarly, fluorescence titrations were performed with a fixed BSA concentration. A micropipette was used to manually add the compounds to both the absorbance and emission titrations.

#### IV.2.6.1. CD Spectral Study

Circular dichroism (CD) measurements were obtained by employing JASCO (J-815) spectropolarimeter at 298 K using a quartz cuvette of 1 cm cell path length. The spectra were carried out by keeping a constant BSA concentration (0.48  $\mu\text{M}$ ) and the spectra were recorded in the absence and presence of the three complexes. The CD results were expressed in terms of the mean residual ellipticity (MRE) in  $\text{deg cm}^2 \text{dmol}^{-1}$  according to the following equation (eq 1).

$$\text{MRE} = \text{observed CD (mdeg)} / 10C_p n l \quad (1)$$

Where,  $C_p$  represents the molar concentration of the protein,  $n$  stands for the number of amino acid residues (583 for BSA) and  $l$  is the path length of the cell (1 cm). The  $\alpha$ -helical (%) contents of the free and bound BSA were calculated from the mean MRE values at 208 nm using the following equation (eq 2).

$$\alpha\text{-helix (\%)} = [(-\text{MRE}_{208} - 4000) / (33,000 - 4000)] \times 100 \quad (2)$$

Where,  $\text{MRE}_{208}$  is the MRE value observed at 208 nm, 4000 is the MRE of the  $\beta$ -form and random coil conformation at 208 nm, and 33000 is the MRE value of a pure  $\alpha$ -helix at 208 nm.

#### IV.2.6.2. Förster Resonance Energy Transfer (FRET)

The value of  $R_0$  was calculated using equation (3).

$$R_0 = 0.2018 \{[\kappa^2 \phi_D \eta^{-4} J(\lambda)]^{1/6}\} \text{ \AA} \quad (3)$$

where the orientation factor between the emission dipole of the donor and the absorption dipole of the acceptor  $\kappa^2$  is taken as 2/3, the fluorescence quantum yield of the donor  $\phi_D$  is 0.118, the refractive index of the medium ( $\eta$ ) is 1.33, and  $J(\lambda)$  is the extent of spectral overlap of donor (BSA) emission and the acceptor (complex) absorption spectra.<sup>58</sup> The value of  $J(\lambda)$  can be calculated using eqn (4).<sup>59</sup>

$$J(\lambda) = \int_0^\infty \bar{I}_D(\lambda) \varepsilon_A(\lambda) \lambda^4 d\lambda \quad M^{-1} \text{cm}^{-1} \text{nm}^4 \quad (4)$$

Where,  $\bar{I}_D(\lambda)$  denotes the normalized fluorescence emission of the donor BSA at the wavelength  $\lambda$ , and  $\varepsilon_A(\lambda)$  represents the molar extinction coefficient of the acceptor metal complex at the wavelength  $\lambda$ .

#### IV.2.7. In Vitro Cytotoxicity Study

##### IV.2.7.1. Cell Culture

The human breast adenocarcinoma (MDA-MB-231) cell line was obtained from the National Centre for Cell Science (NCCS) in Pune, India. The cells were cultured in Dulbecco's



modified Eagle's medium (DMEM) with high glucose, supplemented with 10% heat-inactivated fetal bovine serum (FBS) from Gibco™, USA, and 1% Penicillin-Streptomycin (Gibco™, USA). The cell culture was maintained in a 5% CO<sub>2</sub> atmosphere at 37°C in a humidified incubator. When the cells reached approximately 70-80% confluency, they were harvested using a 0.25% Trypsin-EDTA (Gibco™, USA) solution and then seeded at an appropriate density to allow them to re-equilibrate before the start of the experiment. This process ensures that the cells are in a suitable state for subsequent experimental procedures.

#### IV.2.7.2. Cell Viability Assay

To determine cell viability, the MTT [(4,5-dimethyl-thiazol-2-yl)-2,5-diphenyl tetrazolium bromide] assay was performed using MTT reagent obtained from Sigma Aldrich, USA. In this assay, MDA-MB-231 cells were seeded in a 96-well plate at a density of 10,000 cells per well. The cells were then treated with different concentrations of **C3** (0, 5, 10, 15, 20, 25, 30, 35, 40, 45, and 50 µM). After the treatment, the plates were incubated for 24 hours at 37°C in a humidified CO<sub>2</sub> (5%) incubator. Following the incubation period, the cells were washed thoroughly with phosphate-buffered saline (PBS). Subsequently, MTT solution with a concentration of 4 mg/mL was added to each well, and the plates were returned to the incubator for 4 hours. After the incubation with MTT, the intracellular formazan salt formed was solubilized by adding dimethyl sulfoxide (DMSO). Cell viability was assessed using absorbance measurements to determine cell proliferation. The absorbance values were used to calculate cell viability using the formula:  $\text{Cell viability (\%)} = (\text{OD}_{\text{control}} - \text{OD}_{\text{sample}}) / \text{OD}_{\text{control}} \times 100$ . In this formula, OD<sub>control</sub> represents the absorbance of untreated cells, while OD<sub>sample</sub> represents the absorbance of treated cells. To ensure the reliability of the results, the experiments were conducted multiple times, allowing for the reduction of experimental variability and ensuring the consistency and reproducibility of the findings. The absorbance of the solubilized formazan salt was measured at 595 nm using an ELISA reader (EMax, Molecular Device, USA). This measurement provided an indication of cell viability, as the intensity of the absorbance was proportional to the number of viable cells in each well.

#### IV.2.7.3. Quantification of Apoptosis Using Flow Cytometry

To analyze apoptosis, flow cytometry was performed using the Dead Cell Apoptosis Kit with Annexin V obtained from Invitrogen™, USA.<sup>60-62</sup> Treated cells at a density of  $1 \times 10^6$  were harvested and stained with Annexin-V-FITC and propidium iodide (PI) following the manufacturer's instructions. The staining procedure involved the labeling of cells with

Annexin-V-FITC, which binds to phosphatidylserine exposed on the outer membrane of apoptotic cells. PI was used to stain cells with compromised cell membranes, such as necrotic cells. The staining allowed for the differentiation of viable, apoptotic (early and late), and necrotic cells. After staining, flow cytometry analysis was performed using a BD LSRFortessa flow cytometer (San Jose, CA, USA). The flow cytometer measured the fluorescence emitted by Annexin-V-FITC and PI to determine the proportions of viable, apoptotic, and necrotic cells within the cell population. This analysis provided quantitative information about the induction of apoptosis and the extent of cell death in the treated cell samples.

#### **IV.2.7.4. Measurement of Mitochondrial Membrane Potential Using Flow Cytometry**

For assessing mitochondrial membrane potential, treated cells were incubated with JC-1, a cationic carbocyanine dye obtained from Invitrogen™, USA. The dye accumulates in the mitochondria in a potential-dependent manner. It undergoes a fluorescence emission shift from green (525 nm) to red (590 nm) when the mitochondrial membrane potential is intact. After incubation with JC-1, flow cytometric analysis was performed following the manufacturer's protocol. The flow cytometer measured the fluorescence emitted by JC-1 monomers and aggregates, allowing the determination of the percentage of depolarized and hyperpolarized mitochondria within the cell population. Depolarized mitochondria exhibit a decreased red/green fluorescence ratio, indicating a loss of mitochondrial membrane potential, while hyperpolarized mitochondria display an increased red/green fluorescence ratio, indicating intact mitochondrial membrane potential. By analyzing the fluorescence changes of JC-1, the flow cytometry data provided information about the mitochondrial membrane potential status in the treated cells, allowing the assessment of mitochondrial dysfunction or perturbation induced by the experimental treatment.

#### **IV.2.7.5. Determination of Intracellular ROS (iROS)**

To investigate the production of reactive oxygen species (ROS) within the treated cells, we utilized the fluorescent probe 2',7'-dichlorofluorescein diacetate (H<sub>2</sub>DCFH-DA) obtained from Invitrogen™. H<sub>2</sub>DCFH-DA is a non-fluorescent compound that can enter the cells and be converted into the fluorescent molecule 2',7'-dichlorofluorescein (DCF) in the presence of ROS. The treated cells were incubated with 10 mM H<sub>2</sub>DCFH-DA at 37 °C for 25 minutes. During this incubation period, the H<sub>2</sub>DCFH-DA was taken up by the cells and intracellularly converted to DCF in the presence of ROS. The intensity of DCF fluorescence directly reflects

the level of ROS generated inside the cells. After incubation, the cells were analyzed using a flow cytometry (BD LSRFortessa, Becton Dickinson, Franklin Lakes, NJ, USA). The mean fluorescence intensity of DCF was measured, providing a quantitative assessment of intracellular ROS levels. The increment in DCF fluorescence intensity correlates with an increase in ROS production, indicating oxidative stress within the cells. This analysis allows us to evaluate the impact of the treatment on ROS generation and provides insights into the cellular response to oxidative stress induced by the experimental conditions.

#### **IV.2.7.6. Confocal Microscopy**

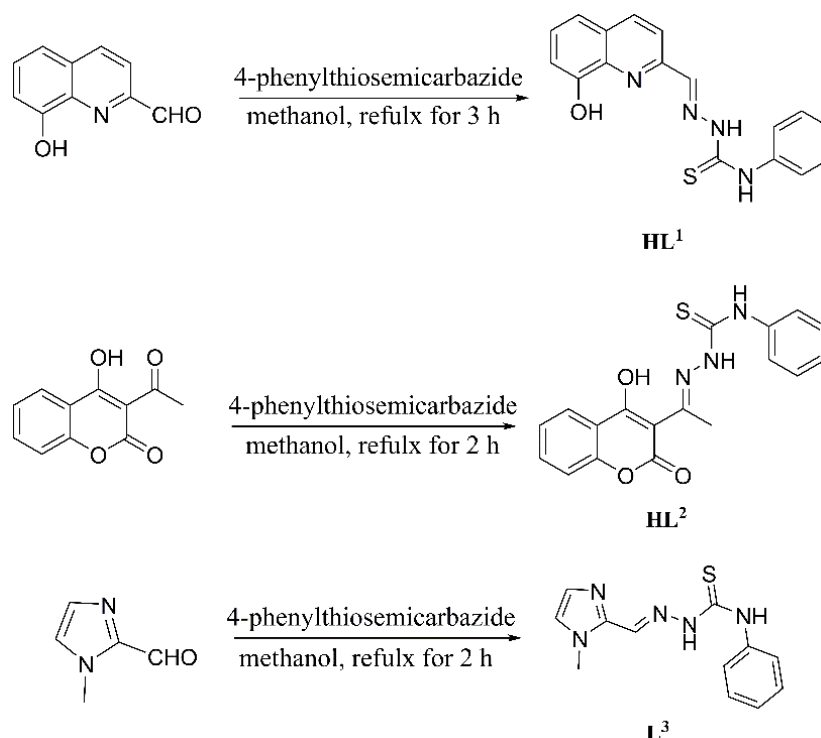
To examine the expression of apoptotic markers, including Caspase-3, Casase-9, Cytochrome C, BCL-2, p53, and p21, confocal microscopy was performed. The following steps were carried out: Control and treated MDA-MB-231 cells were washed twice with PBS (0.01 M) for 5 minutes each to remove any residual media or reagents. The cells were then fixed with a 4% Paraformaldehyde solution in PBS and incubated for 15 minutes at room temperature. This fixation step helps preserve the cellular structure. After fixation, the cells were incubated in a blocking solution containing 2% normal bovine serum and 0.3% Triton X-100 in PBS for 1 hour. Blocking helps reduce nonspecific binding of antibodies and enhances the specificity of the staining. Following the blocking step, the cells were incubated overnight at 4 °C with the respective primary antibodies targeting Caspase-3, Casase-9, Cytochrome C, BCL-2, p53, and p21. These primary antibodies (obtained from CST, USA) specifically bind to their respective targets within the cells. After the overnight incubation, the cells were washed to remove unbound primary antibodies and then incubated with fluorophore-conjugated secondary antibodies for 4 hours. The secondary antibodies, such as anti-mouse/rabbit/goat Alexa Fluor-555, Alexa Fluor-647, and Alexa Fluor-488 (obtained from CST, USA), bind to the primary antibodies and enable visualization of the target proteins. To visualize the cell nuclei, the stained cells were counterstained with 6-diamidino-2-phenylindole (DAPI) obtained from Sigma, USA, for 5 minutes. DAPI binds to DNA, highlighting the nuclei of the cells. Finally, the slides containing the stained cells were mounted using Fluorescent Mounting Media, Aqueous obtained from Sigma, USA. This mounting media helps preserve the fluorescence and protect the slides. The stained cells were examined using a confocal laser scanning microscope (ZEISS LSM-980, Germany). The microscope allows the visualization of fluorescence signals with high resolution and the collection of optical sections through the cells. The acquired images were analyzed using ZEN 3.4 Blue edition software, which enables the quantification and analysis of the fluorescence signals from the

different channels. This analysis helps determine the localization and expression levels of the apoptotic markers within the cells. By performing confocal microscopy and image analysis, we can gain insights into the spatial distribution and expression patterns of the apoptotic markers, providing valuable information about the cellular response to the treatment.

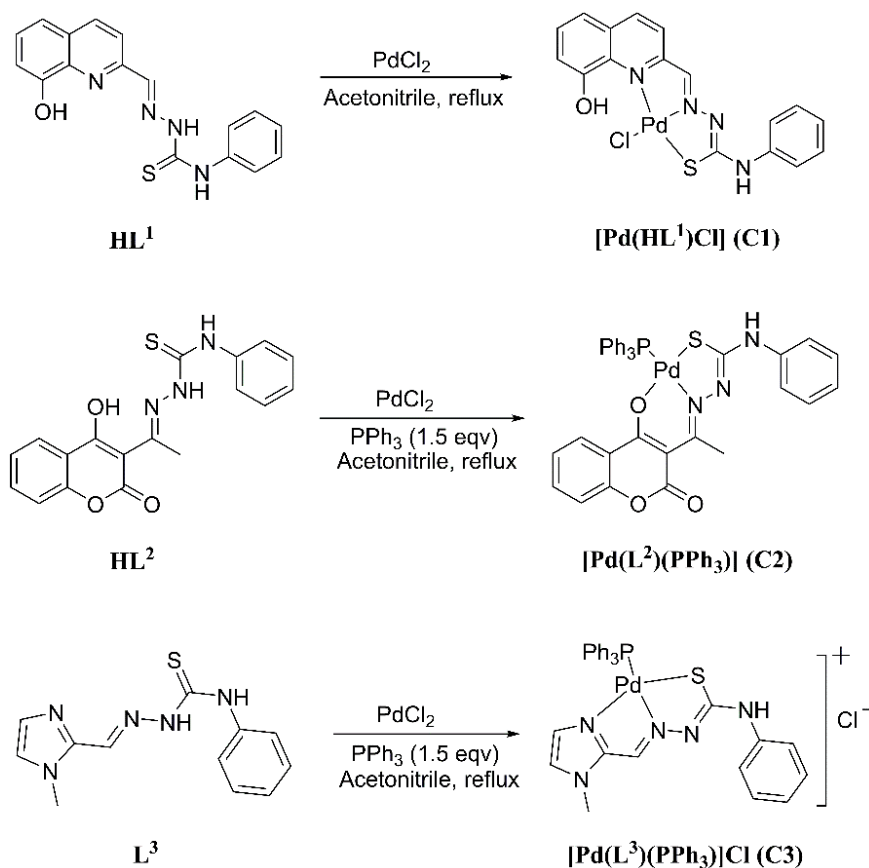
### IV.3. Results and Discussion

#### IV.3.1. Synthesis and Characterization

At first, three thiosemicarbazide based Schiff base ligands (**HL**<sup>1</sup>, **HL**<sup>2</sup> and **L**<sup>3</sup>) were designed by reacting 4-phenylthiosemicarbazide with the carbonyls in methanol solvent (Scheme IV.1). **C1** was obtained by the reaction of **HL**<sup>1</sup> with PdCl<sub>2</sub> in 1 : 1 molar ration in refluxing condition. Synthesis of **C2** and **C3** involved the reaction of PdCl<sub>2</sub> with **HL**<sup>2</sup> and **L**<sup>3</sup> respectively followed by the addition of 1.5 equivalent of PPh<sub>3</sub> in acetonitrile medium (Scheme IV.2). All the compounds were thoroughly characterized by NMR, IR, UV-Vis spectroscopy and mass spectrometry. The molecular structure of the complexes was confirmed using single crystal X-ray crystallography technique.



Scheme IV.1. Synthesis routes of the ligands **HL**<sup>1</sup>, **HL**<sup>2</sup> and **L**<sup>3</sup>

Scheme IV.2. Synthetic routes of the complexes **C1**, **C2** and **C3**

Ligand **HL**<sup>1</sup> displays a broad band at 3624 cm<sup>-1</sup> in the IR spectra corresponds to O–H stretching while N–H stretching band observed at 3398 cm<sup>-1</sup> and 3256 cm<sup>-1</sup>. Imine (C=N) stretching band appears at 1592 cm<sup>-1</sup> which shifted to 1531 cm<sup>-1</sup> in **C1** because of coordination of imine nitrogen atom with metal ion (Figure IV.4 and IV.15). Similar case was observed in **C2** and **C3** where C=N stretching frequencies (1600 and 1541 cm<sup>-1</sup> respectively) are lower than in their respective ligands **HL**<sup>2</sup> and **L**<sup>3</sup> (1605 and 1593 cm<sup>-1</sup>). In case of **HL**<sup>2</sup>, O–H stretching band appears at 3325 cm<sup>-1</sup> and this band is disappeared in **C2** due to the coordination of oxygen atom with metal centre (Pd<sup>2+</sup> ion). The C=S stretching band at 1200, 1228 and 1192 cm<sup>-1</sup> were observed for **HL**<sup>1</sup>, **HL**<sup>2</sup> and **L**<sup>3</sup> respectively and these are lifted to 760–740 cm<sup>-1</sup> in the respective complexes since sulphur atom coordinate to palladium ion (Figures IV.8, IV.11, IV.18 and IV.20).

<sup>1</sup>H NMR spectra of the ligands and complexes were taken in DMSO-d<sub>6</sub> medium. In **HL**<sup>1</sup>, O–H proton singlet peak appears at 9.9 ppm which is retain in **C1** at 9.7 ppm while two N–H

proton peak noticed at 10.38 and 12.26 ppm. Imine ( $-\text{CH}=\text{N}$ ) proton signal observed at 8.39 ppm in **HL**<sup>1</sup> and it was shifted to 8.45 ppm in **C1** indicating the coordination of imine nitrogen atom with palladium ion (Figure IV.1 and IV.13). Similar case was observed for **C3** where imine ( $-\text{CH}=\text{N}$ ) proton peak appears at 8.51 ppm which is deshielded compared to its free ligand **L**<sup>3</sup> (8.19 ppm) (Figure IV.9 and IV.19). A broad singlet peak for the phenolic O–H proton in **HL**<sup>2</sup> is appeared at 15.66 ppm and the disappearance of this peak in **C2** suggest that the coordination of oxygen atom with palladium(II) ion (Figure IV.5 and IV.16). The aromatic and triphenylphosphine protons are appear in the region of 7–7.7 ppm in **C2** and **C3** complexes. <sup>13</sup>C NMR spectrum of ligands were investigated in DMSO-*d*<sub>6</sub> medium and given in Figures IV.2, IV.6 and IV.10.

HRMS spectra of the compounds were recorded in acetonitrile solution in positive ion mode (Figures IV.3, IV.7, IV.12, IV.14, IV.17 and IV.21). The molecular ion peak (*m/z*) corresponding to  $[\text{M} - \text{Cl}]^+$  for  $[\text{Pd}(\text{HL}^1)\text{Cl}]$  (**C1**) shows at 426.9903 while  $[\text{Pd}(\text{L}^2)(\text{PPh}_3)]$  (**C2**) exhibits *m/z* peak at 720.0710 corresponds to  $[\text{M} + \text{H}]^+$ . In case of  $[\text{Pd}(\text{L}^3)(\text{PPh}_3)]\text{Cl}$  (**C3**), the molecular ion peak displays at (*m/z* value) 625.9386 which correspond to  $\text{M}^+$  ion.

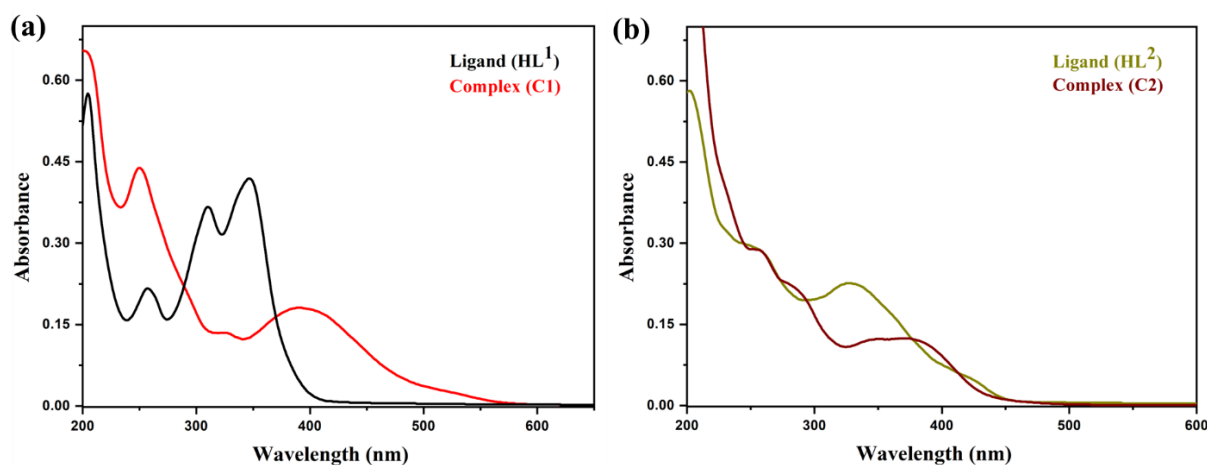


Figure IV.22. UV-Vis spectra of (a) **HL**<sup>1</sup> and **C1**, and (b) **HL**<sup>2</sup> and **C2** in acetonitrile.

Absorption spectra of the compounds were recorded in acetonitrile solution (Figure IV.22 and IV.23). **C1** exhibits one low energy broad band at 391 nm ( $\epsilon$ , 3045  $\text{M}^{-1} \text{cm}^{-1}$ ) while the free ligand **HL**<sup>1</sup> shows a sharp peak at 346 nm ( $\epsilon$ , 29944  $\text{M}^{-1} \text{cm}^{-1}$ ) along with a shoulder band at 310 nm. **C2** display a broad band at 372 nm ( $\epsilon$ , 4018  $\text{M}^{-1} \text{cm}^{-1}$ ) with two shoulders at 287 nm and 252 nm whereas its free ligand **HL**<sup>2</sup> shows a band at 327 nm ( $\epsilon$ , 11255  $\text{M}^{-1} \text{cm}^{-1}$ )

due to intra-ligand charge transfer transition ( $\pi \rightarrow \pi^*$ , ILCT). Similarly, a broad band is observed at 348 nm ( $\epsilon$ , 8121 M<sup>-1</sup> cm<sup>-1</sup>) for **C3** along with a high energy shoulder at 257 nm.

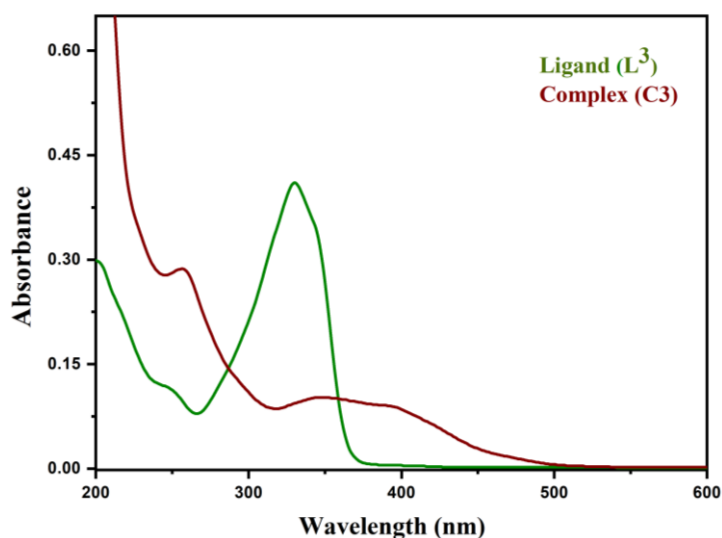


Figure IV.23. UV-Vis spectra of **L<sup>3</sup>** and **C3** in acetonitrile

### IV.3.2. Crystal Structure Description

The crystal structure of the ligand (**L<sup>3</sup>**) and the complexes (**C1**, **C2** and **C3**) were established by single crystal X-ray diffraction method. The ORTEP views of all the compounds are shown in Figure IV.24. The crystallographic data and some selected bond lengths and bond angles of the ligand (**L<sup>3</sup>**) and complexes are given in Tables IV.1–3. The complex **C1** crystallized in monoclinic crystal system having  $P2_1/n$  space group and here ligand **HL<sup>1</sup>** coordinate to palladium metal ion through two nitrogen atoms (N1 and N2) and one sulphur atom (S1) via the generation of two five membered chelate ring [N1-C8-C10-N2-Pd1 and N2-N3-C11-S1-Pd1]. The Pd1-N2(imine) bond distance (1.952(5) Å) is shorter compared to Pd1-N1(pyridyl) length (2.225(5) Å) suggest that the solid interaction between Pd(II) and imine nitrogen atom (N2). In addition, two trans angles  $\angle$ N1-Pd1-S1 and  $\angle$ N2-Pd1-C11 [163.07(15)° and 167.45(16)° respectively] are turned from the ideal trans angle of 180° causing the distorted square planar ( $\tau_4 = 0.209$ ) geometry around the metal ion. The Pd1-S1 and Pd1-C11 bond distances [2.232(2) Å and 2.3221(18) Å respectively] and the bond angles  $\angle$ S1-Pd1-N2, (83.65(18)°);  $\angle$ N1-Pd1-N2, (80.1(2)°);  $\angle$ N1-Pd1-C11, (108.31(15)°); and  $\angle$ S1-Pd1-C11, (88.53(7)°) are well matched with the previously reported complexes.<sup>12,63</sup> There are two types of hydrogen bonds and an extensive  $\pi \cdots \pi$  interactions present in the 3D supramolecular architecture of the complex **C1** as shown in Figure IV.25. The potential inter-



and intra-molecular hydrogen bonds are  $\text{N4-H4}\cdots\text{O1}$  (2.131 Å) and  $\text{O1-H1}\cdots\text{C11}$  (2.159 Å) respectively along with the  $\pi\cdots\pi$  interactions between Cg4 (C1–C2–C3–C4–C5–C9) and Cg5 ring (C12–C13–C14–C15–C16–C17) with a distance of 3.743 Å.

Complex **C2** was crystallized in triclinic crystal system with *P*-1 space group where ligand **HL**<sup>2</sup> act as O N S donor through the formation of one six membered (O1–C1–C9–C10–N1–Pd1) and one five membered (N1–N2–C12–S1–Pd1) chelate ring and the fourth position of the square plane was coordinated by phosphorus atom (from  $\text{PPh}_3$  group). Here both the trans angles [ $\angle\text{N1-Pd1-P1}$ , 177.57(5)°;  $\angle\text{O1-Pd1-S1}$ , 175.60(5)°] are almost equal in value leading to the square planar ( $\tau_4 = 0.048$ ) geometry around metal ion. Moreover, the bond lengths are [ $\text{Pd1-O1}$ , 2.0082(15) Å;  $\text{Pd1-N1}$ , 2.0301(16) Å;  $\text{Pd1-S1}$ , 2.2274(6) Å;  $\text{Pd1-P1}$ , 2.2755(5) Å] well corroborated with the reported work.<sup>12,13,44,64</sup>

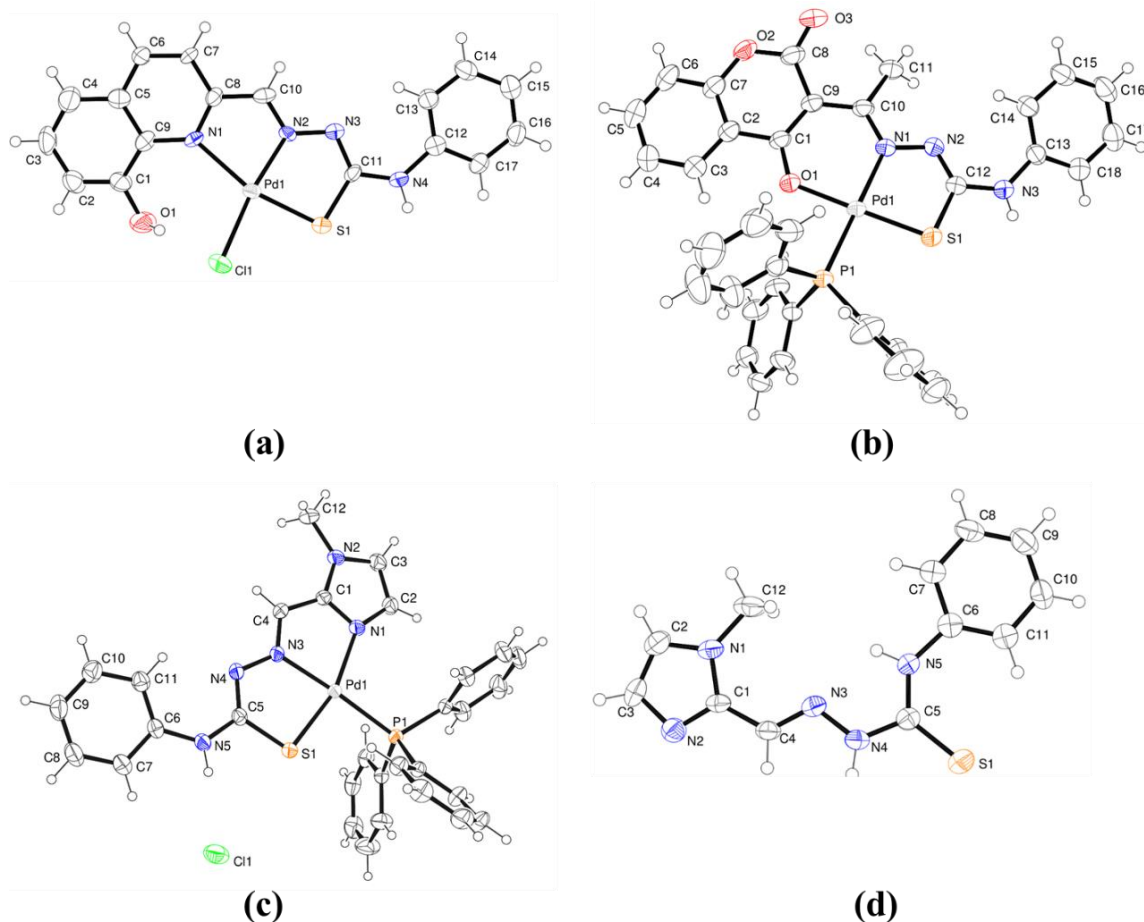


Figure IV.24. ORTEP view of the complexes (a) **C1**, (b) **C2**, (c) **C3** and (d) **L<sup>3</sup>** with 50% ellipsoidal probability.

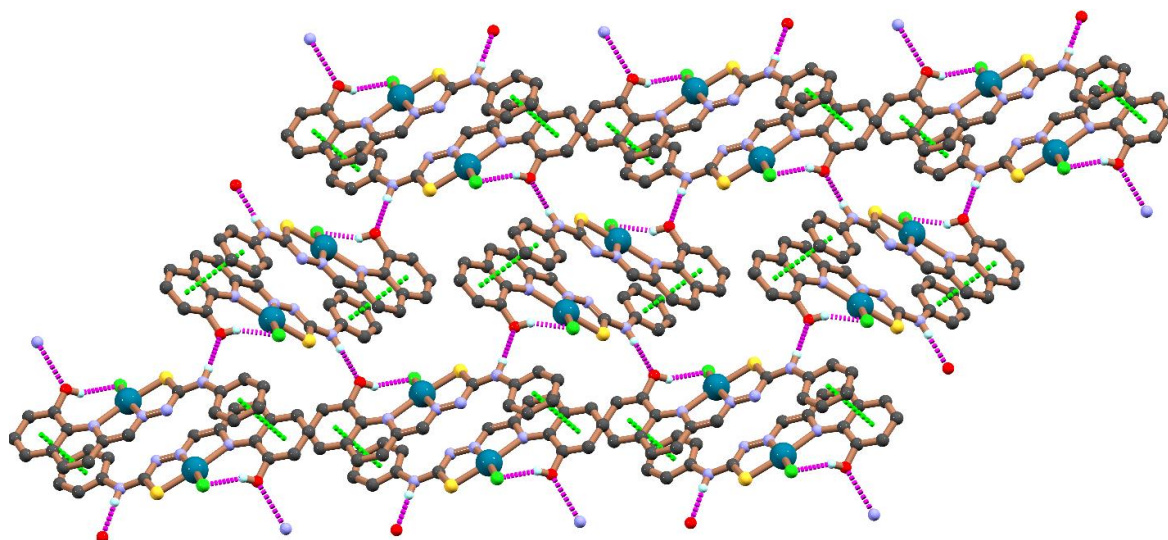


Figure IV.25. 3D architecture of **C1** shows hydrogen bonds (purple color) and  $\pi\cdots\pi$  interactions (green color).

The 3D supramolecular assembly of **C2** shows a hydrogen bond, C–H $\cdots\pi$  interactions and  $\pi\cdots\pi$  interaction (Figure IV.26). The two C–H $\cdots\pi$  interactions were between H5 and Cg6 ring (C19–C20–C21–C22–C23–C24) and between H30 and Cg4 ring (C2–C3–C4–C5–C6–C7) with a distance of 2.738 Å and 2.824 Å respectively. Beside the C–H $\cdots\pi$  interactions, intermolecular H-bond was N3–H3 $\cdots$ O3 (2.567 Å) and an extensive  $\pi\cdots\pi$  interactions between Cg3 (O2–C7–C2–C1–C9–C8) and Cg4 ring with 3.741 Å distance.

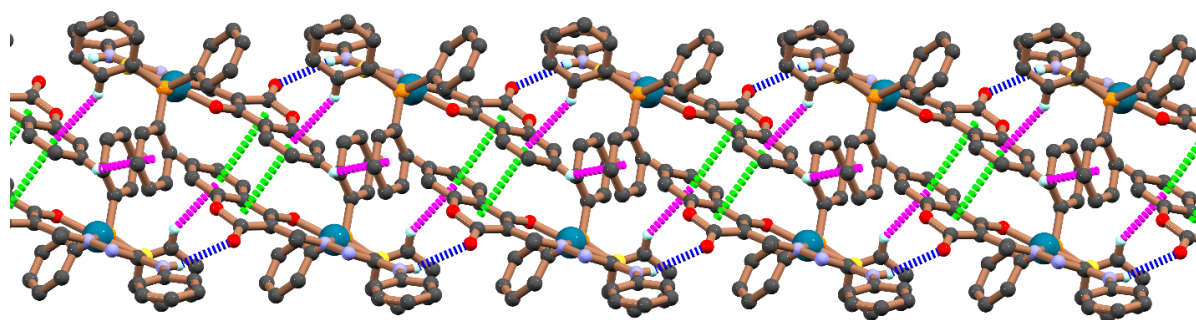


Figure IV.26. 3D supramolecular aggregate of **C2** along 'b' axis, constructed by hydrogen bond (blue color), C–H $\cdots\pi$  interactions (purple color) and  $\pi\cdots\pi$  interactions (green color).

Ligand **L<sup>3</sup>** and complex **C3** were crystallized in orthorhombic and monoclinic crystal system with  $P 2_1 2_1 2_1$  and  $P 1 2_1/c 1$  space group respectively. In **C3** metal ion attached to **L<sup>3</sup>** through

two nitrogen atoms (N1 and N3) and one sulphur atom (S1). The primary valency of the complex ion is satisfied by a chloride ion. The solid-state geometry of the complex is slight distorted square planar ( $\tau_4 = 0.157$ ) in nature as the two trans angles [ $\angle\text{N3-Pd1-P1}$ ,  $175.13(5)^\circ$ ;  $\angle\text{N1-Pd1-S1}$ ,  $162.73(5)^\circ$ ] are much deviated from  $180^\circ$ . The imidazole C=N bond length ( $1.341(3) \text{ \AA}$ ) is slightly increases compared to its ligand **L<sup>3</sup>** ( $1.310(6) \text{ \AA}$ ) which indicates the coordination of imidazole nitrogen atom with Pd(II) ion. The C–S bond distance for the complexes **C1**, **C2** and **C3** [ $1.759(7) \text{ \AA}$ ,  $1.755(2) \text{ \AA}$  and  $1.782(2) \text{ \AA}$  respectively] are significant longer than the free ligand ( $\sim 1.669(5) \text{ \AA}$ ) suggest the coordination of S atom with Pd(II) ion.<sup>13,44,63</sup> The hydrogen bonds and C–H $\cdots\pi$  interaction present in the 2D supramolecular network of **L<sup>3</sup>** are given in the Figure IV.27.

Table IV.1. Crystallographic data and refinement parameters of the compounds

Complex	<b>L<sup>3</sup></b>	<b>C1</b>	<b>C2</b>	<b>C3</b>
Formula	C <sub>12</sub> H <sub>13</sub> N <sub>5</sub> S	C <sub>17</sub> H <sub>13</sub> ClN <sub>4</sub> OPdS	C <sub>36</sub> H <sub>28</sub> N <sub>3</sub> O <sub>3</sub> PPdS	C <sub>31</sub> H <sub>31</sub> ClN <sub>5</sub> OPPdS
Formula Weight	259.33	463.22	720.04	694.49
Crystal System	<i>orthorhombic</i>	<i>monoclinic</i>	<i>triclinic</i>	<i>monoclinic</i>
Space group	<i>P 2<sub>1</sub> 2<sub>1</sub> 2<sub>1</sub></i>	<i>P 2<sub>1</sub>/n</i>	<i>P -1</i>	<i>P 1 2<sub>1</sub>/c 1</i>
a, b, c [ $\text{\AA}$ ]	5.8089(7), 14.2010(16), 15.6248(18)	7.7834(7), 15.0155(12), 14.8258(14)	10.1721(5), 12.4372(7), 13.8990(7)	8.3304(4), 18.3189(8), 20.2464(10)
$\alpha$	90	90	75.234(2)	90
$\beta$	90	99.513(3)	72.327(2)	94.350(2)
$\gamma$	90	90	76.3060(10)	90
V [ $\text{\AA}^3$ ]	1288.9(3)	1708.9(3)	1595.66(15)	3080.8(3)
Z	4	4	2	4
D(calc) [ $\text{g/cm}^3$ ]	1.336	1.800	1.499	1.428
Mu(MoKa) [ $\text{/mm}$ ]	0.241	1.377	0.738	0.836
F(000)	544	920	732	1416
$\theta(\text{Min-Max}) [^\circ]$	2.869 - 25.499	2.713 - 25.093	2.133 - 33.244	2.692 - 27.511
Dataset (h; k; l)	-7 to 7, -17 to 17, -18 to 18	-9 to 9, -17 to 17, - 15 to 17	-15 to 15, -18 to 19, -21 to 21	-10 to 10, -23 to 23, -26 to 26
R, wR <sub>2</sub>	0.0719, 0.0965	0.0807, 0.0839	0.0608, 0.0871	0.0335, 0.0666
Goodness of fit(S)	1.158	1.069	1.143	1.065

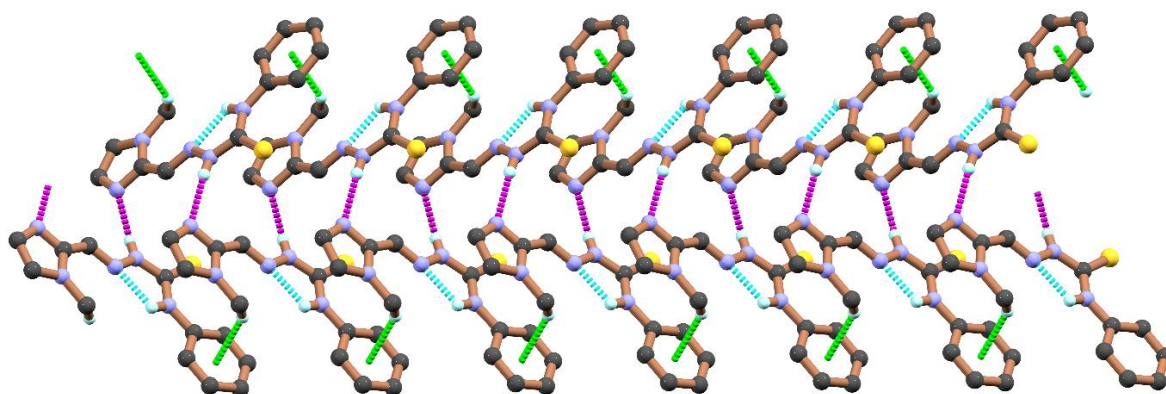


Figure IV.27. 2D supramolecular arrangement of ligand **L<sup>3</sup>** formed by N5–H5···N3 hydrogen bond [2.08 Å, intramolecular; sky-blue color], N4–H4···N2 hydrogen bond [2.14 Å, intermolecular; purple color] and C–H··· $\pi$  interactions [2.75 Å, symmetry: -1+X, Y, Z; green color].

Table IV.2. Selected X-ray and calculated bond distances (Å) and angles (°) of **C1** and **C2**

<b>C1</b>			<b>C2</b>		
Bonds (Å)	X-ray	Calc.	Bonds (Å)	X-ray	Calc.
Pd(1)–N(2)	1.952(5)	1.99551	Pd(1)–O(1)	2.0082(15)	2.04543
Pd(1)–N(1)	2.225(5)	2.23844	Pd(1)–N(1)	2.0301(16)	2.05388
Pd(1)–S(1)	2.232(2)	2.28890	Pd(1)–S(1)	2.2274(6)	2.28770
Pd(1)–Cl(1)	2.3221(18)	2.34635	Pd(1)–P(1)	2.2755(5)	2.34078
N(2)–N(3)	1.367(7)	1.35171	N(1)–N(2)	1.399(2)	1.38418
N(3)–C(11)	1.320(8)	1.32305	N(2)–C(12)	1.292(3)	1.29814
S(1)–C(11)	1.759(7)	1.77376	S(1)–C(12)	1.755(2)	1.77998
O(1)–C(1)	1.366(8)	1.34684			
Angle (°)					
N(2)–Pd(1)–N(1)	80.1(2)	79.70245	O(1)–Pd(1)–N(1)	91.83(6)	91.16451
N(2)–Pd(1)–S(1)	83.65(18)	83.35854	O(1)–Pd(1)–S(1)	175.60(5)	174.90059
N(1)–Pd(1)–S(1)	163.07(15)	162.94703	N(1)–Pd(1)–S(1)	85.79(5)	84.54383
N(2)–Pd(1)–Cl(1)	167.45(16)	170.18396	O(1)–Pd(1)–P(1)	88.32(4)	88.37824
N(1)–Pd(1)–Cl(1)	108.31(15)	104.83510	N(1)–Pd(1)–P(1)	177.57(5)	179.49192
S(1)–Pd(1)–Cl(1)	88.53(7)	92.20575	S(1)–Pd(1)–P(1)	94.220(19)	95.90218
C(11)–S(1)–Pd(1)	95.8(2)	94.87738			

Table IV.3. Selected X-ray and calculated bond distances (Å) and angles (°) of **L<sup>3</sup>** and **C3**

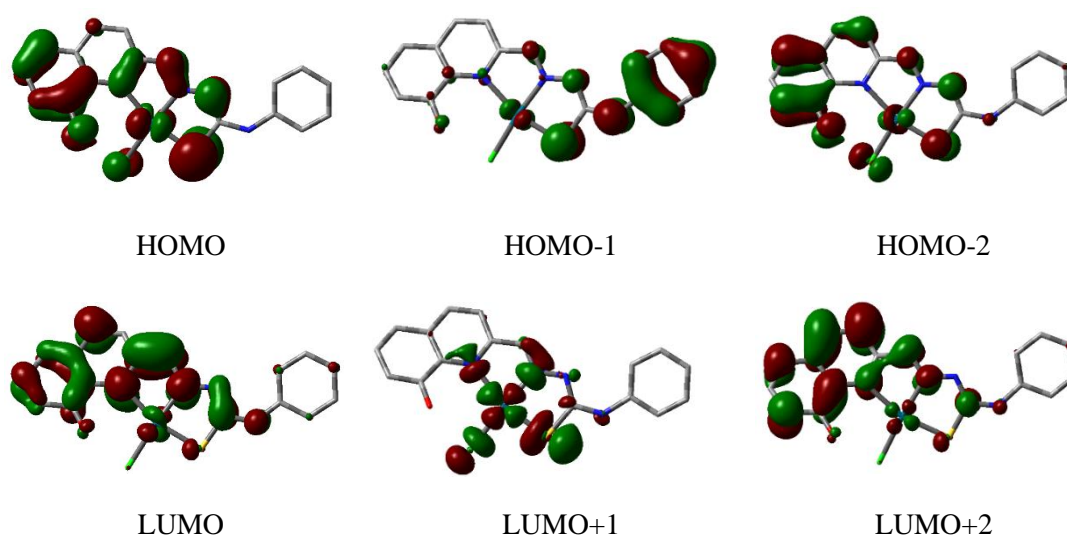
<b>L<sup>3</sup></b>			<b>C3</b>		
Bonds (Å)	X-ray	Calc.	Bonds (Å)	X-ray	Calc.
S(1)-C(5)	1.669(5)	1.67702	Pd(1)-N(3)	2.0336(16)	2.07722
N(2)-C(1)	1.310(6)	1.33421	Pd(1)-N(1)	2.1023(17)	2.13760
N(3)-C(4)	1.292(6)	1.29255	Pd(1)-S(1)	2.2484(5)	2.30684
N(3)-N(4)	1.368(5)	1.35785	Pd(1)-P(1)	2.2690(5)	2.34282
N(4)-C(5)	1.359(6)	1.38411	N(1)-C(1)	1.341(3)	1.34720
C(1)-C(4)	1.443(6)	1.44333	N(3)-N(4)	1.373(2)	1.34476
			N(4)-C(5)	1.314(3)	1.32283
			S(1)-C(5)	1.782(2)	1.79025
<b>C3</b>					
Angles (°)					
N(3)-Pd(1)-N(1)	80.15(7)	79.28193			
N(3)-Pd(1)-S(1)	83.14(5)	82.02555			
N(1)-Pd(1)-S(1)	162.73(5)	161.16674			
N(3)-Pd(1)-P(1)	175.13(5)	176.45113			
N(1)-Pd(1)-P(1)	104.40(5)	104.18273			
S(1)-Pd(1)-P(1)	92.442(19)	94.54144			

### IV.3.3. DFT Study

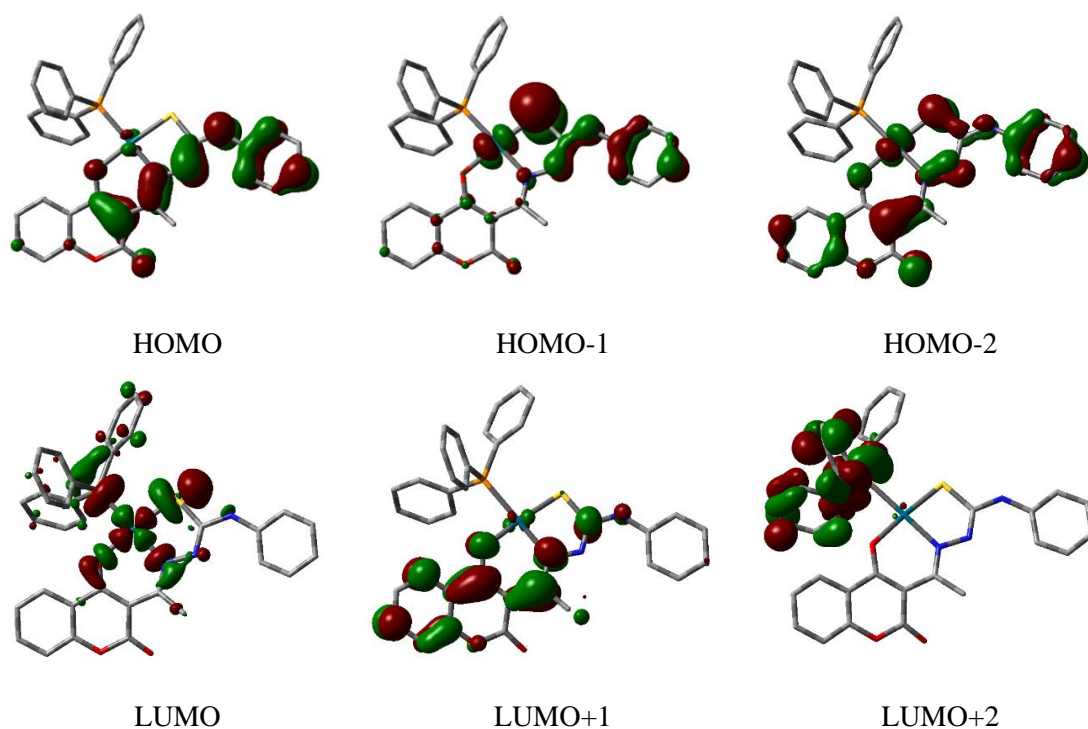
The crystal structure of all the complexes were optimized by DFT/B3LYP method. All the bond parameters of compounds calculated by DFT study are in well agreement with the X-ray crystal structures data. Energy and composition of selected molecular orbitals of the complexes are given in Tables IV.4 and IV.5. Contour plots of selected MOs of **C1**, **C2** and **C3** are given in Figures IV.28-30. In case of **C1** HOMO has 83% involvement of ligand **HL<sup>1</sup>** and Pd(d $\pi$ ) orbital contributes 13% and the LUMO has 95% contribution from ligand  $\pi^*$  orbital. While for **C2**, ligand contributes 98% to HOMO and LUMO has 38% participation of ligand **L<sup>2</sup>**, 36% contribution of Pd(d $\pi$ ) orbital and 26% from PPh<sub>3</sub>  $\pi^*$  orbital. The HOMO and LUMO of the complex **C3** have 100% and 93% of ligand (**L<sup>3</sup>**)  $\pi$  and  $\pi^*$  orbital contribution respectively.

Table IV.4. Energy and % of composition of some selected molecular orbitals of **C1** and **C2**

MO	<b>C1</b>				<b>C2</b>			
	Energy	% of composition			Energy	% of composition		
		Pd	HL <sup>1</sup>	Cl		L <sup>2</sup>	Pd	PPh <sub>3</sub>
LUMO+5	-0.14	02	98	00	-0.59	11	8	81
LUMO+4	-0.33	00	100	00	-0.75	02	04	94
LUMO+3	-0.65	01	99	00	-0.97	04	02	94
LUMO+2	-1.59	03	97	00	-1.15	01	01	98
LUMO+1	-2.46	44	45	11	-1.48	94	02	04
LUMO	-3.02	05	95	00	-1.88	38	36	26
HOMO	-5.89	13	83	04	-5.13	98	02	00
HOMO-1	-6.07	05	94	01	-5.62	84	15	01
HOMO-2	-6.38	05	88	07	-6.17	90	10	00
HOMO-3	-6.71	52	24	23	-6.32	94	06	00
HOMO-4	-6.82	34	20	46	-6.43	69	27	04
HOMO-5	-6.97	50	16	34	-6.59	75	13	12
HOMO-6	-7.13	00	100	00	-6.61	42	26	32
HOMO-7	-7.42	05	82	13	-6.91	92	04	04
HOMO-8	-7.66	13	66	21	-6.96	93	07	00
HOMO-9	-8.02	26	72	04	-7.19	24	11	65
HOMO-10	-8.16	27	49	24	-7.2	05	02	93

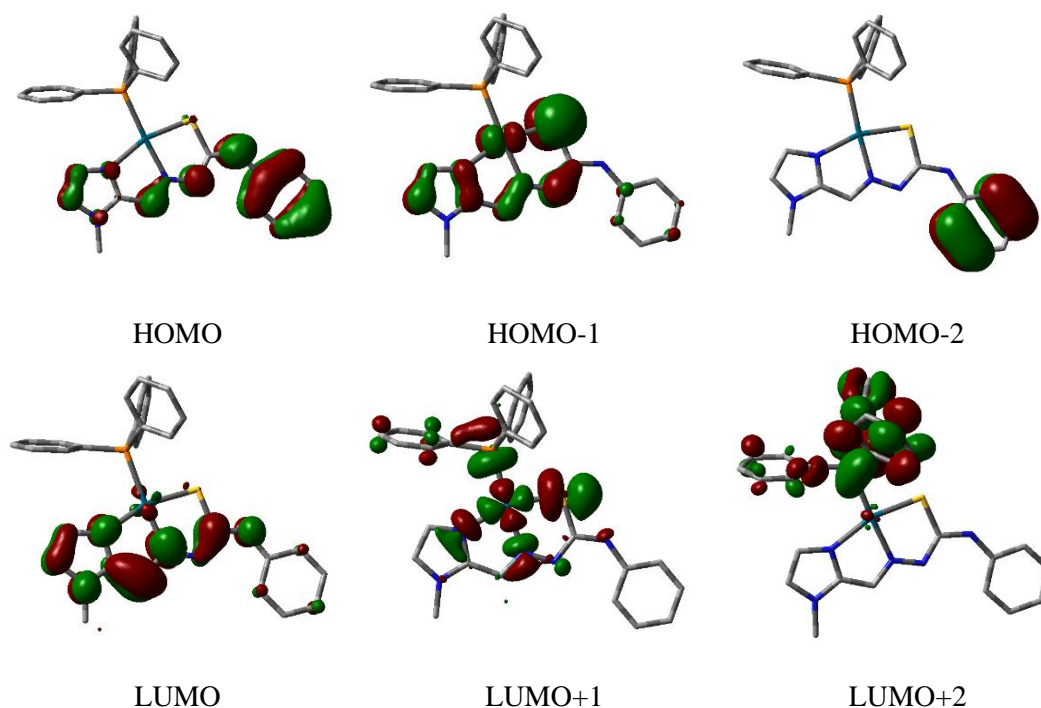
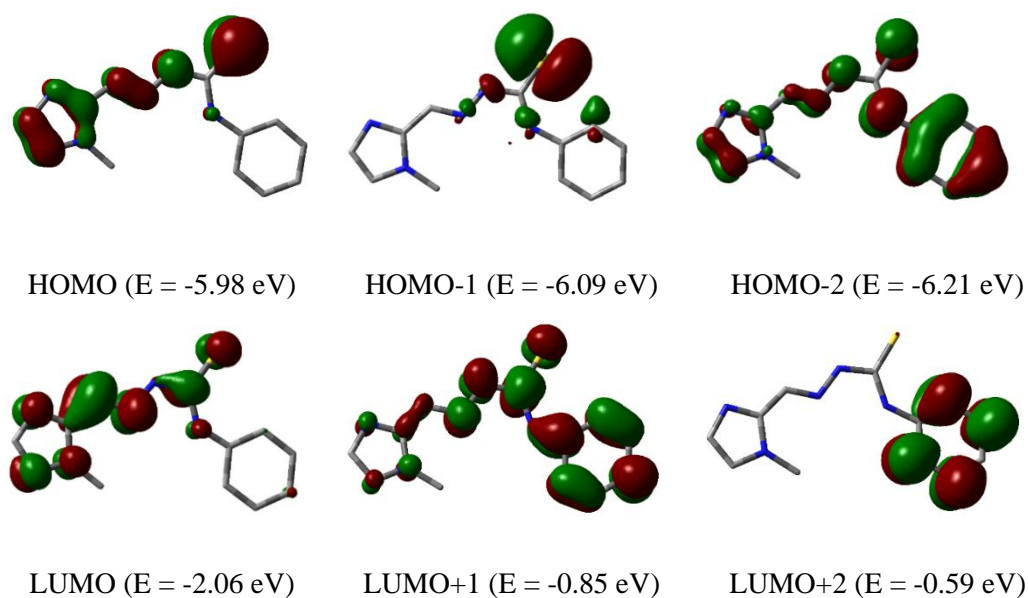
Figure IV.28. Contour plots of some selected molecular orbital of **C1**



Figure IV.29. Contour plots of some selected molecular orbital of **C2**.Table IV.5. Energy and % of composition of some selected molecular orbitals of **C3**

MO	Energy	% of composition		
		Pd	L <sup>3</sup>	PPh <sub>3</sub>
LUMO+5	-2.94	06	02	92
LUMO+4	-2.95	05	03	92
LUMO+3	-3.15	06	02	92
LUMO+2	-3.41	00	02	98
LUMO+1	-4.87	39	38	23
LUMO	-5.00	06	93	01
HOMO	-8.06	00	100	00
HOMO-1	-8.39	14	84	02
HOMO-2	-8.9	00	100	00
HOMO-3	-9.16	14	06	80
HOMO-4	-9.3	01	01	98
HOMO-5	-9.33	08	09	83
HOMO-6	-9.42	24	23	53
HOMO-7	-9.47	12	24	64
HOMO-8	-9.52	11	68	21
HOMO-9	-9.65	08	14	78
HOMO-10	-9.68	04	04	92



Figure IV.30. Contour plots of some selected molecular orbital of **C3**Figure IV.31. Contour plots of some selected molecular orbital of **L<sup>3</sup>**

TDDFT (time dependent density functional theory) study of the optimized structures were performed to illustrate the electronic transitions (Table IV.6). **C1** has a low energy transition

(HOMO-2→LUMO) at 435 nm ( $f = 0.2465$ ) having ILCT character corresponds to experimental band at 391 nm ( $\epsilon$ , 3045 M<sup>-1</sup> cm<sup>-1</sup>) and a high energy transition (HOMO-10→LUMO+1) at 251 nm ( $f = 0.1504$ ) having both ILCT and LMCT character corresponds to experimentally observed band at 250 nm. For **C2** the experimental band at 372 nm is well corroborated with the HOMO→LUMO+1 transition at 385 nm ( $f = 0.3897$ ) having ILCT character. In case of **C3**, an ILCT transition (HOMO-1→LUMO) at 402 nm ( $f = 0.5296$ ) corresponds to 348 nm experimental band. Another high energy transition at 281 nm (HOMO-10→LUMO+1,  $f = 0.1239$ ) having XMCT (X = PPh<sub>3</sub>) character is observed which corresponds to 257 nm from UV study.

Table IV.6. Vertical electronic transition calculated by TDDFT/CPCM method of **C1**, **C2**, **C3** and **L<sup>3</sup>**

Compd.	$\lambda$ (nm)	E (eV)	Osc. Strength (f)	Key excitations	Character	$\lambda_{\text{expt.}}$ (nm) ( $\epsilon$ , M <sup>-1</sup> cm <sup>-1</sup> )
<b>C1</b>	452.38	2.7407	0.2604	(21%) HOMO→LUMO+1	ILCT / LMCT	
	435.63	2.8461	0.2465	(80%) HOMO-2→LUMO	ILCT	391 (3045)
	306.43	4.0461	0.1908	(54%) HOMO-8→LUMO	ILCT / XLCT	325 (2274)
	305.09	4.0639	0.2060	(33%) HOMO-8→LUMO		
	251.08	4.9381	0.1504	(28%) HOMO-10→LUMO+1	ILCT/LMCT	250 (7370)
<b>C2</b>	396.40	3.1277	0.1494	(26%) HOMO-4→LUMO	ILCT/LMCT	
	385.56	3.2157	0.3897	(73%) HOMO→LUMO+1	ILCT	372 (4018)
	325.88	3.8046	0.1536	(53%) HOMO-5→LUMO	ILCT/LMCT	
	299.61	4.1382	0.0939	(21%) HOMO→LUMO+3	LXCT	
	287.79	4.3082	0.1737	(27%) HOMO→LUMO+4	LXCT	287
	255.16	4.8590	0.1070	(38%) HOMO→LUMO+9	ILCT	252
<b>C3</b>	448.55	2.7641	0.1353	(46%) HOMO→LUMO	ILCT	
	402.57	3.0798	0.5296	(43%) HOMO-1→LUMO	ILCT	348 (8121)
	336.76	3.6817	0.1227	(14%) HOMO-3→LUMO+1	XLCT/XMCT	
	281.29	4.4077	0.1239	(32%) HOMO-10→LUMO+1	XLCT/XMCT	257 (22837)
<b>L<sup>3</sup></b>	348.61	3.5565	0.1812	(70%) HOMO-2→LUMO	n(L)→ $\pi^*$ (L)	
	346.92	3.5738	0.8068	(75%) HOMO→LUMO	n(L)→ $\pi^*$ (L)	330 (30770)
	320.17	3.8725	0.2173	(89%) HOMO-1→LUMO	n(L)→ $\pi^*$ (L)	
	256.99	4.8244	0.1440	(61%) HOMO-1→LUMO+1	$\pi$ (L)→ $\pi^*$ (L)	
	250.18	4.9558	0.1826	(57%) HOMO→LUMO+2	$\pi$ (L)→ $\pi^*$ (L)	246 (8735)

#### IV.3.4. Catalysis Study

To assess the Suzuki-Miyaura (S-M) cross coupling reaction in presence of the Pd(II) complexes as catalyst, reaction between iodobenzene and phenylboronic acid takes as a model reaction. To get an ideal reaction condition, a series of experiments were conducted to examine the influence of different parameters such as solvent, base, temperature and catalyst loading (Tables IV.7-9). Initially we focused on the influence of different solvent in the coupling reaction. It was observed that polyethylene glycol 400 (PEG-400) is the optimal solvent which gave the maximum yield (97% for **C2**). Under the optimized solvent condition, we also optimized the reaction time and temperature for the coupling reaction.

Table IV.7. Optimization of reaction conditions using catalyst **C1** for the model reaction

Entry	Solvent	Base	<b>C1</b> <sup>a</sup> (mol%)	Temp. (°C)	Time (h)	Yield <sup>b</sup> (%)	TON
1	EtOH	K <sub>2</sub> CO <sub>3</sub>	1	90	7	71	71
2	H <sub>2</sub> O	K <sub>2</sub> CO <sub>3</sub>	1	90	7	7	7
3	MeCN	K <sub>2</sub> CO <sub>3</sub>	1	90	7	22	22
4	i-PrOH	K <sub>2</sub> CO <sub>3</sub>	1	90	7	53	53
5	PEG-400	K <sub>2</sub> CO <sub>3</sub>	1	70	7	68	68
6	PEG-400	K <sub>2</sub> CO <sub>3</sub>	1	80	7	81	81
7	PEG-400	K <sub>2</sub> CO <sub>3</sub>	1	90	7	90	90
8	PEG-400	K <sub>2</sub> CO <sub>3</sub>	1	100	7	90	90
9	PEG-400	K <sub>2</sub> CO <sub>3</sub>	1	90	6	85	85
10	PEG-400	K <sub>2</sub> CO <sub>3</sub>	1	90	4	67	67
11	PEG-400	K <sub>2</sub> CO <sub>3</sub>	0.5	90	7	66	132
12	PEG-400	K <sub>2</sub> CO <sub>3</sub>	0.8	90	7	84	105
13	PEG-400	Na <sub>2</sub> CO <sub>3</sub>	1	90	7	88	88
14	PEG-400	NaOH	1	90	7	65	65

<sup>a</sup> Reaction conditions: **C1** (1 mol%), iodobenzene (1 mmol), phenylboronic acid (1 mmol), K<sub>2</sub>CO<sub>3</sub> (2 mmol), solvent 6 mL, 70-90°C, 7 h.

<sup>b</sup> The yields were determined by GC using n-decane as internal standard.

The Pd-complex catalyzed S-M coupling reaction was almost completed within 6–7 h at 90°C. In presence of catalyst **C1**, time taken for completion of the coupling reaction was almost 7 h while catalyst **C2** and **C3** takes 6 h for the completion of reactions. The catalyst

loading was optimized by using 1 mol% of catalyst. When the amount of catalyst was reduced to 0.8 mol% and 0.5 mol%, the yields decreased to 84% and 66% for **C1**, 92% and 76% for **C2**, and 89% and 74% for **C3**. Among the several bases screened,  $K_2CO_3$  gives maximum yield for all the three catalysts. Thus, under aerobic condition the cross-coupling between phenylboronic acid and iodobenzene impart maximum yields with 1 mol% catalyst in PEG-400 solvent at 90°C for 6 h of reaction in refluxing condition. The  $^1H$ -NMR spectra of the coupling products are given in Figure IV.32.

Table IV.8. Optimization of reaction conditions using catalyst **C2** for the model reaction

Entry	Solvent	Base	<b>C2</b> <sup>a</sup> (mol%)	Temp. (°C)	Time (h)	Yield <sup>b</sup> (%)	TON
1	EtOH	$K_2CO_3$	1	90	6	78	78
2	H <sub>2</sub> O	$K_2CO_3$	1	90	6	13	13
3	MeCN	$K_2CO_3$	1	90	6	36	36
4	i-PrOH	$K_2CO_3$	1	90	6	63	63
5	PEG-400	$K_2CO_3$	1	70	6	74	74
6	PEG-400	$K_2CO_3$	1	80	6	90	90
7	PEG-400	$K_2CO_3$	1	90	6	97	97
8	PEG-400	$K_2CO_3$	1	100	6	97	97
9	PEG-400	$K_2CO_3$	1	90	5	92	92
10	PEG-400	$K_2CO_3$	1	90	4	84	84
11	PEG-400	$K_2CO_3$	0.5	90	6	76	152
12	PEG-400	$K_2CO_3$	0.8	90	6	92	115
13	PEG-400	$Na_2CO_3$	1	90	6	96	96
14	PEG-400	NaOH	1	90	6	71	71

<sup>a</sup> Reaction conditions: **C2** (1 mol%), iodobenzene (1 mmol), phenylboronic acid (1 mmol),  $K_2CO_3$  (2 mmol), solvent 6 mL, 70-90°C, 6 h.

<sup>b</sup> The yields were determined by GC using n-decane as internal standard.

Under the above optimized reaction conditions, the possibility of the coupling reactions was carried out using different aryl halides having electron donating and electron withdrawing groups with phenylboronic acid (Table IV.10). It was observed that aryl halides give the yields in the order of Cl < Br < I. Additionally, Aryl halide having electron donating group

(such as  $-\text{CH}_3$ ) gives yield greater than that of having electron withdrawing group (such as  $-\text{NO}_2$ ) for the three catalysts. Moreover, it was noticed that the yield was maximum in presence of catalyst **C2** and the catalytic efficiency of the catalysts follow the order **C2** > **C3** > **C1**. The catalytic efficacy of our Pd-complexes was further compared with the some reported Pd-complex with ONS donor ligands (Table IV.11) and it was found that our catalysts exhibit excellent catalytic performance in terms of high yields.

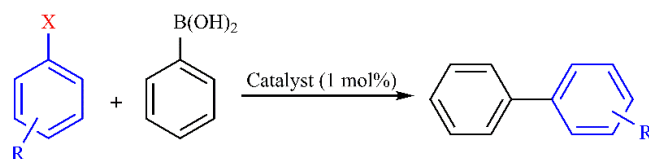
Table IV.9. Optimization of reaction conditions using catalyst **C3** for the model reaction

Entry	Solvent	Base	<b>C3</b> <sup>a</sup> (mol%)	Temp. (°C)	Time (h)	Yield <sup>b</sup> (%)	TON
1	EtOH	K <sub>2</sub> CO <sub>3</sub>	1	90	6	76	76
2	H <sub>2</sub> O	K <sub>2</sub> CO <sub>3</sub>	1	90	6	18	18
3	MeCN	K <sub>2</sub> CO <sub>3</sub>	1	90	6	37	37
4	i-PrOH	K <sub>2</sub> CO <sub>3</sub>	1	90	6	65	65
5	PEG-400	K <sub>2</sub> CO <sub>3</sub>	1	70	6	75	75
6	PEG-400	K <sub>2</sub> CO <sub>3</sub>	1	80	6	87	87
7	PEG-400	K <sub>2</sub> CO <sub>3</sub>	1	90	6	95	95
8	PEG-400	K <sub>2</sub> CO <sub>3</sub>	1	100	6	95	95
9	PEG-400	K <sub>2</sub> CO <sub>3</sub>	1	90	5	90	90
10	PEG-400	K <sub>2</sub> CO <sub>3</sub>	1	90	4	77	77
11	PEG-400	K <sub>2</sub> CO <sub>3</sub>	0.5	90	6	74	148
12	PEG-400	K <sub>2</sub> CO <sub>3</sub>	0.8	90	6	89	111
13	PEG-400	Na <sub>2</sub> CO <sub>3</sub>	1	90	6	93	93
14	PEG-400	NaOH	1	90	6	66	66

<sup>a</sup> Reaction conditions: **C3** (1 mol%), iodobenzene (1 mmol), phenylboronic acid (1 mmol), K<sub>2</sub>CO<sub>3</sub> (2 mmol), solvent 6 mL, 70-90°C, 6 h.

<sup>b</sup> The yields were determined by GC using n-decane as internal standard.

Table IV.10. Suzuki-Miyaura cross-coupling reaction of different aryl halides with phenylboronic acid using three catalysts

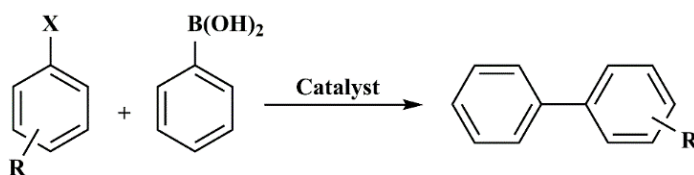


Entry	Aryl halide	Yield (%) <sup>b</sup>		
		Catalyst <sup>a</sup> <b>C1</b>	Catalyst <sup>a</sup> <b>C2</b>	Catalyst <sup>a</sup> <b>C3</b>
1	Iodobenzene	90	97	95
2	Bromobenzene	85	94	91
3	Chlorobenzene	78	88	85
4	4-methyliodobenzene	86	95	92
5	4-methylbromobenzene	81	94	90
6	4-methoxyiodobenzene	85	94	91
7	4-methoxybromobenzene	82	93	89
8	4-bromonitrobenzene	73	87	83
9	4-bromobenzaldehyde	75	88	85

<sup>a</sup> Reaction conditions: Iodobenzene (1 mmol), phenylboronic acid (1 mmol), catalyst (1 mol%), K<sub>2</sub>CO<sub>3</sub> (2 mmol), PEG-400 (6 mL), 90°C, 6-7 h.

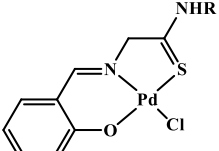
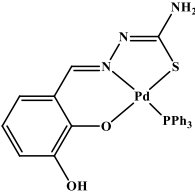
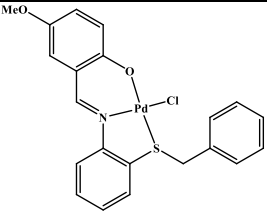
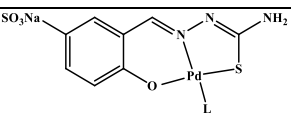
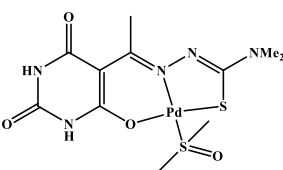
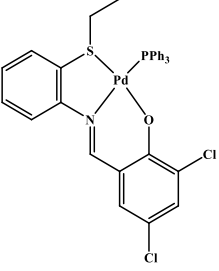
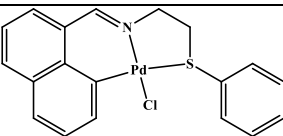
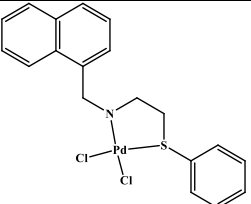
<sup>b</sup> The yields were determined by GC using n-decane as internal standard.

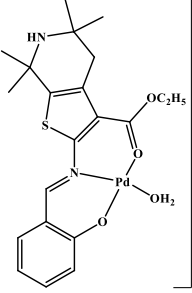
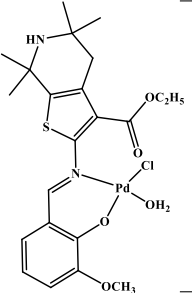
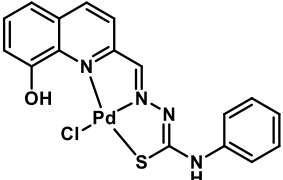
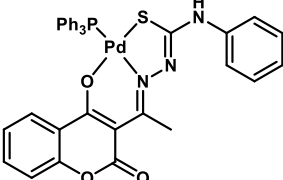
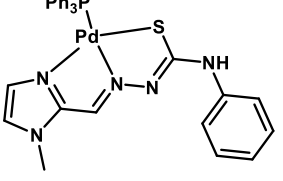
Table IV.11. Comparison of catalytic efficiency and reaction conditions of Suzuki-Miyaura cross-coupling reactions by palladium complexes with O N S donor ligands.



Catalysts	R	X	Mol% (cat.)	Solvent	Temp . (°C)	Time (h)	Yield (%)	Ton	Ref.
	H	Br	0.2	DMF/ H <sub>2</sub> O	100	24	45	225	65
	OCH <sub>3</sub>	Br					25		
	NO <sub>2</sub>	Br					100		
								500	

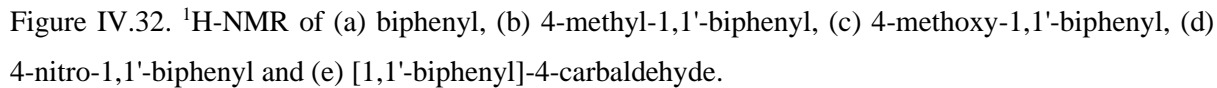
R = H, CH(CH<sub>2</sub>CH<sub>3</sub>)<sub>2</sub>

 R = H, Et	H	Br	0.1	DMF/ H <sub>2</sub> O	100	24	71	710	66
	OCH <sub>3</sub>	Br					53	530	
	NO <sub>2</sub>	Br					83	830	
	H	Cl					30	300	
	H	Br	0.08	i-PrOH	80	6	92	1150	67
	H	I	1	MeOH	65	24	92	92	68
	H	Br					90	90	
 L = PPh <sub>3</sub> , PTA	H	Br	1	H <sub>2</sub> O	70	24	76	76	69
	CH <sub>3</sub>	Br					72	72	
	OCH <sub>3</sub>	Br					93	93	
	H	Br	2	DMF	140	24	46	23	70
	H	Cl					21	11	
	OCH <sub>3</sub>	Br					66	33	
	NO <sub>2</sub>	Br					78	39	
	H	Cl	1	PEG-400	100	10	83	83	71
	H	Br					93	93	
	H	I					96	96	
	CH <sub>3</sub>	Br					90	90	
	OCH <sub>3</sub>	Br					93	93	
	NO <sub>2</sub>	Br					88	88	
 (Complex 1)	H	Br	0.05/0.1	DMF/ H <sub>2</sub> O	90	6/2	80/96	1600/960	72
	OCH <sub>3</sub>	Br	0.1			6	88	880	
	NO <sub>2</sub>	Br	0.01			2	96	9600	
	CH <sub>3</sub>	Br	0.05/0.1			6/2	71/97	1420/970	
 (Complex 3)	H	Br	0.05/0.1	DMF/ H <sub>2</sub> O	90	6/2	21/74	420/740	
	OCH <sub>3</sub>	Br	0.1			6	68	680	
	NO <sub>2</sub>	Br	0.01			2	94	9400	
	CH <sub>3</sub>	Br	0.05/0.1			6/2	69/88	1380/880	

 <b>(1)</b>	H	Br	0.01	EtOH/H <sub>2</sub> O	80	2	98	9800	73
	CH <sub>3</sub>	Br					67	6700	
	OCH <sub>3</sub>	Br					91	9100	
	CHO	Br					91	9100	
 <b>(2)</b>	H	Br	0.01	EtOH/H <sub>2</sub> O	80	2	99	9900	
	CH <sub>3</sub>	Br					71	7100	
	OCH <sub>3</sub>	Br					70	7000	
	CHO	Br					95	9500	
 <b>(C1)</b>	H	I	1	PEG-400	90	7	90	90	
	H	Br					85	85	
	H	Cl					78	78	
	CH <sub>3</sub>	I					86	86	
	CH <sub>3</sub>	Br					81	81	
	OCH <sub>3</sub>	I					85	85	
	OCH <sub>3</sub>	Br					82	82	
	NO <sub>2</sub>	Br					73	73	
 <b>(C2)</b>	H	I	1	PEG-400	90	6	97	97	
	H	Br					94	94	
	H	Cl					88	88	
	CH <sub>3</sub>	I					95	95	
	CH <sub>3</sub>	Br					94	94	
	OCH <sub>3</sub>	I					94	94	
	OCH <sub>3</sub>	Br					93	93	
	NO <sub>2</sub>	Br					87	87	
 <b>(C3)</b>	H	I	1	PEG-400	90	6	95	95	
	H	Br					91	91	
	H	Cl					85	85	
	CH <sub>3</sub>	I					92	92	
	CH <sub>3</sub>	Br					90	90	
	OCH <sub>3</sub>	I					91	91	
	OCH <sub>3</sub>	Br					89	89	
	NO <sub>2</sub>	Br					83	83	

This  
Work





#### IV.3.5.1. Absorption Spectral Titration

The interaction of metal complexes with DNA is one of the most well-known biomolecular interactions. The binding fashion of the complexes with DNA are depend on the stability of the complexes. Stable complexes may interact with DNA non-covalently by  $\pi$ - $\pi$  stacking, intercalation or groove binding while for unstable one, labile ligand may bind covalently with

N-base pairs of DNA.<sup>74</sup> Herein we used calf thymus DNA (CT DNA) to assess the binding pattern of complexes (**C1–C3**) with DNA by utilizing UV-Vis and fluorescence technique. In the absorption spectra the change in absorbance was noticed upon incremental addition of CT DNA to the complex solutions. Gradual addition of CT DNA to the complexes **C1–C3**, a decrease in absorbance (hypochromic shift) was observed in the range 350-400 nm and an increase in the absorptivity was noticed in the range 260-264 nm with a common isosbestic point at 300 nm (Figures IV.33a–35a). The observed hypochromism in the spectra suggest the interaction may occur via non-covalent intercalation binding. The binding constant value ( $K_b$ ) was calculated by using the following Wolfe-Shimmer equation (eq. A). The  $K_b$  values were found to be  $(3.23 \pm 0.16) \times 10^5$ ,  $(3.01 \pm 0.12) \times 10^5$  and  $(4.55 \pm 0.17) \times 10^5 \text{ M}^{-1}$  for **C1**, **C2** and **C3** respectively and these values reflects the great binding efficacy of the complexes with CT DNA (Figures IV.33b–35b).

$$[\text{DNA}]/(\epsilon_a - \epsilon_f) = [\text{DNA}]/(\epsilon_b - \epsilon_f) + 1/K_b(\epsilon_a - \epsilon_f) \quad (\text{A})$$

Where,  $[\text{DNA}]$  represents the concentration of DNA, and  $\epsilon_a$ ,  $\epsilon_f$  and  $\epsilon_b$  represents the apparent extinction coefficient ( $A_{\text{obs}}/[\text{complex}]$ ), the extinction coefficient for the complex in the absence of DNA and the extinction coefficient for complex when fully bound to CT DNA respectively.

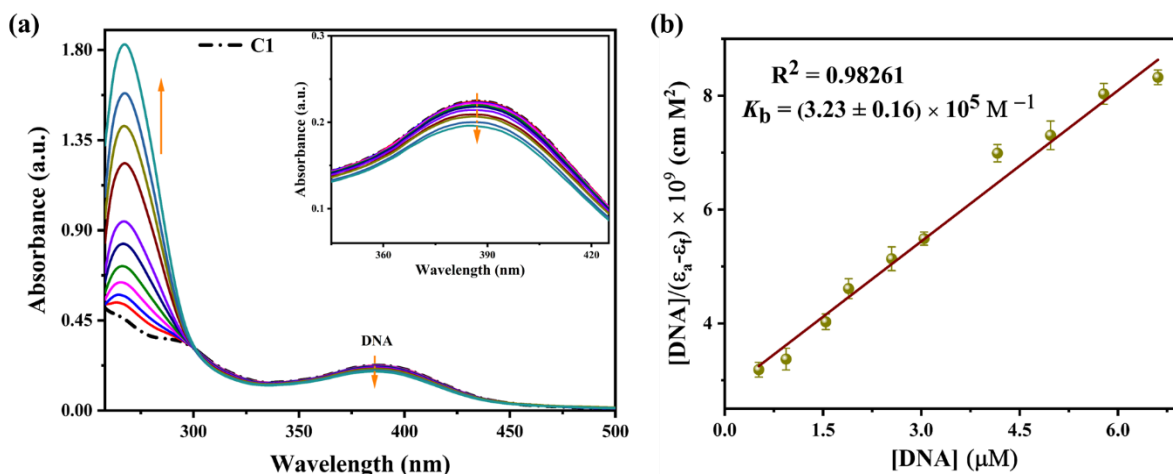


Figure IV.33. (a) UV-Vis titration of **C1** ( $2 \times 10^{-5} \text{ M}$ ) with the gradual addition of CT-DNA in Tris-HCl/NaCl buffer and (b) Wolfe-Shimmer plot of  $[\text{DNA}]/(\epsilon_a - \epsilon_f)$  vs  $[\text{DNA}]$ .

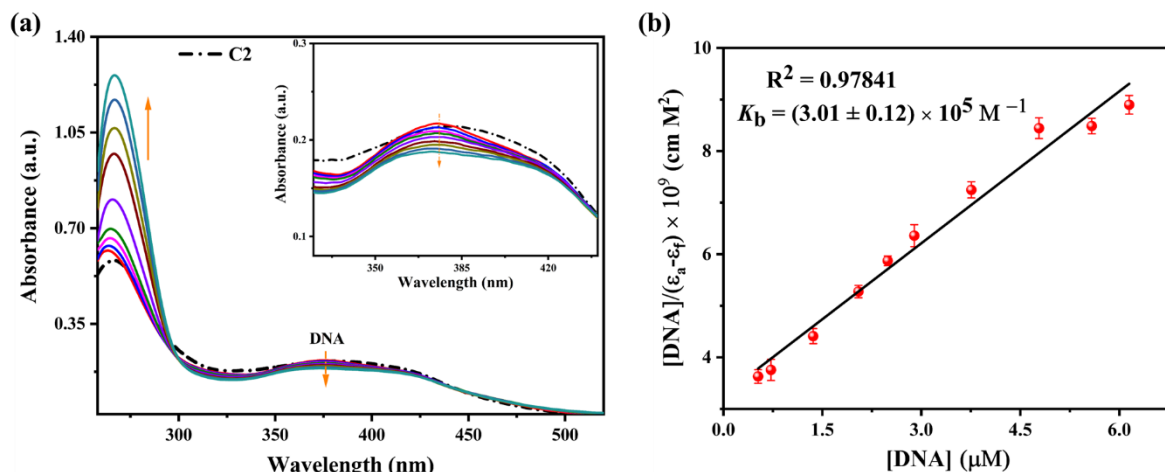


Figure IV.34. (a) UV-Vis titration of **C2** ( $2 \times 10^{-5}$  M) with the gradual addition of CT-DNA in Tris-HCl/NaCl buffer and (b) Wolfe-Shimmer plot of  $[DNA]/(\epsilon_a - \epsilon_f)$  vs  $[DNA]$ .

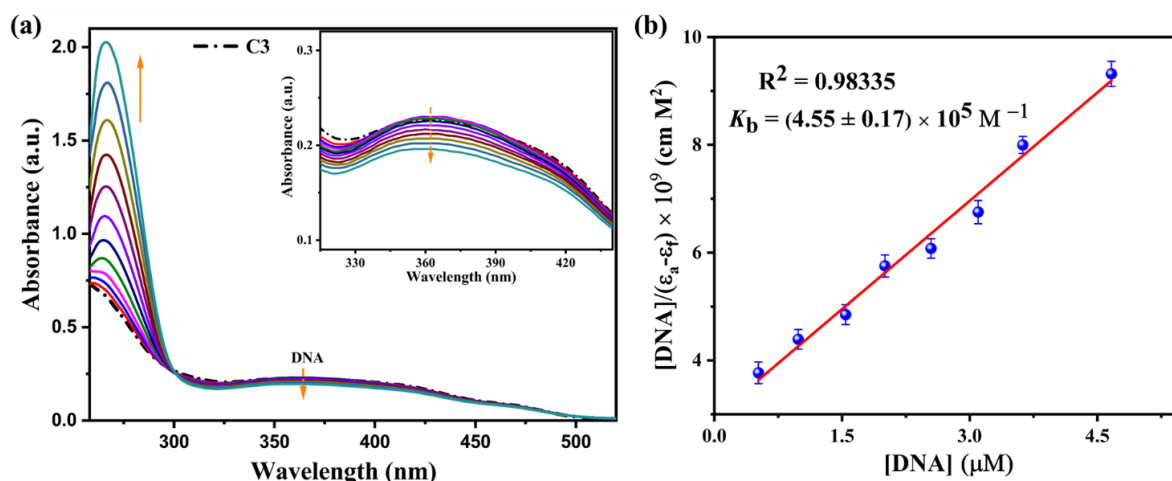


Figure IV.35. (a) UV-Vis titration of **C3** ( $2 \times 10^{-5}$  M) with the gradual addition of CT-DNA in Tris-HCl/NaCl buffer and (b) Wolfe-Shimmer plot of  $[DNA]/(\epsilon_a - \epsilon_f)$  vs  $[DNA]$ .

#### IV.3.5.2. Ethidium Bromide (EB) Displacement Studies

Ethidium bromide (EB) displacement study were performed to assess the binding mode and binding strength of the complexes with CT DNA. EB is the well-known classical intercalator and it shows an intense fluorescence at 605 nm when bound with nitrogen base pairs of DNA.<sup>75</sup> The fluorescence intensity of EB-DNA system decreases with the increasing amount of complex suggested the interaction of complex with CT-DNA via removal of EB from EB-DNA system (Figures IV.36a–38a). This fluorescence quenching experiment can be

understood by calculating the quenching constant using the following classical Stern–Volmer equation (eq B).

$$F_0/F = 1 + K_{sv} [Q] \quad (B)$$

where  $F_0$  and  $F$  are the emission intensity in the absence and presence of the complex,  $[Q]$  is the concentration of the added complex, and  $K_{sv}$  is the Stern-Volmer quenching constant. The calculated  $K_{sv}$  values are  $(2.97 \pm 0.14) \times 10^5$ ,  $(2.71 \pm 0.11) \times 10^5$  and  $(3.78 \pm 0.08) \times 10^5 \text{ M}^{-1}$  for **C1**, **C2** and **C3** respectively (Figures IV.36b–38b). Therefore, the binding ability of the complexes with EB-DNA system follows the order **C3** > **C1** > **C2**, which exactly matches with the results from absorption study. Hence, from these results we can conclude the said complexes interact with CT DNA via intercalative mode which are consistent with absorption studies.

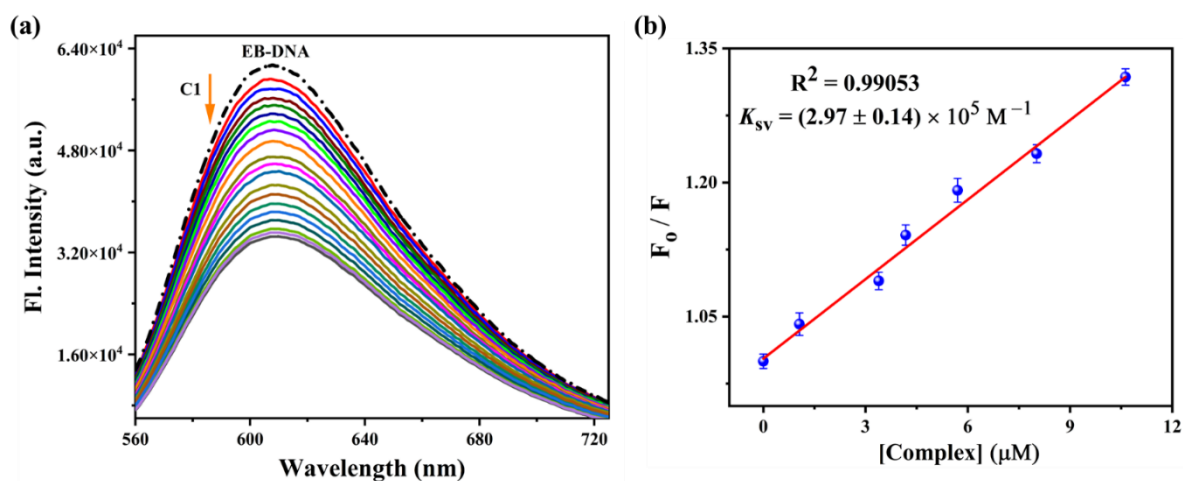


Figure IV.36. (a) Fluorescence titration of EB-CT DNA with the increasing amount of **C1** and (b) Stern-Volmer quenching plot of **C1**.

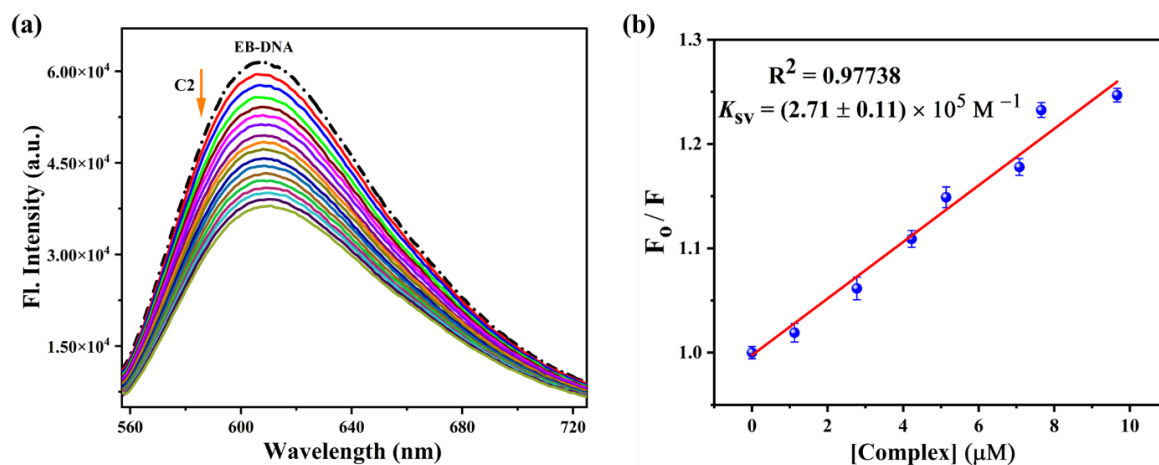


Figure IV.37. (a) Fluorescence titration of EB-CT DNA with the increasing amount of **C2** and (b) Stern-Volmer quenching plot of **C2**.

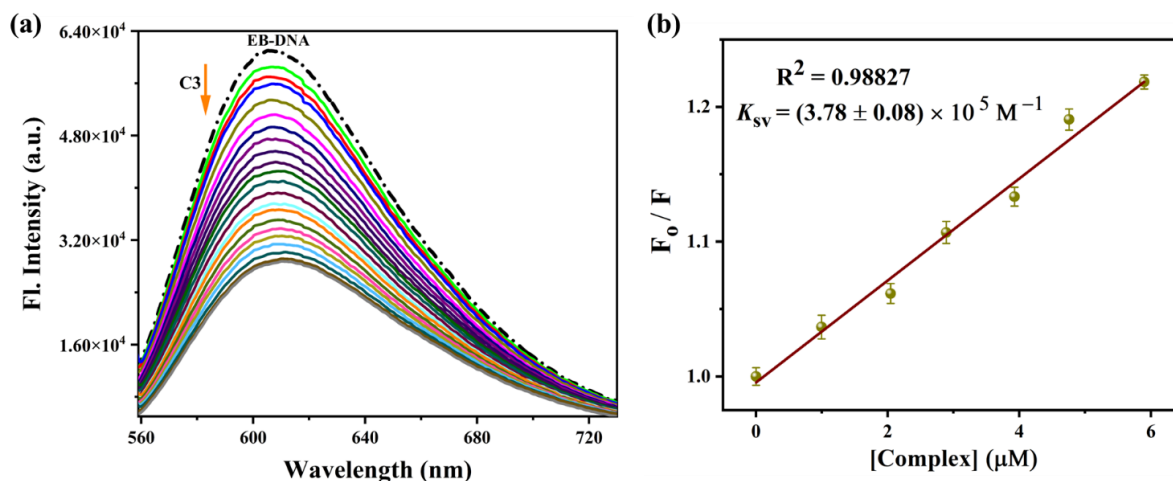


Figure IV.38. (a) UV-Vis titration of **C3** ( $2 \times 10^{-5}$  M) with the gradual addition of CT-DNA in Tris-HCl/NaCl buffer and (b) Wolfe-Shimmer plot of  $[\text{DNA}]/(\epsilon_a - \epsilon_f)$  vs  $[\text{DNA}]$ .

#### IV.3.5.3. Viscosity Measurements

Viscosity measurements were performed prior to drawing any definitive conclusions about the binding fashion of the metal complexes with DNA. Intercalative binding involves inserting a metal complex between DNA base pairs, which lengthens the DNA and increases its viscosity while groove interaction involves twisting or bending the DNA double strand, which shortens the DNA and slightly reduces its viscosity. A traditional DNA intercalator, such as ethidium bromide (EB), makes the DNA viscous. The relative viscosity of DNA solution steadily increased with the addition of the complexes in increasing concentrations (Figure IV.39), suggesting that the DNA's length had risen.<sup>63</sup> Therefore, we can conclude that the complexes (**C1–C3**) were effective for interacting with DNA in a strong intercalative mode.

#### IV.3.6. BSA Protein Binding Experiment

The binding of the complexes with bovine serum albumin (BSA) protein was investigated by different techniques which are fluorescence spectroscopy, CD spectra and FRET mechanism. Among the three amino acid residues (tryptophan, tyrosine and phenylalanine) of BSA protein, the inherent fluorescence of BSA is mostly due to Tryptophan residue at 340 nm.<sup>76</sup> Gradual addition of the complexes to the BSA solution, the fluorescence intensity at 340 nm decreases (Figures IV.40a-42a). This indicates the interactions of the complexes with BSA and may leads to the change in secondary structure of tryptophan residue. This quenching

phenomenon can also be described by calculating the Stern-Volmer quenching constant ( $K_{SV}$ ) using the equation (eq B).

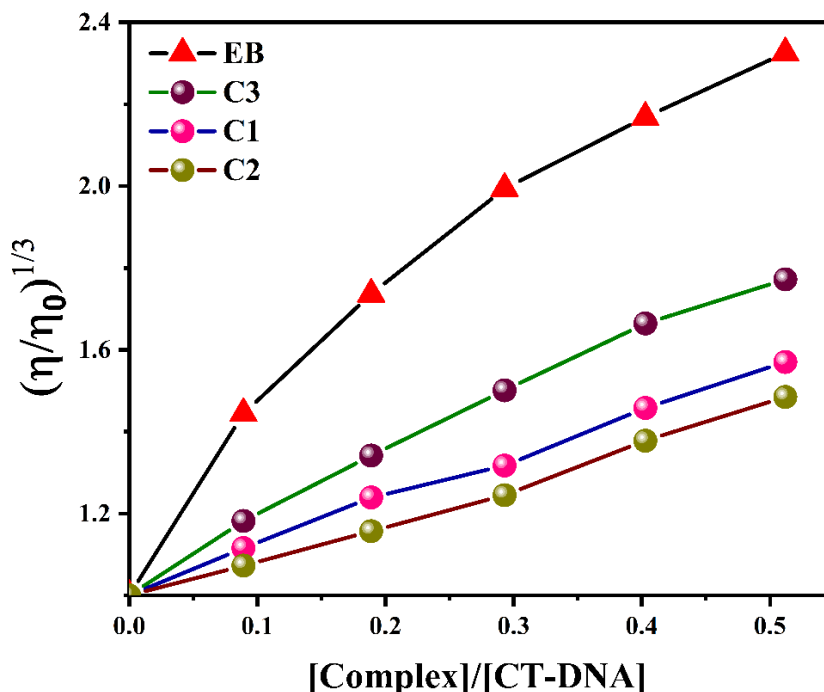


Figure IV.39. Effect of increasing concentrations of EB and complexes (C1–C3) on the relative viscosity of CT-DNA (30  $\mu$ M) at 298 K.

Furthermore, the equilibrium binding constant ( $K_b$ ) and the number of binding site available ( $n$ ) were also determined from the plot of  $\log[(F_0 - F)/F]$  versus  $\log[\text{complex}]$  (Figures IV40a–42a inset) using the following Scatchard equation (eq C).<sup>77</sup>

$$\log (F_0 - F/F) = \log K_b + n \log [Q] \quad (C)$$

Where,  $F_0$ ,  $F$ , and  $[Q]$  are the same as above equation (eq B),  $K_b$  is the binding constant of the complex with BSA and  $n$  is the number of binding sites per BSA molecule. Quenching constant ( $K_{SV}$ ), binding constant ( $K_b$ ) and binding site number ( $n$ ) for all the complexes are given in Table IV.12. The high  $K_{SV}$  represents the higher quenching ability of the C3, similarly the high binding constant ( $K_b$ ) value indicates effective binding capabilities of the complexes with BSA. Number of binding sites ( $n$ ) for C1–C3 were found to be nearly one suggest the binding fashion of the complexes with BSA protein in the molar ratio of 1 : 1.

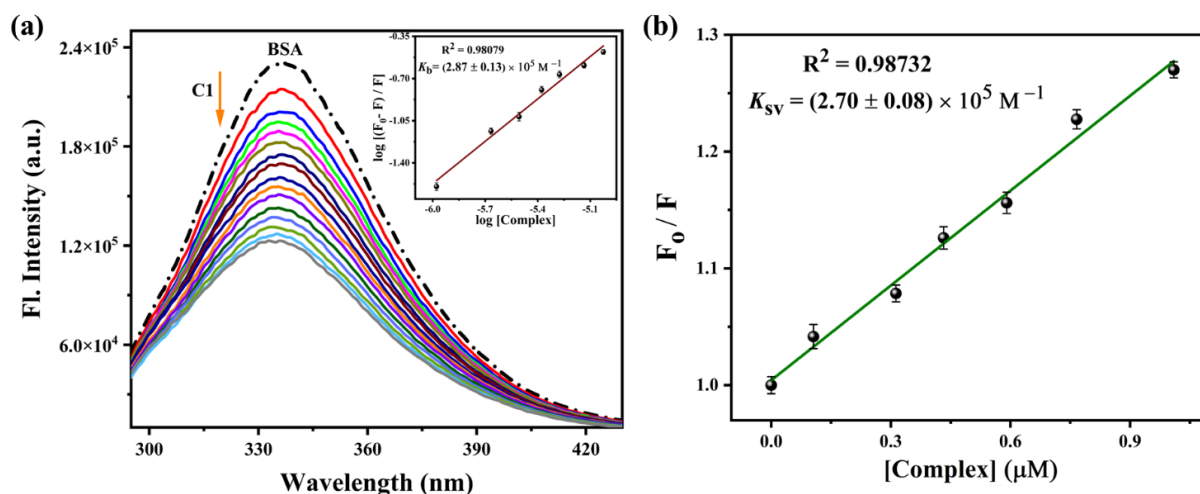


Figure IV.40. (a) Fluorescence quenching titration of BSA (5  $\mu\text{M}$ ) with incremental addition of **C1**. [Inset: Scatchard plot]. (b) Stern-Volmer plot of BSA for **C1**.

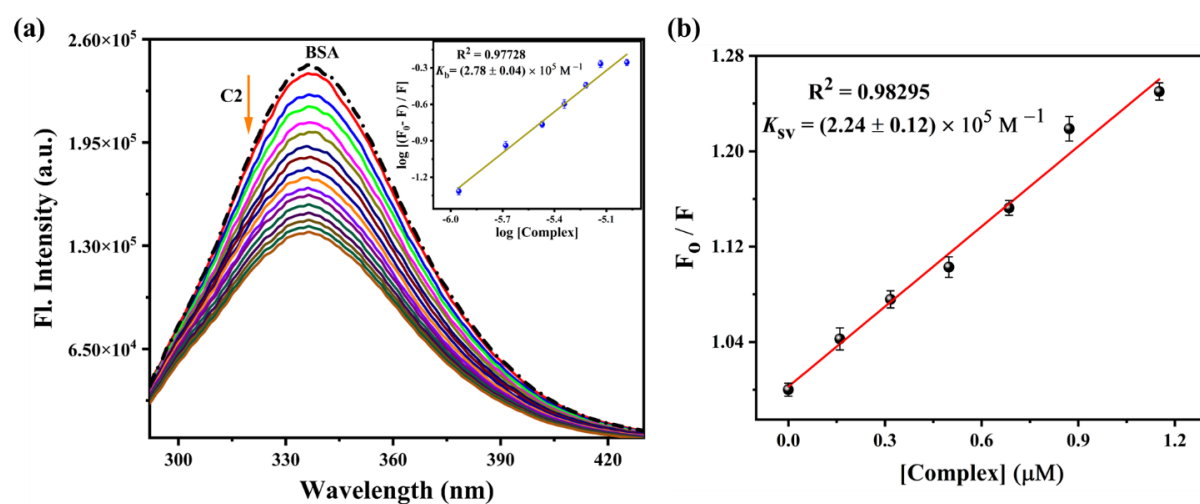


Figure IV.41. (a) Fluorescence quenching titration of BSA (5  $\mu\text{M}$ ) with incremental addition of **C2**. [Inset: Scatchard plot]. (b) Stern-Volmer plot of BSA for **C2**.

Table IV.12. BSA Binding Parameters of the Complexes **C1–C3**

complex	Stern-Volmer constant $K_{SV}$ ( $10^5 \text{ M}^{-1}$ )	binding constant $K_b$ ( $10^5 \text{ M}^{-1}$ )	no. of binding sites ( $n$ )
<b>C1</b>	$2.70 \pm 0.08$	$2.87 \pm 0.13$	$1.07 \pm 0.06$
<b>C2</b>	$2.24 \pm 0.12$	$2.78 \pm 0.04$	$1.13 \pm 0.07$
<b>C3</b>	$3.00 \pm 0.10$	$3.07 \pm 0.15$	$1.12 \pm 0.06$



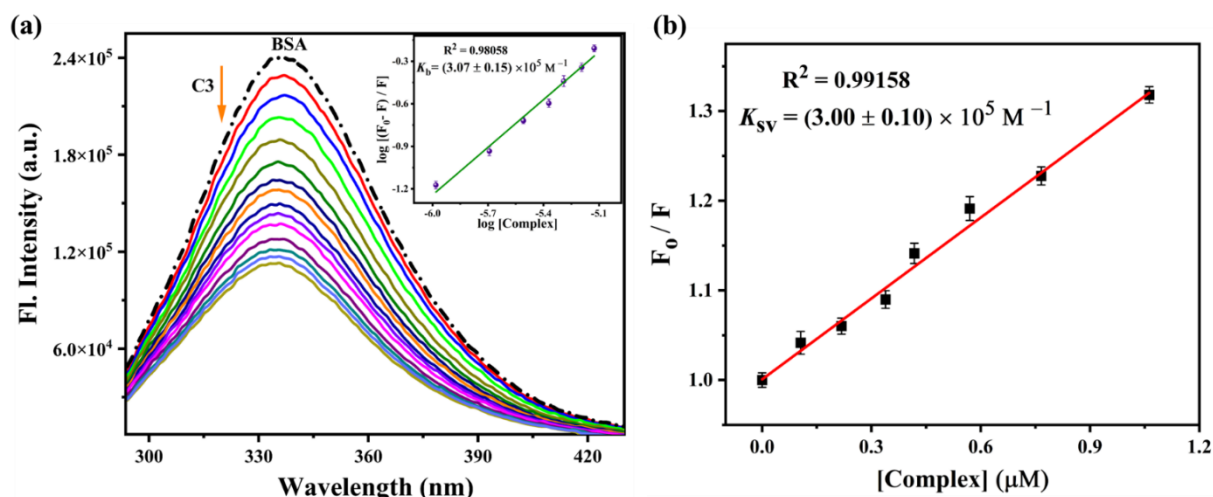


Figure IV.42. (a) Fluorescence quenching titration of BSA (5  $\mu\text{M}$ ) with incremental addition of **C3**. [Inset: Scatchard plot]. (b) Stern-Volmer plot of BSA for **C3**.

#### IV.3.6.1. CD Spectral Study

For more details about the change in the secondary structure of BSA in presence of the metal complex, circular dichroism (CD) spectral studies were performed. BSA shows two negative band at 208 nm ( $\pi \rightarrow \pi^*$ ) and 220 nm ( $n \rightarrow \pi^*$ ) which are characteristic nature of  $\alpha$ -helical structure.<sup>76</sup> The Cd spectra of the BSA in the absence and presence of the complexes are given in Figure IV.43. After the addition of equimolar concentration of the complexes individually to the BSA solution, the band intensity at 208 nm and 220 nm were decreases without any noticeable shift of these bands. These change in the spectra indicates the interaction of the complexes with the secondary structure of BSA protein.<sup>76,78</sup> The percentage change in the  $\alpha$ -helix content of BSA after bound with the complexes was calculated by the equations (1) and (2) given in experimental section, Supporting Information and the values were 38.5 % for **C1**, 43.2 % for **C2** and 30.7 % for **C3**. Hence, these results confirmed the penetration of the complexes in the BSA moiety causing alteration of secondary structure.

#### IV.3.6.2. Energy Transfer Between Complexes and BSA

Förster resonance energy transfer (FRET) is a nondestructive method by which it was possible to measure the energy transfer efficiency ( $E$ ) between the donor and acceptor as well as the distance between them. FRET takes place whenever the fluorophore's (donor, here BSA) emission spectra cross over with the quencher's (acceptor, here complex) absorption spectrum.<sup>57,76</sup>



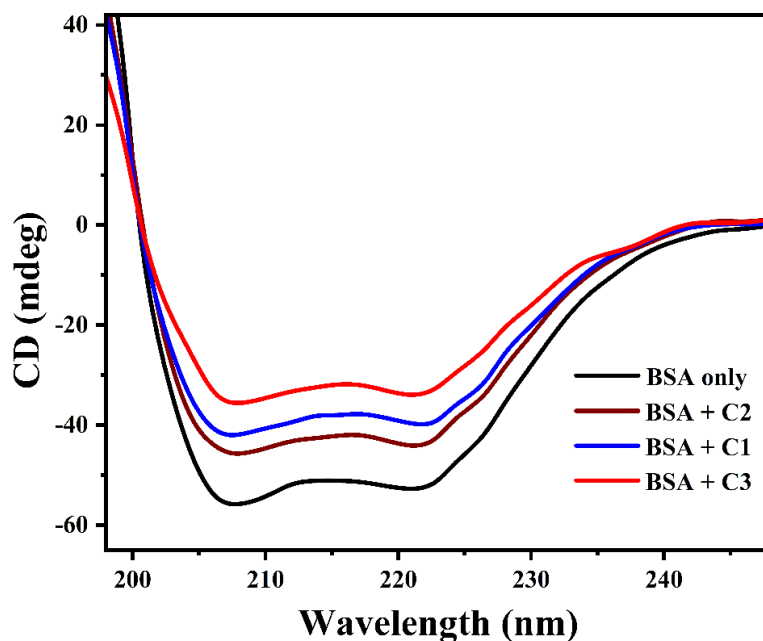


Figure IV.43. CD spectra of free BSA and BSA in presence of equimolar concentration of complexes C1–C3.

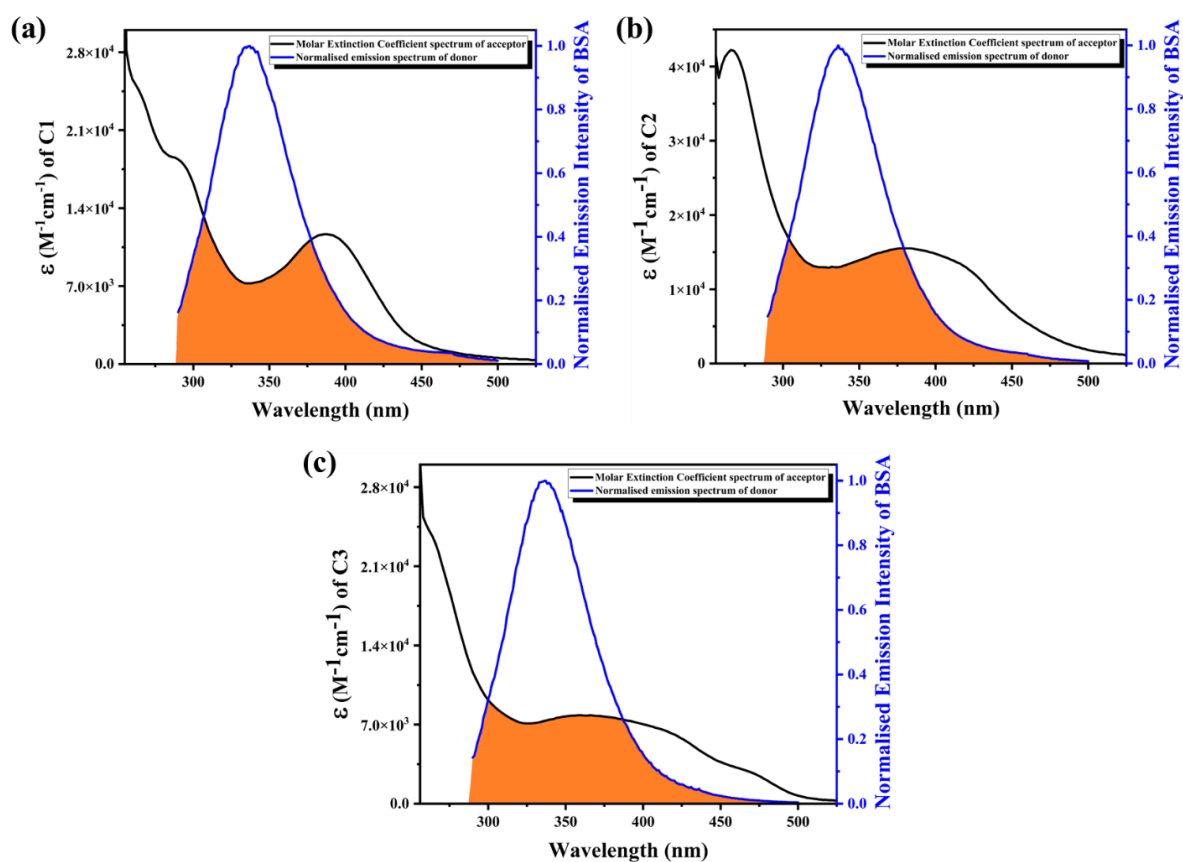
Energy transfer efficiency ( $E$ ) and the distance between donor and acceptor were calculated using the following equation (eq D).

$$E = \frac{R_0^6}{R_0^6 + r^6} = 1 - \frac{F}{F_0} \quad (D)$$

Where,  $F$  and  $F_0$  are the fluorescence intensity of BSA after and before the addition of Pd(II) complexes respectively and  $R_0$  is the distance when energy transfer efficiency is 50%. The spectral overlap of the donor emission and acceptor absorption determines the value of  $R_0$  which is calculated using the equation (3), Experimental Section. The  $J$  value was calculated by integrating the overlapping region of the normalised emission spectrum of the donor (BSA) with the molar extinction coefficient spectrum of acceptor (complex) by using the equation (4) (Figure IV.44). All the calculated parameters are given in the Table IV.13. The donor-to-acceptor distance ( $r$ ) of the complexes should be in the range of 2–8 nm, for efficient energy transfer between BSA and the complexes.<sup>57,76</sup> From the calculated data ( $r = 4.27$ – $5.09$ ), it was confirmed that the energy transfer was highly reasonable. Additionally, the  $r$  value follows the order  $0.5R_0 < r < 1.5R_0$ , which implies that the energy transfer occurs in the quenching interaction between BSA and complexes.<sup>79</sup>

Table IV.13. FRET parameters obtained from the energy transfer between BSA and complexes **C1**–**C3**

complex	$E$	$J(\lambda)$ ( $\text{M}^{-1} \text{cm}^{-1} \text{nm}^4$ )	$R_0$ (nm)	$r$ (nm)
<b>C1</b>	0.45	$4.86 \times 10^{15}$	4.49	4.64
<b>C2</b>	0.42	$7.54 \times 10^{15}$	4.83	5.09
<b>C3</b>	0.52	$3.89 \times 10^{15}$	4.33	4.27

Figure IV.44. FRET between BSA and complexes (a) **C1**, (b) **C2** and (c) **C3**. Normalised emission spectra of donor (blue), molar extinction coefficient spectrum of acceptor (black) and the orange shaded area represent the spectral overlap.

### IV.3.7. Cytotoxicity Study

#### IV.3.7.1. Cell Viability Assay

The Cytotoxicity of **C1**, **C2** and **C3** was evaluated using the MTT assay on MDA-MB-231 triple-negative breast cancer cells. The cells were treated with various concentrations of the complexes (ranging from 0 to 50  $\mu\text{M}$ ). The results showed significant cytotoxicity for all three compounds, with calculated  $\text{IC}_{50}$  values of  $10 \pm 2.90 \mu\text{M}$  for **C3**,  $35 \pm 3.38 \mu\text{M}$  for **C2**, and  $40 \pm 2.72 \mu\text{M}$  for **C1** (Figure IV.45a). Based on these findings, **C3** was chosen for further investigation in the study. To compare the Cytotoxicity of **C3** with a known chemotherapeutic drug, the positive control 5-fluorouracil was included.<sup>80-82</sup> The  $\text{IC}_{50}$  value for 5-fluorouracil was determined to be  $10.15 \pm 2.15 \mu\text{g/mL}$ . Additionally, the Cytotoxicity of **C3** was assessed on normal HEK-293 cells (Figure IV.45b). The results revealed significantly lower toxicity of these compounds towards normal cells compared to MDA-MB-231 cells. This observation highlights the potential of **C3** as a promising candidate for further investigation in the treatment of breast cancer. In summary, the MTT assay demonstrated significant Cytotoxicity of the complexes on MDA-MB-231 cells, with **C3** showing the most potent effect. The compounds exhibited lower toxicity towards normal cells, suggesting their potential as effective and selective agents for breast cancer treatment.

#### IV.3.7.2. C3 Induced ROS generation in Cancer Cells

In order to investigate the mechanism of cell death induced by **C3**, we focused on the generation of reactive oxygen species (ROS) as a potential factor. Elevated ROS levels are known to trigger programmed cell death, or apoptosis. To assess ROS levels, they utilized  $\text{H}_2\text{DCFDA}$ , a non-fluorescent molecule that becomes oxidized to 2',7'-dichlorofluorescein (DCF) in the presence of ROS, emitting strong fluorescence.<sup>60,61</sup> Using flow cytometry, we quantified the fluorescence intensity of DCF and observed a concentration-dependent increase in ROS levels. Upon **C3** treatment, the DCF fluorescence intensity increased in a concentration-dependent manner, indicating elevated ROS levels (Figure IV.45c and IV.45d). This suggests that **C3** treatment leads to an increase in oxidative stress within the cells, which is associated with programmed cell death. By demonstrating the elevation of ROS levels upon **C3** treatment, this experiment provides evidence for a potential mechanism through which **C3** induces cell death. Further research is needed to explore the specific pathways and molecular mechanisms involved in this process.

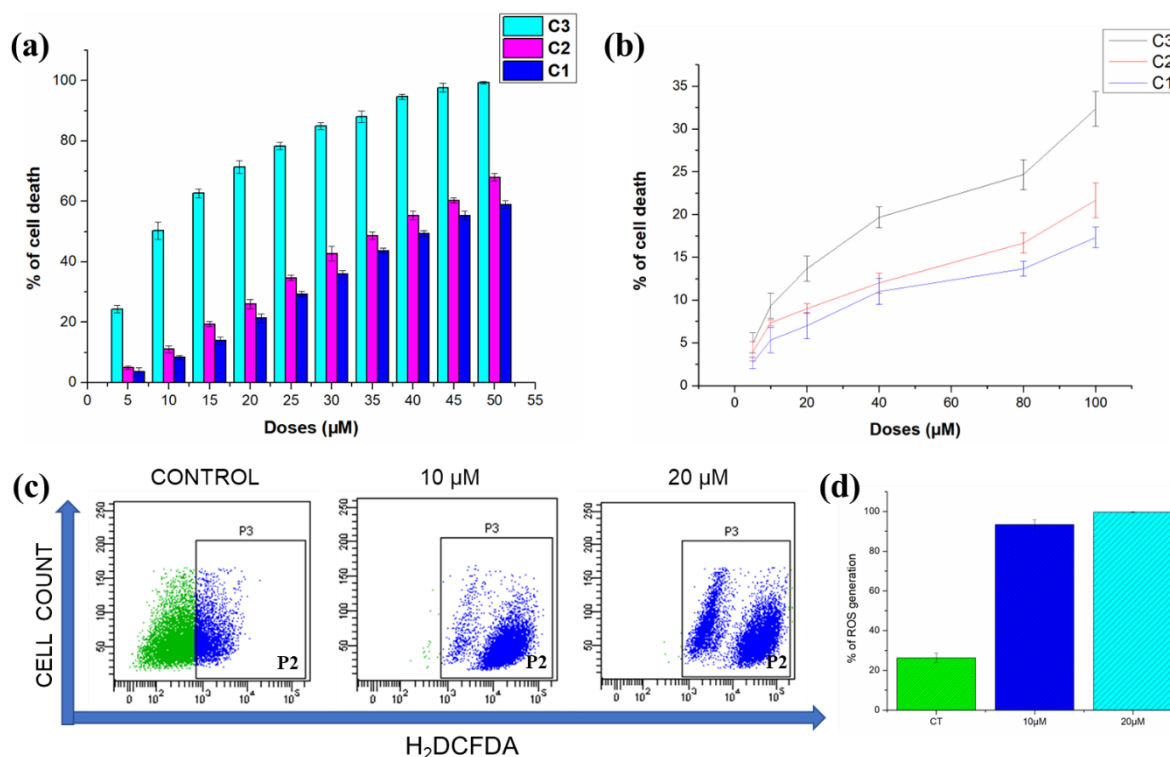


Figure IV.45. Assessment of cell viability using MTT assay. Viability of (a) MDA-MB-231 and (b) HEK-293 cells were assessed by treating different doses of complexes **C1–C3**. Assessment of intracellular ROS following the treatment of **C3**, (c) Intracellular ROS were measured using Flow cytometry and (d) Comparison of DCFDA positive cell population.

#### IV.3.7.3. Apoptotic analysis by annexin-V-FITC/PI Staining

To determine the type of cell death induced by **C3**, we performed flow cytometric analysis using Annexin-V-FITC/propidium iodide (PI) staining. This staining method allows for the detection of phosphatidylserine exposed on the outer membrane of apoptotic cells, which is a characteristic feature of apoptosis. The results of the analysis showed a concentration-dependent increase in the percentage of apoptotic cells, both in the early apoptotic (EA) and late apoptotic (LA) stages, following treatment with **C3**. The percentages of apoptotic cells (both early and late apoptosis) increased as the **C3** concentration increased: 30.1% early apoptosis and 8.4% late apoptosis for 10  $\mu\text{M}$ , 47.8% early apoptosis and 8.1% late apoptosis for 20  $\mu\text{M}$ , and 1.8% early apoptosis and 1% late apoptosis for the control group (Figure IV.46a). These findings suggest that **C3**-induced cell death in MDA-MB-231 cells is associated with cytotoxicity followed by apoptosis.<sup>62,83,84</sup> The combination of the MTT assay, ROS generation analysis, and flow cytometric analysis indicates that **C3** exhibits significant

cytotoxicity, induces ROS generation, and promotes apoptotic cell death in MDA-MB-231 cells.

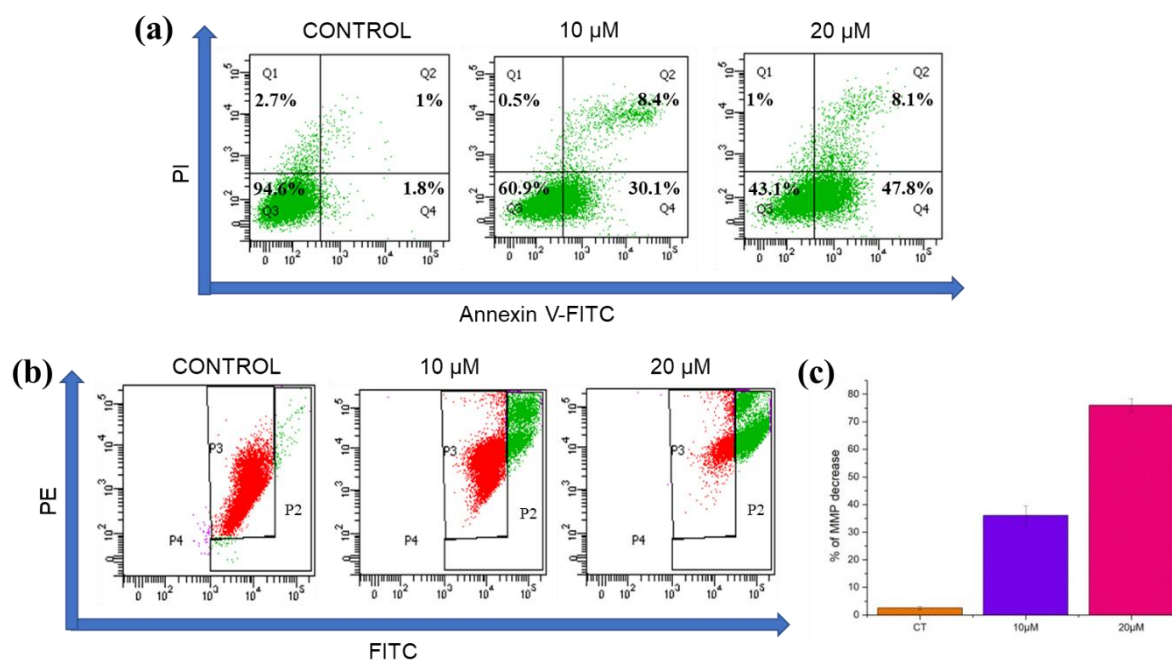


Figure IV.46. (a) Determination of apoptosis using Annexin V-FITC/ PI upon treatment of different concentration of **C3**. Effect of **C3** on Mitochondrial membrane potential (MMP), (b) JC1 Fluorescence measurement in MDA-MB-231 cells and (c) Comparison of MMP decrease.

#### IV.3.7.4. Mitochondrial Membrane Potential (MMP)

The regulation of apoptosis can occur through two main pathways, the mitochondria-dependent (intrinsic) pathway and the mitochondria-independent (extrinsic) pathway. Mitochondria, which are responsible for ATP production and often referred to as the powerhouses of cells, play a crucial role in initiating apoptosis in a controlled manner.<sup>85</sup> One important aspect of this process is the dysfunction of mitochondria, leading to the release of Cytochrome C from the mitochondria into the cytosol. To investigate the involvement of mitochondria in the cell death induced by **C3**, we initially examined the loss of mitochondrial membrane potential, which is a critical step in the apoptosis pathway.<sup>86</sup> Using MDA-MB-231 cells in this study, we observed that treatment with **C3** induced cell death through a mitochondria-dependent apoptotic pathway. We found a concentration-dependent increase in the loss of mitochondrial membrane potential upon **C3** treatment. The percentages of mitochondrial membrane potential loss were 30.3% for 10  $\mu$ M and 72.5% for 15  $\mu$ M, compared to 1.6% in the control group (Figure IV.46b and IV.46c). This increase in

mitochondrial membrane potential loss was attributed to the enlargement of the mitochondrial membrane pore, as indicated by the elevated level of JC1 green fluorescence intensity in **C3**-treated MDA-MB-231 cells. JC1 is a fluorescent dye that exhibits a shift in color from red to green when the mitochondrial membrane potential is disrupted. These findings suggest that **C3**-induced cell death in MDA-MB-231 cells involves a mitochondria-dependent apoptotic pathway. The observed loss of mitochondrial membrane potential and the release of Cytochrome C support the involvement of mitochondria in the apoptotic process triggered by **C3** treatment. In summary, the study provides evidence that **C3** induces cell death through a mitochondria-dependent apoptotic pathway, as demonstrated by the concentration-dependent increase in mitochondrial membrane potential loss and the enlargement of the mitochondrial membrane pore.

#### **IV.3.7.5. Immunofluorescence Assay**

In the study, we observed a decrease in BCL-2 expression in cells treated with **C3** compared to control cells. This decrease suggests a shift towards a proapoptotic state, as BCL-2 proteins are known to inhibit apoptosis. The decrease in BCL-2 expression was confirmed through fluorescence analysis of confocal images, which provided additional evidence for the involvement of mitochondria in the apoptotic process. These apoptotic stimuli triggered the release of Cytochrome C from the mitochondria to the cytosol. Cytochrome C is a key player in caspase activation, which initiates the cellular events leading to cell death. Collectively, the evaluation of P53 and BCL-2 protein expression (Figure IV.47) strengthens the evidence for **C3**-induced cell death through the apoptosis pathway.<sup>87-91</sup> The observed decrease in BCL-2 expression, in conjunction with the increased ROS levels and the release of Cytochrome C, further supports the involvement of mitochondria in the apoptotic process induced by **C3** treatment.

#### **IV.3.7.6. Caspase Activity Assay**

Caspase are a family of proteases that play a critical role in initiating apoptosis, the programmed cell death process.<sup>92,93</sup> These enzymes are responsible for cleaving specific cellular proteins and are activated by the release of Cytochrome C from the inner mitochondria to the cytosol.<sup>94</sup> The upregulation of Cytochrome C (Figure IV.48) triggers caspase activation, which serves as a key event in initiating apoptosis. In the conducted study, we observed a gradual increase in the levels of caspase-3 and caspase-9 in a concentration-

dependent manner (Figure IV.49). This finding suggests that treatment with **C3** induces cell death in MDA-MB-231 cells through the apoptosis pathway.

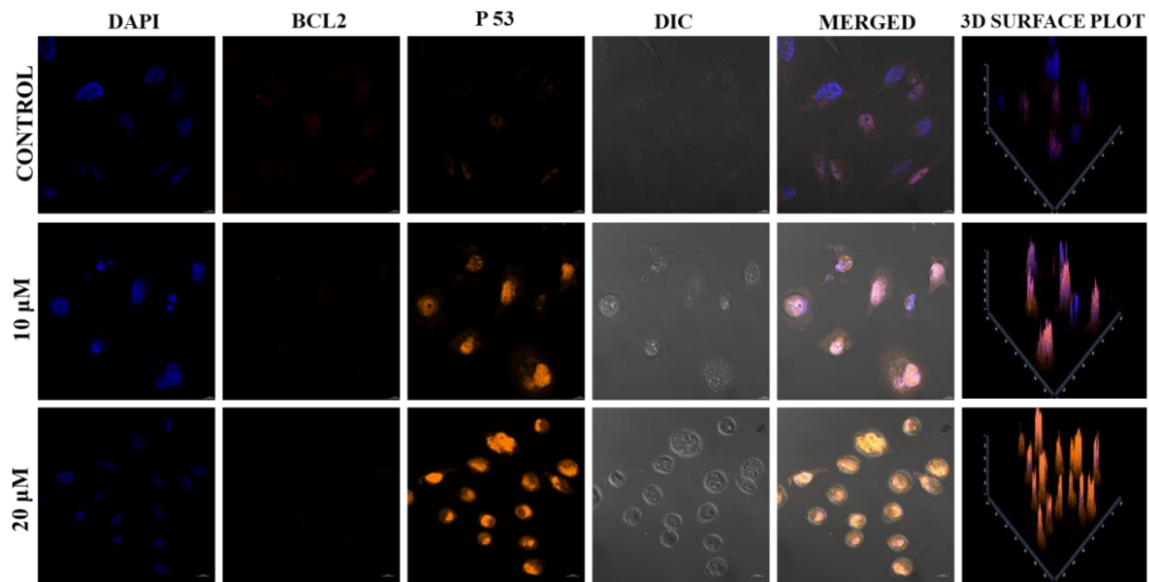


Figure IV.47. Immunofluorescence images showing the expression of BCL2 and P53. DAPI was used for nuclear staining.

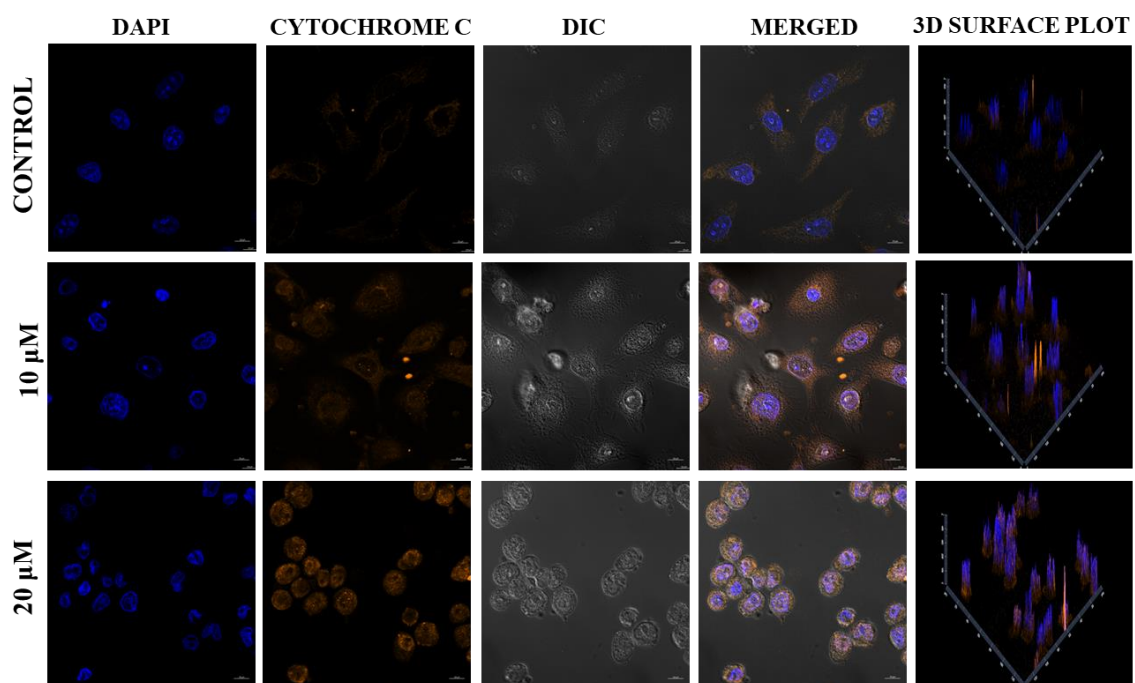


Figure IV.48. Immunofluorescence images showing the expression of Cytochrome C. DAPI was used for nuclear staining.



The increased levels of caspase-3 and caspase-9 indicate their activation and involvement in executing the cellular events leading to apoptosis. Furthermore, the observed expression of P53 and BCL-2 proteins, along with the activity of caspase-3 and caspase-9, provides additional confirmation of the involvement of the apoptosis pathway in **C3**-induced cell death. P53, a tumor suppressor protein, is known to regulate various aspects of apoptosis, including mitochondrial-dependent pathways.<sup>95</sup> The decrease in BCL-2 expression observed in the study indicates a shift towards a proapoptotic state. Taken together, the findings of increased caspase-3 and caspase-9 levels, along with the expression of P53 and BCL-2 proteins, provide strong evidence for the involvement of the apoptosis pathway in **C3**-induced cell death.<sup>96</sup> These molecular and biochemical changes support the conclusion that **C3** treatment triggers apoptosis in MDA-MB-231 cells.

Thus, the ability of the complex **C3** to induce cell death via mitochondria-dependent apoptotic pathway suggests its potential as a therapeutic agent for this subtype of breast cancer. By targeting key players in this pathway, such as BCL-2, Cytochrome C, caspase-3, caspase-9 and P53, **C3** may hold promise as a targeted treatment approach for triple-negative breast cancer.

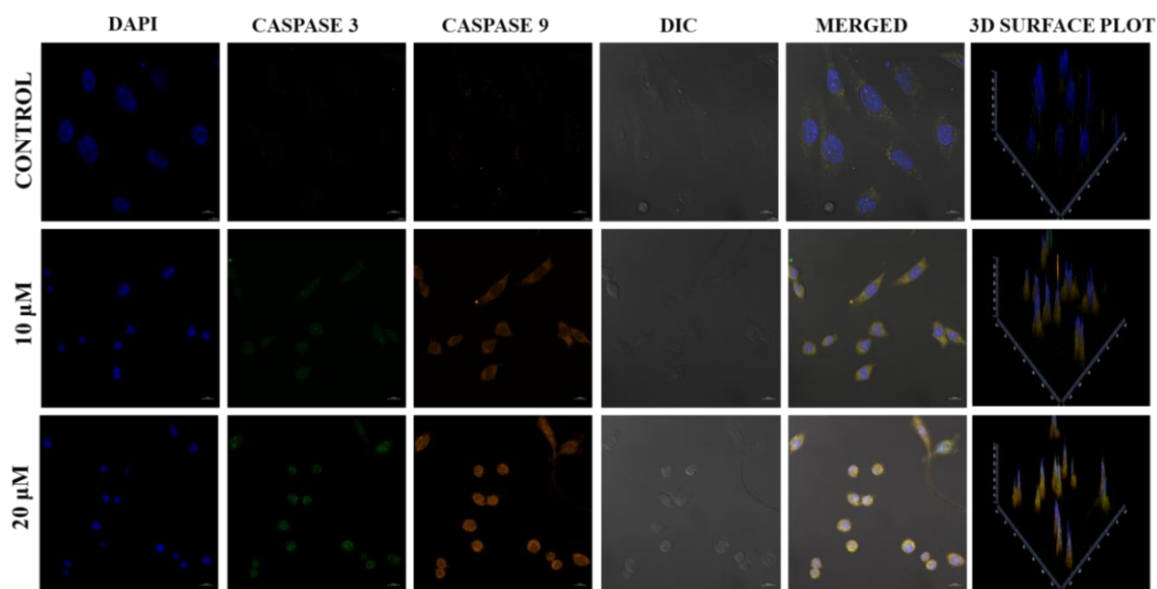


Figure IV.49. Immunofluorescence images showing the expression of Caspase 3 and Caspase 9. DAPI was used for nuclear staining.



#### IV.4. Conclusion

In summary, here we have designed three new heterocyclic thiosemicarbazone based Pd(II) complexes **C1**–**C3** having coligands Cl and PPh<sub>3</sub>. All the compounds were characterized thoroughly by various spectroscopic techniques and X-ray structures of the complexes revealed that complex **C2** have square planar geometry around the metal center while the same for **C1** and **C3** was distorted square plane. Catalytic activity of the complexes was done toward Suzuki-Miyaura cross coupling reaction and it was observed that complex **C2** showed highest catalytic activity followed by **C3** and **C1**. DNA binding study revealed that all the complexes bind with CT-DNA via intercalative mode. From the spectroscopic studies, it was observed that complex **C3** displayed maximum binding activity with  $K_b = (4.55 \pm 0.17) \times 10^5 \text{ M}^{-1}$ . The BSA interaction study was assessed using fluorescence, CD and FRET techniques and the interaction capability of the complexes with BSA protein follows the order **C3** > **C1** > **C2**. Finally, the cytotoxicity study was investigated against human triple negative breast cancer (TNBC) cells MDA-MB-231 and the MTT assay showed that complex **C3** was more toxic ( $\text{IC}_{50} = 10 \pm 2.90 \text{ }\mu\text{M}$ ) than the other two complexes. All the complexes showed lower toxicity toward normal cell line HEK-293. Apoptotic analysis was done by annexin-V-FITC/PI binding assay, mitochondrial membrane potential study, immunofluorescence assay and caspase activity assay. The results showed that the **C3** induced apoptosis was occurred via mitochondrial-dependent (intrinsic) pathway.

## IV.5. References

1. I. I. Ozturk, K. Turk, A. M. Grzeŝkiewicz, M. Kubicki, C. N. Banti and S. K. Hadjikakou, *New J. Chem.*, 2023, **47**, 12779–12789.
2. A. Fuior, D. Cebotari, M. Haouas, J. Marrot, G. M. Espallargas, V. Guérineau, D. Touboul, R. V. Rusnac, A. Gulea and S. Floquet, *ACS Omega*, 2022, **7**, 16547–16560.
3. G. Kalaiarasi, R. Jain, H. Puschman, S. Poorna Chandrika, K. Preethi and R. Prabhakaran, *New J. Chem.* 2017, **41**, 2543–2560.
4. K. Bajaj, R. M. Buchanan and C. A. Grapperhaus, *J. Inorg. Biochem.* 2021, **225**, 111620.
5. A. Haseloer, L. M. Denkler, R. Jordan, M. Reimer, S. Olthof, I. Schmidt, K. Meerholz, G. Hörner and A. Klein, *Dalton Trans.* 2021, **50**, 4311–4322.
6. N. Balakrishnan, J. Haribabu, M. Dharmasivam, J. P. Jayadharini, D. Anandakrishnan, S. Swaminathan, N. Bhuvanesh, C. Echeverria and R. Karvembu, *Organometallics*, 2023, **42**, 259–275.
7. H. S. Adhikari, A. Garai, K. Das Manandhar and P. N. Yadav, *ACS Omega*, 2022, **7**, 30978–30988.
8. R. Anjum, D. Palanimuthu, D. S. Kalinowski, W. Lewis, K. C. Park, Z. Kovacevic, I. U. Khan and D. R. Richardson, *Inorg. Chem.*, 2019, **58**, 13709–13723.
9. D. L. Sun, S. Poddar, R. D. Pan, E. W. Rosser, E. R. Abt, J. V. Valkenburgh, T. M. Le, V. Lok, S. P. Hernandez, J. Song, J. Li, A. Turlik, X. Chen, C. -A. Cheng, W. Chen, C. E. Mona, A. D. Stuparu, L. Vergnes, K. Reue, R. Damoiseaux, J. I. Zink, J. Czernin, T. R. Donahue, K. N. Houk, M. E. Jung and C. G. Radu, *RSC Med. Chem.*, 2020, **11**, 392–410.
10. A. I. Matesanz, J. Perles and P. Souza, *Dalton Trans.*, 2012, **41**, 12538–12547.
11. C. M. Almeida, P. H. S. Marcon, É. C. M. Nascimento, J. B. L. Martins, M. A. S. Chagas, M. Fujimori, P. G. F. De Marchi, E. L. França, A. C. Honório-França and C. C. Gatto, *Appl. Organomet. Chem.*, 2022, **36**, e6761.
12. A. Shanmugapriya, G. Kalaiarasi, M. Ravi, H. A. Sparkes, P. Kalaivani and R. Prabhakaran, *New J. Chem.*, 2021, **45**, 20227–20240.
13. J. Haribabu, M. M. Tamizh, C. Balachandran, Y. Arun, N. S. P. Bhuvanesh, A. Endo, and R. Karvembu, *New J. Chem.*, 2018, **42**, 10818–10832.
14. H. Sung, J. Ferlay, R. L. Siegel, M. Laversanne, I. Soerjomataram, A. Jemal and F. Bray, *CA-Cancer J. Clin.*, 2021, **71**, 209–249.
15. J. Lopes, C. M. P. Rodrigues, M. M. Gaspar and C. P. Reis, *Cancers*, 2022, **14**, 4652.
16. (a) T. C. Johnstone, K. Suntharalingam and S. J. Lippard, *Chem. Rev.*, 2016, **116**, 436–3486; (b) J. J. Wilson and S. J. Lippard, *Chem. Rev.*, 2014, **114**, 4470–4495.
17. I. B. Lozada, B. Huang, M. Stilgenbauer, T. Beach, Z. Qiu, Y. Zheng and D. E. Herbert, *Dalton Trans.*, 2020, **49**, 6557–6560.

18. L. Gourdon, K. Cariou and G. Gasser, *Chem. Soc. Rev.*, 2022, **51**, 1167–1195.
19. Q. Du, L. Guo, M. Tian, X. Ge, Y. Yang, X. Jian, Z. Xu, Z. Tian and Z. Liu, *Organometallics*, 2018, **37**, 2880–2889.
20. E. Bortolamiol, F. Fama, Z. Zhang, N. Demitri, L. Cavallo, I. Caligiuri, F. Rizzolio, T. Scattolin and F. Visentin, *Dalton Trans.*, 2022, **51**, 11135–11151.
21. A. Kumar, A. Naaz, A. P. Prakasham, M. K. Gangwar, R. J. Butcher, D. Panda and P. Ghosh, *ACS Omega*, 2017, **2**, 4632–4646.
22. A. Krstic, A. Pavic, E. Avdovic, Z. Markovic, M. Stevanovic and I. Petrovic, *Molecules*, 2022, **27**, 2115.
23. M. Vojtek, M. P. M. Marques, I. M. P. L. V. O. Ferreira, H. Mota-Filipe and C. Diniz, *Drug Discov. Today*, 2019, **24**, 1044–1058.
24. R. D. Graham, D. R. Williams, *J. Inorg. Nucl. Chem.*, 1979, **41**, 1245–1249.
25. Z. Wang, J. Li, R. Liu, X. Jia, H. Liu, T. Xie, H. Chen, L. Pan and Z. Ma, *J. Inorg. Biochem.*, 2023, **244**, 112219.
26. R. Ouyang, S. Wang, K. Feng, C. Liu, D. Z. Silva, Y. Chen, Y. Zhao, B. Liu, Y. Miao and S. Zhou, *J. Inorg. Biochem.*, 2023, **244**, 112205.
27. S. Zehra, T. Roisnel and F. Arjmand, *ACS Omega*, 2019, **4**, 7691–7705.
28. G. Sahu, A. Banerjee, R. Samanta, M. Mohanty, S. Lima, E. R. T. Tiekink and R. Dinda, *Inorg. Chem.*, 2021, **60**, 15291–15309.
29. V. Sharma, O. Yañez, C. Zúñiga, A. Kumar, G. Singh and P. Cantero-López, *Chem. Phys. Lett.* 2020, **747**, 137349.
30. M. Ghosh, N. Sepay, C. Rizzoli, C. K. Ghosh, A. Banerjee and S. Saha, *New J. Chem.* 2021, **45**, 2995–3006.
31. B. Bera, S. Mondal, S. Mandal, K. Das Saha and T. K. Mondal, *Appl. Organomet. Chem.*, 2023, **37**, e7185.
32. J. Diccianni, Q. Lin and T. Diao, *Acc. Chem. Res.*, 2020, **53**, 906–919.
33. Y. Xia and J. Wang, *J. Am. Chem. Soc.*, 2020, **142**, 10592–10605.
34. A. Das and N. T. Patil, *ACS Catal.*, 2023, **13**, 3847–3853.
35. B. Sardar, N. Biswas and D. Srimani, *Organometallics*, 2023, **42**, 55–61.
36. S. Yang, H. Li, X. Yu, J. An and M. Szostak, *J. Org. Chem.*, 2022, **87**, 15250–15260.
37. J. Li, X. Zhang, Y. Yao, Y. Gao, W. Yang and W. Zhao, *J. Org. Chem.*, 2022, **87**, 6951–6959.
38. G. K. Rao, A. Dutta, N. Yadav, P. Oswal, A. Kumar and A. K. Singh, *New J. Chem.*, 2023, **47**, 4218–4227.
39. P. Elumalai, H. Mamlouk, W. Yiming, L. Feng, S. Yuan, H. -C. Zhou and S. T. Madrahimov, *ACS Appl. Mater. Interfaces*, 2018, **10**, 41431–41438.
40. W. Mansour, M. Fettouhi and B. El Ali, *Appl. Organomet. Chem.*, 2020, **34**, e5636.

41. H. Matsumoto, Y. Hoshino, T. Iwai, M. Sawamura and Y. Miura, *Ind. Eng. Chem. Res.*, 2020, **59**, 15179–15187.
42. S. Let, G. K. Dam, P. Samanta, S. Fajal, S. Dutta and S. K. Ghosh, *J. Org. Chem.*, 2022, **87**, 16655–16664.
43. R. Martin and S. L. Buchwald, *Acc. Chem. Res.*, 2008, **41**, 1461–1473.
44. B. Agrahari, S. Layek, Anuradha, R. Ganguly and D. D. Pathak, *Inorg. Chim. Acta*, 2018, **471**, 345–354.
45. P. Paul, P. Sengupta and S. Bhattacharya, *J. Organomet. Chem.*, 2013, **724**, 281–288.
46. D. Pandiarajan, R. Ramesh, Y. Liu and R. Suresh, *Inorg. Chem. Commun.*, 2013, **33**, 33–37.
47. P. Paul, R. J. Butcher and S. Bhattacharya, *Inorg. Chim. Acta*, 2015, **425**, 67–75.
48. Bruker. SAINT v8.38A. Bruker AXS Inc., Madison, Wisconsin, USA.
49. L. Krause, R. Herbst-Irmer, G. M. Sheldrick and D. Stalke, *J. Appl. Crystallogr.*, 2015, **48**, 3–10.
50. (a) G. M. Sheldrick, *Acta Crystallogr. A*, 2008, **64**, 112–122; (b) G. M. Sheldrick, *Acta Crystallogr. C*, 2015, **71**, 3–8.
51. (a) A. D. Becke, *J. Chem. Phys.*, 1993, **98**, 5648; (b) C. Lee, W. Yang and R. G. Parr, *Phys. Rev. B: Condens. Matter Mater. Phys.*, 1988, **37**, 785.
52. (a) P. J. Hay and W. R. Wadt, *J. Chem. Phys.*, 1985, **82**, 270; (b) W. R. Wadt and P. J. Hay, *J. Chem. Phys.*, 1985, **82**, 284; (c) P. J. Hay and W. R. Wadt, *J. Chem. Phys.*, 1985, **82**, 299.
53. M. J. Frisch, G. W. Trucks, H. B. Schlegel, G. E. Scuseria, M. A. Robb, J. R. Cheeseman, G. Scalmani, V. Barone, B. Mennucci, G. A. Petersson, H. Nakatsuji, M. Caricato, X. Li, H. P. Hratchian, A. F. Izmaylov, J. Bloino, G. Zheng, J. L. Sonnenberg, M. Hada, M. Ehara, K. Toyota, R. Fukuda, J. Hasegawa, M. Ishida, T. Nakajima, Y. Honda, O. Kitao, H. Nakai, T. Vreven, J. A. Montgomery, Jr., J. E. Peralta, F. Ogliaro, M. Bearpark, J. J. Heyd, E. Brothers, K. N. Kudin, V. N. Staroverov, R. Kobayashi, J. Normand, K. Raghavachari, A. Rendell, J. C. Burant, S. S. Iyengar, J. Tomasi, M. Cossi, N. Rega, J. M. Millam, M. Klene, J. E. Knox, J. B. Cross, V. Bakken, C. Adamo, J. Jaramillo, R. Gomperts, R. E. Stratmann, O. Yazyev, A. J. Austin, R. Cammi, C. Pomelli, J. W. Ochterski, R. L. Martin, K. Morokuma, V. G. Zakrzewski, G. A. Voth, P. Salvador, J. J. Dannenberg, S. Dapprich, A. D. Daniels, O. Farkas, J. B. Foresman, J. V. Ortiz, J. Cioslowski and D. J. Fox, Gaussian 09, Revision D.01, Gaussian, Inc., Wallingford CT, **2009**.
54. (a) R. Bauernschmitt and R. Ahlrichs, *Chem. Phys. Lett.*, 1996, **256**, 454; (b) R. E. Stratmann, G. E. Scuseria and M. J. Frisch, *J. Chem. Phys.*, 1998, **109**, 8218; (c) M. E. Casida, C. Jamorski, K. C. Casida and D. R. Salahub, *J. Chem. Phys.*, 1998, **108**, 4439.
55. (a) V. Barone and M. Cossi, *J. Phys. Chem. A*, 1998, **102**, 1995; (b) M. Cossi and V. Barone, *J. Chem. Phys.*, 2001, **115**, 4708; (c) M. Cossi, N. Rega, G. Scalmani and V. Barone, *J. Comput. Chem.*, 2003, **24**, 669.

56. N. M. O'Boyle, A. L. Tenderholt and K. M. Langner, *J. Comput. Chem.*, 2008, **29**, 839.
57. S. Mandal, R. Naskar, A. Sau Mondal, B. Bera and T. K. Mondal, *Dalton Trans.*, 2023, **52**, 5983–5998.
58. A. Banerjee, M. Mohanty, S. Lima, R. Samanta, E. Garribba, T. Sasamori and R. Dinda, *New J. Chem.*, 2020, **44**, 10946–10963.
59. S. U. Parsekar, P. Velankanni, S. Sridhar, P. Haldar, N. A. Mate, A. Banerjee, P. K. S. Antharjanam, A. P. Koley and M. Kumar, *Dalton Trans.*, 2020, **49**, 2947–2965.
60. A. Brozovic, A. Ambriović-Ristov and A. Osmak, *Crit. Rev. toxicol.*, 2010, **40**, 347–359.
61. Y. Li, Z. Gu, C. Zhang, S. Li, L. Zhang, G. Zhou, S. Wang and J. Zhang, *Eur. J. Med. Chem.*, 2018, **144**, 662–671.
62. R. B. Birge, S. Boeltz, S. Kumar, J. Carlson, J. Wanderley, D. Calianese, M. Barcinski, R. A. Brekken, X. Huang, J. T. Hutchins, B. Freimark, C. Empig, J. Mercer, A. J. Schroit, G. Schett and M. Herrmann, *Cell Death Differ.*, 2016, **23**, 962–978.
63. W. Li, S. Li, Z. Zhang, G. Xu, X. Man, F. Yang and H. Liang, *J. Med. Chem.*, 2023, **66**, 8564–8579.
64. J. Haribabu, S. Srividya, D. Mahendiran, D. Gayathri, V. Venkatramu, N. Bhuvanesh and R. Karvembu, *Inorg. Chem.*, 2020, **59**, 17109–17122.
65. I. D. Kostas, B. R. Steele, A. Terzis, S. V. Amosova, A. V. Martynov and N. A. Makhaeva, *Eur. J. Inorg. Chem.*, 2006, **2006**, 2642–2646.
66. I. D. Kostas, F. J. Andreadaki, D. Kovala-Demertzi, P. Christos and M. A. Demertzis, *Tetrahedron Lett.*, 2005, **46**, 1967–1970.
67. B. Agrahari, S. Layek, Anuradha, R. Ganguly and D. D. Pathak, *Inorg. Chim. Acta*, 2018, **471**, 345–354.
68. M. Kalita, K. J. Tamuli, P. Barman, B. Sarma, R. Baruah and H. P. D. Boruah, *Polyhedron*, 2015, **97**, 140–147.
69. L. C. Matsinha, J. Mao, S. F. Mapolie and G. S. Smith, *Eur. J. Inorg. Chem.*, 2015, **2015**, 4088–4094.
70. A. Castiñeiras, N. Fernández-Hermida, I. García-Santos and L. Gómez-Rodríguez, *Dalton Trans.*, 2012, **41**, 13486–13495.
71. C. K. Manna, R. Naskar, B. Bera, A. Das and T. K. Mondal, *J. Mol. Struct.*, 2021, **1237**, 130322.
72. R. Bhaskar, A. K. Sharma, M. K. Yadav and A. K. Singh, *Dalton Trans.*, 2017, **46**, 15235–15248.
73. A. Akdeniz and N. Turan, *J. Mol. Struct.*, 2023, **1287**, 135724.
74. Y. -C. Huang, J. Haribabu, C. -M. Chien, G. Sabapathi, C. -K. Chou, R. Karvembu, P. Venuvanalingam, W. -M. Ching, M. -L. Tsai and S. C. N. Hsu, *J. Inorg. Biochem.*, 2019, **194**, 74–84.

75. Y. Ma, G. Zhang and J. Pan, *J. Agric. Food Chem.*, 2012, **60**, 10867–10875.
76. G. Sahu, A. Banerjee, R. Samanta, M. Mohanty, S. Lima, E. R. T. Tiekink and R. Dinda, *Inorg. Chem.*, 2021, **60**, 15291–15309.
77. A. Papadopoulou, R. J. Green and R. A. Frazier, *J. Agric. Food Chem.*, 2005, **53**, 158–163.
78. M. Bashir, A. A. Dar and I. Yousuf, *ACS Omega*, 2023, **8**, 3026–3042.
79. M. Mohanty, G. Sahu, A. Banerjee, S. Lima, S. A. Patra, A. Crochet, G. Sciortino, D. Sanna, V. Ugone, E. Garribba and R. Dinda, *Inorg. Chem.*, 2022, **61**, 4513–4532.
80. D. S. Heo, J. -G. Park, K. Hata, R. Day, R. B. Herberman and T. L. Whiteside, *Cancer Res.*, 1990, **50**, 3681–3690.
81. L. Niu, G. Ren, T. Hou, X. Shen, and D. Zhu, *Inorg. Chem. Commun.*, 2021, **130**, 108737.
82. S. Rubino, V. D. Stefano, A. Attanzio, L. Tesoriere, M. A. Girasolo, F. Nicolò, G. Bruno, S. Orecchio and G. C. Stocco, *Inorganica Chim. Acta*, 2014, **418**, 112–118.
83. G. Zhang, V. Gurtu, S. R. Kain and G. Yan, *Biotechniques*, 1997, **23**, 525–531.
84. M. D. Coskun, F. Ari, A. Y. Oral, M. Sarimahmut, H. M. Kutlu, V. T. Yilmaz and E. Ulukaya, *Bioorg. Med. Chem.*, 2013, **21**, 4698–4705.
85. A. Mallick, P. More, S. Ghosh, R. Chippalkatti, B. A. Chopade, M. Lahiri and S. Basu, *ACS Appl. Mater. Interfaces*, 2015, **7**, 7584–7598.
86. S. Sivagnanam, K. Das, I. Pan, A. Barik, A. Stewart, B. Maity and P. Das, *ACS Appl. Bio Mater.*, 2023, **6**, 836–847.
87. F. A. Serrano, A. L. Matsuo, P. T. Monteforte, A. Bechara, S. S. Smaili, D. P. Santana, T. Rodrigues, et al. *BMC Cancer*, 2011, **11**, 1–16.
88. M. J. Hosseini, I. Jafarian, S. Farahani, R. Khodadadi, S. H. Tagavi, P. Naserzadeh, A. Mohammadi-Bardbori and N. Arghavanifard, *Metallomics*, 2016, **8**, 252–259.
89. S. Zhang, A. Long and A. J. Link, *ACS Synth. Biol.*, 2012, **1**, 89–98.
90. A. Sharma, P. Anand, Y. S. Padwad and S. K. Maurya, *ACS Omega*, 2022, **7**, 49, 45036–45044.
91. P. Bhanja, S. Mishra, K. Manna, K. Das Saha and A. Bhaumik, *ACS Omega*, 2018, **3**, 529–535.
92. C. Ye, S. Zheng, D. Jiang, J. Lu, Z. Huang, Z. Liu, H. Zhou, C. Zhuang and J. Li, *Int. J. Mol. Sci.*, 2021, **22**, 12942.
93. X. Wen, Z. Q. Lin, B. Liu and Y. Q. Wei, *Cell Prolif.*, 2012, **45**, 217–224.
94. K. González-Arzola, A. Velázquez-Cruz, A. Guerra-Castellano, M. Á. Casado-Combreras, G. Pérez-Mejías, A. Díaz-Quintana, I. Díaz-Moreno and M. A. De la Rosa, *FEBS Lett.*, 2019, **593**, 3101–3119.
95. S. Jamil, I. Lam, M. Majd, S. -H. Tsai and V. Duronio, *Cancer Cell Int.*, 2015, **15**, 1–11.
96. A. Mondal and L. L. Bennett, *Biomed. Pharmacother.*, 2016, **84**, 1906–1914.

## **CHAPTER - V**

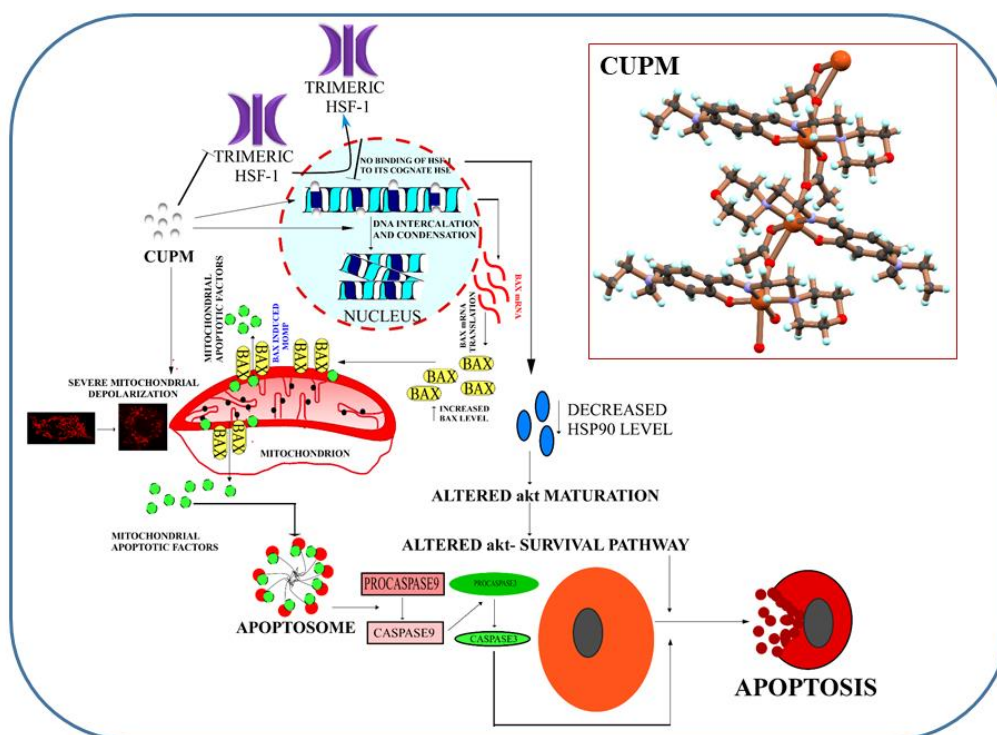
**Synthesis of acetate bridged copper(II) 1D  
polymer containing morpholine based NNO  
donor Schiff base ligand: Exploration of potential  
catalytic and biological activity**



## *Synthesis of acetate bridged copper(II) 1D polymer containing morpholine based NNO donor Schiff base ligand: Exploration of potential catalytic and biological activity*

### Abstract

Herein we have report a new one dimensional Cu(II) coordination polymer (**CUPM**) fabricated from a morpholine based NNO donor ligand, (E)-5-(diethylamino)-2-(((2-morpholinoethyl)imino)methyl)phenol (**L**). The ligand as well as the complex were methodically characterized by NMR, IR, mass, and UV-vis spectral studies. The stability of the coordination polymer was checked by UV-Vis, TGA, PXRD techniques. The bio-inspired catalytic activity of the synthesized polymer was spectrophotometrically evaluated for the aerial oxidation of 3,5-di-tert-butylcatechol (3,5-DTBC) in acetonitrile. The biological activity of **CUPM** towards DNA and BSA protein were thoroughly investigated by several spectral studies like UV-Vis, fluorescence and viscosity study, the results of which show great binding affinity of **CUPM** towards DNA and BSA proteins. Furthermore, the biological assessment of **CUPM** as a potent anticancer drug candidate was focused against MDA-MB-231, a human TNBC (triple negative breast cancer) cell line, and the mechanism of its cytotoxicity has been assessed and explained via various biochemical assays and imaging techniques.





## V.1. Introduction

One of the fastest developing fields of research in the recent era, is the application of coordination polymers in the area of chemistry, physics, biology, and material science.<sup>1-5</sup> Coordination polymers are captivating, extremely methodical, malleable solid hybrid materials created by metal ions cluster and organic ligands in an extended assortment.<sup>6,7</sup> These compounds have the potential of application in a vast range of areas including device production, absorption and separation of gases, magnetic resources, catalysis, ion exchange, drug delivery, identification of selected molecules, etc. due to their diverse structural capacity.<sup>8-15</sup> Amid numerous homonuclear polymeric coordination complexes, Cu(II)-azido coordination complexes are one of the furthestmost fascinating and common systems for chemists owing to their adaptable and discrete structural dimensionality and tractability of Cu(II) ions in coordination numbers and geometries.<sup>16-18</sup> Alternatively, NNO donor Schiff base ligands have been extensively used for fabricating several homonuclear polymeric coordination complexes when distinguishable co-ligands like azido, thiocyanato, cyanato, carboxylato etc. are present.<sup>19-22</sup>

The exponential growth of cancer has become a foremost universal challenge to human wellbeing.<sup>23-25</sup> Breast cancer (BC) caseload is thought to cross the grim mark of 2 million cases by 2030; and in India, BC, especially triple negative breast cancer (TNBC) claimed 90,408 deaths, or 10.6% of the total cancer load in the country in 2020.<sup>26-28</sup> However, a methodical breast cancer treatment still faces a major blockage. Among numerous accessible cancer cure alternatives, chemotherapy is a prized option in most cases owing to its high effectiveness.<sup>29</sup> In order to cure several different types of cancers, various platinoids, viz., oxaliplatin, carboplatin, cisplatin, etc., have been in clinical use for a very long time although there still remain some rigorous side effects that include neurotoxicity, ototoxicity, nephrotoxicity and cardiotoxicity.<sup>30-32</sup> However, in recent years, research, screening, and testing of other metal-containing prospective chemotherapeutic agents has gained momentum. This range of metal-based candidates excluding platinum, and predominantly being transition metals, have proved to pose a tough fight against cancer.<sup>33</sup>

In order to fabricate first-hand cancer therapeutics, metal complexes lead the way in the drug advancement field.<sup>34-37</sup> A new category of chemotherapeutic agents have emerged from the field of inorganic chemistry, touted as medicinal inorganics, since the effective application of platinum-based anticancer drugs.<sup>38-41</sup> However, as their disadvantages (low solubility, elevated price, toxicity and multifactorial resistance) constrain the worldwide usability of

platinum-based anticancer drugs in chemotherapy,<sup>42-44</sup> copper has emerged as a fine platinum-alternative among the series of extensively researched biologically significant metals. The significant metabolic effects of copper along with its homeostatic effects obtained in studies on a range of cancer types, in addition to distinctive selectivity toward malignant cells are responsible for selecting copper as a major substitute metal.<sup>45-50</sup> A huge array of copper complexes have been developed in this regard in order to get reviewed as anticancer agents.<sup>51-54</sup>

Copper-based therapeutics have attracted significant amount of interest as platinum-alternatives given that copper is an essential feature of organisms as a noteworthy constituent of the active sites of several metalloproteins like hemocyanin, catecholase and tyrosinase.<sup>55-57</sup> Therefore, based on the idea that normal cells are toxicologically very little affected by endogenous metals unlike cancer cells, as well as, normal and cancer cellular responses towards copper ions are different, copper complexes have been monitored for cancer chemotherapeutics.<sup>58</sup> Moreover owing to its oxidoreduction activity, copper could be deadly when bioaccumulated in increased concentrations. Also, in case of cancers of the breast, prostate, lung, and brain, the rate of absorption of copper is found to be amplified in cells showing neoplastic tendencies, thereby allowing its complexes further selectivity towards cancer cells. It is to note that, most cancer therapeutics find DNA to be their core target. The interactions between DNA and candidate drugs hamper DNA replication thus averting the unrestrained growth of malignant cells.<sup>59-62</sup> The fact that bivalent copper Cu(II) can coordinate to guanine in DNA via its N-7 atom is an invigorative finding, along with the information that the specific oxidoreductive activity of Cu(II) smoothens ROS (reactive oxygen species) production, eventually causing DNA damage and subsequent apoptosis. Many copper complexes have been recognized with a method of action that may help in resolving the drug resistance crisis, to be pitched as alternatives to platinum-based therapeutic agents which are effluxed from cancer cells/ cancer cells develop resistance to them.<sup>58,59</sup> Such copper complexes have good potential for utilization in the fabrication of cancer therapeutics. Tumor growth has also been reported to be hindered by several Cu (II) complexes *in vivo*.<sup>63</sup> Thus, copper complexes have turned out to be a novel promising cancer chemotherapeutic agent, despite that their mechanism of anticancer activity has not been recognized indisputably as of yet.

Lately, fast development and discovery in the metallopolymer field, that might have massive prospect for manufacturing optimistic-properties bearing materials, has been established.<sup>64,65</sup> Inspection of the therapeutic potentialities of various metallopolymer in treatment of cancer

has taken noteworthy strides.<sup>66-68</sup> Until now, the development, design and fabrication of copper-based potentially chemotherapeutic metallopolymer has seen significant advancements.<sup>69</sup> In this work, we have designed a morpholine based NNO donor Schiff base ligand, (*E*)-5-(diethylamino)-2-(((2-morpholinoethyl)imino)methyl)phenol (**L**) to fabricate a new one dimensional copper(II) coordination polymer (**CUPM**). The ligand and the coordination complex were characterized by UV-Vis, IR, NMR, and mass spectral studies, beside SCXRD (single crystal X-ray diffraction) analyses. The interactions of **CUPM** with DNA and BSA protein were investigated thoroughly along with the catecholase activity of **CUPM**. The DFT (density functional theory) and TD-DFT (time dependent density functional theory) studies were performed to elucidate the electronic structure and UV-vis spectra of the polymer. Cytotoxicity analyses of **CUPM** against cancer cells were focused on human triple TNBC (triple negative breast cancer) cells MDA-MB-231. The mechanism of the cytotoxic activity was explained in detail via cell viability studies, live cell imaging, FESEM, FACS based MMP disruption and ROS generation studies, simulation and biophysical studies, and immunoblotting.

## V.2. Experimental

### V.2.1. Reagents and physical measurements

All reagents and solvents used in this synthesis were purchased from Aldrich. All other organic chemicals and inorganic salts were available from commercial sources and used without further purification. <sup>1</sup>H and <sup>13</sup>C NMR spectra were recorded on Bruker 300 MHz instrument in CDCl<sub>3</sub>. Chemical shifts are expressed in  $\delta$  units and <sup>1</sup>H-<sup>1</sup>H and <sup>1</sup>H-C coupling constants in Hz. HRMS mass spectra were recorded on Waters quadrupole time-of-flight mass spectrometer (Xevo G2 Q-TOF). Electronic spectra were taken on a Shimadzu UV-1900i spectrophotometer. IR spectra were recorded on a Perkin-Elmer Spectrum Two FT-IR Spectrometer (4000–400 cm<sup>-1</sup>). Powder X-ray diffraction (PXRD) was measured on a Bruker D8 ADVANCE X-ray diffractometer instrument using Cu K $\alpha$  radiation ( $\lambda = 10548 \text{ \AA}$ ) at 40kV and 40 mA in a  $2\theta$  range of 5–50°. On a PerkinElmer Pyris Diamond TG/DTA instrument, thermal stability was measured under nitrogen atmosphere (20 mL/min) using platinum crucible with alpha alumina powder in a temperature range of 30–800 °C at 10 °C/min.

## V.2.2. Synthesis

### V.2.2.1. Synthesis of (E)-5-(diethylamino)-2-(((2-morpholinoethyl)imino)methyl)phenol (**L**)

To a solution of 4-(diethylamino)-2-hydroxybenzaldehyde (0.37 g, 1.915 mmol) in ethanol (10 mL), 4-(2-ethylamino)morpholine (0.25 g, 1.915 mmol) was added. The solution was refluxed for 4 h. The reaction mixture was cooled to room temperature and evaporated. After cooling to room temperature, the reaction mixture was allowed to evaporate completely to yield a solid product. Yield was 0.467 g, 80%.

Anal. Calc. for  $C_{17}H_{27}N_3O_2$ : C, 50.25; H, 4.40; N, 10.19. Found: C, 49.97; H, 4.21; N, 9.95.  $^1H$  NMR (300 MHz,  $CDCl_3$ ):  $\delta$  1.23 (t,  $J = 7.14$  Hz, 6H), 2.56-2.64 (m, 6H), 3.39-3.46 (m, 4H), 3.68-3.75 (m, 6H), 6.09 (s, 1H), 6.28 (d,  $J = 8.85$  Hz, 1H), 7.28 (d,  $J = 8.85$  Hz, 1H), 8.19 (s, 1H), 10.35 (s, 1H).  $^{13}C$  NMR (75 MHz,  $CDCl_3$ ) in ppm:  $\delta$  12.58, 44.82, 66.45, 67.24, 96.64, 104.37, 111.37, 135.39, 154.21, 164.37, 191.89. HRMS: calculated for  $C_{17}H_{27}N_3O_2$   $[M + H]^+$  ( $m/z$ ) = 306.2182; found = 306.1221. IR ( $cm^{-1}$ ) in KBr: 3340  $\nu$ (O-H); 2971, 2929, 2852, 2815  $\nu$ (C-H); 1610  $\nu$ (C=N). UV-Vis (in  $CH_3CN$ ),  $\lambda_{max}$  ( $\epsilon$ ,  $M^{-1}cm^{-1}$ ): 344 (54961).

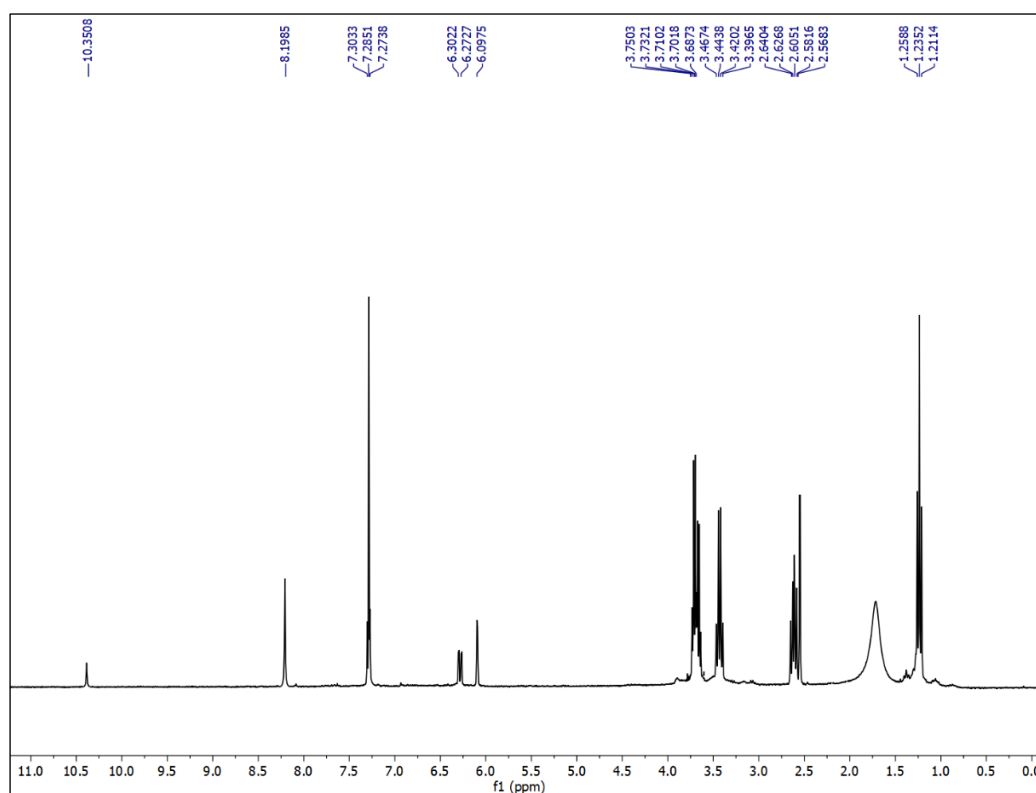


Figure V.1.  $^1H$ -NMR spectrum of ligand (**L**) in  $CDCl_3$

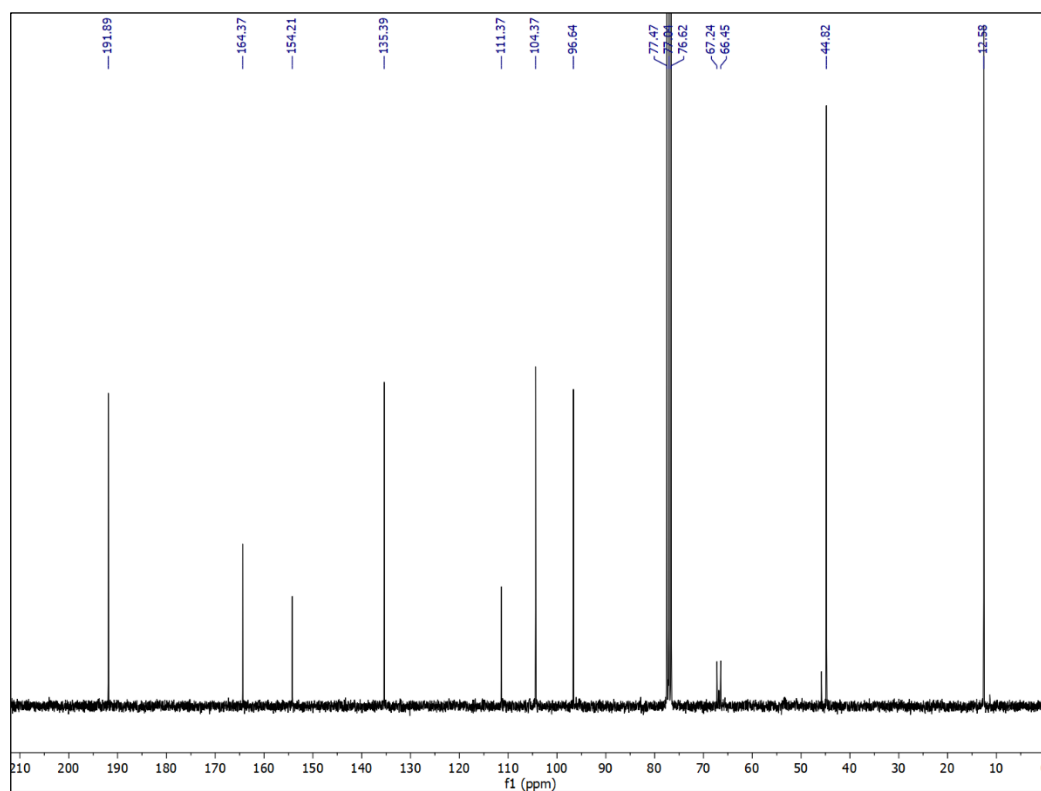
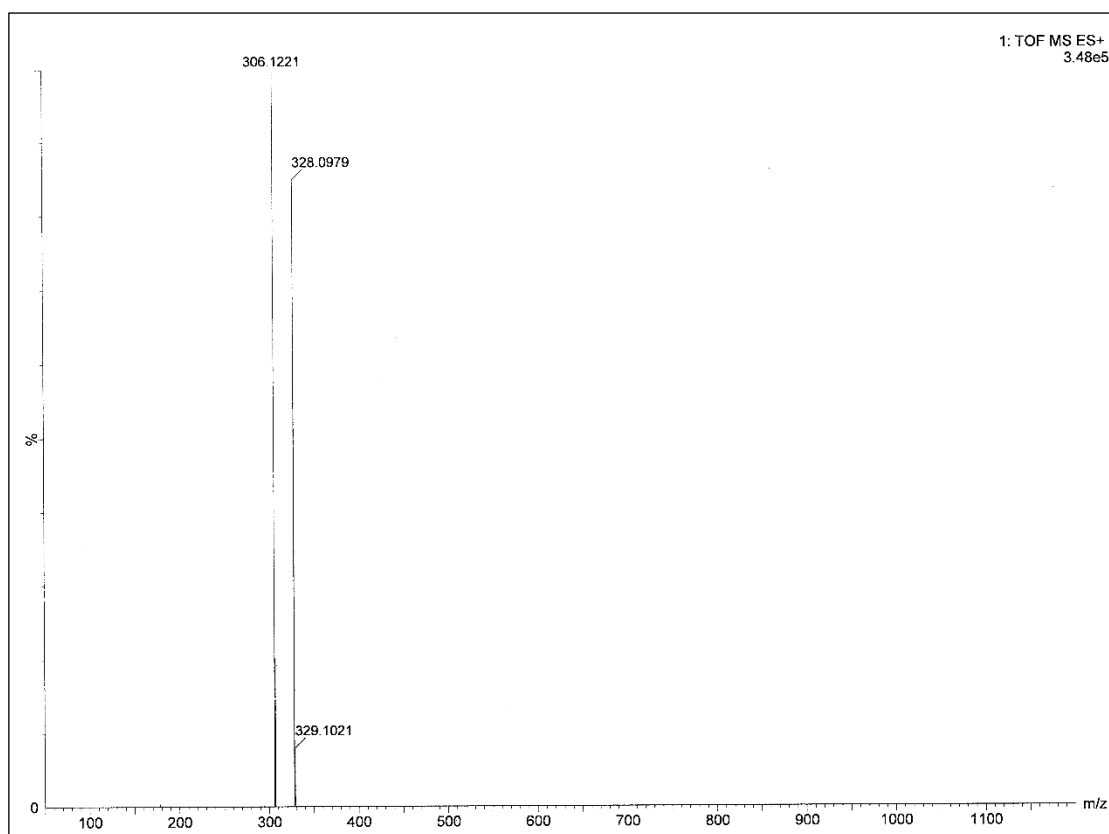
Figure V.2.  $^{13}\text{C}$  NMR spectrum of ligand (L) in  $\text{CDCl}_3$ 

Figure V.3. HRMS of ligand (L)

### V.2.2.2. Synthesis of copper polymer (CUPM)

To a methanolic solution (8 ml) of the ligand **L** (0.244 g, 0.8 mmol), a solution of copper acetate monohydrate  $[\text{Cu}(\text{OAc})_2 \cdot \text{H}_2\text{O}]$  (0.16 g, 0.8 mmol) in methanol (7 ml) was added. Then the mixture was refluxed for 12 h. After cooled to room temperature, green solution was filtered and filtrate part was kept at R.T for slow evaporation of solvent. After one week, green crystal were obtained and suitable for X-ray crystallography study. Yield: 0.27 g, 76%. Anal. calc. for  $\text{C}_{19}\text{H}_{29}\text{CuN}_3\text{O}_4$ : C, 42.12; H, 5.26; N, 24.6. Found: C, 42.26; H, 5.30; N. HRMS: calculated for  $\text{C}_{17}\text{H}_{26}\text{CuN}_3\text{O}_2 [\text{M} - \text{H}]^+$  (m/z): 367.1321; found: 367.0913. UV-Vis (in  $\text{CH}_3\text{CN}$ ),  $\lambda_{\text{max}}$  ( $\epsilon$ ,  $\text{M}^{-1}\text{cm}^{-1}$ ): 214 (61283), 238 (58448), 360 (87661), 633 (902). IR ( $\text{cm}^{-1}$ ) in KBr: 2965, 2923, 2898, 2862  $\nu(\text{C-H})$ ; 1597  $\nu(\text{C=N})$ ; 1337  $\nu(\text{C-O phenol})$ .

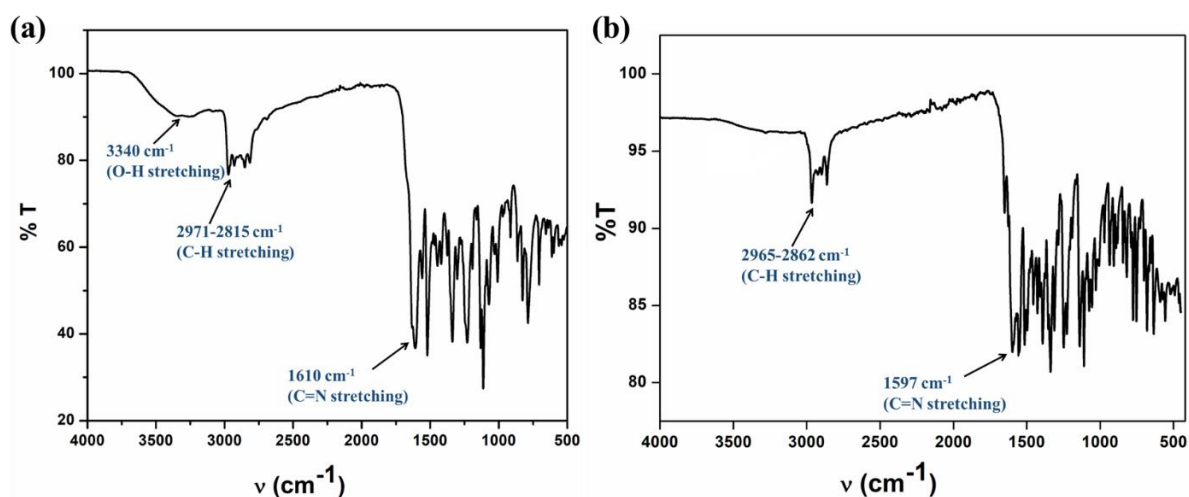


Figure V.4. IR spectra of (a) ligand and (b) CUPM

### V.2.3. X-ray crystallography

The X-ray diffraction data was collected using Bruker AXS D8 Quest CMOS diffractometer using graphite monochromatized  $\text{Mo-K}\alpha$  radiation ( $\lambda = 0.71073 \text{ \AA}$ ) at 293 K. The data integration and reduction were carried out with the SAINT program,<sup>70</sup> and the absorption corrections were made with SADABS.<sup>71</sup> Reflection data were recorded using the  $\omega$  scan technique. All data were corrected for Lorentz and polarization effects, and the non-H atoms were refined anisotropically. Hydrogen atoms were included in the refinement process as per the riding model. The structures were solved by direct method and refined using SHELXL-2016/6 program<sup>72</sup> by full-matrix least-squares techniques.

### V.2.5. Catecholase activity

Catalytic activity of the present polymeric Cu(II) complex **CUPM** towards the aerial oxidation of the substrate 3,5-ditert-butyl catechol (3,5-DTBC) to 3,5-di-tert-butyl-o-quinone (3,5-DTBQ) was explored spectrophotometrically under aerobic conditions at 298K. The kinetic parameters were estimated by capturing the steady growth of characteristic absorption intensity around 400 nm which corresponds to the oxidation product 3,5-DTBQ. Because the substrate, complexes, and their products are extremely soluble in acetonitrile, all the studies were carried out in this medium.  $10^{-5}$  (M) solution of complex was reacted with at least 100-fold more concentrated substrate to maintain pseudo-first order reaction conditions.<sup>73</sup> The rate of a reaction was determined from the initial rate method and catalytic rate constant values were evaluated applying Michaelis–Menten enzyme kinetics and Lineweaver–Burk double reciprocal plots.<sup>74</sup> Blank experiments without catalyst (complex) were also performed under identical conditions to discard the phenomenon of auto-oxidation of the substrate by air.

#### V.2.5.1. Rationalization of kinetic parameters

The kinetics of 3,5-DTBC oxidation to 3,5-DTBQ catalysed by **CUPM** was estimated using the initial rate method, recording the amplification of 400 nm absorption intensity at 298K. For a set of catalyst–substrate concentration, the rate constant was calculated by plotting  $\Delta A$  (change in absorbance at 400 nm) vs.  $t$  (time). The conversion of the reaction rate units from  $\Delta A/s$  to  $M/s$  was done using  $\epsilon$  value  $1630\text{ M}^{-1}\text{cm}^{-1}$  for DTBQ.<sup>75</sup>

One demo calculation of catecholase activity of **CUPM** was demonstrated below:

$1 \times 10^{-5}$  (M) acetonitrile solution of complex **CUPM** was mixed with  $4 \times 10^{-3}$  (M) solution of 3,5-DTBC in acetonitrile at 298K under aerobic conditions. The concentration of the catalyst as well as the substrate are halved after mixing; i.e,  $[\text{catalyst}] = 5 \times 10^{-6}$  (M) and  $[\text{DTBC}] = 2 \times 10^{-3}$  (M).

Slope of “ $\Delta A$  (change in absorbance at 400 nm) vs.  $t$  (time)” plot = Rate  $(\frac{dA}{dt}) = 0.014010499\text{ min}^{-1}$  (See Fig. 13).

$$\text{Rate (V)} = \frac{1}{\epsilon L} \times \frac{dA}{dt} = \frac{0.014010499\text{ min}^{-1}}{(1630\text{ M}^{-1}\text{cm}^{-1}) \times 1\text{cm}} = 8.59 \times 10^{-6}\text{ M.min}^{-1}$$

So, at  $[\text{DTBC}] = 2 \times 10^{-3}\text{ M}$ ;  $V = 8.59 \times 10^{-6}\text{ M.min}^{-1}$

$$\frac{1}{\text{DTBC}} = 500\text{ M}^{-1}; \frac{1}{V} = 1.16 \times 10^5\text{ M}^{-1}.\text{min}$$

Now keeping the catalyst (here **CUPM**) concentration constant ( $5 \times 10^{-6}$  M), the substrate (3, 5-DTBC) concentration was varied from  $10^{-3}$  (M) to  $10^{-2}$  (M) to explore the rate dependence on the substrate concentration. Lineweaver–Burk (double reciprocal) plot was constructed to extract all the kinetic parameters, such as the maximum initial reaction rate ( $V_{max}$ ), Michaelis–Menten binding constant ( $K_M$ ) and turnover numbers ( $K_{cat}$ ) which are shown below:

$$V_{max} = 1.84 \times 10^{-5} \text{ M} \cdot \text{min}^{-1}$$

$$K_M = 2.31 \times 10^{-3} \text{ M}$$

$$K_{cat} = \frac{V_{max}}{C_0} = \frac{1.84 \times 10^{-5} \text{ M} \cdot \text{min}^{-1}}{5 \times 10^{-6} \text{ M}} = 3.68 \text{ min}^{-1} = 220.8 \text{ h}^{-1}$$

### V.2.6. DNA interaction studies

The interaction of **CUPM** with CT DNA has been carried out by UV-Vis absorption spectroscopy to calculate the binding constant to CT DNA. The  $K_b$  value has been determined for a constant concentration ( $2.49 \times 10^{-6}$  M) of **CUPM** in the absence or presence of CT DNA using Wolfe–Shimer eqn. (1),<sup>76</sup> from the plot of  $[DNA]/(\epsilon_a - \epsilon_f)$  versus  $[DNA]$ , where  $[DNA]$  represents the concentration of DNA, and  $\epsilon_a$ ,  $\epsilon_f$  and  $\epsilon_b$  represents the apparent extinction coefficient ( $A_{obs}/[CUPM]$ ), the extinction coefficient for free **CUPM**, and the extinction coefficient for **CUPM** when fully bound to CT DNA respectively.

$$[DNA]/(\epsilon_a - \epsilon_f) = [DNA]/(\epsilon_b - \epsilon_f) + 1/K_b(\epsilon_a - \epsilon_f) \quad (1)$$

The competitive studies of **CUPM** with EB were investigated with fluorescence spectroscopy in order to examine whether the compound can displace EB from its EB-CT DNA complex. The EB-CT DNA adduct was prepared by adding 15  $\mu$ M EB and 30  $\mu$ M CT DNA in buffer (Tris-HCl/NaCl buffer at pH 7.4). The influence of the addition of **CUPM** to the EB-CT DNA complex solution has been obtained by recording the variation of the fluorescence emission spectra, the observed quenching is attributed to the displacement of EB from its EB-CT DNA adduct. The Stern–Volmer plots of EB-CT DNA have been used in order to study the quenching of EB bound to DNA by the compound according to the linear Stern–Volmer equation (2).

$$F_0/F = 1 + K_{sv} [Q] \quad (2)$$

where  $F_0$  and  $F$  are the emission intensity in the absence and presence of the quencher,  $[Q]$  is the concentration of the added quencher, and  $K_{sv}$  is the quenching constant.



The viscosity of the CT-DNA solution (34.8  $\mu\text{M}$ ) was measured by increasing the concentration of **CUPM** using an Ostwald viscometer placing in a thermostated water bath at 20.0  $^{\circ}\text{C}$ . Flow time has been measured three times for each concentration of the compound and then the average flow time was calculated. Viscosity values were calculated from the observed flow time of DNA-containing solutions ( $t$ ) corrected for the flow time of buffer alone ( $t_0$ ),  $\eta = t - t_0$ . The data is reported as  $(\eta / \eta_0)^{1/3}$  versus the ratio of the concentration of the compound to CT-DNA ( $R$ ), where  $\eta$  is the viscosity of CT-DNA in the presence of the compound and  $\eta_0$  is the viscosity of CT-DNA solution alone.

### V.2.7. Protein binding studies

The interaction of BSA protein with **CUPM** were studied by emission spectroscopy. A BSA solution (10  $\mu\text{M}$ ) was prepared by using phosphate buffer saline (PBS) at pH 7.4 and stored in the dark at 4 $^{\circ}$  C. The **CUPM** solution (25  $\mu\text{M}$ ) was prepared in DMSO solvent and was suitably diluted with PBS whenever necessary. The fluorescence titration was done at a constant BSA concentration by increasing the concentration of **CUPM**. In fluorescence experiment, tryptophan fluorescence of BSA was recorded in the range 290–500 nm at an excitation wavelength of 280 nm. For synchronous fluorescence spectra, the same concentrations of BSA and the complex were also used and the spectra were measured at two different  $\Delta\lambda$  values (difference between the excitation and emission wavelengths of BSA), such as 15 and 60 nm.

The 3D fluorescence spectra of BSA were recorded with and without complex. To a fixed concentration of BSA solution, 10  $\mu\text{M}$  of **CUPM** was added and the 3D fluorescence spectra were recorded by scanning excitation wavelength in the range of 200–400 nm and emission wavelength from 200 to 500 nm at an interval of 2 nm. The scanning parameters were the same as in the fluorescence quenching experiments.

### V.2.8. Cytotoxicity studies

#### V.2.8.1. Cell culture

Human TNBC MDAMB-231 and normal kidney epithelial (NKE) cells were firstly cultured in DMEM (Dulbecco's modified eagle medium) that was supplemented with growth serum (10% fetal bovine serum; FBS), antibacterial and antifungal agents (50  $\mu\text{g/ml}$  pen-strep (penicillin + streptomycin), gentamycin (50 mg/ml), amphotericin B (2.5  $\mu\text{g/ml}$ )), and other growth agents viz., 1 mM L-glutamine and non-essential amino acids, and were maintained at 37 $^{\circ}\text{C}$  and 5%  $\text{CO}_2$  in a humidified incubator.

**V.2.8.2. Cell viability assay**

To determine the cytotoxicity of the prepared polymer **CUPM**, a cell viability assay was done using MTT reagent [3-(4,5-diethylthiazol-2-yl)-2,5- diphenyltetrazolium bromide]. Briefly, MDAMB-231 were seeded onto 48-well cell culture plates and maintained according to protocol stated above. Upon reaching 70% confluency, they were treated with the compound at various concentrations and vehicle (DMSO). 24 hours following treatment, cells were subjected to MTT incubation (Himedia-RM1131) for 4 hours (MTT solution concentration = 0.5 mg/ml). After completion of incubation, the cells were further treated with DMSO after discarding MTT solution. Finally, a plate reader was used to analyze OD of the cells at 570 nm. The MTT assay was carried out multiple times to get an idea about the concentration-dependent effects of the compound, based on whose results, further experiments were conducted. Each experiment was performed in triplicate.

**V.2.8.3. Clonogenic assay**

6-well culture plates were used to seed MDAMB-231 cells (500 cells/well), and 1.5 ml growth media supplementation was done per well. They were treated with DMSO (vehicle) or varying **CUPM** concentrations for 24 hours. The cells were left to incubate in freshly supplemented media for 6 division cycles, following which formaldehyde (3.7%) fixation and crystal violet (0.05% in 20% methanol) (SRL, India) staining was carried out solution for 1 hour. After thorough washing of excess stain in 1X PBS, the cells were dried, following which, they were imaged in a Gel-Doc system (Biorad). Image analysis and estimation of band densities were later carried out via Image J.

**V.2.8.4. Scratch assay**

Scratch, or wound-healing assay was carried out in the *in vitro* system to study the anti-migratory capacity of **CUPM**, if any. Briefly, a 12-well culture plate was used to grow MDAMB-231 cells until they were 70% confluent, following which, a scratch was introduced across the well surfaces using a 20  $\mu$ l pipette tip. PBS was used to thoroughly wash each well so that the loose cells uprooted in the scratched area are removed. The remaining cells were treated with desired **CUPM** concentrations, and incubated for 24 hours in a 5% serum supplemented growth medium. The scratch width was viewed and photographed under a microscope (phase-contrast; Leica) at time  $t_0$ , that is, immediately after the scratch, and then at time points  $t_1$  and  $t_2$ , that is, the end of the incubation period at 24 hours and 48 hours respectively.

**V.2.8.5. Chromatin condensation assay**

**CUPM** induced chromatin condensation of live MDA-MB-231 cells was assessed by nuclear stain, Hoechst 33342. About 8000 cells were seeded in confocal dishes and next day cells were treated with 25µg/ml of **CUPM** and/or DMSO (vehicle control) for 12h and then the cells were washed with 1xPBS and incubated with 5µg/ml of hoechst33342 and visualized through Leica stellaris 5 super resolution confocal microscope.

**V.2.8.6. Cell cycle analysis**

Flow cytometry was used to analyze cell cycle by staining cells with propidium iodide (PI). Briefly, MDAMB-231 cells were grown in growth supplemented media in 6-well plates ( $\sim 3 \times 10^5$  cells/well) up to 70% confluency, after which, they were treated with desired **CUPM** concentrations and incubated for one division cycle (24 hours). They were then harvested by trypsinization, and fixed in chilled ethanol (80%) by keeping at  $-20^{\circ}\text{C}$  for 16 hours. After this, the fixed cells were subject to PBS washing (1X, chilled) and resuspension; before 2 hours of incubation at  $4^{\circ}\text{C}$ . RNA degradation followed this step, using 20 µM RNase A treatment and incubation at  $37^{\circ}\text{C}$  for 2 hours. Finally, PI staining was performed (5 µl PI) on the cells and kept for not more than 20 minutes, before being analyzed for cell cycle determination by a BD-FACS Verse analyser.

**V.2.8.7. Apoptosis**

Apoptotic potential of **CUPM** was studied via flow cytometric analysis of FITC-Annexin V/PI double staining on treated cells. MDAMB-231 cells were grown as per standard protocol and treated with desired concentrations of **CUPM** after reaching 70% confluency. 24 hours following treatment, the cells were trypsinized; after which, 1X binding buffer (BD Pharmingen) was used to wash and resuspend them. Following this, the experimental cells were treated with FITC-Annexin V and incubated for 25 minutes in dark conditions. Finally, they were stained with PI and subsequently analyzed via BD-FACS Verse.

**V.2.8.8. Ultrastructure analysis of CUPM treated cells**

Ultrastructure analysis of **CUPM** treated MDAMB231 cells was done by variable pressure scanning electron microscopy (SEM). Samples were prepared by using a protocol reported by Ali et al., (2021) and Heckman et al., (2007) with some necessary adjustments. Breast cancer cells MDAMB-231 were seeded ( $2 \times 10^4$  cells/cover slip) on a glass cover slip (sterilized) within a 6-well plate. Next day, **CUPM** treatment was performed on the cells in desired concentrations and cells were left to incubate for 24 hours. Following optimal incubation, the

cellular media was discarded and cells were rapidly incubated with pre-warmed (at 37°C) 3.7% glutaraldehyde (electron microscopy grade, from Merck) at room temperature for 15 minutes; no PBS wash was done in between to maintain the native structures of cells as best as possible. Then glutaraldehyde was removed and PBS wash was performed 3 times. Then the cells were treated with 1% osmium tetroxide (OsO<sub>4</sub>) (EM grade) (Sigma-Aldrich) under room temperature conditions for 15 minutes, followed by subjecting cells to PBS wash thrice. Cells were then dehydrated with gradually increasing concentrations of ethanol (molecular biology grade; Merck) (30%, 50%, 70%, 90%, and 100%) for 20 minutes for each concentration. Then hexamethyldisilazane (HMDS) treatment was performed on the cells under room temperature for 10 minutes, as a chemical alternative for critical point drying (CPD). Finally, cells were coated with platinum-palladium by a sputter-coater (Quorum 150T ES) and examined by a variable pressure scanning electron microscope (SEM; Zeiss EVO 18 special edition, Zeiss microscope, Germany).<sup>77,78</sup>

#### **V.2.8.9. Study of mitochondrial ROS (mtROS) generation**

Mitochondrial ROS generated, if any, was assessed by MitoSox Red staining. Around 8000 cells (MDAMB-231) were seeded in a confocal dish (35 mm) (SPL Life Technologies) with 200 µL media. When cells were properly seeded, the plates were flooded with 1.5 ml media. Next day **CUPM** treatment in desired concentrations was performed on the cells, along with vehicle (DMSO) and positive control (doxorubicin), and incubated for 5 hours; and then they were incubated with MitoSox Red reagent (5 µM final concentration in serum free media) (catalog no. M36007 from ThermoFisher Scientific, Waltham, MA, USA) for 30 minutes at 37°C within a humidified chamber (from OKO lab, attached with Leica Stellaris 5 super-resolution confocal microscope, Germany), and co-stained with Hoechst33342 to stain the nuclei, followed by warm PBS wash. Finally, live cell images were acquired by Stellaris 5 super-resolution confocal microscope (63X oil) (Leica Microsystems, Germany); analysis of intensity was done on LAS-X (Leica Microsystems, Germany) and represented via bar graph.<sup>79,80</sup>

#### **V.2.8.10. Determination of Mitochondrial Membrane Potential (MMP)**

The change in MMP upon treatment of MDAMB-231 cells by **CUPM** was determined by Tetramethyl rhodamine methyl ester (TMRM) staining. About 8000 MDAMB-231 cells were seeded in 35mm confocal dish (SPL Life Technologies) with 200 µL of complete media followed by addition of 1.5ml media. Next day, treatment was performed on cells with

desired concentrations of **CUPM** and /or vehicle (DMSO) along with doxorubicin (positive control); then they were incubated for 12 hours. The drug-containing media was removed and the cells were subjected to warm 1X PBS wash. Next, the cells were incubated with TMRM (final concentration to be 100 nM in serum-free media) for 30 minutes at 37°C within a humidified chamber (from OKO lab, attached with Leica Stellaris 5 super-resolution confocal microscope, Germany) (Hoechst33342 was used as nuclear stain), and this was again followed by warm PBS wash. Finally live cell images were taken via Stellaris 5 super-resolution confocal microscope (63X oil) (Leica Microsystems, Germany). The intensity was analyzed by LAS-X (Leica Microsystems, Germany) and represented with bar graph.<sup>81</sup>

#### **V.2.8.11. Immunoblot assay**

MDAMB-231 cells were harvested after treatment with vehicle/desired concentrations of **CUPM** and subsequently lysed using the cell lysis buffer prepared with 20 mM Tris-HCl (pH 7.5), 300 mM NaCl, 5% glycerol, 1% Triton X-100, in addition to 1 mM Phenylmethyl sulfonylfluoride (PMSF), 10 µg/mL aprotinin, 10 µg/mL leupeptin, 20 mM sodium orthovanadate, and 20 mM sodium fluoride. Bradford assay was used to determine the total protein concentration of the hence prepared whole-cell lysate, following protocol provided by the manufacturer (BioRad). The whole cell lysate was subsequently electrophoresed (protein concentration per sample = 50 µg) in a denaturing polyacrylamide gel (ratio of acrylamide to bisacrylamide being 29:1) and a BioRad wet transfer apparatus was used to transfer proteins to a PVDF membrane (EMD Millipore; activated with methanol). Thereafter, membranes containing proteins were blocked in a solution containing 5% BSA in PBST for 1 hour under room temperature conditions (PBST was prepared with PBS containing 2.7 mM KCl, 137 mM NaCl, 10 mM Na<sub>2</sub>HPO<sub>4</sub>, 1.8 mM KH<sub>2</sub>PO<sub>4</sub> at pH 7.4, finally supplemented with 0.1% Tween 20). After blocking, the membranes were incubated with primary antibodies of our choice (antibody dilution ratio = 1:1000) overnight, kept at 4°C. The following day, the membranes were thoroughly washed with PBST, and then further incubated with secondary antibody (anti-rabbit secondary antibody, at a dilution of 1:5000) at room temperature for 1 hour. The PVDF membranes were finally washed in PBST and developed using an ECL Western Blotting Substrate (Clarity BioRad).

### V.2.9. Biophysical studies

#### V.2.9.1. Fluorescence Polarization (FP) Assay

5'-Fluorescein Amide (FAM) labelled double-stranded oligonucleotide containing the canonical HSE sequence was used for FP assay. Single-stranded complementary oligonucleotides were purchased from Sigma-Aldrich and annealed before use. Proteins (trimeric/oligomeric form of human HSF1 and HSF1-DBD) were titrated against 1nM labelled oligo, both in the absence and presence (10 $\mu$ M) of **CUPM** in HSF1 buffer [25mM HEPES-NaOH (pH 7.4), 150mM NaCl & 10% (v/v) glycerol]. Fluorescence Polarization values were noted for each concentration of protein using a Horiba Nanolog spectrofluorometer. These values were then plotted against protein concentrations to obtain a binding curve, and the dissociation constant ( $K_d$ ) value was obtained using a one-site-specific binding fit of the curve in GraphPad Prism 5.<sup>82</sup>

#### V.2.9.2. Dynamic Light Scattering (DLS) Assay

DLS assay was done to determine the oligomeric status of trimeric/oligomeric HSF1 protein in the absence and presence of **CUPM** in the above mentioned HSF1 buffer. For this purpose, Zetasizer Nano S (Malvern Instruments, UK) was used. 2 $\mu$ M protein was used for the assay, and the final concentration of **CUPM** was kept at 10 $\mu$ M. Scans were obtained at 25°C. Each data was an average of 10 scans. The protein's hydrodynamic radius was computed by the instrument's software using the standard Stokes-Einstein equation.

#### V.2.9.3. Bioinformatics studies

Open Babel was used for conversion of different file formats, needed in different softwares.<sup>83</sup> AutoDock tool was used for PDBQT generation and AutoDock Vina was used for molecular docking.<sup>84</sup> Pymol was used for visualization of protein-ligand interactions. The X-Ray crystallographic structure of Heat Shock Factor-1 DNA Binding Domain (HSF-1 DBD) with PDBID, 5D5U was downloaded from protein category under site [www.ncbi.nlm.gov](http://www.ncbi.nlm.gov) (which is a 1-123 amino acid-residue containing domain of HSF-1 protein, located at N-terminal end of the protein); along with that, shelx.cif was prepared and arranged for *in silico* process as ligand, and then the said ligand was docked with 5D5U PDB. After docking of drug, the first conformation was taken as best, which was already reflected in the log table generated by AutoDock Vina.

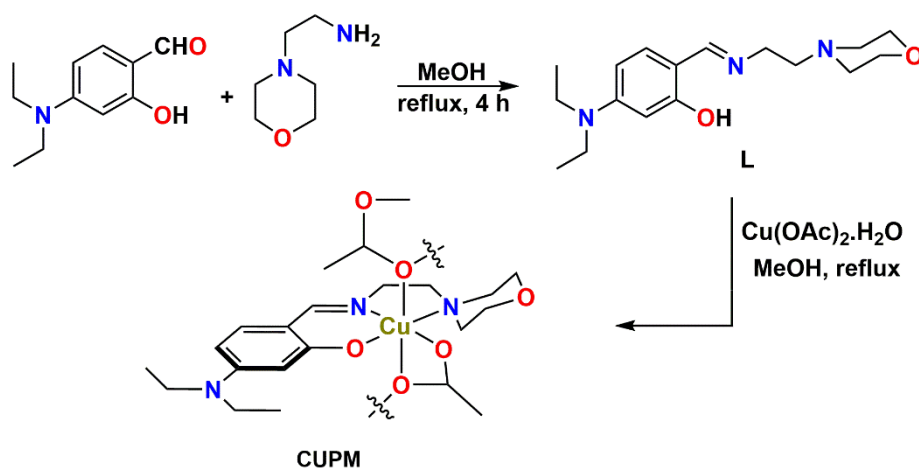
#### V.2.9.4. Statistical analysis

Graphs for each observation were plotted and analysed for statistical significance using GraphPad Prism 8.0 software by one-way or ANOVA method. Individual data points in box-plots as well as error bars were plotted as per mean  $\pm$  SD. Only those values were taken to be significant statistically, were those with a P value  $< 0.05$ .

### V.3. Results and Discussion

#### V.3.1. Synthesis and Characterization of the Cu(II) polymer (CUPM)

The 1D-Cu(II) polymer was generated by dissolving the ligand (E)-5-(diethylamino)-2-(((2-morpholinoethyl)imino)methyl)phenol (**L**) in methanol, to it a methanolic solution of copper acetate monohydrate  $[\text{Cu}(\text{OAc})_2 \cdot \text{H}_2\text{O}]$  was added at a molar ratio of 1:1 under reflux condition for 12 h that gave green colour crystals after slow evaporation of solvent (Scheme V.1). The 1D-Cu(II) polymer (**CUPM**) was fully characterized by elemental analysis, FT-IR spectroscopy, HRMS mass spectrometry and the chemical structure was confirmed by X-ray diffraction analysis.



Scheme V.1. Synthetic route of the ligand (**L**) and Cu(II) polymer (**CUPM**)

In IR spectra of ligand **L**, a broad band was observed at  $\sim 3340 \text{ cm}^{-1}$  which corresponded to O-H stretching. Polymer **CUPM** displayed a peak range of  $\sim 2857\text{--}2975 \text{ cm}^{-1}$  corresponding to C-H ( $\text{sp}^3$  and  $\text{sp}^2$ ) stretching. In free ligand, C=N stretching exhibited a strong band at  $1610 \text{ cm}^{-1}$  which was lifted to  $1597 \text{ cm}^{-1}$  (for **CUPM**) after the coordination of nitrogen atom with Cu metal ion and a typical peak at  $\sim 1337 \text{ cm}^{-1}$  was obtained due to the vibration of



phenolic C–O moieties (Figure V.4). The HRMS mass spectra of **CUPM** was collected in methanol and showed a characteristic molecular ion peak ( $m/z$ ) at 367.0913 associated with the  $[\text{C}_{17}\text{H}_{27}\text{CuN}_3\text{O}_2\text{--H}]^+$  molecular fragment. Another fragmented molecular ion peak was noticed at 793.1772. The characteristic molecular ion peak of the ligand (**L**) was observed at 306.1221 which was associated with  $[\text{M} + \text{H}]^+$  (Figure V.3 and V.5).

Absorption spectra of the compounds were taken in acetonitrile solution ( $10^{-5}$  M). Ligand (**L**) displayed a sharp band at 344 nm ( $\epsilon$ , 55000  $\text{M}^{-1}\text{cm}^{-1}$ ) which was due to intra-ligand charge transfer transition and confirmed the presence of imine ( $\text{HC}=\text{N}$ ) bond. The polymer showed a high energy absorption band at 360 nm ( $\epsilon$ , 87661  $\text{M}^{-1}\text{cm}^{-1}$ ) which could be attributed to the LMCT transition and this informed the coordination of ligand with Cu(II) ion. Another very low energy broad band was observed for the polymer at 633 nm ( $\epsilon$ , 902  $\text{M}^{-1}\text{cm}^{-1}$ ) which corresponded to the d–d transition (Figure V.6).

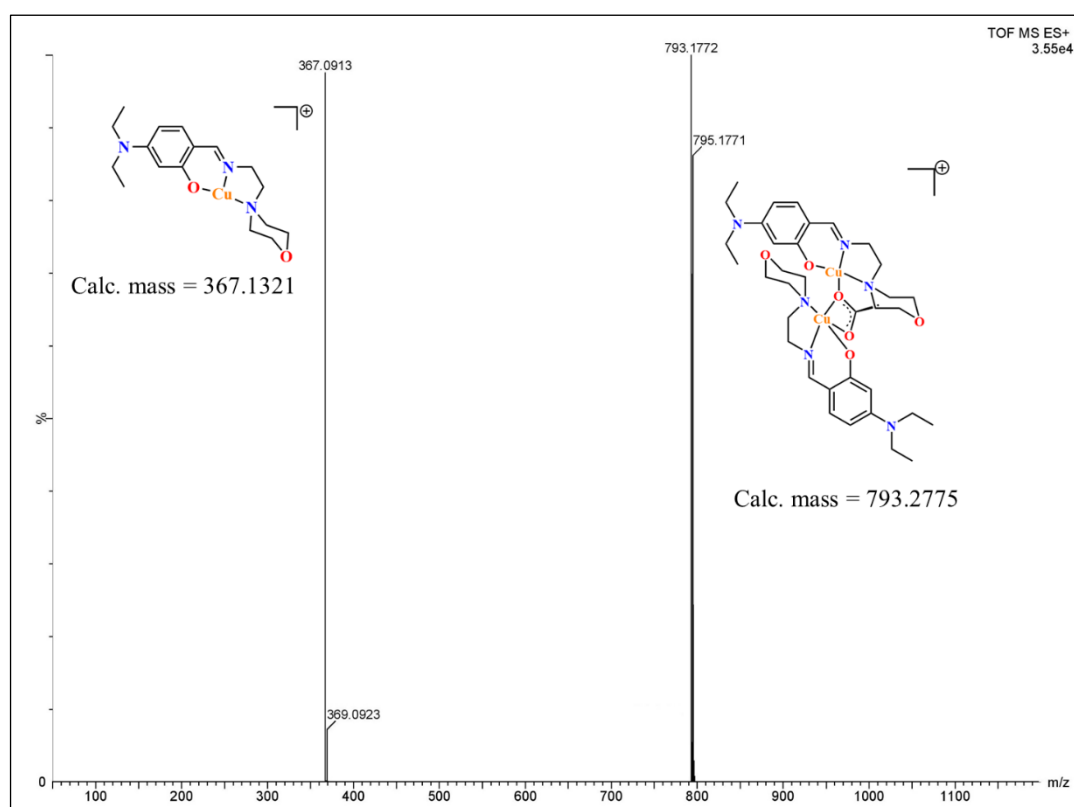


Figure V.5. HRMS of **CUPM** in methanol



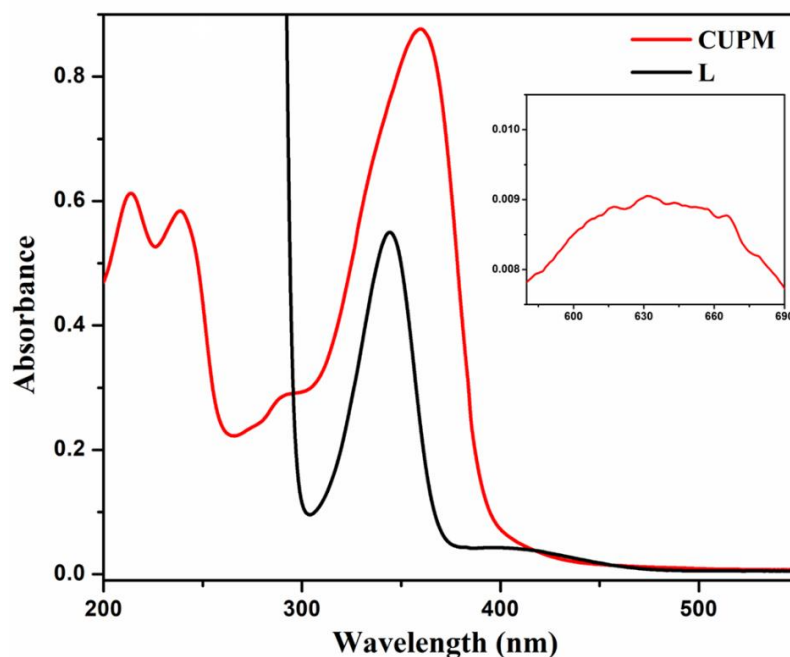


Figure V.6. Absorption spectra of ligand (**L**) and **CUPM** in acetonitrile [inset: d-d transition band at 633 nm of **CUPM**]

### V.3.2. Crystallographic study

The molecular and crystal structures of ligand (**L**) and **CUPM** were determined by single crystal X-ray diffraction method. Details of crystal analysis, data collection and structure refinement data for **L** and **CUPM** is given in Table V.1 and the ORTEP view of the compounds are given in Figure V.7 and V.8(a). Ligand, **L** crystallized in triclinic system with *P*-1 space group while **CUPM** crystallized in the monoclinic crystal system with space group *P*2<sub>1</sub>/*c*. Here the **L** served as tridentate ligand and Cu(II) ion coordinated with the ligand through imine nitrogen atom (N2), morpholine nitrogen atom (N1) and oxygen atom (O1) by the formation of one six membered chelate ring [Cu1-N2-C7-C8-C9-O1] and one five membered chelate ring [Cu1-N2-C6-C5-N1]. In the helical chain structure, acetate ion acted as bridging ligand where two oxygen atom of acetate group coordinated to Cu(II) ion. In the monomer unit Cu(II) ion was coordinated to two acetate ion where oxygen atom (O3) was situated in both the axial position of Cu(II) ion by forming a hexa-coordinated geometry where N1-N2-O1-O4 formed a square plane around the metal ion and overall structure showed a distorted octahedral geometry as the trans angles  $\angle$ N2-Cu1-O4; (169.10(16)°) and  $\angle$ O1-Cu1-N1; (174.92(15)°) were deviated from the ideal trans angle of 180° and the axial

bite angles were also turned from  $90^\circ$  [ $\angle\text{O1-Cu1-O3}$ ,  $94.19(14)^\circ$ ;  $\angle\text{O4-Cu1-O3}$ ,  $95.32(14)^\circ$ ]. The equatorial Cu1-O4 bond length ( $1.971(4)$  Å) was much shorter than axial Cu1-O3 bond distance ( $2.313(4)$  Å), which was lengthened because of the Jahn–Teller distortion. Imine bond length, N2-C7 [ $1.304(2)$  Å in ligand;  $1.272(6)$  Å in complex] was decreased after the coordination of imine nitrogen atom (N2) with Cu(II) ion which might have been because of the charge transfer from metal to ligand. Although the monomer complex units were connected in an endless chain in the structure one dimensionally with Cu–Cu distance of  $4.777$  Å (Figure V.8(b)). Here, Cu1-N2 bond distance ( $1.944(4)$  Å) was significantly shorter than Cu1-N1 bond distance ( $2.119(4)$  Å) which suggested the strong interaction of Cu(II) ion with imine nitrogen atom (N2). The selected bond distances and angles of ligand and complex are listed in Tables S3, supporting information. All the above bond distances were in well agreement with the reported values.<sup>22,58,85</sup>

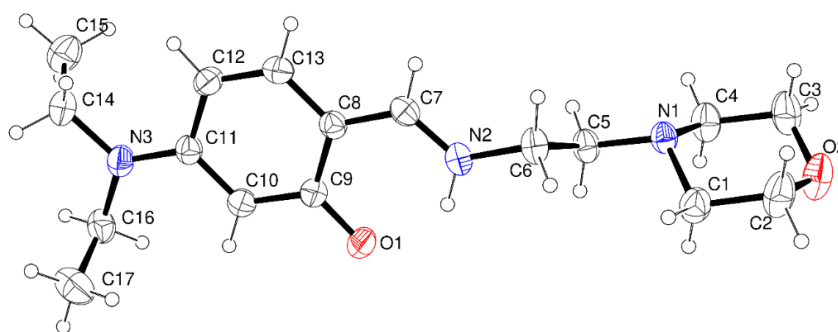


Figure V.7. ORTEP view of the ligand (**L**) with 35% ellipsoidal probability

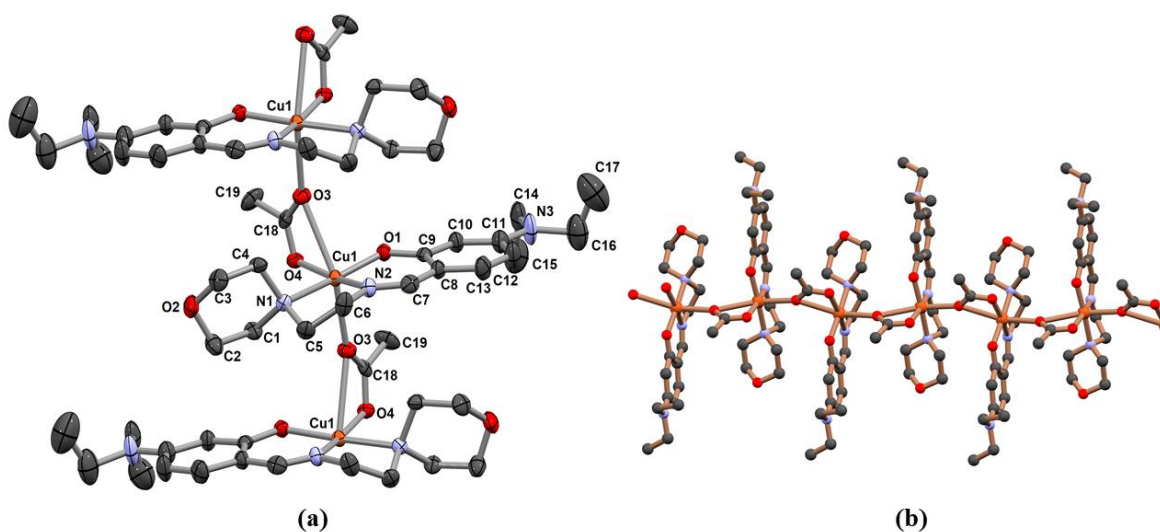


Figure V.8. (a) ORTEP view of the polymer **CUPM** and (b) One dimensional polymeric chain of the **CUPM** along *b* axis.

Table V.1. Crystallographic data and refinement parameters of the compounds

Complex	Ligand (L)	CUPM
Formula	C17 H33 N3 O5	C19 H31 Cu N3 O5
Formula Weight	359.46	445.01
Crystal System	<i>Triclinic</i>	<i>monoclinic</i>
Space group	<i>P -1</i>	<i>P 21/c</i>
a, b, c [Å]	8.2976(6), 8.5109(6), 14.9473(11)	8.771(5), 27.560(5), 9.491(5)
$\alpha$	86.856(2)	90.000(5)
$\beta$	85.220(2)	115.603(5)
$\gamma$	72.410(2)	90.000(5)
V [Å <sup>3</sup> ]	1002.24(13)	2069.0(17)
Z	2	4
D(calc) [g/cm <sup>3</sup> ]	1.191	1.429
Mu(MoKa) [ /mm]	0.087	1.090
F(000)	392	940
Temperature (K)	293(2)	293(2)
Radiation [Å]	0.71073	0.71073
$\theta$ (Min-Max) [°]	2.512 – 27.245	2.679 – 25.993
Dataset (h; k; l)	-10 to 10, -10 to 10, -19 to 19	-10 to 10, -33 to 33, -11 to 11
R, wR <sub>2</sub>	0.0614, 0.1526	0.0753, 0.1150
Goodness of fit(S)	1.040	1.074

Table V.2. Selected X-ray and calculated bond distances (Å) and angles (°) of L and CUPM

L		CUPM	
Bonds (Å)	X-ray	Bonds (Å)	X-ray
O(1)-C(9)	1.298(2)	Cu(1)-O(1)	1.939(3)
O(2)-C(3)	1.417(3)	Cu(1)-N(2)	1.944(4)
O(2)-C(2)	1.417(3)	Cu(1)-O(3)	2.313(4)
N(1)-C(5)	1.463(2)	Cu(1)-O(4)	1.971(4)
N(1)-C(1)	1.467(2)	Cu(1)-N(1)	2.119(4)
N(1)-C(4)	1.470(2)	N(1)-C(1)	1.478(6)
N(2)-C(7)	1.304(2)	N(2)-C(7)	1.272(6)
Angles (°)			
C(3)-O(2)-C(2)	110.21(17)	O(1)-Cu(1)-N(2)	92.97(17)
C(5)-N(1)-C(1)	112.03(14)	O(1)-Cu(1)-N(1)	174.92(15)
C(5)-N(1)-C(4)	110.42(13)	N(2)-Cu(1)-N(1)	83.40(17)
C(1)-N(1)-C(4)	108.36(15)	O(1)-Cu(1)-O(3)	94.19(14)
C(7)-N(2)-C(6)	124.25(17)	N(2)-Cu(1)-O(4)	169.10(16)

### V.3.3. Purity and stability of CUPM

**CUPM** readily dissolved in acetonitrile ( $\text{CH}_3\text{CN}$ ), methanol and dimethyl sulfoxide (DMSO), by forming a green colour solution but solubility in water was poor. The bulk phase purity of the polymer was checked by using powder X-ray diffraction analysis. PXRD pattern showed the high crystalline nature of the polymer and the whole pattern was in well agreement with the simulated data from single crystal X-ray data (Figure V.9). To study the anticancer activity of compounds, one of the most important factors is their stability. So, we prepared some solution of **CUPM** in  $\text{CH}_3\text{CN}$ , 50%  $\text{CH}_3\text{CN}$ /50%  $\text{H}_2\text{O}$  (v/v), DMSO, 50% DMSO/50%  $\text{H}_2\text{O}$  (v/v) and 20% DMSO/80% Tris-HCl buffer (v/v) (at pH 7.4) and studied their UV-Vis spectra. The result showed no noticeable change in absorption spectra of **CUPM** after 12 h (Figure V.10). Furthermore, Thermogravimetry analysis (TGA) was performed to ensure about the thermal stability of the polymer within the temperature range of 30–800°C under nitrogen atmosphere which showed **CUPM** was stable up to about 459 K (Figure V.11). Therefore, it could be concluded that our complex was quite stable for further studies.

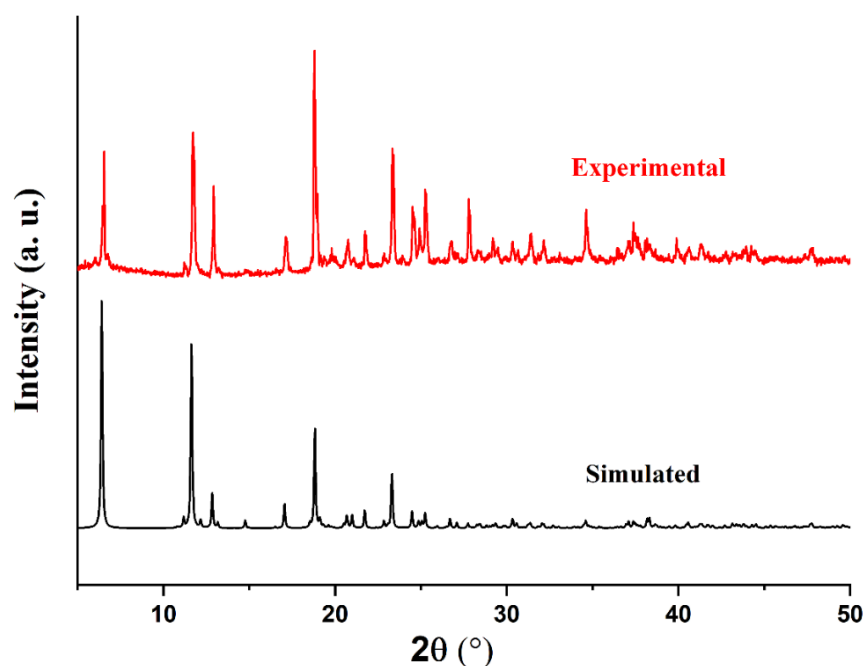


Figure V.9. PXRD plot of **CUPM**, simulated data is obtained from the crystal cif file and the experimental data is collected from powder X-ray diffraction analysis.

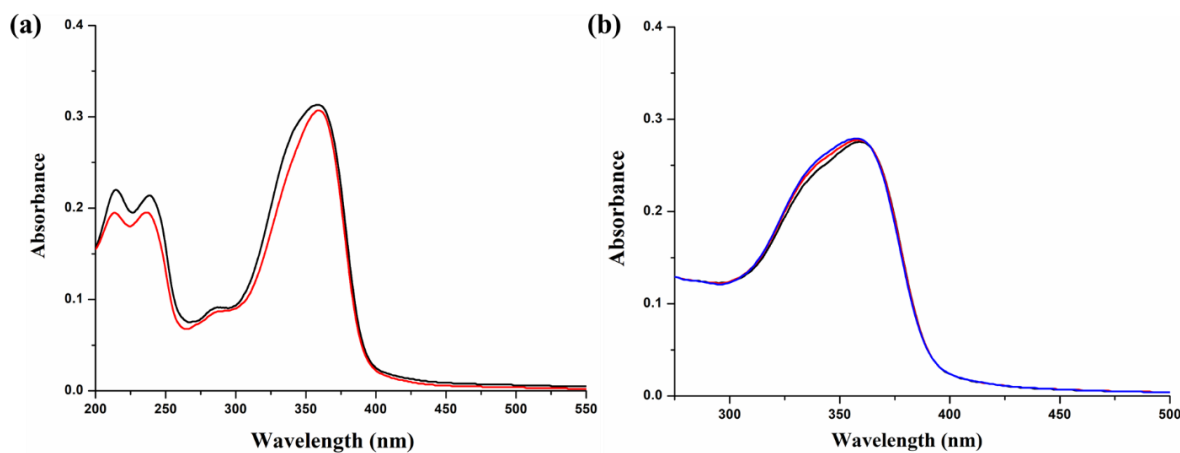


Figure V.10. Left side, UV-vis spectra of **CUPM** in ACN (black) and in 50% ACN + 50% H<sub>2</sub>O (red). Right side, UV-vis spectra of **CUPM** in DMSO (blue), in 50% DMSO + 50% H<sub>2</sub>O (red) and in 20% DMSO + Tris-HCl buffer (black) after 12h.

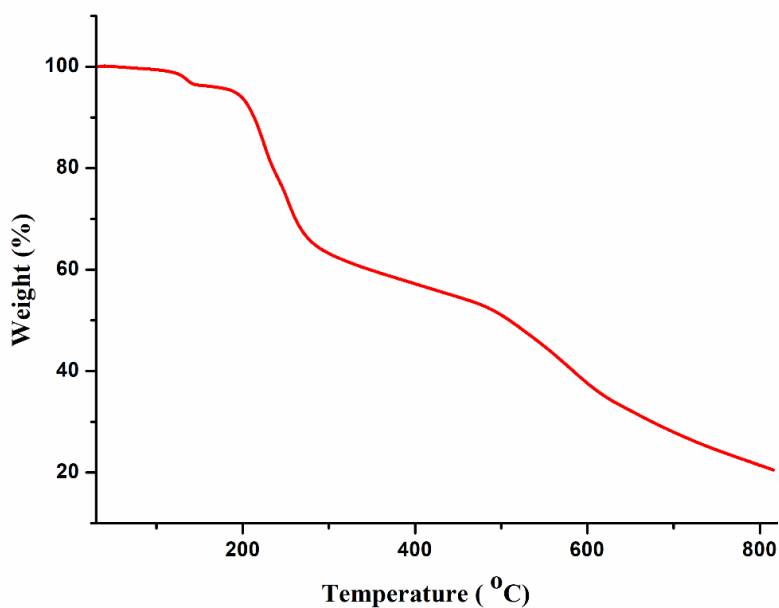
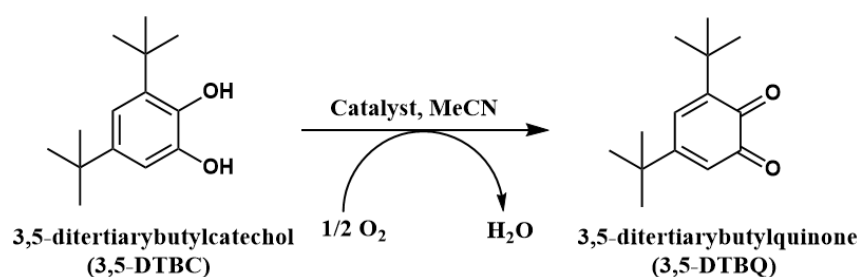


Figure V.11. TGA plot of **CUPM** under nitrogen atmosphere

#### V.3.4. Catechol oxidase-like activity

3,5-DTBC (3,5-Di-tert-butylcatechol) is a widely used substrate to measure the catecholase activity of Cu(II) coordination complexes.<sup>85-87</sup> Bulky tert-butyl groups present in the ring lower the quinone-catechol reduction potential, facilitating quicker 3,5-DTBC oxidation by increasing the oxidizability of the catechol.<sup>88</sup> Moreover, it protects the ring from over-

oxidation and polymerization. 3,5-DTBQ (3,5-di-tert-butylquinone), which is produced by its oxidation, is particularly stable in acetonitrile and has a distinctive absorption peak at 400 nm (Scheme V.2). In order to test the complex's ability to mediate the oxidation of 3,5-DTBC,  $1 \times 10^{-5}$  M acetonitrile solution of **CUPM** was combined with  $4 \times 10^{-3}$  M 3,5-DTBC in acetonitrile at 298 K in an aerobic environment. This maintained the requirement for the pseudo-first order response. The colourless solution ultimately turned dark brown as this time-dependent spectrum scan showed a steadily increasing strength of the unique quinone absorption peak at 400 nm (see Figure V.14(a)). The data clearly showed that the compound has substantial catecholase activity. There was no catalytic activity in the control experiments using ligand (**L**) and Cu(II)-perchlorate  $[\text{Cu}(\text{ClO}_4)_2 \cdot 6\text{H}_2\text{O}]$  salts (Figure V.12).



Scheme V.2. Catechol oxidation catalyzed by **CUPM**

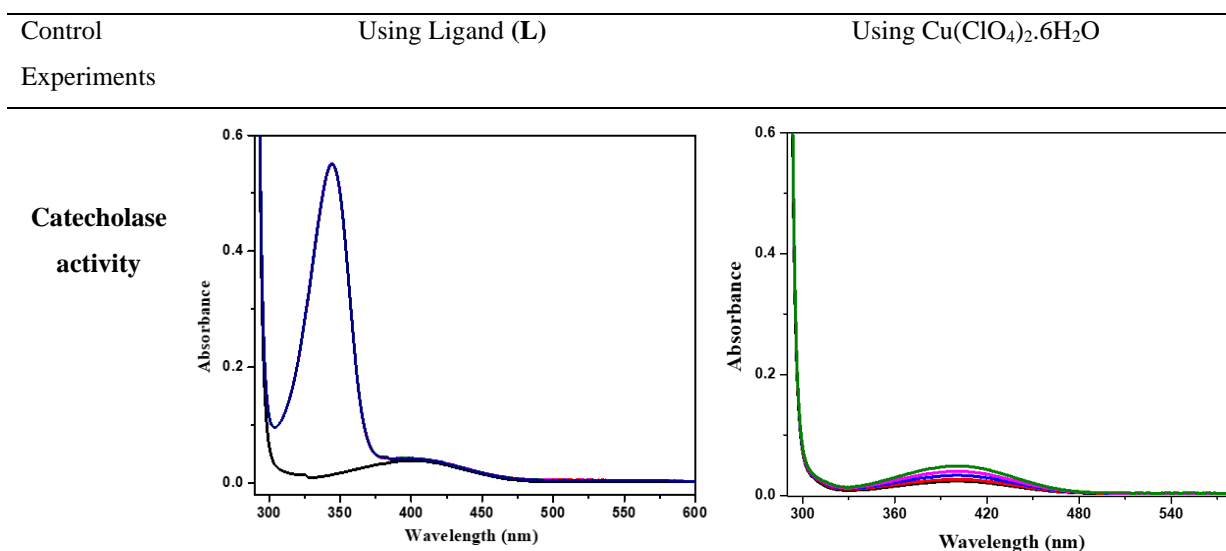


Figure V.12. Control Experiments Using Ligand (**L**) and  $\text{Cu}(\text{ClO}_4)_2 \cdot 6\text{H}_2\text{O}$  salt for Catechol oxidase activity.

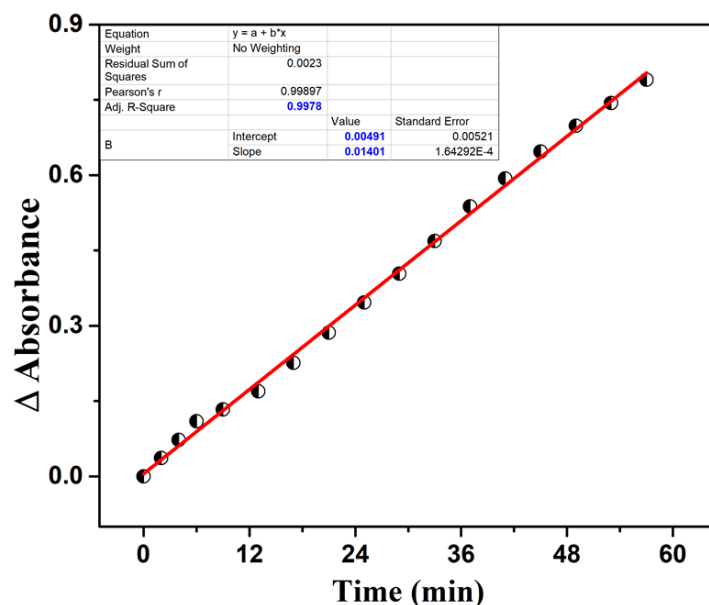
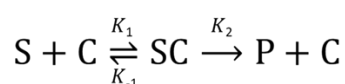


Figure V.13.  $\Delta A$  (change in absorbance at 400 nm) vs.  $t$  (time) plot of the catalytic oxidation of 3,5-DTBC by complex **CUPM**.

#### V.3.4.1. Rationalization of kinetic parameters

Utilizing the initial rate approach and measuring the amplified 400 nm absorption intensity at 298 K, the kinetics of 3,5-DTBC oxidation to 3,5-DTBQ catalyzed by **CUPM** were determined. The rate constant was determined for a set of catalyst-substrate concentrations by graphing  $\Delta A$  (change in absorbance) vs  $t$  (time) at 400 nm (Figure V.13). The  $\epsilon$  value,  $1630 \text{ M}^{-1}\text{cm}^{-1}$  (for DTBQ) was used to convert the reaction rate units from  $\Delta A/\text{s}$  to  $\text{M}/\text{s}$ .<sup>89</sup> To investigate the rate dependence on the substrate concentration, the concentration of the substrate (3,5-DTBC) was changed from  $10^{-3} \text{ M}$  to  $10^{-2} \text{ M}$  while the catalyst concentration (here **CUPM**) remained constant ( $5 \times 10^{-6} \text{ M}$ ) (Figure V.14(b)). The figure depicted a first order kinetics at low substrate concentrations, but as the substrate concentration increased, it gradually deviated from linearity until it reached a flat plateau, signifying saturation. This research on saturation kinetics makes excellent use of the Michaelis-Menten model of enzyme catalysis.<sup>88</sup> The fundamental premise is that the initial process leads to the formation of a substrate-catalyst complex (SC), which later disintegrates into the product (P) and free catalyst (C).<sup>90</sup>



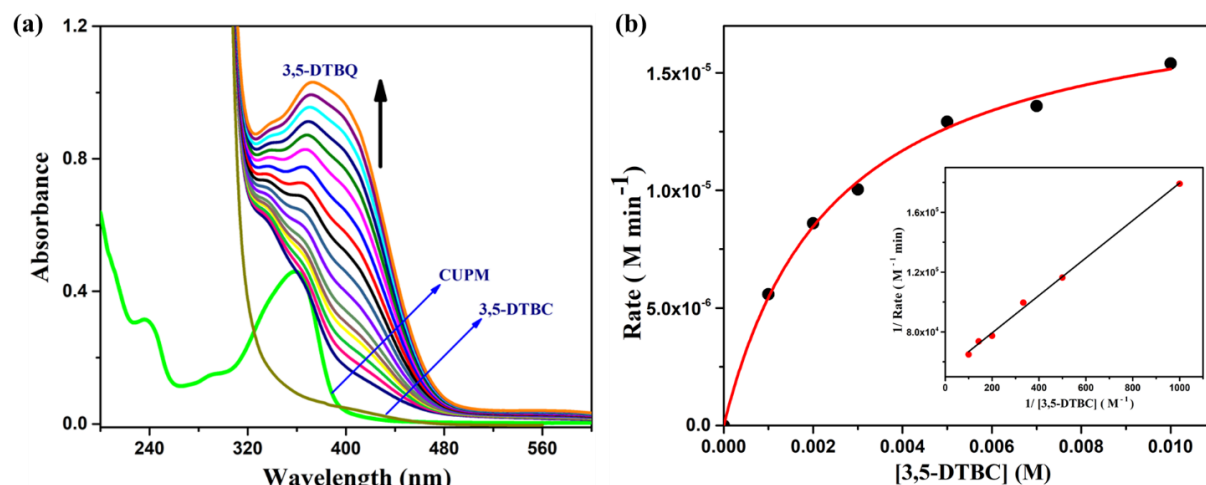


Figure V.14. (a) Time dependent UV–Vis spectral growth of 3, 5-DTBQ at  $\sim 400$  nm upon addition of  $4.0 \times 10^{-3}$  M substrate to  $1.0 \times 10^{-5}$  M of **CUPM** in acetonitrile medium at room temperature. (b) Dependence of rate of catechol oxidation on 3,5-DTBC concentration [Inset: Lineweaver–Burk plot].

All the kinetic parameters, including the maximal initial reaction rate ( $V_{\max}$ ) and Michaelis-Menten binding constant ( $K_M$ ) were calculated from the Lineweaver-Burk (double reciprocal) plot (see inset of Figure V.14(b)).<sup>91</sup> To get the turnover numbers ( $K_{\text{cat}}$ ) for this oxidation reaction,  $V_{\max}$  value was divided by the corresponding concentration of the catalyst **CUPM**. All these kinetic parameters are listed in Table V.3. Several previously reported copper-based complexes with enzyme mimicking activities have been tabulated in Table V.3 together with their  $K_{\text{cat}}$  values to enable comparisons with the activity of our designed Cu(II)-polymer.

Table V.3. Kinetic parameters of catecholase activity at 298K for the reported Cu(II) complexes

Complex	$V_{\max}$ (M min <sup>-1</sup> )	$K_M$ (M)	$K_{\text{cat}}$ (h <sup>-1</sup> )	Ref
<b>CUPM</b>	<b><math>1.84 \times 10^{-5}</math></b>	<b><math>2.31 \times 10^{-3}</math></b>	<b>220.8</b>	<b>This work</b>
[Cu(L)(NCS)] (1)	$4.11 \times 10^{-5}$	$2.87 \times 10^{-3}$	49.3	92a
[Cu(L)(N <sub>3</sub> )] (2)	$4.33 \times 10^{-5}$	$2.99 \times 10^{-3}$	52	
[Cu(L)(NO <sub>3</sub> )] (3)	$5.76 \times 10^{-5}$	$4.49 \times 10^{-3}$	69.1	
[Cu(L) <sub>2</sub> ]	$1.32 \times 10^{-4}$	$4.52 \times 10^{-3}$	475	92b
[Cu <sub>2</sub> L <sub>4</sub> (OH)]ClO <sub>4</sub>	$3.89 \times 10^{-4}$	$4.60 \times 10^{-3}$	233.40	92c
C <sub>26</sub> H <sub>26</sub> C <sub>12</sub> Cu <sub>2</sub> N <sub>6</sub> O <sub>4</sub> S <sub>2</sub> ·2Cl <sup>-</sup> ·6H <sub>2</sub> O	$4.275 \times 10^{-3}$	0.8715	256.5	92d
[Cu <sub>2</sub> (L <sup>2</sup> )Ce(NO <sub>3</sub> ) <sub>3</sub> ]	-	-	346.5	92e
[Cu <sup>II</sup> <sub>2</sub> (L) <sub>2</sub> Cl <sub>4</sub> ]	$3.63 \times 10^{-4}$	$6.20 \times 10^{-4}$	218.0	92f



### V.3.5. DNA interaction studies

The interaction mode of metal complexes with DNA mostly depends on the structure of the complexes and the nature of the ligands. Labile ligands may interact with DNA by forming covalent bond via replacement of ligand by a nitrogen atom of a DNA base, e.g; guanine N-7, while stable complexes may interact non-covalently by  $\pi$ - $\pi$  stacking, intercalation or groove-binding.<sup>93</sup> Thus such activities are highly beneficial for designing an efficient anticancer therapeutic agent. Cu(II) complexes displayed good DNA binding and cleavage affinities.<sup>58,94</sup> Therefore, we tested how **CUPM** interacted with CT DNA in order to investigate the new molecule's potential as an anticancer medication.

The absorption spectra of **CUPM** were carried out, in which the DNA solution (0-50  $\mu$ M) was gradually added to a constant concentration of **CUPM** ( $2.49 \times 10^{-6}$  M). The absorption maxima at 360 nm gradually decreased along with a slight blue shift of 3 nm which suggested a strong interaction of **CUPM** with CT DNA involving the intercalative binding mode (Figure V.15a). The binding constant ( $K_b$ ) value was calculated by using the Wolfe–Shimmer eqn (1) in the experimental section (supporting information). The  $K_b$  value of **CUPM** with CT DNA was found to be  $(3.06 \pm 0.07) \times 10^5 \text{ M}^{-1}$  (see Figure V.15a inset), implying a strong binding affinity of the compound with CT DNA. The aforesaid  $K_b$  value was determined to be fairly substantial when compared with the previously reported copper complexes.<sup>22,58,95,96</sup>

Further, we carried out ethidium bromide (EB) displacement assay using a fluorescence spectroscopic approach. EB is a known intercalating agent and it is commonly used for finding the binding propensity of metal complexes with DNA. EB shows an intense fluorescence in the presence of CT DNA at 606 nm ( $\lambda_{em}$ ) due to its strong intercalation with DNA base pairs. Upon gradual addition of **CUPM** to EB-CT DNA system, the emission intensity decreased progressively with a noticeable red shift of 4 nm (Figure V.15b). This quenching phenomenon could be attributed to the replacement of EB by **CUPM** from the EB-CT DNA system. The traditional Stern-Volmer equation (eqn (2) in the experimental section) was used to determine the quantitative evaluation of the interaction. The Stern-Volmer constant ' $K_{SV}$ ' value was determined to be  $(2.98 \pm 0.12) \times 10^5 \text{ M}^{-1}$  for **CUPM** (Figure V.15b inset). These findings supported the absorption investigations and suggested the intercalative mechanism of interactions.

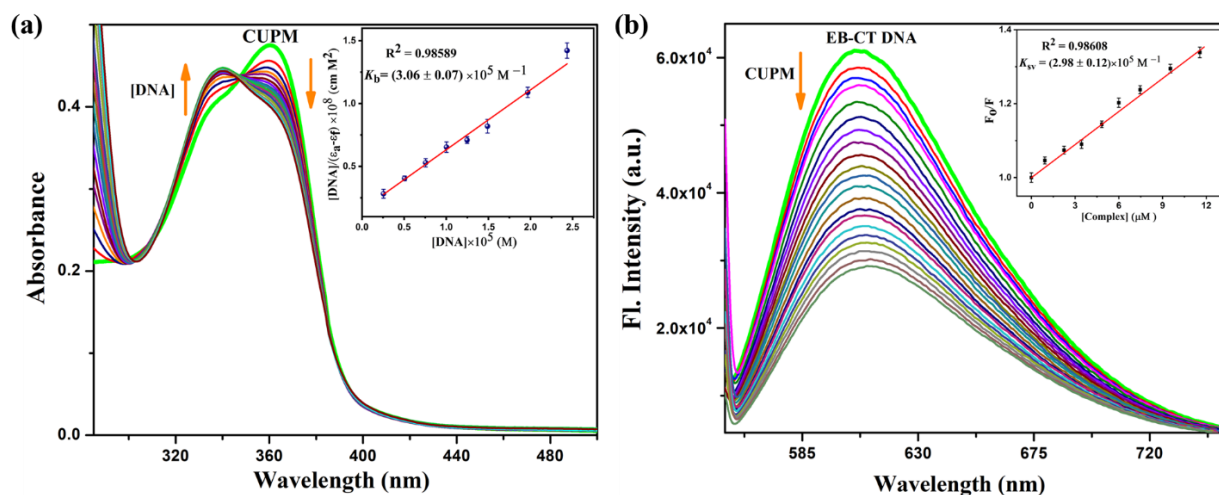


Figure V.15. (a) UV-Vis titration of **CUPM** ( $2.49 \times 10^{-6}$  M) with the gradual addition of CT DNA in Tris-HCl/NaCl buffer [inset:  $[DNA]/(\epsilon_a - \epsilon_f)$  vs  $[DNA]$  plot]. (b) Fluorescence titration of EB-CT DNA with the increasing amount of **CUPM** ( $2.49 \times 10^{-5}$  M) [Inset: Stern-Volmer quenching plot].

### V.3.5.1. Viscosity study

Before coming to any clear conclusion regarding the binding fashion of the metal polymer with DNA, viscosity measurements were carried out. The insertion of metal polymer between the base pairs of DNA increases the length of DNA (intercalative binding) resulting in increase in the viscosity while if the binding fashion is groove interaction, the twisting or bending of double strand of DNA reduces the length of DNA leading to a slight decrease in the viscosity. A classical DNA intercalator like ethidium bromide (EB) causes an increase in viscosity of the DNA. Upon addition of increasing concentrations of **CUPM** to the CT DNA solution, the relative viscosity gradually increased (Figure V.16) which suggested the increase in the length of DNA.<sup>22</sup> Therefore, it could be concluded that **CUPM** is efficient for the interaction with DNA in a strong intercalative mode.

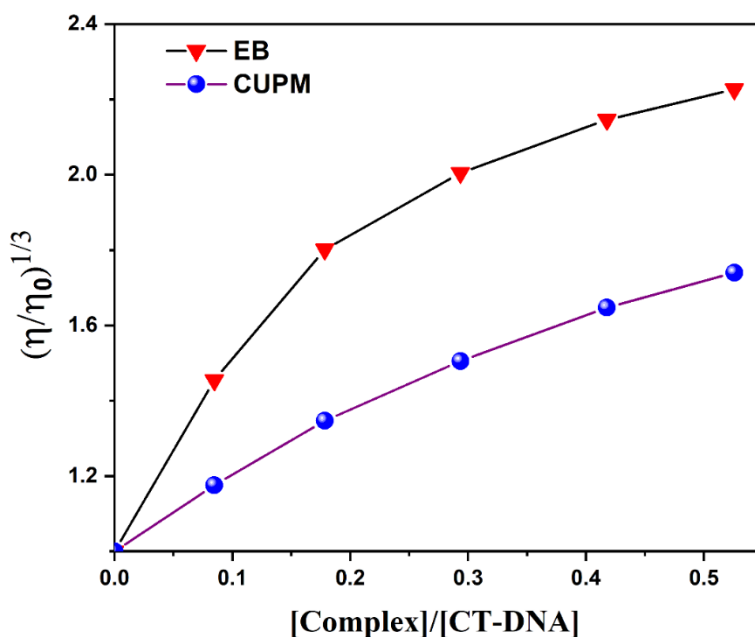


Figure V.16. Effect of increasing concentrations of EB and complexes (**CUPM**) on the relative viscosity of CT-DNA (30  $\mu$ M) at 298 K.

### V.3.6. Protein binding studies

Serum albumin is a widely known blood protein which carries small molecules, metal ions, drugs and metal complexes via blood to the cells, tissues and other biological targets.<sup>97,98</sup> In this context, it was important to investigate the binding of the biologically active compound (**CUPM**) with serum albumin, which might provide paths for drug transportation. Here bovine serum albumin (BSA) was used to study the binding affinity and interaction mechanism of **CUPM**. The fluorescence property of BSA is mainly due to the presence of tryptophan (Trp) and tyrosine (Tyr) residue but the intrinsic fluorescence property is for the tryptophan chromophore at 340 nm. Addition of **CUPM** resulted in quenching (53.15 %) of the emission intensity of tryptophan of BSA at 340 nm along with a noticeable blue shift (Figure V.17a). This result indicated the binding of **CUPM** to BSA and might lead to changes in the tryptophan environment. Stern-Volmer equation could be used to explain fluorescence quenching:<sup>99</sup>

$$F_0/F = 1 + K_{SV} [Q]$$

where  $K_{SV}$  is the Stern-Volmer quenching constant,  $[Q]$  is the concentration of the quencher (here **CUPM**), and  $F_0$  and  $F$  were the fluorescence intensities of BSA in the absence and presence of the **CUPM**, respectively. The high  $K_{SV}$  [ $(1.33 \pm 0.06) \times 10^5 \text{ M}^{-1}$ ] value showed that **CUPM** had effective fluorescence quenching properties (Figure V.17b).

For the details about quenching phenomenon, the equilibrium binding constant ( $K_b$ ) and number of binding sites ( $n$ ) available for the complex were assessed from the plot of  $\log[(F_0 - F)/F]$  versus  $\log[\text{CUPM}]$  (Figure V.17a inset) using the following equation below:<sup>94</sup>

$$\log (F_0 - F/F) = \log K_b + n \log [Q]$$

Where,  $F_0$ ,  $F$ , and  $[Q]$  were the same as above equation,  $n$  was the number of binding sites per albumin molecule and  $K_b$  was the binding constant of the **CUPM** with BSA respectively. The value of  $K_b$  and  $n$  were determined from the slope and the intercept of the plot of  $\log[(F_0 - F)/F]$  versus  $\log[\text{CUPM}]$  (Figure V.17a inset) and the value of  $n$  ( $= 0.9304$ ), which is almost equal to 1, suggested that the complex formed a system with BSA in the molar ratio of 1:1.<sup>100,101</sup> Since the value of  $K_b$   $[(6.34 \pm 0.21) \times 10^4 \text{ M}^{-1}]$  was less compared to non-covalent interactions between avidin-biotin ( $10^{15} \text{ M}^{-1}$ ), the complex might be liberated from the protein in target cells.<sup>96,102</sup>

#### V.3.6.1. Characteristics of the synchronous fluorescence spectra

Synchronous fluorescence technique was used to access information about the microenvironment of protein. In the synchronous fluorescence spectra, tyrosine residue was visible at a wavelength interval ( $\Delta\lambda$ ) of 15 nm while the tryptophan residue of BSA was visible at  $\Delta\lambda$  of 60 nm. When **CUPM** was added to BSA solution, fluorescence intensity at 340 nm decreased (51.02 % quenching) accompanied by a blue shift of  $\sim 6$  nm but slight decrease in intensity was observed (22 % quenching) at 300 nm without any change in spectra for tyrosine residue (Figure V.18a and V.18b). So, from these studies, we could conclude that the binding of **CUPM** with BSA affected the conformation of tryptophan only and not the microenvironment of tyrosine. Therefore, the complex bound to the BSA active site and changed the protein's secondary structure conformationally.

#### V.3.6.2. Three-dimensional fluorescence spectroscopy

The conformational changes of BSA proteins could be more precisely described using three-dimensional fluorescence techniques. The change in the microenvironment of BSA was examined by comparing the spectral properties of BSA in the absence and presence of the **CUPM**. The 3D spectra and the contour are given in Figure V.19. The normal fluorescence peaks (assigned as C and D) were located in the lower right of the Rayleigh scattering regions.<sup>103</sup> A fluorescence peak was found which was assigned as peak 'A' that mainly indicated the spectral character of the tryptophan and tyrosine moieties while another peak (peak 'B') which was observed might have displayed the emission characteristics of the

polypeptide backbone structures.<sup>104,105</sup> Hence the emission peaks ‘A’ and ‘B’ of BSA were quenched upon incorporation of **CUPM** and the change in intensity of the two peaks reflected the binding of **CUPM** to BSA causing some structural and microenvironment changes in BSA.<sup>106,107</sup>

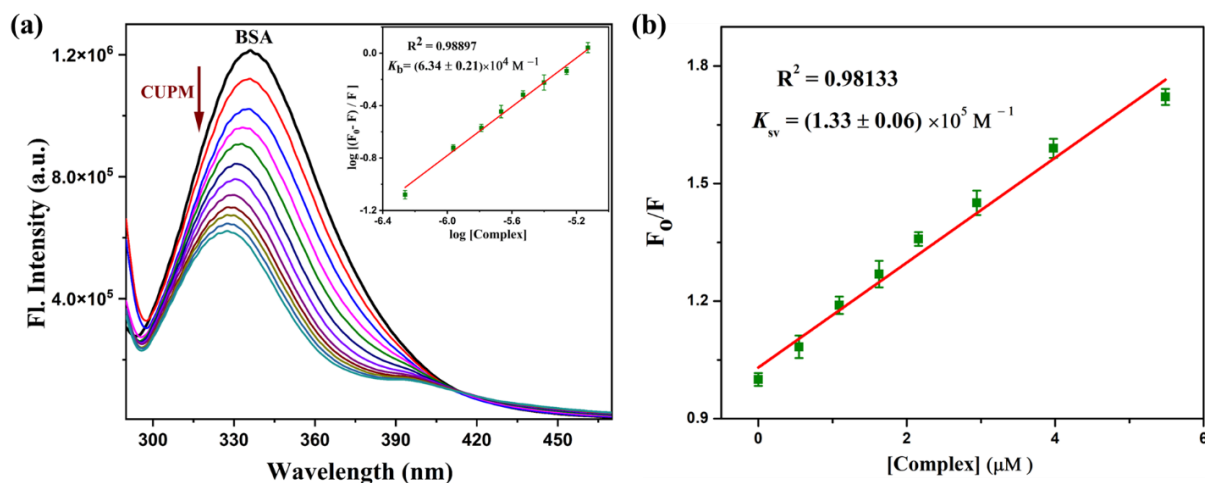


Figure V.17. (a) Fluorescence quenching titration of BSA with incremental addition of **CUPM**. [Inset: Scatchard plot]. (b) Stern-Volmer plot of BSA for **CUPM**.

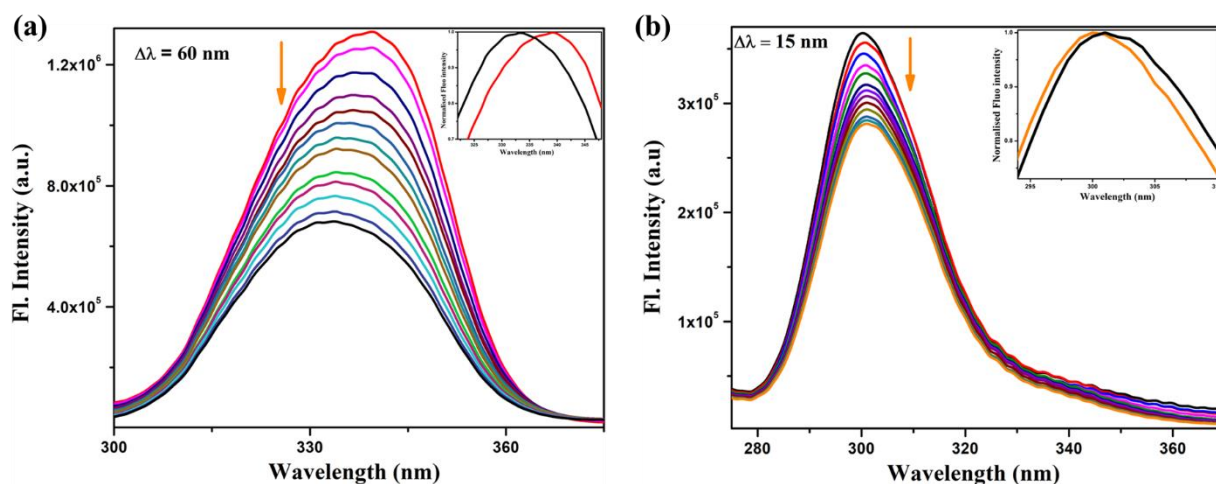


Figure V.18. Synchronous fluorescence spectral titration of BSA using **CUPM** at (a)  $\Delta\lambda = 60$  nm for Tryptophan residue of BSA and at (b)  $\Delta\lambda = 15$  nm for Tyrosine residue of BSA.

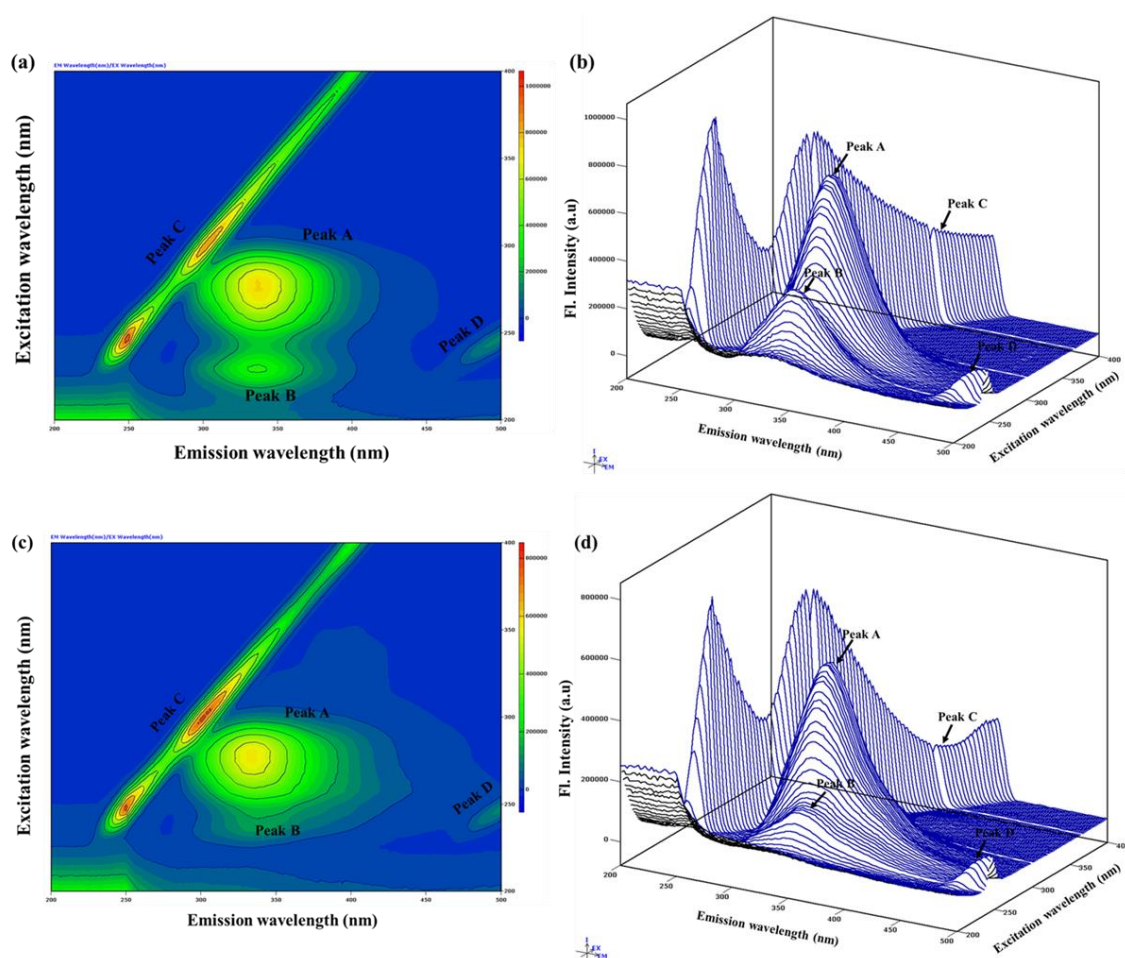


Figure V.19. Contour plot and 3D spectra of BSA only [(a) and (b) respectively] and BSA+CUPM [(c) and (d) respectively] using  $\lambda_{\text{ex}} = 200 - 400$  nm and  $\lambda_{\text{em}} = 200 - 500$  nm.

### V.3.7. Antiproliferative activity

#### V.3.7.1. CUPM is toxic to triple negative human breast cancer cells and inhibits their migration

Sensitivity of **CUPM** towards MDAMB-231 was tested via MTT assay with varying concentrations of **CUPM** and it was found that **CUPM** affected the viability of TNBC cells in a dose-dependent manner. The  $\text{IC}_{50}$  of **CUPM** towards MDAMB-231 cells was 53.87  $\mu\text{g/ml}$ , with an  $r^2$  value of 0.9628. Data obtained in this experiment are depicted via box plot (Figure V.20; A. i. and ii.). The results were corroborated through variable pressure scanning electron microscope (SEM) and phase contrast microscopy. Phase-contrast microscopy of



**CUPM** treated MDA-MB-231 cells for 24 hours showed rounded cellular structures (data not shown); in addition, their growth was also seen to be retarded (data not shown).

SEM studies were conducted to test the ultrastructural changes of MDAMB-231 cells induced by **CUPM** at different concentrations; at 50 µg/ml concentration, lamellipodial connections between two adjacent cells was not disrupted, but distinct structural changes in cellular membrane was found compared to control, and nuclear evasion was also found. As filopodial structures were disrupted (white arrow heads) at this concentration, a relatively less cellular adherence was observed. In groups treated with **CUPM** doses of 100 µg/ml onwards, the intercellular lamellipodial junctions got totally disrupted, and the lamellipodial remnants were found on the coverslip surface. At 150 µg/ml, very less cellular attachment was found along with membrane blebbing, and disrupted lamellipodial structures were still observed on coverslip surface. At 200 µg/ml, root-like blebbed bodies were found and lamellipodial remnants on coverslip surface were absent (Figure V.20C).

*In vitro* scratch assay showed that **CUPM** treatment at a concentration of 50 µg/ml significantly reduced the migratory potential of MDA-MB-231 cells by about 1.68 folds in 24 hours and about 3 folds in 48 hours (Figure V.20; B. i. and ii.) (100 µg/ml dose killed most of the cells, hence data not shown. Only time-dependent data of scratch assay for a single **CUPM** dose of 50 µg/ml was presented).

#### **V.3.7.2. CUPM significantly reduces regenerative capacity of MDA-MB-231 cells**

Clonogenic assay was performed on 6-well plates to determine the effect of **CUPM** on the regenerative capacity of MDA-MB-231 cells. It was found that **CUPM** inhibited the cellular regenerative capacity in a concentration-dependent manner. Even at a dose of 12.5 µg/ml, **CUPM** reduced MDA-MB-231 colony formation by 1.23 folds. At 25 µg/ml, this reduction was increased to 1.58 folds, and then kept on increasing with higher concentrations of 50 µg/ml (2.3 folds) and 100 µg/ml (5.39 folds). At the highest treated dose of 200 µg/ml, the reduction in colony formation of treated cells as compared to control was 8.73 folds (Figure V.20; D. i and ii.).

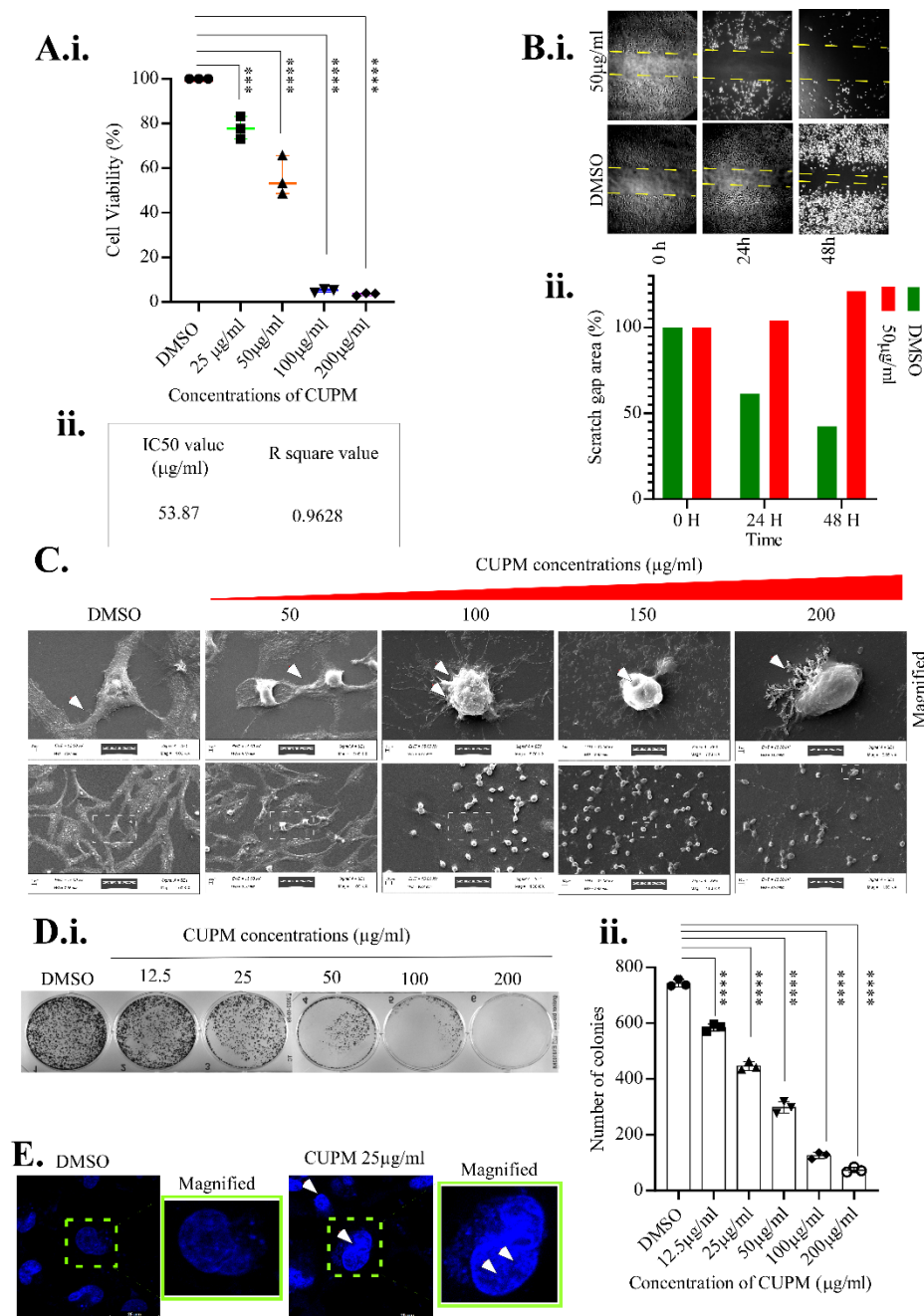


Figure V.20. **A.i.)** Box plot representing cytotoxicity of **CUPM** to MDA-MB-231 cell line as measured by MTT assay after treatment with DMSO or increasing concentrations of **CUPM** (0-200) µg/ml for 24 h. Error bar mean±SD (n=3); \*\*\*P=0.0005; \*\*\*\*P<0.0001 with tabulation of IC<sub>50</sub> value and R square value (**A.ii.**). **B.i.)** Phase contrast image representation of the effect of **CUPM** on migration potential on MDA-MB-231 cells determined wound healing assay. MDA-MB-231 cells were treated with DMSO or **CUPM** for different durations after scratches were made. Bar graph representing an estimation of scratch gap area as indicated (**B.ii.**). **C.)** Ultra-structure analysis of the effects of different **CUPM** concentrations (0-200) µg/ml or DMSO for 24 h. **D.i.)** Regeneration capacity of MDA-MB-231 cells was significantly reduced upon treatment of different concentrations



of **CUPM** and/or DMSO control for 24 h. Cells were stained with crystal violet after fixing with formaldehyde. **D.ii.)** Bar graph representing inhibition of colony formation of MDA-MB-231 cells at different concentrations of **CUPM** (0-200)  $\mu\text{g/ml}$  or DMSO for 24 h. Error bar mean $\pm$ SD (n=3); \*\*\*\*P<0.0001. **E.)** **CUPM**-inducing chromatin condensation in MDA-MB-231 cells. Live cell confocal images were taken after treatment with **CUPM** or DMSO for 12 h at 63x oil lens. Significant chromatin condensation was found at 25  $\mu\text{g/ml}$  **CUPM** concentrations (white arrows) (Hoechst 33342 staining)

#### **V.3.7.3. Chromatin condensation in MDA-MB-231 cells was induced upon CUPM treatment**

Like many other anti-cancer compounds, **CUPM** also caused significant chromatin condensation in MDA-MB-231 cells, indicating that **CUPM** had the capacity of chromatin condensation and subsequent cell cycle arrest (Figure V.20E).

#### **V.3.7.4. Destabilization of mitochondrial membrane potential plays a crucial role in CUPM action in mtROS independent manner**

The action of **CUPM** on mitochondria was assessed by visualizing live MDA-MB-231 cells under a super resolution confocal microscope (Leica Stellaris 5). It was seen that **CUPM** treatment caused a significant decrease in mitochondrial membrane potential (depolarization) in a concentration-dependent manner but with a little change in mitochondrial ROS (mtROS) generation. Average size of live mitochondria in **CUPM** treated groups were significantly reduced compared to control. mtROS, MMP and average mitochondrial length were analyzed qualitatively as well as quantitatively (via LAS-X software). Live cell imaging showed fold changes in intensity of two dyes – Mitosox red and TMRM, that gave indications about the mtROS levels, and polarization state of the mitochondrial membrane, respectively.

#### **V.3.7.5. mtROS**

It was seen that **CUPM** at 50  $\mu\text{g/ml}$  concentration increased Mitosox red positive cells by 1.58 folds, and at 100  $\mu\text{g/ml}$ , increased Mitosox red positive cells by 2.12 folds. Doxorubicin (5  $\mu\text{g/ml}$ ) was used as positive control, which increased Mitosox red positive cells by 3.34 folds. Statistical analysis showed that the change is non-significant at a dose of 50  $\mu\text{g/ml}$ , whereas it is mildly significant at the dose of 100  $\mu\text{g/ml}$ , when compared to control. The change in mtROS induced by the positive control Doxorubicin is highly significant compared to control. No significant difference was found between Mitosox positive signals obtained from cells treated with 50  $\mu\text{g/ml}$  and 100  $\mu\text{g/ml}$  doses (Figure V.21; A. i. and ii.).

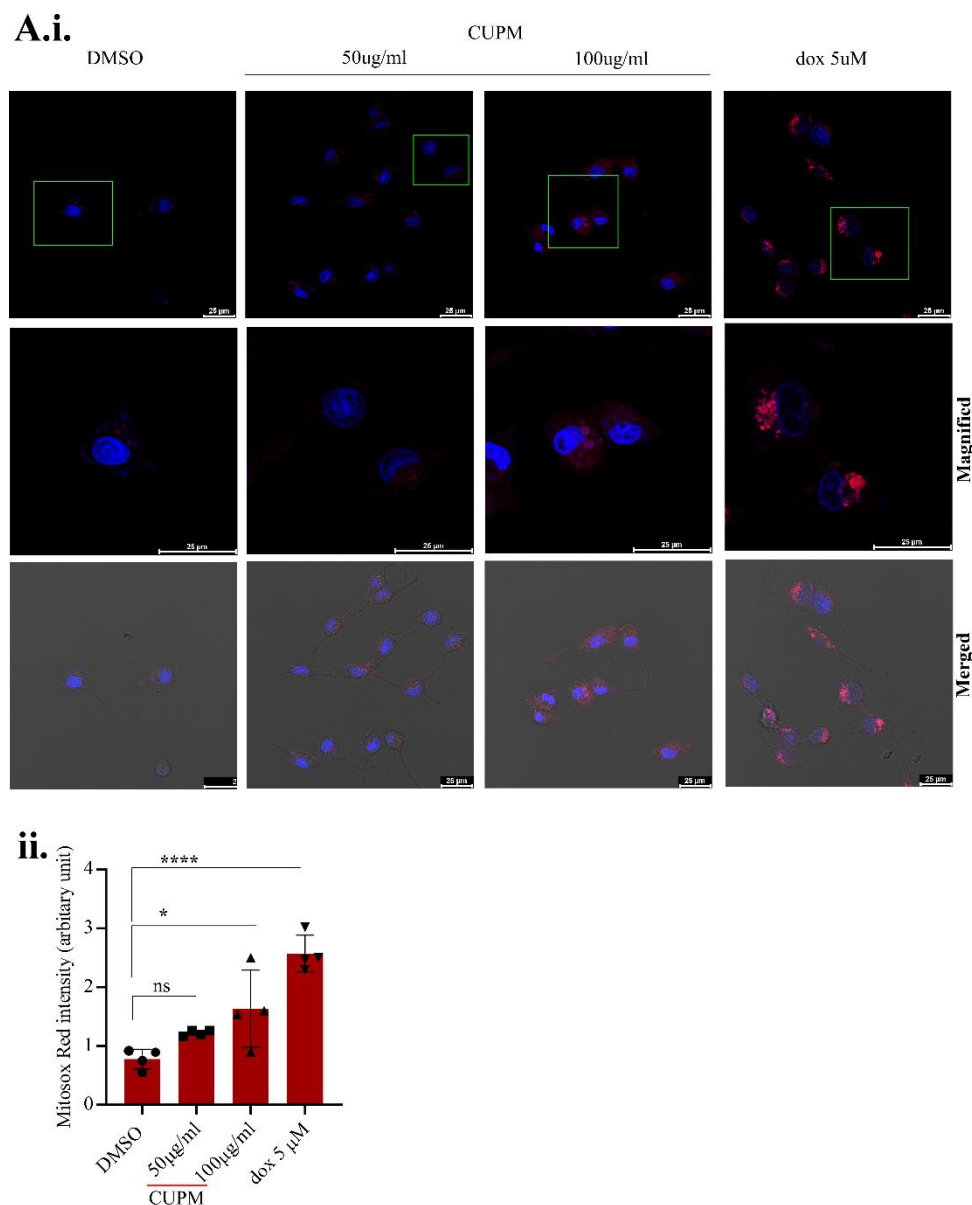


Figure V.21. Effects of **CUPM** on mitochondrial ROS generation. MitoSOX red fluorescence was used to quantify mitochondrial ROS in MDA-MB-231 cell line. **A.i.**) MDA-MB-231 cells were treated gradually with increasing concentrations of **CUPM** (50 and 100  $\mu\text{g/ml}$ ) and/or DMSO as vehicle control and Doxorubicin(Dox) as positive control for 5 h, scale bar 25  $\mu\text{m}$ . Initial pictures of live MDA-MB-231 cells were captured at super-resolution by using 63x oil lens followed by magnified images (from initial fields depicted in the green box) and merged with bright fields (63x) respectively (from top to bottom) (Nuclear co-staining with Hoechst 33342). **A.ii.**) Summarized bar graph showing mean mitochondrial ROS generation upon **CUPM** treatment at indicated concentrations. Error bar, mean $\pm$ SD (n=4); ns, non-significant; \*P=0.0184; \*\*\*\*p<0.001.

**V.3.7.6. MMP**

Interestingly, even though **CUPM** doesn't increase mtROS significantly, but, successive results showed that it significantly destabilizes MMP in a dose-dependent manner.

Live healthy mitochondria from control cells gave the highest TMRM signals. A **CUPM** dose of 50 µg/ml reduced the mean TMRM intensity by about 4-folds (depolarization). At a dose of 100 µg/ml, **CUPM** decreased the TMRM intensity by about 40-folds (40-fold was calculated from DMSO-treated cells that showed arbitrary fluorescence at 40 units, and no TMRM signal was found from the 100 µg/ml **CUPM** treated cells). In both cases, the significance was found to be very high which ultimately indicated mitochondrial damage, as well as activation of caspases followed by PARP1 cleavage, leading to **CUPM** induced apoptosis in MDA-MB-231 cells.

Further, to determine mitochondrial health, mitochondrial length was quantified via LAS-X. At 50 µg/ml dose of **CUPM**, the average mitochondrial length was reduced by 3.21 folds, but at 100 µg/ml of **CUPM**, no mitochondrial signal was found (hence unable to determine change in mitochondrial length) (Figure V.22; A. i. ii. And iii.). This decreased mitochondrial length and increase in their number in treated group indicated mitochondrial fission which triggers release of different mitochondrial apoptotic factors, leading to cell death.

**V.3.7.7. CUPM induces cell cycle arrest in MDA-MB-231 cells at sub G<sub>0</sub>/G<sub>1</sub> stage, and induces apoptosis**

Whether or not **CUPM** has any effect on the cell cycle of MDA-MB-231 cells was assessed by FACS analysis of MDAMB-231 cells treated with **CUPM** at varying concentrations. It was seen that sub G<sub>0</sub>/G<sub>1</sub> arrest was induced in the treated cells in a dose-dependent manner (Figure V.23; B. i and ii.). Apoptosis was also seen to be induced by **CUPM**. At 50 µg/ml concentration, the cell survival percentage was 40.72%, which significantly decreased to 0.29% at a dose of 100 µg/ml (Figure V.23; A. i. and ii.).

**V.3.7.8. CUPM induces intrinsic apoptotic pathway by activation of bax and caspase 9, leading to PARP1 cleavage**

By following the results of annexin V/PI assay, we carried out immunoblotting to identify the probable molecular signalling responsible for MDA-MB-231 cell death induced by **CUPM**. **CUPM** treatment significantly increased BAX levels in a concentration dependent way. This high level of cytosolic BAX formed porous BAX-channels at the outer membrane of mitochondria, resulting in mitochondrial outer membrane permeabilization or MOMP, finally

resulting in release of different mitochondrial apoptotic factors into cytosol,<sup>108</sup> culminating in Caspase9 cleavage through “Wheel of Death” (apoptosome) formation. Activated cleaved Caspase9 then caused activation of Caspase3 by proteolytic cleavage,<sup>109</sup> followed by PARP-1 cleavage, resulting in cellular apoptosis (Figure V.23C).<sup>110</sup>

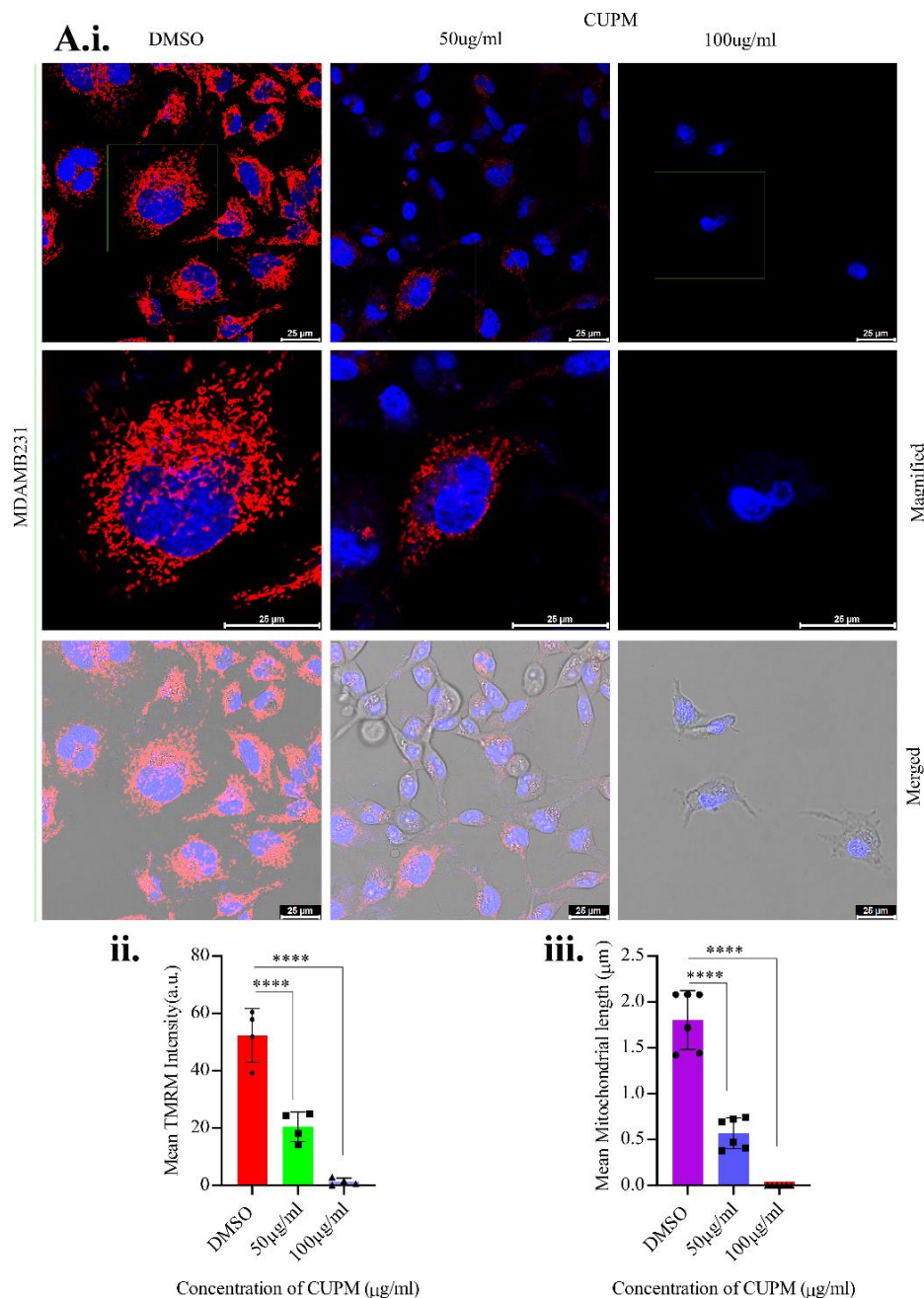


Figure V.22. **CUPM** affects mitochondrial membrane potential (MMP) and induced mitochondrial fission, and TMRM fluorescence to quantify MMP and mitochondrial health in MDA-MB-231 cells. **A.i.)** MDA-MB-231 cells were gradually treated with increasing concentrations of **CUPM** (50 and 100 μg/ml) and/or DMSO as vehicle control for 12 h, scale bar 25 μm. Initial pictures of live MDA-MB-231 cells were captured at super-resolution by using a 63x oil lens followed by magnified images

(from initial fields depicted in the green box) at 250x and merged with bright fields (63x) respectively (from top to bottom) (Nuclear co-staining with Hoechst 33342). **A.ii.)** Summarized bar graph showing mean mitochondrial membrane depolarization upon **CUPM** treatment at indicated concentrations. Error bar, mean $\pm$ SD (n=4); \*\*\*\*P<0.0001; **A.iii.)** Summarized bar graph showing mean mitochondrial length upon **CUPM** treatment at indicated concentrations. Error bar, mean $\pm$ SD (n=6); \*\*\*\*P<0.0001.

#### **V.3.7.9. CUPM inhibits MDAMB-231 cell survival by downregulating HSP90 and its client protein AKT**

HSP90, a cellular chaperone, plays an important role in cancer cell survival by mediating a number of cellular activities like maturation of different survival proteins (Li and Luo 2023) and stability of its client, AKT in complex.<sup>111,112</sup> AKT, also known as Protein Kinase B (PKB),<sup>113</sup> helps in oncogenic promotion by either activation of a number of cell survival proteins<sup>114</sup> or by inhibiting pro-apoptotic factors by its kinase property.<sup>115</sup> **CUPM** treatment towards MDAMB-231 cells did not alter cellular HSF1 protein level but significantly reduced HSP90 level in a dose dependent manner. Biophysical studies indicated that **CUPM** significantly decreased the binding affinity of trimeric HSF-1 towards its cognate HSE (Figure V.24; A. i., ii and iii.), resulting in decreased formation of cellular chaperones like HSP90, leading to failure of maintenance of its client, AKT. This caused inhibition of AKT driven cell-survival pathways, resulting in cancer cell death (Figure V.23C).

#### **V.3.7.10. CUPM decreases the binding affinity of the trimeric/ oligomeric form of Heat Shock Transcription Factor1 (HSF1) with its cognate Heat Shock Element (HSE)**

Heat Shock Factor1 (HSF1) is a stress-inducible transcription factor that helps in maintaining cellular proteostasis (protein homeostasis) upon exposure to various stressful conditions by upregulating the expression of chaperones. Stress exposure of cells causes a monomer-to-multimer transition and post-translational modifications of HSF1, which then binds with Heat Shock Elements (HSEs) present in the promoters of its target genes and turns on the expression of molecular chaperones. These chaperones in turn help in the proper folding of proteins that were misfolded by stress.<sup>116</sup>

Cancer cells, in contrast to normal cells, keep the HSF1 protein constitutively active, as they need a continuous supply of molecular chaperones to support their rapid proliferation and survival. Moreover, cancer cells orchestrate a unique transcriptional program (distinct from the normal proteotoxic stress response described above), which targets genes involved in

cellular energy metabolism, apoptosis, cell cycle, etc.<sup>117</sup> Thus, small molecule-mediated inhibition of HSF1 activity in cancer cells could render them more susceptible to standard anticancer drugs.

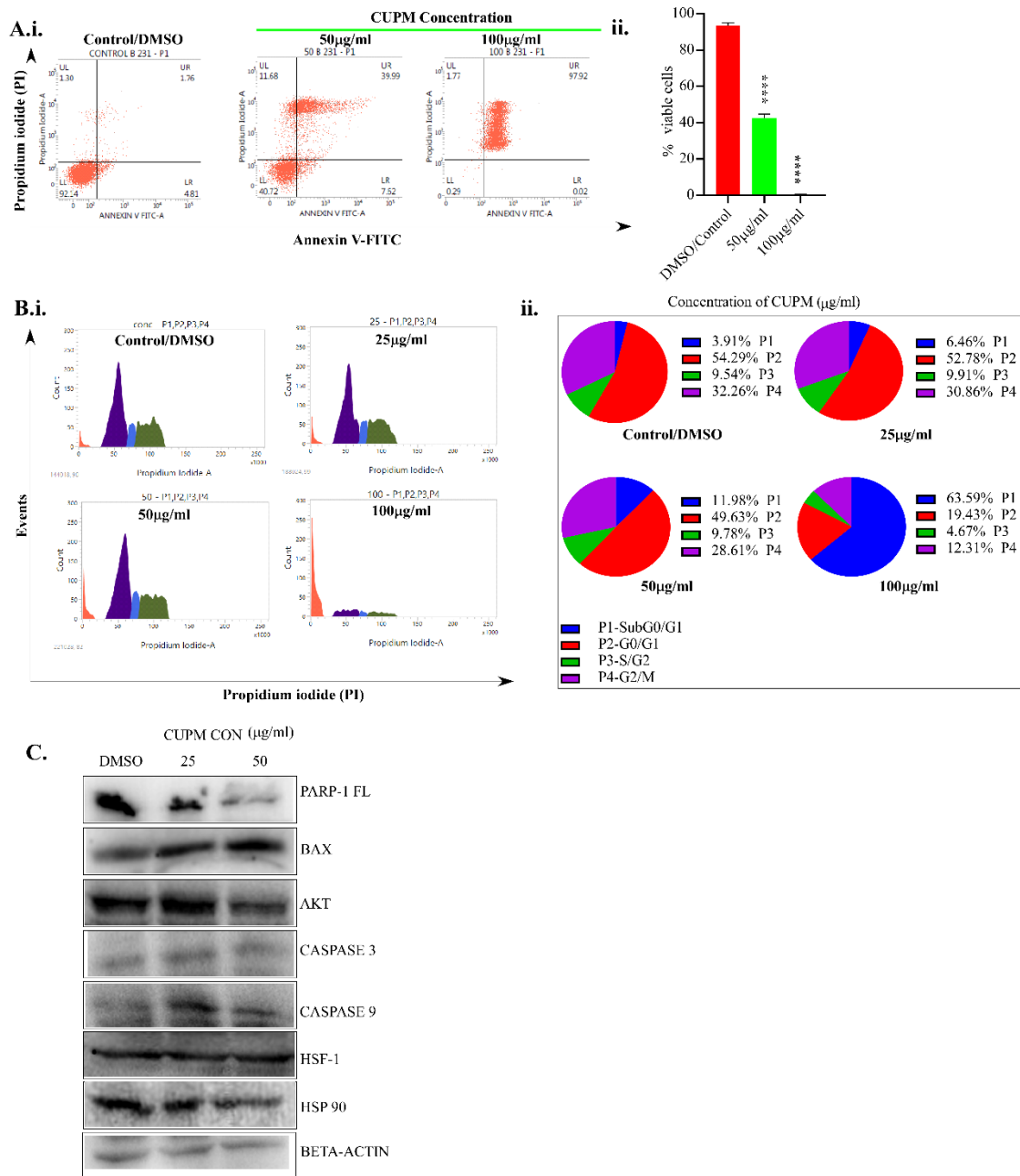


Figure V.23. **CUPM**-induced apoptosis in MDA-MB-231 cells. A.i.) Representative flow-cytometry plots with Annexin V/PI double staining for control/DMSO (0.2%), cells exposed to 50 and 100 µg/ml of **CUPM** respectively for 24 h, A.ii.) Summary data through bar-graph representation. Error bar, mean±SD (n=3), \*\*\*\*p<0.0001 compared to control. B.i.) Flow-cytometry plots, representing **CUPM** induced-distribution of MDA-MB-231 cells in different cell cycle phases through propidium staining. Cells were treated with indicated concentrations of **CUPM** and/or DMSO for 24 h. B.ii.)



Summary data through pi graph representation with **CUPM**-induced distribution of MDA-MB-231 cells in different cell cycle phases. C.) Immunoblot representing the effect of **CUPM** on different cellular markers, BETA-ACTIN levels was determined as the internal loading control.

To this end, we tested the effect of **CUPM** on the interaction of the constitutively active trimeric/oligomeric form of HSF1 with its cognate HSE sequence by an *in vitro* Fluorescence Polarization Assay. Interestingly, the presence of **CUPM** in the reaction mixture was found to compromise the binding of trimeric/ oligomeric HSF1 with HSE, as evident from an increase in the  $K_d$  value of this interaction compared to the control condition (Figure V.24 A. i., ii. And iii.). Also, Dynamic Light Scattering (DLS) studies on trimeric/ oligomeric HSF1 in the presence of **CUPM** showed a slight increase in the protein's hydrodynamic radius compared to the control condition (Figure V.24 A. iv.), which could be caused by structural destabilization of the protein by **CUPM**. Taken together, **CUPM** induced structural destabilization of trimeric/ oligomeric HSF1, which was responsible for the decrease in its affinity for HSE. Our cell-based immunoblot assay showed a decrease in the hsp90 protein level upon **CUPM** treatment in the MDAMB-231 cell line (Figure 9C.), which could be due to impaired binding of hsf-1 with HSE. Thus, our cell-based studies were found to be in good agreement with our *in vitro* binding assays.

Furthermore, we checked the effect of **CUPM** on the HSE binding affinity of purified HSF1-DNA Binding Domain (HSF1-DBD). It is located at the N-terminus of the protein and consists of residues 1-123.<sup>82</sup> As the name suggests, it helps trimeric/ oligomeric HSF1 bind to its cognate HSE and is the only domain whose crystal structure is known. In our study, the presence of **CUPM** in the reaction mixture was shown to decrease the binding affinity of HSF1-DBD with HSE compared to the control condition (Figure V.24 B. i., ii. And iii.), which was consistent with our findings on trimeric/ oligomeric HSF1 (Figure V.24 A. i., ii., iii., and iv).

#### V.3.7.11. Lysine-80 of hsf-1 DBD is the probable site of CUPM interaction

After docking, the score of the mentioned ligand (**CUPM**) obtained from the log table was tabulated, and the best score was -5.6. It was found that **CUPM** formed a hydrogen bond with LYS-80 residue of HSF1-DBD, with a bond distance of 2.6 Å. All the mentioned amino acids had values below 5 Å, which were ALA-67, ARG-71, ASN-74, MET-66, VAL-70, GLN-49, THR-97 and LYS-80 (Figure V.24 C. i., ii. and iii.).

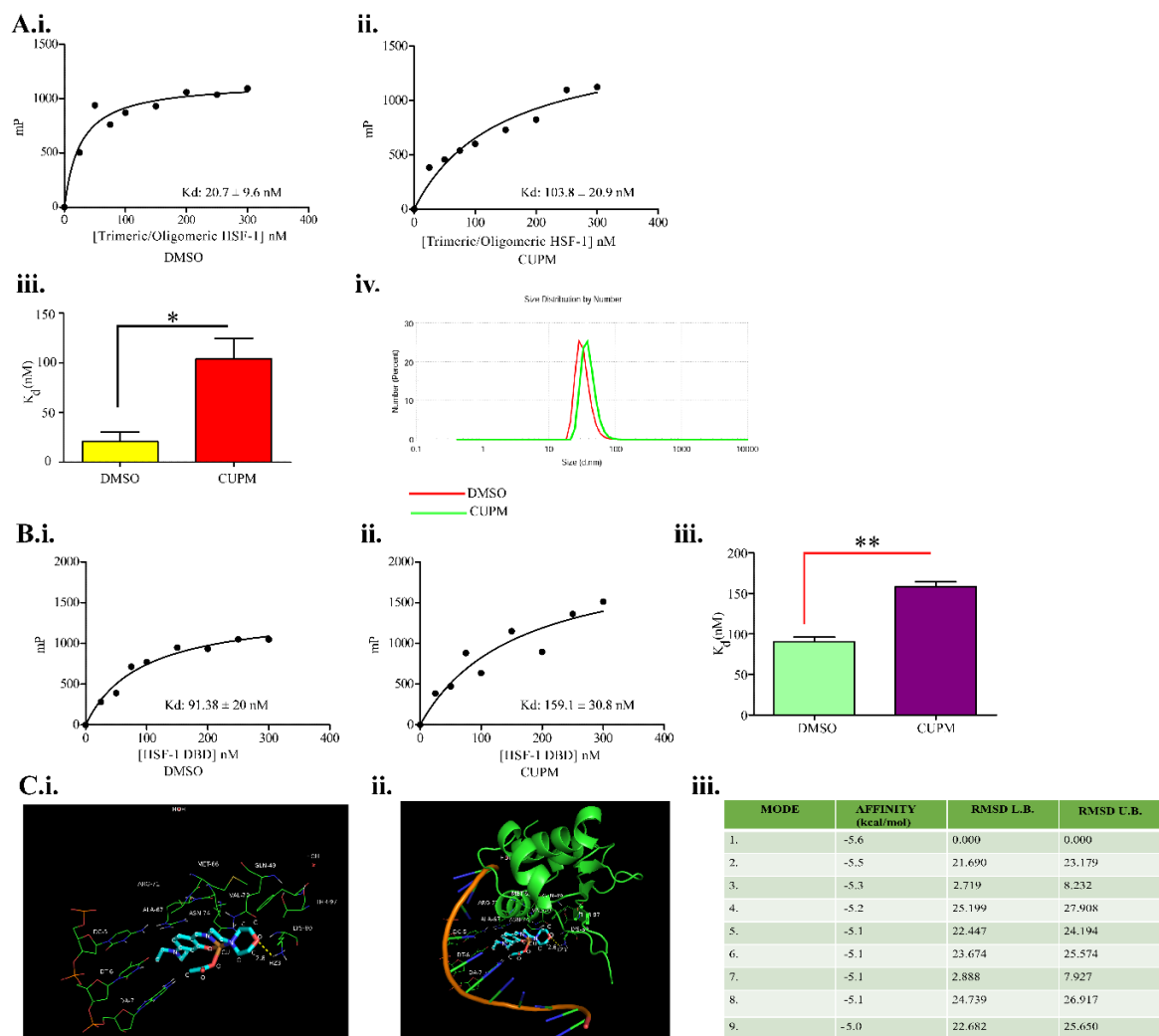


Figure V.24. Studying the interaction of constitutively trimeric/ oligomeric form of HSF1 with **CUPM** by Fluorescence Polarization Assay and Dynamic Light Scattering.

A.i.) A representative curve showing the binding of the protein with fluorescein-labeled HSE in the absence of **CUPM**. The dissociation constant ( $K_d$ ) value is shown as mean  $\pm$  SEM. A.ii.) A representative curve showing the binding of the protein with fluorescein-labelled HSE in the presence of 10  $\mu$ M **CUPM**. The dissociation constant ( $K_d$ ) value is shown as mean  $\pm$  SEM. A.iii.) Bar graph showing the comparison of  $K_d$  values of the binding reaction in the absence and presence of **CUPM**. Statistical analysis was done using a two-tailed unpaired student's t-test at a 95% confidence interval using GraphPad Prism software; p values < 0.05 were statistically significant. Here, p=0.0227. A.iv.) Dynamic Light Scattering (DLS) results showing the oligomeric status of the protein in the absence and presence of **CUPM**. The red curve depicts the protein's size distribution in the presence of vehicle (DMSO). The green curve with a slightly increased hydrodynamic radius shows the protein's size distribution in the presence of **CUPM**. Representative binding curves depicting the binding of HSF1-DBD with fluorescein-labelled HSE in the absence (B.i.) and presence (B.ii.) of **CUPM**. B.iii).



Bar graph showing the comparison of  $K_d$  values of the binding reaction in the absence and presence of **CUPM**. Statistical analysis was done using a two-tailed unpaired student's  $t$  test at 95% confidence interval using GraphPad Prism software;  $p$  values  $< 0.05$  were considered to be statistically significant. Here,  $p=0.0013$ . C.i and ii.) Bioinformatics analysis of the probable binding site of **CUPM** with HSF-1 DBD. C.iii.) Log table, depicting modes, the affinity of binding (Kcal/mol), root-mean-square deviations (RMSD) with lower bound (LB), and upper bound (UB) values.

## Discussion

Cancer is a global health hazard and currently stands at a dangerous rate nearing an epidemic, with very high mortality, next only to cardiovascular diseases.<sup>26</sup> While surgery and radiation are conducted in extreme cases, chemotherapy still remains as the first line of treatment. The high neoplastic cell-turnover and drug efflux makes it difficult to treat till date.<sup>118</sup> In this study, we found that a 1D copper coordination polymeric compound **CUPM**, developed by our group, could easily target neoplastic cells and make them prone to death. In **CUPM**, L served as a tridentate ligand (N N O donor) and acetate ion acted as a bridging co-ligand, through which monomeric units expanded out one-dimensionally. The synthetic compound showed characteristic peaks in infrared and mass spectra, and a peak corresponding to ligand-metal charge transfer (LMCT) in UV-Vis spectrum, confirming its synthesis. Single-crystal and powder XRD gave coordinated results, where it could be seen that the monomer units in the polymer were linked to one another forming a 1-D chain. Moreover, it was highly stable thermally, as well as in solution. It possessed excellent catalytic properties for the oxidation of 3,5-DTBC; additionally, **CUPM** showed high binding propensity for DNA and changes in the microenvironment of BSA protein which was confirmed from synchronous fluorescence study.

It is widely established that metal complexes lead the way in the synthesis of anticancer compounds.<sup>34-37</sup> Previous studies have established that copper could be a safer alternative to platinum, a metal that is widely used in today's date.<sup>55-57</sup> Normal and cancer cells respond to copper differentially, owing to it being a noteworthy constituent of the active sites of several metalloproteins like hemocyanin, catecholase and tyrosinase.<sup>57</sup> Hence, we attempted to synthesize a polymer based on copper, that would keep copper's cancer-cell precision intact, while increasing its anticancer activity. Initially, we found from DNA binding studies, that **CUPM** showed excellent DNA binding and intercalation, as well as DNA condensation.

Fast proliferation and migration are hallmarks of cancer cells, and these were seen to be disrupted by **CUPM**.<sup>119,120</sup> The anticancer potential of **CUPM** was evaluated in human triple

negative breast cancer cells by analysing the sensitivity of TNBC cells, MDAMB-231 towards **CUPM** and comparing it with that of human normal kidney epithelial cells (NKE). Results showed that **CUPM** was significantly toxic to MDAMB-231 cells and not as much to NKE cells, in line with properties of copper as a potent alternative to platinum. **CUPM** induced cell death in a dose-dependent manner in MDAMB-231. The treated cells showed rounding, that is, attachment towards culture plate was getting loosened, indicative of impending apoptotic death. Scanning electron micrographs of the treated cells showed disruption of intercellular lamellipodia and presence of severely apoptotic blebbed bodies, indicating strong anti-cancer effects. **CUPM** restricted the colony formation of MDAMB-231 cells manifolds, thus indicating it slowed down or stopped or reverted the regenerative potential of the highly proliferative cells. It also restricted the migratory potential of these TNBC cells in a dose-dependent manner, thus showing a potential anti-metastatic effect. **CUPM** condensed the nuclear chromatin and induced a sub G<sub>0</sub>/G<sub>1</sub> cell cycle arrest in MDAMB-231 cells in a concentration-dependent manner.

Presently, cisplatin, doxorubicin, 5-Fluorouracil, etc. are commonly used drugs to treat cancer in clinical chemotherapy but problem associated with such clinically approved compounds are drug-induced cytotoxicity and chemoresistance.<sup>121,122</sup> So, emergence of new anti-cancer regimens with lesser toxicity and chemoresistance is the golden rule of fight against cancer on today's date. The mechanisms involved in cancer maintenance and progression are many, but ROS has been proven to play a very important role as a double-edged sword.<sup>123</sup> Cancer cells have higher ROS than normal cells, but ROS inducers that can target cancer cells tilt the ROS levels on the higher side, leading to oxidative stress and subsequent cell death.<sup>124,125</sup> **CUPM** treatment significantly induced mitochondrial depolarization and mitochondrial fission in comparison to mtROS generation, indicating that **CUPM**-induced mitochondrial depolarization was mtROS independent. **CUPM** also increased cellular BAX levels that probably incorporated into mitochondrial outer membrane as homodimeric BAX channel, and caused mitochondrial outer membrane permeabilization (MOMP), resulting in release of different mitochondrial apoptotic factors into cytosol.<sup>108</sup> This led to the formation of apoptosome or 'Wheel of Death',<sup>126</sup> that caused proteolytic cleavage of Procaspase9 to active Caspase9, which in turn converted Procaspase3 to Caspase3.<sup>109</sup> This caused PARP1 cleavage,<sup>110</sup> finally resulting in cancer cell death. In our study, we also found that **CUPM** treatment reduced HSP90 levels significantly, without changing cellular HSF1 levels. Biophysical studies indicated that purified oligomeric HSF1 binding, as well as the binding of purified HSF1-DNA binding domain (HSF-1DBD) to its cognate HSE, was compromised

greatly upon **CUPM** treatment, causing an altered cellular proteotoxic stress response (PSR).<sup>127</sup> This resulted in decreased production of cellular chaperones (like HSP 90),<sup>128</sup> which in turn caused altered maintenance of different proteins like AKT (as AKT levels were found to be decreased upon **CUPM** treatment).<sup>112</sup> This resulted in altered AKT-driven cell-survival pathways, finally causing cell death.<sup>114,115</sup> Studies through bioinformatics tools also confirmed that there was a possible binding pocket in HSF1-DBD to which **CUPM** bound through a hydrogen bond (H-bond with Lys80 of HSF1-DBD). Lys80 residue is involved in the binding of HSF1 with HSE; and this residue is known to be acetylated by the histone acetyltransferase P300 during the later phase of the heat shock response, thereby causing HSF1 to get dissociated from HSE.<sup>129</sup> In our study, the interaction of **CUPM** with Lys80 might have compromised the binding of HSF1 with HSE, thereby causing functional inactivation of HSF1 and resulting in an altered proteotoxic stress response in breast cancer cells.

#### V.4. Conclusions

In summary, we have fabricated a morpholine based new one dimensional Cu(II) coordination polymer (**CUPM**) and characterized comprehensively by several spectroscopic techniques. Single crystal X-ray diffraction study displayed **L** served as tridentate ligand (N N O donor) and acetate ion acted as a bridging coligand through which monomeric units expanded out one dimensionally in **CUPM**. Catalytic activity of our synthesized complex was investigated and it possessed excellent catalytic properties for the oxidation of 3,5-DTBC. Additionally, binding affinity of our complex towards CT-DNA and BSA protein were evaluated using several spectroscopic methods. **CUPM** shows high binding propensity for DNA and changes in the microenvironment of BSA protein which was confirmed from synchronous fluorescence study. Finally *in vitro* cytotoxicity study was assessed against human TNBC cells MDAMB-231. It showed a high anti-neoplastic activity and killed cancer cells by inhibiting their growth as well as migration, moreover, it induced apoptosis in these cells by depolarization of the mitochondrial membrane potential in a mitochondrial ROS-independent manner, a very rare characteristics that is found in the anticancer drug cohort. Thus, we can conclusively pitch **CUPM** as a potent candidate molecule against triple negative breast cancer as well as a potential commercial candidate as an HSF-1 and AKT inhibitor, which could be of great help to find newer cellular signalling pathways in future.

## V.5. References

1. M. H. Mir, L. L. Koh, G. K. Tan, J. J. Vittal, *Angew. Chem. Int. Ed.*, 2010, **49**, 390-393.
2. L. K. Das, C. J. Gómez-García, A. Ghosh, *Dalton Trans.*, 2015, **44**, 1292-1302.
3. L. K. Das, C. Diaz, A. Ghosh, *Cryst. Growth Des.*, 2015, **15**, 3939-3949.
4. H. Li, Y. Wang, Y. He, Z. Xu, X. Zhao, Y. Han, *New J. Chem.*, 2017, **41**, 1046-1056.
5. P. Mahapatra, M. G. B. Drew, A. Ghosh, *Cryst. Growth Des.*, 2017, **17**, 6809-6820.
6. C. Janiak, J. K. Vieth, *New J. Chem.*, 2010, **34**, 2366-2388.
7. N. N. Adarsh, P. Dastidar, *Chem. Soc. Rev.*, 2012, **41**, 3039-3060.
8. K. Biradha, C.-Y. Su, J. J. Vittal, *Cryst. Growth Des.*, 2011, **11**, 875-886.
9. S. Ganguly, P. Kar, M. Chakraborty, A. Ghosh, *New J. Chem.*, 2018, **42**, 9517-9529.
10. T. Kundu, S. Mitra, P. Patra, A. Goswami, D. Díaz Díaz, R. Banerjee, *Chem. Eur. J.*, 2014, **20**, 10514-10518.
11. S. Khan, S. Halder, P. P. Ray, S. Herrero, R. González-Prieto, M. G. B. Drew, S. Chattopadhyay, *Cryst. Growth Des.*, 2018, **18**, 651-659.
12. S. Roy, A. Dey, P. P. Ray, J. Ortega-Castro, A. Frontera, S. Chattopadhyay, *Chem. Commun.*, 2015, **51**, 12974-12976.
13. Y. Zhang, J. Yang, D. Zhao, Z. Liu, D. Li, L. Fan, T. Hu, *CrystEngComm.*, 2019, **21**, 6130-6135.
14. L. Fan, Y. Zhang, J. Liang, X. Wang, H. Lv, J. Wang, L. Zhao, X. Zhang, *CrystEngComm.*, 2018, **20**, 4752-4762.
15. J. Wang, N. N. Chen, C. Zhang, L. Y. Jia, L. Fan, *CrystEngComm.*, 2020, **22**, 811-820.
16. G. Lazari, T. C. Stamatatos, C. P. Raptopoulou, V. Psycharis, M. Pissas, S. P. Perlepes, A. K. Boudalis, *Dalton Trans.*, 2009, 3215-3221.
17. Y. S. You, J. H. Yoon, H. C. Kimb, C. S. Hong, *Chem. Commun.*, 2005, 4116-4118.
18. E. Q. Gao, S. Q. Bai, C. F. Wang, Y. F. Yue, C. H. Yan, *Inorg. Chem.*, 2003, **42**, 8456-8464.
19. M. Mondal, P. M. Guha, S. Giri, A. Ghosh, *J. Mol. Catal. A Chem.*, 2016, **424**, 54-64.
20. M. Mondal, S. Giri, P. M. Guha, A. Ghosh, *Dalton Trans.*, 2017, **46**, 697-708.
21. R. Biswas, C. Diaz, A. Bauzá, M. Barceló-Oliver, A. Frontera, A. Ghosh, *Dalton Trans.*, 2014, **43**, 6455-6467.
22. M. Das, S. Mukherjee, Md. M. Islam, I. Choudhuri, N. Bhattacharyya, B. C. Samanta, B. Dutta, T. Maity, *ACS Omega*, 2022, **7**, 23276-23288.
23. F. Bray, J. Ferlay, I. Soerjomataram, R. L. Siegel, L. A. Torre, A. Jemal, *Ca-Cancer J. Clin.*, 2018, **68**, 394-424.
24. K. L. Pogrebniak, C. Curtis, *Trends Genet.*, 2018, **34**, 639-651.
25. E. Koren, Y. Fuchs, *Drug Resist. Updates*, 2016, **28**, 1-12.

26. S. Chatterjee, U. Hossain, P. C. Sil, *Modulation of Oxidative Stress in Heart Disease*, 2019, 457-487.
27. R. Mehrotra, K. Yadav, *World J. Clin. Oncol.*, 2022, **13**, 209-218.
28. R. L. Siegel, K. D. Miller, H. E. Fuchs, A. Jemal, *CA Cancer J. Clin.*, 2022, **72**, 7-33.
29. P. Huang, D. Wang, Y. Su, W. Huang, Y. Zhou, D. Cui, X. Zhu, D. Yan, *J. Am. Chem. Soc.*, 2014, **136**, 11748-11756.
30. B. Rosenberg, *Cisplatin* 1980, pp. 9-20.
31. Y. Jung, S. J. Lippard, *Chem. Rev.*, 2007, **107**, 1387-1407.
32. T. C. Johnstone, G. Y. Park, S. J. Lippard, *Anticancer Res.*, 2014, **34**, 471-476.
33. A. Eskandari, A. Kundu, C. Lu, S. Ghosh, K. Suntharalingam, *Dalton Trans.*, 2018, **47**, 5755-5763.
34. S. Banerjee, A. K. Chakravarty, *Acc. Chem. Res.*, 2015, **48**, 2075-2083.
35. M. Galanski, M. A. Jakupec, B. K. Keppler, *Curr. Med. Chem.*, 2005, **12**, 2075-2094.
36. B. Rosenberg, L. VanCamp, J. E. Trosko, V. H. Mansour, *Nature*, 1969, **222**, 385-386.
37. X. Qiao, Z. Y. Ma, C. Z. Xie, F. Xue, Y. W. Zhang, J. Y. Xu, Z. Y. Qiang, J. S. Lou, G. J. Chen, S. P. Yan, *J. Inorg. Biochem.*, 2011, **105**, 728-737.
38. S. A. Elsayed, E. A. Saad, S. Mostafa, *Mini-Rev. Med. Chem.*, 2019, **19**, 913-922.
39. A.-M. Florea, D. Büsselberg, *Cancers*, 2011, **3**, 1351.
40. K. T. Tadele, T. W. Tsega, *Anticancer Agents Med. Chem.*, 2019, **19**, 1786-1795.
41. U. M. Rafi, D. Mahendiran, A. K. Haleel, R. P. Nankar, M. Doble, A. K. Rahiman, *New J. Chem.*, 2016, **40**, 2451-2465.
42. L. Qi, Q. Lou, Y. Zhang, F. Jia, Y. Zhao, F. Wang, *Chem. Res. Toxicol.*, 2019, **32**, 1469-1486.
43. R. Oun, Y. E. Moussa, N. J. Wheate, *Dalton Trans.*, 2018, **47**, 6645-6653.
44. R. Y. Tsang, T. Al-Fayea, H. Au, *Drug Saf.*, 2009, **32**, 1109-22.
45. J. Jin, J. Hu, Y. Qin, J. Zhang, J. Zhao, L. Yue, H. Hou, *New J. Chem.*, 2019, **43**, 19286-19297.
46. B. B. Hasinoff, X. Wu, A. A. Yadav, D. Patel, H. Zhang, D. Wang, Z. Chen, J. C. Yalowch, *Biochem. Pharmacol.*, 2015, **93**, 266-276.
47. X. Shi, Z. Chen, Y. Wang, Z. Guo, X. Wang, *Dalton Trans.*, 2018, **47**, 5049-5054.
48. A. Gupte, R. J. Mumper, *Cancer Treat. Rev.*, 2009, **35**, 32-46.
49. F. Tisato, C. Marzano, M. Porchia, M. Pellei, C. Santini, *Med. Res. Rev.*, 2010, **30**, 708-749.
50. L. M. Balsa, V. Ferraresi-Curotto, M. J. Lavecchia, G. A. Echeverría, O. E. Piro, J. García-Tojal, R. Pis-Diez, A. C. González-Baró, I. E. León, *Dalton Trans.*, 2021, **50**, 9812-9826.
51. C. Santini, M. Pellei, V. Gandin, M. Porchia, F. Tisato, C. Marzano, *Chem. Rev.*, 2014, **114**, 815-862.
52. L. Ruiz-Azuara, M. E. B. Gomez, *Curr. Med. Chem.*, 2010, **17**, 3606-3615.
53. S. Tabassum, S. Amir, F. Arjmand, C. Pettinary, R. Marchetti, N. Masciocchi, G. Lupidi, R. Pettinary, *Eur. J. Med. Chem.*, 2013, **60**, 216-232.

54. J. Zuo, C. Bi, Y. Fan, D. Buak, C. Nardon, K. G. Daniel, Q. P. Dou, *J. Inorg. Biochem.*, 2013, **118**, 83-93.
55. A. Paul, S. Anbu, G. Sharma, M. L. Kuznetsov, B. Koch, M. F. C. G. da Silva, A. J. L. Pombeiro, *Dalton Trans.*, 2015, **44**, 19983-19996.
56. C. Marzano, M. Pellei, F. Tisato, C. Santini, *Anti-Cancer Agents Med. Chem.*, 2009, **9**, 185–211.
57. C. Santini, M. Pellei, V. Gandin, M. Porchia, F. Tisato, C. Marzano, *Chem. Rev.*, 2014, **114**, 815-862.
58. M. Usman, R. A. Khan, M. R. Khan, M. A. Farah, I. I. BinSharfan, W. Alharbi, J. P. Shaik, N. Reddy Parine, A. Alsalme, S. Tabassum, *Dalton Trans.*, 2021, **50**, 2253-2267.
59. B. J. Pages, D. L. Ang, E. P. Wright, J. R. Aldrich-Wright, *Dalton Trans.*, 2015, **44**, 3505-3526.
60. T. Bal-Demirci, G. Congur, A. Erdem, S. Erdem-Kuruca, N. Özdemir, K. Akgün-Dar, B. Varol, B. Ülküseven, *New J. Chem.*, 2015, **39**, 5643-5653.
61. J. K. Muenzner, T. Rehm, B. Biersack, A. Casini, I. A. M. De Graaf, P. Worawutputtapong, A. Noor, R. Kempe, B. Bravec, J. Kasperkova, R. Schobert, *J. Med. Chem.*, 2015, **58**, 6283-6292.
62. L. Jia, J. Xu, X. L. Zhao, S. S. Shen, T. Zhou, Z. Q. Xu, T. F. Zhu, R. H. Chen, T. L. Ma, J. Xie, K. Dong, J. C. Huang, *J. Inorg. Biochem.*, 2016, **159**, 107-119.
63. L. Yang, X. Tan, Z. Wang, X. Zhang, *Chem. Rev.*, 2015, **115**, 7196-7239.
64. W. L. Leong, J. J. Vittal, *Chem. Rev.*, 2011, **111**, 688-764.
65. Y. Yan, J. Zhang, L. Ren, C. Tang, *Chem. Soc. Rev.*, 2016, **45**, 5232–5263.
66. Z. Ma, B. Moulton, *Coord. Chem. Rev.*, 2011, **255**, 1623-1641.
67. D. Liu, C. Poon, K. Lu, C. He, W. Lin, *Nat. Commun.*, 2014, **5**, 1-11.
68. W. Zhu, J. Zhao, Q. Chen, Z. Liu, *Coord. Chem. Rev.*, 2019, **398**, 113009.
69. X. -H. Bu, W. Chen, S. -L. Lu, R. -H. Zhang, D. -Z. Liao, W. -M. Bu, M. Shionoya, F. Brisse, J. Ribas, *Angew. Chem.*, 2001, **113**, 3301-3303.
70. Bruker. SAINT v8.38A. Bruker AXS Inc., Madison, Wisconsin, USA.
71. L. Krause, R. Herbst-Irmer, G. M. Sheldrick, D. Stalke, *J. Appl. Cryst.*, 2015, **48**, 3-10.
72. (a) G. M. Sheldrick, *Acta Cryst.*, 2008, **A64**, 112-122. (b) G. M. Sheldrick, *Acta Cryst.*, 2015, **C71**, 3-8.
73. N. Sarkar, K. Harms, S. Chattopadhyay, *Polyhedron*, 2018, **141**, 198-207.
74. (a) S. K. Dey, A. Mukherjee, *New J. Chem.*, 2014, **38**, 4985-4995; (b) E. Monzani, L. Quinti, A. Perotti, L. Casella, M. Gullotti, L. Randaccio, S. Geremia, G. Nardin, P. Faleschini, G. Tabbi, *Inorg. Chem.*, 1998, **37**, 553-562.
75. (a) S. Dutta, P. Bhunia, J. Mayans, M. G. B. Drew, A. Ghosh, *Dalton Trans.*, 2020, **49**, 11268-11281; (b) S. Dutta, T. K. Ghosh, P. Mahapatra, A. Ghosh, *Inorg. Chem.*, 2020, **59**, 14989-15003; (c) A. Das, K. Bhattacharya, L. K. Das, S. Giri, A. Ghosh, *Dalton Trans.*, 2020, **49**, 3369-3371.



76. A. Wolfe, G. H. Jr. Shimer, T. Meehan, *Biochemistry*, 1987, **26**, 6392–6396.
77. R. Ali, K. El-Boubbou, M. Boudjelal, *MethodsX*, 2021, **8**, 101521.
78. C. Heckman, S. Kanagasundaram, M. Cayer, J. Paige, *Protocol Exchange*, 2007, November. <https://doi.org/10.1038/nprot.2007.504>.
79. K. M. Robinson, M. S. Janes, J. S. Beckman, *Nat. Protoc.*, 2008, **3**, 941–947.
80. P. C. Liao, S. Franco-Iborra, Y. Yang, L. A. Pon, *Methods Cell Biol.*, 2020, **155**, 295–319.
81. Y. Jiang, S. Krantz, X. Qin, S. Li, H. Gunasekara, Y. M. Kim, A. Zimnicka, M. Bae, K. Ma, P. T. Toth, Y. Hu, A. N. Shajahan-Haq, H. H. Patel, S. Gentile, M. G. Bonini, J. Rehman, Y. Liu, R. D. Minshall, *Redox Biol.*, 2022, **52**, 102304.
82. A. M. Jaeger, L. N. Makley, J. E. Gestwicki, D. J. Thiele, *J. Biol. Chem.*, 2014, **289**, 30459–30469.
83. N. M. O'Boyle, M. Banck, C. A. James, C. Morley, T. Vandermeersch, G. R. Hutchison, *J. Cheminform*, 2011, **3**, 33.
84. O. Trott, A. J. Olson, *J. Comput. Chem.*, 2010, **31**, 455–461.
85. S. Saha, N. Biswas, A. Sasmal, C. J. Gómez-García, E. Garribba, A. Bauza, A. Frontera, G. Pilet, G. M. Rosair, S. Mitra, C. R. Choudhury, *Dalton Trans.*, 2018, **47**, 16102–16118.
86. Z. -Z. Chen, W. -Z. Zhang, T. Zhang, Y. Zhang, W. -K. Dong, *New J. Chem.*, 2020, **44**, 19836.
87. A. Banerjee, S. Sarkar, D. Chopra, E. Colacio, K. K. Rajak, *Inorg. Chem.*, 2008, **47**, 4023–4031.
88. N. Balakrishnan, J. Haribabu, A. K. Dhanabalan, S. Swaminathan, S. Sun, D. F. Dibwe, N. Bhuvanesh, S. Awale, R. Karvembu, *Dalton Trans.*, 2020, **49**, 9411–9424.
89. A. Das, K. Bhattacharya, L. K. Das, S. Giri, A. Ghosh, *Dalton Trans.*, 2020, **49**, 3369–3371.
90. R. Sanyal, P. Kundu, E. Rychagova, G. Zhigulin, S. Ketkov, B. Ghosh, S. K. Chattopadhyay, E. Zangrando, D. Das, *New J. Chem.*, 2016, **40**, 6623–6635.
91. M. S. Ahmad, M. Khalid, M. S. Khan, M. Shahid, M. Ahmad, Monika, A. Ansari, M. Ashafaq, *New J. Chem.*, 2020, **44**, 7998–8009.
92. (a) S. Mandal, R. Naskar, A. Sau Mondal, B. Bera, T. K. Mondal, *Dalton Trans.*, 2023, **52**, 5983–5998; (b) S. Mukherjee, C. K. Pal, M. Kotakonda, M. Joshi, M. Shit, P. Ghosh, A. R. Choudhury, B. Biswas, *J. Mol. Struct.*, 2021, **1245**, 131057; (c) A. Biswas, L. K. Das, M. G. B. Drew, C. Diaz, A. Ghosh, *Inorg. Chem.*, 2012, **51**, 10111–10121; (d) N. Balakrishnan, J. Haribabu, A. K. Dhanabalan, S. Swaminathan, S. Sun, D. F. Dibwe, N. Bhuvanesh, S. Awale, R. Karvembu, *Dalton Trans.*, 2020, **49**, 9411–9424; (e) Z. -Z. Chen, W. -Z. Zhang, T. Zhang, Y. Zhang, W. -K. Dong, *New J. Chem.*, 2020, **44**, 19836; (f) D. Mondal, A. K. Ghosh, A. Chatterjee, R. Ghosh, *Inorg. Chim. Acta*, 2019, **486**, 719–723.
93. G. Barone, A. Terenzi, A. Lauria, A. M. Almerico, J. M. Leal, N. Busto, B. García, *Coord. Chem. Rev.*, 2013, **257**, 2848–2862.
94. D. -H. Cai, B. -H. Chen, Q. -Y. Liu, X. -Y. Le, L. He, *Dalton Trans.*, 2022, **51**, 16574–16586.

95. A. Paul, P. Singh, P. M. Kuznetsov, A. Karmakar, M. F. C. Guedes da Silva, B. Koch, A. J. L. Pombeiro, *Dalton Trans.*, 2021, **50**, 3701-3716.
96. F. Jozefíková, F. Perontsis, M. Šimunková, M. Barbieriková, L. Švorc, M. Valko, G. Psomas, J. Moncol', *New J. Chem.*, 2020, **44**, 12827-12842.
97. M. Das, S. Mukherjee, P. Brandao, S. K. Seth, S. Giri, S. S. Mati, B. S. Samanta, S. Laha, T. Maity, *ACS Omega*, 2021, **6**, 3659–3674.
98. D. Senthil Raja, N. S. P. Bhuvanesh, K. Natarajan, *Inorg. Chem.*, 2011, **50**, 12852–12866.
99. C. Kalaivanan, M. Sankarganesh, M. Y. Suvaikin, G. B. Karthi, S. Gurusamy, R. Subramanian, R. N. Asha, *J. Mol. Liq.*, 2020, **320**, 114423.
100. R. Aggarwal, M. Hooda, P. Kumar, N. Jain, G. P. Dubey, H. Chugh, R. Chandra, *J. Org. Chem.*, 2022, **87**, 3952–3966.
101. F. Darabi, H. Hadadzadeh, J. Simpson, A. Shahpiri, *New J. Chem.*, 2016, **40**, 9081-9097.
102. V. Rajendiran, R. Karthik, M. Palaniandavar, H. Stoeckli-Evans, V. S. Periasamy, M. A. Akbarsha, B. S. Srinag, H. Krishnamurthy, *Inorg. Chem.*, 2007, **46**, 8208–8221.
103. X. L. Han, P. Mei, Y. Liu, Q. Xiao, F. L. Jiang, R. Li, *Spectrochim. Acta, Part A*, 2009, **74**, 781–787.
104. S. Rahman, M. T. Rehman, G. Rabbani, P. Khan, M. F. AlAjmi, M. I. Hassan, G. Muteeb, J. Kim, *Int. J. Mol. Sci.*, 2019, **20**, 2727.
105. A. Hussain, M. F. AlAjmi, M. T. Rehman, S. Amir, F. M. Husain, A. Alsalmeh, M. A. Siddiqui, A. A. AlKhedhairi, R. A. Khan, *Sci Rep.*, 2019, **9**, 5237.
106. J. Juárez, S. G. López, A. Cambón, V. Mosquera, P. Taboada, *J. Phys. Chem. B*, 2009, **113**, 10521–10529.
107. A. Shanmugapriya, F. Dallemer, R. Prabhakaran, *New J. Chem.*, 2018, **42**, 18850-18864.
108. S. Dadsena, A. Jenner, A. J. García-Sáez, *Cell. Mol. Life Sci.*, 2021, **78**, 3777–3790.
109. Q. Bao, Y. Shi, *Cell Death Differ*, 2007, **14**, 56–65.
110. G. V. Chaitanya, J. S. Alexander, P. P. Babu, *Cell Commun Signal*, 2010, **8**, 31.
111. R. Zhang, D. Luo, R. Miao, L. Bai, Q. Ge, W. C. Sessa, W. Min, *Oncogene*, 2005, **24**, 3954–3963.
112. A. D. Basso, D. B. Solit, G. Chiosis, B. Giri, P. Tsichlis, N. Rosen, *J. Biol. Chem.*, 2002, **277**, 39858–39866.
113. B. D. Manning, L. C. Cantley, *Cell.*, 2007, **129**, 1261–1274.
114. G. M. Nitulescu, M. V. D. Venter, G. Nitulescu, A. Ungurianu, P. Juzenas, Q. Peng, O. T. Olaru, D. Grădinaru, A. Tsatsakis, D. Tsoukalas, D. A. Spandidos, D. Margina, *Int. J. Oncology*, 2018, **53**, 2319–2331.
115. S. -J. Jeong, A. Dasgupta, K. -J. Jung, J. -H. Um, A. Burke, H. U. Park, J. N. Brady, *Virology*, 2008, **370**, 264–272.
116. S. W. Kmiecik, M. P. Mayer, *Trends biochem. Sci.*, 2022, **47**, 218-34.



117. C. Dai, L. Whitesell, A. B. Rogers, S. Lindquist, *Cell.*, 2007, **130**, 1005-1018.
118. M. Kundu, P. Sadhukhan, N. Ghosh, S. Chatterjee, P. Manna, J. Das, P. C. Sil, *J. Adv. Res.*, 2019, **18**, 161-172.
119. J. Fares, M. Y. Fares, H. H. Khachfe, H. A. Salhab, Y. Fares, *Sig. Transduct Target. Ther.*, 2020, **5**, 28.
120. D. Hanahan, R. A. Weinberg, *Cell.*, 2011, **144**, 646-74.
121. M. V. Blagosklonny, *Oncotarget*, 2023, **14**, 193-206.
122. A. Ramos, S. Sadeghi, H. Tabatabaeian, *Int. J. Mol. Sci.*, 2021, **22**, 9451.
123. P. Sadhukhan, S. Saha, P. C. Sil, *Biochem. Anal. Biochem.*, 2015, **4**, 236.
124. S. J. Kim, H. S. Kim, Y. R. Seo, *Oxid. Med. Cell Longev.*, 2019, **2019**, 5381692.
125. G. Y. Liou, P. Storz, *Free Radic. Res.*, 2010, **44**, 479-496.
126. B. Fadeel, A. Ottosson, S. Pervaiz, *Cell Death Differ.*, 2008, **15**, 443-452.
127. C. Dai, *Philosophical Transactions of the Royal Society B: Biological Sciences*, 2017, **373**, 20160525.
128. C. Prodromou, *Biochem. J.*, 2016, **473**, 2439-2452.
129. R. Takii, M. Fujimoto, K. Tan, E. Takaki, N. Hayashida, R. Nakato, K. Shirahige, A. Nakai, *Mol. Cell Biol.*, 2015, **35**, 11-25.

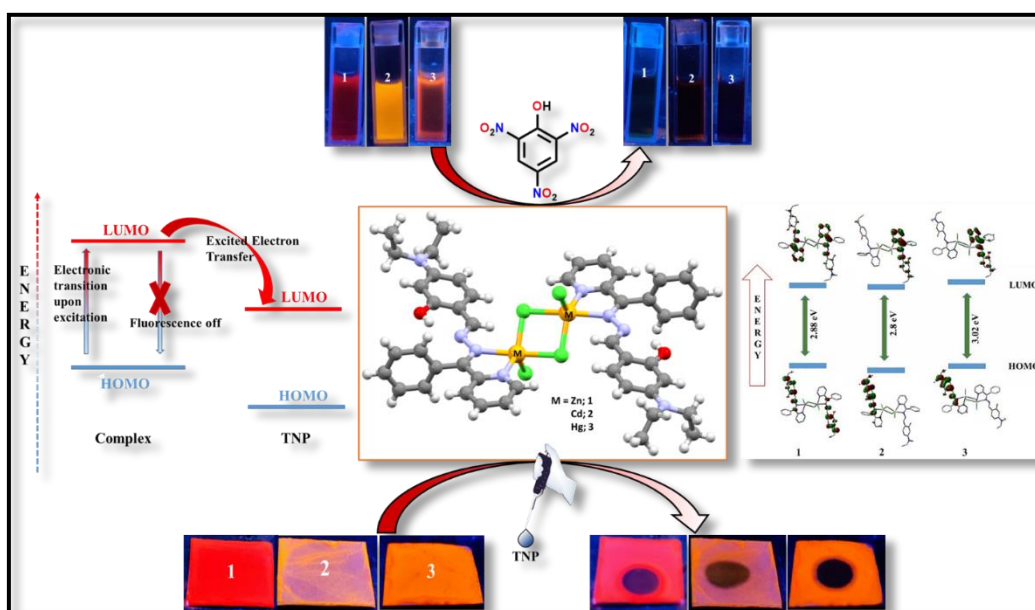
## **CHAPTER - VI**

**Heavy metal based binuclear luminescent complexes for selective and swift sensing of nitro-explosives in solution and solid phase**

## *Heavy metal based binuclear luminescent complexes for selective and swift sensing of nitro-explosives in solution and solid phase*

### Abstract

Discerning detection of 2,4,6-trinitrophenol (TNP) like mutagenic pollutant and other NACs using robust luminescent metal complexes has been always a potential research field. Herein, we report the synthesis of three novel luminescent chloro-bridged heavy metal complexes of formulation  $[M_2(\mathbf{HL})_2\text{Cl}_4]$  where  $M$  stands for  $\text{Zn}^{2+}$ ,  $\text{Cd}^{2+}$  and  $\text{Hg}^{2+}$  for complex **1**, **2** and **3** respectively, by refluxing the mixture of ligand **HL** and metal chloride salts. Single-crystal X-ray study, spectroscopic ( $^1\text{H}$  NMR, FT-IR, UV-Vis, and emission spectroscopy) techniques, DFT and TDDFT calculations have all been used to fully characterize the complexes. All the three complexes exhibit excellent fluorescence responses which gets quenched in presence of different NACs. Interestingly, the fluoroprobes (**1-3**) are more selective and sensitive towards TNP over several other comparative NACs with high (in the order of  $\sim 10^4 \text{ M}^{-1}$ ) quenching constants ( $K_{\text{sv}}$ ) and nanomolar detection limit (LOD) and also, complex-coated TLC plate was used to detect TNP in solid state. Among the three, complex **3** is the most efficacious with  $K_{\text{sv}} (5.19 \pm 0.12) \times 10^4 \text{ M}^{-1}$  and LOD of 180.2 nM. In addition, DFT and UV-Vis absorption of probes with TNP proved that the quenching phenomenon could be primarily ascribed to photo-induced electron transfer (PET) and the resonance energy transfer (RET).



## VI.1. Introduction

The lucid design and fabrication of distinct multinuclear metal complexes have attracted significant attention due to their structural variety, remarkable magnetic properties, and probable applications in the fields of luminescence, catalysis, gas adsorption and functional materials.<sup>1-7</sup> There are some reports of heterometallic and homometallic complexes of  $\text{Ni}^{2+}$ ,  $\text{Zn}^{2+}$ ,  $\text{Co}^{2+}$ ,  $\text{Cu}^{2+}$  in the literature.<sup>8-11</sup> These complexes have been designed mostly to explore their magnetic properties. This field of research involving the multinuclear metal complexes still remains uncultivated. Lately, numerous research groups have been occupied with the precise design and fabrication of chemosensors for the distinct recognition of metal ions, anions, a range of toxic organic analytes and explosive compounds due to their major impact on environment as well as on human life.<sup>12-20</sup> Zinc(II) Schiff base complexes have been explored by the inorganic chemists for an elongated time period owing to its effortlessness in synthetic schemes and remarkable coordination of zinc. Another good advantage of these zinc Schiff base complexes is that they exhibit excellent fluorescent properties which are utilized in a number of fluorescence-based applications.<sup>21,22</sup> Among numerous metal ions,  $\text{Zn}^{2+}$  is the second most significant metal ion after iron in the human body.<sup>23,24</sup> On the other hand, cadmium is a non-essential substance for the organism, and is even classified as a human carcinogen.<sup>25</sup> Several fluorescence chemosensors for  $\text{Zn}^{2+}$  and  $\text{Cd}^{2+}$  ions have been published in the literature till date and amid them, turn-on fluorescent sensors have secured hugely advantageous position in the field of molecular recognition and in sensing different analytes.<sup>26-28</sup> Now among them, zinc(II) Schiff base complexes have been found mainly to be used as chemosensors for the detection of nitroaromatics by diverse research groups.<sup>29-31</sup>

The effectual recognition of nitroaromatic-based explosives (NACs) and dangerous metal ions has achieved lots of attention in present time owing to the threat towards security and human wellbeing.<sup>32-34</sup> NACs are non-biodegradable lethal pollutants that are in deliberate use in separate industries such as dye industry, pharma industry etc.<sup>35</sup> NACs can also be attained without difficulty and are a reason of distress owing to the growing terrorist actions. These are the reasons behind the utmost necessity of detecting these nitroaromatics in very minute level. Scientists are putting great efforts in developing chemosensors which can not only recognize NACs at a very tiny level but at the same time, it should be cost-effective.<sup>36,37</sup> Of all the nitro explosives, 2,4,6-trinitrophenol (TNP) has gained the most attention because it is more powerful explosive than the others.<sup>38</sup> The casual release of TNP residues not only contaminates the environment, but also results in organ impairment.<sup>39</sup> Moreover, with the

growth in industrial segments, NACs have been broadly used in dyes, fireworks, leathers, medicines and pesticides.<sup>40</sup> Also, due to the high toxicity of TNP, it may become the source of numerous diseases which can cause immense danger to human wellbeing and biological atmosphere.<sup>41-47</sup> Hence, proficient recognition of TNP is vital.

Accordingly, the approach towards a portable and competent recognition strategy has captivated significant minds all over the globe.<sup>48</sup> Some swift and sensitive techniques have been evolved, such as gas chromatography-mass spectrometry (GC-MS), high-performance liquid chromatography (HPLC) and surface-enhanced Raman spectroscopy (SERS).<sup>49-51</sup> Still, the large-scale production and low cost-effectiveness have restricted their extensive application.<sup>52,53</sup> As a result, it is vital to construct ecologically aware, economical and portable approaches to proficiently and selectively detect TNP. Predominantly fluorescence sensing have awakened immense interest for their high sensitivity, admirable selectivity, rapid response and reasonably priced cost.<sup>54-58</sup> The sensitive fluorescence quenching by nitroaromatic derivatives have been inspected broadly both in solid as well as in solution phases at low concentrations with discrete sensitivity and selectivity.<sup>59-61</sup> In the recent years, a number of fluorescent probes were published for recognizing NACs, such as metal-organic frameworks, polymer-based substances, aggregation-induced emission-active molecules and quantum dots.<sup>62-65</sup> Even though there are several reports of organic fluorescent sensors and coordination polymers which identify the presence of nitroaromatics, the fabrication of a greatly selective and capable AIE-active metal complex-based TNP probe is still very exceptional.<sup>66,67</sup>

Even though there are several reports of TNP sensors, most of them revolve around the coordination polymers.<sup>68-72</sup> So furthermore research is highly necessary in this area. In this present report, we have fabricated three heavy metal complexes comprising  $\text{Zn}^{2+}$ ,  $\text{Cd}^{2+}$  and  $\text{Hg}^{2+}$  and each of these metal-based probes show quenching in presence of TNP selectively. To the best of our knowledge, this is the first report of three heavy metal complex-based probes which selectively recognize TNP. So herein we have introduced three binuclear chloro-bridged metal complexes having molecular formula  $[\text{Zn}_2(\text{HL})_2\text{Cl}_4](\mathbf{1})$ ,  $[\text{Cd}_2(\text{HL})_2\text{Cl}_4](\mathbf{2})$  and  $[\text{Hg}_2(\text{HL})_2\text{Cl}_4](\mathbf{3})$  and thoroughly characterized them by elemental analysis,  $^1\text{H}$ -NMR, FT-IR, UV-Vis and emission spectroscopy along with single crystal X-ray diffraction technique. Here Schiff base ligand, 5-(diethylamino)-2-((E)-(((E)-phenyl(pyridin-2-yl)methylene)hydrazono)methyl)phenol (**HL**) was synthesized by using hydrazine, 2-benzoylpyridine and 4-(diethylamino)salicylaldehyde.<sup>73</sup> This type of Schiff base ligand act like pincer, multifaceted ligands with variety of flexible donors and are capable of

coordinating with different transition metals. Their adaptable ligating nature enables the metal center to adopt varied geometries and coordination numbers, resulting in a diverse range of photophysical and luminescence properties. Our lab is actively involved in the design and fabrication of a wide spectrum of transition metal complexes of such Schiff base, which prompted us to choose the ligand (**HL**) for the synthesis of the above-mentioned compounds. We have then executed the sensing study of these complexes in presence of different nitroaromatic compounds in acetonitrile solution. All the three binuclear complexes display high selectivity towards TNP over other nitroaromatic explosives in nanomolar level. The plausible quenching mechanism includes photo-induced electron transfer (PET) and resonance energy transfer (RET). In case of RET mechanism, the extent of overlapping zone for the complexes follows the order **3** > **2** > **1**, which explains the higher quenching ability of complex **3** towards TNP than the other two. To establish the quenching behavior of these complexes in presence of TNP, we have utilized fluorescence spectroscopy, time resolved spectrofluorometer, <sup>1</sup>H-NMR titration and paper strip based solid state detection.

## VI.2. Experimental

### VI.2.1. Materials and Physical measurements

All the chemicals and solvents used in this work were bought from Aldrich. So, all the chemicals were utilized without any further purification. Ligand **HL** was synthesized by previous procedure.<sup>73</sup> Infrared spectra (IR) were recorded on a Perkin-Elmer FT-IR spectrometer (4000–400 cm<sup>-1</sup>) in KBr pellets. <sup>1</sup>H NMR spectra of the compounds were collected from a Bruker 300 MHz instrument in CDCl<sub>3</sub> and DMSO-d<sub>6</sub> medium (mentioned in each spectrum). Absorption spectra were obtained by using a Shimadzu UV-1900i spectrophotometer. On a Shimadzu RF-6000 spectro-fluorophotometer, fluorescence studies were carried out at room temperature. Luminescence lifetime studies were performed in a time-resolved spectrofluorometer from IBH, UK.

### VI.2.2. Synthesis

#### VI.2.2.1. Synthesis of the Complex [Zn<sub>2</sub>(**HL**)<sub>2</sub>Cl<sub>4</sub>] (**1**)

To a solution of **HL** (100 mg, 0.268 mmol) in acetonitrile (10 mL), a solution of ZnCl<sub>2</sub> (36.5 mg, 0.268 mmol) in acetonitrile (5 mL) was added and refluxed for 6 hours. A wine-red coloured solution was appeared which is filtered and kept in a beaker for slow evaporation of solvent. Single crystals of the complex were obtained after 3 days at room temperature.

Yield 0.196 g (72%). Anal. Calc. for  $C_{46}H_{48}Cl_4N_8O_2Zn_2$ : C, 54.3; H, 4.76; N, 11.01. Found: C, 53.97; H, 4.31; N, 10.87. IR ( $cm^{-1}$ ) in KBr: 3452  $\nu(O-H)$ ; 3076 – 2871  $\nu(C-H)$ ; 1628  $\nu(imine, -HC=N-)$ ; 1572  $\nu(pyridyl, -HC=N-)$ .  $^1H$  NMR (300 MHz,  $CDCl_3$ ):  $\delta$  1.2 (t,  $J = 7$  Hz, 6H), 3.36-3.43 (m, 4H), 6.04 (s, 1H), 6.29 (d,  $J = 9$  Hz, 1H), 7.44-7.54 (m, 5H), 7.65 (s, 1H), 7.73 (t,  $J = 8$  Hz, 1H), 8.04 (t,  $J = 8$  Hz, 2H), 8.88 (d,  $J = 6$  Hz, 1H), 9.02 (s, 1H), 10.7 (s, 1H). UV-Vis (in  $CH_3CN$ ),  $\lambda_{max}$  ( $\epsilon$ ,  $M^{-1}cm^{-1}$ ): 501 nm (14983), 430 nm (24429), 350 nm (5704), 290 nm (8280).

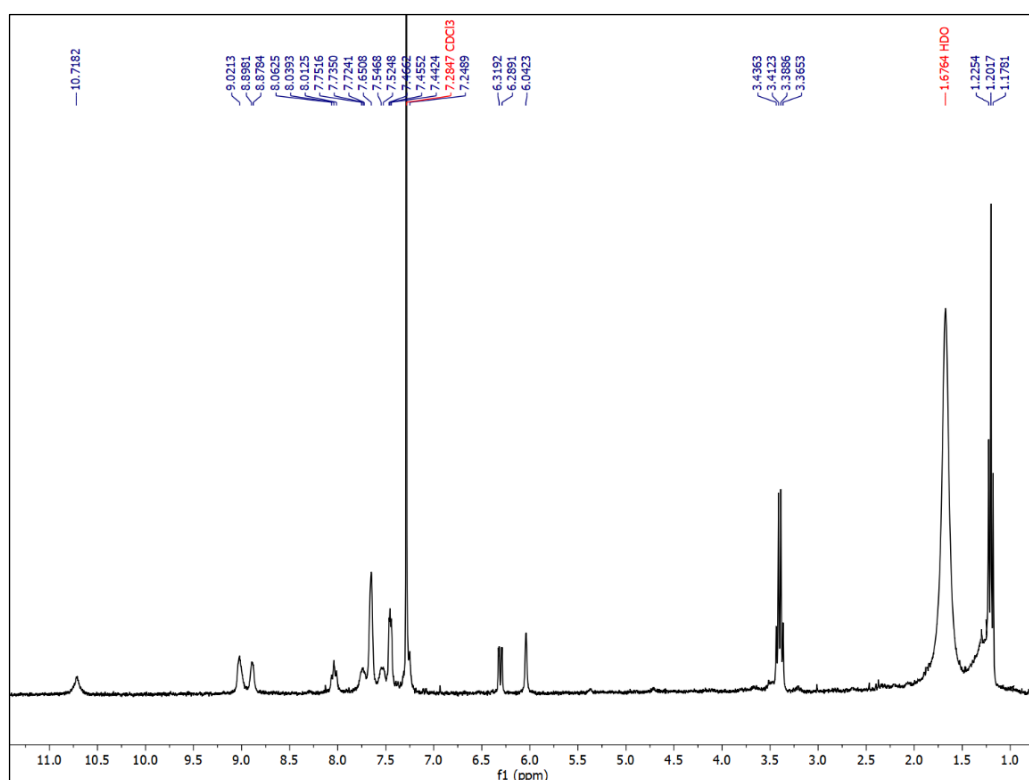


Figure VI.1.  $^1H$  NMR spectra of complex **1** in  $CDCl_3$

#### VI.2.2.2. Synthesis of the Complex $[Cd_2(HL)_2Cl_4]$ (**2**)

An acetonitrile solution (5 mL) of  $CdCl_2 \cdot H_2O$  (40 mg, 0.2 mmol) was poured to 10 mL solution ligand **HL** (74 mg, 0.2 mmol) in acetonitrile and was refluxed for 3 hours. After completion of reaction, orange coloured precipitate was observed which is filtered and collected. Suitable orange-coloured single crystals of the complex were obtained from a DCM/Hexane layer of the residue after few days.

Yield 0.155 g (70%). Anal. Calc. for  $C_{46}H_{48}Cl_4N_8O_2Cd_2$ : C, 49.71; H, 4.35; N, 10.08. Found: C, 49.4; H, 4.08; N, 9.91. IR ( $cm^{-1}$ ) in KBr: 3490  $\nu(O-H)$ ; 3075 – 2871  $\nu(C-H)$ ; 1628  $\nu(imine -HC=N-)$ ; 1574  $\nu(pyridyl -HC=N-)$ .  $^1H$  NMR (300 MHz,  $CDCl_3$ ):  $\delta$  1.08 (t,  $J = 6.8$



Hz, 6H), 3.4-3.47 (m, 4H), 5.98 (s, 1H), 6.3 (d,  $J = 8.4$  Hz, 1H), 7.28 (d,  $J = 8.4$  Hz, 2H), 7.43-7.5 (m, 5H), 7.95 (t,  $J = 7$  Hz, 1H), 8.57 (d,  $J = 5.9$  Hz, 1H), 8.78 (s, 1H), 11.3 (s, 1H). UV-Vis (in  $\text{CH}_3\text{CN}$ ),  $\lambda_{\text{max}}$  ( $\epsilon$ ,  $\text{M}^{-1}\text{cm}^{-1}$ ): 444 nm (25247), 330 nm (3869), 298 nm (6894), 240 nm (12639).

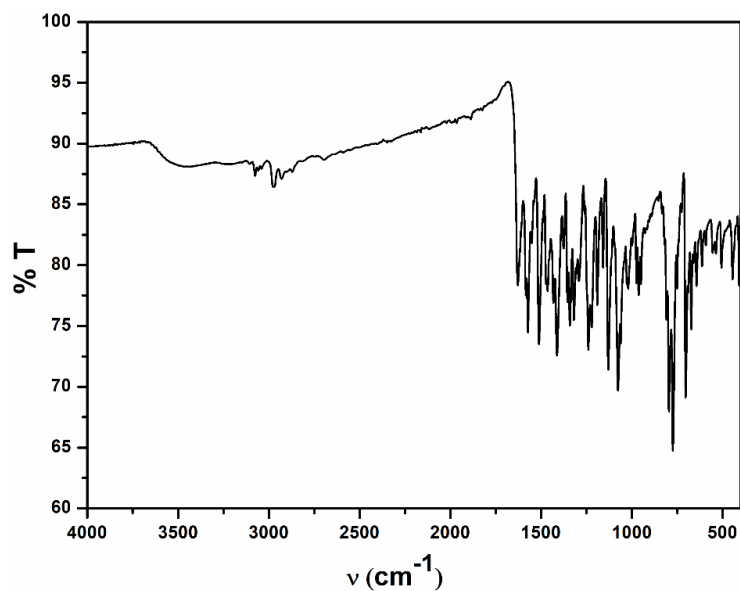
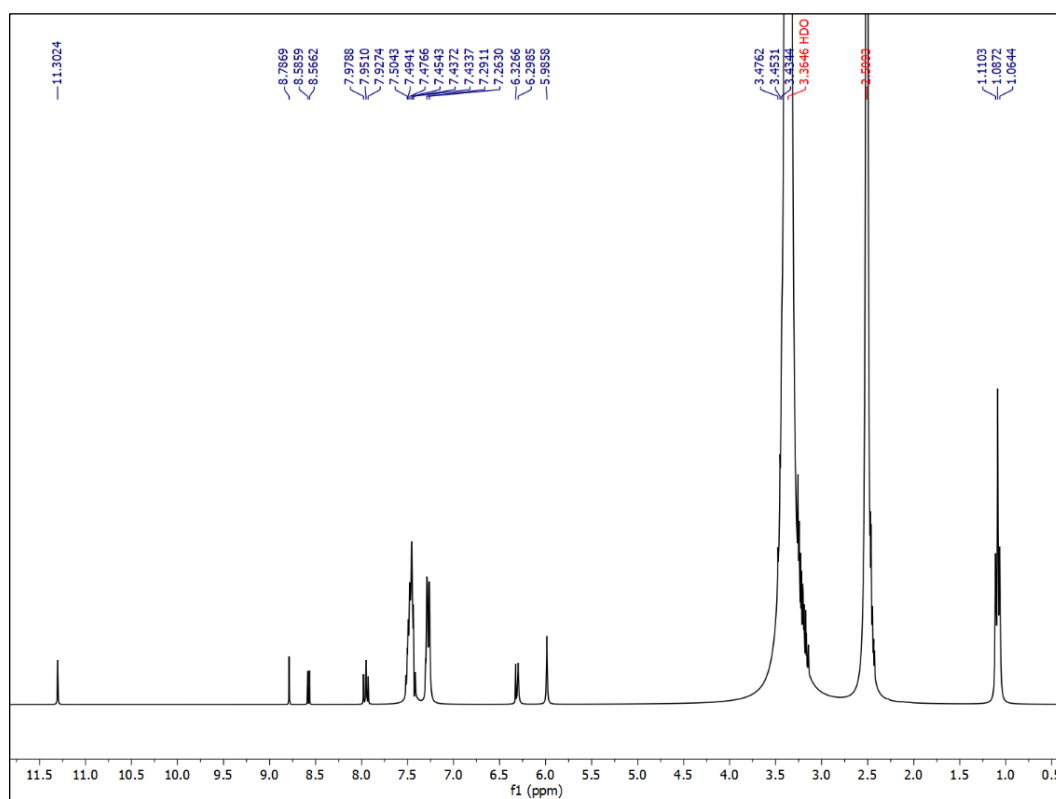
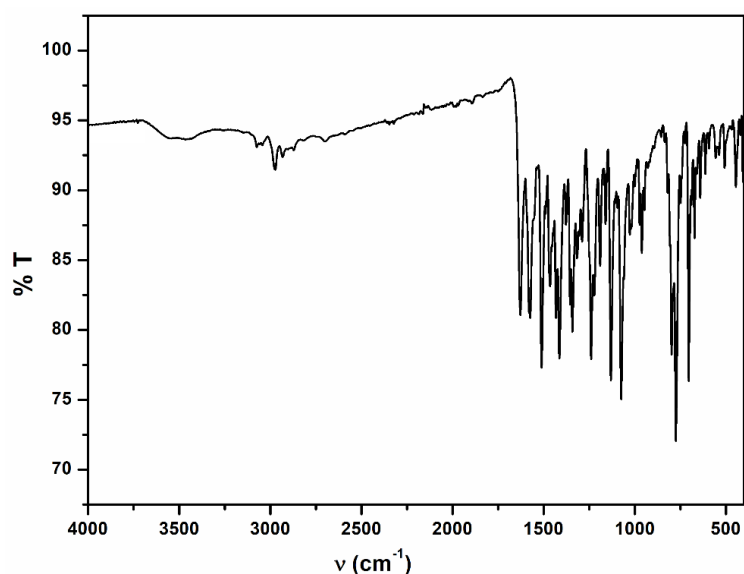


Figure VI.2. FT-IR spectra of complex 1

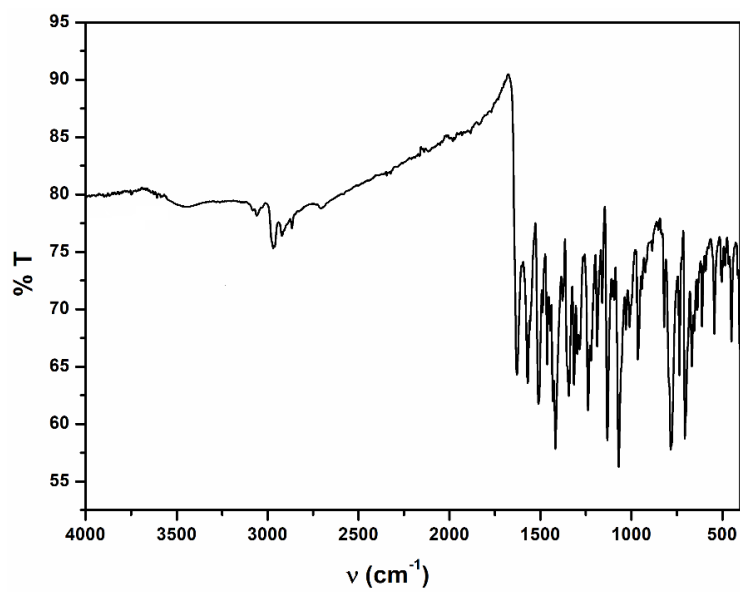
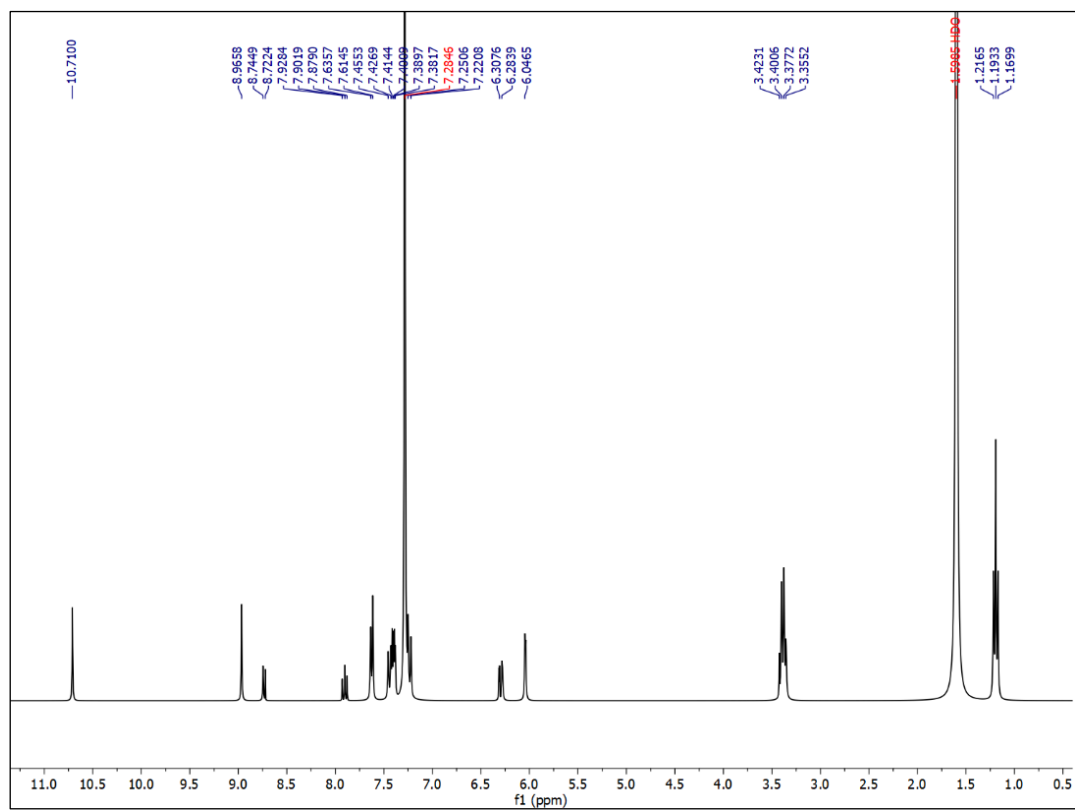
Figure VI.3.  $^1\text{H}$  NMR spectra of complex 2 in  $\text{CDCl}_3$

Figure VI.4. FT-IR spectra of complex **2**

### VI.2.2.3. Synthesis of the Complex $[\text{Hg}_2(\text{HL})_2\text{Cl}_4]$ (**3**)

A solution of  $\text{HgCl}_2$  (54 mg, 0.2 mmol) in acetonitrile (6 mL) was added to a solution of **HL** (75 mg, 0.2 mmol) in acetonitrile (10 mL) and refluxed for 4 hours. After the completion of reaction, deep wine-red coloured crystalline precipitate was obtained which is filtered. After few days, wine-red coloured single crystals were obtained on slow diffusion of a DCM/Hexane mixture of the residue in a layer.

Yield 0.13 g (70%). Anal. Calc. for  $\text{C}_{46}\text{H}_{48}\text{Cl}_4\text{N}_8\text{O}_2\text{Hg}_2$ : C, 42.9; H, 3.76; N, 8.7. Found: C, 42.65; H, 3.48; N, 8.41. IR ( $\text{cm}^{-1}$ ) in KBr: 3480  $\nu(\text{O-H})$ ; 3070 – 2870  $\nu(\text{C-H})$ ; 1626  $\nu(\text{imine, } -\text{HC}=\text{N}-)$ ; 1572  $\nu(\text{pyridyl, } -\text{HC}=\text{N}-)$ .  $^1\text{H}$  NMR (300 MHz,  $\text{CDCl}_3$ ):  $\delta$  1.19 (t,  $J = 7$  Hz, 6H), 3.35-3.42 (m, 4H), 6.04 (s, 1H), 6.29 (d,  $J = 7.1$  Hz, 1H), 7.24 (d,  $J = 8.9$  Hz, 1H), 7.38-7.45 (m, 5H), 7.62 (d,  $J = 6.36$  Hz, 2H), 7.9 (t,  $J = 6.8$  Hz, 1H), 8.73 (d,  $J = 6.7$  Hz, 1H), 8.96 (s, 1H), 10.7 (s, 1H). UV-Vis (in  $\text{CH}_3\text{CN}$ ),  $\lambda_{\text{max}}$  ( $\epsilon$ ,  $\text{M}^{-1}\text{cm}^{-1}$ ): 430 nm (21780), 328 nm (3807), 277 nm (9456).

Figure VI.5. FT-IR spectra of complex **3**Figure VI.6.  $^1\text{H}$  NMR spectra of complex **3** in  $\text{CDCl}_3$

### VI.2.3. Crystal structure determination and refinement

X-ray Diffraction data was collected using Bruker AXS D8 Quest CMOS diffractometer using graphite monochromatized Mo-K $\alpha$  radiation ( $\lambda = 0.71073 \text{ \AA}$ ) at 293°C. Reflection data were recorded using the  $\omega$  scan technique. The data were integrated using the SAINT program<sup>74</sup>, and the absorption corrections were made with SADABS<sup>75</sup>. All data were corrected for Lorentz and polarization effects, and the non-hydrogen atoms were refined anisotropically. Hydrogen atoms were included in the refinement process as per the riding model. The structures were solved by direct method and refined using SHELXL-2016/6 program<sup>76</sup> by full-matrix least-squares techniques.

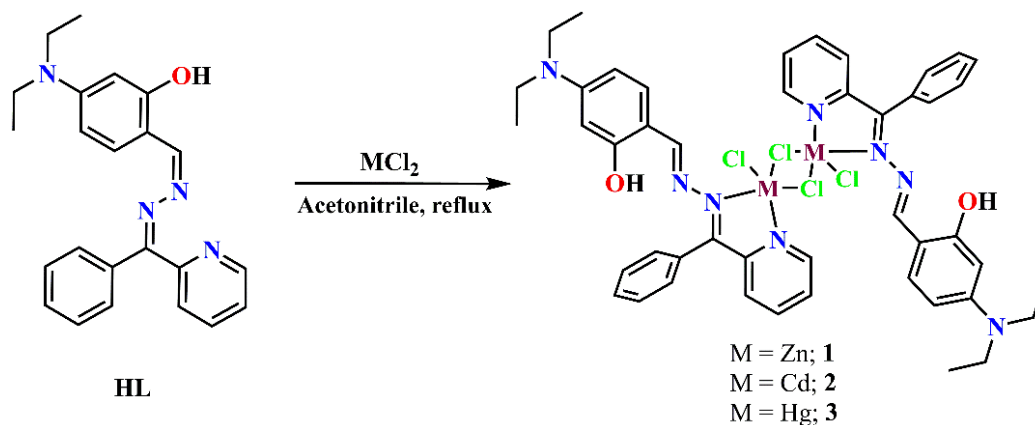
### VI.2.4. Theoretical study

Geometry optimizations were carried out by density functional theory (DFT) method using B3LYP<sup>77</sup> function for the complexes. All calculations were performed with Gaussian09 program<sup>78</sup> with the aid of the Gauss-View, Version 5 visualization program. All elements were assigned the 6-31G(d) basis set except the metals. Basis set used for the metals (Zn, Hg and Cd) was LanL2dz.<sup>79</sup> Electronic transitions were calculated using the time-dependent density functional theory (TDDFT) formalism<sup>80</sup> using conductor-like polarizable continuum model (CPCM)<sup>81</sup> in acetonitrile to simulate the solvent. GaussSum<sup>82</sup> was used to calculate the fractional contributions of various groups to each molecular orbital.

## VI.3. Results and Discussion

### VI.3.1. Synthesis and Characterization of **1** – **3**

The fabrication of the complexes (**1–3**) was carried out via the reaction of metal salts (ZnCl<sub>2</sub>, CdCl<sub>2</sub>.H<sub>2</sub>O and HgCl<sub>2</sub>) with the ligand **HL**<sup>73</sup> in 1 : 1 molar ratio in acetonitrile solvent (scheme VI.1). Single crystals of the complexes **2** and **3** were collected from the DCM/hexane layer of the respective compounds while single crystals of **1** was obtained in a beaker by slow evaporating the resulting reaction mixture. All the complexes are methodically characterized by elemental analysis, IR, UV-Vis and <sup>1</sup>H-NMR spectroscopy. The molecular structures of complexes were established by single crystal X-ray diffraction method.

Scheme VI.1. Synthetic layout of the complexes **1–3**.

In the IR spectra of the complexes **1–3**, vibration bands which are in the range 3450 - 3490  $\text{cm}^{-1}$ , were observed due to the presence of phenolic O–H group. Multiple bands were detected in the range 2866 – 3075  $\text{cm}^{-1}$  for all the complexes, which are responsible for C–H stretching ( $\text{sp}^2$  and  $\text{sp}^3$ ). Imine bond ( $-\text{CH}=\text{N}-$ ) vibrations were noticed at around 1628  $\text{cm}^{-1}$  while pyridyl  $\text{CH}=\text{N}-$  bond vibrations were visible at around 1572  $\text{cm}^{-1}$  for the complexes **1–3** (Figure VI.2, VI.4 and VI.5).  $^1\text{H}$ -NMR spectra of the complexes were done in  $\text{CDCl}_3$  (**1** and **3**) and  $\text{DMSO-d}_6$  (complex **2**). Characteristic phenolic O–H proton peak was noticed around 11 ppm for all the complexes. Imine proton ( $\text{CH}=\text{N}-$ ) peaks (singlet) were observed at 9.02, 8.78 and 8.96 ppm while pyridyl  $\text{CH}=\text{N}-$  proton peaks (doublet) appeared at 8.88, 8.57 and 8.73 ppm for **1**, **2** and **3** respectively (Figure VI.1, VI.3 and VI.6). Absorption spectra of the complexes were studied in acetonitrile medium. The high intensity absorption bands shown by the complexes are due to intra-ligand charge transfer ( $\pi \rightarrow \pi^*$ ) transitions (Figure VI.7).

### VI.3.2. Crystal Structure Descriptions

Single crystal X-ray diffraction analysis reflects that all the three complexes were crystallized in triclinic system with space group  $\text{P}\bar{1}$ . The crystallographic refinement parameters of the complexes are given in Table VI.1 and some selected bond distances and bond angles are listed in Table VI.2 and VI.3. X-ray method showed that ligand, **HL** was coordinated to metal through pyridine nitrogen atom (N1) and imine nitrogen atom (N2) by forming a five membered chelate ring ( $\text{N1-C5-C6-N2-M}$ ;  $\text{M} = \text{Zn, Cd and Hg}$ ) and surprisingly, the structural environment of **1**, **2** and **3** were similar where the geometry around the metal centres was distorted square pyramidal. All the three complexes **1**, **2** and **3** have  $\mu_2$  bridged binuclear structure where two metal centres were bridged by two chloride ions ( $\text{Cl}_2$ ) in the

equatorial positions and the fifth coordination site (axial position) of the metal ions was fulfilled by chlorine atom (Cl1) (Figure VI.8 and VI.9).

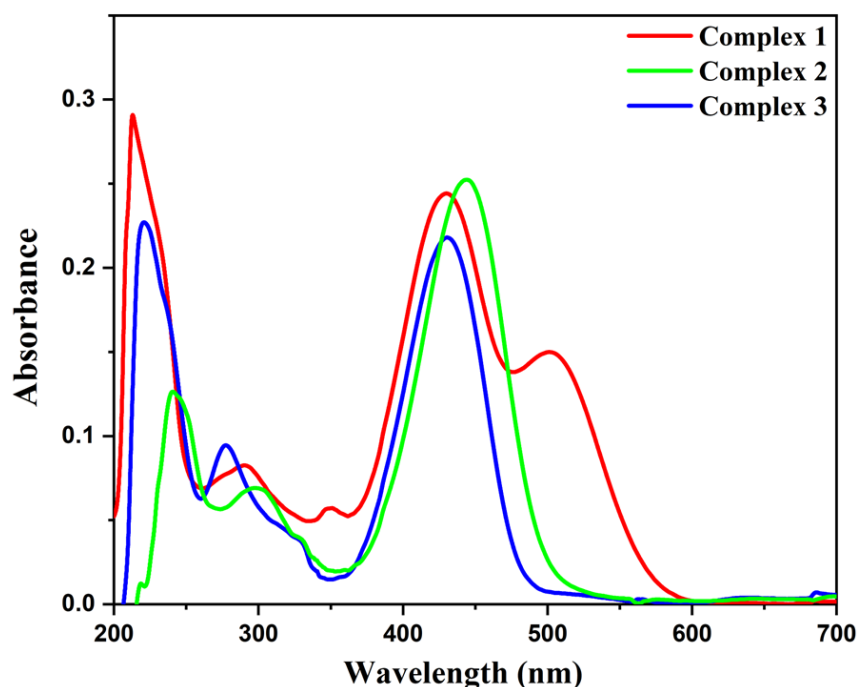


Figure VI.7. Absorption spectra of complexes **1-3** in acetonitrile

In complex **1**, Zn(II)–N (pyridyl) bond distance (2.091(2) Å) was significantly shorter than Zn(II)–N (imine) bond distance (2.2278(19) Å), which clearly stated that the interaction between Zn(II) ion and pyridine nitrogen atom (N1) was stronger than that of between Zn(II) and imine nitrogen atom (N2). Similar scenarios were noticed for complex **2** and **3**, where, Cd(II)–N1, Cd(II)–N2, Hg(II)–N1 and Hg(II)–N2 bond lengths were, 2.315(4) Å, 2.403(4) Å, 2.307(7) Å, and 2.453(8) Å respectively. Unexpectedly, the bond distances between metal ion (Zn(II), Cd(II) and Hg(II)) and two  $\mu_2$  bridged chloride ions (Cl2) were dissimilar, in complex **1**, two Zn(II)–Cl2 bond distances were 2.3160(7) and 2.5751(7) Å while in **2**, two Cd(II)–Cl2 lengths were 2.5593(16) and 2.6006(15) Å and in case of complex **3**, two Hg(II)–Cl2 distances were 2.570(3) and 2.680(3) Å, which suggested that the geometry around metal ion was distorted square and it was also found that in the binuclear structure, one metal ion was significantly in upward position while another metal ion was significantly in downward position from the distorted square planes which could be explained from the bond angles. The two trans angles  $\angle \text{Cl2}^i\text{-Zn1-N1}$  and  $\angle \text{Cl2-Zn1-N2}$  of complex **1** were 129.24(6)° and 162.07(6)° respectively and these were much deviated from the ideal trans angle 180°, and

the other two angles  $\angle N1-Zn1-Cl1$  and  $\angle N2-Zn1-Cl1$  were  $116.79(6)^\circ$  and  $98.76(6)^\circ$  respectively which were deviated from the actual axial angle of  $90^\circ$  which led to a distorted geometry around metal centre. Similar case was observed for the complexes **2** and **3**. The structural environment of the metal centres for each complex could also be illustrated by Addison parameter<sup>83</sup>  $\tau_5$  value [ $\tau_5 = (\alpha - \beta)/60^\circ$ , where  $\alpha$  and  $\beta$  are the two largest angles around the metal centre] which were 0.547, 0.355 and 0.372 for both the metal centres of the complexes **1**, **2** and **3** respectively. These values reflected that the geometry around each metal centres were between square pyramidal and trigonal bipyramidal shape ( $\tau_5 = 0$  for a perfect square pyramidal and  $\tau_5 = 1$  for a perfect trigonal bipyramidal). The intramolecular M–M distances were 3.620 Å, 3.767 Å and 3.859 Å in complexes **1**, **2** and **3** respectively.

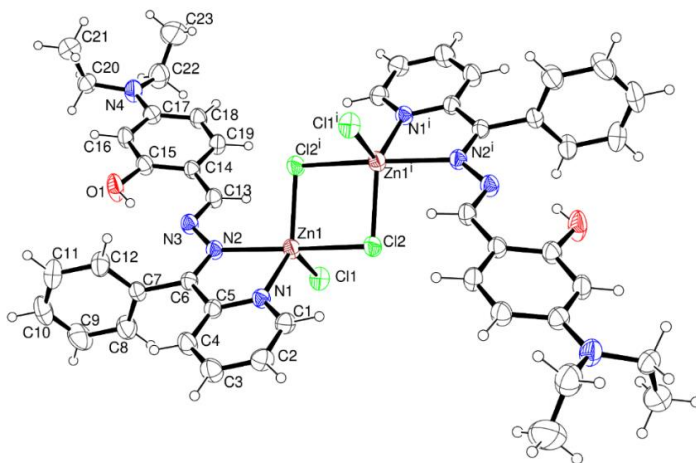


Figure VI.8. ORTEP view of complex **1** with 35% ellipsoidal probability

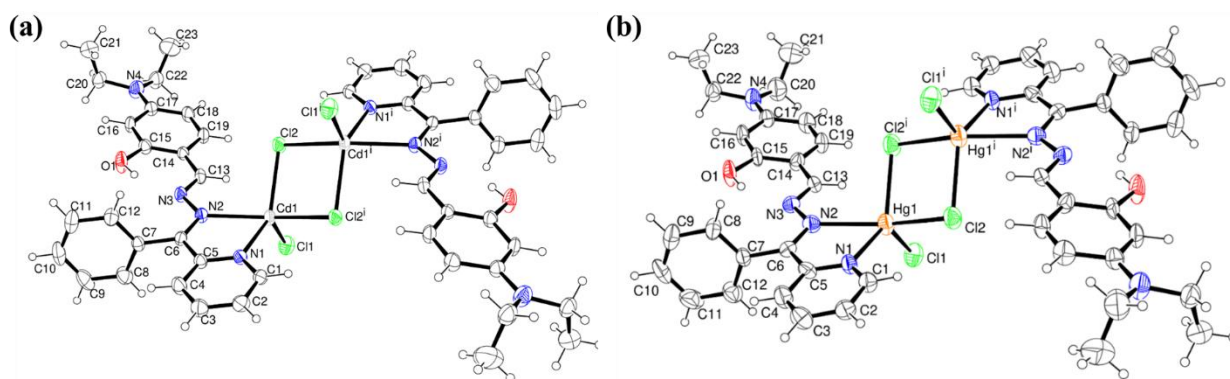


Figure VI.9. ORTEP view of (a) complex **2** and (b) complex **3** with 35% ellipsoidal probability



### VI.3.3. DFT studies

The structure of the complexes (**1–3**) were optimized by using DFT/B3LYP method where all complexes are in singlet state. The optimized bond length and angles are given in Table VI.2 and VI.3. The GaussSum calculations have been carried out to establish the partial contributions of the components present in the complexes and to get energy values of the molecular orbitals which were given in Table VI.4. For all the complexes, higher energy occupied molecular orbital (HOMO) has 100% contribution from the ligand and low-lying virtual orbital, LUMO also has 99% contribution from ligand  $\pi^*$  orbital.

Table VI.1. Crystallographic data and refinement parameters of **1–3**

Complex	<b>1</b>	<b>2</b>	<b>3</b>
Formula	C <sub>46</sub> H <sub>48</sub> Cl <sub>4</sub> N <sub>8</sub> O <sub>2</sub> Zn <sub>2</sub>	C <sub>46</sub> H <sub>48</sub> Cd <sub>2</sub> Cl <sub>4</sub> N <sub>8</sub> O <sub>2</sub>	C <sub>46</sub> H <sub>48</sub> Cl <sub>4</sub> Hg <sub>2</sub> N <sub>8</sub> O <sub>2</sub>
Formula Weight	1017.46	1111.52	1287.90
Crystal System	<i>triclinic</i>	<i>triclinic</i>	<i>triclinic</i>
Space group	<i>P</i> -1	<i>P</i> -1	<i>P</i> -1
a, b, c [Å]	8.1332(7), 10.0113(8), 16.2865(13)	7.9691(7), 10.2773(8), 16.2847(14)	7.9488(15), 10.1294(17), 16.347(3)
$\alpha$	106.643(3)	107.387(2)	106.835(11)
$\beta$	92.361(3)	90.544(3)	90.555(12)
$\gamma$	110.595(3)	110.202(3)	110.296(11)
V [Å <sup>3</sup> ]	1174.37(17)	1185.00(17)	1172.6(4)
Z	1	1	1
D(calc) [g/cm <sup>3</sup> ]	1.439	1.558	1.824
Mu(MoKa) [/mm]	1.295	1.169	6.813
F(000)	524	560	624
Temperature (K)	293(2)	293(2)	293(2)
Radiation [Å]	0.71073	0.71073	0.71073
$\theta$ (Min-Max) [°]	2.25 - 25	2.642 - 25	2.22 - 25
Dataset (h; k; l)	-10 to 10, -13 to 12, - 19 to 21	-9 to 9, -12 to 12, -19 to 19	-9 to 9, -12 to 12, -18 to 19
R, wR <sub>2</sub>	0.0727, 0.0956	0.0598, 0.0849	0.0549, 0.0867
Goodness of fit(S)	0.962	1.110	0.890

Table VI.2. Some selected X-ray and calculated bond distances and angles of **1** and **2**

<b>1</b>			<b>2</b>		
Bonds(Å)	X-ray	Calc.	Bonds(Å)	X-ray	Calc.
Zn(1)-N(1)	2.091(2)	2.19204	Cd(1)-N(1)	2.315(4)	2.39297
Zn(1)-N(2)	2.2278(19)	2.36880	Cd(1)-N(2)	2.403(4)	2.54428
Zn(1)-Cl(1)	2.2254(8)	2.28537	Cd(1)-Cl(1)	2.4158(18)	2.46061
Zn(1)-Cl(2)	2.3160(7)	2.40725	Cd(1)-Cl(2)	2.5593(16)	2.61460
Zn(1)-Cl(2) <sup>i</sup>	2.5751(7)	2.56962	Cl(2)-Cd(1)	2.6006(15)	2.70285
N(3)-C(13)	1.294(3)	1.31152	N(3)-C(13)	1.294(6)	1.31166
N(2)-N(3)	1.390(3)	1.36754	N(2)-N(3)	1.388(6)	1.36993
N(1)-C(1)	1.335(3)	1.33858	N(1)-C(1)	1.336(6)	1.33842
N(1)-C(5)	1.356(3)	1.35520	N(1)-C(5)	1.348(6)	1.35367

Angles (°)					
N(1)-Zn(1)-N(2)	76.06(8)	72.46122	N(1)-Cd(1)-N(2)	70.38(15)	67.46837
N(1)-Zn(1)-Cl(1)	116.79(6)	119.02298	N(1)-Cd(1)-Cl(1)	118.29(12)	128.01365
Cl(1)-Zn(1)-N(2)	98.76(6)	97.87872	Cl(1)-Cd(1)-N(2)	99.93(12)	99.72513
N(1)-Zn(1)-Cl(2) <sup>i</sup>	129.24(6)	115.13014	N(1)-Cd(1)-Cl(2)	133.31(12)	104.18041
Cl(2)-Zn(1)-N(1)	90.81(6)	91.95150	N(1)-Cd(1)-Cl(2) <sup>i</sup>	90.40(11)	89.03910
Cl(1)-Zn(1)-Cl(2) <sup>i</sup>	113.90(3)	124.58921	Cl(1)-Cd(1)-Cl(2)	107.68(6)	125.91938
N(2)-Zn(1)-Cl(2) <sup>i</sup>	94.16(5)	87.39360	N(2)-Cd(1)-Cl(2)	94.97(11)	86.64052
N(2)-Zn(1)-Cl(2)	162.07(6)	159.19579	N(2)-Cd(1)-Cl(2) <sup>i</sup>	154.61(11)	153.30864
Cl(1)-Zn(1)-Cl(2)	98.05(3)	101.80560	Cl(1)-Cd(1)-Cl(2) <sup>i</sup>	103.86(6)	104.92346

Table VI.3. Some selected X-ray and calculated bond distances and angles of **3**

Bonds(Å)	X-ray	Calc.
Hg(1)-N(1)	2.307(7)	2.48857
Hg(1)-N(2)	2.453(8)	2.69583
Hg(1)-Cl(1)	2.388(3)	2.42182
Hg(1)-Cl(2)	2.570(3)	2.50221
Hg(1)-Cl(2) <sup>i</sup>	2.680(3)	3.03930
N(3)-C(13)	1.299(10)	1.31065
N(2)-N(3)	1.383(10)	1.36985
N(1)-C(1)	1.326(11)	1.33713
N(1)-C(5)	1.345(11)	1.35133

Angles (°)		
N(1)-Hg(1)-N(2)	69.3(3)	64.22917
N(1)-Hg(1)-Cl(1)	121.3(2)	120.21886
Cl(1)-Hg(1)-N(2)	103.1(2)	99.98354
N(1)-Hg(1)-Cl(2) <sup>i</sup>	129.4(2)	95.62491

Cl(2)-Hg(1)-N(1)	89.9(2)	86.66443
Cl(1)-Hg(1)-Cl(2) <sup>i</sup>	108.61(10)	143.89736
N(2)-Hg(1)-Cl(2) <sup>i</sup>	93.23(19)	91.40793
N(2)-Hg(1)-Cl(2)	151.8(2)	150.43067
Cl(1)-Hg(1)-Cl(2)	104.06(9)	99.21748

For details about the electronic transitions, time-dependent density functional theory (TDDFT) calculations were done on the optimized structures of the complexes (Table VI.5). In complex **1**, low energy HOMO–1  $\rightarrow$  LUMO+1 transition at 488 nm ( $f = 1.7667$ ) corresponds to experimental band at 501 nm ( $\epsilon$ , 14983 M<sup>-1</sup>cm<sup>-1</sup>) having ILCT character, another high energy transitions, HOMO–4  $\rightarrow$  LUMO+1 ( $\lambda$ , 364 nm;  $f$ , 0.0881) have mixed ILCT and XLCT (halogen to ligand charge transfer) character, HOMO–1  $\rightarrow$  LUMO+2 ( $\lambda$ , 337 nm;  $f$ , 0.4728) and HOMO–1  $\rightarrow$  LUMO+4 ( $\lambda$ , 306 nm;  $f$ , 0.6172) have ILCT character. For **2**, significant HOMO  $\rightarrow$  LUMO+1 transition ( $\lambda$ , 476 nm;  $f$ , 1.7245) have intra-ligand charge transfer (ILCT) character which is correspond to the experimental band at 444 nm ( $\epsilon$ , 25247 M<sup>-1</sup>cm<sup>-1</sup>) and another high energy transition is HOMO–1  $\rightarrow$  LUMO+4 at 304 nm ( $f = 0.2810$ ) and this is correspond to the experimental band at 298 nm ( $\epsilon$ , 6894 M<sup>-1</sup>cm<sup>-1</sup>). In case of **3**, low energy HOMO–1  $\rightarrow$  LUMO+1 transition at 465 nm ( $f = 1.8827$ ) resembles to experimental band at 430 nm ( $\epsilon$ , 21780 M<sup>-1</sup>cm<sup>-1</sup>) have ILCT character.

Table VI.4. Energy and % of composition of some selected molecular orbitals of **1–3**

MO	<b>1</b>				<b>2</b>				<b>3</b>			
	Energy (eV)	% Composition			Energy (eV)	% Composition			Energy (eV)	% Composition		
		Zn	Lig	Cl		Cd	Lig	Cl		Hg	Lig	Cl
LUMO+5	-0.64	01	99	00	-0.64	03	72	08	-0.98	20	72	08
LUMO+4	-0.64	01	99	00	-0.73	02	96	01	-1.02	03	96	01
LUMO+3	-1.16	01	99	00	-1.13	02	38	20	-1.17	42	38	20
LUMO+2	-1.16	01	99	00	-1.21	01	12	23	-1.46	65	12	23
LUMO+1	-2.31	01	99	00	-2.28	01	99	00	-2.18	01	99	00
LUMO	-2.31	01	99	00	-2.37	01	99	00	-2.18	01	99	00
HOMO	-5.19	00	100	00	-5.17	00	100	00	-5.20	00	100	00
HOMO-1	-5.19	00	100	00	-5.25	00	100	00	-5.20	00	100	00
HOMO-2	-5.92	00	100	00	-5.91	00	100	00	-5.95	00	100	00
HOMO-3	-5.92	00	100	00	-5.98	00	100	00	-5.95	00	100	00

HOMO-4	-6.03	01	21	78	-6.16	02	73	22	-6.34	05	73	22
HOMO-5	-6.06	02	20	78	-6.22	02	68	26	-6.34	06	68	26
HOMO-6	-6.25	03	06	91	-6.33	04	44	51	-6.63	05	44	51
HOMO-7	-6.25	04	02	94	-6.38	04	63	34	-6.65	04	63	34
HOMO-8	-6.55	04	51	45	-6.63	05	46	50	-6.70	04	46	50
HOMO-9	-6.60	06	26	68	-6.67	05	64	33	-6.70	03	64	33
HOMO-10	-6.72	00	96	04	-6.72	00	02	92	-6.78	06	02	92

Table VI.5. Vertical electronic transitions calculated by TDDFT/CPCM method of **1** – **3**

Compd.	$\lambda$ (nm)	E (eV)	Osc. Strength (f)	Key excitations	Character	$\lambda_{\text{expt.}}$ (nm) ( $\epsilon$ , $\text{M}^{-1}\text{cm}^{-1}$ )
<b>1</b>	487.94	2.5410	1.7667	(56%)HOMO-1 $\rightarrow$ LUMO+1	ILCT	501 (14983)
	364.82	3.3985	0.0881	(37%)HOMO-4 $\rightarrow$ LUMO+1	ILCT/XLCT	430 (24429)
	336.89	3.6803	0.4728	(51%)HOMO-1 $\rightarrow$ LUMO+2	ILCT	350 (5704)
	324.76	3.8177	0.0825	(34%)HOMO-6 $\rightarrow$ LUMO	XLCT/ILCT	
	305.92	4.0528	0.6172	(25%)HOMO-1 $\rightarrow$ LUMO+4	ILCT	290 (8280)
<b>2</b>	476.27	2.6032	1.7245	(73%) HOMO $\rightarrow$ LUMO+1	ILCT	444 (25247)
	331.35	3.7417	0.3123	(55%)HOMO-1 $\rightarrow$ LUMO+3	ILCT	330 (3869)
	304.52	4.0715	0.2810	(42%)HOMO-1 $\rightarrow$ LUMO+4	ILCT	298 (6894)
	303.93	4.0793	0.2684	(38%) HOMO $\rightarrow$ LUMO+5	ILCT	
<b>3</b>	465.01	2.6663	1.8827	(34%)HOMO-1 $\rightarrow$ LUMO+1	ILCT	430 (21780)
	391.13	3.1699	0.0707	(93%)HOMO $\rightarrow$ LUMO+2	LMCT/LXCT/ILCT	
	374.02	3.3149	0.0354	(24%)HOMO-5 $\rightarrow$ LUMO	ILCT/XLCT	
	369.17	3.3585	0.0438	(28%)HOMO-2 $\rightarrow$ LUMO+1	ILCT	
	345.74	3.5860	0.0649	(87%)HOMO-1 $\rightarrow$ LUMO+3	LMCT/ILCT/LXCT	
	324.25	3.8237	0.2918	(55%) HOMO $\rightarrow$ LUMO+4	ILCT	328 (3807)
	316.19	3.9212	0.1097	(30%)HOMO-6 $\rightarrow$ LUMO+1	XLCT/ILCT	
	300.99	4.1192	0.2761	(27%)HOMO-10 $\rightarrow$ LUMO+1	XLCT	277 (9456)

### VI.3.4. Photoluminescence Properties

The absorption spectra of **1** showed a moderate intensity band at 501 nm and a high intensity band at 430 nm which was also showed by complex **3** while complex **2** was observed to be excited at 444 nm and all these band were mostly due to ligand  $\pi \rightarrow \pi^*$  (ILCT) transition which is suggested from TDDFT study (Table VI.5). As the  $\pi$ -conjugated ligand and its

complexes having metal ion with  $d^{10}$  system usually show strong luminescence properties, fluorescence measurements of the complexes (**1–3**) were performed in acetonitrile solution (Figure VI.10). Complex **1** showed an emission maximum at 677 nm. Upon excitation at 470 nm, an intensified broad emission band at 649 nm was appeared for complex **2** upon irradiation at 450 nm while a sharp intensify emission band appeared at 480 nm for complex **3** upon excitation at 430 nm. As the metal ions have  $d^{10}$  system ( $d-d$  transition forbidden), the fluorescence intensity of the complexes may be originated from the coordinating conjugated ligand backbone via ligand to metal charge transfer (LMCT) or intra-ligand charge transfer (ILCT,  $\pi^* \rightarrow \pi$  or  $\pi^* \rightarrow n$ ) transition. Moreover, as a result of coordination with metal ions, a rigid chelate ring was formed and the electronic vibration between ligand and metal ions might intensify the luminescence character.<sup>70,72</sup> As the explosive nitro-aromatic compounds are highly electron deficient in nature, so in presence of the explosive NACs, the inherent fluorescence of the  $\pi$ -electron rich complexes might be diminished due to the transfer of photoelectron from the complex (donor) to the NACs (acceptor). Hence this significant high luminescence properties of the complexes could be utilized in various field of applications especially in the detection of explosive nitro-aromatics.

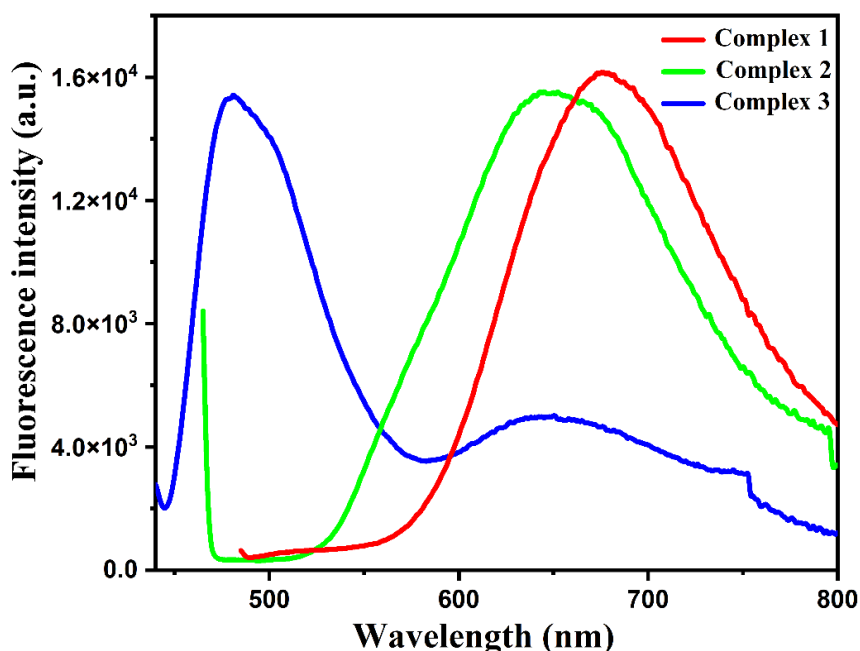


Figure VI.10. Emission spectra of **1-3** in acetonitrile

### VI.3.5. TNP Sensing Study

In this circumstance, taking into consideration of the homeland security and to maintain the human wellbeing and ecological harmony, sensitive and distinguished identification of explosive nitro groups (NACs) is one of the worthy concerns. Herein, the high intensity emissive properties of these heavy metal prompted us to execute a broad analysis towards recognition of a series of explosive nitro groups containing aromatic compounds (NACs) such as 2-nitrophenol (2-NP), 4-nitrophenol (4-NP), nitrobenzene (NB), 4-nitroaniline (4-NA), 4-nitrobenzoic acid (4-NBA), 4-nitrotoluene (4-NT), 2,4-dinitrophenol (DNP), and 2,4,6-trinitrophenol (picric acid, TNP). Each of the analyte solutions (NACs) was added into a well-dispersed solution of the complexes in the same quantity ( $10^{-4}$  M) to study the selective detection. Addition of these NACs into the well-dispersed probe solutions (complex **1**, **2**, **3**) displayed a sharp quenching of the original fluorescence intensity of the complexes in presence of TNP, whereas other analytes revealed a weak outcome. The sensing studies of the explosive nitroaromatic compounds (NACs) were evaluated further through fluorescence titration experiments. This observation showed that the complexes **1-3** could be utilized as potential sensors for discerning recognition of nitroaromatics. The more electron deficient nature of the nitroaromatics compared to other aromatics may be the cause for the considerably high quenching of emission intensity of the complexes. The considerable quenching of fluorescence intensity was detected upon addition of picric acid in contrast to other NACs (Figure VI.12, VI.13 and VI.14). So, the fluorescence titrations of complexes **1-3** have been executed in acetonitrile on gradual incremental addition of PA.

Initially, the solution of complex **1** revealed a wine-red fluorescence with the emission band at 677 nm (ex ~470 nm) while complex **2** showed an emission maxima at 649 nm (ex ~450 nm) with a bright orange fluorescence and in case of complex **3**, the emission band was noticed at 480 nm (ex ~430 nm) with orangish red fluorescence. The emission intensities of the three complexes continued to decrease with an increase in the concentration of TNP ( $10^{-4}$  M) as displayed in Figure VI.11. The titration study exhibited that the quenching of the emission intensity follows the order complex **3** (83.41%) > complex **2** (70.24%) > complex **1** (69%) (Figure VI.15). The quenching efficiencies of TNP in case of the three complexes were quantitatively studied by the Stern-Volmer equation:  $I_0/I = 1 + K_{SV}[Q]$ , where  $I_0$  and  $I$  are the fluorescence intensities before and after the addition of TNP respectively,  $[Q]$  is the concentration of the quencher and  $K_{SV}$  is the Stern-Volmer quenching constant. The Stern-Volmer quenching constants ( $K_{SV}$ ) was calculated from the slope of the linearly fitted curve and is found to be  $(4.51 \pm 0.21) \times 10^4 \text{ M}^{-1}$  ( $R^2 = 0.98397$ ) for complex **1**,  $(5.02 \pm 0.15) \times 10^4$

$M^{-1}$  ( $R^2 = 0.97509$ ) for complex **2** and in case of complex **3**,  $K_{sv}$  is calculated to be  $(5.19 \pm 0.12) \times 10^4 M^{-1}$  ( $R^2 = 0.99309$ ) (Figure VI.16. (a)i, (b)i and (c)i respectively). Similarly, the limit of detection of TNP was calculated using the equation:  $LOD = 3\sigma/k$ , where  $\sigma$  is standard deviation of blank measurements and  $k$  is the slope of the plot of fluorescence intensity of complex vs [TNP] and the value was found to be 212 nM for complex **1**, for complexes **2** and **3**, detection limits were determined to be 201.4 nM and 180.2 nM respectively (Figure VI.16. (a)ii, (b)ii and (c)ii respectively) which were much lower than the reported sensors for TNP (Table VI.6). From these calculated parameters one could conclude that the quenching ability of TNP was greater for the complex **3** compare to other two complexes.

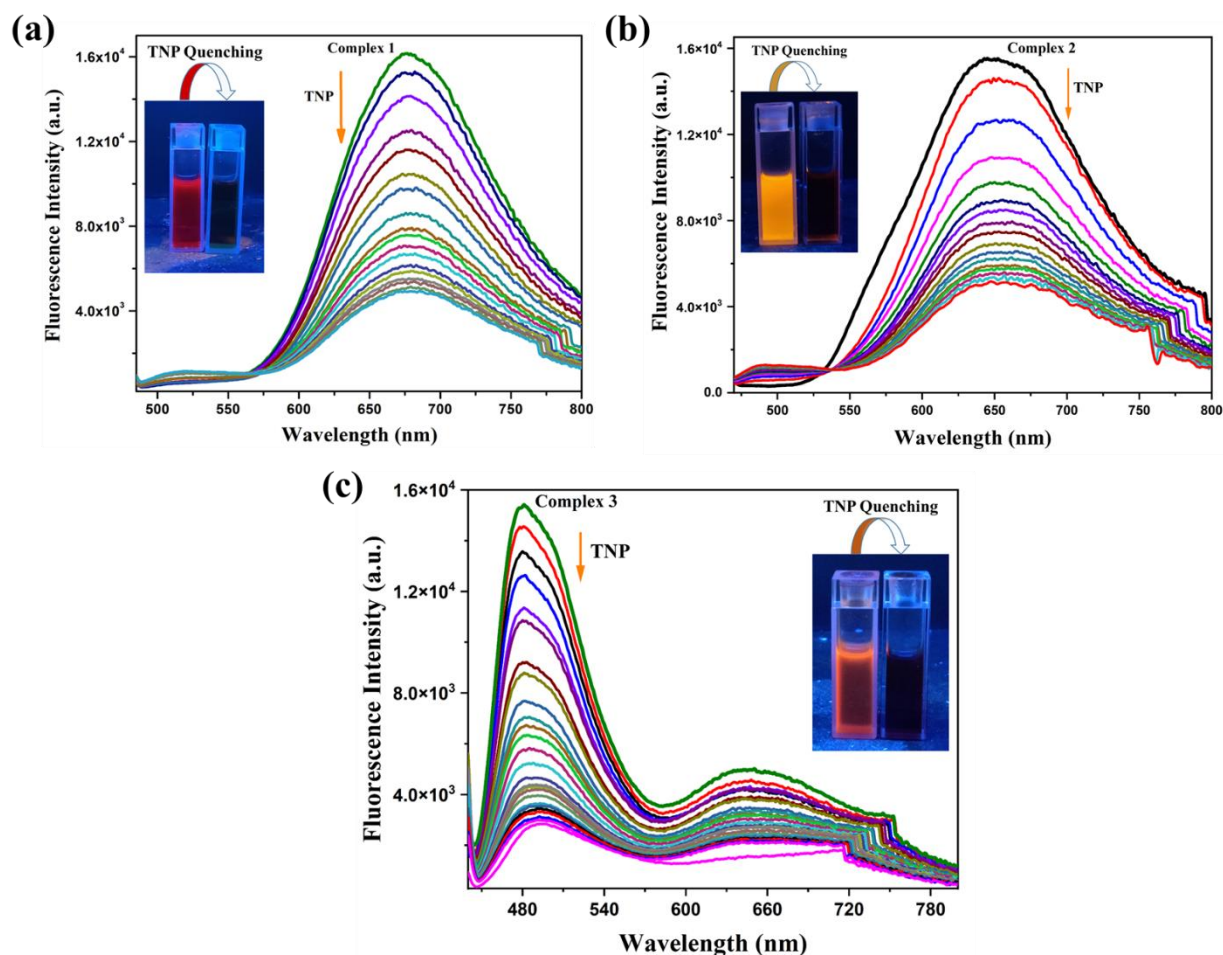


Figure VI.11. Fluorescence emission spectral titration of (a) **1**, (b) **2** and (c) **3** (20  $\mu M$ ) in acetonitrile with TNP ( $10^{-4} M$ ) ( $\lambda_{ex} = 470$  nm) [Inset: Visual effect of complexes in acetonitrile before and after the addition of TNP under UV chamber].

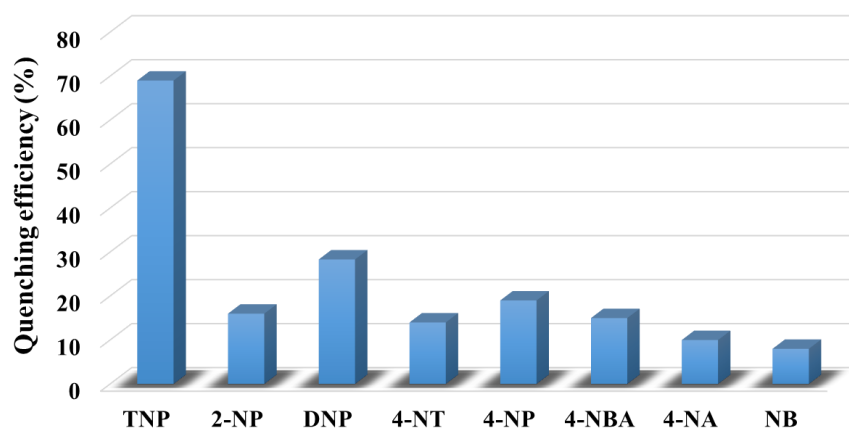


Figure VI.12. Quenching efficiency of nitro-aromatics towards the fluorescence intensity of complex 1

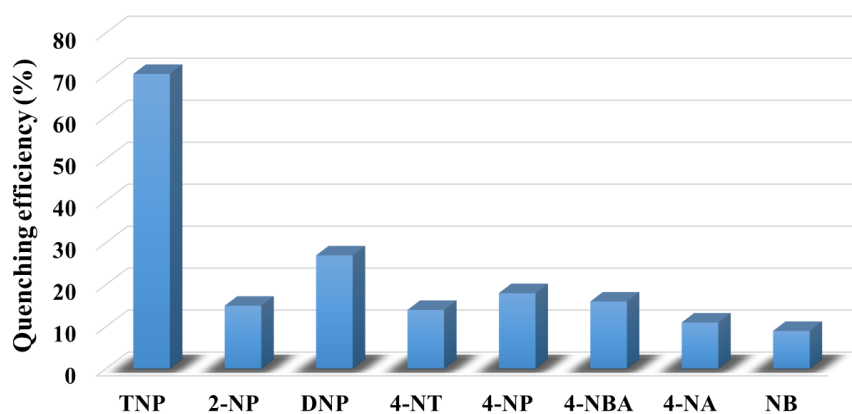


Figure VI.13. Quenching efficiency of nitro-aromatics towards the fluorescence intensity of complex 2

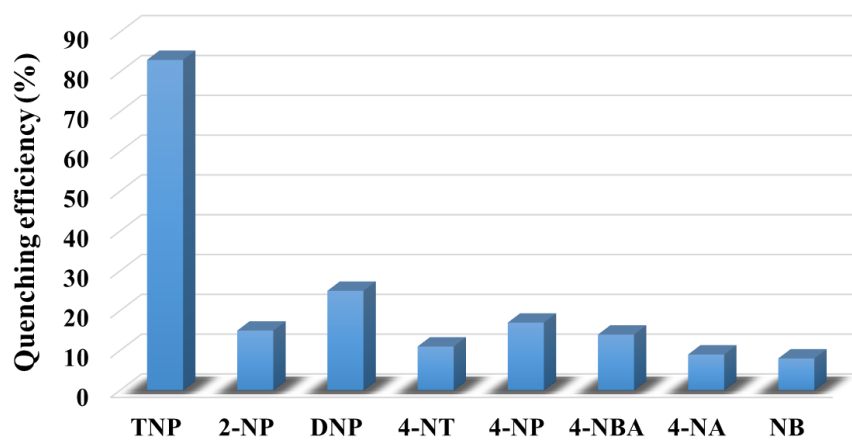


Figure VI.14. Quenching efficiency of nitro-aromatics towards the fluorescence intensity of complex 3



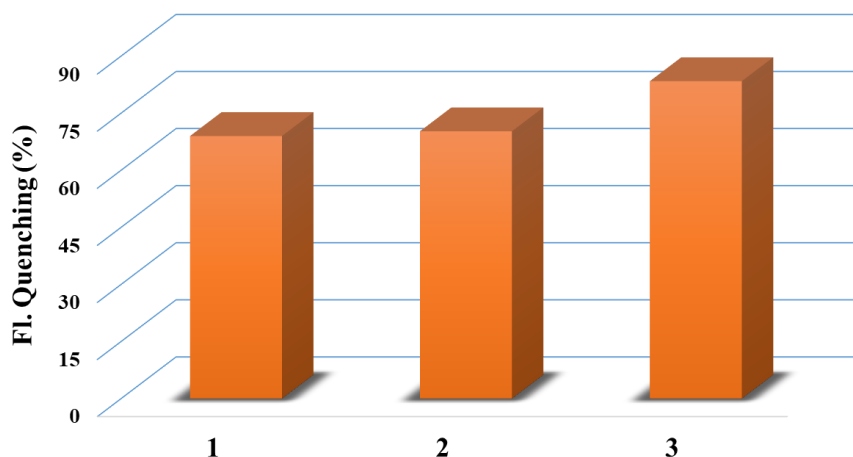


Figure VI.15. Fluorescence quenching percentage of the complexes by TNP

In order to determine the binding mechanism of picric acid with the complexes in solution, we performed  $^1\text{H}$ -NMR titration with varying amounts of TNP (0, 1 and 2 equiv.) in  $\text{CDCl}_3/\text{DMSO}-d_6$  solvent (Figure VI.17–VI.19). It was noticed that all the protons are shifted slightly to downfield region for all the complexes because of the withdrawn of electron density by the electron deficient TNP from the electron rich metal complexes and shifted the protons to deshielded zone. Also, a new signal appeared (at 9.19 ppm for **1**, at 8.58 ppm for **2** and at 9.09 ppm for **3**) which was a characteristic proton peak of TNP. So, from  $^1\text{H}$  NMR spectral titration it was confirmed that there was no change in structure of the complex or structural collapse during or after the interaction with TNP.

The time-resolve fluorescence spectra were taken for the complexes in presence of TNP to check the quenching mechanism i.e., whether it was static or dynamic quenching. Interestingly, the lifetimes of the excited states of the complexes **1**, **2** and **3** were found to be 0.74 ns, 0.76 ns and 0.79 ns respectively but after the addition of TNP, it was found that the lifetime of the fluorophores decreased (0.25 ns, 0.23 ns and 0.19 ns for **1**, **2** and **3** respectively) which implied that the quenching pathway was dynamic in nature (Figure VI.20 and VI.21).<sup>72</sup>

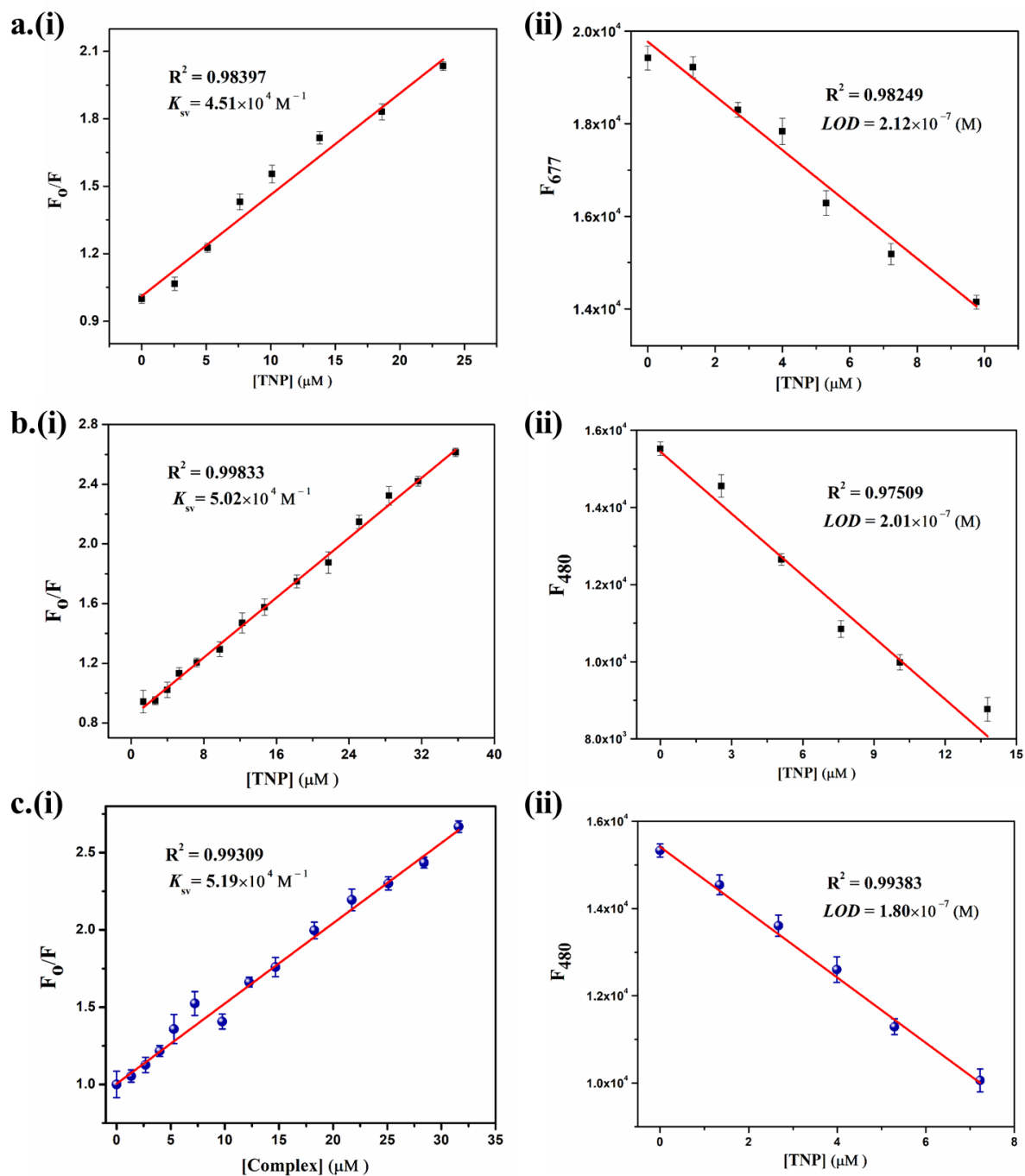
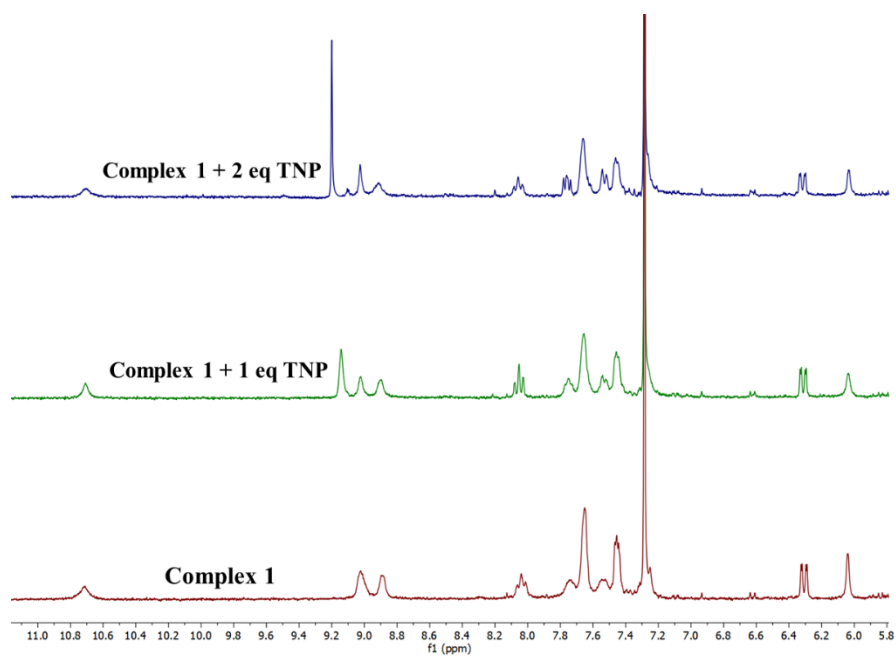
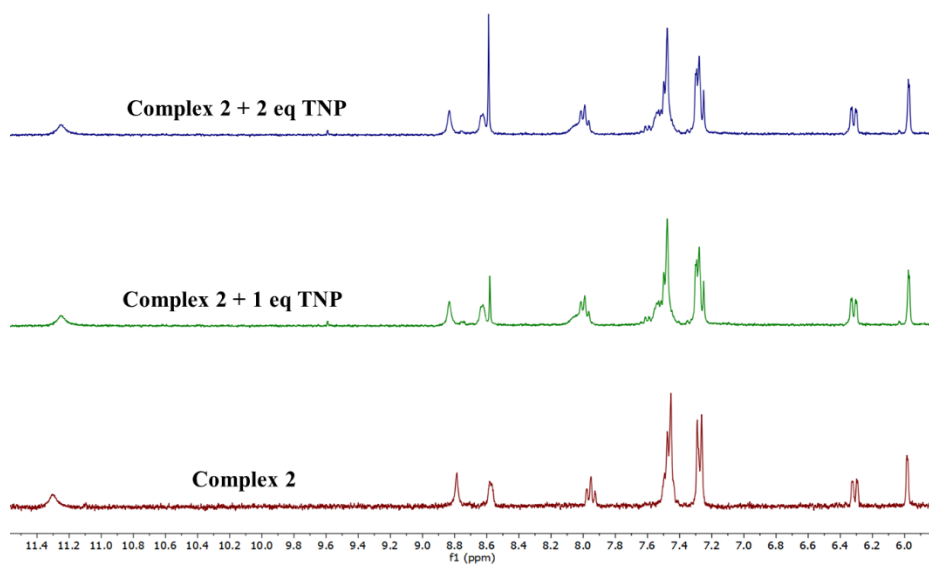
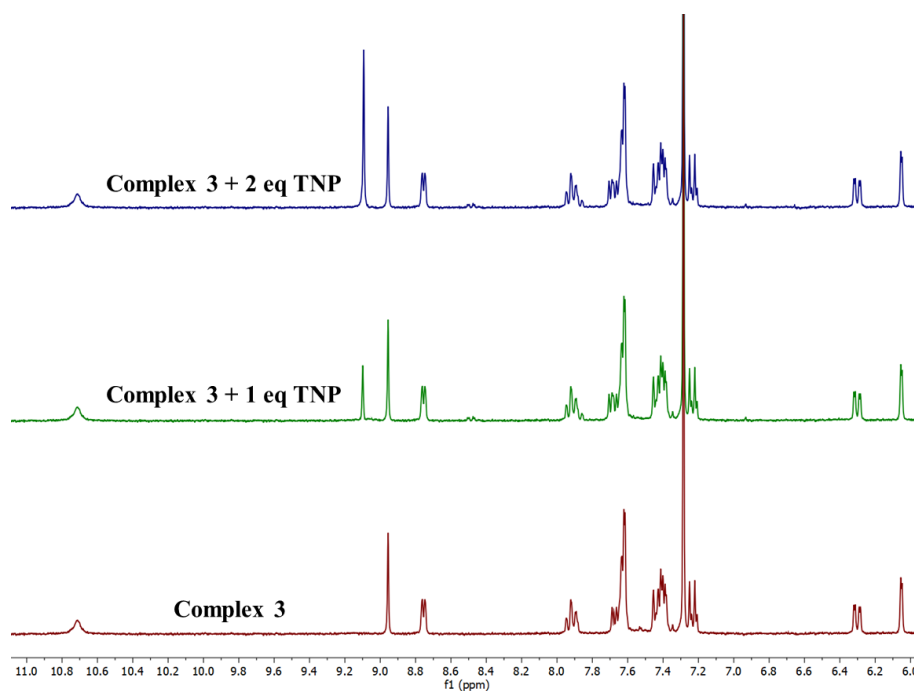
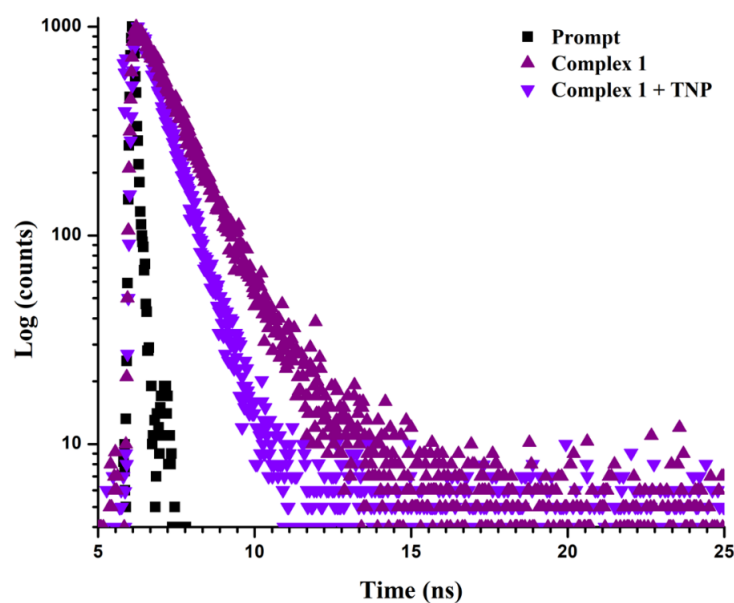


Figure VI.16. (i) Stern–Volmer plot and (ii) LOD plot of TNP for the complexes (a) **1**, (b) **2** and (c) **3**

Figure VI.17.  $^1\text{H}$  NMR titration of complex **1** with TNP in  $\text{CDCl}_3$ Figure VI.18.  $^1\text{H}$  NMR titration of complex **2** with TNP in  $\text{CDCl}_3$

Figure VI.19.  $^1\text{H}$  NMR titration of complex **3** with TNP in  $\text{CDCl}_3$ Figure VI.20. Fluorescence lifetime decay plot of **1** without and with TNP

The emission quenching response time spectra of the fluorophores in presence of TNP in acetonitrile solution was performed. It was observed that the emission intensities were quenched instantly i.e., the quenching kinetics was very fast after the addition of picric acid

and remains unaltered over an extended period of 3 mins (Figure VI.22). Thus, the fast-quenching kinetics suggested the quick response of the fluorophores towards TNP.

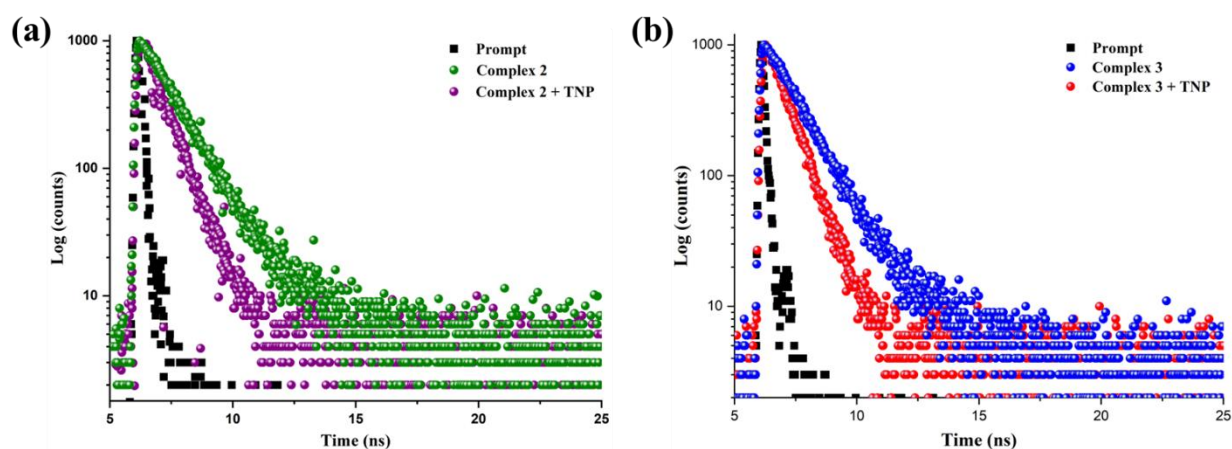


Figure VI.21. Fluorescence lifetime decay plot of (a) **2** and (b) **3** without and with TNP

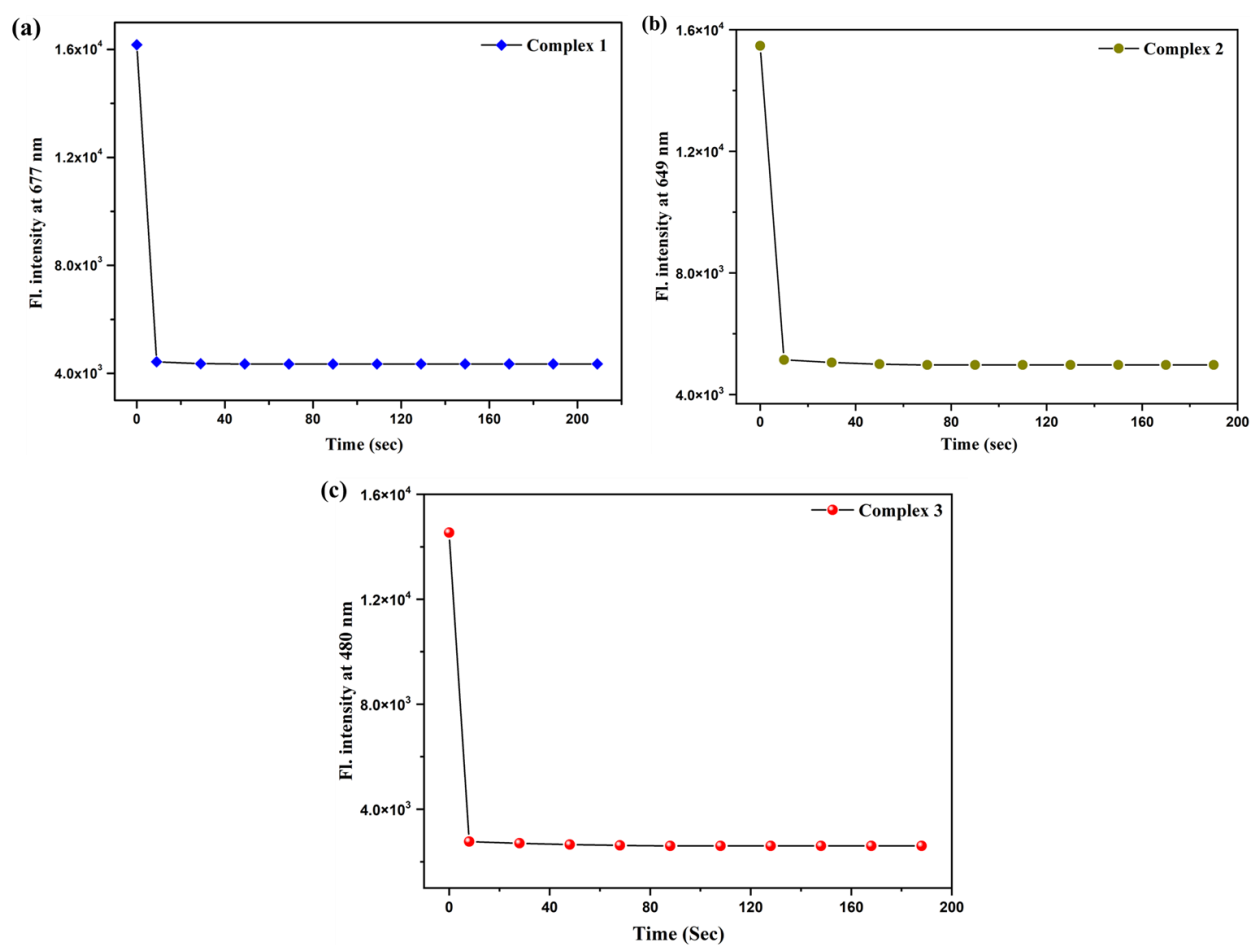


Figure VI.22. Time dependent quenching response of the complexes (a) **1**, (b) **2** and (c) **3**

Table VI.6. Comparison table with recently reported works related to NACs detection

Sl. No.	Compound	Synthetic process	Selective NACs	LOD (M)	Quenching Constant, $K_{SV}$ ( $M^{-1}$ )	Real Sample Analysis	Ref.
1	$[Zn_2(valpn)_2Dy_2Ir(L)(ppy)_2(DMF)_6(H_2O)_2]^{5+}$	Stirring, slow evaporation	Different NAs	$1.07 \times 10^{-5}$	$2.3 \times 10^4$	No	84
2	$[Cd(NDI-A)(glu)(H_2O)]$ (Com-2)	Ultrasonication, 100°C, 12 h	TNP	$2.98 \times 10^{-6}$	$3.66 \times 10^4$	No	85
3	$[Cd(L1)(N(CN)_2)]_n$ (1)	Stirring, slow evaporation	TNP	$0.68 \times 10^{-6}$	$7.49 \times 10^4$	Yes	72
4	$[Cd(L1)(NCS)]_n$ (2)	Stirring, slow evaporation	TNP	$0.41 \times 10^{-6}$	$8.01 \times 10^4$	Yes	
5	$[Cd_2(L2)_2(NCS)_2]_n$ (3)	Stirring, slow evaporation	TNP	$1.18 \times 10^{-6}$	$8.1 \times 10^4$	Yes	
6	$[Zn(nip)(cis-nvp)(H_2O)].CH_3OH$	Slow diffusion	TNP, DNP	$0.72 \times 10^{-6}$	$6.3 \times 10^4$	Yes	68
7	$\{[Zn(adc)(avp)_2(H_2O)].(H_2O)_3\}_n$	Layer diffusion	TNP	$0.51 \times 10^{-6}$	$39.38 \times 10^4$	No	69
8	$\{[Cd(adc)(avp)_2(H_2O)].(H_2O).(CH_3OH)\}_n$	Layer diffusion	TNP	$0.45 \times 10^{-6}$	$44.07 \times 10^4$	No	
9	$[Cd(HL_2)_2(N(CN)_2)_2]_n$ (3)	Stirring, slow evaporation	TNP	$1.6 \times 10^{-7}$	$1.82 \times 10^4$	No	70
10	$[Zn(PBBA)(H_2O)].3DMF.2H_2O$	Sonication and then in oven, 95°C, 24 h	TNP DNP	$1 \times 10^{-6}$ $0.96 \times 10^{-6}$	$4.4 \times 10^4$ $5.3 \times 10^4$	No No	86
12	$Zn_2(TZBPDC)(\mu_3-OH)(H_2O)_2$	85°C, 48 h, Hydrothermal reaction	TNP	$2.78 \times 10^{-4}$	$4.9 \times 10^4$	No	87
13	$\{[Hg(L)_2].(ClO_4)_2\}_n$	Heating at 70°C, 12 h	Nitro-derivatives	$2.4 \times 10^{-6}$	$3.25 \times 10^5$	No	88
14	$[Zn_2LCl_2(H_2O)]$ (1)	Stirring, slow evaporation	TNP	$3.98 \times 10^{-9}$	$8.06 \times 10^4$	No	89
15	$[Zn_2L(SCN)_2(H_2O)].H_2O$ (2)	Stirring, slow evaporation	TNP	$3.97 \times 10^{-9}$	$7.98 \times 10^4$	No	
16	$[Zn_2L(N_3)(CH_3CO_2)]$ (3)	Stirring, slow evaporation	TNP	$3.91 \times 10^{-9}$	$8.51 \times 10^4$	No	
<b>Present Work</b>							
17	$[Zn_2(HL)_2Cl_4]$ (1)	Reflux, Slow evaporation	TNP	$2.12 \times 10^{-7}$	$4.51 \times 10^4$	Yes	<b>This Work</b>
18	$[Cd_2(HL)_2Cl_4]$ (2)	Reflux, Slow evaporation	TNP	$2.014 \times 10^{-7}$	$5.02 \times 10^4$	Yes	
19	$[Hg_2(HL)_2Cl_4]$ (3)	Reflux, Slow evaporation	TNP	$1.802 \times 10^{-7}$	$5.19 \times 10^4$	Yes	

### VI.3.6. Insight into fluorescence quenching mechanism

The distinct fluorescence quenching response of complexes **1**, **2** and **3** after interacting with TNP may be accredited to the host-guest interaction mechanism which comprised of several sensing mechanisms. Initially, the photo-induced electron transfer (PET) may be ascribed for the quenching of emission intensity through viable transfer of excited state electron from the donor fluorophore unit to the low lying vacant  $\pi^*$  orbital of the acceptor (here TNP).<sup>68,72,90-92</sup> This indicated that lower the LUMO as well as higher the electron deficiency of the quencher, higher will be the rate of accepting tendency of excited electron from the fluorophore i.e., PET enhances. Thus, the highest electron deficient analyte, TNP unveiled the highest emission quenching efficacy over other relative analytes. Also, from Density Functional Theory (DFT) studies utilizing B3LYP functional and Lanl2dz basis set, the HOMO and LUMO energy values were calculated for the three complexes and nitro-compounds (Table VI.4 and VI.7). The Energy profile diagram showed that the LUMO of all the nitro explosives exist nearly in lower energy state as compared to the LUMO of the three complexes continuing a driving force for simple electron transfer from complexes to electron deficit nitro compounds. However, TNP having the lowest LUMO energy level as compared to other nitro explosives validates the maximum quenching effectiveness of TNP (Figure VI.23 (a)). Hence, herein the sensing mechanism based on PET comprised of the photo excitation of electron from HOMO to LUMO of **1-3** and facile transfer of the excited electron to the low lying vacant LUMO of TNP (Figure VI.23 (b)) resulting in the eminent quenching of fluorescence of **1-3**. The reason that PET was not the sole factor responsible for the fluorescence quenching phenomenon was due to the difference in HOMO-LUMO energy levels of all the NACs and non-accordance of a corresponding sequence of observed quenching efficiency.

Apart from PET, resonance energy transfer (RET) mechanism may also be accounted for the quenching phenomenon noticed in this article. The RET involved attainable spectral overlap between the emission band of donor (complex **1-3**) and absorption band of analytes (TNP) (Figure VI.24). However, the extent of overlapping portion was greater for **3** compare to other two complexes, which corroborated with the higher response of complex **3**. This overlapping could be used to rationalize the quenching efficacy and selectivity of complex **1-3** towards TNP.

Table VI.7. HOMO and LUMO energies of explosive nitro-aromatics (NACs) from GaussSum calculation.

NACs	LUMO (eV)	HOMO (eV)	Band gap (eV)
NB	-2.43	-7.59	5.16
4-NA	-2.47	-6.6	4.13
2-NP	-2.67	-7.19	4.52
4-NP	-2.22	-6.92	4.7
4-NT	-2.79	-7.65	4.86
4-NBA	-3.4	-8.19	4.79
2,4-DNP	-3.31	-8.05	4.74
2,4,6-TNP	-4.32	-8.59	4.27

So, in conclusion, one could say that the chosen quenching mechanisms followed PET-RET paths with credible host-guest interaction between fluorescent probes, i.e., the complexes **1-3** and TNP.<sup>92,93</sup> Hence this affords a distinct fluorescent chemosensor for distinctive and sensitive recognition of TNP like nitroaromatic compound.

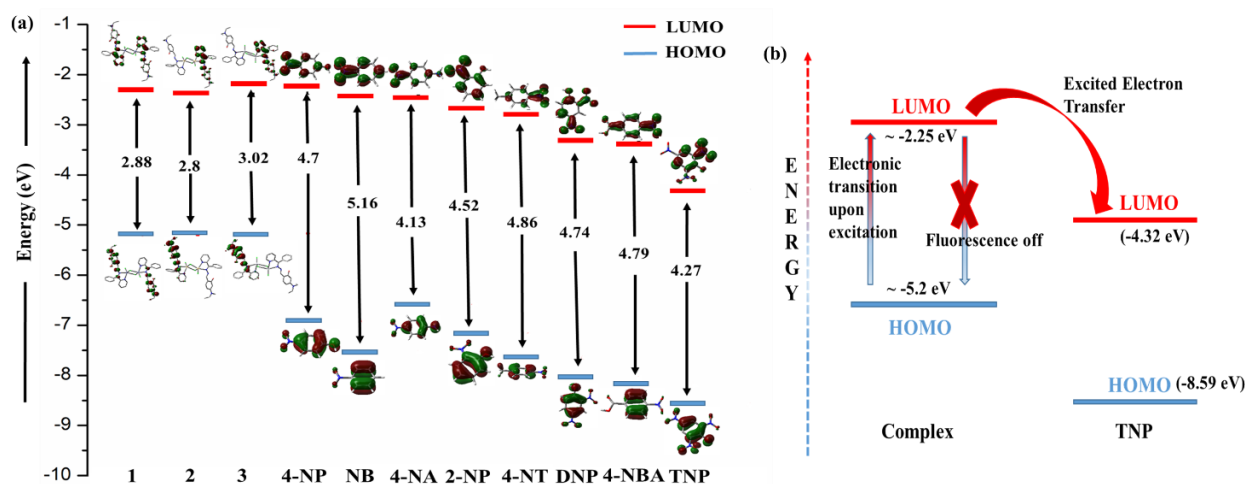


Figure VI.23. (a) HOMO and LUMO energies of the three complexes and nitro-compounds obtained from DFT study and (b) PET-induced quenching mechanism of the complex in the presence of TNP.



### VI.3.7. Optical detection of TNP in solid state using a TLC plate

For real-world application, the quenching of fluorescence intensities of **1-3** towards TNP was also investigated in solid state. We prepared portable test strips by transferring the acetonitrile solution of the complexes on silica coated aluminum TLC plates. The complex-coated TLC plates showed the luminescence properties under a UV lamp (365nm). Then onto the complex-coated TLC plates, TNP solution was introduced by a drop and immediately the TNP applied portion was fully quenched which was seen under the UV lamp (Figure VI.25). This result explained the efficacy of the complexes for the immediate detection of trace amounts of TNP.

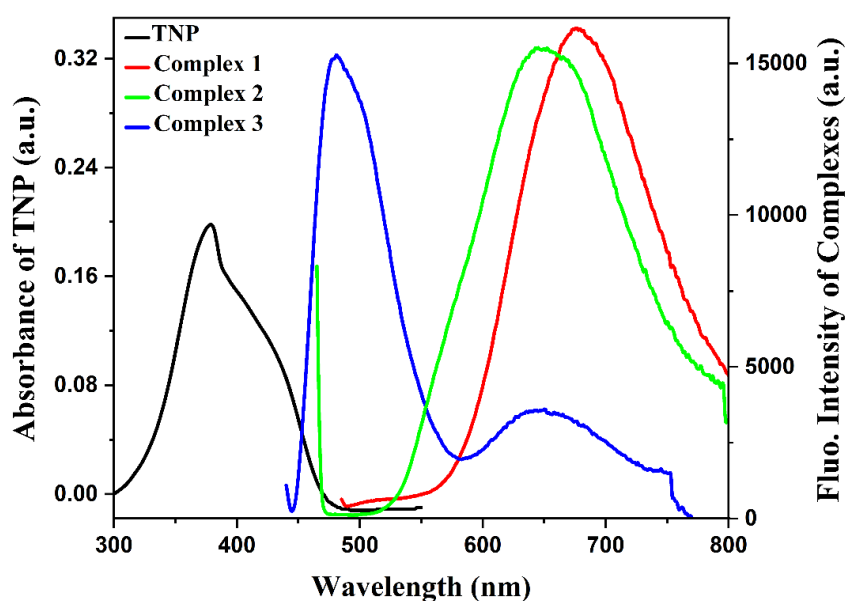


Figure VI.24. Overlay of the absorption spectra of TNP and emission spectra of the complexes **1-3**.

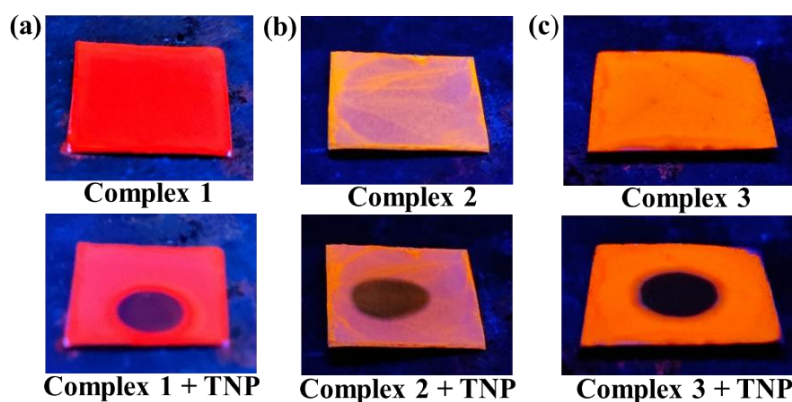


Figure VI.25. Fluorescence quenching upon introduction of TNP on the complex-coated TLC plate of (a) **1**, (b) **2** and (c) **3**.

### VI.3.8. Real Field sensing application

Fluorescence quenching response of our probe (**1-3**) towards nitroaromatics, especially TNP with high selectivity, sensitivity (nanomolar level), rapidity over a broad pH range (4-10), made it ideal for practical applications for real samples. In order to further verify the reliability of **1-3** towards detection of TNP in real field water samples, we have collected water sample from the river Ganges, centrifuged for 15 min and filtered with Whatman filter paper (pH was checked and it was around 7.2). At first, a blank experiment was done to check the presence of any dissolved NBs in the water samples but found to be negative based on absence of change in fluorescence intensity of the probe. The goal here was not to determine the TNP contained in them, but to use these in place of distilled water to prepare TNP solutions and to carry out experiments. Herein, TNP was spiked in the mentioned water sample for preparing a known concentration of TNP solution. Progressive addition of this TNP solution to our probe solutions displayed quenching response similar to the controlled titration experiments (Figure VI.26). The recovery measurements were evaluated and percentage recovery was greater than 90% (Table VI.8). Therefore, regardless of the source, it could be inferred that the fluorescence emission of **1-3** will always be reduced in the presence of TNP in environmental sample.

Table VI.8. Determination of TNP concentration and corresponding recovery from river water sample.

water sample	probes	added in $\mu\text{M}$	found in $\mu\text{M}$	recovery (%)
river water	<b>1</b>	1	0.98	98
		4	3.76	94
	<b>2</b>	1	0.0958	95.8
		4	3.643	91
	<b>3</b>	1	0.976	97.6
		4	3.812	95.3

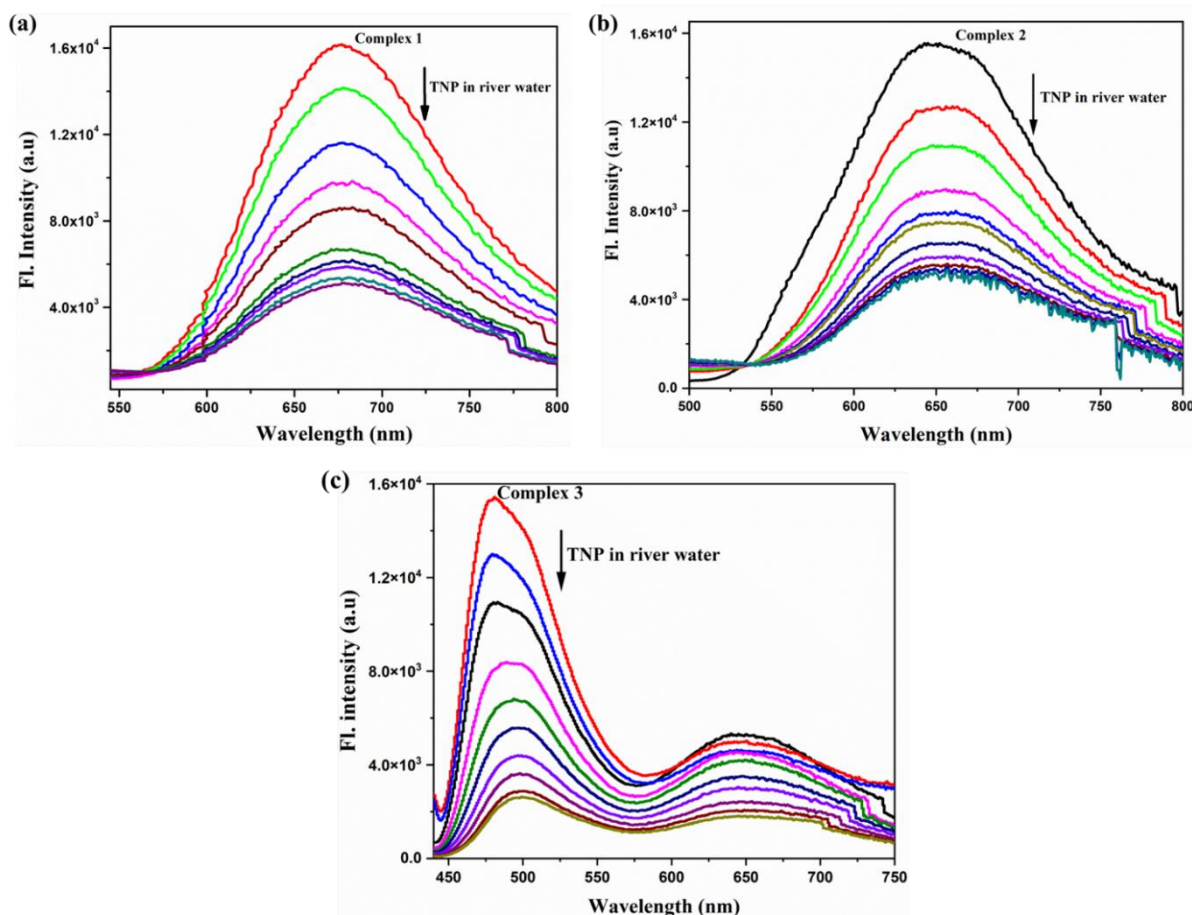


Figure VI.26. Fluorescence spectral titration of the complexes (a) **1**, (b) **2** and (c) **3** with the incremental addition of TNP in river water.

#### VI.4. Conclusions

In summary, we have fabricated three new binuclear chloro-bridged heavy metal complexes (**1**, **2** and **3**) and characterized thoroughly. Single crystal X-ray diffraction study showed that **HL** was a bidentate ligand (N N donor) and structure of the complexes was similar in fashion. The emission study showed the inherent fluorescence of the complexes which instigated us in detecting explosives nitro-compounds (NACs). From the fluorescence titration spectra and calculated  $K_{SV}$  and LOD value, 2,4,6-trinitrophenol (TNP) showed a great quenching efficacy among other nitro-compounds in acetonitrile solution which was well explained by PET-RET mechanistic paths and the order of quenching percentage of the fluorophore was  $\mathbf{3} > \mathbf{2} > \mathbf{1}$ . Moreover, quick response in solid state and high recovery of TNP in environmental water sample suggested the reliability and practicability of the metal fluorophores.

## VI.5. References

1. I. A. Riddell, Y. R. Hristova, J. K. Clegg, C. S. Wood, B. Breiner and J. R. Nitschke, *J. Am. Chem. Soc.*, 2013, **135**, 2723-2733.
2. B. M. Ahmed and G. Mezei, *Chem. Commun.*, 2017, **53**, 1029-1032.
3. P. Mahapatra, M. G. B. Drew and A. Ghosh, *Cryst. Growth Des.*, 2017, **17**, 6809-6820.
4. J. A. Sheikh, H. S. Jena, A. Clearfield and S. Konar, *Acc. Chem. Res.*, 2016, **49**, 1093-1103.
5. A. N. Părvulescu, G. Marin, K. Suwinska, V. C. Kravtsov, M. Andruh, V. Părvulescu and V. I. Părvulescu, *J. Mater. Chem.*, 2005, **15**, 4234-4240.
6. X. Li, B. L. Wu, C. Y. Niu, Y. Y. Niu and H. Y. Zhang, *Cryst. Growth Des.*, 2009, **9**, 3423-3431.
7. M. Chen, S. S. Chen, T. Okamura, Z. Su, M. S. Chen, Y. Zhao, W. Y. Sun and N. Ueyama, *Cryst. Growth Des.*, 2011, **11**, 1901-1912.
8. L. Botana, J. Ruiz, J. M. Seco, A. J. Mota, A. Rodríguez-Diéguez, R. Sillanpää and E. Colacio, *Dalton Trans.*, 2011, **40**, 12462-12471.
9. Q. W. Xie, S. Q. Wu, C. M. Liu, A. L. Cui and H. Z. Kou, *Dalton Trans.*, 2013, **42**, 11227-11233.
10. Q. W. Xie, S. Q. Wu, W. B. Shi, C. M. Liu, A. L. Cui and H. Z. Kou, *Dalton Trans.*, 2014, **43**, 11309-11316.
11. L. Botana, J. Ruiz, A. J. Mota, A. Rodríguez-Diéguez, J. M. Seco, I. Oyarzabal and E. Colacio, *Dalton Trans.*, 2014, **43**, 13509-13524.
12. S. K. Asthana, A. Kumar, Neeraj, Shweta, S. K. Hira, P. P. Manna and K. K. Upadhyay, *Inorg. Chem.*, 2017, **56**, 3315-3323.
13. P. S. Yao, Z. Liu, J. Z. Ge, Y. Chen and Q. Y. Cao, *Dalton Trans.*, 2015, **44**, 7470-7476.
14. Z. Hu, B. J. Deibert and J. Li, *Chem. Soc. Rev.*, 2014, **43**, 5815-5840.
15. P. A. Gale and C. Caltagirone, *Chem. Soc. Rev.*, 2015, **44**, 4212-4227.
16. B. Chen, L. Wang, F. Zapata, G. Qian and E. B. Lobkovsky, *J. Am. Chem. Soc.*, 2008, **130**, 6718-6719.
17. T. Moradpour, A. Abbasi and K. Van Hecke, *J. Solid State Chem.*, 2015, **228**, 36-41.
18. Z. Hu, B. J. Deibert and J. Li, *Chem. Soc. Rev.*, 2014, **43**, 5815-5840.
19. D. Wang, L. Zhang, G. Li, Q. Huo and Y. Liu, *RSC Adv.*, 2015, **5**, 18087-18091.
20. K. Acharyya and P. S. Mukherjee, *Chem. Commun.*, 2014, **50**, 15788-15791.
21. A. N. Gusev, M. A. Kiskin, E. V. Braga, M. A. Kryukova, G. V. Baryshnikov, N. N. Karaush-Karmazin, V. A. Minaeva, B. F. Minaev, K. Ivaniuk, P. Stakhira, H. Ågren and W. Linert, *ACS Appl. Electron. Mater.*, 2021, **3**, 3436-3444.
22. I. P. Oliveri, S. Failla, A. Colombo, C. Dragonetti, S. Righetto and S. D. Bella, *Dalton Trans.*, 2014, **43**, 2168-2175.

23. J. M. Berg and Y. Shi, *Science*, 1996, **271**, 1081–1085.
24. B. L. Vallee and K. H. Falchuk, *Physiol. Rev.*, 1993, **73**, 79–105.
25. N. Behera and V. Manivannan, *J. Photochem. Photobiol. A*, 2018, **353**, 77–85.
26. X. Liu, P. Wang, J. Fu, K. Yao, K. Xue and K. Xu, *J. Lumin.*, 2017, **186**, 16–22.
27. P. S. Yao, Z. Liu, J. Z. Ge, Y. Chen and Q. Y. Cao, *Dalton Trans.*, 2015, **44**, 7470–7476.
28. R. Singh, A. Gogoi and G. Das, *RSC Adv.*, 2016, **6**, 112246–112252.
29. A. Sarkar, A. Chakraborty, T. Chakraborty, S. Purkait, D. Samanta, S. Maity and D. Das, *Inorg. Chem.*, 2020, **59**, 9014–9028.
30. Y. Rachuri, B. Parmar, K. K. Bisht and E. Suresh, *Cryst. Growth Des.*, 2017, **17**, 1363–1372.
31. F. Qian, C. Zhang, Y. Zhang, W. He, X. Gao, P. Hu and Z. Guo, *J. Am. Chem. Soc.*, 2009, **131**, 1460–1468.
32. J. Li, X. Luo, Y. Zhou, L. Zhang, Q. Huo and Y. Liu, *Cryst. Growth Des.*, 2018, **18**, 1857–1863.
33. L. Li, S. Zhang, L. Xu, L. Han, Z. -N. Chen and J. Luo, *Inorg. Chem.*, 2013, **52**, 12323–12325.
34. S. Senthilkumar, R. Goswami, V. J. Smith, H. C. Bajaj and S. Neogi, *ACS Sustainable Chem. Eng.*, 2018, **6**, 10295–10306.
35. J. Tiwari, P. Tarale, S. Sivanesan and A. Bafana, *Environ. Sci. Pollut. Res.*, 2019, **26**, 28650–28667.
36. W. Lu, J. Zhang, Y. Huang, P. Théato, Q. Huang and T. Chen, *ACS Appl. Mater. Interfaces.*, 2017, **9**, 23884–23893.
37. A. Sil, D. Giri and S. K. Patra, *J. Mater. Chem. C*, 2017, **5**, 11100–11110.
38. Y. Salinas, R. Martínez-Máñez, M. D. Marcos, F. Sancenón, A. M. Costero, M. Parra and S. Gil, *Chem. Soc. Rev.*, 2012, **41**, 1261–1296.
39. P. C. Ashbrook and T. A. Houts, *Chem. Health Saf.*, 2003, **10**, 27.
40. J. Zhang and J. M. Shreeve, *J. Am. Chem. Soc.*, 2014, **136**, 4437–4445.
41. S. Xing, Q. Bing, H. Qi, J. Liu, T. Bai, G. Li, Z. Shi, S. Feng and R. Xu, *ACS Appl. Mater. Interfaces*, 2017, **9**, 23828–23835.
42. G. Yuqian, Q. Yuancheng, Z. Kui, W. Qing, S. Jinwen, Q. Liyou and M. Wanzhi, *Sens. Actuators B*, 2018, **257**, 553–560.
43. S. S. Dhankhar, N. Sharma, S. Kumar, T. J. D. Kumar and C. M. Nagaraja, *Chemistry*, 2017, **23**, 16204–16212.
44. X. Yin, S. Meng and J. Xie, *J. Cluster Sci.*, 2018, **29**, 411–416.
45. J. Zhang, J. Wu, L. Gong, J. Feng and C. Zhang, *ChemistrySelect*, 2017, **2**, 7465–7473.
46. Y. Zhang, B. Li, H. Ma, L. Zhang and W. Zhang, *J. Mater. Chem. C*, 2017, **5**, 4661–4669.
47. R. Dalapati and S. Biswas, *Sens. Actuators B*, 2017, **239**, 759–767.
48. X. C. Sun, Y. Wang and Y. Lei, *Chem. Soc. Rev.*, 2015, **44**, 8019–8061.

49. M. M. Alam, A. M. Asiri, M. T. Uddin, M. A. Islam, M. R. Awual and M. M. Rahman, *New J. Chem.*, 2019, **43**, 8651–8659.
50. M. M. Alam, A. M. Asiri, M. T. Uddin, Inamuddin, M. A. Islam, M. R. Awual and M. M. Rahman, *New J. Chem.*, 2019, **43**, 4849–4858.
51. T. A. Sheikh, M. M. Rahman, A. M. Asiri, H. M. Marwani and M. R. Awual, *J. Ind. Eng. Chem.*, 2018, **66**, 446–455.
52. J. Zhang, J. Wu, G. Tang, J. Feng, F. Luo, B. Xu and C. Zhang, *Sens. Actuators B*, 2018, **272**, 166–174.
53. S. S. Nagarkar, B. Joarder, A. K. Chaudhari, S. Mukherjee and S. K. Ghosh, *Angew. Chem., Int. Ed.*, 2013, **125**, 2953–2957.
54. S. -R. Zhang, J. Li, D. -Y. Du, J. -S. Qin, S. -L. Li, W. -W. He, Z. -M. Su and Y. -Q. Lan, *J. Mater. Chem. A*, 2015, **3**, 23426–23434.
55. R. M. Kamel, A. Shahat, W. H. Hegazy, E. M. Khodier and M. R. Awual, *J. Mol. Liq.*, 2019, **285**, 20–26.
56. M. M. Rahman, M. M. Hussain, M. N. Arshad, M. R. Awual and A. M. Asiri, *New J. Chem.*, 2019, **43**, 9066–9075.
57. M. R. Awual, *Chem. Eng. J.*, 2015, **266**, 368–375.
58. K. T. Kubra, M. S. Salman, M. N. Hasan, A. Islam, M. M. Hasan and M. R. Awual, *J. Mol. Liq.*, 2021, **336**, 116325–116335.
59. S. Sanda, S. Parshamoni, S. Biswas and S. Konar, *Chem. Commun.*, 2015, **51**, 6576–6579.
60. V. Bhalla, S. Kaur, V. Vij and M. Kumar, *Inorg. Chem.*, 2013, **52**, 4860–4865.
61. S. Dey, A. Maity, M. Shyamal, D. Das, S. Maity, P. K. Giri, N. Mudi, S. S. Samanta, P. Hazra and A. Misra, *Photochem. Photobiol. Sci.*, 2019, **18**, 2717–2729.
62. Z. Hu, B. J. Deibert and J. Li, *Chem. Soc. Rev.*, 2014, **43**, 5815–5840.
63. X. Liu, Y. Xu and D. Jiang, *J. Am. Chem. Soc.*, 2012, **134**, 8738–8741.
64. A. A. Tehrani, L. Esrafil, S. Abedi, A. Morsali, L. Carlucci, D. M. Proserpio, J. Wang, P. C. Junk and T. Liu, *Inorg. Chem.*, 2017, **56**, 1446–1454.
65. W. Liu, H. -l. Cui, J. Zhou, Z. -t. Su, Y. -z. Zhang, X. -l. Chen and E. -l. Yue, *ACS Omega*, 2023, **8**, 24635–24643.
66. M. Raizada, F. Sama, M. Ashafaq, M. Shahid, M. Ahmad and Z. A. Siddiqi, *J. Mater. Chem. C*, 2017, **5**, 9315–9330.
67. J. Sahoo, S. B. Waghmode, P. S. Subramanian and M. Albrecht, *ChemistrySelect*, 2016, **1**, 1943–1948.
68. B. Dutta, A. Hazra, S. Datta, C. Sinha, P. Banerjee and M. H. Mir, *ACS Appl. Polym. Mater.*, 2022, **4**, 2841–2850.
69. S. Khan, A. Hazra, B. Dutta, Akhtaruzzaman, M. J. Raihan, P. Banerjee, M. H. Mir, *Cryst. Growth Des.*, 2021, **21**, 3344–3354.



70. P. Ghorai, A. Dey, A. Hazra, B. Dutta, P. Brandão, P. P. Ray, P. Banerjee, A. Saha, *Cryst. Growth Des.*, 2019, **19**, 6431-6447.
71. S. Tripathi, D. Bardhan and K. D. Chand, *Inorg. Chem.*, 2018, **57**, 11369–11381.
72. P. Ghorai, A. Hazra, J. Mandal, S. Malik, P. Brandão, P. Banerjee and A. Saha, *Inorg. Chem.*, 2023, **62**, 98–113.
73. B. Bera, S. Mondal, S. Gharami, R. Naskar, K. Das Saha and T. K. Mondal, *New J. Chem.*, 2022, **46**, 11277-11285.
74. Bruker. SAINT v8.38A. Bruker AXS Inc., Madison, Wisconsin, USA
75. L. Krause, R. Herbst-Irmer, G. M. Sheldrick and D. Stalke, *J. Appl. Crystallogr.*, 2015, **48**, 3–10.
76. (a) G. M. Sheldrick, *Acta Crystallogr. A*, 2008, **64**, 112-122; (b) G. M. Sheldrick, *Acta Crystallogr. C*, 2015, **71**, 3–8.
77. (a) A. D. Becke, *J. Chem. Phys.*, 1993, **98**, 5648; (b) C. Lee, W. Yang and R. G. Parr, *Phys. Rev. B: Condens. Matter Mater. Phys.*, 1988, **37**, 785.
78. M. J. Frisch, G. W. Trucks, H. B. Schlegel, G. E. Scuseria, M. A. Robb, J. R. Cheeseman, G. Scalmani, V. Barone, B. Mennucci, G. A. Petersson, H. Nakatsuji, M. Caricato, X. Li, H. P. Hratchian, A. F. Izmaylov, J. Bloino, G. Zheng, J. L. Sonnenberg, M. Hada, M. Ehara, K. Toyota, R. Fukuda, J. Hasegawa, M. Ishida, T. Nakajima, Y. Honda, O. Kitao, H. Nakai, T. Vreven, J. A. Montgomery, Jr., J. E. Peralta, F. Ogliaro, M. Bearpark, J. J. Heyd, E. Brothers, K. N. Kudin, V. N. Staroverov, R. Kobayashi, J. Normand, K. Raghavachari, A. Rendell, J. C. Burant, S. S. Iyengar, J. Tomasi, M. Cossi, N. Rega, J. M. Millam, M. Klene, J. E. Knox, J. B. Cross, V. Bakken, C. Adamo, J. Jaramillo, R. Gomperts, R. E. Stratmann, O. Yazyev, A. J. Austin, R. Cammi, C. Pomelli, J. W. Ochterski, R. L. Martin, K. Morokuma, V. G. Zakrzewski, G. A. Voth, P. Salvador, J. J. Dannenberg, S. Dapprich, A. D. Daniels, O. Farkas, J. B. Foresman, J. V. Ortiz, J. Cioslowski and D. J. Fox, Gaussian 09, Revision D.01, Gaussian, Inc., Wallingford CT, 2009.
79. (a) P. J. Hay and W. R. Wadt, *J. Chem. Phys.*, 1985, **82**, 270; (b) W. R. Wadt and P. J. Hay, *J. Chem. Phys.*, 1985, **82**, 284; (c) P. J. Hay and W. R. Wadt, *J. Chem. Phys.*, 1985, **82**, 299.
80. (a) R. Bauernschmitt and R. Ahlrichs, *Chem. Phys. Lett.*, 1996, **256**, 454; (b) R. E. Stratmann, G. E. Scuseria and M. J. Frisch, *J. Chem. Phys.*, 1998, **109**, 8218; (c) M. E. Casida, C. Jamorski, K. C. Casida and D. R. Salahub, *J. Chem. Phys.*, 1998, **108**, 4439.
81. (a) V. Barone and M. Cossi, *J. Phys. Chem. A*, 1998, **102**, 1995; (b) M. Cossi and V. Barone, *J. Chem. Phys.*, 2001, **115**, 4708; (c) M. Cossi, N. Rega, G. Scalmani and V. Barone, *J. Comput. Chem.*, 2003, **24**, 669.
82. N. M. O'Boyle, A. L. Tenderholt and K. M. Langner, *J. Comput. Chem.*, 2008, **29**, 839.
83. A. W. Addison, T. N. Rao, J. Reedijk, J. van Rijn and G. C. Verschoor, *J. Chem. Soc., Dalton Trans.*, 1984, 1349–1356.

84. M. Zeng, Z. -Y. Zhou, X. -R. Wu, C. -M. Liu and H. -Z. Kou, *Inorg. Chem.*, 2022, **61**, 14275–14281.
85. C. Wang, G. Zeng, Z. -X. You, Y. -H. Xing, F. -Y. Bai and L. -X. Sun, *Inorg. Chem.*, 2022, **61**, 10066–10078
86. W. Liu, J. Qiao, J. Gu and Y. Liu, *Inorg. Chem.*, 2023, **62**, 1272–1278.
87. Y. Hu, M. Ding, X. -Q. Liu, L. -B. Sun and H. -L. Jiang, *Chem. Commun.*, 2016, **52**, 5734–5737.
88. S. Tripathi, D. Bardhan and K. D. Chand, *Inorg. Chem.*, 2018, **57**, 11369–11381.
89. A. Das, S. Jana and A. Ghosh, *Cryst. Growth Des.*, 2018, **18**, 2335–2348.
90. X. X. Wu, H. R. Fu, M. L. Han, Z. Zhou and L. F. Ma, *Cryst. Growth Des.*, 2017, **17**, 6041–6048.
91. X. G. Yang, Z. M. Zhai, X. M. Lu, Y. Zhao, X. H. Chang and L. F. Ma, *Dalton Trans.*, 2019, **48**, 10785–10789.
92. S. Bhattacharjee, S. Bera, R. Das, D. Chakraborty, A. Basu, P. Banerjee, S. Ghosh and A. Bhaumik, *ACS Appl. Mater. Interfaces*, 2022, **14**, 20907–20918.
93. S. S. Nagarkar, A. V. Desai and S. K. Ghosh, *CrystEngComm*, 2016, **18**, 2994–3007.





**LIST OF PUBLICATIONS**

1. Palladium(II) and platinum(II) complexes with ONN donor pincer ligand: Synthesis, characterization and *in vitro* cytotoxicity study.  
**Biswajit Bera**, Sanchaita Mondal, Saswati Gharami, Rahul Naskar, Krishna Das Saha\* and Tapan K. Mondal\*, *New J. Chem.*, 2022, **46**, 11277-11285.
2. New palladium(II) and platinum(II) complexes with coumarin based O,N,N pincer: Synthesis, structure elucidation, BSA protein binding studies and anticancer activity.  
**Biswajit Bera**, Sanchaita Mondal, Subrata Mandal, Krishna Das Saha\* and Tapan K. Mondal\*, *Appl. Organomet. Chem.*, 2023, **37**, e7185.
3. Heavy metal based binuclear luminescent complexes for selective and swift sensing of nitro-explosives in solution and solid phase.  
**Biswajit Bera**, Subrata Mandal, Saswati Gharami and Tapan Kumar Mondal\*, *Cryst. Growth Des.*, 2023, **23**, 6631–6640.
4. Efficient solid and solution state emissive reusable solvatochromic fluorophore for colorimetric and fluorometric detection of CN<sup>−</sup>.  
Atanu Maji, Amitav Biswas, Krishnendu Aich, Saswati Gharami, **Biswajit Bera** and Tapan Kumar Mondal\*, *Analyst*, 2024, Accepted Manuscript.
5. A chemodosimetric approach for the visual detection of nerve agent simulant diethyl chlorophosphate (DCP) in liquid and vapour phase.  
Atanu Maji, Amitav Biswas, **Biswajit Bera** and Tapan Kumar Mondal\*, *Anal. Methods*, 2023, **15**, 6417–6424.
6. Facile synthesis of novel NNO-tethered copper(II) complexes: characterization details, theoretical studies, promising enzyme-like activities, and biomolecular interactions.  
Subrata Mandal, Rahul Naskar, Apurba Sau Mondal, **Biswajit Bera** and Tapan K. Mondal\*, *Dalton Trans.*, 2023, **52**, 5983–5998.
7. A new palladium(II) phosphino complex with ONS donor Schiff base ligand: Synthesis, characterization and catalytic activity towards Suzuki-Miyaura cross-coupling reaction.  
Chandan Kumar Manna, Rahul Naskar, **Biswajit Bera**, Akash Das, Tapan Kumar Mondal\*, *J. Mol. Struct.*, 2021, **1237**, 130322.



Cite this: DOI: 10.1039/d2nj01894b

# Palladium(II) and platinum(II) complexes with ONN donor pincer ligand: synthesis, characterization and *in vitro* cytotoxicity study†

Biswajit Bera,<sup>a</sup> Sanchaita Mondal,<sup>b</sup> Saswati Gharami,<sup>a</sup> Rahul Naskar,<sup>a</sup> Krishna Das Saha <sup>\*b</sup> and Tapan K. Mondal <sup>\*a</sup>

New Pd(II) and Pt(II) complexes, [Pd(HL)Cl<sub>2</sub>] (**C1**) and [Pt(L)Cl] (**C2**) with ONN donor pincer ligand, 5-(diethylamino)-2-((Z)-((E)-(phenyl(pyridin-2-yl)methylene)hydrazono)methyl)phenol (HL) were synthesized and thoroughly characterized using spectroscopic techniques. X-ray structures of the complexes revealed that HL acts as bidentate *N,N* and tridentate *O,N,N* chelator in Pd(II) and Pt(II) complexes, respectively. The antiproliferative activity of the complexes was explored against four different human cancer (MCF-7, HCT116, A549, HepG2) cell lines. However, the maximum cytotoxicity was seen in the HepG2 cell line [IC<sub>50</sub> = 6–12 μM] for both the complexes. IC<sub>50</sub> for both complexes, **C1** and **C2**, toward human peripheral blood mononuclear cells (hPBMC) cells were found to be >200 μM. The cytotoxicity of platinum complex (**C2**) was comparable to that of the cisplatin in HepG2 cell lines.

Received 17th April 2022,  
Accepted 11th May 2022

DOI: 10.1039/d2nj01894b

rsc.li/njc

## Introduction

According to the WHO, cancer is the second major reason for death worldwide.<sup>1</sup> Therefore any new effective anticancer agents with nominal side effects remain of crucial significance to the world research society.<sup>2–4</sup> The advancement of drug resistance and disease relapse are the foremost challenges in anticancer drug design.<sup>5</sup> Metals have always been handy in dealing with a variety of illnesses found globally.<sup>6</sup> Owing to their exclusive nature, metal complexes, particularly those consisting of transition metals have achieved remarkable consideration as anticancer agents.<sup>7</sup> Transition metal complexes as antitumor agents have been broadly utilized after *cis*-platin proved to be as successful as an anti-cancer drug. Lately, *cis*-platin has been recognized as one of the most extensively used antitumor drugs in the world due to its high effectiveness for testicular and ovarian cancers and in the treatment of cervical, bladder and many other varieties of carcinoma.<sup>8</sup> Nevertheless, regardless of the positive outcomes of platinum compounds in destroying cancer cells, they also have lethal side effects which include nausea, vomiting, lessening of blood cell

and platelet production in bone marrow thereby affecting response to infection.<sup>9</sup> Hence to prevail over these drawbacks, numerous platinum complexes were designed and fabricated and examined for their anticancer activities.<sup>10–12</sup> The cytotoxic properties of these Pt(II) complexes were evaluated with respect to cell growth inhibition against different types of human cancer cell lines.

On the other hand, other than the platinum compounds, the palladium(II) compounds are the ones that are being used for cancer treatment as palladium(II) derivatives have antitumor activity similar to the *cis*-platin drug and they also show a lesser amount of kidney toxicity.<sup>13–15</sup> Thus, the development of new palladium-based anti-cancer drugs is very crucial for effective and efficient use as chemotherapeutic agents. Thus far, significant importance has been given to studying Pd(II) complexes as anticancer drugs,<sup>16–20</sup> among all other metal ions owing to their much resemblance with Pt(II). Although one obstacle to these Pd-based anticancer drugs is that the ligand exchange and aquation rates of Pd(II) complexes are about 105 times faster than that of the Pt(II) analogues.<sup>21</sup> Thus, palladium could prevent the interaction with the target DNA by associating with the other donor groups present in the bloodstream, thereby enhancing their toxicity and diminishing their beneficial potential. Hence, an appropriate choice of ligands is vital in order to fabricate better and more competitive palladium, complex-based anticancer agents.<sup>15</sup> Additionally, the palladium compounds have improved solubilities compared to Pt(II) analogues generally. Recent studies revealed that numerous Pd(II) compounds demonstrated a vastly proficient biological

<sup>a</sup> Department of Chemistry, Jadavpur University, Kolkata-700032, India.  
E-mail: [tapank.mondal@jadavpuruniversity.in](mailto:tapank.mondal@jadavpuruniversity.in)

<sup>b</sup> Cancer Biology & Inflammatory Disorder Division, CSIR-Indian Institute of Chemical Biology, Kolkata-700 032, India. E-mail: [krishna@iicb.res.in](mailto:krishna@iicb.res.in)

† Electronic supplementary information (ESI) available: NMR, IR and MS of all new compounds, X-ray structure analysis, DFT calculation etc. CCDC 2123838 and 2123839. For ESI and crystallographic data in CIF or other electronic format see DOI: <https://doi.org/10.1039/d2nj01894b>

## RESEARCH ARTICLE

# New palladium (II) and platinum (II) complexes with coumarin based O,N,N pincer: Synthesis, structure elucidation, BSA protein binding studies, and anticancer activity

Biswajit Bera<sup>1</sup>  | Sanchaita Mondal<sup>2</sup>  | Subrata Mandal<sup>1</sup>  |  
Krishna Das Saha<sup>2</sup>  | Tapan K. Mondal<sup>1</sup> 

<sup>1</sup>Department of Chemistry, Jadavpur University, Kolkata, India

<sup>2</sup>Cancer Biology and Inflammatory Disorder Division, CSIR-Indian Institute of Chemical Biology, Kolkata, India

## Correspondence

Tapan K. Mondal, Department of Chemistry, Jadavpur University, Kolkata 700032, India.

Email: [tapank.mondal@jadavpuruniversity.in](mailto:tapank.mondal@jadavpuruniversity.in)

Krishna Das Saha, Cancer Biology and Inflammatory Disorder Division, CSIR-Indian Institute of Chemical Biology, Kolkata 700032, India.

Email: [krishna@iicb.res.in](mailto:krishna@iicb.res.in)

## Funding information

Science and Engineering Research Board, Grant/Award Number: EEQ/2018/000226; Council of Scientific and Industrial Research, Grant/Award Number: 09/096 (0995)/2019-EMR-1

New Pd (II) and Pt (II) complexes (**C1/C2**) with a O,N,N donor pincer ligand, 4-hydroxy-3-((*E*)-1-(((*Z*)-phenyl (pyridin-2-yl)methylene)hydrazono)ethyl)-2H-chromen-2-one (**HL**) were synthesized and methodically characterized by several spectroscopic and XRD techniques. Absorption and fluorescence techniques were used to assess the mechanism of interaction of the complexes with bovine serum albumin protein. MTT assay was executed to investigate the antiproliferative activity of the complexes with several cancer cell lines (MCF-7, HCT116, A549, and HepG2) along with a normal cell line (PBMC). Both **C1** and **C2** showed better antiproliferative activity with HepG2 cell line (IC<sub>50</sub> value of 15.3 and 5.1 μM, respectively). A cytotoxicity study was performed, and complex **C2** exhibited a better antiproliferative activity as compared to **C1**. The morphological changes were also examined by staining methods, and fragmented DNA unveiled that the cell death took place through apoptosis.

## KEYWORDS

antiproliferative activity, BSA interaction study, computational study, synthesis, X-ray structure

## 1 | INTRODUCTION

Unquestionably, one of the most important health problems that modern society faces is cancer, which is a key focus in the field of medicinal chemistry. Therefore, every new and effective anticancer treatment with few side effects stands out as being of utmost significance to the global scientific community.<sup>1–3</sup> The emergence of drug resistance and illness relapse is the fundamental obstacles in the development of anti-cancer medications.<sup>4</sup> Metals have constantly been utilized to take care of an

array of disorders around the world.<sup>5</sup> Due to their elite nature, anticancer activity of transition metal complexes is comprehensively explored.<sup>6</sup> Following the incredibly successful adoption of cisplatin as an anti-cancer therapy in 1965, these transition metal complexes are widely used as antitumor medicine.<sup>7,8</sup> Due to its superior efficacy, particularly in the treatment of cervical, ovarian, bladder, metastatic testicular, and several other types of cancers, cisplatin has recently been recognized as one of the most extensively and exclusively utilized anticancer drug in the globe along with the more effectual and less fatal

## Heavy Metal-Based Binuclear Luminescent Complexes for Selective and Swift Sensing of Nitro-Explosives in Solution and Solid Phases

Biswajit Bera, Subrata Mandal, Saswati Gharami, and Tapan Kumar Mondal\*

Cite This: *Cryst. Growth Des.* 2023, 23, 6631–6640

Read Online

ACCESS |



Metrics &amp; More

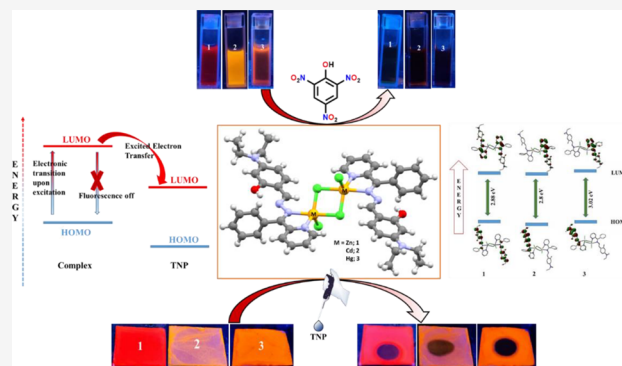


Article Recommendations



Supporting Information

**ABSTRACT:** Discerning the detection of 2,4,6-trinitrophenol (TNP)-like mutagenic pollutants and other nitroaromatic-based explosives (NACs) using robust luminescent metal complexes has been always a potential research field. Herein, we report the synthesis of three novel luminescent chloro-bridged heavy metal complexes of formulation  $[M_2(HL)_2Cl_4]$  where M stands for  $Zn^{2+}$ ,  $Cd^{2+}$ , and  $Hg^{2+}$  for complexes 1, 2, and 3, respectively, by refluxing the mixture of ligand HL and metal chloride salts. Single-crystal X-ray study, spectroscopic ( $^1H$  NMR, FT-IR, UV-vis, and emission spectroscopy) techniques, DFT, and TDDFT calculations have all been used to fully characterize the complexes. All the three complexes exhibit excellent fluorescence responses which get quenched in the presence of different NACs. Interestingly, the fluoroprobes (1–3) are more selective and sensitive toward TNP over several other comparative NACs with high (in the order of  $\sim 10^4 M^{-1}$ ) quenching constants ( $K_{SV}$ ) and nanomolar detection limit (LOD), and complex-coated TLC plates were used to detect TNP in the solid state. Moreover, our probes were quite sensitive for the trace detection of TNP in real samples. Among the three, complex 3 is the most efficacious with  $K_{SV}$   $(5.19 \pm 0.12) \times 10^4 M^{-1}$  and LOD of 180.2 nM.  $^1H$  NMR and fluorescence lifetime titration of probes with TNP shed light on the nature of the interaction (dynamic quenching) of probes with TNP. In addition, DFT and UV-vis absorption of probes with TNP proved that the quenching phenomenon could be primarily ascribed to photo-induced electron transfer (PET) and resonance energy transfer (RET).



## ■ INTRODUCTION

The lucid design and fabrication of distinct multinuclear metal complexes have attracted significant attention due to their structural variety, remarkable magnetic properties, and probable applications in the fields of luminescence, catalysis, gas adsorption, and functional materials.<sup>1–7</sup> There are some reports of heterometallic and homometallic complexes of  $Ni^{2+}$ ,  $Zn^{2+}$ ,  $Co^{2+}$ , and  $Cu^{2+}$  in the literature.<sup>8–11</sup> These complexes have been designed mostly to explore their magnetic properties. This field of research involving multinuclear metal complexes still remains uncultivated. Lately, numerous research groups have been occupied with the precise design and fabrication of chemosensors for the distinct recognition of metal ions, anions, a range of toxic organic analytes, and explosive compounds due to their major impact on the environment as well as on human life.<sup>12–19</sup> Zinc(II) Schiff base complexes have been explored by inorganic chemists for an elongated time period owing to their effortlessness in synthetic schemes and remarkable coordination of zinc. Another good advantage of these zinc Schiff base complexes is that they exhibit excellent fluorescent properties which are utilized in a number of fluorescence-based applications.<sup>20,21</sup> Among numerous metal ions,  $Zn^{2+}$  is the second most significant metal ion after iron in the human body.<sup>22,23</sup> On the other

hand, cadmium is a nonessential substance for the organisms and is even classified as a human carcinogen.<sup>24</sup> Several fluorescence chemosensors for  $Zn^{2+}$  and  $Cd^{2+}$  ions have been published in the literature to date, and amid them, turn-on fluorescent sensors have secured a hugely advantageous position in the field of molecular recognition and in sensing different analytes.<sup>13,25,26</sup> Now among them, zinc(II) Schiff base complexes have been found mainly to be used as chemosensors for the detection of nitroaromatics by diverse research groups.<sup>27–29</sup>

The effectual recognition of nitroaromatic-based explosives (NACs) and dangerous metal ions has achieved a lot of attention in the present time owing to the threat toward security and human wellbeing.<sup>30–32</sup> NACs are nonbiodegradable lethal pollutants that are in deliberate use in separate industries such as dye industry, pharma industry, etc.<sup>33</sup> NACs

Received: May 5, 2023

Revised: July 24, 2023

Published: August 4, 2023



## PAPER

[View Article Online](#)  
[View Journal](#)

Cite this: DOI: 10.1039/d3an01697h

# Efficient solid- and solution-state emissive reusable solvatochromic fluorophores for colorimetric and fluorometric detection of $\text{CN}^-$ †

Atanu Maji, Krishnendu Aich,  Amitav Biswas, Saswati Gharami, Biswajit Bera and Tapan K. Mondal  \*

In this work, a novel organic receptor, CPI [(*E*)-3-(4-(9*H*-carbazol-9-yl)phenyl)-2-(1*H*-benzo[*d*]imidazol-2-yl)acrylonitrile], was rationally designed and successfully fabricated for selective and sole recognition of  $\text{CN}^-$  ions over other competitive anions through an obvious chromogenic and ratiometric emission change in DMSO. The distinct and prominent color change upon the addition of  $\text{CN}^-$  can be attributed to the typical ICT process, which is induced by the deprotonation of acidic NH protons in the imidazole moiety. The sensor displayed strong solvatochromic effects in commonly used organic solvents such as *n*-hexane, toluene, diethyl ether, DCM, THF, DMF and DMSO. The chemical structure of the sensor was characterized by single-crystal X-ray diffraction,  $^1\text{H}$ NMR,  $^{13}\text{C}$ NMR, IR and mass spectroscopy. Significantly, the probe can function as a fluorescence-based sensor for the efficient detection of low-level water in organic solvents. The solid-state emission properties of CPI were successfully applied to recognise cyanide in a solid-state platform with naked eye-visualized distinct color change. The probe can be made reusable by adding TFA into the  $\text{CN}^-$  treated probe solution. The detection limit of CPI towards  $\text{CN}^-$  was determined to be  $4.48 \times 10^{-8}$  M. More importantly, the sensor is capable of detecting  $\text{CN}^-$  in food samples and has been employed for wastewater treatment. Besides, easy-to-prepare CPI-coated test strips provide a simple, reusable and easy-to-handle protocol for the qualitative identification of  $\text{CN}^-$  conveniently. Finally, density functional theory and time-dependent density functional theory were performed to verify the experimental outcomes theoretically.

Received 5th October 2023,  
Accepted 13th January 2024

DOI: 10.1039/d3an01697h

[rsc.li/analyst](https://rsc.li/analyst)

## Introduction

Many researchers have recently paid attention to the development of anionic chemosensors due to their broad application in many fields including chemical, biological, medical and technological processes.<sup>1–6</sup> Among various anions, cyanide ion is one of the deadliest poisonous anions towards human beings. Even trace amounts of  $\text{CN}^-$  ions can affect human health in many ways, and it may lead to several health risks because of their excellent binding affinity towards  $\text{Fe}^{3+}$  ions in cytochrome c oxidase, eventually leading to the incapability to produce ATP in cells, which subsequently results in respiratory arrest and ultimately death.<sup>7–10</sup> Some insects and food samples such as sprouting potatoes, bitter almonds, apple seeds as well as cassava contain cyanide, and it reaches to the

environment through the hydrolysis process of cyanogenic glycosides.<sup>11–14</sup> Despite its toxicity, cyanide has been extensively used in many industrial production such as petrochemicals, electroplating, steel production, photography, metallurgy, gold mining, and synthesis of resins and fibres due to its critical role in multi-functional reactions.<sup>15</sup> Therefore, water pollution and food safety issues by toxic cyanide pose a serious threat to human health and environment nowadays.<sup>16–18</sup> The maximum intake of  $\text{CN}^-$  ions as per the guidelines approved by WHO and USEPA is 1.9  $\mu\text{M}$  (200  $\mu\text{g L}^{-1}$ ).<sup>19</sup> In view of its vital role in industries and toxicity, the development of a new method to monitor trace amounts of  $\text{CN}^-$  ions in biological and environmental samples is one of the most sensitive hotspots among researchers. In the past few decades, numerous types of chemosensors based on coordination,<sup>20–22</sup> the Sonogashira cross-coupling,<sup>23–25</sup> nucleophilic addition reaction,<sup>26,27</sup> hydrogen-bonding interactions<sup>28,29</sup> and many other mechanisms have been reported for the sole detection of poisonous cyanide. However, these methods have many limitations such as complicated synthetic steps, poor sensitivity and selectivity, use of sophisti-

Department of Chemistry, Jadavpur University, Kolkata- 700032, India.

E-mail: [tapank.mondal@jadavpuruniversity.in](mailto:tapank.mondal@jadavpuruniversity.in)† Electronic supplementary information (ESI) available: NMR and MS of all new compounds, limit of detection determination, quantum yield calculation. See DOI: <https://doi.org/10.1039/d3an01697h>



## PAPER

View Article Online  
View Journal | View Issue

Cite this: *Anal. Methods*, 2023, 15, 6417

# A chemodosimetric approach for the visual detection of nerve agent simulant diethyl chlorophosphate (DCP) in liquid and vapour phase†

Atanu Maji, Amitav Biswas, Biswajit Bera and Tapan Kumar Mondal \*

In this work, a novel fluorescent ratiometric switch, 8-((6-(1*H*-benzo[d]imidazol-2-yl)pyridin-2-yl)methoxy)quinoline (BIPQ), has been introduced for sensing an organophosphorus (OP) chemical vapor threat, diethyl chlorophosphate (DCP), the low-toxic mimic of the real nerve agent sarin (GB). BIPQ is efficient at detecting DCP in both solution and gaseous phase and has potential practical application with high sensitivity and selectivity. The probe shows significant ratiometric emission in the presence of DCP along with a distinct color change from blue to cyan under UV light. The sensing mechanism of the chemodosimeter is based on the generation of a new adduct, BIPQ–DCP, through a nucleophilic substitution reaction with DCP followed by a ring-closure process to form the final product. The detection limit of BIPQ for DCP was determined to be in the order of  $10^{-8}$  (M) in the liquid state. DFT and TDDFT computational techniques were carried out in order to interpret the electronic properties theoretically.

Received 27th July 2023  
Accepted 31st October 2023

DOI: 10.1039/d3ay01296d

rsc.li/methods

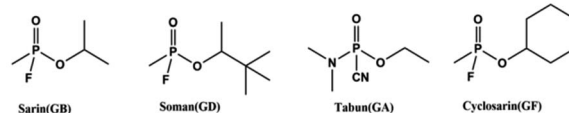
## Introduction

Nowadays organophosphorus compounds are used in preparing many pesticides and herbicides in modern agriculture. Organophosphorus compounds are conceived as one of the most exceptionally hazardous nerve agents and are extremely harmful to the nervous system of every living being if inhaled or ingested through any kind of contamination of food or drink.<sup>1–4</sup> Some known nerve agents including tabun (GA), soman (GD) and sarin (GB) are extremely dangerous organophosphates (Scheme 1), which bear excellent leaving groups owing to which they are known as essential phosphorylating and phosphorylating agents.<sup>5–9</sup> These poisonous chemicals along with their advantages of cheapness, simplicity in manufacture and destructive effects on civilians encourage terrorism. The phosphate group present in these chemicals binds irreversibly with the hydroxyl group present in acetylcholinesterase (AChE), blocks the hydrolysis of acetylcholine neurotransmitters and restrains the decomposition of acetylcholine.<sup>10–13</sup> The excessive storage of acetylcholine causes neuromuscular paralysis, neurological imbalance in the cholinergic synapse, resistance to muscle relaxation, and organ failure, leading to sudden death.<sup>14–20</sup> So they have become a massive threat to all mankind. As most of these compounds are odorless, colorless and tasteless, making them very difficult to detect,<sup>21</sup> it is very urgent to develop a very sensitive, reliable and rapid method for easy and

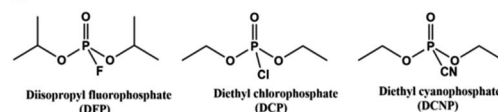
quick detection of these substances in both solution and vapour phase. Our present work is based on the recognition of highly volatile sarin (GB) as it is one of the forbidden CWAs used by terrorists. But due to its too toxic nature and difficult availability, an associated substance, diethyl chlorophosphate (DCP), has been used as a nerve-gas-mimicking agent for experiments because it has a similar chemical structure and comparable reactivity but very low toxicity.

In recent years, many research groups have already introduced a variety of noteworthy tools for detecting nerve-agent-mimicking substances, including colorimetry,<sup>22–24</sup> fluorometry,<sup>25–27</sup> electro-chemistry,<sup>28–30</sup> mass spectrometry,<sup>31–33</sup> interferometry,<sup>34</sup> enzyme-based biosensors,<sup>35–38</sup> surface acoustic wave (SAW) devices,<sup>39,40</sup> enzymatic assays,<sup>41</sup> photoacoustic spectroscopy,<sup>42</sup> PET based probes,<sup>43</sup> ion mobility spectroscopy,<sup>44</sup> cyclization reactions,<sup>45</sup> photonic crystals,<sup>46</sup> nucleophilic substitution reactions,<sup>47,48</sup> lanthanide luminescence,<sup>49</sup> complex

### Nerve agents



### Simulants



**Scheme 1** The structures of chemical warfare agents (CWAs) and their less toxic simulants.

Department of Chemistry, Jadavpur University, Kolkata-700 032, India. E-mail: tapank.mondal@jadavpuruniversity.in

† Electronic supplementary information (ESI) available. See DOI: <https://doi.org/10.1039/d3ay01296d>

## PAPER

[View Article Online](#)  
[View Journal](#) | [View Issue](#)

Cite this: *Dalton Trans.*, 2023, **52**, 5983

# Facile synthesis of novel NNO-tethered copper(II) complexes: characterization details, theoretical studies, promising enzyme-like activities, and biomolecular interactions†

Subrata Mandal, Rahul Naskar, Apurba Sau Mondal, Biswajit Bera and Tapan K. Mondal \*

Given the ubiquitous and multifaceted role of copper ions in various biological processes, we report herein the one-pot facile synthesis, X-ray structure, Hirshfeld surface analysis, enzyme-like activities, and biomolecular interactions of three mononuclear copper(II) complexes, [Cu(L)(X)] (**1–3**) with a tridentate quinoline-based salicylaldimine Schiff base (**LH**) having an N<sub>2</sub>O donor set where X denotes NCS, N<sub>3</sub>, and NO<sub>3</sub> for complexes **1**, **2**, and **3**, respectively. Single-crystal X-ray study, spectroscopic techniques, DFT, and TD-DFT calculations were all used to fully characterize the complexes. The bio-inspired catalytic activities of the synthesized complexes were spectrophotometrically evaluated for the aerial oxidation of 3,5-di-*tert*-butylcatechol (3,5-DTBC) and 2-aminophenol (OAPH) in acetonitrile. The results of ESI mass spectrometry, EPR analysis of the reaction mixture, and DFT computations established that the aforementioned oxidation is metal-mediated and radical-driven, leading us to propose a viable mechanistic scheme. In complex **3**, coordinated nitrate probably confers greater lability, allowing it to be the most effective enzyme for catecholase and phenoxazane-synthase activities. The biological activity of complexes **1–3** and the ligand **LH** towards calf thymus DNA and proteins (bovine serum albumin (BSA)) was explored using absorption and fluorescence spectral titrations, which affirmed that the compounds underwent avid binding with DNA, with high binding affinities ( $K_b$ ) of approximately  $10^4$ – $10^5$  M<sup>−1</sup>. The observed DNA binding constants and viscosity measurement data suggested an intercalative mode of DNA binding with the copper(II) complexes. Spectral evidence also supports the high binding propensity (on the order of approximately  $10^5$  M<sup>−1</sup>) of the complexes with the protein. They actively suppressed the protein's intrinsic fluorescence in a static quenching mode, as further determined by fluorescence lifetime titration of protein with the complexes. Circular dichroism and synchronous spectroscopic experiments supported the protein's conformational alterations mediated by copper(II) complexes (**1–3**) in the micro-environment of the tryptophan residue of the protein. The typical binding distance between BSA and complexes was also computed using fluorescence resonance energy transfer. Of the three complexes (**1–3**), complex **3** stands out as the most efficacious.

Received 30th December 2022,  
Accepted 28th March 2023

DOI: 10.1039/d2dt04170g

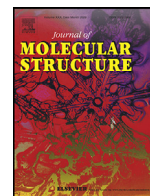
[rsc.li/dalton](https://rsc.li/dalton)

Department of Chemistry, Jadavpur University, Kolkata 700032, India.  
E-mail: [tapank.mondal@jadavpuruniversity.in](mailto:tapank.mondal@jadavpuruniversity.in)

† Electronic supplementary information (ESI) available: Experimental details of synthesis and characterization (FT-IR, UV-Vis, fluorescence, EPR, and ESI-mass spectra) of all new compounds, their X-ray structure and Hirshfeld surface analyses, DFT calculations, plots of DNA/protein binding studies, enzyme-like activities, and mechanistic schemes. CCDC 2233475–2233477 for complexes **1**, **2**, and **3**. For ESI and crystallographic data in CIF or other electronic format see DOI: <https://doi.org/10.1039/d2dt04170g>

## Introduction

The use of molecular oxygen for oxidation of a large variety of organic molecules is beneficial as well as environmentally benevolent<sup>1–3</sup> because it produces no perilous byproducts, and nature provides a bountiful supply of it. Unfortunately, triplet spin in the ground state of molecular oxygen generates kinetic inertness towards such oxidation under ambient conditions. However, in many biochemical reactions,<sup>4–8</sup> metalloenzymes of different transition metals assist the spin-forbidden reaction between dioxygen and organic matter by switching the spin state of molecular oxygen from triplet to singlet. In this regard, copper-containing metalloenzymes are ubiquitous in



# A new palladium(II) phosphino complex with ONS donor Schiff base ligand: Synthesis, characterization and catalytic activity towards Suzuki-Miyaura cross-coupling reaction

Chandan Kumar Manna, Rahul Naskar, Biswajit Bera, Akash Das, Tapan Kumar Mondal\*

Department of Chemistry, Inorganic Chemistry Section, Jadavpur University, Kolkata, 700032, India

## ARTICLE INFO

### Article history:

Received 14 December 2020

Revised 5 March 2021

Accepted 15 March 2021

Available online 26 March 2021

### Keywords:

Palladium(II) phosphino complex

ONS donor Schiff base ligand

X-ray structure

DFT computation

Suzuki-Miyaura cross coupling

## ABSTRACT

New palladium(II) phosphino complex,  $[\text{Pd}(\text{PPh}_3)(\text{L})](\text{ClO}_4)$  (**1**) with thioether containing ONS donor Schiff base ligand (HL) is synthesized by the reaction of HL with sodium tetrachloropalladate ( $\text{Na}_2\text{PdCl}_4$ ) and  $\text{PPh}_3$ . The complex is thoroughly characterized by several spectroscopic techniques. The square planar geometry of the complex is confirmed by single crystal X-ray crystallography. Cyclic voltammetric study in acetonitrile exhibits ligand based irreversible oxidation and reduction peaks at +1.18 V and -1.25 V respectively versus Ag/AgCl reference electrode. Electronic structure and UV-vis spectrum of the complex are interpreted by DFT and TDDFT calculations. Catalytic property of the complex towards Suzuki-Miyaura cross coupling reactions is explored and excellent catalytic conversions (86–97%) are observed with various substituted aryl halides and phenylboronic acid at 100 °C.

© 2021 Elsevier B.V. All rights reserved.

## 1. Introduction

Since the first report of palladium-catalyzed Suzuki-Miyaura C-C cross-coupling reaction in 1979 [1,2], it is used as the most efficient and effective method for the synthesis of a wide variety of biaryl compounds, used in pharmaceutical applications and various chemical industries [3–6]. The efficiency of catalytic cross-coupling reactions is significantly varied with the ligand environment around the palladium center [7–10]. Moreover, palladium(0/II) phosphine complexes are known to be the most efficient catalysts for C-C cross coupling reactions [11–17]. Several palladium(II) triphenylphosphine-Schiff base complexes are also reported to be effective catalysts towards Suzuki-Miyaura cross-coupling reaction [18–20]. Again, the chemistry of transition metal complexes with ONS donor ligand are extensively studied because of their potential use in industrial and synthetic processes such as catalysis, photochemistry, and biological systems [21–25]. So far, several palladium(II) complexes with tridentate ONS donor ligands are synthesized, characterized and explored their catalytic and biological activities [26–28]. Palladium(II) complexes with ONS donor Schiff base ligands are successfully utilized as effective catalyst towards Suzuki-Miyaura cross-coupling reactions [29–33]. Herein,

we report the synthesis of a new palladium(II) triphenylphosphine complex,  $[\text{Pd}(\text{PPh}_3)(\text{L})](\text{ClO}_4)$  (**1**) with ONS based thioether containing Schiff base ligand (HL). Structure of the complex is confirmed by single crystal X-ray diffraction method. Electronic structure and redox properties are interpreted by DFT studies. The complex is proved to be an efficient catalyst in Suzuki-Miyaura cross-coupling reactions of phenyl boronic acid with various aryl halides.

## 2. Experimental

### 2.1. Material and methods

All the reagents and solvents were purchased from commercial sources and were used as received. 3,5-Dichlorosalicylaldehyde, 2-aminothiophenol, triphenyl phosphine and  $\text{Na}_2\text{PdCl}_4$  were purchased from Sigma Aldrich. 2-(Ethylthio)aniline was synthesized following the reported method [34].

Microanalyses (C, H, N) data were obtained using a PerkinElmer Series-II CHN-2400 CHNS/O elemental analyzer. Electronic spectra were measured on a Lambda 750 PerkinElmer spectrophotometer in dichloromethane. IR spectra were recorded on a RX-1 PerkinElmer spectrometer in the range of 4000–400  $\text{cm}^{-1}$  with the samples in the form of KBr pellets. HRMS mass spectra were recorded on a Waters (Xevo G2 Q-TOF) mass spectrometer.  $^1\text{H}$ -NMR spectra were recorded in  $\text{CDCl}_3$  on a Bruker (AC) 300 MHz

\* Corresponding author.

E-mail address: [tapank.mondal@jadavpuruniversity.in](mailto:tapank.mondal@jadavpuruniversity.in) (T.K. Mondal).